CRANFIELD UNIVERSITY

SCHOOL OF MECHANICAL ENGINEERING

PhD THESIS

Academic Year 1996-1999

YIGUANG LI

Three-Dimensional Flow and Performance Simulation of Multistage Axial Flow Compressors

Supervisors: Prof. R. L. Elder
Dr. A. Tourlidakis

March 2000

ABSTRACT

With the current development in computer technology and Computational Fluid Dynamics techniques, the simulation within axial flow compressors becomes more and more practical and beneficial to the compressor designs. Due to the insufficient capability of today's computers for three-dimensional unsteady flow modelling of multistage axial flow compressors, sophisticated models of steady state flow and performance modelling of the compressors deserve to be thoroughly investigated.

In multistage compressor simulations with steady state methods, frame of reference is fixed on blades and the computational domains for rotors and stators have relative rotation. One of the difficulties in such simulations is how to pass information across the interfaces between blade rows without losing continuity. Two major steady state modelling approaches, a mixing plane approach based on Denton's circumferentially non-uniform mixing plane model and a deterministic stress approach based on Adamczyk's average passage model, are investigated and compared with each other through the flow predictions of the third stage of Cranfield Low Speed Research Compressor at peak efficiency operating condition.

In the deterministic stress approach, overlapped solution domains are introduced to calculate deterministic stresses in order to "close" the time-averaged governing equation system and the influence of the downstream blade row of the blade row under investigation has to be imposed through the simulation of bodyforce and blade blockage effect of the downstream blade row. An effective method of simulating bodyforce and blade blockage effect has been developed and proven to be simple in programming.

Conventionally, boundary conditions are specified in CFD calculations based on experimental data or other empirical calculations. By taking advantage of the special flow features in rear stages of multistage axial flow compressors where each rear stage behaves like a repeating stage of its neighbouring stages in terms of flow pattern at the inlet and the exit of these stages, a repeating stage model has been developed aiming at significantly simplifying the boundary conditions when simulating rear stages of a multistage axial flow compressor with only mass flow rate and stage exit average static pressure required as global input.

A computer simulation system *MSTurbo3D* has been developed to investigate and assess different steady state simulation models within multistage compressor environment. It has been proven that with the mixing plane model *MSTurbo3D* is able to predict flows in multistage low speed axial flow compressors with acceptable accuracy. Application of the repeating stage model to the third stage of *LSRC* shows that the prediction with this model has equivalent accuracy to the prediction with the conventional boundary setting, and proves that the repeating stage model is an effective alternative to the expensive complete compressor simulation. The deterministic stress model provides more information of rotor-stator interaction and slightly better performance prediction than the mixing plane model, but the benefits of the model is not significant when applied to low speed axial flow compressors.

Acknowledgements

The course of this doctoral study was financially supported by the Overseas Research Students Awards Scheme (*ORS*) organized by the Comittee of Vice-Chancellors and Principals of the Universities of the United Kingdom and the department grant of Cranfield University.

The author is greatly indebted to Professor R. L. Elder for his continuous guidance and support throughout the research, and to Dr. A. Tourlidakis for his technical advice and proof-reading of this thesis. Their invaluable advice and supervision are extremely appreciated. Acknowledgement also to the Laboratory of Thermal Turbomachines of the National Technical University of Athens for their kind permission to use *ELISA* code at the initial phase of the project.

I would also like to acknowledge all my friends and colleagues at Cranfield for their valuable discussion, generous help and encouragement during the course period, especially Mr. C. Lookwood, Mr. W.T.Yeoh, Mr. Michael Sandling and some of those in Cranfield Chinese Society.

Last but not least, my sincere thanks to my wife Yuhua and my son Bicen for their love, patience, understanding and encouragement, and also to my parents in China for their continuous support and encouragement throughout my life. This research project would had never been finished without their support.

Contents

List of Figures

List of Tables

Nomenclature

A	area
$\mathbf{A}$	coefficient matrix
a	variable
$\vec{\mathbf{a}}$	acceleration vector in absolute frame
$\vec{\mathbf{a}}'$	acceleration vector in relative frame
$\mathbf{B}$	coefficient matrix of pressure correction equation
B, B^u, B^v, B^w	coefficients in pressure correction equation
b	variable
bf	bodyforce
blk	blockage effect
C, C^u, C^v, C^w	coefficients in pressure correction equation
C_D	constant in turbulence model
C_p	specific heat at constant pressure
C_{p_s}	static pressure scaling factor
C_v	specific heat at constant volume; velocity scaling factor
C_μ	constant in eddy viscosity equation
C_1, C_2	constants in turbulence model
D	diffusion term coefficient
D, D^u, D^v, D^w	coefficients in pressure correction equation
dts	deterministic stress
E	total energy; constant in wall function
ϵ	internal energy
F	mass flux; convection term coefficient
$\vec{\mathbf{F}}$	blending function vector
F_s	shear force
$\vec{\mathbf{f}}$	force
f_P, f_M	interpolation coefficients

g^{ij}	contravariant base matrix components
H	total enthalpy
h	enthalpy
I	unit tensor
I^C	convection term
I^D	diffusion term
I^{DC}	cross diffusion term
I^{DN}	normal diffusion term
I^{S_Φ}	volume integral of source terms
J	Jacobian matrix
k	thermal conductivity coefficient; turbulence kinetic energy
$\mathbf{L}$	lower triangular matrix
l	length in turbulence model
l_m	mixing length (m)
$\dot{m}$	mass flow rate (m/s)
max	maximum
min	minimum
m_p	mass source term in pressure correction equation
N	sample number; blade number of a blade row
P	total pressure; effective pressure
$\mathbf{P}$	coefficient matrix
P_e	Peclet number
P_r	Prandtl number
p	static pressure
$\vec{\mathbf{p}}'$	pressure correction vector
Q	transformation matrix; external heat transfer
$\vec{\mathbf{q}}$	heat transfer vector
R	specific gas constant
$\mathbf{R}$	residual matrix
$\vec{\mathbf{R}}$	coordinate vector
R_{ij}	composite stress
r	radial coordinate in cylindrical coordinates
$\vec{\mathbf{r}}$	position vector
rho	density (kg/m^3)
S	surface area of control volume (m^2);

	source term: total entropy (W/K)
$\vec{\mathbf{S}}$	coordinate vector
$\vec{\mathbf{S}}^*$	"mass source" vector in pressure correction equation
S^{CDT}	cross diffusion terms as part of source term
S_ϵ	control volume surface
S^{HOT}	hight order source term from $QUICK$ scheme
S^{OT}	other source terms
S^{PGT}	pressure gradient term as part of source term
s	specific entropy (J/kgK)
s'	generation rate of specific entropy (W/kgK)
T	temperature (K); time (s)
t	time (s)
U	internal energy
U, V, W	velocity component in general coordinates (m/s)
$\mathbf{U}$	upper triangular matrix
U_m	tangential blade velocity at midspan (m/s)
U_p	mean flow velocity (m/s)
u, v, w	velocity components in Cartesian coordinates (m/s);
u, v	coordinates in parametric plane
u_τ	friction velocity in wall function (m/s);
$\vec{\mathbf{V}}$	velocity vector in absolute frame; intermediate variable vector
V_p	volume of control volume (m^3)
v	coordinate in parametric plane; specific volume
$\vec{\mathbf{W}}$	velocity vector in relative frame
W, w_f	work done by external bodyforces
$\vec{\mathbf{X}}$	coordinate vector in absolute frame
X	space length (m)
x, y, z	Cartesian coordinate components

Greek Symbols

β	acceleration parameter
Γ	diffusion coefficient
γ	ratio of specific heats
δ	Kronecker delta function
ϵ	dissipation rate of turbulence kinetic energy

ε_{ijk}	alternating tensor
ε_{ν}	dissipation term
η_c	compressor stage efficiency
θ	tangential coordinate in cylindrical coordinate system
κ	Von Karman's constant
λ	second viscosity coefficient
μ	molecular viscosity coefficient
μ_T	turbulent eddy viscosity coefficient
ξ, η, ζ	coordinates in computational space
ρ	density
Π	stress tensor
$\sigma_k, \sigma_\epsilon$	constants in the k-ϵ turbulence model
τ	viscous shear stress tensor
Φ	scalar variable; variable vector
ϕ	potential function
ψ	stream function
Ω	angular velocity vector
ω	quantity in turbulence model; relaxation factor

Subscripts

a	axial; area averaging
c	circumferential
cal	calculated
$cell$	cell
dns	downstream
eff	effective
$exit$	exit
ext	external
i, j, k	coordinate indices
int	internal
M	neighbouring cell
m	coordinate index; mass averaging
mid	interpolated value at control volume surface
mix	corresponding to mixing plane
n	coordinate index
P	cell centre

p	coordinate index
r	radial
ref	reference
s	space; static
T	turbulent
t	time; stagnation or total
ups	upstream
x, y, z	in Cartesian coordinate direction
θ	circumferential
Φ	corresponding to variable Φ
0	at the same initial and boundary condition

Superscripts

(n)	iteration number
$'$	random fluctuation; correction value in pressure correction equation
$+$	non-dimensional quantity in wall function
$-$	average; ensemble average; distance
$=$	ensemble and time average
$\equiv$	ensemble, time and passage-to-passage average
$\hat{-}$	periodic fluctuation
$\hat{=}$	aperiodic fluctuation
$\sim$	normalised variable
$*$	previous iteration value; provisional value

Abbreviation

AC3A	Advanced Civil Core Compressor Aerodynamics
ADI	Alternating Direct Iteration
Comp.	Sub-Computation
CU	Cranfield University
DSM	Deterministic Stress Model
EULER	Exponential Upwinding or Linear Exprapolation Refinement
FDM	Finite Difference Method
FEM	Finite Element Method
FVM	Finite Volume Method
HP	High Pressure
IGV	Inlet Guide Vane
LDS	Lumped Deterministic Stresses
LSRC	Low Speed Research Compressor
MPM	Mixing Plane Model
MSI	Modified Strongly Implicit procedure
NVD	Normalised Variable Diagram
OGV	Outlet Guide Vane
PISO	Pressure Implicit with Splitting of Operators
PVM	Parallel Vitual Machine
QUICK	Quadratic Upstream Interpolation for Convection Kinetics
SIP	Strongly Implicit Procedure
SIMPLE	Semi-Implicit Method for Pressure Linked Equations
SIMPLER	*SIMPLE*-Revised
SIMPLEC	*SIMPLE*-Consistent
SMART	Sharp and Monotonic Algorithm for Realistic Transport by convection

SOR	Successive Over Relaxation
SOUCOUP	Second-Order Upwind Central differencing first-Order UPwind
STOIC	Second and Third Order Interpolation for Convection
TDMA	Tri-Diagonal-Matrix-Algorithm

Chapter 1

Introduction

1.1 Introduction

The flow field in turbomachinery is extremely complicated and this complexity was well described by McNally et al.[123]. Turbomachinery flows can be described as three-dimensional, transitional and turbulent, and also separated flows are frequently encountered. The flow is dominated by vortical flows: secondary, leakage, trailing, horseshoe vortices. In a multistage environment both the relative and absolute flows are unsteady. Large axial, radial and centrifugal pressure gradients exist within the flow passages due to the turning of the flow within blade rows. This turning redistributes the incoming vorticity field and generates cross flows. Strong shocks may exist within the blade passages. These can be complex and interacting, and often cause separation and additional loss. Geometrical parameters are also complex and many: camber, blade and blade-row spacing, varying thickness from hub-to-tip and from leading-to-trailing edge, stagger and skew, lean, twist, aspect ratio, hub/tip ratio, tip clearance, leading and trailing edge radii, etc. Typical flow features are described schematically in Figure 1.1.

The application of numerical methods to turbomachinery dates back to 1950's, even before the advent of the digital computers. Fully three-dimensional CFD methods first became available in the early 1980's and made the predictions more accurate as compared with previous methods. With the rapid development of computer architecture and pre- and post-data processing during the last two decades, computational techniques are able to provide efficient methods for the analysis and design of turbomachinery. Nowadays Computational Fluid Dynamics (CFD) plays a more and more important role in the aerodynamic design of turbomachinery. The design of modern compressors and turbines has become unthinkable without the

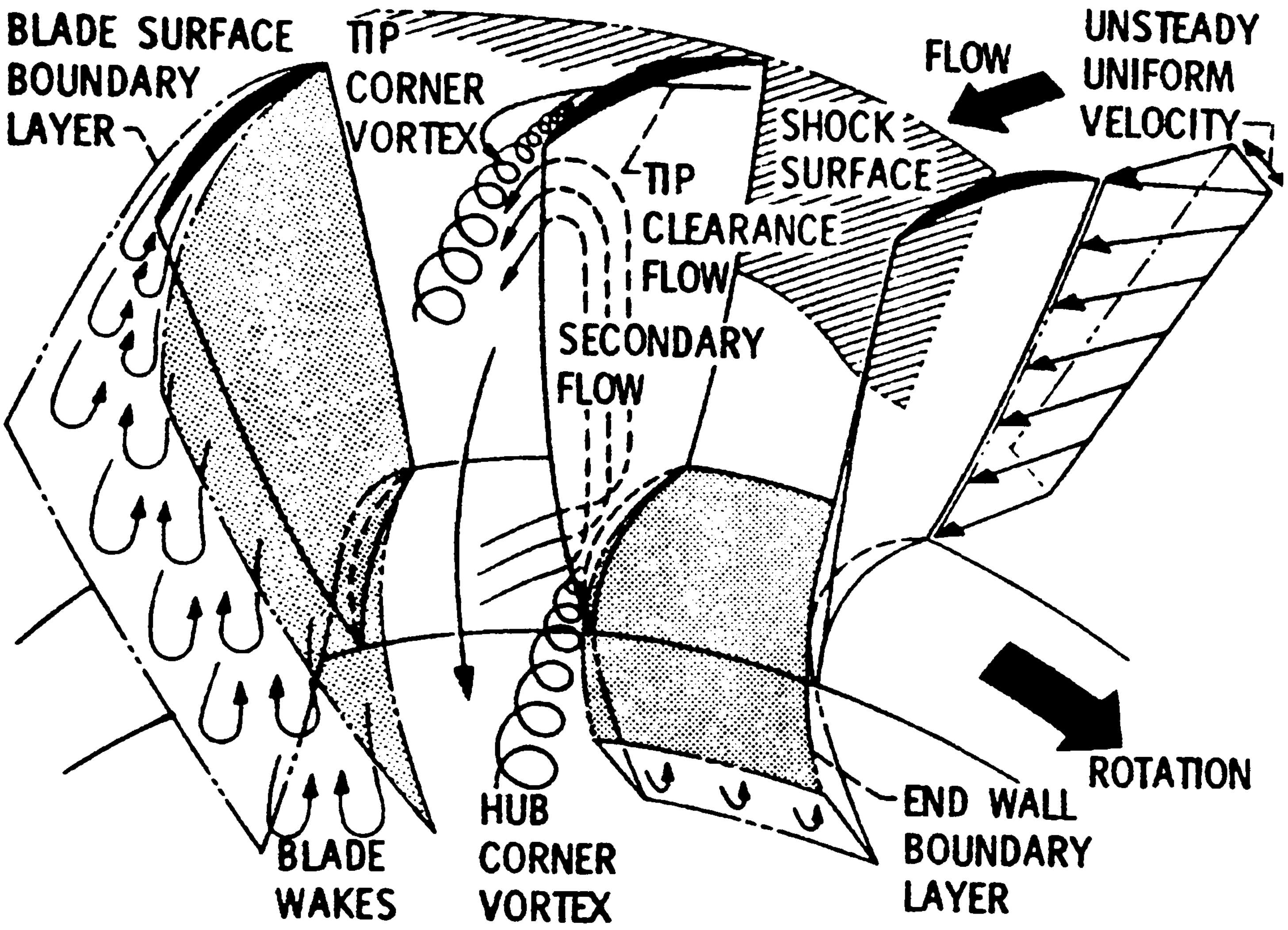

Figure 1.1: **Flow features in an axial flow compressor (McNally et al. [123])**

help of CFD. Combined with measurements, CFD provides an efficient tool for simulation, design, optimisation and, most importantly, analysis of complex three-dimensional flows hitherto inaccessible to the engineer. In many cases, it is the only simulation available, because the actual testing of turbomachinery, including detailed measurement in rotating passages, is cumbersome and even impossible.

In the aeroengine industry of the 1980's, a typical iterative design procedure for a multistage axial flow compressor would take up to three years to develop and cost as much as twenty million dollars (LeJambre et al. [109]). However, the resulting designs were not optimum. No detailed understanding of the internal fluid mechanics was gained; it was not then possible to break from a previous design with any confidence.

In the 1990's, design methods based on solving the Navier-Stokes equations became more accurate and practical for isolated cascades of airfoils such as fans. As computers became more powerful, it became more practical to routinely solve multiple rows of airfoils in order to evaluate new design concepts.

More recently, efficient prediction methods for multistage turbomachinery have been developed and have shown great potential in design application. Under these circumstances, the research work in recent years has been aimed towards the development and computational implementation of methods for internal flow and performance simulation and the improvement of 3D design and prediction tools of multistage turbomachinery. The proposed methods should be able:

- to predict the most significant flow phenomena and global aerodynamic performance of multistage turbomachinery.
- to investigate the better setting of boundary conditions in the simulation of multistage turbomachinery.
- to investigate and develop different models for passing information between neighbouring blade rows.
- to make the code sufficiently flexible and robust for different turbomachinery applications.

Right now, the capability of flow simulation for multistage turbomachinery is still limited by the capability of today's computers and therefore a direct solution of Navier-Stokes equations or even an unsteady solution of Reynolds averaged Navier-Stokes equations for three-dimensional flows in multistage turbomachinery are very difficult or even impossible.

The general aim of this study is to investigate and improve a set of models and a computer code in order to efficiently predict the global performance and detailed internal flows of multistage axial flow compressors with defined geometries and global aerodynamic boundary conditions. A thorough comparison of the predictions against available in-house experimental data and analysis of flow phenomena inside compressor flow passages are also required.

1.2 Brief Review on Turbomachinery CFD

The current review of CFD methods for turbomachinery flows is based on Lakshminarayana [104], McNally et al. [123], Hirsch et al. [81], Denton and Dawes [49], Adamczyk [6] and other recent publications, and only the major categories are described here. The development of CFD in turbomachinery may be classified in six model groups based on the simplification of the Navier-Stokes equations.

1.2.1 Mean-line Model

This is a model of one-dimensional calculation where the fluid properties and velocities are estimated along the mean line by empirical corrections of experimental data. This model is also called quasi-one-dimensional model.

The accuracy of the mean-line model is one dimensional in space and relies heavily on a large empirical database. This class of methods continues to be developed and used for the preliminary estimation of performance, Howell and Calvert [89].

1.2.2 Axisymmetric Flow Models

The flow field in turbomachinery can be assumed to be axisymmetric when the incoming and exiting flow is supposed to be axisymmetric and steady. This axisymmetric flow representation is described by through flow models. If the blade thickness is allowed to be ignored while the aerodynamic loading is maintained, the blade row can be regarded as an "actuating disk". Across the disk, there is an aerodynamic force acting on the fluid and energy inputed in (for compressors) or extracted from (for turbines) the fluid. The axisymmetric flow field is divided into two kinds of regions: the core region and the endwall regions. The impact of the endwall region is accounted for by means of a flow blockage and needs to be estimated with empirical data. There are basically three types of axisymmetric flow calculations normally used. They are through-flow, cascade flow and quasi-three-dimensional flow calculations which are described as follows.

Through-flow and Cascade Flow Calculations

The ultimate equations to be solved in most internal flows are the Reynolds-averaged Navier-Stokes equations. These equations are often reduced to a simpler form, the Euler equations, by neglecting the viscous terms. The calculation methods for through-flows and cascade flows may be classified as follows based on different simplification of governing equations:

1. **Streamline Curvature Method.**
   This analysis method is based on the direct determination, through iterative calculation, of the traces or projections of streamlines on a prescribed surface, for example on a meridional section of a turbomachine. Velocities and fluid properties are predicted at locations on the streamlines corresponding to control surface intersections.

The influence on the hub-to-shroud flow patterns due to the terms in the radial component of the equation of motion representing streamline slope (due to radial velocity) and curvature (due to radial velocity change) was first described by Traupel [175], and later by Wu and Welfonstein [196] and Hamrick, Ginsbury and Osborn [74]. Wu [191] provided the basis for a hub-to-shroud flow field calculation including locations internal to blade rows and some design procedures tracing streamlines through blade rows were reported during the 1950s. Between 1960 and 1976 a substantial number of computer codes for axial-flow turbomachinery analysis were developed using streamline curvature methods.

The starting point of the methods is a family of pseudo streamlines deduced, by similarity, from the profile geometry. The transverse pressure gradients are connected to the curvature of these streamlines; a transverse velocity distribution is derived, and, by iteration on the continuity equation, the shape of the streamline is changed until a convergence of the process is reached, Wilkinson [189] and Bindon [16]. The main advantage of the method is the rapidity of the computation, also for subsonic compressible flows. Difficulties arise for transonic flow because of the discontinuity of the streamline curvature at the shocks. Another drawback lies in the lack of accuracy in areas with strong curvature (leading and trailing edges).

2. **Stream Function Method**

The continuity equation allows definition of a stream function which combined with the condition of irrotationality provides a second order, non-linear equation for compressible flow. This equation is generally discretised in an orthogonal grid. by means of a scheme suitable for an elliptic type problem (subsonic flow).

The stream function is defined by postulating that the mass flow components, ρu and ρv, are obtained from a scalar function as follows:

$$\rho u = \frac{\partial \psi}{\partial y}, \qquad \rho v = -\frac{\partial \psi}{\partial x} \tag{1.1}$$

where ψ is the stream function.

The stream function equations for turbomachinery S1(blade-to-blade) and S2 (hub-to-tip) stream surfaces were firstly introduced by Wu [192]. Katsanis [97] published a method for isentropic blade-to-blade flows applicable to any fixed or rotating axial, radial or mixed flow in turbomachinery blade rows. Marsh [120] developed a stream function analysis for hub-to-shroud surfaces. Marsh's technique was also applied to axial, radial and mixed flow turbomachinery. In 1970, Smith and Frost [158] applied these methods to flow on general blade-to-blade stream surfaces.

The discretised finite difference equation was solved by relaxation techniques, Katsanis [96] and Fenain [57], or by a matrix technique, Calvert and Smith [25].

3. **Velocity Potential Method**

Another approach to circumventing the problems inherent in the full Euler equations is to assume that the velocity components u and v are derivatives of a scalar function ϕ:

$$u = \frac{\partial \phi}{\partial x}, \qquad v = \frac{\partial \phi}{\partial y} \tag{1.2}$$

Such a flow is automatically isentropic with constant total temperature and zero vorticity (irrotational). Substitution of these relations into the continuity equation yields a second order equation in ϕ. As with the stream function, the potential equation can be solved by different relaxation techniques. Furthermore, it permits the solution of 3D as well as 2D flows. The isentropic assumption implies that shock waves captured in the transonic regime must be limited in Mach number to a value less than 1.3.

The pioneering work on such methods was performed by Murman and Cole [127] and Jameson [92]. Hafez et al.[68] later introduced a concept of artificial compressibility to accomplish the same objective when the conservation form of the full equation is used. Three major discretization methods, i.e., finite differences, finite volumes and finite elements, are used to obtain a set of algebraic equations for solution.

Potential methods are very useful for the flow analysis in the subsonic, fully supersonic and low transonic (i.e. free of strong shocks) flow regimes during the preliminary design stages of turbomachinery.

4. **Solution to Steady State Euler Equations for Inviscid Flows**

For inviscid flows, the viscous terms in Navier-Stokes equations are ignored and the equations are simplified to the Euler equations. In this situation, the problem raised by the mixed elliptic-hyperbolic nature of the Euler equations for steady transonic motion with intense shocks can be solved by non-steady type of methods, Magnus and Yoshihara [117] [118]. Such methods offer the great advantage of being applicable to any transonic flow; however, they require very long computation time for the asymptotic condition to be achieved. As the asymptotic solution is the only solution retained, the intermediate states do not need to have a physical significance, and the non-steady terms can be modified in order to accelerate the achievement of the final solution. Methods based on such an idea are called time marching methods.

The time marching methods of the Euler equations can be classified into two major categories: explicit and implicit.

The explicit method is the one in which all spatial derivatives are evaluated using known conditions at the old time level. All such methods are limited by the so-called Courant, Friedrichs, and Lewy (CFL) stability limit, which states that the domain of independence of the numerical scheme must contain the domain of dependence of the original equations.

MacCormack [116] introduced a two-step prediction-correction method, which alternates between forward and backward differencing on the two steps. McDonald [122] used another method for 2D transonic flows in axial turbine cascade, in which the conservation laws in an integral form are written and applied to local control volumes surrounding each grid point. Denton [43] [44] [50] has developed a somewhat simpler method for both 2D and 3D turbomachinery flows. Bosman and Highton [18] have developed a method for 3D flows which employs two overlapping grids with density and internal energy evaluated at one set of nodes and velocities evaluated at the second set. Ni [130] has developed another method that is equivalent to the second order Lax-Wendroff procedures. A pseudo-unsteady method has been developed by Viviand and Veuillet [182] [181].

In implicit methods the equations are backward differenced in time, and the nonlinear terms at the new time are linearised about their values at the previous time level. Introductions of difference gives a large system of algebraic equations for the unknowns at the new time level. These equations are solved by block alternating-direction-implicit (block ADI) techniques.

The first of these methods was introduced by Briley and McDonald [22, 23], primarily for compressible Navier-Stokes equations. Beam and Warming [13] independently developed a similar method for Euler equations. Steger [165] [166] has developed a curvilinear coordinate version of the Beam-Warming algorithm for viscous as well as inviscid flows. Denton [45] has extended his earlier Euler method by employing a simpler more accurate differencing scheme. Both Ecer and Akay [52] and Lacor and Hirsch [103] have developed methods for solving the steady Euler equations. Another hybrid streamline curvature-Euler solver developed by Giles & Drela [62] is now proving very popular due to its ability to work with a coupled boundary layer calculation and to work in both direct and inverse mode.

5. **The Pressure-Based Methods for Viscous Flows**

In the pressure-based techniques, usually the solution algorithm is based on a semi-implicit scheme which utilises the continuity equation for the derivation of a Poisson Type equation for the calculation of the pressure in order to satisfy a divergence free velocity field. In the first step a guessed pressure field is the pre-condition for the solution of the momentum equation which are decoupled and expressed in a linearised form and in the second step an equation for the pressure or pressure correction is solved to update the pressure field and promote the satisfaction of the continuity condition. The density is then calculated using the perfect gas law.

This technique was originally suggested by Chorin [33, 34]. The semi-implicit method for pressure-linked equations (SIMPLE) algorithm due to Patankar and Spalding [136] provided a remarkably successful scheme and has dominated the field of numerical simulation of incompressible flows. Patankar [135] introduced the SIMPLER method, in which an extra equation was solved for the evaluation of static pressure. The SIMPLEST procedure was developed by Spalding [160], who recommended an explicit treatment of the convection and implicit treatment of diffusion in the momentum equations. Another variant is the SIMPLEC procedure described by Von Doormal and Raithby [183] which uses a consistent under-relaxation of the momentum and pressure corrections. Vanka [179] has used the multi-grid method with a coupled solution. He proposed an explicit smoothing technique called Symmetrical Coupled Gauss-Seidel (SCGS) and improved both convergence and CPU time. Most earlier techniques utilised a staggered grid system in order to remove unphysical pressure oscillation. Rhie and Chow [147] used a pressure weighted method to suppress pressure oscillations and developed a differencing scheme for a curvilinear coordinate system on a non-staggered grid. Kirtley and Lakshminarayana [100] developed a coupled pressure-based method in which all the equations were solved simultaneously. The pressure-based methods have been applied successfully to incompressible, compressible, laminar, turbulent, low and high Reynolds number flows for a large class of geometries. The grid system may be orthogonal or non-orthogonal. The method is flexible; either the finite difference or finite volume formulation can be employed. The pressure-based methods are efficient and have reached a high level of sophistication; they are highly recommended for incompressible and subsonic turbomachinery flows, Lakshminarayana [104]. One of the successful applications of the pressure-based methods is the commercial code *TASCflow3D*, which is capable of solving diverse and complex multi-dimensional fluid flow problems and provides solutions for incompressible or compressible, steady or transient, laminar or turbulent single-phase fluid flow in complex geometries [171].

6. **Time-Marching Methods.**

   In these techniques, the time derivative in the Navier-Stokes equations is retained. Very efficient techniques have been developed to solve the equations for external and internal flows. There are two classes of methods of solving the time-dependent hyperbolic equations: explicit and implicit.

   In the explicit scheme, the spatial derivatives are evaluated using known conditions at the old time level. The explicit schemes used widely for the computations of turbomachinery flows are as follows:

   - The Lax-Wendroff scheme [108] is second-order accurate in time and space.
   - The predictor-corrector method due to MacCormack [116] is a modified version of the Lax-Wendroff scheme and has been in use for external aerodynamics for a long time. Many early turbomachinery computations were performed with this scheme.
   - The Runge-Kutta type scheme (Jameson et al. [93]) has found wide application in both the internal and external flows.

   The explicit techniques are highly successful in predicting complex flow fields in turbomachinery.

   Implicit methods, where the unknown variables are derived from a simultaneous solution of a set of equations, on the other hand, usually allow for larger time steps and faster convergence and are attractive for both steady and unsteady flows.

One of the widely used implicit techniques is the approximate factorisation due to Briley and McDonald [23] and Beam and Warming [14]. This technique is widely used, with modifications, to predict viscous flow fields in cascades, stators, and rotors. Another one is the upwind schemes developed by Osher and Solomon [134] which are used to capture strong shocks without requiring arbitrary smoothing parameters (artificial dissipation), which may alter the physics of the problems.

The calculation methods may also be categorised based on different numerical discretization techniques used:

(a) **Finite Difference Methods**

The method is based on the initial definition of a system of grid points throughout the flow passage under study. Finite difference equations are written for each grid point. Then the equations are solved to determine the distributions of fluid properties and velocities at the nodal points. Finite difference methods for turbomachinery analysis were first suggested and utilised between 1950 and 1960, Wu [190] [191] [193] [194] [195].

(b) **Finite Element Methods**

The flow passage to be studied is subdivided by a network of lines into elements. Nodal points are located on the lines forming the boundary of each element. The physical laws and empirical input are formulated so that the fluid properties and velocities may be determined at each nodal point by iteration.

Finite element methods initially appeared as usable through-flow analysis techniques during the middle 1970s, Hirsch and Warzee [82], Adler and Krimerman [8], and also developed by Whitehead [187]. The finite element mesh can be adapted readily to quite complex geometries and also can be developed for three-dimensional analysis.

The methods are based on an approximation of dependent variables in the form of polynomials, and on integral definition of the problem, Krimerman and Adler [102] and Morice [125].

The benefits of this technique are as follows:

- Possibility of giving an optimum grid distribution, especially by using curvilinear meshes;
- Automatic treatment of natural boundary conditions;

- Preservation of symmetry in the discretization of differential operators.

(c) **Finite Volume Methods**

The flow passage is subdivided into a large number of small volume elements, fitted to the passage geometry. The physical laws and empirical information governing the calculation are used to generate integral conservation equations for each small volume. The equations are solved, typically by an iterative time-matching process or pressure based methods, to reach a converged distribution of velocities and properties for the finite volume surfaces.

The application of finite volume methods to hub-to-tip flow fields and their strong potential for extension to an effective three-dimensional analysis have been reported by Denton and Singh [50], Farn and Whirlow [55], and Ivanov and Kimasov [91]. The finite volume regions can also be generated to conform to complex passage geometries.

Quasi-Three-Dimensional Flow Model

With the development of digital computers, the through-flow models were replaced by quasi-three dimensional flow models. The quasi-three-dimensional model is the numerical coupling between an axisymmetric flow model and a cascade flow model. The axisymmetric flow model provides the streamline surfaces on which the cascades are defined and the cascade flow model provides the blade force distribution required as input to the axisymmetric flow model. This class of methods was pioneered by Wu [191].

A major development paving the way for analysis of turbomachinery flows was the series of early papers by Wu, particularly [192], which derived the stream function equation for S1 (blade-to-blade) and S2 (hub-to-shroud) stream surfaces of turbomachinery. Smith [159] described both the meridional and the blade-to-blade analysis, which was the first description of the meridional and blade-to-blade methods used together.

In 1976 Bosman [17] presented an iterative approach to couple S1 and S2 analysis. A more elaborate iterative procedure was described by Adler and Krimerman [7]-[9]. Hirsch [82] presented the first solution of the meridional stream function equation based on the finite element method. Later, Hirsch [83] developed an iterative analysis in which meridional and blade-to-blade finite element analysis were combined for application to axial turbomachinery.

Davis [37, 38] demonstrated a method for a single full stage machine. On the other hand, the methods of Katsanis [98, 99], and Bosman [17] were applied to a single blade row. Hafez [69] has extended the solution of the stream function equation to transonic flow by using techniques developed for the potential equation. Two publications, Howard and Gallimore [87] and Gallimore [58], are the representative of recent development of axisymmetric flow models.

Most of the computational methods which have evolved from Wu's theory depend strongly on empiricism to account for viscous effects of flow deviation and blockage and their predictive capability is limited in separated flow regions.

1.2.3 Three-Dimensional Single Blade Row Approaches

Initially the CFD-based models which were introduced into turbomachinery calculation ignored the impact of the unsteady, deterministic flow which exists within actual multistage turbomachinery. Based on this assumption, the governing equations are simplified to the Reynolds-Averaged steady-state Navier-Stokes equations.

Many flow features in turbomachinery, such as the effects of blade lean and sweep, of tip leakage and secondary flow, are fully three-dimensional and can only be predicted by 3D methods. Three dimensional methods have evolved over the past 20 years and now are most commonly used as a final check on designs. Inverse methods in 3D are relatively difficult. A few inverse 3D methods have been reported, Demeulenaere et al. [42], but they are not yet widely used in industry.

Only a limited number of numerical schemes have been applied to 3D turbomachinery flow. The most common are time marching solutions of the Euler or Navier-Stokes equations, Denton [46] and Dawes [39]. Another type is pressure correction methods initially used by Moore and Moore [124], Hah [70] and more recently in the commercial code $TASCflow3D$.

In a typical design system for multistage turbomachinery, preliminary blading is defined using through-flow calculations with empirical corrections for 3D viscous effects. 2D airfoil cross sections are defined and stacked to form 3D airfoils. Then simple 2D viscous CFD calculations are performed to check blade loadings, flow separation, etc. After that, a series of rig tests are undertaken to match the stages. Finally, engine hardware is defined and built for a full scale engine test. The design is assessed after each step and can be changed. This iterative procedure is very expensive and time consuming, LeJambre [109].

Computational methods for a single blade row in turbomachinery are now highly developed and commonly used in industry. However, few turbomachines operate as isolated blade rows. Generally, three-dimensional CFD based methods for multistage turbomachinery, without taking into account the impact of unsteady, deterministic variation generated by neighbouring blade rows, are categorised into two types:

1. **Successive Analysis of Isolated Blade Rows**
   Given an analysis code for an isolated blade row, multistage turbomachinery is simulated by analysing successive blade rows from inlet to exit, using average flow properties from the exit of one blade row as inlet boundary conditions for the next. This method is simple, but it introduces many modelling issues. For example, the boundary conditions for a single blade row working in a multistage environment are difficult to set, mass flow rate and spanwise flow properties are difficult to match between the neighbouring blade rows and the method ignores physical processes such as wake mixing and migration. acoustic interaction, and other unsteady effects that may be important in real turbomachinery. Because of the simplicity of this method, it was used by several researchers such as Boyle et al. [20] and Politis et al. [140].

2. **Mixing-Plane Methods**
   Simple mixing-plane methods analyse multistage turbomachines by exchanging spanwise distributions of averaged flow quantities at a common grid surface between the blade rows, Denton [47] and Dawes [41]. These methods have the advantage of maintaining spanwise consistency and preserving general radial variation between blade rows although circumferential averaging of flow properties are introduced.

   More recently, an improved mixing-plane treatment has been developed, Denton [47], in which the circumferential variation of fluxes at the mixing plane is obtained by extrapolation from the upstream and downstream planes while adjusting the level of the fluxes to satisfy the overall conservation. Thus the fluxes "seen" by the blade rows are circumferentially nonuniform at the mixing plane with different circumferential variations, but the same average values, being "seen" by the upstream and downstream rows. With this model the mixing-plane is allowed to be located very close to the leading or trailing edges of the blade rows and the flow calculations for multiple blade rows and even for whole multistage compressors and turbines becomes possible.

Chen et al.[31] derived another method from the Beam and Warming implicit approximation factorisation (AF) finite difference scheme and used the mixing plane model from Denton [47] to predict 3D multistage turbomachinery flows.

1.2.4 Time Averaged Flow Model

This type of methods was developed by Adamczyk [2] [3] and Adamczyk et al. [5] as a rigorous means of modelling unsteady blade row interaction using a steady state analysis. This flow model describes the time averaged flow field within a typical passage of a blade row embedded within a multistage configuration. The unsteady deterministic stresses resulted from a time averaging on the governing equations are the result of flow processes directly linked to shaft rotational speed and are responsible for the recovery of wake mixing loss in compressors, flow blockage, and the spanwise redistribution of momentum, Adamczyk [6]. The flow quantities are split into a steady component, an unsteady deterministic (periodic) component, and an unsteady random (turbulent) component. The flow equations are integrated in time using procedures analogous to Reynolds-Averaging to produce the average-passage equations. The average-passage approach has the advantage of a rigorous foundation for modelling unsteady blade-row interaction, although little data is available for modelling the deterministic stresses. The method requires that the computational grids for each blade overlap one neighbouring blade row on each side, adding to programming complexity and computational difficulties.

The solution methodology of this model was developed by Celestina et al. [29] and Rhie et al. [148]. A computer code called NASTAR based on average passage equations was applied by LeJambre et al. [109] to the design of a P&W's eleven stage HP compressor. The application of the code was assessed to achieve 2% higher efficiency at no overall stall margin loss and yield up to 50% reduction in the compressor development time and cost, LeJambre et al. [109]. Sondak et al. [161] demonstrated a "lumped" deterministic stress (LDS) model where the unsteady flow effects are modelled with lower order (inviscid) time dependent simulation as source terms in viscous steady flow equations. These source terms, expressed with lumped deterministic stresses, are employed to drive steady flow solution procedures to produce the time averaged solution of an unsteady flow field. The LDS model was recently used by Busby et al. [24] and Orkwis et al. [133] to investigate turbine hot streaks.

More recently, further efforts have been made to investigate the effects and modelling of deterministic stresses and closure approaches to the average passage equations. In general, the passage equations for multistage turbomachinery applications require the pitchwise mesh lines with no variation in axial and radial direction. Such a requirement is due to the original implication of the model for the deterministic stresses which close the average passage equations. Kirtley et al. [101] introduced a more general implementation of the closure model that permits the use of general meshes with high distortion especially near blunt leading edges or around highly staggered airfoils. This methodology was applied to the complete turbine for the GE90 turbofan engine, Turner et al. [177]. In addition, the deterministic stresses were quantitatively analysed with a time-dependent CFD tool for the Pennsylvania State University Research Compressor (PSRC), Hall [73] and a combined strategy of mixing plane/deterministic stress modelling was proposed by Hall [73]. An experimental study of velocity decomposition and unsteadiness at downstream of an embedded stator was made by Prato et al. [144] and the experimental analysis of deterministic stresses and heat flux distribution at the downstream of the same compressor stator was studied by Suryavamshi [168].

1.2.5 Fully Unsteady Flow Simulation

Fully unsteady methods, pioneered by Rai [145] and Whitfield et al.[185], involve direct solution of unsteady rotor-stator interaction. These methods presumably avoid all modelling questions except for turbulence but are very expensive computationally and still require averaging at the end to produce useful results. The practical application of this model in design processes must await the further development of more powerful computers.

In the application of these methods, the publications of Gundy-Burlet et al. [64] [65] [66] [67], Chen et al. [30], Dorney et al. [51], Giles [61], Hodson and Dawes [84], Rai and Dring [146], Sharma et al. [157] and Davis et al. [36] have proven that these models are very useful in numerical experiments to quantify the impact of the unsteady deterministic flow on turbomachinery aerodynamic performance and durability, Adamczyk [6]. More recently, unsteady three-dimensional viscous flow simulation in a multistage turbomachinery application was carried out by several researchers such as Chima [32], Nozaki et al. [132], Hall [72], He [76] and Bell and He [15], etc..

1.2.6 Direct Navier-Stokes Simulation

The advantage of this approach is that apart from the empirical information required to model the physical and thermodynamic properties of a fluid, no other empirical information is required to solve the Navier-Stokes equations. The direct solution of the Navier-Stokes equations for Reynolds numbers typical of aero and industrial turbomachinery configurations would produce a non-deterministic or turbulent flow state. Theoretically, this model could provide the most accurate flow information than any other models mentioned above. However, the computer requirement of this model to solve the Navier-Stokes equations and support the aerodynamic design far exceed the capability of today's most advanced computers in both CPU speed and memory size.

1.3 Contribution of the Present Study

As seen from the literature review, there are several types of methods for the simulation of multistage turbomachinery. Unfortunately, because of the limitation of computer capabilities, some of these methods are still under development and are not sophisticated. It is the purpose of this study to develop and improve the numerical models for this kind of prediction based on steady state methods, with the main focus on multistage axial flow compressors.

The contribution of the present study is as follows:

- Implementation of the mixing plane models which are used to transfer information between neighbouring blade rows; analysis of the discontinuity at mixing planes and the limitation of the mixing plane models.
- Development of repeating stage models applicable to the flow simulation in rear stages of multistage axial flow compressors.
- Improvement of a deterministic stress model with focus on a practical way of simulating the influence of a relatively rotating blade row on a flow field by imposing the approximated bodyforce and blade blockage effect generated by the blade row.
- Development of computer code MSTurbo3D which is applicable to the simulation of single or multiple blade rows of axial flow compressors with the above models.

- Assessment of different simulation approaches by comparing the predicted results against experimental data.
- Understanding of detailed flow phenomena inside compressor flow passages, interaction between flow and blade rows and losses resulted from various stresses.

1.4 Structure of the Thesis

Chapter 2 describes a surface fitting method which is used in this project to generate boundary grid points for the flow passage of a blade row using existing discrete networked points that define the blade surface. Then an algebraic grid generation and grid clustering method is applied to create interior grid points.

In Chapter 3 general forms of governing equations for turbomachinery flows and the transformed form of the governing equations in a non-orthogonal curvilinear coordinate system and in different frames of reference are shown. Then three averaging procedures – ensemble, time and passage-to-passage averagings – are applied to the governing equations.

Chapter 4 presents the closure approaches to the system of governing equations for multistage turbomachinery applications. The closure issues include turbulence modelling, an overlapped solution approach and the modelling of deterministic stresses, bodyforce and blade blockage effect. A standard wall function is introduced to simplify the treatment of near wall regions. In addition, repeating stage models are developed aiming at simplifying the global aerodynamic boundary conditions for the flow simulation of rear stages of multistage axial flow compressors.

Chapter 5 describes the spatial discretization process of the governing equations. Subsequently, different numerical schemes for the treatment of the convective term of the momentum equations are described in detail. A pressure correction method is described followed by the discussion of the application of under-relaxation, the use of collocated grids and the remedies to pressure oscillations.

In Chapter 6 the developed numerical approaches and the corresponding computer code are applied to the third stage and the complete 4 stages of the Cranfield

4-stage Low Speed Research Compressor (*LSRC*) on the peak efficiency operating condition. Analysis and comparison between the numerical results from different simulation approaches and experimental data are carried out. Efforts are also made to simulate the performance of the third stage working at off-design operating conditions and to analyse the losses of the flow by calculating the distribution of entropy generation rate and entropy rise.

Finally in Chapter 7, conclusions from the present research project are drawn and ideas for further work are suggested.

Chapter 2

Surface Modelling and Grid Generation

2.1 Introduction

Normally in turbomachinery applications, the three dimensional surfaces of compressor blades are defined by sets of discrete networked points. In this chapter, a three-dimensional surface fitting method, Weatherill [184] and Faux and Pratt [56] is applied to generate surface grids on the blade surfaces to form the boundary conditions for the interior grid generation. An algebraic grid generation technique with grid point clustering capabilities are used to generate interior grids.

2.2 Surface Grid Generation

Surface grid generation is one of the most difficult and yet important aspects in grid generation. The surface grid influences the field grid close to the configuration, the region where flow gradients are important and need to be resolved accurately. Surface grid lines have the same requirement for smoothness and continuity as the field grid lines for which they act as boundary conditions, and in addition, they are required to conform and describe accurately the configuration surfaces, including lines of component intersection, and to model regions of high surface curvature.

Geometrical surface modelling is a means by which a continuous surface can be defined from a discrete set of points. Such a definition of a surface is valuable for the generation of surface grids which, in general, will not coincide with the original geometry definition. The parametric representation of a surface which is described in detail in Appendix A, is straightforward to construct and therefore, a surface in three-dimensional space can be defined in just two independent parametric coordinates.

In this sense, surface grid generation can be viewed as a transformation from two dimensional parametric space where the grid is generated and mapped to the physical space $\vec{\mathbf{R}} \rightarrow \vec{\mathbf{X}}(x, y, z)$ by the mapping

$$\vec{\mathbf{X}}(x, y, z) = \vec{\mathbf{F}}(u) Q \vec{\mathbf{F}}^T(v) \tag{2.1}$$

where $\vec{F}$ is a blending function vector and Q a matrix, which are defined in Appendix A. Thus, three dimensional surface grid generation is simplified to grid generation in two dimensions within the finite parametric domain. Such grids can be defined by any grid generation method.

2.3 Interior Grid Generation

In order to numerically solve the governing equations of fluid mechanics, the fluid domains firstly need to be divided into finite volumes where the governing equations are going to be discretised and solved. Therefore, some techniques are necessary to specify the grid points that define the finite volumes as well as the boundaries of the domain.

Typically, the computational domain is chosen to be rectangular in shape where the interior grid points are distributed along grid lines. Therefore, the grid points can be identified easily with reference to the appropriate grid lines. This type of grid is called the **structured grid**, Hoffmann and Chiang [85], and is used in the present study. If the fluid domain is rectangular and the grid points are uniformly spaced inside the domain, the generation of the grid is simple and the specification of boundary conditions is not complicated. Unfortunately, the majority of the physical domains of interest are not rectangular. So, applying a Cartesian grid on an arbitrary physical domain requires some sort of interpolation for the implementation of the boundary conditions. This will cause serious numerical error near boundaries because the boundary conditions can not be described accurately, and create programming difficulties when grid points are not uniformly distributed.

To overcome these difficulties, a general coordinate system is introduced and a transformation from the physical to the computational space is utilised. This transformation is accomplished by specifying the general coordinate system which will map a non-rectangular grid in the physical space to a rectangular uniform grid

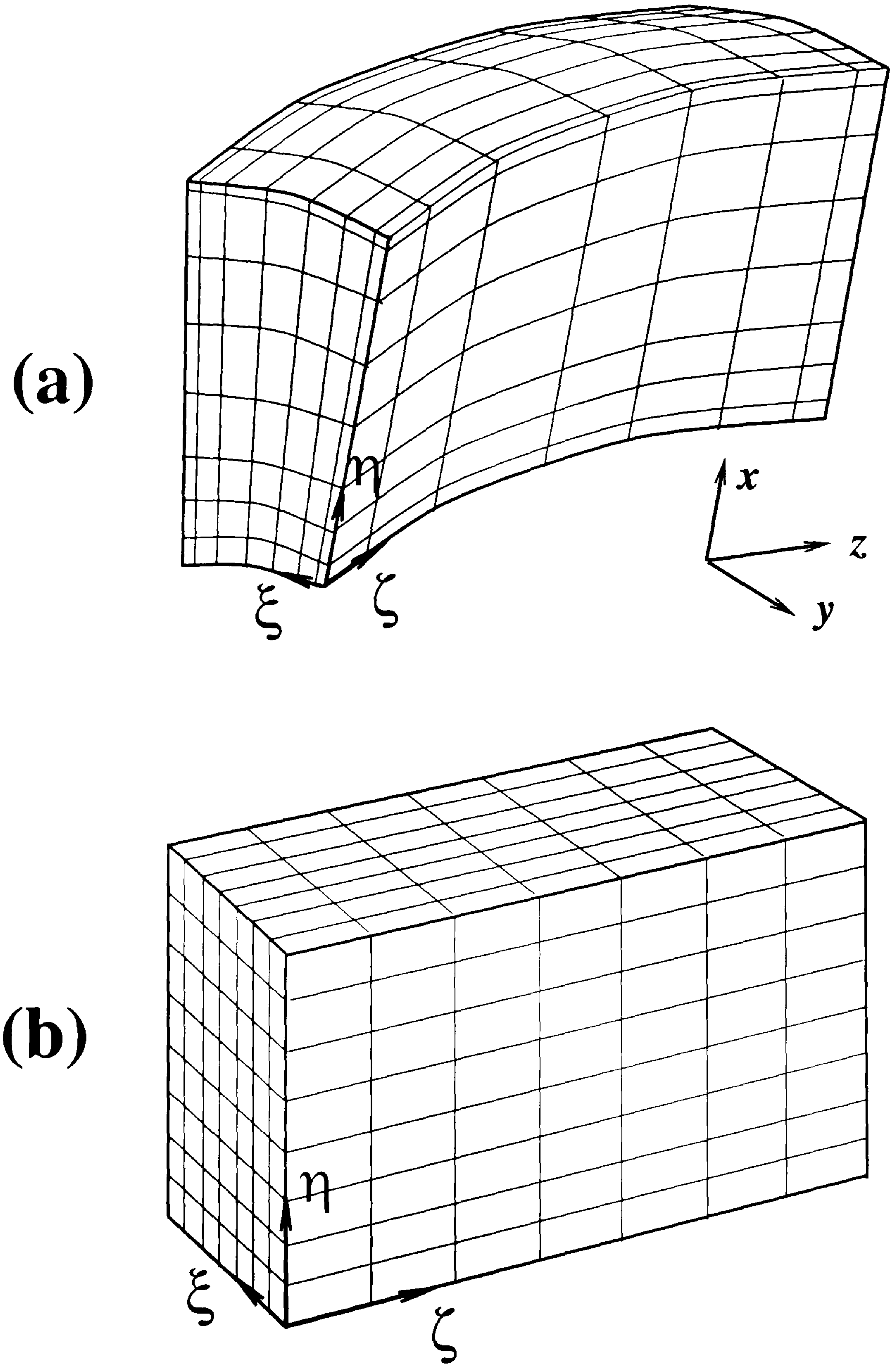

Figure 2.1: **Grid in (a) physical and (b) computational spaces**

in the computational space. Such a transformation is defined with the following expressions:

$$\begin{aligned} \xi &= \xi(x, y, z) \\ \eta &= \eta(x, y, z) \\ \zeta &= \zeta(x, y, z) \end{aligned} \tag{2.2}$$

Accordingly, the governing equations expressed in the Cartesian coordinate system also need to be transformed to the general non-orthogonal coordinate system, which will be described in the next chapter. This mapping is schematically expressed in Figure 2.1, where the physical space is expressed with Cartesian coordinates (x, y, z) and the computational space is expressed with general coordinates (ξ, η, ζ).

The purpose of the grid generation is to identify the location of the grid points in the physical space and create the relationship between the coordinates in the physical space and in the computational space. It is desirable that a grid system has the following features:

- One-to-one correspondent mapping to ensure grid lines of the same family do not cross with each other;
- Smoothness of the grid point distribution;
- Orthogonality or near orthogonality of the grid lines;
- Options for grid point clustering

In general, grid generation methods may be classified as:

- algebraic methods
- methods based on partial differential equations
- conformal mappings based on complex variables

Conformal mapping are limited to two-dimensional problems and the determination of the mapping function is sometimes a difficult task. Therefore, this type of method is not used here.

Compared with algebraic methods, the methods based on partial differential equations may provide grids with better smoothness and orthogonality. In the case of interest where there is a requirement for the pitchwise grid lines to have no variation in the axial and the radial directions, algebraic methods are more suitable than others and are used in the present study.

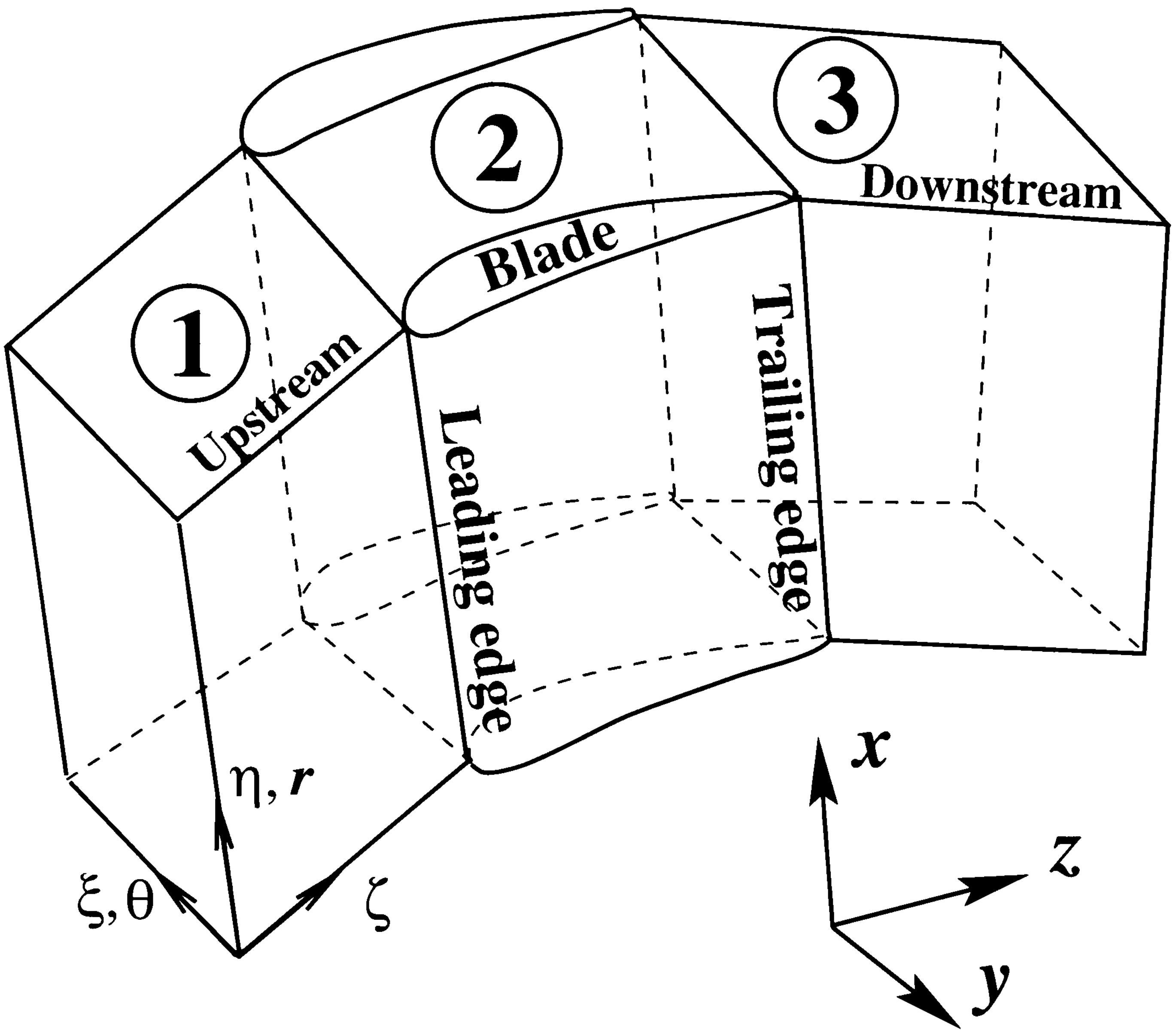

Figure 2.2: **Division of flow passage**

The algebraic method is theoretically simple and has the advantage of fast speed with which a grid can be generated. Different algebraic methods are selectable to generate required interior grid points between specified boundaries.

Direct three-dimensional grid generation with algebraic methods can be complicated for programming. Based on the features of the problems concerned which will be discussed in the following chapters, the grid generation can be simplified to a two-dimensional problem which will be described in detail below.

The flow passage between two neighbouring blades in an axial flow compressor and the applied coordinate systems are schematically shown in Figure 2.2. This passage is divided into three sub-domains: the upstream domain, the domain between the blades and the downstream domain. The grids of these domains are generated separately and connected together to a single domain.

For each of these three sub-domains, two-dimensional grid points on $\xi-\zeta$ planes

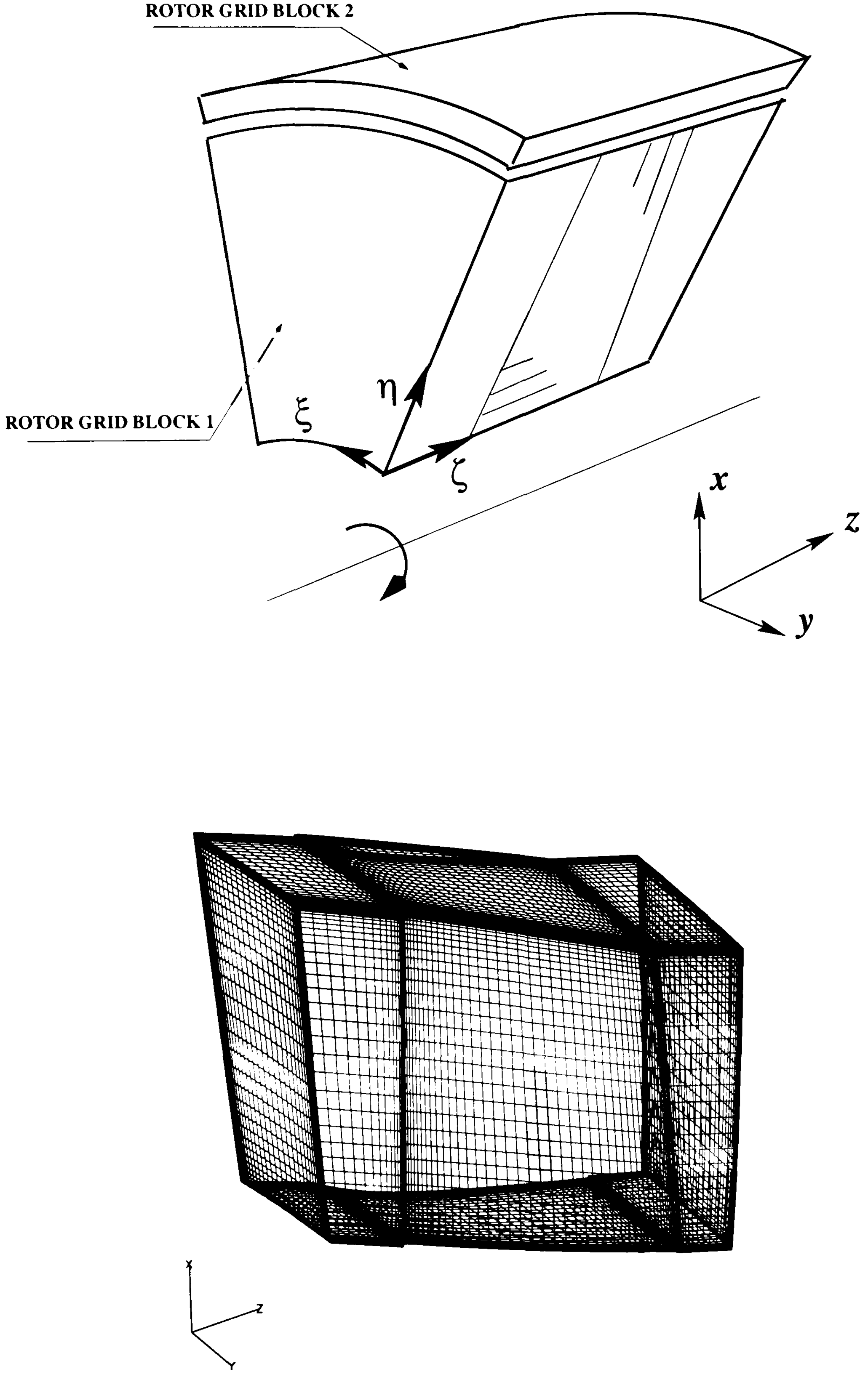

Figure 2.3: **Grid for the third rotor of** *LSRC*

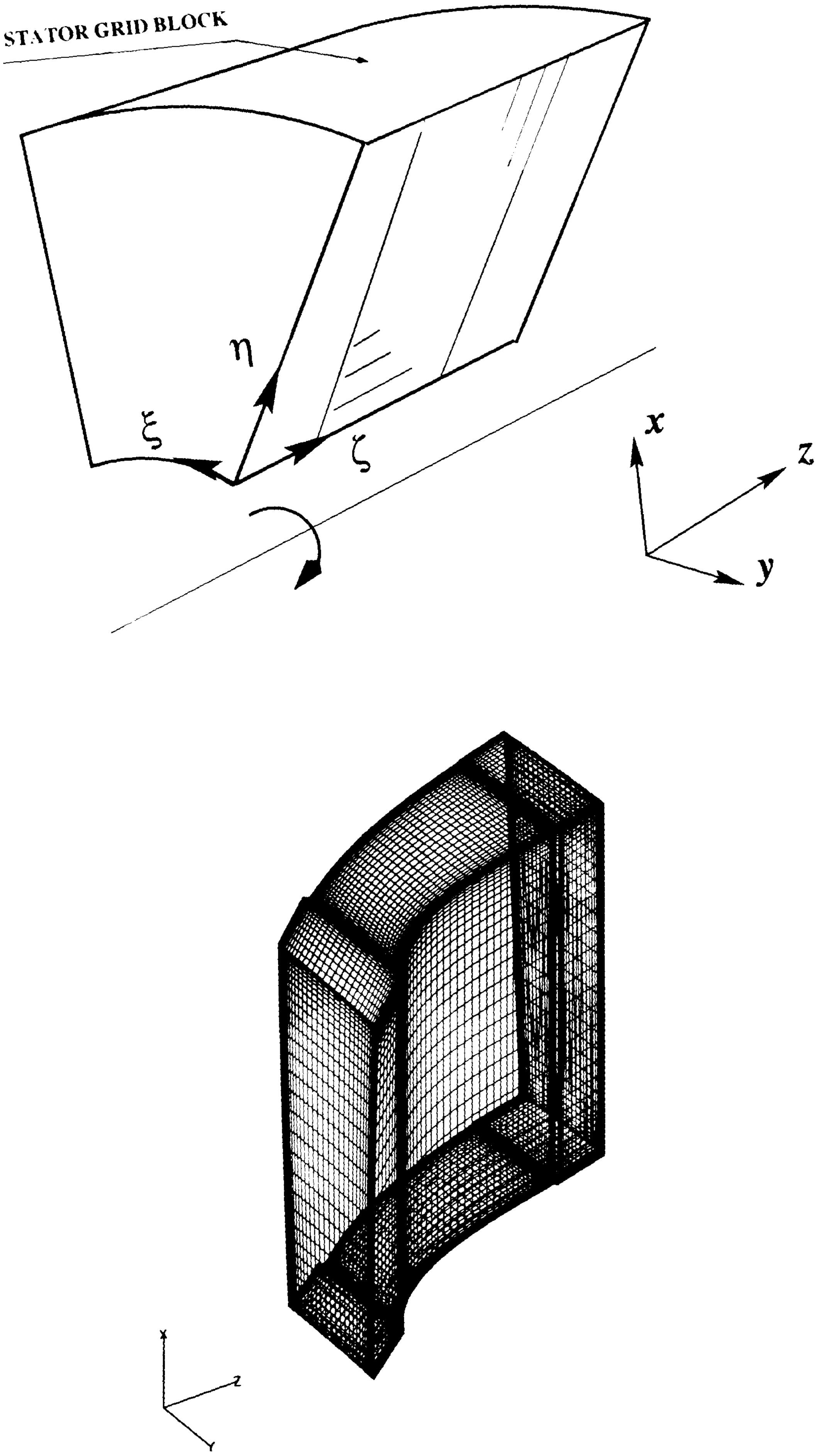

Figure 2.4: **Grid for the third stator of** *LSRC*

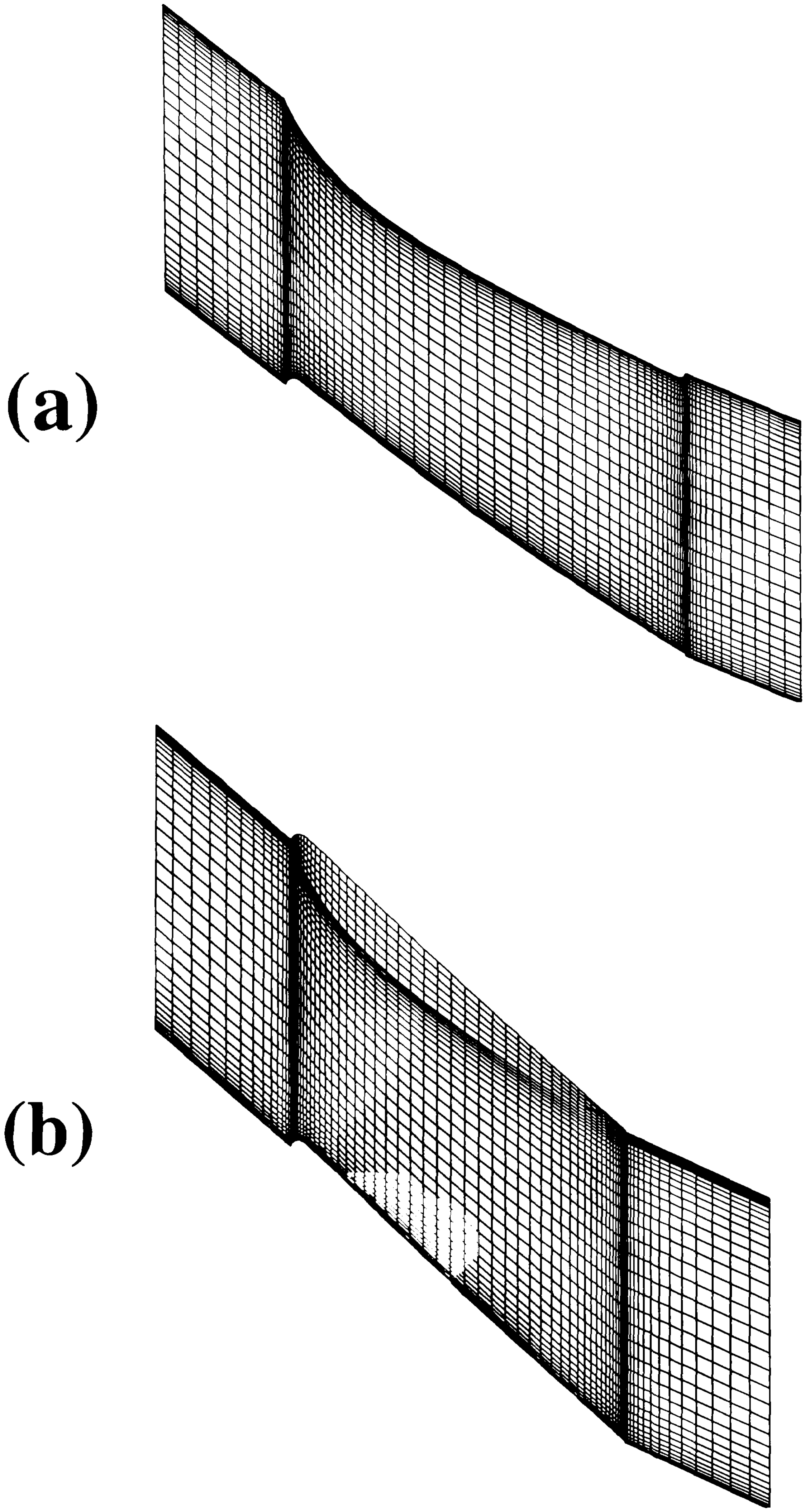

Figure 2.5: **Blade-to-blade view of rotor grid at (a) midspan and (b) inside the tip region**

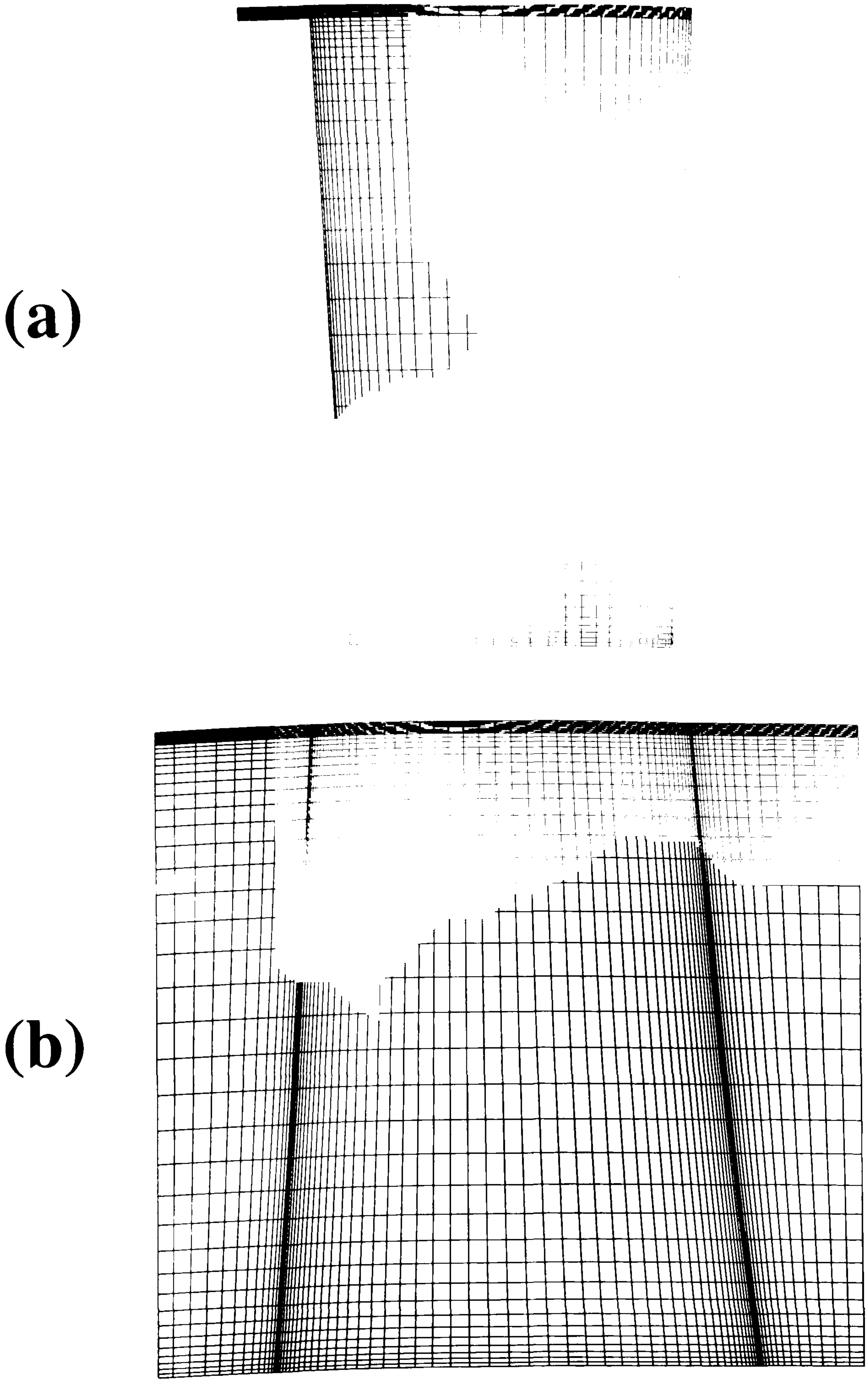

Figure 2.6: **(a) Front view and (b) side view of rotor grid**

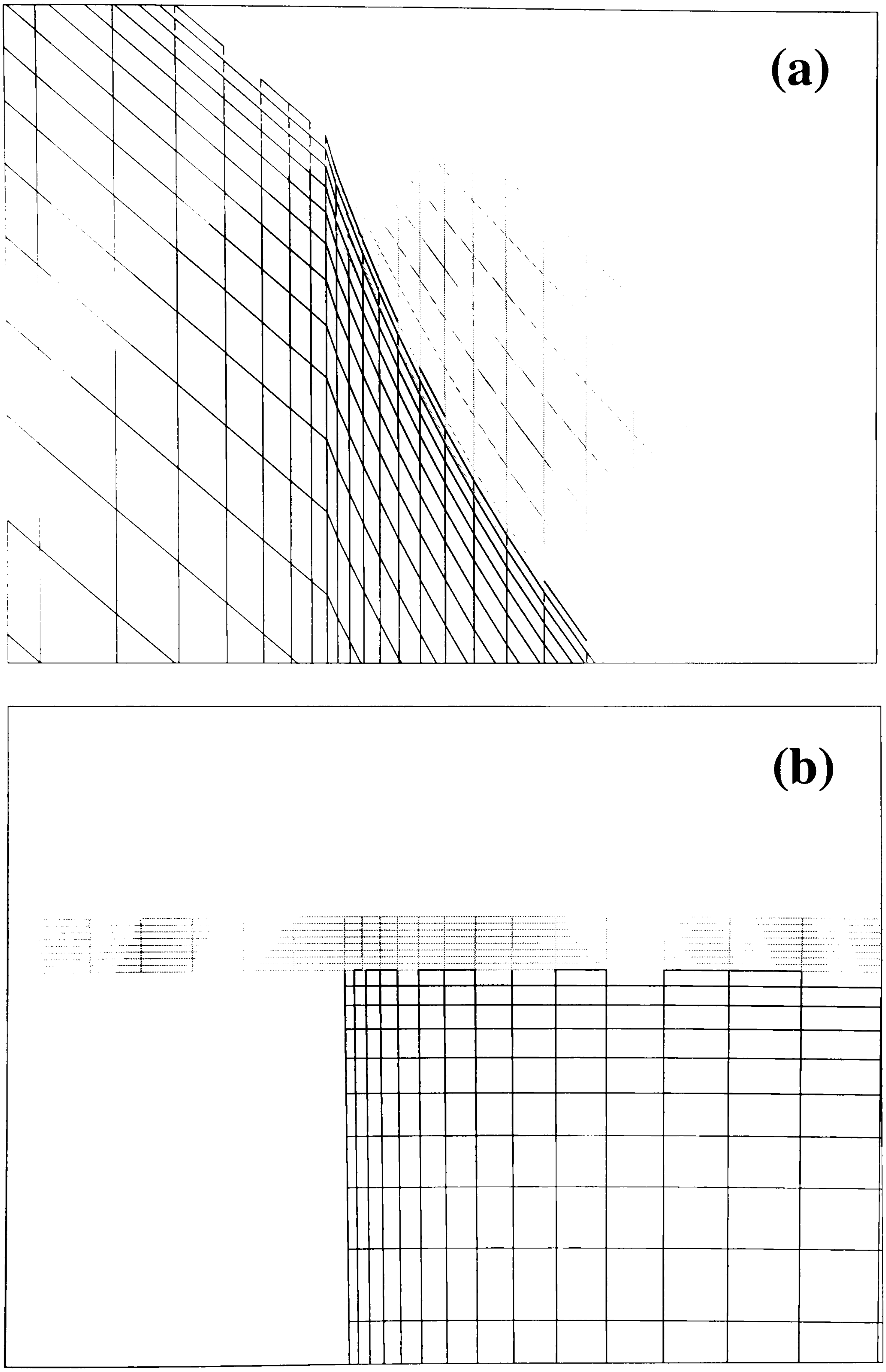

Figure 2.7: **Grid distribution inside the tip region (a) blade-to-blade view; (b) front view**

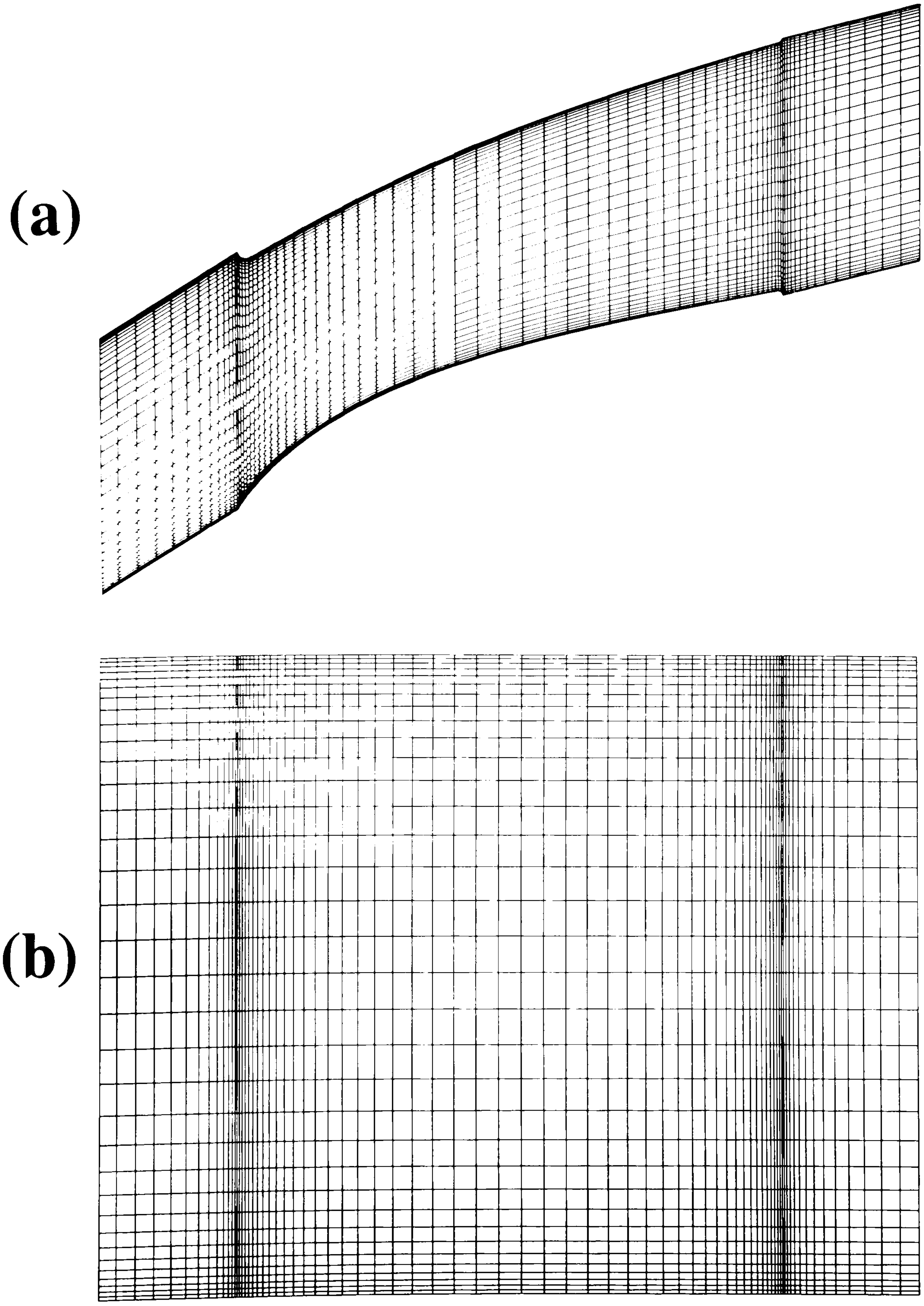

Figure 2.8: (a) **Blade-to-blade view and (b) side view of stator grid**

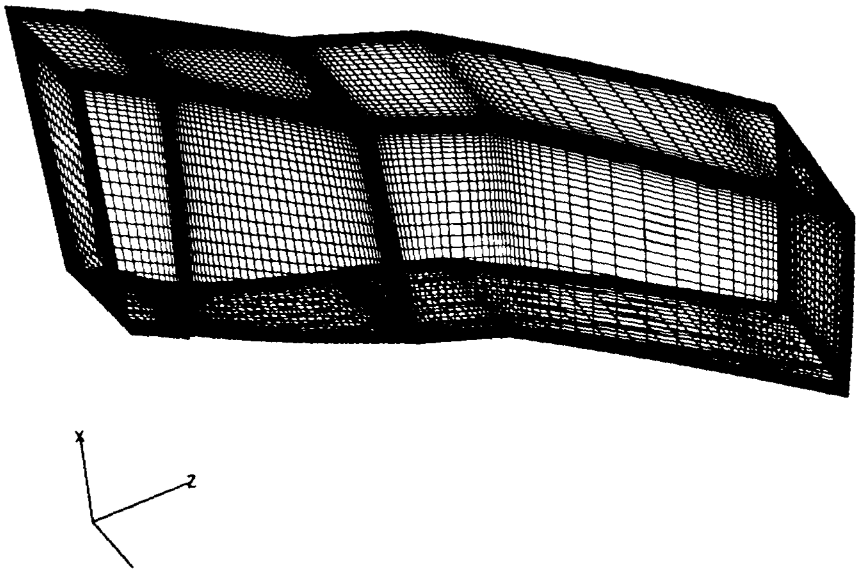

Figure 2.9: **Grids with downstream extension for the third rotor of** *LSRC*

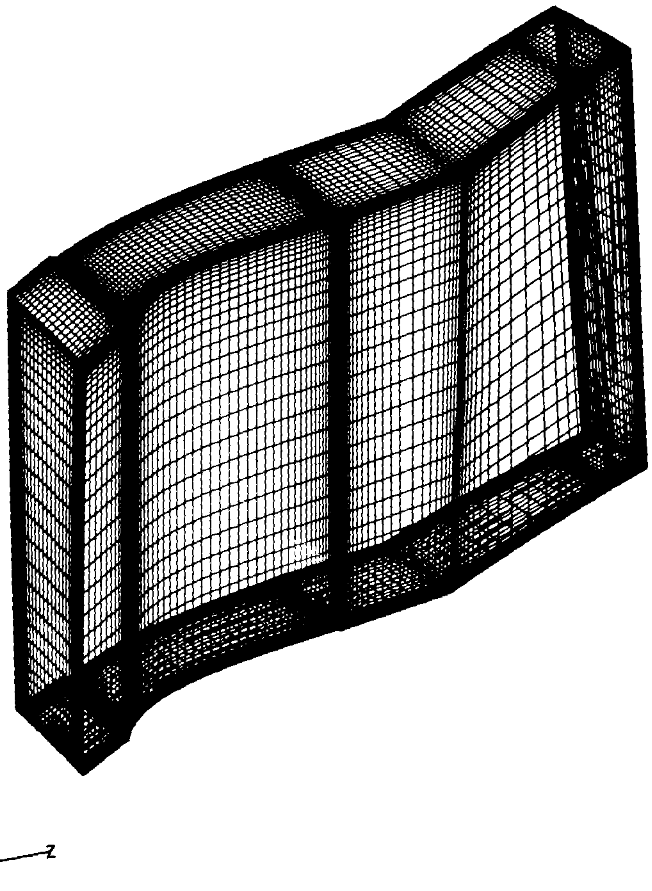

Figure 2.10: **Grids with downstream extension for the third stator of** *LSRC*

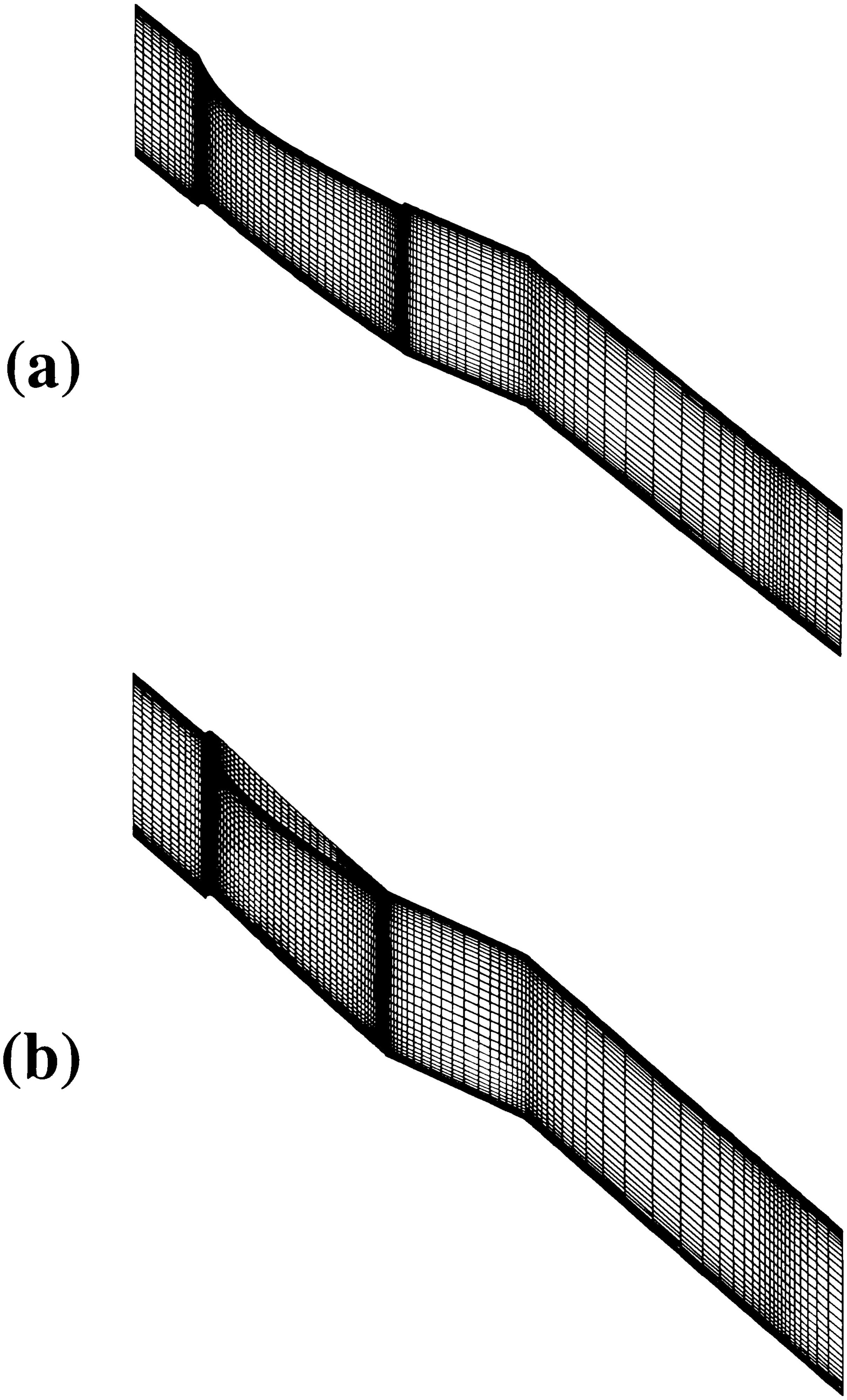

Figure 2.11: **Blade-to-blade view of rotor grid with downstream extension (a) at midspan; (b) inside the tip region**

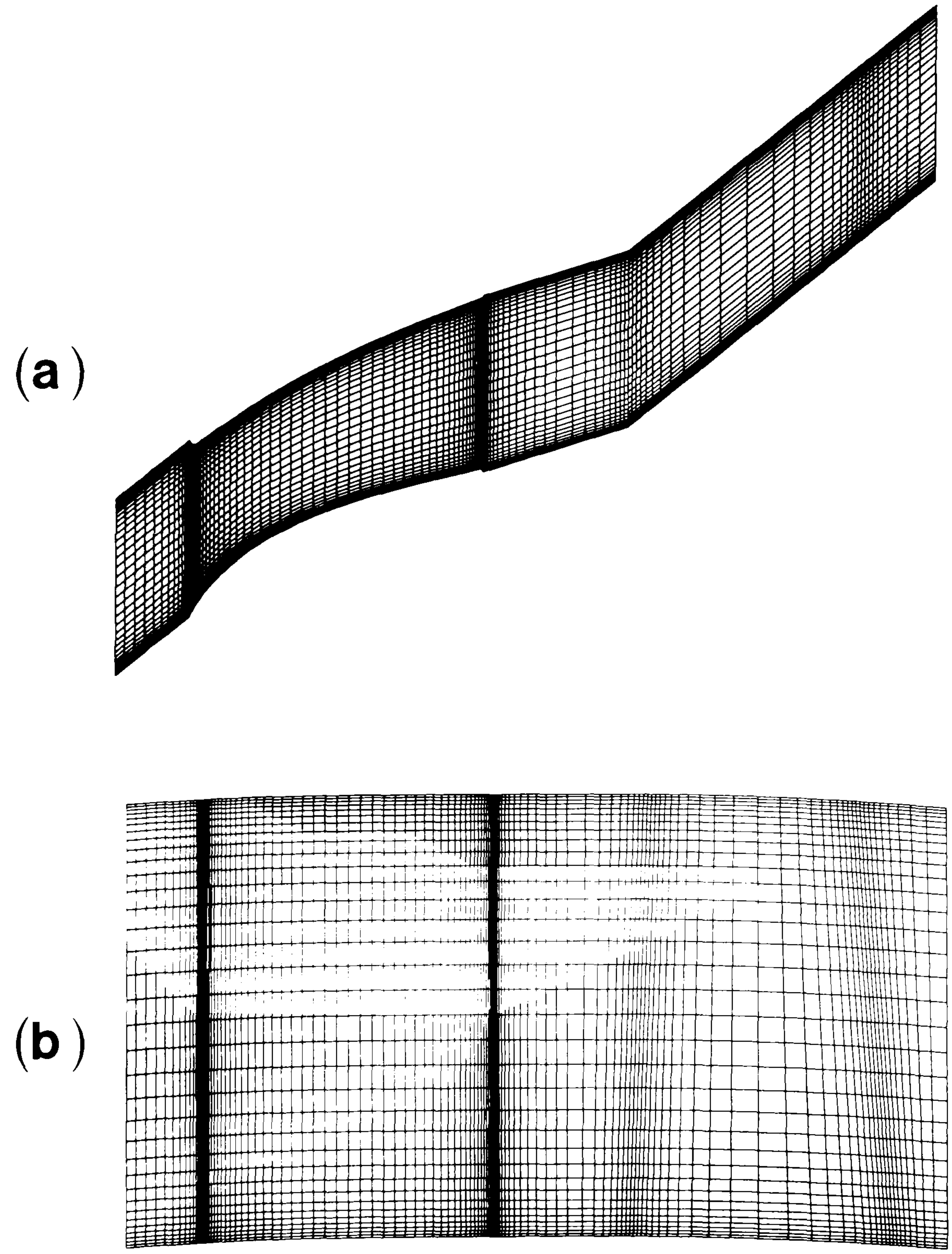

Figure 2.12: **Blade-to-blade view of stator grid with downstream extension (a) blade-to-blade view; (b) side view**

are generated separately when it is supposed that the grid points on each $\xi - \zeta$ plane have the same radius. Then, two-dimensional grids are stacked radially from blade hub to blade tip to form a three-dimensional grid.

In order to control the grid distribution to make it suitable for CFD computation, grid clustering must be considered near boundaries or in the regions where there are large gradients of aerodynamic variables. Many algebraic schemes, such as those described by Hoffmann,K.A. [85], can be introduced for this purpose.

2.4 Results and Discussion

The compressor used in this study is the Cranfield University 4-stage Low Speed Research Compressor (*LSRC*) which is described in detail in Appendix B. For this compressor, it is only necessary to generate grids for a rotor and a stator passages because the compressor has the same geometry for every stage. The grid generation procedure for both the boundary surface and the interior passage were described in the previous sections.

In the rotor passage, a two-block grid system is used in order to describe the geometry of both the main blade passage and the blade tip clearance accurately, Figure 2.3. The pair of grids are H-type grids ending at a common surface, which corresponds to a notional blade-to-blade surface at the blade tip radius. The first grid fills the main passage, defined by two successive blade surfaces, their upstream and downstream extensions, the inner annular wall and the axisymmetric blade-to-blade surface at the blade tip radius. The second grid fills the remaining part of the flow domain, lying between the blade tip radius and the second annulus. This grid covers the full length of the domain and provides the convenience of imposing a periodic boundary condition along its side surface for the CFD computation. The two dimensional blade-to-blade view, front view and side view of the rotor passage grid are shown in Figures 2.5 and 2.6. The $\xi - \zeta$ 2-D grid layout of the tip domain is made identical to that at the same locations in the main passage domain in most area. In the remaining part, the grid line at boundary in the tip domain moves from blade suction side to blade pressure side. More grid lines are introduced in this part and they are linearly distributed in the ξ direction. The difference of the grid distribution of the two grids can be seen in Figure 2.7. Grid clustering is applied to the regions near the walls, inlet, blade leading edge and trailing edge for both grid domains.

In the case of the stator, a single grid block, Figure 2.4, is used as there is no hub clearance in the shrouded stator. The generated H-type grid is similar to that of the main grid in the rotor passage, whose blade-to-blade and side views are shown in Figure 2.8.

In the application of using a deterministic stress model which will be described in Chapter 6, the grids need to be extended further downstream to cover the following blade passage. Under these circumstances, each 2-D grid is extended downstream before stacking, keeping the same radius and following the same ζ grid line direction as that of the upstream blade extension. The three-dimensional grid for the rotor and the stator are shown in Figures 2.9 and 2.10 respectively and the grid distribution in the $\xi - \zeta$ planes for the rotor and the stator passages in this situation are shown in Figures 2.11 and 2.12 respectively.

This set of grid generation tool is relatively simple, but quick and effective to generate grids of computational domains for both rotors and stators of axial flow compressors.

Chapter 3

Governing Equations

3.1 Introduction

The theoretical foundation of Computational Fluid Dynamics (CFD) in turbomachinery is the universal laws of conservation of fluid dynamics :

- Conservation of Mass → Mass Continuity Equation
- Conservation of Momentum (Newton's Second Law) → Momentum Equation
- Conservation of Energy (First Law of Thermodynamics) → Energy Equation

Additionally, the relationship between fluid properties, e.g. the equation of state, which relates pressure (p), density (ρ) and temperature (T), is also necessary in order to close the system of equations. The derivation of the governing equations of fluid dynamics is described in many textbooks (such as Versteeg et al. [180], Anderson [10], Hirsch [79], etc.) and will not be discussed here.

In turbomachinery applications, it is sometimes assumed that the fluid is steady in the relative frame of reference, incompressible and therefore the governing equations can be simplified to be suitable for numerical simulations.

Three averaging operators are applied to the Navier-Stokes equations, Adamczyk [2]. The first averaging operator, referred to as the **ensemble averaging operator**, is introduced to eliminate the need to resolve the structure of turbulent flows and yields the Reynolds-Averaged form of these equations. The second is the **time averaging operator** which is used to average the deterministic unsteady equations in time at every point in space. This operator removes unsteady time scales that are of the order of the period of shaft rotation. The third operator, called the **passage-to-passage averaging operator**, averages out the details of the passage-to-passage variation in the flow field.

In order to treat the fluid flow in turbomachinery with complex geometries, the equations are transformed to a semi-Cartesian form in a generalised non-orthogonal coordinate system.

All the above treatments aim to simplify the description of the actual physical phenomena and the system of governing equations and make major physical processes to be predicted easily. At the same time, they raise closure issues which will be discussed in the next chapter.

3.2 Transformation of Coordinate Systems

To enhance the efficiency and accuracy of numerical schemes and to simplify the implementation of boundary conditions, a general non-orthogonal curvilinear coordinate system is introduced and a transformation from a physical space to a computational space is performed. The computational domain has a rectangular shape which is divided into an equally spaced grid system. In order to solve the governing equations of flow mechanics in the physical space, a transformation of the equations from the physical space into the computational space is required, which is described in detail by Tourlidakis [173].

3.2.1 Relationship Between Two Spaces

A relationship exists between the physical space (x, y, z) and the computational space (ξ, η, ζ) which is as follows:

$$\xi = \xi(x, y, z) \tag{3.1}$$

$$\eta = \eta(x, y, z) \tag{3.2}$$

$$\zeta = \zeta(x, y, z) \tag{3.3}$$

Consider the following differential expressions:

$$d\xi = \xi_x dx + \xi_y dy + \xi_z dz \tag{3.4}$$

$$d\eta = \eta_x dx + \eta_y dy + \eta_z dz \tag{3.5}$$

$$d\zeta = \zeta_x dx + \zeta_y dy + \zeta_z dz \tag{3.6}$$

These three equations can be expressed in a matrix form as:

$$\begin{bmatrix} d\xi \\ d\eta \\ d\zeta \end{bmatrix} = \begin{bmatrix} \xi_x & \xi_y & \xi_z \\ \eta_x & \eta_y & \eta_z \\ \zeta_x & \zeta_y & \zeta_z \end{bmatrix} \begin{bmatrix} dx \\ dy \\ dz \end{bmatrix} \tag{3.7}$$

or

$$\vec{\mathbf{Y}} = \underline{\mathbf{A}}\vec{\mathbf{X}} \tag{3.8}$$

Similarly, the inverse relations between the coordinates of the two spaces are obtained:

$$x = x(\xi, \eta, \zeta) \tag{3.9}$$

$$y = y(\xi, \eta, \zeta) \tag{3.10}$$

$$z = z(\xi, \eta, \zeta) \tag{3.11}$$

and

$$\begin{bmatrix} dx \\ dy \\ dz \end{bmatrix} = \begin{bmatrix} x_\xi & x_\eta & x_\zeta \\ y_\xi & y_\eta & y_\zeta \\ z_\xi & z_\eta & z_\zeta \end{bmatrix} \begin{bmatrix} d\xi \\ d\eta \\ d\zeta \end{bmatrix} \tag{3.12}$$

or

$$\vec{\mathbf{X}} = \underline{\mathbf{\Lambda}}\vec{\mathbf{Y}} \tag{3.13}$$

Therefore, comparing the above expressions,

$$\begin{bmatrix} \xi_x & \xi_y & \xi_z \\ \eta_x & \eta_y & \eta_z \\ \zeta_x & \zeta_y & \zeta_z \end{bmatrix} = \begin{bmatrix} x_\xi & x_\eta & x_\zeta \\ y_\xi & y_\eta & y_\zeta \\ z_\xi & z_\eta & z_\zeta \end{bmatrix}^{-1} \tag{3.14}$$

or

$$\underline{\mathbf{\Lambda}} = \underline{\mathbf{A}}^{-1} \tag{3.15}$$

or

$$\underline{\mathbf{\Lambda}} \cdot \underline{\mathbf{A}} = \mathbf{I} \tag{3.16}$$

where **I** is the unit matrix. From the above relations, a series of relationships between the coordinates in the two spaces are obtained:

$$\xi_x = \frac{y_\eta z_\zeta - y_\zeta z_\eta}{J}, \qquad \xi_y = \frac{x_\zeta z_\eta - x_\eta z_\zeta}{J}, \qquad \xi_z = \frac{x_\eta y_\zeta - x_\zeta y_\eta}{J} \tag{3.17}$$

$$\eta_x = \frac{y_\zeta z_\xi - y_\xi z_\zeta}{J}, \qquad \eta_y = \frac{x_\xi z_\zeta - x_\zeta z_\xi}{J}, \qquad \eta_z = \frac{x_\zeta y_\xi - x_\xi y_\zeta}{J} \tag{3.18}$$

$$\zeta_x = \frac{y_\xi z_\eta - y_\eta z_\xi}{J}, \qquad \zeta_y = \frac{x_\eta z_\xi - x_\xi z_\eta}{J}, \qquad \zeta_z = \frac{x_\xi y_\eta - x_\eta y_\xi}{J} \tag{3.19}$$

where J is the Jacobian of the transformation defined as:

$$J = \frac{\partial(x, y, z)}{\partial(\xi, \eta, \zeta)} = \begin{vmatrix} x_\xi & x_\eta & x_\zeta \\ y_\xi & y_\eta & y_\zeta \\ z_\xi & z_\eta & z_\zeta \end{vmatrix} \tag{3.20}$$

The Jacobian J expresses the ratio of the volume of an element in the physical space to the volume of the element in the computational space, Hoffmann [85] and must obtain non-zero positive values for the transformation without any singularities.

3.2.2 Chain Rule Expressions

The chain rule of partial differentiation provides the following relations between the Cartesian coordinate system and the curvilinear coordinate system for a general scalar variable Φ:

$$\frac{\partial \Phi}{\partial x} = \xi_x \frac{\partial \Phi}{\partial \xi} + \eta_x \frac{\partial \Phi}{\partial \eta} + \zeta_x \frac{\partial \Phi}{\partial \zeta} \tag{3.21}$$

$$\frac{\partial \Phi}{\partial y} = \xi_y \frac{\partial \Phi}{\partial \xi} + \eta_y \frac{\partial \Phi}{\partial \eta} + \zeta_y \frac{\partial \Phi}{\partial \zeta} \tag{3.22}$$

$$\frac{\partial \Phi}{\partial z} = \xi_z \frac{\partial \Phi}{\partial \xi} + \eta_z \frac{\partial \Phi}{\partial \eta} + \zeta_z \frac{\partial \Phi}{\partial \zeta} \tag{3.23}$$

In order to transform the Navier-Stokes equations from the Cartesian coordinate system to the curvilinear coordinate system, another form of chain rule expressions is necessary. In this case, Equation (3.21) may be rearranged to give:

$$\frac{\partial \Phi}{\partial x} = \frac{\partial}{\partial \xi}(\xi_x \Phi) + \frac{\partial}{\partial \eta}(\eta_x \Phi) + \frac{\partial}{\partial \zeta}(\zeta_x \Phi) - \Phi \left(\frac{\partial \xi_x}{\partial \xi} + \frac{\partial \eta_x}{\partial \eta} + \frac{\partial \zeta_x}{\partial \zeta} \right) \tag{3.24}$$

However, it can be proved by a simple expansion that:

$$-\frac{1}{J}\frac{\partial J}{\partial x} = \frac{\partial \xi_x}{\partial \xi} + \frac{\partial \eta_x}{\partial \eta} + \frac{\partial \zeta_x}{\partial \zeta} \tag{3.25}$$

Substituting Expression (3.25) into the previous Equation (3.24) leads to the alternative chain rule expression:

$$\frac{\partial \Phi}{\partial x} = \frac{1}{J}\left[\frac{\partial}{\partial \xi}(J\xi_x \Phi) + \frac{\partial}{\partial \eta}(J\eta_x \Phi) + \frac{\partial}{\partial \zeta}(J\zeta_x \Phi) \right] \tag{3.26}$$

Similarly

$$\frac{\partial \Phi}{\partial y} = \frac{1}{J}\left[\frac{\partial}{\partial \xi}(J\xi_y\Phi) + \frac{\partial}{\partial \eta}(J\eta_y\Phi) + \frac{\partial}{\partial \zeta}(J\zeta_y\Phi)\right] \tag{3.27}$$

$$\frac{\partial \Phi}{\partial z} = \frac{1}{J}\left[\frac{\partial}{\partial \xi}(J\xi_z\Phi) + \frac{\partial}{\partial \eta}(J\eta_z\Phi) + \frac{\partial}{\partial \zeta}(J\zeta_z\Phi)\right] \tag{3.28}$$

The above equations represent the fully conservative form of the chain rule, Lapworth [105].

3.2.3 Generalised Velocity Components

The scaled velocity components U, V, W in general coordinate system are related to the Cartesian velocity components u, v, w by the following relationship:

$$U = J(\xi_x u + \xi_y v + \xi_z w) \tag{3.29}$$

$$V = J(\eta_x u + \eta_y v + \eta_z w) \tag{3.30}$$

$$W = J(\zeta_x u + \zeta_y v + \zeta_z w) \tag{3.31}$$

or in a compact form

$$U^i = J\frac{\partial \xi_i}{\partial x_j}u_j, \qquad (i = 1, 2, 3) \tag{3.32}$$

where index j means a summation for $j = 1, 2, 3$.

The components U, V and W have an important physical meaning, Tourlidakis (1992). In fact, $U/J\sqrt{\xi_x^2 + \xi_y^2 + \xi_z^2}$, $V/J\sqrt{\eta_x^2 + \eta_y^2 + \eta_z^2}$ and $W/J\sqrt{\zeta_x^2 + \zeta_y^2 + \zeta_z^2}$ are the velocities normal to the constant ξ, η and ζ planes respectively. In other words, U, V and W are the contravariant velocity components scaled by the Jacobian of the transformation.

With the definitions, the Cartesian velocity components may be expressed by the inverse relations:

$$u = \frac{1}{J}(x_\xi U + x_\eta V + x_\zeta W) \tag{3.33}$$

$$v = \frac{1}{J}(y_\xi U + y_\eta V + y_\zeta W) \tag{3.34}$$

$$w = \frac{1}{J}(z_\xi U + z_\eta V + z_\zeta W) \tag{3.35}$$

or

$$u_i = \frac{1}{J}\frac{\partial x_i}{\partial \xi_j}U^j, \qquad (i = 1, 2, 3) \tag{3.36}$$

where j means a summation for $j = 1, 2, 3$.

3.3 Governing Equations in Cartesian Coordinate System

The equations that govern the flow mechanics in turbomachinery are the conservation equations for mass, momentum and energy. They are also called the **Navier-Stokes equations**. In order to simplify the solution process, these equations are transformed to a general non-orthogonal curvilinear coordinate system in a relative frame of reference fixed on a rotating passage or in absolute frame of reference on stationery passage and then are averaged with averaging operators, which will be described later in this chapter. Different forms of Navier-Stokes equations are described as follows.

3.3.1 The Conservation Equation for Mass

The conservation of mass expresses that the rate of increase of mass of a fluid element equals the net rate of flow mass into the fluid element. In other words, mass cannot disappear from nor be created in a fluid system. On the other hand, we will not consider multiphase fluids and hence no sources due to chemical reaction will have to be introduced.

The general conservation equation then becomes:

$$\frac{\partial}{\partial t}\int_{V_p} \rho dV_p + \oint_S \rho\vec{\mathbf{V}} \cdot d\vec{\mathbf{S}} = 0 \tag{3.37}$$

and in a differential form:

$$\frac{\partial \rho}{\partial t} + \nabla \cdot (\rho\vec{\mathbf{V}}) = 0 \tag{3.38}$$

In the Cartesian coordinate system, it may be written as:

$$\frac{\partial \rho}{\partial t} + \frac{\partial}{\partial x_j}(\rho v_j) = 0 \tag{3.39}$$

where ρ is the fluid density, $\vec{\mathbf{V}}$ the fluid velocity, S the surface area and V_p the volume of the element. Equations (3.37) to (3.39) are the different forms of the unsteady, three-dimensional mass conservation or continuity equation for a compressible fluid.

3.3.2 The Conservation Equation for Momentum

The Newton's second law of motion states that the rate of change of momentum of a fluid particle equals the sum of the forces exerted on the particle. These forces consist of external volume forces $\vec{\mathbf{f}}_{ext}$ and internal forces $\vec{\mathbf{f}}_{int}$. The former are also called bodyforces such as gravitational force, magnetic force. centrifugal force, etc. The latter are dependent on the nature of the fluid concerned and are applied by the external stresses on the fluid element. The external stresses consist of normal stresses and shear stresses and are expressed by

$$\vec{\mathbf{f}}_{int} = \nabla \cdot \mathbf{\Pi} \tag{3.40}$$

where $\mathbf{\Pi}$ is the stress tensor. The integral form of the momentum conservation equation is

$$\frac{\partial}{\partial t}\int_{V_p}(\rho\vec{\mathbf{V}})dV_p + \int_{V_p}\nabla\cdot\left(\rho\vec{\mathbf{V}}\times\vec{\mathbf{V}}\right)dV_p = \int_{V_p}\rho\vec{\mathbf{f}}_{ext}dV_p + \int_{V_p}\nabla\cdot\mathbf{\Pi}dV_p \tag{3.41}$$

which leads to the differential conservation form of the momentum equation:

$$\frac{\partial}{\partial t}\left(\rho\vec{\mathbf{V}}\right) + \nabla\cdot\left(\rho\vec{\mathbf{V}}\times\vec{\mathbf{V}}\right) = \nabla\cdot\mathbf{\Pi} + \rho\vec{\mathbf{f}}_{ext} \tag{3.42}$$

It is assumed that the fluid is Newtonian, and therefore the stress tensor $\mathbf{\Pi}$ is taken to be:

$$\mathbf{\Pi} = -p\mathbf{I} + \tau \tag{3.43}$$

where $\mathbf{I}$ is the unit tensor. Here the existence of the isotropic pressure component $-pI$ is introduced and τ is the viscous shear stress tensor, equals to

$$\tau = \mu\left[grad\vec{\mathbf{V}} + \left(grad\vec{\mathbf{V}}\right)^T\right] - \frac{2}{3}\mu\left(\nabla\cdot\vec{\mathbf{V}}\right)\cdot\mathbf{I} \tag{3.44}$$

or in the most general form:

$$\tau = \mu\left[grad\vec{\mathbf{V}} + \left(grad\vec{\mathbf{V}}\right)^T\right] + \lambda\left(\nabla\cdot\vec{\mathbf{V}}\right)\cdot\mathbf{I} \tag{3.45}$$

where μ is the dynamic viscosity of the fluid and λ the second viscosity coefficient. μ and λ are related by the Stokes relation:

$$2\mu + 3\lambda = 0 \tag{3.46}$$

The stress tensor component Π_{ij} can also be expressed by

$$\Pi_{ij} = -p\delta_{ij} + \tau_{ij} \qquad (i,j = 1,2,3) \tag{3.47}$$

where δ_{ij} is the Kronecker delta function:

$$\delta_{ij} = \begin{cases} 1, & \text{if } i = j \\ 0, & \text{if } i \neq j \end{cases}$$

and

$$\tau_{ij} = \mu\left[\frac{\partial v_i}{\partial x_j} + \frac{\partial v_j}{\partial x_i}\right] - \frac{2}{3}\mu\delta_{ij}\frac{\partial v_k}{\partial x_k} \qquad (i,j,k = 1,2,3) \tag{3.48}$$

Upon substituting Equations (3.47) and (3.48) into Equation (3.42) and expanding Equation (3.42), the momentum equation in the i–direction becomes:

$$\frac{\partial}{\partial t}(\rho v_i) + \frac{\partial}{\partial x_j}(\rho v_i v_j) = \frac{\partial}{\partial x_j}\left\{\mu\left[\frac{\partial v_i}{\partial x_j} + \frac{\partial v_j}{\partial x_i} - \frac{2}{3}\delta_{ij}\frac{\partial v_k}{\partial x_k}\right]\right\} - \frac{\partial p}{\partial x_i} + \rho f_i \tag{3.49}$$

3.3.3 The Conservation Equation for Energy

The energy equation is derived from the first law of thermodynamics which states that the rate of change of energy of a fluid particle is equal to the rate of heat adding to the fluid particle plus the rate of work done on the particle. In a fluid element the total energy to be considered in the conservation equation is the sum of its internal energy e and its kinetic energy per unit mass $V^2/2$. Therefore, the total energy per unit mass E may be expressed as:

$$E = e + \frac{V^2}{2} \tag{3.50}$$

The energy conservation equation in an integral form is:

$$\begin{gathered}\frac{\partial}{\partial t}\int_{V_p}\rho E\,dV_p + \oint_S\left(\rho E\vec{\mathbf{V}}\cdot d\vec{\mathbf{S}}\right) = \\ \frac{\partial}{\partial t}\int_{V_p} Q\,dV_p - \oint_S \vec{\mathbf{q}}\cdot d\vec{\mathbf{S}} + \int_{V_p} w_f\,dV_p + \oint_S\left(\mathbf{\Pi}\cdot\vec{\mathbf{V}}\right)d\vec{\mathbf{S}}\end{gathered} \tag{3.51}$$

and in a differential form is:

$$\frac{\partial}{\partial t}(\rho E) + \nabla\cdot(\rho\vec{\mathbf{V}}E) = \frac{\partial Q}{\partial t} - \nabla\cdot\vec{\mathbf{q}} + w_f + \nabla\cdot(\mathbf{\Pi}\cdot\vec{\mathbf{V}}) \tag{3.52}$$

The first term on the left-hand side of Equation (3.52) represents the rate of increase of total energy per unit volume in the control volume while the second term represents the rate of total energy lost through convection (per unit volume) through the control volume surface. The first term on the right-hand side of the Equation (3.52) is the rate of heat produced by external sources (i.e. radiation, chemical reactions, etc.) while the second term is the rate of heat lost by conduction (per unit volume) through the control volume surface. Fourier's law for heat transfer by conduction will be assumed so that the heat transfer $\vec{\mathbf{q}}$ can be expressed as

$$\vec{\mathbf{q}} = -k\nabla T \tag{3.53}$$

where k is the thermal conductivity coefficient and T is the absolute temperature. The third term w_f on the right-hand side of Equation (3.52) is the work done on the control volume (per unit volume) by the body forces

$$w_f = \rho \vec{\mathbf{f}}_{ext} \cdot \vec{\mathbf{V}} \tag{3.54}$$

while the fourth term represents the work done on the control volume (per unit volume) by the surface forces. An extra relation is often used to determine the coefficient of thermal conductivity k once μ is known:

$$k = \frac{\mu c_p}{P_r} \tag{3.55}$$

where P_r is the Prandtl number, μ the viscosity and c_p the specific heat at constant pressure.

Substituting Equations (3.43), (3.53) and (3.54) into Equation (3.52) produces:

$$\frac{\partial}{\partial t}(\rho E) + \nabla \cdot (\rho \vec{\mathbf{V}} E) = \frac{\partial Q}{\partial t} + \nabla \cdot (k \nabla T) + \rho \vec{\mathbf{f}}_{ext} \cdot \vec{\mathbf{V}} + \nabla \cdot (\mathbf{\Pi} \cdot \vec{\mathbf{V}}) \tag{3.56}$$

Clarifying the term $\nabla \cdot (\mathbf{\Pi} \cdot \vec{\mathbf{V}})$ in Equation (3.52) and introducing the enthalpy h of the fluid leads to the following alternative expression in a differential form:

$$\frac{\partial(\rho H)}{\partial t} + \nabla \cdot \left(\rho \vec{\mathbf{V}} H\right) = \frac{\partial Q}{\partial t} + \nabla \cdot (k \nabla T) + \rho \vec{\mathbf{f}}_{ext} \cdot \vec{\mathbf{V}} + \frac{\partial p}{\partial t} + \nabla \cdot \left(\tau \cdot \vec{\mathbf{V}}\right) \tag{3.57}$$

where the stagnation, or total, enthalpy H is introduced:

$$H = e + \frac{p}{\rho} + \frac{V^2}{2} = h + \frac{V^2}{2} = E + \frac{p}{\rho} \tag{3.58}$$

3.3.4 Equation of State

In aerodynamics, it is generally reasonable to assume that the fluid is a perfect gas (which assumes that intermolecular forces are negligible). For a perfect gas, the equation of state is

$$p = \rho R T \tag{3.59}$$

where R is the specific gas constant. Additionally for a perfect gas the following relationships are defined:

$$e = C_v T \tag{3.60}$$

$$h = C_p T \tag{3.61}$$

$$C_v = \frac{R}{\gamma - 1} \tag{3.62}$$

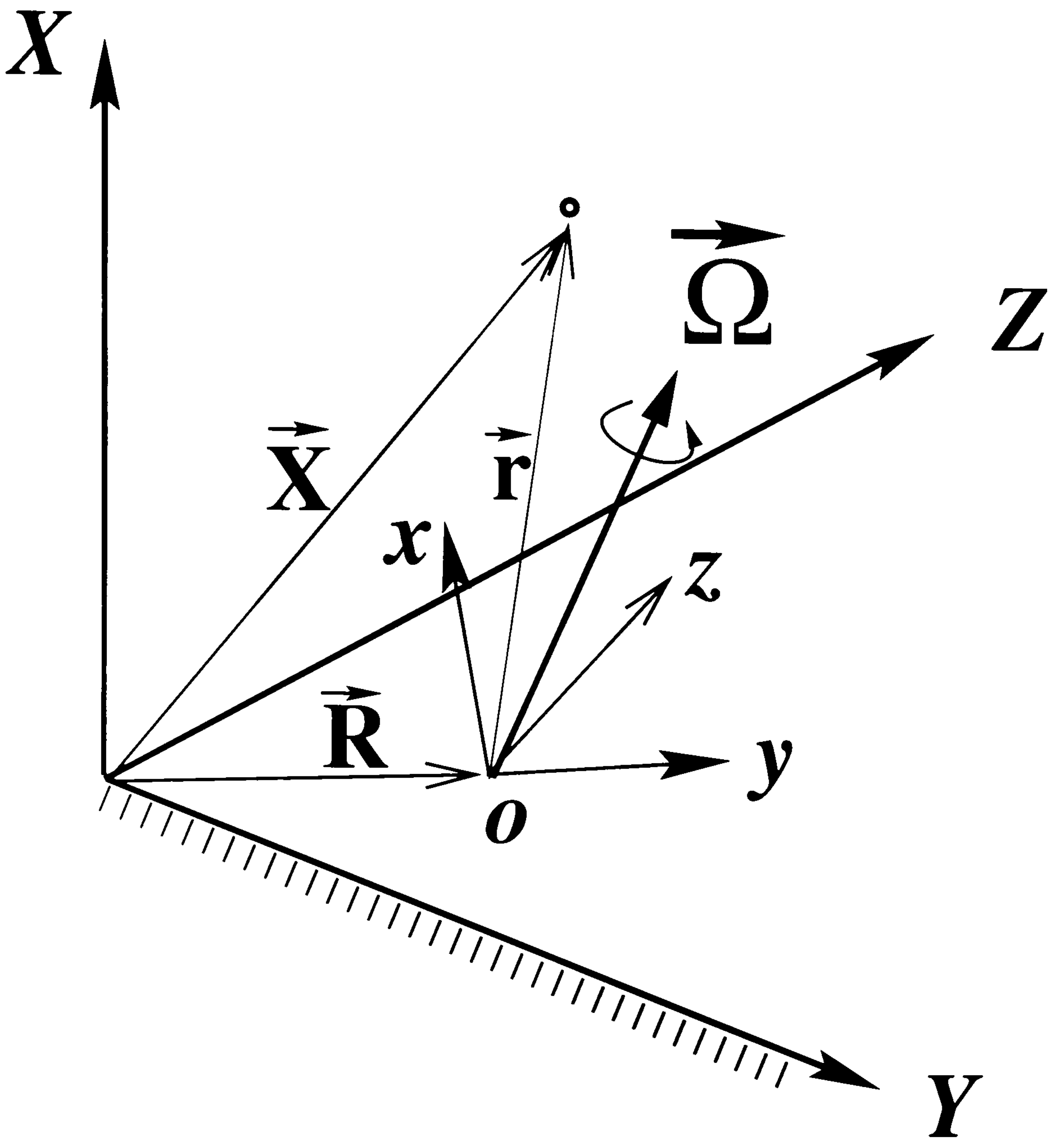

Figure 3.1: **Absolute and relative coordinate systems**

$$C_p = \frac{\gamma R}{\gamma - 1} \tag{3.63}$$

$$\gamma = \frac{C_p}{C_v} \tag{3.64}$$

where C_v is the specific heat at constant volume, C_p is the specific heat at constant pressure and γ is the ratio of specific heats.

3.4 Governing Equations in Rotating Frame of Reference

In turbomachinery applications we have to deal with rotating systems. It is necessary to be able to describe the flow behaviour relative to a rotating frame of reference. Figure 3.1 represents a schematic relation between a stationary and a rotating system. It is assumed that the coordinates z and Z are aligned (so $\vec{\mathbf{R}} = \vec{\mathbf{0}}$) and the moving system (x, y, z) is rotating steadily in the absolute frame of reference (X, Y, Z) with a constant angular velocity $\vec{\boldsymbol{\Omega}}$ around the axis z (or Z), Figure 3.1. Defining $\vec{\mathbf{r}}$ as the position vector of a particle relative to the rotating frame of reference and $\vec{\mathbf{X}}$ as the position vector of the particle relative to the absolute frame of reference. We have

$$\vec{\mathbf{X}} = \vec{\mathbf{r}} \tag{3.65}$$

Defining $\vec{\mathbf{W}}$ as the velocity vector of the particle relative to the rotating system, $\vec{\mathbf{V}}$ as the velocity vector of the particle relative to the absolute frame of reference and $(\vec{\boldsymbol{\Omega}} \times \vec{\mathbf{r}})$ as the entrainment velocity , the composition law holds

$$\vec{\mathbf{V}} = \vec{\mathbf{W}} + \vec{\boldsymbol{\Omega}} \times \vec{\mathbf{r}} \tag{3.66}$$

- **Continuity Equation**
  Since the entrainment velocity does not contribute to the mass balance, the continuity equation remains the same form and can be written in the relative system as:

$$\frac{\partial \rho}{\partial t} + \nabla \cdot (\rho \vec{\mathbf{W}}) = 0 \tag{3.67}$$

- **Momentum Equation**
  The acceleration of the particle relative to the absolute frame of reference is

$$\vec{\mathbf{a}} = \frac{\vec{\mathbf{V}}}{dt} = \frac{d\vec{\mathbf{W}}}{dt} + \frac{d}{dt}(\vec{\boldsymbol{\Omega}} \times \vec{\mathbf{r}}) \tag{3.68}$$

Eventually

$$\vec{\mathbf{a}} = \vec{\mathbf{a}}' + 2\vec{\boldsymbol{\Omega}} \times \vec{\mathbf{W}} + \vec{\boldsymbol{\Omega}} \times (\vec{\boldsymbol{\Omega}} \times \vec{\mathbf{r}}) \tag{3.69}$$

where $\vec{\mathbf{a}}'$ is the acceleration of the particle relative to the rotating frame of reference. $2\vec{\boldsymbol{\Omega}} \times \vec{\mathbf{W}}$ is the Coriolis acceleration due to the motion of the particle within the moving frame and $\vec{\boldsymbol{\Omega}} \times (\vec{\boldsymbol{\Omega}} \times \vec{\mathbf{r}})$ is the centrifugal acceleration due to rotation of the moving frame of reference.

Then the differential form of the conservation law for momentum in the relative frame of reference can be derived according to Newton's Second Law of motion:

$$\frac{\partial}{\partial t}\left(\rho\vec{\mathbf{W}}\right) + \nabla\cdot(\rho\vec{\mathbf{W}}\times\vec{\mathbf{W}}) = -\nabla p + \nabla\cdot\tau + \rho\vec{\mathbf{f}}_{ext} \tag{3.70}$$

The extra two external forces, the Coriolis and centrifugal forces acting on a fluid particle in the rotating system, play a very important role in rotating flows, especially when the velocity vector $\vec{\mathbf{W}}$ has large components in the direction perpendicular to $\vec{\mathbf{\Omega}}$ and other external forces, such as gravity, magnetic force, are neglected. The external forces can then be expressed by

$$\vec{\mathbf{f}}_{ext} = \vec{\mathbf{f}}_C + \vec{\mathbf{f}}_c = -2(\vec{\mathbf{\Omega}}\times\vec{\mathbf{W}}) - \vec{\mathbf{\Omega}}\times(\vec{\mathbf{\Omega}}\times\vec{\mathbf{r}}) \tag{3.71}$$

and their components are

$$f_x = \Omega^2 x + 2\Omega v \tag{3.72}$$

$$f_y = \Omega^2 y - 2\Omega u \tag{3.73}$$

$$f_z = 0 \tag{3.74}$$

- **Energy Equation**

  The energy conservation equation in a relative system with a steady rotation is obtained by adding the work of the centrifugal force, since the Coriolis forces do not contribute to the energy balance of the work.

  The differential conservative form of the equation (Hirsch [79]) is

$$\begin{aligned}\frac{\partial}{\partial t}\rho\left(e+\frac{\vec{\mathbf{W}}^2}{2}-\frac{\vec{\mathbf{V}}^2}{2}\right)+\nabla\cdot\left[\rho\vec{\mathbf{W}}\left(h+\frac{\vec{\mathbf{W}}^2}{2}-\frac{\vec{\mathbf{V}}^2}{2}\right)\right] &= \\ \frac{dQ}{dt}+\nabla\cdot(k\nabla T)+\rho\vec{\mathbf{f}}_{ext}\cdot\vec{\mathbf{W}}+\nabla\cdot(\tau\cdot\vec{\mathbf{W}})\end{aligned} \tag{3.75}$$

3.5 Averaged Forms of Navier-Stokes Equations

The flow field in multistage turbomachinery is extremely complex in terms of vast range of time and length scales, which make the direct numerical simulation practically impossible. The original form of the governing equations which describes the flow mechanics in turbomachinery is also too complicated for practical application. In order to simplify the equation system based on the problems concerned, it is assumed that the flow is incompressible and adiabatic.

One of the practical ways of simplifying the governing equations is to use some kind of approximately averaged set of equations which can be obtained with the following three averaging operators, Adamczyk [2]. The first averaging operator, refered to as the **ensemble averaging** or **Reynolds averaging**, is introduced to eliminate the need to resolve the structure of turbulent flows and yields the Reynolds-averaged form of these equations. The second is the **time-averaging operator** which is used to average the deterministic unsteady equations in time at every point in space. This operator removes unsteady time scales that are of the order of the period of shaft rotation. The third operator, called the **passage-to-passage averaging operator**, averages out the details of the passage-to-passage variation in the flow field.

3.5.1 Original Form of Navier-Stokes Equations

For the problem concerned in the simulation of internal flows in multistage axial flow compressors, the governing equations in general form can be simplified by using a relative frame of reference for rotor blade rows and an absolute frame of reference for stator blade rows. It is supposed that the flows are incompressible and adiabatic for low speed, low pressure ratio axial flow compressors, so the density ρ is constant and the energy equation is not applied in the application.

Under these circumstances, the continuity and the momentum equations in the Cartesian coordinate system are rewritten in a relative frame of reference as follows:

- **Continuity Equation**

$$\frac{\partial \rho}{\partial t}+\frac{\partial(\rho v_j)}{\partial x_j}=0 \tag{3.76}$$

where j is a summation for $j=1,2,3$.

- **i–Momentum Equation**

$$\frac{\partial}{\partial t}(\rho v_i)+\frac{\partial}{\partial x_j}(\rho v_j v_i)=-\frac{\partial p}{\partial x_i}+\frac{\partial}{\partial x_j}\left[\mu\left(\frac{\partial v_j}{\partial x_i}+\frac{\partial v_i}{\partial x_j}\right)-\frac{2}{3}\mu\left(\delta_{ij}\frac{\partial v_k}{\partial x_k}\right)\right]+\rho f_i \tag{3.77}$$

where

$$f_i=-2\varepsilon_{ijk}\Omega_j v_k-(\Omega_n x_n)\Omega_i+(\Omega_m\Omega_m)x_i \tag{3.78}$$

ε_{ijk} is the alternating tensor, which is equal to 1 if ijk is cyclic (123, 231, 312), is -1 if ijk is anti-cyclic (321, 213, 132) and is 0 otherwise; i= 1, 2, 3, corresponding to x, y, z directions; j, k, m and n are summations for each index varying from 1 to 3.

- **General Scalar Equation**

  The continuity and momentum equations all can be expressed in a general form of scalar equation:

$$\frac{\partial}{\partial t}(\rho\Phi) + \frac{\partial}{\partial x_j}(\rho v_j \Phi) = \frac{\partial}{\partial x_j}\left(\Gamma_\Phi \frac{\partial \Phi}{\partial x_j}\right) + S_\Phi \qquad (3.79)$$

  where Φ is a scalar quantity, Γ_Φ is a diffusion coefficient and S_Φ is a source term and has specific meanings for different Φ. It can also be expressed by the following form:

$$\begin{bmatrix} Unsteady \\ term \end{bmatrix} + \begin{bmatrix} Convection \\ terms \end{bmatrix} = \begin{bmatrix} Diffusion \\ terms \end{bmatrix} + \begin{bmatrix} Source \\ terms \end{bmatrix}$$

3.5.2 Ensemble-Averaging Procedure

Turbulent fluid motion is defined as an irregular condition of flow in which the various quantities show a random variation with time and space coordinates, so that statistically distinct average values can be discerned, Hinze [78].

If the value of a variable Φ can be considered as the ensembled mean value $\overline{\Phi}$ plus a fluctuating component about the average Φ', we get

$$\Phi = \overline{\Phi} + \Phi' \qquad (3.80)$$

where the overbar denotes the average value, then by definition

$$\overline{\Phi'} = 0 \qquad (3.81)$$

The variable Φ is the function of time and space. If it is averaged with time at a certain location then:

$$\overline{\Phi}_t(x_0) = \lim_{T\to\infty} \frac{1}{2T}\int_{-T}^{+T} \Phi(x_0, t)dt \qquad (3.82)$$

In the case of a homogeneous turbulence flow field, averaging with respect to space can be considered:

$$\overline{\Phi}_s(t_0) = \lim_{X\to\infty} \frac{1}{2X}\int_{-X}^{+X} \Phi(x, t_0)dx \qquad (3.83)$$

If the flow field is neither steady nor homogeneous, we then speak of an ensemble mean value. In other words, an average is taken over a large number of experiments that have the same initial and boundary conditions.

$$\overline{\Phi}(x_0, t_0) = \frac{\sum_{n=1}^{N} \Phi_n(x_0, t_0)}{N} \tag{3.84}$$

where N is the sample number. The expression (3.84) is suitable for incompressible turbulent flows. For the analysis of a compressible turbulent flow, it is recommended to use a density-weighted average.

Actually, turbulent flow in reality is neither stationary nor homogeneous. So in the application of turbomachinery calculations ensemble averaging is used as the first averaging operator.

When averaging procedures are carried out on products of quantities, the overbars have the following properties:

Let $a = \overline{a} + a'$ and $b = \overline{b} + b'$. Thus

$$\overline{a'} = 0 \qquad \overline{b'} = 0 \tag{3.85}$$

$$\overline{a} = \overline{a} + \overline{a'} \tag{3.86}$$

$$\overline{\overline{a}\,\overline{b}} = \overline{a}\,\overline{b} \tag{3.87}$$

$$\overline{\overline{a}\,\overline{b'}} = \overline{\overline{a'}\,\overline{b}} = 0 \tag{3.88}$$

$$\overline{ab} = \overline{(\overline{a} + a')(\overline{b} + b')} = \overline{a}\,\overline{b} + \overline{a'b'} \tag{3.89}$$

$$\overline{\frac{\partial a}{\partial x}} = \frac{\partial \overline{a}}{\partial x} \tag{3.90}$$

where a, b and x are independent variables. These properties are often taken for granted in deriving the following averaged Navier-Stokes equations.

When the first averaging operator is applied on the Navier-Stokes equations, the derived ensemble averaged equations are as follows:

- **Continuity Equation**

$$\frac{\partial \overline{\rho}}{\partial t} + \frac{\partial}{\partial x_j}(\overline{\rho}\overline{v}_j) = 0 \tag{3.91}$$

- i**–Momentum Equation**

$$\frac{\partial}{\partial t}(\overline{\rho}\overline{v}_i) + \frac{\partial}{\partial x_j}(\overline{\rho}\overline{v}_i\overline{v}_j) = -\frac{\partial \overline{p}}{\partial x_i} + \frac{\partial}{\partial x_j}\left(\overline{\tau}_{ij} - \overline{\rho v_i' v_j'}\right) + \overline{\rho} f_i \tag{3.92}$$

where

$$\overline{\tau}_{ij} = \mu\left(\frac{\partial \overline{v_i}}{\partial x_j} + \frac{\partial \overline{v_j}}{\partial x_i} - \frac{2}{3}\delta_{ij}\frac{\partial \overline{v_k}}{\partial x_k}\right)$$

- **General Scalar Equation**

$$\frac{\partial}{\partial t}\left(\overline{\rho\Phi}\right)+\frac{\partial}{\partial x_j}\left(\overline{\rho v_j\Phi}\right)=\frac{\partial}{\partial x_j}\left(\Gamma_\Phi\frac{\partial\overline{\Phi}}{\partial x_j}-\overline{\rho v_i'\Phi'}\right)+\overline{S}_\Phi \qquad (3.93)$$

The new turbulent quantities, $-\overline{\rho v_i' v_j'}$ produced from the ensemble averaging process, are Reynolds stresses due to the transport of momentum by turbulent fluctuation. In order to close the equation system, an approximate turbulence modelling is required, which will be discussed in Chapter 4.

In some cases, the Equations (3.91) to (3.93) are simplified by ignoring the unsteady terms on the left-hand side of the equations when it is assumed that the unsteady, deterministic flow produced by neighbouring blade rows is not taken into account.

3.5.3 Time-Averaging Procedure

The second operator for averaging in the turbomachinery flow field is the time-averaging operator. This operator is used to average the deterministic unsteady equations in time at every point in space and removes the periodic unsteadiness in the flow field. The definition of this averaging operator is given by the integral:

$$\overline{\overline{\Phi}}=\frac{1}{T}\int_{t_1}^{t_1+T}\overline{\Phi}dt \qquad (3.94)$$

So the ensemble-averaged mean value $\overline{\Phi}$ can be considered as the time-averaged value $\overline{\overline{\Phi}}$ plus a primary time resolved periodic fluctuation $\hat{\overline{\Phi}}$:

$$\overline{\Phi}=\overline{\overline{\Phi}}+\hat{\overline{\Phi}} \qquad (3.95)$$

With this definition, the time-averaged unsteady term in ensemble averaged governing equations in relative frame of reference becomes zero:

$$\overline{\frac{\partial(\overline{\rho}\overline{\Phi})}{\partial t}}=\frac{1}{T}\int_{t_1}^{t_1+T}\left[\frac{\partial(\overline{\rho}\overline{\Phi})}{\partial t}\right]dt=0 \qquad (3.96)$$

Introducing the decomposition Equations (3.94) to (3.96) into Equations (3.91) to (3.93), upon time averaging, results in the following time-averaged form of the Navier-Stokes equations in the relative frame of reference:

- **Continuity Equation**

$$\frac{\partial}{\partial x_j}\left(\overline{\rho}\overline{\overline{v}}_j\right)=0 \qquad (3.97)$$

- **i–Momentum Equation**

$$\frac{\partial}{\partial x_j}(\overline{\bar{\rho}\bar{\bar{v}}_i\bar{\bar{v}}_j}) = -\frac{\partial \bar{\bar{p}}}{\partial x_i} + \frac{\partial}{\partial x_j}\left(\bar{\bar{\tau}}_{ij} - \bar{\rho}\overline{v_i'v_j'} - \overline{\bar{\rho}\hat{\bar{v}}_i\hat{\bar{v}}_j}\right) + \bar{\rho}f_i \qquad (3.98)$$

where

$$\bar{\bar{\tau}}_{ij} = \mu\left(\frac{\partial\bar{\bar{v}}_i}{\partial x_j} + \frac{\partial\bar{\bar{v}}_j}{\partial x_i} - \frac{2}{3}\delta_{ij}\frac{\partial\bar{\bar{v}}_k}{\partial x_k}\right)$$

- **General Scalar Equation**

$$\frac{\partial}{\partial x_j}(\overline{\bar{\rho}\bar{\bar{v}}_j\bar{\bar{\Phi}}}) = \frac{\partial}{\partial x_j}\left(\Gamma_\Phi\frac{\partial\bar{\bar{\Phi}}}{\partial x_j} - \bar{\rho}\overline{v_i'\Phi'} - \overline{\bar{\rho}\hat{\bar{v}}_i\hat{\bar{\Phi}}}\right) + \bar{\bar{S}}_\Phi \qquad (3.99)$$

We can see from Equations (3.97) to (3.99) that the unsteady terms on the left-hand side of the equations have disappeared and instead extra terms, the deterministic unsteady terms, appear on the right-hand side of Equations (3.98) and (3.99). The importance of this change means that a complex unsteady problem now is converted into a relatively simple steady state problem by introducing deterministic unsteady terms into the governing equations.

3.5.4 Passage-to-Passage Averaging Procedure

For a multistage machine in which the number of blades varies from row to row, the steady flow will not, in general, be identical from blade passage to blade passage. In this case, a third averaging operator is introduced and the passage-to-passage average of a variable will in general be different for each blade row. The decomposition of the time averaged variable $\bar{\bar{\Phi}}$ into a passage-to-passage averaged component $\bar{\bar{\bar{\Phi}}}$ and an aperiodic component $\hat{\bar{\bar{\Phi}}}$ is as follows:

$$\bar{\bar{\Phi}} = \bar{\bar{\bar{\Phi}}} + \hat{\bar{\bar{\Phi}}} \qquad (3.100)$$

When the above decomposition is introduced into Equations (3.97) to (3.99), the resultant continuity, momentum and scalar equations become:

- **Continuity Equation**

$$\frac{\partial}{\partial x_j}\left(\overline{\bar{\rho}\bar{\bar{\bar{v}}}_j}\right) = 0 \qquad (3.101)$$

- **i–Momentum Equation**

$$\frac{\partial}{\partial x_j}\left(\overline{\bar{\rho}\bar{\bar{\bar{v}}}_i\bar{\bar{\bar{v}}}_j}\right) = -\frac{\partial\bar{\bar{\bar{p}}}}{\partial x_i} + \frac{\partial}{\partial x_j}\left(\bar{\bar{\bar{\tau}}}_{ij} - \bar{\rho}\overline{v_i'v_j'} - \overline{\bar{\rho}\hat{\bar{v}}_i\hat{\bar{v}}_j} - \overline{\bar{\rho}\hat{\bar{\bar{v}}}_i\hat{\bar{\bar{v}}}_j}\right) + \bar{\rho}f_i \qquad (3.102)$$

where

$$\overline{\overline{\overline{\tau}}}_{ij} = \mu\left(\frac{\partial\overline{\overline{\overline{v}}}_i}{\partial x_j} + \frac{\partial\overline{\overline{\overline{v}}}_j}{\partial x_i} - \frac{2}{3}\delta_{ij}\frac{\partial\overline{\overline{\overline{v}}}_k}{\partial x_k}\right)$$

- **General Scalar Equation**

$$\frac{\partial}{\partial x_j}\left(\overline{\rho\overline{\overline{\overline{v}}}_j\overline{\overline{\overline{\Phi}}}}\right) = \frac{\partial}{\partial x_j}\left(\Gamma_\Phi\frac{\partial\overline{\overline{\overline{\Phi}}}}{\partial x_j} - \overline{\rho v_i'\Phi'} - \overline{\rho\hat{\bar{v}}_i\bar{\hat{\bar{\Phi}}}} - \overline{\rho\bar{\hat{\bar{v}}}_i\hat{\bar{\bar{\Phi}}}}\right) + \overline{\overline{\overline{S}}}_\Phi \qquad (3.103)$$

We can see from Equations (3.102) to (3.103) that extra aperiodic unsteady terms appear on the right-hand side of the equations. In order to model the aperiodic flow features, further techniques need to be investigated to close the equation system, which will not be discussed in this study.

3.6 Governing Equations in General Coordinate System

In general, the Navier-Stokes equations consist of four basic terms: the unsteady term, the convection terms, the diffusion terms and the source terms and their general form of Equation (3.79) is rewritten here for convenience.

$$\frac{\partial}{\partial t}(\rho\Phi) + \frac{\partial}{\partial x_j}(\rho v_j\Phi) = \frac{\partial}{\partial x_j}\left(\Gamma_\Phi\frac{\partial\Phi}{\partial x_j}\right) + S_\Phi(x, y, z) \qquad (3.104)$$

When the governing equations are transformed into a general coordinate system, the unsteady term keeps the same form and the source terms can be transformed with chain rules described in Section 3.2. The transformation of the convection terms and the diffusion terms is more complicated and they are derived in more detail in the following two sections. Subsequently, the governing equations in a general coordinate system are derived.

3.6.1 Convection Terms

The convection terms in Equation (3.104) may be expressed as:

$$\frac{\partial(\rho v_j\Phi)}{\partial x_j} = \frac{\partial}{\partial x}(\rho u\Phi) + \frac{\partial}{\partial y}(\rho v\Phi) + \frac{\partial}{\partial z}(\rho w\Phi) \qquad (3.105)$$

Using the conservative form of chain rule, the expression for the convection terms in a general coordinate system is obtained as:

$$\begin{aligned}\frac{\partial}{\partial x_j}(\rho v_j \Phi) = \; & \frac{1}{J}\frac{\partial}{\partial \xi}\left[J\rho\Phi(\xi_x u + \xi_y v + \xi_z w)\right] + \\ & \frac{1}{J}\frac{\partial}{\partial \eta}\left[J\rho\Phi(\eta_x u + \eta_y v + \eta_z w)\right] + \\ & \frac{1}{J}\frac{\partial}{\partial \zeta}\left[J\rho\Phi(\zeta_x u + \zeta_y v + \zeta_z w)\right]\end{aligned} \tag{3.106}$$

or it can be expressed in a compact form as:

$$\frac{\partial}{\partial x_j}(\rho v_j \Phi) = \frac{1}{J}\frac{\partial}{\partial \xi_j}(\rho U^j \Phi) \qquad (j = 1, 2, 3) \tag{3.107}$$

where

$$U^j = J\frac{\partial \xi_j}{\partial x_k} v_k \qquad j, k = 1, 2, 3$$

3.6.2 Diffusion Terms

The diffusion terms in Equation (3.104) may be expressed as:

$$\frac{\partial}{\partial x_j}\left(\Gamma\frac{\partial \Phi}{\partial x_j}\right) = \frac{\partial}{\partial x}\left(\Gamma\frac{\partial \Phi}{\partial x}\right) + \frac{\partial}{\partial y}\left(\Gamma\frac{\partial \Phi}{\partial y}\right) + \frac{\partial}{\partial z}\left(\Gamma\frac{\partial \Phi}{\partial z}\right) \tag{3.108}$$

In a similar way, the conservative form of chain rule are used in the diffusion terms and gives:

$$\begin{aligned}\frac{\partial}{\partial x_j}\left(\Gamma\frac{\partial \Phi}{\partial x_j}\right) = \; & \frac{1}{J}\frac{\partial}{\partial \xi}\left[J\Gamma\left(\xi_x\frac{\partial \Phi}{\partial x} + \xi_y\frac{\partial \Phi}{\partial y} + \xi_z\frac{\partial \Phi}{\partial z}\right)\right] + \\ & \frac{1}{J}\frac{\partial}{\partial \eta}\left[J\Gamma\left(\eta_x\frac{\partial \Phi}{\partial x} + \eta_y\frac{\partial \Phi}{\partial y} + \eta_z\frac{\partial \Phi}{\partial z}\right)\right] + \\ & \frac{1}{J}\frac{\partial}{\partial \zeta}\left[J\Gamma\left(\zeta_x\frac{\partial \Phi}{\partial x} + \zeta_y\frac{\partial \Phi}{\partial y} + \zeta_z\frac{\partial \Phi}{\partial z}\right)\right]\end{aligned} \tag{3.109}$$

If the Cartesian derivatives of Φ are replaced by non conservative chain rule, the resultant diffusion terms may be written as:

$$\begin{aligned}\frac{\partial}{\partial x_j}\left(\Gamma\frac{\partial \Phi}{\partial x_j}\right) = \; & \frac{1}{J}\frac{\partial}{\partial \xi}\left[J\Gamma\left(g^{11}\frac{\partial \Phi}{\partial \xi} + g^{12}\frac{\partial \Phi}{\partial \eta} + g^{13}\frac{\partial \Phi}{\partial \zeta}\right)\right] + \\ & \frac{1}{J}\frac{\partial}{\partial \eta}\left[J\Gamma\left(g^{21}\frac{\partial \Phi}{\partial \xi} + g^{22}\frac{\partial \Phi}{\partial \eta} + g^{23}\frac{\partial \Phi}{\partial \zeta}\right)\right] + \\ & \frac{1}{J}\frac{\partial}{\partial \zeta}\left[J\Gamma\left(g^{31}\frac{\partial \Phi}{\partial \xi} + g^{32}\frac{\partial \Phi}{\partial \eta} + g^{33}\frac{\partial \Phi}{\partial \zeta}\right)\right]\end{aligned} \tag{3.110}$$

or in a compact form:

$$\frac{\partial}{\partial x_j}\left(\Gamma\frac{\partial\Phi}{\partial x_j}\right) = \frac{1}{J}\frac{\partial}{\partial\xi_j}\left(J\Gamma g^{jk}\frac{\partial\Phi}{\partial\xi_k}\right) \qquad (j,k=1,2,3) \tag{3.111}$$

where the metric components g^{jk} are defined as:

$$g^{11} = \xi_x^2 + \xi_y^2 + \xi_z^2 \tag{3.112}$$

$$g^{22} = \eta_x^2 + \eta_y^2 + \eta_z^2 \tag{3.113}$$

$$g^{33} = \zeta_x^2 + \zeta_y^2 + \zeta_z^2 \tag{3.114}$$

$$g^{12} = g^{21} = \xi_x\eta_x + \xi_y\eta_y + \xi_z\eta_z \tag{3.115}$$

$$g^{13} = g^{31} = \xi_x\zeta_x + \xi_y\zeta_y + \xi_z\zeta_z \tag{3.116}$$

$$g^{23} = g^{32} = \eta_x\zeta_x + \eta_y\zeta_y + \eta_z\zeta_z \tag{3.117}$$

3.6.3 Governing Equations in General Coordinate System

In a more general case, the Navier-Stokes equations in Cartesian coordinate system (3.101) to (3.103) can be transfered to those in a general coordinate system by using the relations (3.107) and (3.111) and the chain rules described in Section 3.2. They may be expressed in the following form:

- **Continuity Equation**

$$\frac{1}{J}\frac{\partial}{\partial\xi_j}\left(J\overline{\rho}\overline{\overline{\overline{V}}}^j\right) = 0 \tag{3.118}$$

- **i–Momentum Equation**

$$\begin{aligned}\frac{1}{J}\frac{\partial}{\partial\xi_j}\left(J\overline{\rho}\overline{\overline{\overline{V}}}^j\overline{\overline{\overline{v}}}_i\right) = & -\frac{1}{J}\frac{\partial}{\partial\xi_j}\left(J\frac{\partial\xi_j}{\partial x_i}\overline{\overline{\overline{p}}}\right)\\ & +\frac{1}{J}\frac{\partial}{\partial\xi_j}\left[J\frac{\partial\xi_j}{\partial x_k}\left(\overline{\overline{\overline{\tau}}}_{ij} - R_{ij}\right)\right] + \overline{\rho}f_i\end{aligned} \tag{3.119}$$

$$R_{ij} = \overline{\rho}\,\overline{v_i'v_j'} + \overline{\overline{\rho}\,\widehat{\overline{v}}_i\widehat{\overline{v}}_j} + \overline{\overline{\rho}\,\widehat{\overline{\overline{v}}}_i\widehat{\overline{\overline{v}}}_j}$$

- **General Scalar Equation**

  With the transformation relations mentioned above, the transformed general transport equation in the curvilinear coordinate system may be written as:

$$\frac{1}{J}\frac{\partial}{\partial\xi_j}\left(\overline{\rho}\overline{\overline{\overline{V}}}^j\overline{\overline{\overline{\Phi}}}\right) = \frac{1}{J}\frac{\partial}{\partial\xi_j}\left(J\Gamma_\Phi g^{jk}\frac{\partial\overline{\overline{\overline{\Phi}}}}{\partial\xi_k}\right) + S_\Phi(\xi,\eta,\zeta) \tag{3.120}$$

where $S_\Phi(\xi, \eta, \zeta)$ are the transformed form of the source terms $S_\Phi(x, y, z)$. Expression (3.120) may also be expressed as:

$$\begin{gathered}\frac{1}{J}\frac{\partial}{\partial \xi_j}\left(\overline{\rho}\,\overline{\overline{\overline{V}}}^{j}\,\overline{\overline{\overline{\Phi}}}\right) = \\ \frac{1}{J}\frac{\partial}{\partial \xi_j}\left(J\Gamma_\Phi g^{jj}\frac{\partial \overline{\overline{\overline{\Phi}}}}{\partial \xi_j}\right) + \left[S_\Phi(\xi, \eta, \zeta) + \frac{1}{J}\frac{\partial}{\partial \xi_j}\left(J\Gamma_\Phi g^{jk}\frac{\partial \overline{\overline{\overline{\Phi}}}}{\partial \xi_k}\right)_{j \neq k}\right]\end{gathered} \tag{3.121}$$

where the non-orthogonal "cross diffusion" terms have been lumped into the source terms. This transformation allows fluid dynamics problems involving complex geometries to be handled in a general and precise manner.

Chapter 4

Closure Modelling Issues

4.1 Introduction

The averaged forms of governing equations derived in Chapter 3 can not be solved directly without further information. In order to close the equation system different numerical models are introduced to provide sufficient information for the total mixing stresses which consist of the Reynolds stresses, stresses generated by an unsteady velocity field linked to the rotational speed and stresses due to the steady, aperiodic velocity field:

$$R_{ij} = \bar{\rho}\overline{v_i' v_j'} + \bar{\rho}\overline{\widehat{\bar{v}}_i \widehat{\bar{v}}_j} + \bar{\rho}\overline{\widehat{\bar{\bar{v}}}_i \widehat{\bar{\bar{v}}}_j} \qquad (i, j = 1, 2, 3) \tag{4.1}$$

Their evaluation, along with the application of overlapped solution domains and mixing planes and the simulation of bodyforce and blade blockage effect, constitutes the closure problems for the equation system in a multistage environment.

In this chapter, different steady state simulation approaches are discussed. When only the turbulent fluctuation is taken into account by ignoring the deterministic and the aperiodic unsteady fluctuations, the flow is assumed to be steady in a relative frame of reference and mixing plane models are introduced to pass information between blade rows to make the multistage simulation of axial flow compressors practicable.

When deterministic unsteady fluctuation is accounted, a deterministic stress model is applied based on the idea of Adamczyk [2]. This approach is more rigorous and also more complicated.

A more rigorous description of the flow in multistage axial flow compressors with a steady state approach should account for the aperiodic unsteady flow. The aperiodic unsteady effect is ignored in the current study because it is much smaller than other unsteady effects and therefore this simplification will not produce obvious error to the predictions.

In addition, repeating stage models are developed in this study and described afterwards. These models effectively simplify the global aerodynamic boundary conditions required for the flow simulation of rear stages of multistage axial flow compressors.

4.2 Turbulence Modelling

The determination of the Reynolds stress term, $-\bar{\rho}\overline{v'_i v'_j}$, is carried out through turbulence models.

The most commonly used turbulence models can be classified in terms of the number of differential equations solved in addition to the mean flow Navier-Stokes equations, Nallasamy [128].

1. Zero equation models
2. One equation models
3. Two equation models
4. Reynolds stress equation models

Most of the models, (1) to (3), use the Boussinesq eddy viscosity model whose concept is based on the assumption that the Reynolds stresses follow the same type of stress-strain relation as in the laminar flow:

$$-\bar{\rho}\overline{v'_i v'_j} = \mu_T\left(\frac{\partial \bar{v}_i}{\partial x_j} + \frac{\partial \bar{v}_j}{\partial x_i} - \frac{2}{3}\delta_{ij}\frac{\partial \bar{v}_k}{\partial x_k}\right) - \frac{2}{3}\bar{\rho}k\delta_{ij} \tag{4.2}$$

$$k = \frac{1}{2}\overline{v'_k v'_k}$$

where μ_T is a turbulent eddy viscosity coefficient and k the turbulent kinetic energy. The advantage of this assumption is that the turbulent flow equations have the same form as the laminar flow equations with the molecular viscosity μ replaced by an effective viscosity

$$\mu_{eff} = \mu + \mu_T$$

Thus, the effects of turbulence are completely simulated by the turbulent viscosity and the system of ensemble averaged Navier-Stokes equations becomes:

- **Continuity Equation**

$$\frac{\partial}{\partial x_j}(\overline{\rho v_j}) = 0 \tag{4.3}$$

- ***i*–Momentum Equation**

$$\frac{\partial}{\partial x_j}(\overline{\rho v_i}\overline{v_j}) = -\frac{\partial \overline{P}}{\partial x_i} + \frac{\partial}{\partial x_j}\tau_{ij} + \overline{\rho} f_i \tag{4.4}$$

where

$$\tau_{ij} = (\mu + \mu_T)(\frac{\partial \overline{v}_i}{\partial x_j} + \frac{\partial \overline{v}_j}{\partial x_i} - \frac{2}{3}\delta_{ij}\frac{\partial \overline{v}_k}{\partial x_k})$$

$$\overline{P} = \overline{p} + \frac{2}{3}\overline{\rho}k$$

This is the easiest closure approach to the ensemble averaged Navier-Stokes equations. Various turbulence models in this group are distinguished from one another by the way the quantities k and μ_T are estimated. The models most frequently used in turbomachinery applications are described below in detail.

4.2.1 Zero Equation Models

Zero equation models are mostly based on the eddy viscosity concept. The first turbulence model proposed is the Prandtl's mixing length hypothesis, Prandtl [142], which employs the eddy viscosity concept to relate the turbulent transport terms to the local gradient of mean flow quantities. With this model, the distribution of the eddy viscosity is calculated with the mean velocity gradient:

$$\mu_T = C_\mu \rho l_m^2 \left|\frac{\partial U}{\partial y}\right| \tag{4.5}$$

where C_μ is a constant. The mixing length l_m whose distribution over the flow field has to be given with the aid of empirical information. The main drawback of this model is the difficulty of the evaluation of l_m for complex flows, such as recirculating flows and 3-D flows. The incorporation of the effects of curvature, buoyancy or rotation in the model is entirely empirical and the transport and history effects of turbulence are not accounted.

The most popular algebraic turbulence model in turbomachinery applications is the Baldwin-Lomax model, Baldwin and Lomax [11]. Application of the Baldwin-Lomax model to turbomachinery flow problems were reported and summarized by Hirsch [80] and Dawes [40]. This model split the boundary layer into an inner region and an outer region, and the mixing length l_m and the eddy viscosity μ_t are calculated in each region with corresponding empirical relations.

Although the models are simple and computationally economical, theoretical and practical difficulties appear when implementing these models in the flow simulations where corner flows exist. It can be considered that algebraic models provide acceptable accuracy for predictions of well-behaved, attached shear layers.

4.2.2 One Equation Models

In one equation turbulence models, the turbulent kinetic energy k is the solution of an equation which can be derived from the Navier-Stokes equations. The earliest One-Equation Model was described by Prandtl [143], Emmons [53] and Glushko [63] and may be expressed as follows:

$$\rho\frac{\partial k}{\partial t} + \rho v_j\frac{\partial k}{\partial x_j} = \tau_{ij}\frac{\partial v_i}{\partial x_j} - C_D\rho\frac{k^{3/2}}{l} + \frac{\partial}{\partial x_j}\left[(\mu + \frac{\mu}{\sigma_k})\frac{\partial k}{\partial x_j}\right] \tag{4.6}$$

where τ_{ij} is the Reynolds stress tensor and μ_T the eddy viscosity modelled by

$$\mu_T = C_\mu \rho k^{\frac{1}{2}} l \tag{4.7}$$

Before the model can be used in applications, the length scale, l, and the closure coefficients σ_k and C_D must be specified.

Bradshaw, Ferriss and Atwell [21] formulated a one equation model that avoids introducing a gradient-diffusion approximation. The model's skin friction for boundary layers in adverse pressure gradient was closest of the various modes tested in the 1968 Conference to measured values, Wilcox [188].

One equation models were also formulated that based on somthing like the kinetic eddy viscosity other than the turbulence kinetic energy, such as a model developed by Nee and Kovasznay [129]. In early 1990's, Baldwin and Barth [12] and Spalart and Allmaras [163] derived more elaborate model equations for the eddy viscosity. The Baldwin-Barth model includes seven closure coefficients, two empirical function and a function describing the turbulence length scale. The Spalart-Allmaras model is also written in terms of the eddy viscosity and includes eight closure coefficients and three functions.

The early one equation model only performs slightly better than the zero equation models. While the improved models by Baldwin and Barth [12] and Spalart and Allmaras [163] show better predictive capability and have achieved closer agreement with measurement than is possible with zero equation models.

4.2.3 Two Equation Models

The two equation models are widely used in engineering applications. The first attemp to apply the two-equation $k - \epsilon$ model to turbomachinery flows was pioneered by Hah [71]. Application of the $k - \epsilon$ model to various turbomachinery flows, such as subsonic turbine blade and a transonic compressor, were performed by Matuso [121], and Jennions and Turner [94]. The idea of the models is to introduce another differential equation for the calculation of the turbulence length scale in addition to the transport equation for the turbulent kinetic energy.

The length scale equation can, in principle, be derived from the Navier-Stokes equations. Basically, three kinds of two equation models were proposed: $k - kl$, $k - \omega$ and $k - \epsilon$ models, Launder and Spalding [106]. Here l is a length representing the macroscale of turbulence which may be defined in terms of k, ϵ and a constant C_D through

$$l = C_D k^{\frac{3}{2}}/\epsilon \qquad (4.8)$$

where ϵ is the dissipation rate of the turbulence kinetic energy defined as

$$\epsilon = \frac{\mu}{\rho} \overline{\frac{\partial v_i'}{\partial x_j} \frac{\partial v_i'}{\partial x_j}} \qquad (4.9)$$

ω is a quantity having the dimension of $(\mathrm{time})^{-2}$ and can be defined in terms of k, ϵ and C_D:

$$\omega = \epsilon^2/(C_D k)^2 \qquad (4.10)$$

The above definitions imply that:

$$\frac{d(kl)}{kl} = \frac{5}{2}\frac{dk}{k} - \frac{d\epsilon}{\epsilon} \qquad (4.11)$$

$$\frac{d\omega}{\omega} = -2\frac{dk}{k} + 2\frac{d\epsilon}{\epsilon} \qquad (4.12)$$

With these equations, the three models are closely related to one another and it is possible to transform one pair of equations into another. However, the $k - \epsilon$ model becomes the most popular because of the advantage that the ϵ-equation requires no extra terms near walls. In addition, ϵ itself appears in the k-equation and the ϵ-equation requires no secondary source term. Hence, only the $k - \epsilon$ model is described in detail here.

The standard $k - \epsilon$ model, Launder and Spalding [106], employs eddy viscosity and relates it to k and ϵ:

$$\mu_T = C_\mu \rho \frac{k^2}{\epsilon} \qquad (4.13)$$

The two model equations at high Reynolds numbers, one for turbulent kinetic energy and the other for its dissipation rate are given below:

- **Kinetic energy equation**

$$\frac{\partial(\rho \overline{v}_j k)}{\partial x_j} = \frac{\partial}{\partial x_j}(\frac{\mu_T}{\sigma_k}\frac{\partial k}{\partial x_j}) + G_k - \rho\epsilon + G_c \tag{4.14}$$

- **Kinetic energy dissipation rate equation**

$$\frac{\partial(\rho \overline{v}_j \epsilon)}{\partial x_j} = \frac{\partial}{\partial x_j}(\frac{\mu_T}{\sigma_\epsilon}\frac{\partial \epsilon}{\partial x_j}) + \frac{\epsilon}{k}(C_1 G_k - C_2\rho\epsilon + G_c) \tag{4.15}$$

where G_k is the generation rate of turbulence obtained by

$$G_k = \mu_T(\frac{\partial \overline{v}_i}{\partial x_j} + \frac{\partial \overline{v}_j}{\partial x_i})\frac{\partial v_i}{\partial x_j} \tag{4.16}$$

The constants in these equations have been found to take the following values:

$$C_\mu = 0.09, \qquad C_1 = 1.44, \qquad C_2 = 1.92, \qquad \sigma_k = 1.0, \qquad \sigma_\epsilon = 1.3$$

However, these constants need to be changed in order to accommodate effects such as curvature, low Reynolds number, near wall, etc.

4.2.4 Other Models

The two equation models which have been used extensively have their own limitations. The major limitation is the assumption of isotropic eddy viscosity. The same value of μ_T are taken for different $\overline{\rho v_i' v_j'}$ terms. In order to account for the different development of the individual stresses and additional effects, such as curvature and rotation, more advanced turbulence models such as Reynolds Stress Transport Equation models ($RSTE$) and the Large Eddy Simulation (LES) have been introduced. One of the successful Reynolds stress models is due to Rodi [149], who provided an algebraic equation for the Reynolds stresses. The algebraic Reynolds stress model in conjection with the $k-\epsilon$ turbulence model captured rotation and curvature effects, Lakshminarayana [104]. More recently, a turbulent potential model was developed by Tsuei et al. [176] based on the ealier work of Perot et al.[137] and Perot [138], and was implemented into a turbomachinery CFD solver and indicated more benefits than the two widely used turbulence models, the Baldwin-Lomax model and the two equation $k-\epsilon$ model, in their calculations. Unfortunately, the advanced turbulence models still lack universal validity and are in the academic development stage. They suffer from many limitations and lead to a significant increase in computer time. Even so, their application for turbomachinery flows might provide more reliable turbulence modelling in the future. Hirsch [80].

4.3 Wall Function

In a turbulent flow, the flow close to a wall is dominated by viscous effects and the flow properties in boundary layers change steeply. This makes the treatment of wall boundaries more complicated. A detailed description of turbulent boundary layers would require prohibitively large number of grid points. Normally, the "wall function" is employed to represent the effect of the wall boundaries and link the solution in the interior of the domain to the near wall region and avoid the use of a fine grid.

According to Versteeg et al. [180] and Tourlidakis [173], a turbulent boundary layer adjacent to a solid surface is composed of two regions: the inner region which occupies 10% to 20% of the total thickness of the wall layer and the outer region or law-of-the-wake layer occupying the rest of the wall layer which is an inertia-dominated core flow far from the wall. Normally, only the flow behaviour in the inner region is simulated with the "wall function" approach as the control volumes closest to the wall are chosen to be within that region. In the inner region, it is supposed that the mean flow velocity U_p only depends on the distance from the wall y, fluid density ρ, viscosity μ and the wall shear stress τ_w:

$$U_p = f(y, \rho, \mu, \tau_w) \tag{4.17}$$

Dimensional analysis show that

$$u^+ = \frac{U_p}{u_\tau} = f(y^+) \tag{4.18}$$

where

$$y^+ = \frac{\rho u_\tau y}{\mu} \tag{4.19}$$

and u_τ is called friction velocity and defined as

$$u_\tau = \sqrt{\frac{\tau_w}{\rho}} \tag{4.20}$$

Expression (4.18) is called **the law of the wall.**

Within the inner region there are three zones (Figure 4.1):

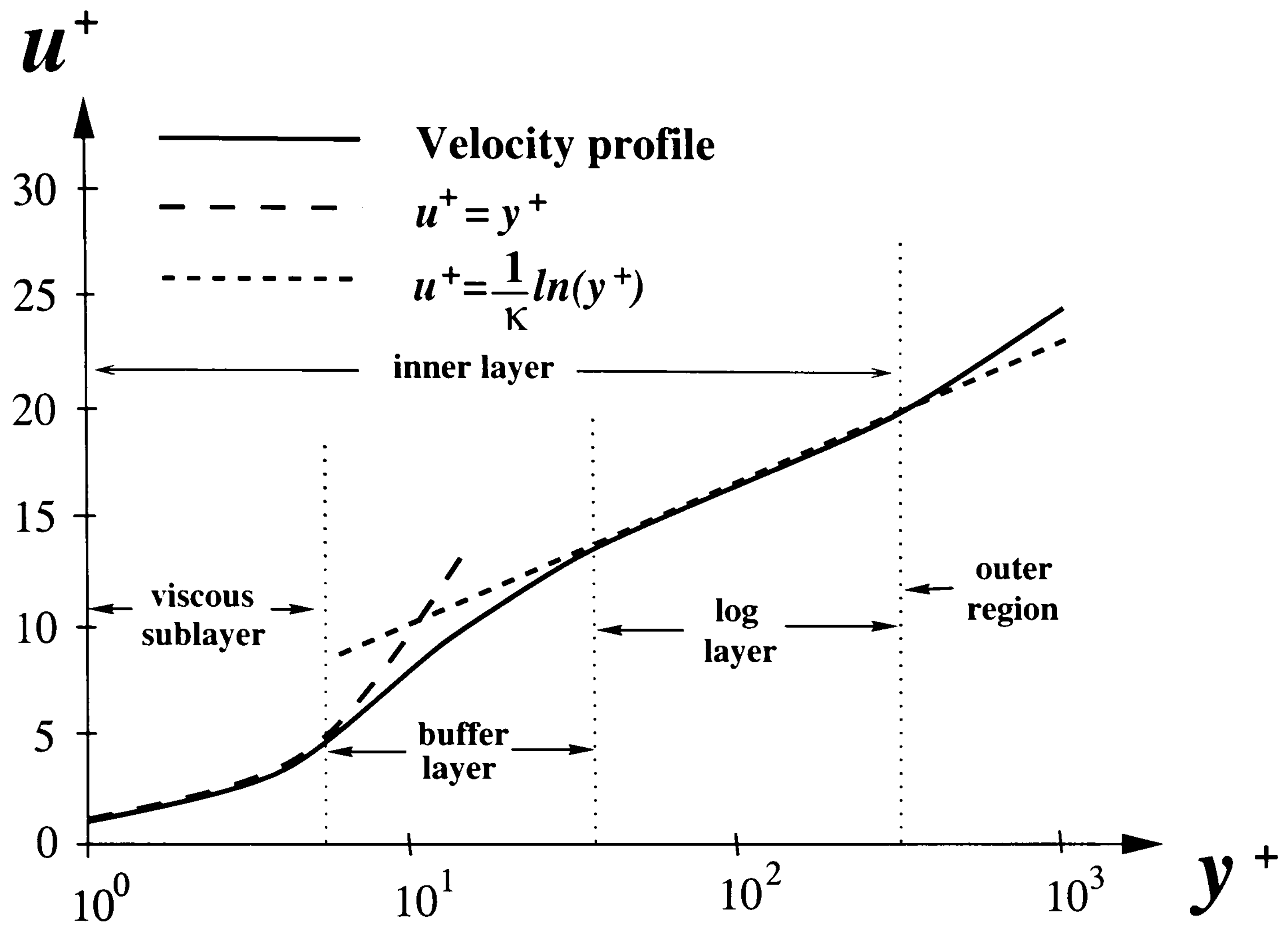

Figure 4.1: **Typical turbulent boundary-layer velocity profile [162]**

- **The Linear Sub-layer**

  At the solid surface the fluid is stationary. In the absence of a turbulent shear stress effect the fluid closest to the wall is dominated by viscous shear. This layer is in practice extremely thin ($y^+ \leq 3$) and we may assume that the shear stress is approximately constant and equal to the wall shear stress τ_w throughout the layer. The following relationship is used to describe the layer:

$$u^+ = y^+ \tag{4.21}$$

- **Log-Law Layer**

  This region ($50 \leq y^+ < 500$) is fully turbulent and dominated by turbulent (Reynolds) stresses. A functional relationship between u^+ and y^+ is used to describe the layer:

$$u^+ = \frac{1}{\kappa}\ln(Ey^+) \tag{4.22}$$

  where κ is Von Karman's constant and equals to 0.41, E is a function of the wall roughness and found to be 9.0 for smooth walls.

- **The buffer Layer**

  This region exists between the linear sub-layer and the Log-law layer, where viscous and turbulent stresses are of similar magnitude. There is a smooth change of the velocity profile in the region. In an engineering application, this layer is ignored and a transition point is found to be at $y^+ \approx 11.5$ to join the linear sub-layer and the Log-law layer.

So in the near wall region, the flow is taken to be laminar if $y^+ \leq 11.5$ and the wall shear stress is assumed to be entirely viscous in origin. If $y^+ > 11.5$ the flow is turbulent and the wall function is used. The relationship between u^+ and y^+ is re-written as follows

$$u^+ = \begin{cases} y^+ & \text{if } y^+ \leq 11.5 \\ \dfrac{1}{\kappa}\ln(Ey^+) & \text{if } y^+ > 11.5 \end{cases} \tag{4.23}$$

The wall force is extended into the discretised momentum equations as sources. The detailed description is stated below.

- <u>**Laminar Flow/Linear Sub-layer**</u>

  In the near wall region when $y^+ \leq 11.5$ the near wall flow is taken to be laminar. The definition of the friction velocity u_τ yields

$$\tau_w = \rho u_\tau^2 \tag{4.24}$$

With the definition of u^+ (4.18) and y^+ (4.19) and Expression (4.21) we get

$$\tau_w = \frac{\mu U_p}{y} \tag{4.25}$$

The shear force F_s is now given by

$$F_s = -\tau_w A_{cell} = -\mu \frac{U_p}{y} A_{cell} \tag{4.26}$$

where A_{cell} is the wall surface area of the control volume.

- <u>**Turbulent Flow**</u>

  If the value of y^+ is greater than 11.5 the flow is considered to be turbulent.

  In the $k - \epsilon$ model, it is assumed that the generation of turbulence kinetic energy k is in equilibrium with the dissipation of turbulence kinetic energy ϵ and the expression of the friction velocity is given through the following expression:

$$u_\tau^2 = k\sqrt{C_\mu} \tag{4.27}$$

Then, substituting the equation (4.27) and (4.20) into (4.18) and (4.19) yields

$$u^+ = \frac{\rho U_p C_\mu^{\frac{1}{4}} k^{\frac{1}{2}}}{\tau_w} \tag{4.28}$$

$$y^+ = \frac{\rho C_\mu^{\frac{1}{4}} \sqrt{k} y}{\mu} \tag{4.29}$$

Substituting Equations (4.29), (4.22), (4.18), (4.27) into (4.20), we get

$$\tau_w = \frac{\kappa C_\mu^{\frac{1}{4}} \sqrt{k} \rho U_p}{\ln(E C_\mu^{\frac{1}{4}} \sqrt{k} \rho y/\mu)} \tag{4.30}$$

The shear force F_s is now expressed by

$$F_s = -\tau_w \cdot A_{cell} = -\frac{\kappa C_\mu \frac{1}{4} \sqrt{k} \rho U_p}{\ln(E C_\mu^{\frac{1}{4}} \sqrt{k} \rho y/y)} A_{cell} \tag{4.31}$$

4.4 Mixing Plane Models

4.4.1 Introduction

The mixing plane model is one of the practical ways of predicting flows in multistage axial flow compressors. The idea of this approach is to simulate multistage turbomachinery flows with the ensemble averaged Navier-Stokes equations by taking into account only turbulent fluctuations. Other unsteady effects, the deterministic and aperiodic unsteady fluctuations, are ignored. It is also assumed that the flow is steady in the relative frame of reference in rotors and in the absolute frame of reference in stators, and therefore the unsteady terms in Navier-Stokes equations disappear. Separate flow simulations can be carried out in computational domains for each blade passage by appropriately setting boundary conditions. Hence, difficulties arise on how to pass information between the two frames of reference with relative rotation and maintain consistency of variables at interfaces.

The first mixing plane model for multi-blade row calculation was introduced by Denton and Singh [50] where aerodynamic information is circumferentially area averaged and passed across a mixing plane to the next blade row. The disadvantage of this model is that the averaging process loses a lot of information and causes errors to the predictions. In order to overcome the above problem, a circumferentially non-uniform mixing plane model was proposed by Denton [47] where both radial and circumferential variations exist on both sides of the mixing planes.

It is obvious that the circumferentially non-uniform mixing plane model is better than the circumferentially uniform mixing plane model. However in some situations when the circumrefentially non-uniform mixing plane model is difficult to apply, such as the transformation of velocity field, the uniform mixing plane model is an effective alternative. Because of this both models are used in the calculations.

4.4.2 Uniform Mixing Plane Model

In this model, a mixing plane is chosen to be located at an axial position approximately halfway between two neighbouring blade rows. Since the flow through two blade rows in relative rotation is inevitably unsteady, the unsteady effects of the real flow are removed through circumferential averaging so the upstream row sees a circumferentially uniform downstream boundary condition and the downstream row sees a circumferentially uniform upstream flow approaching it. This averaging process must, as a minimum, ensure conservation of the mass flow rate, Dawes [41]. It is important to note that although the circumferential information is smeared, the radial variation exists.

The circumferential averaging process may be carried out with area averaging by

$$\overline{\Phi}_a = \frac{\int \Phi r dr d\theta}{\int r dr d\theta} \tag{4.32}$$

or mass averaging by

$$\overline{\Phi}_m = \frac{\int \Phi \rho w r dr d\theta}{\int \rho w r dr d\theta} \tag{4.33}$$

where Φ is a flow parameter, ρ the density, w the axial velocity, r the radius and θ the tangential angle of a control volume, Figure 4.2.

This averaging process is not a physically realistic process unless the blade rows are widely spaced, and can lead to unrealistic predictions of the flow in the regions close to the leading and trailing edges. In other words, the circumferentially uniform flow may be forced to exist too close to the leading edge of the downstream blade row and not allow the flow to adjust circumferentially to the presence of the blade as it would in reality. As a result the leading edge loading on the blade row may be wrong and may even be physically unrealistic. The magnitude of this problem depends on the leading edge loading and thickness and on how close the leading edge is to the mixing plane. A similar problem occurs at the trailing edge of the blade row upstream of the downstream mixing plane, but for subsonic exit

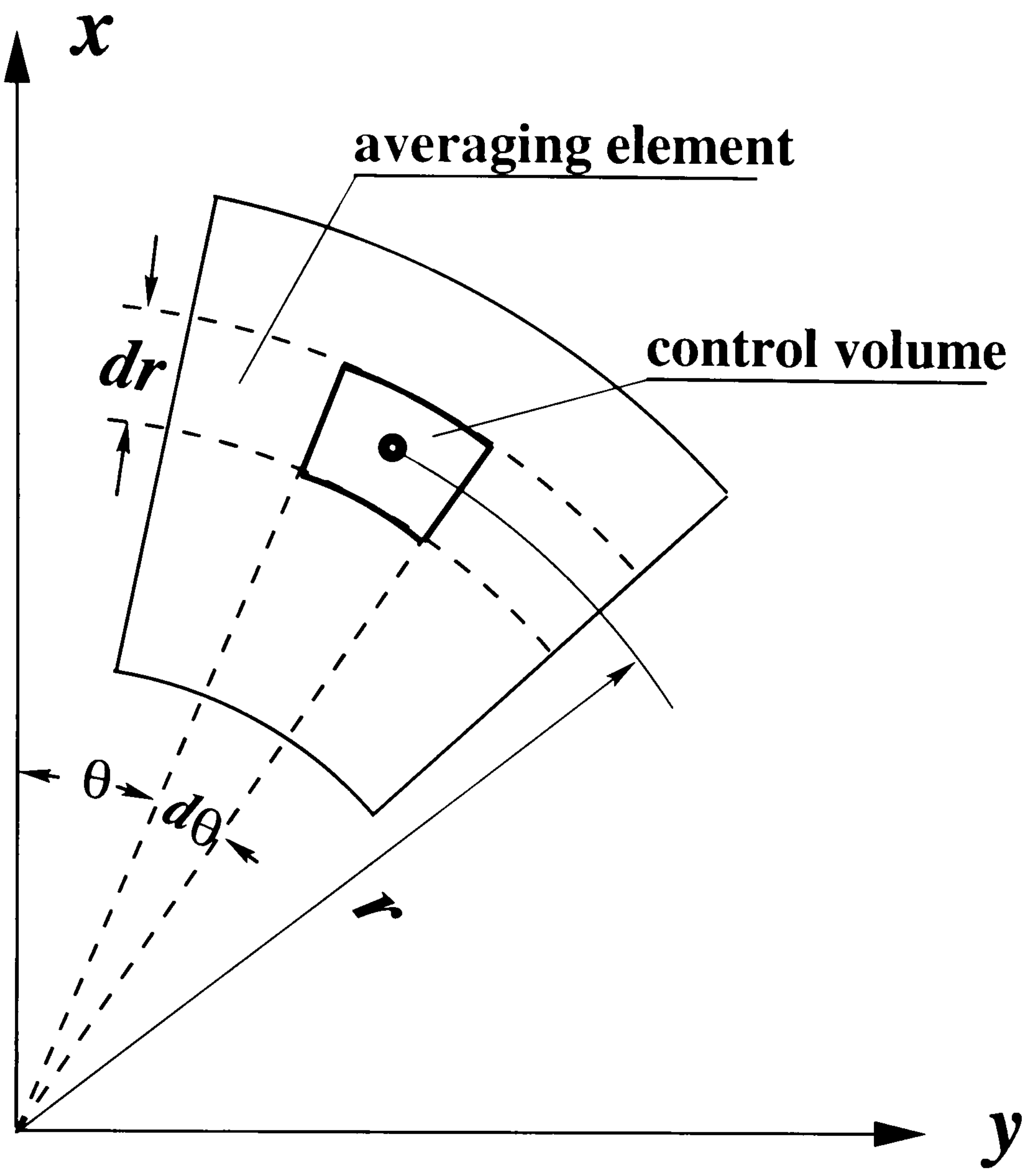

Figure 4.2: **Circumferential averaging element**

flows the problem is not so serious. In this study, the uniform mixing plane model is used to pass velocity profiles across mixing planes.

4.4.3 Non-Uniform Mixing Plane Model

In order to relieve the problem mentioned above, a circumferentially non-uniform mixing plane model is introduced, Denton [47]. The method may be briefly described as obtaining the circumferential variation of fluxes at the mixing plane by extrapolation from the upstream and downstream planes while adjusting the level of the fluxes to satisfy overall conservation. Thus the fluxes "seen" by the blade rows are circumferentially non-uniform at the mixing plane with different circumferential variations, but the same average value, being "seen" by the upstream and downstream blade rows.

In more detail, the circumferential averaging is first applied to the parameters

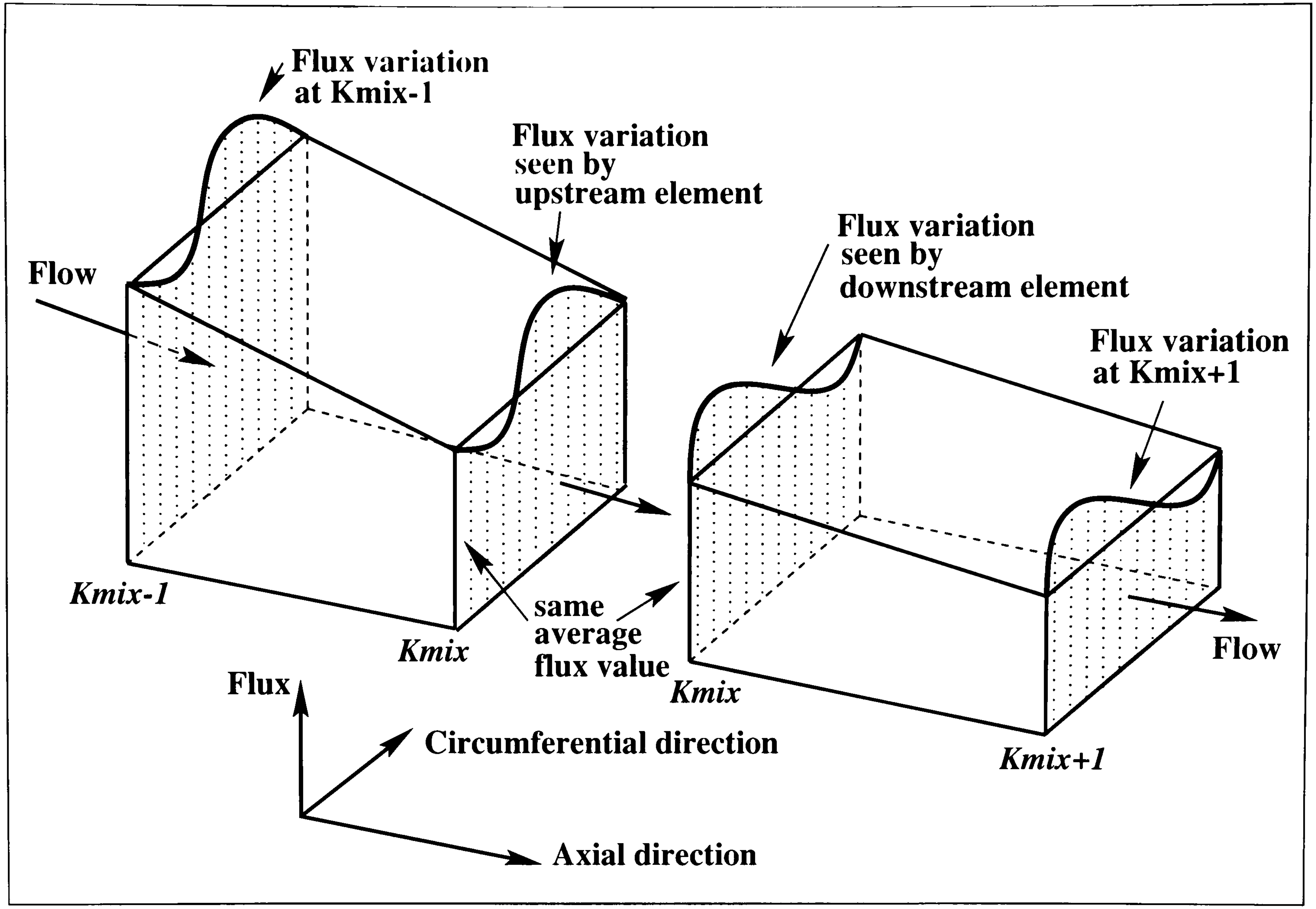

Figure 4.3: Mixing-plane model (Denton [47])

to be transfered across the mixing plane with Equation (4.32) or (4.33). In the process, all the cells at the same spanwise location immediately upstream of the mixing plane are treated as a single large element and the fluxes are conserved between the non-uniform flow entering its upstream face and the uniform flow leaving its downstream face, which is on the mixing plane. However, the fluxes crossing the mixing plane are not taken to be circumferentially uniform. Instead, the fluxes crossing the face of an element immediately upstream of the mixing plane are obtained by multiplying the fluxes through the upstream face by the ratio of the circumferentially averaged fluxes at the mixing plane to the circumferentially averaged fluxes at the upstream plane, i.e.,

$$\Phi_{k_{mix}} = \Phi_{k_{mix-1}} \left(\frac{\overline{\Phi}_{k_{mix}}}{\overline{\Phi}_{k_{mix-1}}} \right) \tag{4.34}$$

Similar treatment is applied to the elements immediately downstream of the mixing plane. At a certain spanwise position, the fluxes entering the face of the element immediately downstream of the mixing plane are obtained by multiplying the fluxes through its downstream plane by the ratio of the circumferentially averaged flux at the mixing plane to the circumferentially averaged fluxes at the downstream plane.

$$\Phi_{k_{mix}} = \Phi_{k_{mix+1}} \left(\frac{\overline{\Phi}_{k_{mix}}}{\overline{\Phi}_{k_{mix+1}}} \right) \tag{4.35}$$

The idea and the symbols are schematically described in Figure 4.3. The flux variation is obtained at every spanwise location and is equivalent to obtaining the circumferential variation in flux from upstream of the propagating direction of the parameters but adjusting their magnitude to satisfy the overall conservation.

The described non-uniform mixing plane model allows the flow entering and leaving the mixing plane to vary circumferentially and is a great improvement compared with the uniform mixing plane model when the mixing plane is close to the leading or trailing edge. In this study, the circumferentially non-uniform mixing plane model is applied to all parameters except the velocity profile and the details of the application of this model will be described in Chapter 6.

4.4.4 Discussion

The mixing plane models have several advantages:

1. The mixing plane models are numerically simple and easy to be implemented into an existing computer code of isolated blade row simulation.

2. They are easy to apply to engineering applications and can provide predictions with acceptable accuracy for multistage turbomachinery working near peak efficiency, which will be demonstrated in Chapter 6.
3. The computer code with the mixing plane models is easy to operate.
4. The mixing plane models provide spanwise consistency of mass flow rate, velocity profile and static pressure profile crossing the mixing planes between blade rows.

Apart from the above advantages, these models also have their disadvantages:

1. They can not maintain spanwise consistency of momentum and total pressure. This inconsistency may not be a serious problem when a machine works near peak efficiency but may be significant when the machine works far away from the design operating condition.
2. The flow prediction with the mixing plane models will have a large prediction error when a compressor works near stall or has extended flow separation areas.

Based on the above discussion, it is suggested that the mixing plane models be used for multistage simulation of turbomachinery flows near peak efficiency. For off-design flow simulation, the mixing plane models need to be improved or other approaches may be considered.

4.5 Deterministic Stress Model

4.5.1 Introduction

The major disadvantage of mixing plane models for multistage axial flow compressor applications based on ensemble averaged Navier-Stokes equations is the discontinuity of several aerodynamic parameters such as momentum, total pressure, etc. at interfaces. This discontinuity may cause large prediction errors when the machines operate away from design operating condition.

The discontinuity at interfaces comes from the deterministic and aperiodic unsteady fluctuations generated by neighbouring blade rows. According to Prato et al. [144], the aperiodic unsteady fluctuations are much smaller than the deterministic unsteady fluctuations. Therefore, the aperiodic unsteadiness is ignored in this study.

When ignoring the aperiodicity of the flow generated by neighbouring blade rows and applying the time-averaging operator to the ensemble averaged Navier-Stokes equations, the introduction of the deterministic stresses along with the bodyforce and blade blockage makes the interfaces between blade rows continuous for momentum, total pressure, etc..

In order to close the time-averaged Navier-Stokes equations where the deterministic stresses are introduced, overlapped computational domains are used to transfer deterministic stresses, bodyforce and blade blocking effect. The function of the body force and blocking effect coming from the neighbouring blade row is to get a correct average flow field in the downstream extended computational domain of the blade row under investigation.

4.5.2 Overlapped Solution Domain

It is assumed that the deterministic (periodic) unsteady influence on the flow in a blade passage only comes from its upstream blade row. In order to "close" the equation system, an overlapped solution domain approach is introduced for the simulation of deterministic stress terms. Figure 4.4 shows how overlapped computational domains are utilised for a blade row in a multistage environment with at least one upstream blade row and one downstream blade row.

For a blade row in a multistage environment, the computational domain starts axially from its upstream interface and ends at the downstream interface of its following blade row. A H-type two-block grid, one for the main passage and the other for the tip clearance ear for a rotor and a H-type single block grid for a shrouded stator are used for accurate simulation of flow phenomena in different flow regions.

The bodyforce and blade blockage effect generated by the downstream blade row are calculated in the computational domain of downstream blade row and applied on the computational domain of current blade row. With the implementation of the bodyforce and blade blockage effect, the predicted flow field in the extended domain of the current blade row reflects the averaged flow nature with the influence of the downstream relatively rotating blade row.

The deterministic stresses generated by the upstream blade row are calculated in the computational domain of the upstream blade row and imposed on the computational domain of the current blade row. With the implementation of the deterministic stresses, the interface between the current and the upstream blade rows becomes continuous for all the aerodynamic parameters except for static pressrue

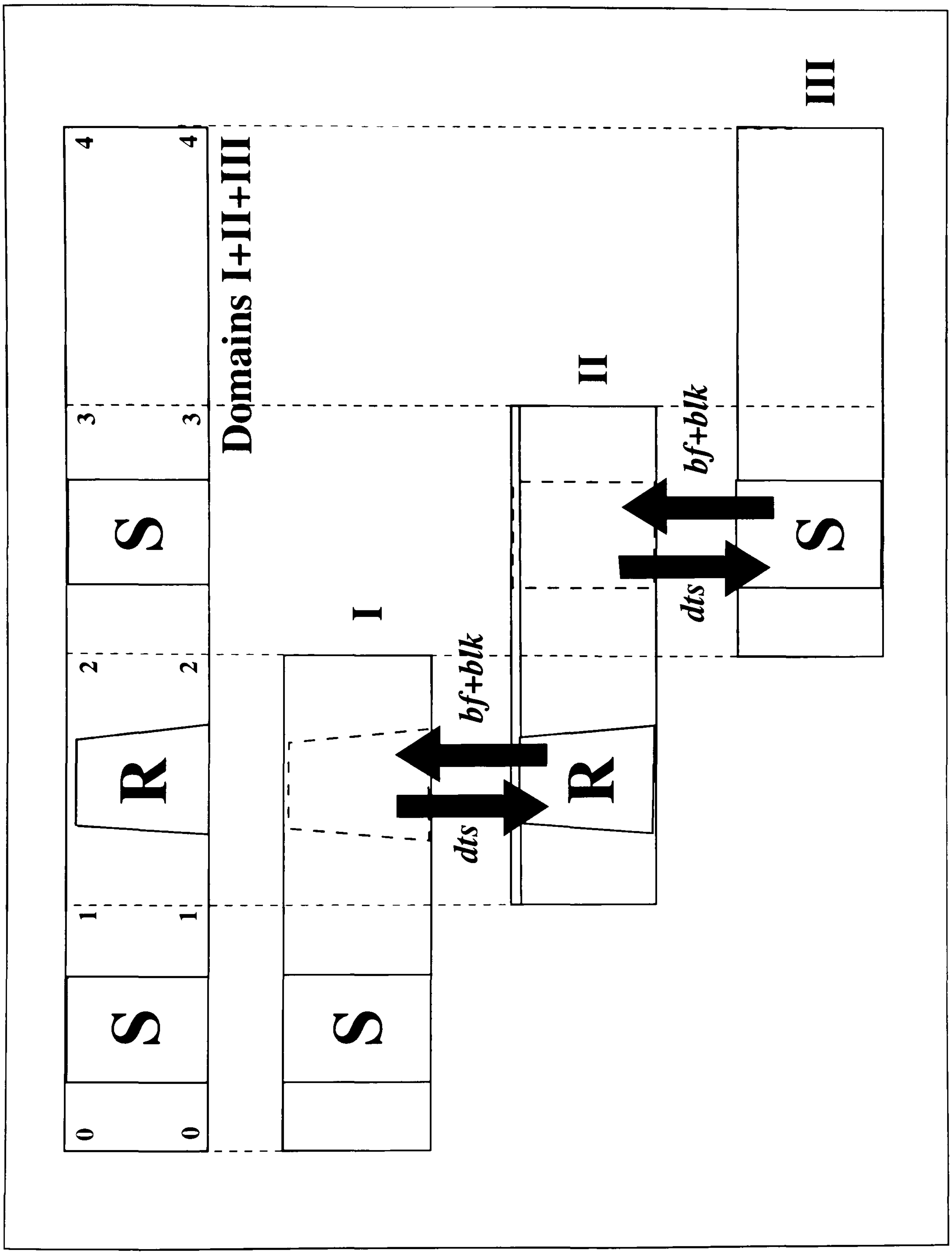

Figure 4.4: **Overlapped computational domains**

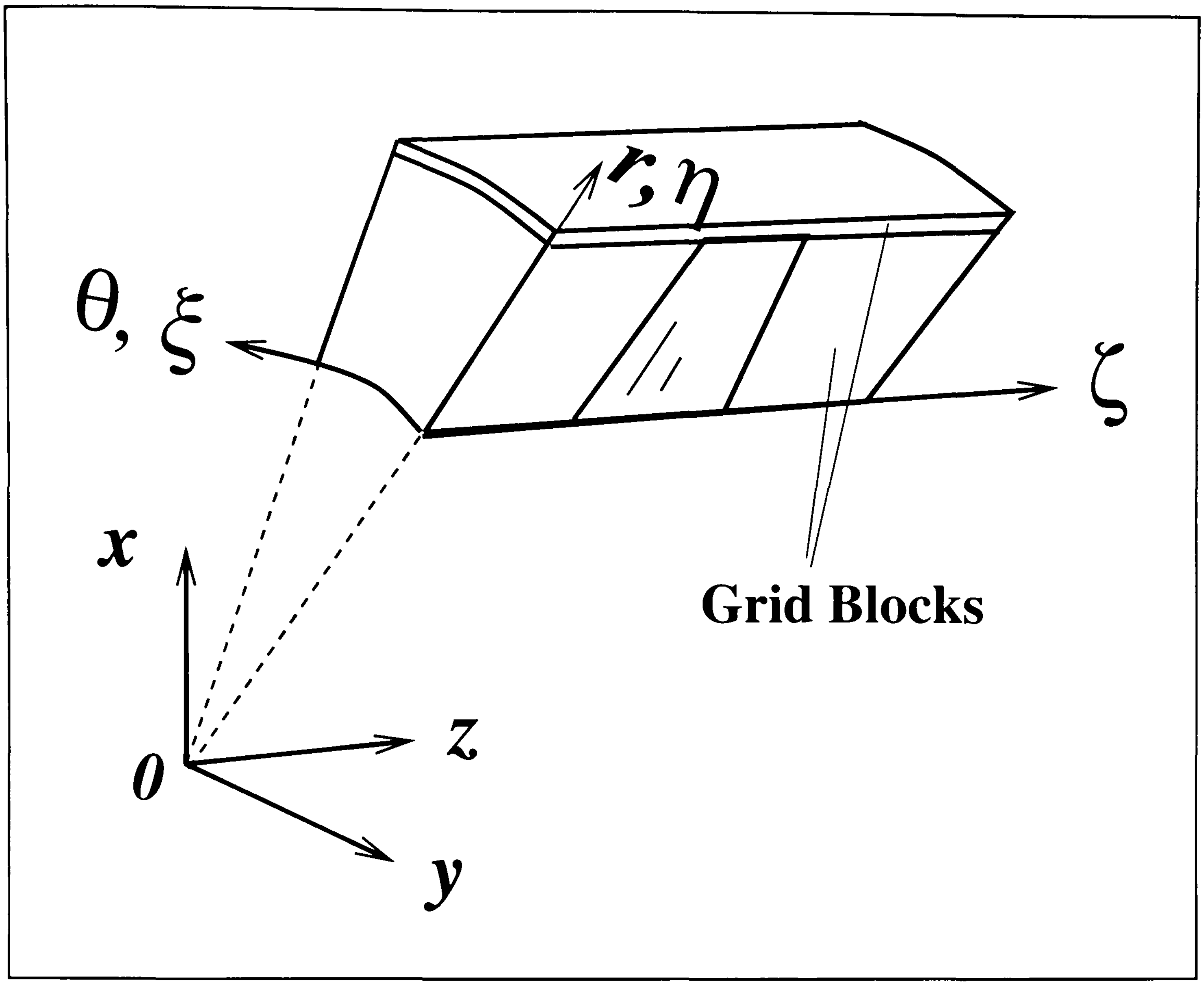

Figure 4.5: **Coordinate systems for deterministic stress approach**

and total pressrue. The inconsistency of the pressure distributions at interfaces will be discussed later.

4.5.3 Special feature of the coordinate system

In the computational system of this study, three coordinate systems, the general non-orthogonal curvilinear coordinate system, the cylindrical coordinate system and the Cartesian coordinate system, are employed simultaneously. The cylindrical coordinate system and the Cartesian coordinate system are two special cases of the general non-orthogonal curvilinear coordinate system. Such an arrangement has two reasons. Firstly, the Navier-Stokes equations are expressed in a general non-orthogonal curvilinear coordinate system with the Cartesian velocity components as unknown variables. Secondly, ξ and η coordinates in general coordinate system are chosen to be aligned with θ and r coordinates in cylindrical coordinate system respectively in order to simplify the CFD computation.

The special features of the coordinate systems used in this study are as follows:

- The coordinate lines ξ and η of the non-orthogonal curvilinear coordinate system are designed to be aligned with the θ and r coordinates of the cylindrical coordinate system respectively, Figure 4.5.
- The grid nodes with the same η have the same r.
- The grid nodes with the same ξ and ζ have the same θ.
- On each η surface the grid nodes with the same ζ have the same z.

Under these circumstances, many calculations are simplified and can be operated in the cylindrical coordinates and then transferred to the Cartesian or non-orthogonal coordinate system.

4.5.4 Deterministic Stresses

The deterministic fluctuations occur on larger space and time scales than the random (turbulent) fluctuations, and are the result of tangential non-uniformity of the flow field generated by neighbouring blade rows. In a three-dimensional simulation, the local deterministic velocity fluctuation can be expressed in a cylindrical coordinate system, Rhie et al.[148] as:

$$\hat{\overline{v}}_i = \overline{v}_i - \overline{\overline{v}}_i \qquad (i = r, \theta, z) \tag{4.36}$$

where $\overline{v}_i$ is the ensemble-averaged velocity and $\overline{\overline{v}}_i$ is the time-averaged velocity calculated by:

$$\overline{\overline{v}}_i = \frac{\int_{\theta_2}^{\theta_3} \overline{v}_i dA}{\int_{\theta_2}^{\theta_3} dA} \tag{4.37}$$

where $dA = rd\theta dr$, θ_2 and θ_3 are explained in Figure 4.6. Velocity decomposition is schematically shown in Figure 4.7 at a certain radial position across one blade pitch from θ_2 to θ_3.

The computational procedure for a time-averaged velocity fluctuation $\hat{\overline{v}}_i$, a normal deterministic stress and its gradient is schematically shown in Figure 4.8. Other deterministic stress terms and their gradients can be calculated in a similar manner.

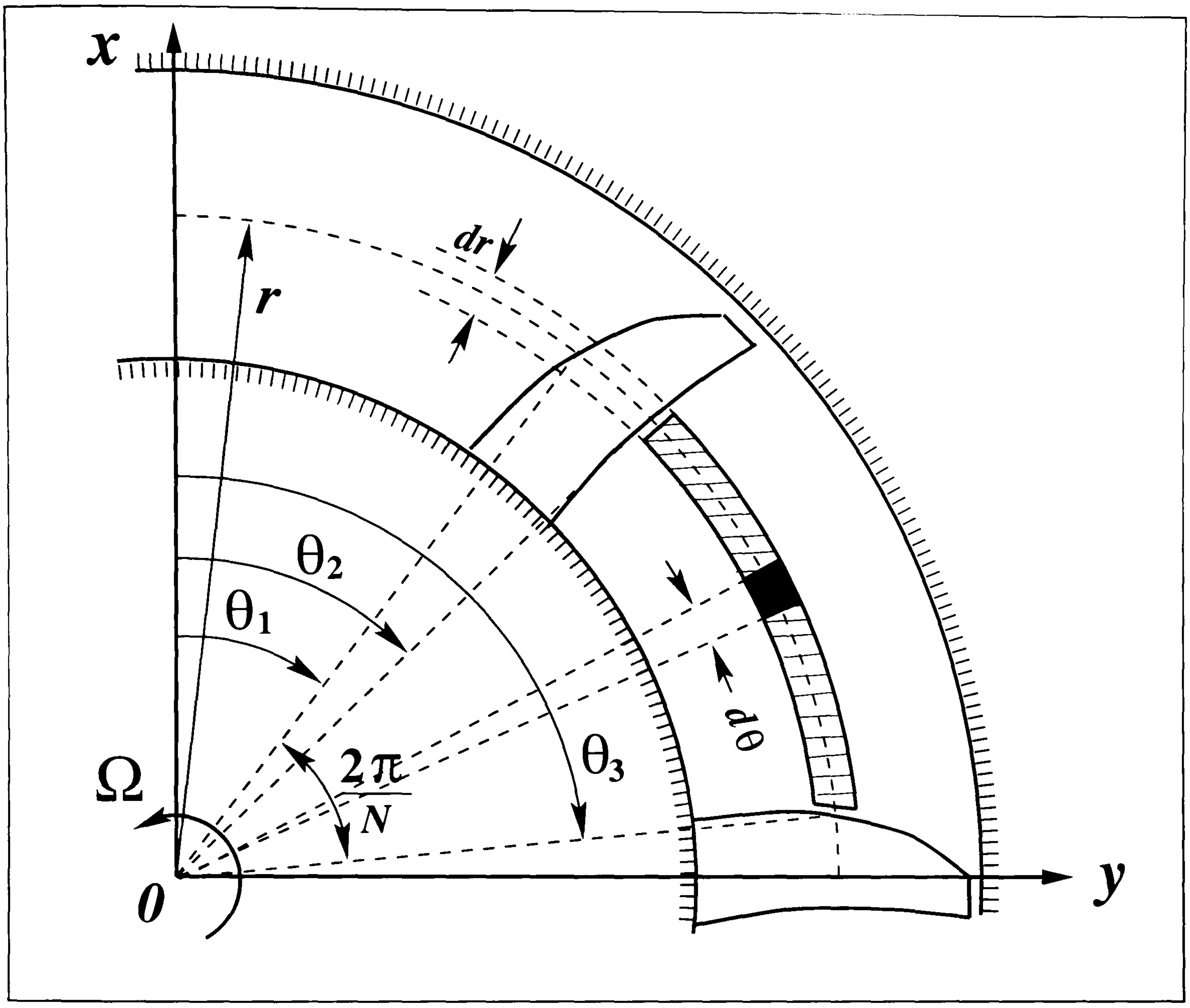

Figure 4.6: **Schematic front view of a blade row**

In order to include the deterministic stresses into the momentum equations, calculated $\hat{\bar{v}}_i, (i = r, \theta)$ in each control volume must be projected to x and y directions:

$$\hat{\bar{v}}_x = \hat{\bar{v}}_r cos\theta - \hat{\bar{v}}_\theta sin\theta \tag{4.38}$$

$$\hat{\bar{v}}_y = \hat{\bar{v}}_r sin\theta + \hat{\bar{v}}_\theta cos\theta \tag{4.39}$$

Consequently, the tangentially area-averaged deterministic stresses can be calculated as:

$$\overline{\rho\hat{\bar{v}}_i\hat{\bar{v}}_j} = \frac{\int_{\theta_2}^{\theta_3} \rho\hat{\bar{v}}_i\hat{\bar{v}}_j dA}{\int_{\theta_2}^{\theta_3} dA} \qquad (i, j = x, y, z) \tag{4.40}$$

In the computational domain of a given blade row, the deterministic stresses generated by its upstream blade row are calculated in the computational domain

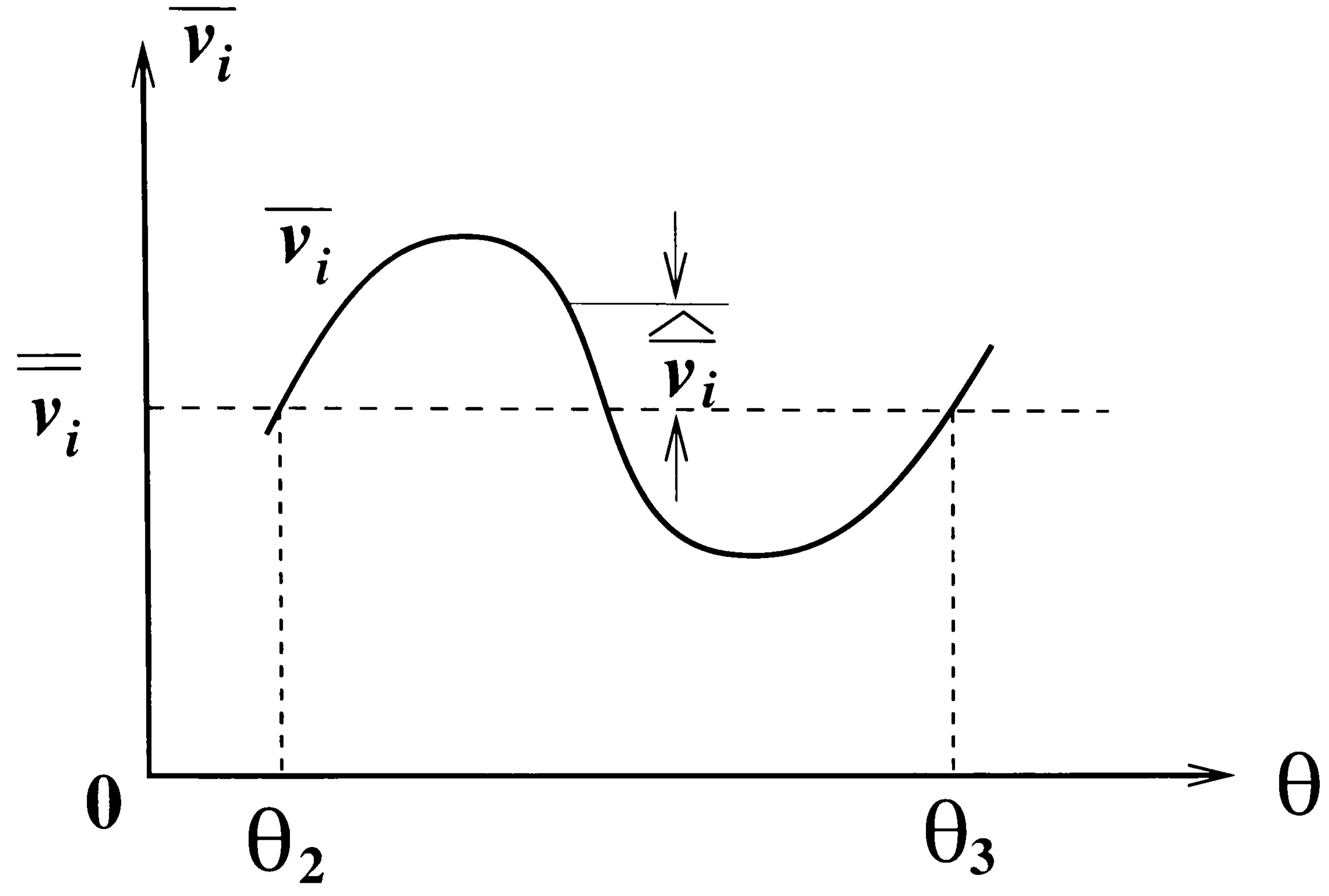

Figure 4.7: **Velocity decomposition**

of the upstream blade row and imposed on the computational domain of the current blade row. These deterministic stresses contribute to the correction of the momentum and make the spanwise continuity of momentum possible at interfaces. The momentum in a circumferential element at certain radius r before and after an interface may be expressed for incompressible flows by the following equation:

$$\underbrace{\int_A (\bar{\rho}\overline{v}_i\overline{v}_j)dA}_{\textbf{before interface}} = \underbrace{\left(\bar{\rho}\overline{\overline{v}}_i\overline{\overline{v}}_j + \bar{\rho}\overline{\hat{\overline{v}}_i\hat{\overline{v}}_j}\right)A}_{\textbf{after interface}} \tag{4.41}$$

In the deterministic stress approach, the area averaged total pressure is continuous as well provided that the static pressure is consistent at interfaces because of the compensation of the deterministic stresses applied:

$$\overline{p}_{t,ups} = \overline{p}_{t,dns} \tag{4.42}$$

where

$$\overline{p}_{t,ups} = \int_A \left[\overline{p}_s + \frac{\bar{\rho}}{2}\left(\overline{u}^2 + \overline{v}^2 + \overline{w}^2\right)\right] dA \tag{4.43}$$

$$\overline{p}_{t,dns} = \overline{\overline{p}}_s + \frac{1}{2}\rho\left(\overline{\overline{u}}^2 + \overline{\overline{v}}^2 + \overline{\overline{w}}^2\right) + \frac{1}{2}\bar{\rho}\left(\overline{\hat{\overline{u}}^2} + \overline{\hat{\overline{v}}^2} + \overline{\hat{\overline{w}}^2}\right) \tag{4.44}$$

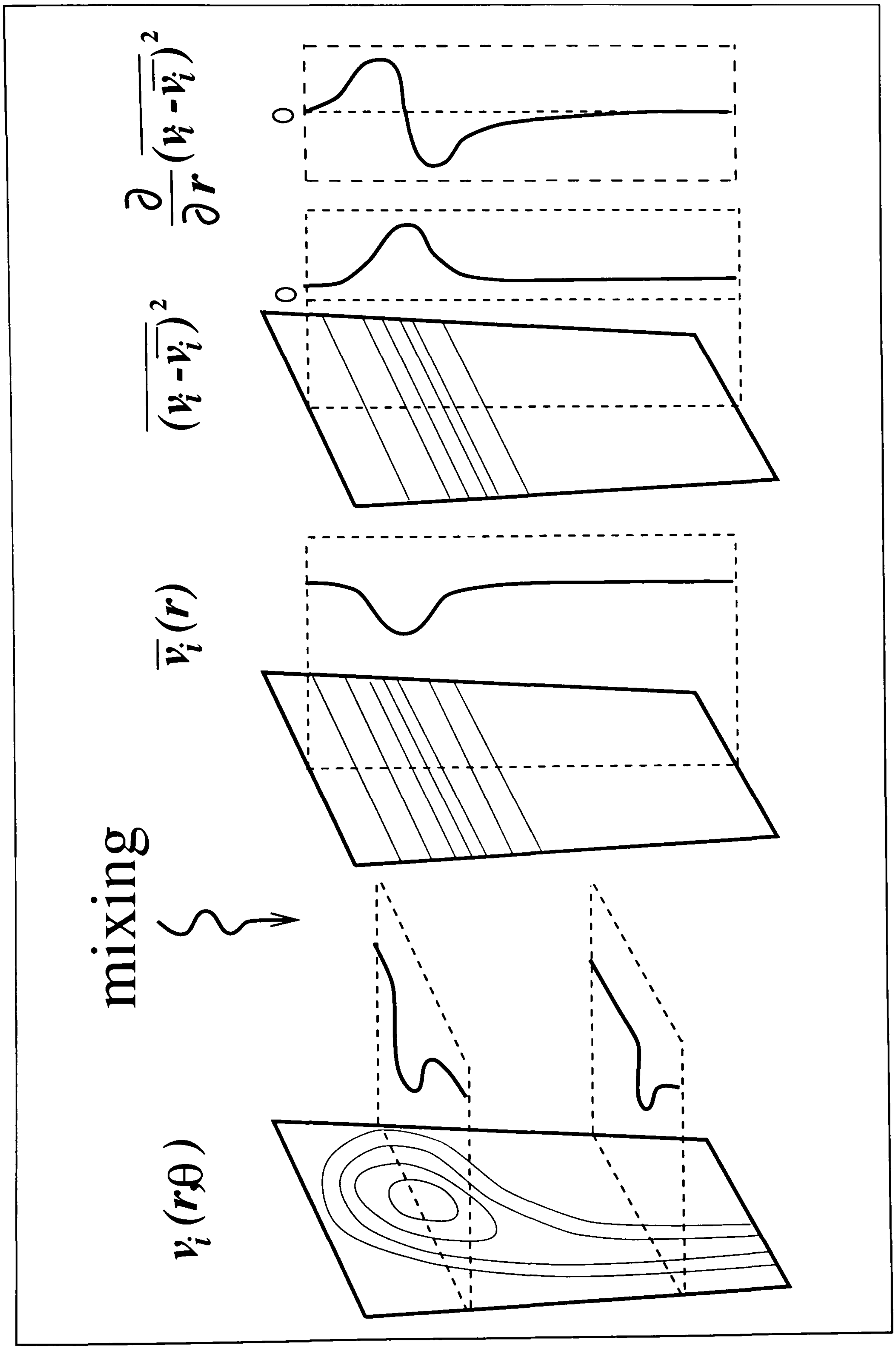

Figure 4.8: **Calculation of deterministic stresses (Denton et al. [49])**

The continuity of mass is satisfied automatically at interfaces when the area averaged mixing process is applied.

4.5.5 Body Force

Body force is caused by the interaction between the flow and blade rows. It is associated with the inviscid and viscous forces acting on the blades. The influence of body force is not only restricted in the blade passage, but on the flow fields upstream and downstream of the blade passage. In a computational domain which covers a blade passage, the flow field can be predicted by removing the blades and instead introducing the bodyforce and blade blockage generated by the blades. The predicted flow field is not the same as the original one but is an equilibrium flow field in terms of axial and radial variation of aerodynamic parameters. The circumferential variation only reflects the development of the wake generated by the upstream blade row. The circumferential variation in the original flow field is smeared just like a flow passing an actuator disk which is equivalent to a rotating blade row.

It is assumed that the body force contributes to the pressure gradient and part of the momentum change of the flow. Another part of the momentum change comes from the impact of the blade blockage which will be discussed in the next section. In a rotating blade passage, centrifugal force also contributes to the bodyforce. Based on this assumption, the body force acting on a control volume is due to the pressure difference around the volume surface and the centrifugal force. It is also assumed that the centrifugal force generated by rotor blade rows only exists in the areas between blades.

This approximation has the advantage that the body force can be easily simulated by calculating the circumferentially area-averaged pressure gradients and centrifugal force(for rotating blade passages) from the current blade computational domain and implementing in the calculation of the upstream blade computational domain.

In the simulation procedure, local pressure gradients in a blade computational domain are first of all calculated in three coordinate directions of the cylindrical coordinate system. Then the circumferentially area averaged bodyforce components at certain radius r are obtained with Equations (4.45), (4.46) and (4.47). Figures 4.9 and 4.10 show the bodyforce imposed on a tangential volume element

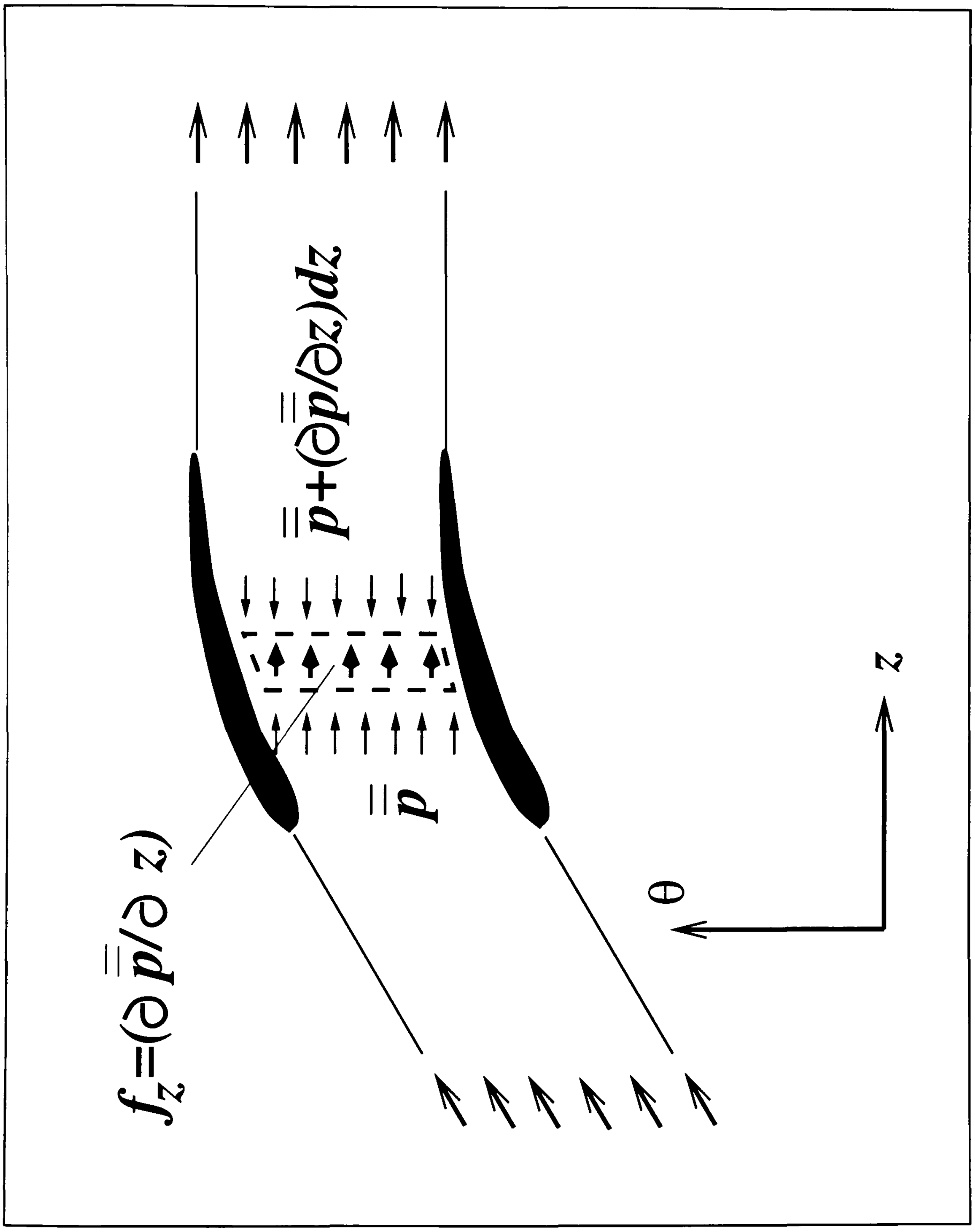

Figure 4.9: **Axial bodyforce component**

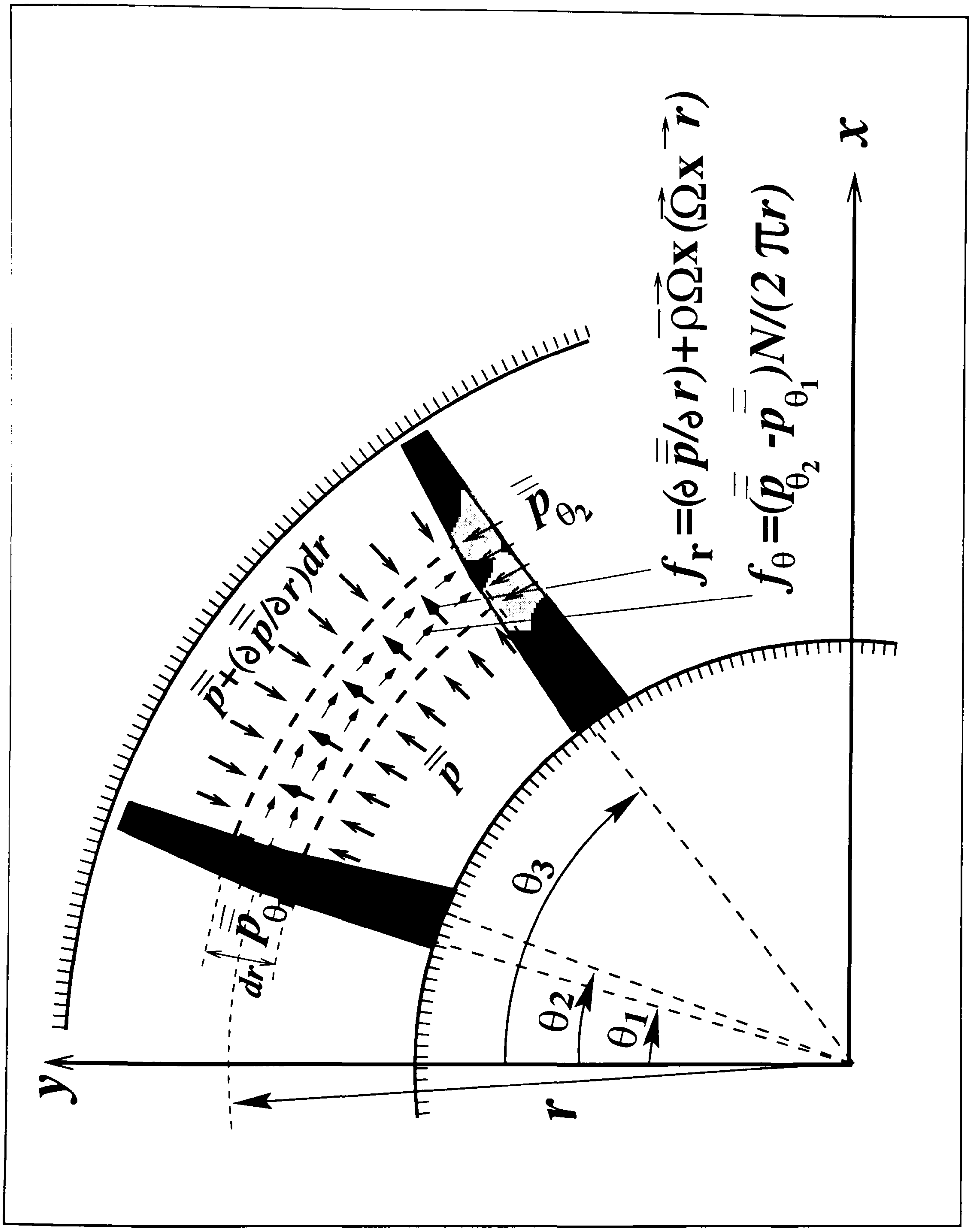

Figure 4.10: **Tangential and radial bodyforce components**

in z, θ and r directions in a cylindrical coordinate system.

$$f_r = \left(\frac{\partial \overline{p}}{\partial r}\right)_r + \overline{\rho}\vec{\Omega} \times (\vec{\Omega} \times \vec{r}) = \frac{\int_{\theta_2}^{\theta_3} \left(\frac{\partial \overline{p}}{\partial r}\right) dA}{\int_{\theta_2}^{\theta_3} dA} + \overline{\rho}\vec{\Omega} \times (\vec{\Omega} \times \vec{r}) \tag{4.45}$$

$$f_\theta = \left(\frac{\partial \overline{p}}{r\partial \theta}\right)_r = \frac{\int_{\theta_2}^{\theta_3} \left(\frac{\partial \overline{p}}{r\partial \theta}\right) dA}{\int_{\theta_2}^{\theta_3} dA} \lambda_R \tag{4.46}$$

$$f_z = \left(\frac{\partial \overline{p}}{\partial z}\right)_r = \frac{\int_{\theta_2}^{\theta_3} \left(\frac{\partial \overline{p}}{\partial z}\right) dA}{\int_{\theta_2}^{\theta_3} dA} \tag{4.47}$$

where λ_R is the local weighting function of blade blockage defined by Adamczyk et al. [2] as

$$\lambda_R = 1 - \frac{|\theta_1 - \theta_2| N}{2\pi} \tag{4.48}$$

(i.e. 1 minus blockage) within a blade passage and $\lambda_R = 1$ outside a blade passage. In Equation (4.48), N is the blade number of a blade row, and the meaning of θ_1 and θ_2 are shown in Figure 4.10.

The function of λ_R here is to average out the tangential pressure gradient on the whole tangential length, including the area occupied by blades because this pressure gradient is supposed to be implemented in the momemtum equations to change the tangential flow momentum in the upstream blade computational domain where the space of blades are occupied by fluid.

Subsequently, the obtained circumferentially area averaged pressure gradients are projected locally to the x, y and z directions, similar to the projection of deterministic stresses.

$$f_x = (f_r)_r\, cos\theta - (f_\theta)_r\, sin\theta \tag{4.49}$$

$$f_y = (f_r)_r\, sin\theta + (f_\theta)_r\, cos\theta \tag{4.50}$$

$$f_z = (f_z)_r \tag{4.51}$$

4.5.6 Blade Blockage Effect

Blade blockage has obvious influence on the flow momentum inside the blocked area. When the flow is blocked, the flow must go faster in the blocking direction

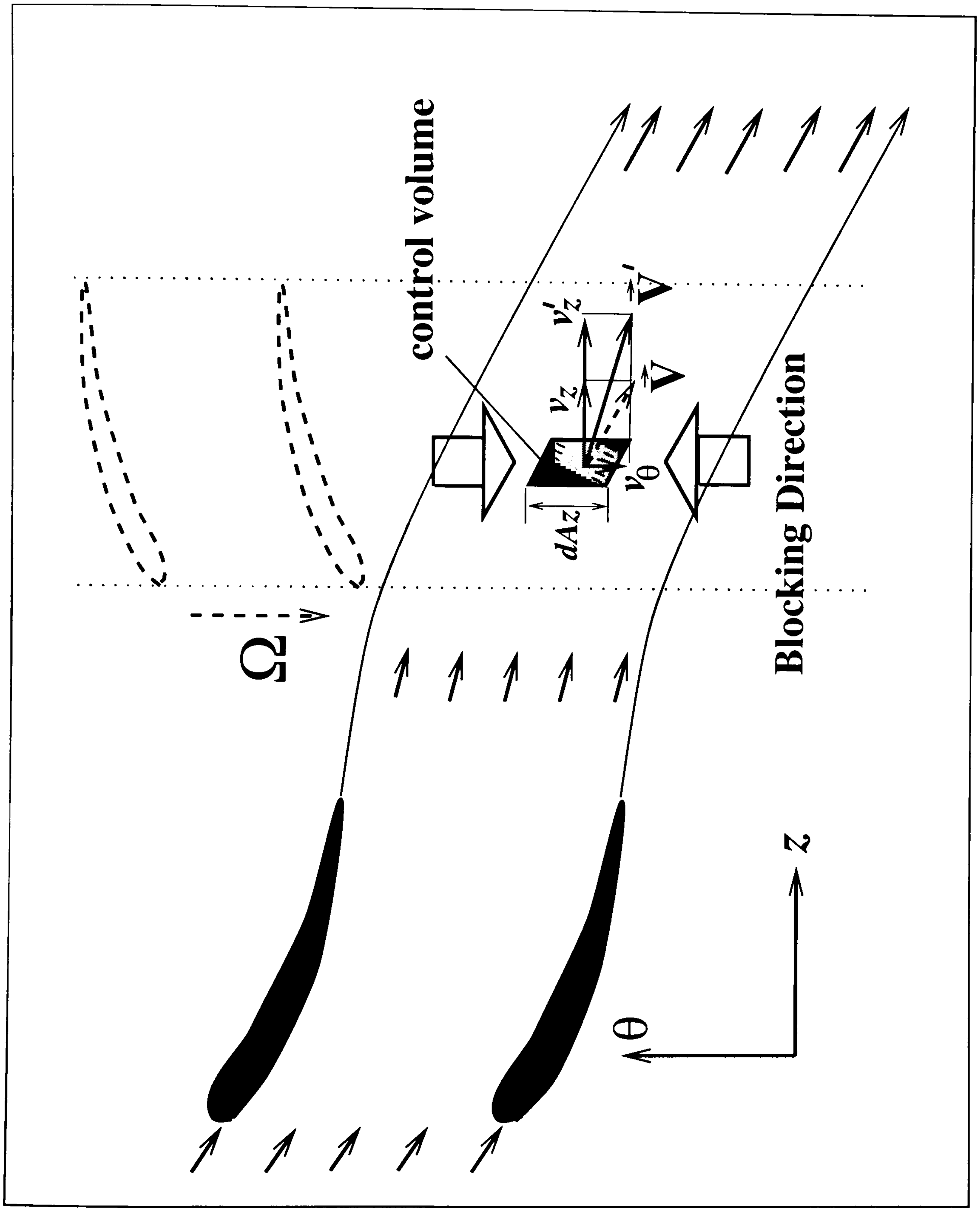

Figure 4.11: **Blockage effect on velocity components** V_z & V_θ

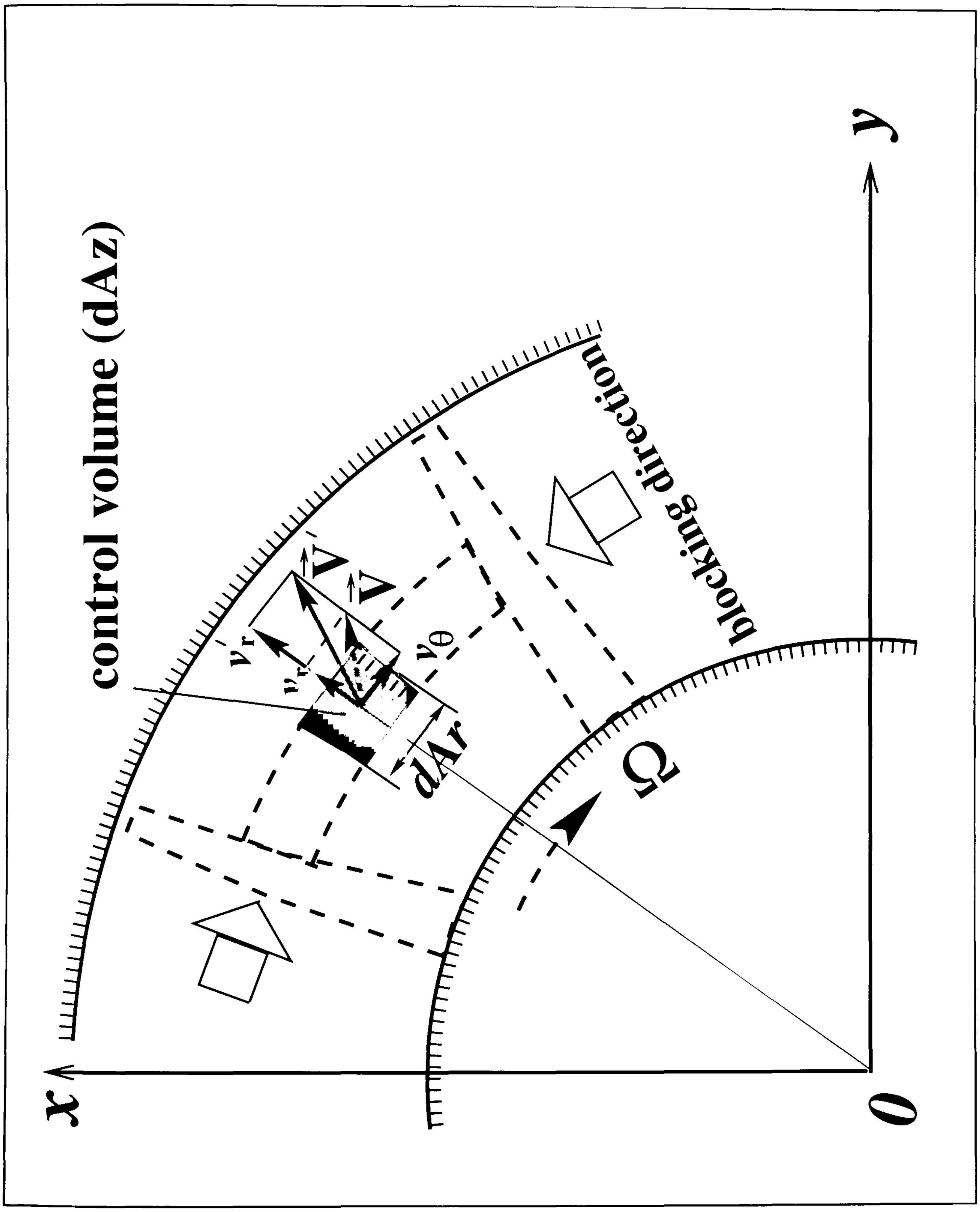

Figure 4.12: **Blockage effect on velocity components** V_r & V_θ

in order to pass the unchanged mass flow rate. Adamczyk [2] implemented the blockage factor (λ_R) into the time-averaged Navier-Stokes equations. Effort has been made for the application of his equation system to the current flow simulation and it was found that the pressure gradient term has unphysically large influence on the flow field and the resulted flow field is far away from reality. Because of this reason, a simplfied approximation for the blade blockage effect is introduced in this study and described as follows.

A typical control volume in the downstream domain of the blade row of interest is shown in Figures 4.11 and 4.12. When blockage occurs to the control volume, the effect of the blockage is just like that when the flow passes through a control volume with a smaller cross area which is drawn in dotted lines, where the projected flow areas are reduced in the z and r directions and keep the same in the θ direction. Assuming that the mass flow rates in the z, r and θ directions remain the same when the flow is blocked, the new velocity components in the cylindrical coordinate system are calculated based on the mass continuity in each direction:

$$\begin{aligned} d\dot{m}_z &= \rho v_z dA_z = \rho v_z^{'}(\lambda_R dA_z) \\ d\dot{m}_r &= \rho v_r dA_r = \rho v_r^{'}(\lambda_R dA_r) \\ d\dot{m}_\theta &= \rho v_\theta dA_\theta \end{aligned} \tag{4.52}$$

and

$$\begin{aligned} v_z^{'} &= v_z/\lambda_R \\ v_r^{'} &= v_r/\lambda_R \\ v_\theta^{'} &= v_\theta \end{aligned} \tag{4.53}$$

The updated velocity components are then projected to the x, y and z directions and the resultant Cartesian velocity components are:

$$\begin{aligned} v_x^{'} &= v_r^{'}cos\theta - v_\theta^{'}sin\theta \\ v_y^{'} &= v_r^{'}sin\theta + v_\theta^{'}cos\theta \\ v_z^{'} &= v_z^{'} \end{aligned} \tag{4.54}$$

This approximation of the blade blockage effect is only applied after a solution to a flow field is converged. During the iterations the volume geometries are actually chosen to be the same to those in the computational domains instead of the blocked ones so the velocity components used in the computation are the Cartesian velocity components corresponding to the cylindrical velocity components v_z, v_r and v_θ rather than $(v_z^{'}), (v_r^{'})$ and $v_\theta^{'}$.

4.5.7 Deficit of Overlapped Solution Approach

Theoretically, the interfaces between blade rows become continuous for all the aerodynamic parameters with the implementation of deterministic stresses. Unfortunately, due to the closure requirement of the time averaged Navier-Stokes equations, the overlapped computational domains have to be used to obtained the deterministic stresses. This type of approach actually causes the inconsistency in spanwise static pressure distribution at interfaces.

For example at the interface 2 in Figure 4.4, the spanwise distribution of static pressure obtained in Domain II is not exactly the same to that obtained in Domain III due to the model error (i.e. the approximation of bodyforce and the blade blockage effect) and numerical error. This spanwise inconsistency also contributes to the spanwise inconsistency in total pressure distribution. Therefore, the deterministic stress model discussed in this section provides interfaces with spanwise continuous mass flow rate, momemtum, k and ϵ but does not garantee the spanwise consistency of static pressure and total pressure in practice, although the influence of the inconsistency is not significant. More analysis can be found in Chapter 6 (Section 6.6).

4.6 Repeating Stage Models

4.6.1 Introduction

In multistage axial flow compressors, it is observed that after a few similar stages the flow develops a radial distribution which repeats itself after every stage. This is particularly obvious in terms of the radial distribution of axial velocity and flow angles, but it is also true for other parameters such as static pressure and total pressure although with different absolute values at the inlet and exit of the stage. The effects of casing, hub friction, tip leakage and hub leakage in the first few blade rows appear to rapidly reach an equilibrium condition similar to fully developed pipe flows. Therefore in repeating stages, the spanwise distribution of velocity, flow angle, k and ϵ at the inlet and the exit of the stages remain almost the same and the spanwise distribution of static pressure and total pressures maintain a radially constant increment across the stages. It is assumed that each rear stage of a multistage axial flow compressor is just like a repeating stage of its neighbouring stages in terms of flow patterns.

The repeating stage concept resulted in a repeating stage model suitable for the flow prediction of rear stages of multistage axial flow compressors, Li et al.[113] and [114]. The major advantage of the repeating stage model is that the inlet and exit spanwise distributions of all the aerodynamic parameters such as velocity, static pressure, total pressure, k and ϵ become the result of the simulation instead of boundary conditions and only the averaged static pressure at the exit of the stage together with the total mass flow rate are required as global input. Two repeating stage models are described in this section.

4.6.2 Repeating Stage Model *I*

In the case of low speed multistage axial flow compressor simulations with a simple mixing plane model, a first repeating stage model was developed by Li et al. [113] and is described as follows.

Figure 4.13 shows how the repeating stage model works. For a typical rear stage of a multistage axial flow compressor there are three mixing planes used to pass circumferentially area-averaged information between the neighbouring blade rows, one at the inlet of the stage located halfway between the current rotor and the upstream stator, one at the interface between the rotor and the stator and another at the exit of the stage located halfway between the current stator and the downstream rotor.

It is assumed that the spanwise velocity profile at the stage inlet is the same to that at the stage exit. The total mass flow rate is used to scale the inlet velocity profile in order to maintain mass continuity during global iterations. The velocity scaling factor C_v is calculated as:

$$C_v = \frac{\dot{m}}{\dot{m}_{cal}} \tag{4.55}$$

where $\dot{m}$ is the specified mass flow rate and $\dot{m}_{cal}$ is the calculated mass flow rate by imposing the stage exit velocity profile at the stage inlet. The three velocity components, axial, tangential and radial, are scaled using the same scaling factor in order to keep the flow angle in a absolute frame of reference unchanged after scaling. The scaling factor becomes unity when global convergence is achieved.

Similarly, the stage inlet k and ϵ profiles are set to be equal to those at the stage exit as they tend to be unchanged when the turbulent flow is fully developed, and hence the scaling factors for k and ϵ profiles are equal to 1.

The way of setting the static pressure at the stage exit is to define the average static pressure for the whole exit area as a given value, maintain the same shape

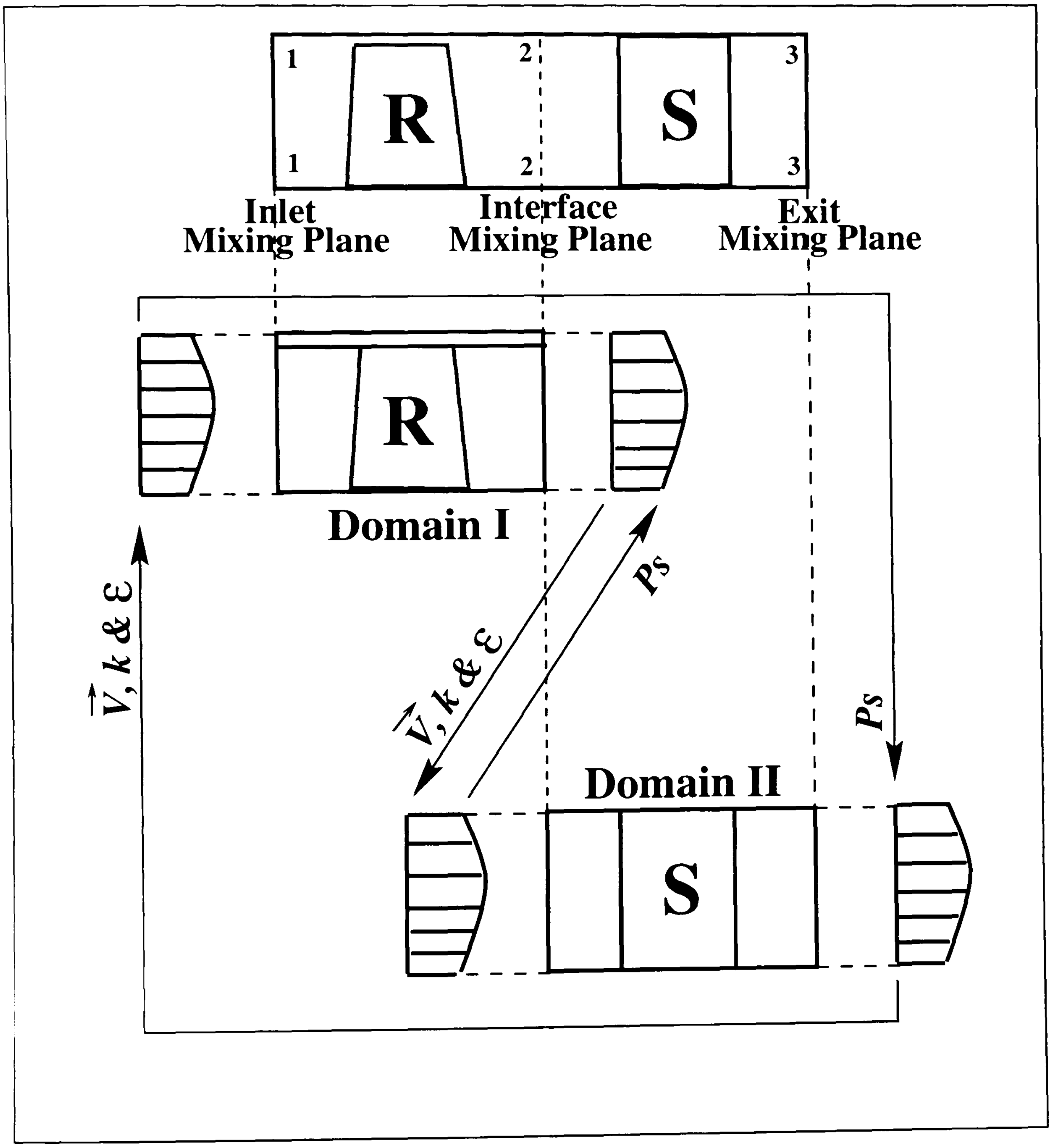

Figure 4.13: Repeating Stage Model I

of spanwise static pressure distribution at the inlet and the exit of the stage and allow pressure variation to exist circumferentially. Firstly, the circumferentially area averaged static pressure profile is shifted from the stage inlet to the stage exit with appropriete interpolation. Then the static pressure at the exit is scaled by a scaling factor C_{p_s}:

$$C_{p_s} = \frac{p_{s,exit}}{p_{s,cal}} \tag{4.56}$$

where $p_{s,exit}$ is the specified value of the average static pressure at the stage exit, $p_{s,cal}$ is the calculated area-averaged static pressure at the stage exit after imposing the stage inlet pressure profile on the exit. This kind of setting also results in the similarity of spanwise total pressure distribution at the inlet and the exit of the stage because the flow is supposed to be incompressible and the total pressure is calculated with static pressure and velocity components.

$$p_t = p_s + \frac{1}{2}\rho(u^2 + v^2 + w^2) \tag{4.57}$$

4.6.3 Repeating Stage Model *II*

In the case of multistage simulation of axial flow compressors where a deterministic stress model is applied, second repeating stage model has been developed in order to provide a better prediction than the repeating stage model *I* and to simplify the global aerodynamic boundary conditions.

The idea of this model is to implement the deterministic stress into the Navier-Stokes equations to make the interfaces between blade rows continuous for aerodynamic parameters. Sondak et al. [161] developed a "lumped" deterministic stress (LDS) model where the deterministic stress field is modelled with a lower order (inviscid) time dependent simulation and then implemented in the viscous steady flow equations as source terms. Unlike the idea of the "lumped" deterministic stress model, the deterministic stress field is simulated in this study with the deterministic stress model described in Section 4.5.

In the flow simulation for rear stages of multistage axial flow compressors with the repeating stage model *II*, there are two individual computations involved in the global iterations of the calculation. One is the major computation (*Computation I*) which is similar to the repeating stage model *I*. The only difference between *Computation I* and the repeating stage model *I* is that the deterministic stresses as additional source terms are implemented in the Navier-Stokes

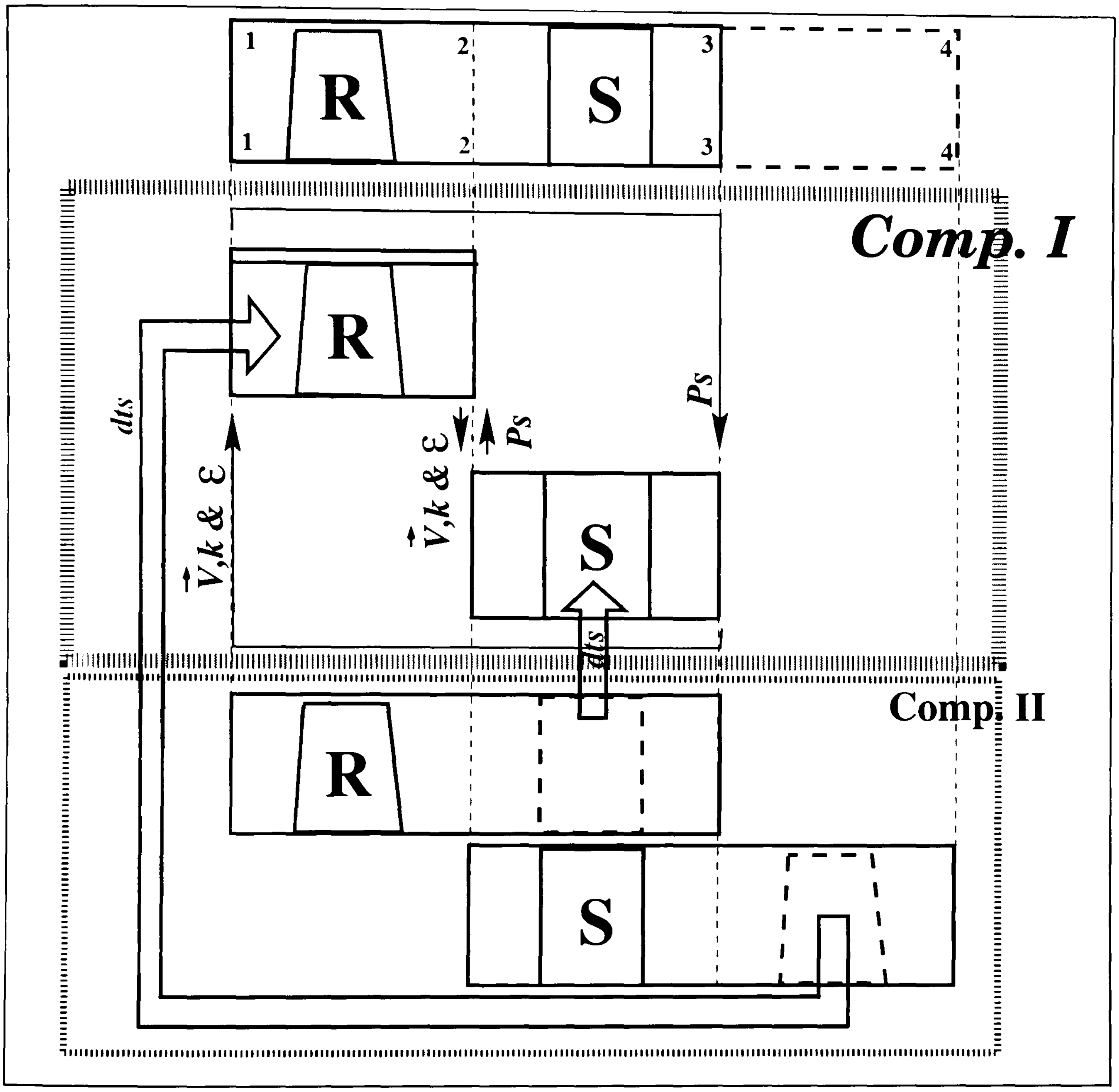

Figure 4.14: **Repeating Stage Model** *II* **(Computation** *I***)**

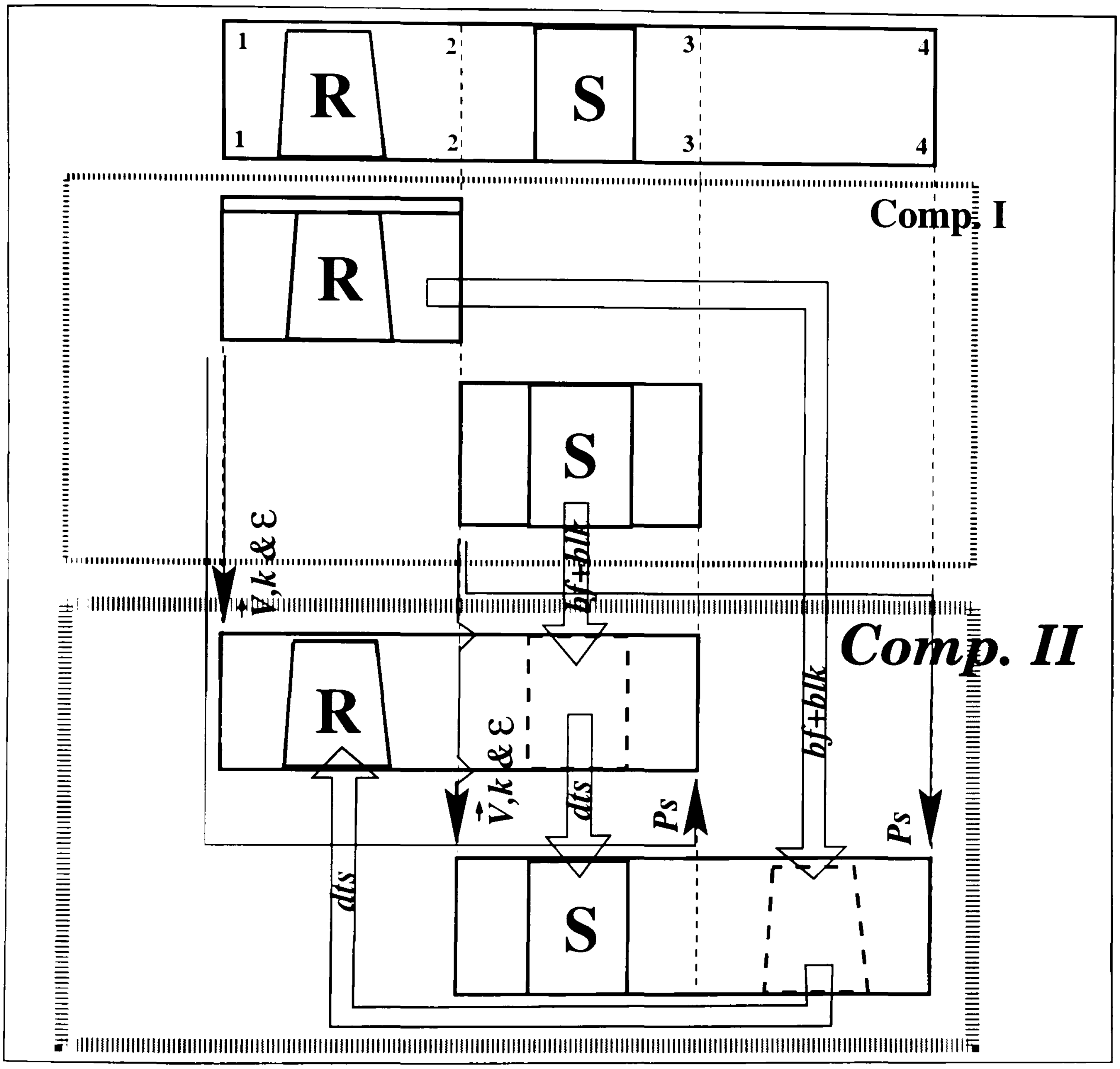

Figure 4.15: **Repeating Stage Model *II* (Computation *II*)**

equations in *Compution I*. The other (*Compution II*) is similar to the flow simulation with the deterministic stress model described in Section 4.5, which is carried out once in every 4 to 5 global iterations of *Computation I*. In *Computation II* the overlapped computational domains are employed. In other words, every computational domain for a blade row has an extended domain covering the flow field of the following blade passage. The purpose of the extended computational domain is to calculate the deterministic stress field resulted from the circumferential non-uniformity of the flow. In order to get a correct circumferentially averaged flow field in the extended computational domain, the bodyforce and blade blockage calculated in *Computation I* have to be implemented. The boundary conditions and bodyforce field required by *Computation II* are obtained from *Computation I* and the deterministic stress field required by *Computation I* is obtained from *Computation II*. The two computations in the repeating stage model *II* are illustrated in Figures 4.14 and 4.15.

It is assumed that mixing planes are located halfway between two neighbouring blade rows. For a typical stage working in a multistage environment there are three mixing planes for the compressor stage in *Computation I*, one (Mixing Plane 1) at the inlet of the rotor, one (Mixing Plane 2) at the interface between the rotor and the stator and another (Mixing Plane 3) at the exit of the stator. For *Computation II* of the same compressor stage there are four mixing planes, the first three mixing planes are the same to those in *Computation I* and the last one (Mixing Plane 4) is at the exit of the following rotor.

The setting of boundary conditions for the computational domains are based on the assumption that the stage under investigation possesses repeating flow nature. In *Computation I* of the repeating stage model *II*, the velocity, k and ϵ profiles at the inlet of the stage are set to be equal to those at the stage exit and the static pressure profile at the stage exit is assumed to have the same shape of the static pressure at the stage inlet but with a given average value. In *Computation II*, the velocity, k and ϵ profiles at the rotor and stator inlet are set to be equal to those at the same locations in *computation I*. The static pressure profiles at the exit of both the rotor and the stator computational domains are assumed to have the same shapes to those at the inlet of the rotor and the stator respectively in *Computation I* but with different average values. In addition, the average value of the static pressure at a computational domain exit needs to be modified in order to satisfy the average value of the static pressure at the blade exit because the given values of static pressure at the domain exit and the blade exit can not be both satisfied in *Computation II* due to the model and numerical errors. For example, the average value of static pressure at mixing plane 4 of the stator computational domain needs to be corrected in every global iteration using Equation (4.58) in order to satisfy the average static pressure at the stator exit (Mixing Plane 3) to a given value.

$$p_4^{n+1} = p_4^n + \omega(p_{exit} - p_3^n) \tag{4.58}$$

where p_{exit} is the specified value of the average static pressure at the stator exit (Mixing Plane 3), p_3^n is the calculated value of the average static pressure at mixing plane 3 for the current iteration in the stator computational domain, p_4^n and p_4^{n+1} are the average values of static pressure at Mixing Plane 4 of the stator computational domain for the current and next global iterations respectively, and ω is the under relaxation factor which normally takes a value between 0.6 and 0.8.

In *Computation II* of the repeating stage model *II*, the deterministic stress field obtained from the downstream extension of the stator passage between Mixing Planes 3 and 4 is shifted upstream and imposed on the rotor computational domain between Mixing Planes 1 and 2 to compensate the discontinuity of momentum for the Mixing Plane 1. Similarly, the deterministic stress field obtained from the downstream extension of the rotor passage between Mixing Planes 2 and 3 is applied to the stator domain (Domain *II*) between the same mixing planes.

With the implementation of deterministic stresses, the interfaces in *Computation I* is continuous for all the aerodynamic parameters and the flow field predicted in *Computation I* is the major result of the repeating stage model *II*. The role of *Computation II* of the model is to provide required deterministic stress field. More details of the prediction with this model and the benefits of the model will be discussed in Chapter 6.

4.6.4 Discussion

The advantage of the repeating stage models for flow prediction of rear stages of multistage axial flow compressors is that they simplify the global aerodynamic boundary conditions. In other words, the boundary distribution of aerodynamic parameters becomes the result of the simulation instead of the aerodynamic boundary setting with only the requirement of total mass flow rate and average static pressure at the stage exit.

However, the above repeating stage models are based on the particular case concerned, where the compressor stages have constant inner and outer diameters, the flow is supposed to be incompressible and the compressor works near peak efficiency. In more general, if the compressor annulus is convergent downstream and the flow is compressible, the current repeating stage models need to be modified. This issue will not be discussed in this thesis.

In addition, if the compressor operates at off-design conditions it is very likely that the flow loses its repeating nature and the repeating stage models can not be applied.

Chapter 5

Numerical Procedures

5.1 Introduction

In this chapter, the detailed description of the discretization and solution procedure of the governing equations is provided.

Firstly, a complete form of governing equations is expanded here to make them easier to be used later.

Secondly, a finite volume method is utilised to discretize the governing equations on each control volume and a general form of the discretized equations is obtained. Different differencing schemes for convection terms are discussed.

Then, a solution procedure for the discretized algebraic equation system and relaxation methodology are described.

A pressure correction method which describes how the continuity equation and momentum equation are used to derive a pressure correction equation and how both momentum and continuity equations are satisfied. In addition, a solution acceleration method to the pressure correction equation and a remedy to pressure oscillations are discussed.

Finally, the $SIMPLE$ algorithm is described for the solution of incompressible flow problems.

5.2 Expanded Forms of Governing Equations

To make the expression of the governing equations simpler, the overbars above variables describing averaging processes in Chapter 2 are omitted in this chapter. The expanded form of the time-averaged governing equations in the transformed coordinates where the $z-$axis coincides with the axis of rotation may be written as follows.

Continuity Equation

$$\frac{\partial(\rho U)}{\partial\xi}+\frac{\partial(\rho V)}{\partial\eta}+\frac{\partial(\rho W)}{\partial\zeta}=0 \tag{5.1}$$

Momentum Equations

u-momentum

$$\begin{aligned}
&\frac{\partial}{\partial\xi}\left[\rho Uu-J\left(\mu+\mu_T\right)\left(g^{11}\frac{\partial u}{\partial\xi}+g^{12}\frac{\partial u}{\partial\eta}+g^{13}\frac{\partial u}{\partial\zeta}\right)\right]+\\
&+\frac{\partial}{\partial\eta}\left[\rho Vu-J\left(\mu+\mu_T\right)\left(g^{21}\frac{\partial u}{\partial\xi}+g^{22}\frac{\partial u}{\partial\eta}+g^{23}\frac{\partial u}{\partial\zeta}\right)\right]+\\
&+\frac{\partial}{\partial\zeta}\left[\rho Wu-J\left(\mu+\mu_T\right)\left(g^{31}\frac{\partial u}{\partial\xi}+g^{32}\frac{\partial u}{\partial\eta}+g^{33}\frac{\partial u}{\partial\zeta}\right)\right]=\\
&=J\rho f_1-J\left(\frac{\partial p}{\partial\xi}\xi_x+\frac{\partial p}{\partial\eta}\eta_x+\frac{\partial p}{\partial\zeta}\zeta_x\right)+\\
&+\frac{\partial}{\partial\xi_s}\left[J\left(\mu+\mu_T\right)\frac{\xi_s}{\partial x_p}\left(\frac{\partial v_p}{\partial\xi_l}\frac{\partial\xi_l}{\partial x}\right)-\frac{2}{3}\delta_{1p}\left(\frac{\partial v_m}{\partial\xi_n}\frac{\partial\xi_n}{\partial x_m}\right)\right]-\\
&-\frac{2}{3}J\frac{\partial(\rho k)}{\partial\xi_j}\frac{\partial\xi_j}{\partial x_i}-\frac{\partial}{\partial\xi_k}\left[J\frac{\partial\xi_k}{\partial x_j}\left(\rho\overline{\hat{u}\hat{v}}_j\right)\right]
\end{aligned} \tag{5.2}$$

where

$$f_1=2\Omega_z v+\Omega^2 x+f_x$$

and f_x is the bodyforce in the x direction generated by neighbouring blade rows.

v-momentum

$$\begin{aligned}
&\frac{\partial}{\partial\xi}\left[\rho Uv-J\left(\mu+\mu_T\right)\left(g^{11}\frac{\partial v}{\partial\xi}+g^{12}\frac{\partial v}{\partial\eta}+g^{13}\frac{\partial v}{\partial\zeta}\right)\right]+\\
&+\frac{\partial}{\partial\eta}\left[\rho Vv-J(\mu+\mu_T)\left(g^{21}\frac{\partial v}{\partial\xi}+g^{22}\frac{\partial v}{\partial\eta}+g^{23}\frac{\partial v}{\partial\zeta}\right)\right]+\\
&+\frac{\partial}{\partial\zeta}\left[\rho Wv-J(\mu+\mu_T)\left(g^{31}\frac{\partial v}{\partial\xi}+g^{32}\frac{\partial v}{\partial\eta}+g^{33}\frac{\partial v}{\partial\zeta}\right)\right]=\\
&=J\rho f_2-J\left(\frac{\partial p}{\partial\xi}\xi_y+\frac{\partial p}{\partial\eta}\eta_y+\frac{\partial p}{\partial\zeta}\zeta_y\right)+\\
&+\frac{\partial}{\partial\xi_s}\left[J(\mu+\mu_T)\frac{\xi_s}{\partial x_p}\left(\frac{\partial v_p}{\partial\xi_l}\frac{\partial\xi_l}{\partial y}\right)-\frac{2}{3}\delta_{2p}\left(\frac{\partial v_m}{\partial\xi_n}\frac{\partial\xi_n}{\partial x_m}\right)\right]-\\
&-\frac{2}{3}J\frac{\partial(\rho k)}{\partial\xi_j}\frac{\partial\xi_j}{\partial x_i}-\frac{\partial}{\partial\xi_k}\left[J\frac{\partial\xi_k}{\partial x_j}\left(\rho\overline{\hat{v}\hat{v}}_j\right)\right]
\end{aligned} \tag{5.3}$$

where

$$f_2 = -2\Omega_z u + \Omega^2 y + f_y$$

and f_y is the bodyforce in the y direction generated by neighbouring blade rows.

w-momentum

$$\begin{aligned}
&\frac{\partial}{\partial\xi}\left[\rho U w - J(\mu+\mu_T)\left(g^{11}\frac{\partial w}{\partial\xi} + g^{12}\frac{\partial w}{\partial\eta} + g^{13}\frac{\partial w}{\partial\zeta}\right)\right] + \\
&+\frac{\partial}{\partial\eta}\left[\rho V w - J(\mu+\mu_T)\left(g^{21}\frac{\partial w}{\partial\xi} + g^{22}\frac{\partial w}{\partial\eta} + g^{23}\frac{\partial w}{\partial\zeta}\right)\right] + \\
&+\frac{\partial}{\partial\zeta}\left[\rho W w - J(\mu+\mu_T)\left(g^{31}\frac{\partial w}{\partial\xi} + g^{32}\frac{\partial w}{\partial\eta} + g^{33}\frac{\partial w}{\partial\zeta}\right)\right] = \\
&= J\rho f_3 - J\left(\frac{\partial p}{\partial\xi}\xi_z + \frac{\partial p}{\partial\eta}\eta_z + \frac{\partial p}{\partial\zeta}\zeta_z\right) + \\
&+\frac{\partial}{\partial\xi_s}\left[J(\mu+\mu_T)\frac{\xi_s}{\partial x_p}\left(\frac{\partial v_p}{\partial\xi_l}\frac{\partial\xi_l}{\partial z}\right) - \frac{2}{3}\delta_{2p}\left(\frac{\partial v_m}{\partial\xi_n}\frac{\partial\xi_n}{\partial x_m}\right)\right] - \\
&-\frac{2}{3}\frac{\partial(\rho k)}{\partial\xi_j}\frac{\partial\xi_j}{\partial x_i} - \frac{\partial}{\partial\xi_k}\left[J\frac{\partial\xi_k}{\partial x_j}\left(\rho\overline{\widehat{w}\widehat{v}_j}\right)\right]
\end{aligned} \tag{5.4}$$

where

$$f_3 = f_z$$

and f_z is the bodyforce in the z direction generated by neighbouring blade rows.

k–Equation

$$\begin{aligned}
&\frac{\partial}{\partial\xi}\left[\rho U k - J\left(\frac{\mu_T}{\sigma_k}\right)\left(g^{11}\frac{\partial k}{\partial\xi} + g^{12}\frac{\partial k}{\partial\eta} + g^{13}\frac{\partial k}{\partial\zeta}\right)\right] + \\
&+\frac{\partial}{\partial\eta}\left[\rho V k - J\left(\frac{\mu_T}{\sigma_k}\right)\left(g^{21}\frac{\partial k}{\partial\xi} + g^{22}\frac{\partial k}{\partial\eta} + g^{23}\frac{\partial k}{\partial\zeta}\right)\right] + \\
&+\frac{\partial}{\partial\zeta}\left[\rho W k - J\left(\frac{\mu_T}{\sigma_k}\right)\left(g^{31}\frac{\partial k}{\partial\xi} + g^{32}\frac{\partial k}{\partial\eta} + g^{33}\frac{\partial k}{\partial\zeta}\right)\right] = G_k - \rho\epsilon
\end{aligned} \tag{5.5}$$

where

$$G_k = \mu_T\left(\frac{\partial v_i}{\partial\xi_l}\frac{\xi_l}{\partial x_j} + \frac{\partial v_j}{\partial\xi_n}\frac{\xi_n}{\partial x_i}\right)\left(\frac{\partial v_i}{\partial\xi_l}\frac{\partial\xi_l}{\partial x_j}\right)$$

ϵ–Equation

$$\frac{\partial}{\partial\xi}\left[\rho U\epsilon - J\left(\frac{\mu_T}{\sigma_\epsilon}\right)\left(g^{11}\frac{\partial\epsilon}{\partial\xi} + g^{12}\frac{\partial\epsilon}{\partial\eta} + g^{13}\frac{\partial\epsilon}{\partial\zeta}\right)\right] +$$

$$\begin{aligned}
&+\frac{\partial}{\partial \eta}\left[\rho V\epsilon - J\left(\frac{\mu_T}{\sigma_\epsilon}\right)\left(g^{21}\frac{\partial \epsilon}{\partial \xi} + g^{22}\frac{\partial \epsilon}{\partial \eta} + g^{23}\frac{\partial \epsilon}{\partial \zeta}\right)\right] + \\
&+\frac{\partial}{\partial \zeta}\left[\rho W\epsilon - J\left(\frac{\mu_T}{\sigma_\epsilon}\right)\left(g^{31}\frac{\partial \epsilon}{\partial \xi} + g^{32}\frac{\partial \epsilon}{\partial \eta} + g^{33}\frac{\partial \epsilon}{\partial \zeta}\right)\right] = \\
&= \frac{\epsilon}{k}\left(C_1 G_k - C_2 \rho \epsilon\right)
\end{aligned} \tag{5.6}$$

General Scalar Equation

$$\begin{aligned}
&\frac{\partial}{\partial \xi}\left[\rho U\Phi - J\Gamma_\Phi\left(g^{11}\frac{\partial \Phi}{\partial \xi} + g^{12}\frac{\partial \Phi}{\partial \eta} + g^{13}\frac{\partial \Phi}{\partial \zeta}\right)\right] + \\
&+\frac{\partial}{\partial \eta}\left[\rho V\Phi - J\Gamma_\Phi\left(g^{21}\frac{\partial \Phi}{\partial \xi} + g^{22}\frac{\partial \Phi}{\partial \eta} + g^{23}\frac{\partial \Phi}{\partial \zeta}\right)\right] + \\
&+\frac{\partial}{\partial \zeta}\left[\rho W\Phi - J\Gamma_\Phi\left(g^{31}\frac{\partial \Phi}{\partial \xi} + g^{32}\frac{\partial \Phi}{\partial \eta} + g^{33}\frac{\partial \Phi}{\partial \zeta}\right)\right] = JS_\Phi
\end{aligned} \tag{5.7}$$

or

$$\begin{aligned}
&\frac{\partial}{\partial \xi}(\rho U\Phi) + \frac{\partial}{\partial \eta}(\rho V\Phi) + \frac{\partial}{\partial \zeta}(\rho W\Phi) = \\
&= \frac{\partial}{\partial \xi}\left(J\Gamma_\Phi g^{11}\frac{\partial \Phi}{\partial \xi}\right) + \frac{\partial}{\partial \eta}\left(J\Gamma_\Phi g^{22}\frac{\partial \Phi}{\partial \eta}\right) + \frac{\partial}{\partial \zeta}\left(J\Gamma_\Phi g^{33}\frac{\partial \Phi}{\partial \zeta}\right) + \\
&+\left\{ JS_\Phi(\xi,\eta,\zeta) + \frac{\partial}{\partial \xi}\left[J\Gamma_\Phi\left(g^{12}\frac{\partial \Phi}{\partial \eta} + g^{13}\frac{\partial \Phi}{\partial \zeta}\right)\right] + \right. \\
&\left. +\frac{\partial}{\partial \eta}\left[J\Gamma_\Phi\left(g^{21}\frac{\partial \Phi}{\partial \xi} + g^{23}\frac{\partial \Phi}{\partial \zeta}\right)\right] + \frac{\partial}{\partial \zeta}\left[J\Gamma_\Phi\left(g^{31}\frac{\partial \Phi}{\partial \xi} + g^{33}\frac{\partial \Phi}{\partial \zeta}\right)\right]\right\}
\end{aligned} \tag{5.8}$$

where the non-orthogonal "cross diffusion" terms have been lumped into the source terms. Thus the scalar equation takes similar form to that in the Cartesian coordinates and allows fluid dynamics problems involving complex geometries to be handled in a similar way.

In the governing equations the coefficients g^{jk} are defined as follows:

$$\begin{aligned}
g^{11} &= \xi_x^2 + \xi_y^2 + \xi_z^2 \\
g^{22} &= \eta_x^2 + \eta_y^2 + \eta_z^2 \\
g^{33} &= \zeta_x^2 + \zeta_y^2 + \zeta_z^2 \\
g^{12} = g^{21} &= \xi_x\eta_x + \xi_y\eta_y + \xi_z\eta_z \\
g^{13} = g^{31} &= \xi_x\zeta_x + \xi_y\zeta_y + \xi_z\zeta_z \\
g^{23} = g^{32} &= \eta_x\zeta_x + \eta_y\zeta_y + \eta_z\zeta_z
\end{aligned} \tag{5.9}$$

The variables in the scalar equation take different forms for different equations and are summarised in Table 5.1.

Equations	Φ	Γ_Φ	S_Φ
Mass	1	0	0
v_i–Momentum $(i = 1,2,3)$	v_i	$\mu + \mu_T$	$\frac{\partial}{\partial \xi_j}\left[J(\mu+\mu_T)\left(g^{jk}\frac{\partial v_i}{\partial \xi_k}\right)_{j\neq k}\right] -$ $-J\frac{\partial p}{\partial \xi_j}\frac{\partial \xi_j}{\partial x_i} + J\rho f_i +$ $+\frac{\partial}{\partial \xi_s}\left[J(\mu+\mu_T)\frac{\partial \xi_s}{\partial x_p}\left(\frac{\partial v_p}{\partial \xi_l}\frac{\partial \xi_l}{\partial x_i}\right) -\right.$ $\left. -\frac{2}{3}\delta_{ip}\left(\frac{\partial v_m}{\partial \xi_n}\frac{\partial \xi_n}{\partial x_m}\right)\right] -$ $-\frac{2}{3}J\frac{\partial(\rho k)}{\partial \xi_j}\frac{\partial \xi_j}{\partial x_i} - \frac{\partial}{\partial \xi_k}\left[J\frac{\partial \xi_k}{\partial x_j}\left(\rho\overline{\hat{\overline{v}}_i\hat{\overline{v}}_j}\right)\right]$
k–Equation	k	$\frac{\mu_T}{\sigma_k}$	$G_k - \rho\epsilon$
ϵ–Equation	ϵ	$\frac{\mu_T}{\sigma_\epsilon}$	$\frac{\epsilon}{k}(C_1 G_k - C_2\rho\epsilon)$

Table 5.1: **Meanings of symbols in scalar equation**

Although the governing equations have different expressions, they take the same form expressed with the scalar equation. This similarity has the advantage that a similar discretization and solution procedures can be followed.

5.3 Discretization Procedure

5.3.1 Finite Volume Integration

There are basically three major discretization methods for fluid dynamics problems: the Finite Difference (FDM), the Finite Volume (FVM) and the Finite Element methods (FEM). The discretization procedure in this study is based on the finite-volume method where the flow domain is firstly divided into small non-overlapped volumes (finite control volumes). Each control volume surrounds a nodal point that is located at the centre of the volume and the flow quantities representing the mean value of the volume are stored at that point. Figure 5.1 illustrates a typical control volume in physical space around node P, along with some neighbouring nodes and mid-nodes and clarifies the notation used hereafter. E, W, N, S, F and B denote the neighbouring grid points per two in the ξ, η and ζ directions respectively and e, w, n, s, f and b correspond to the mid-nodes on

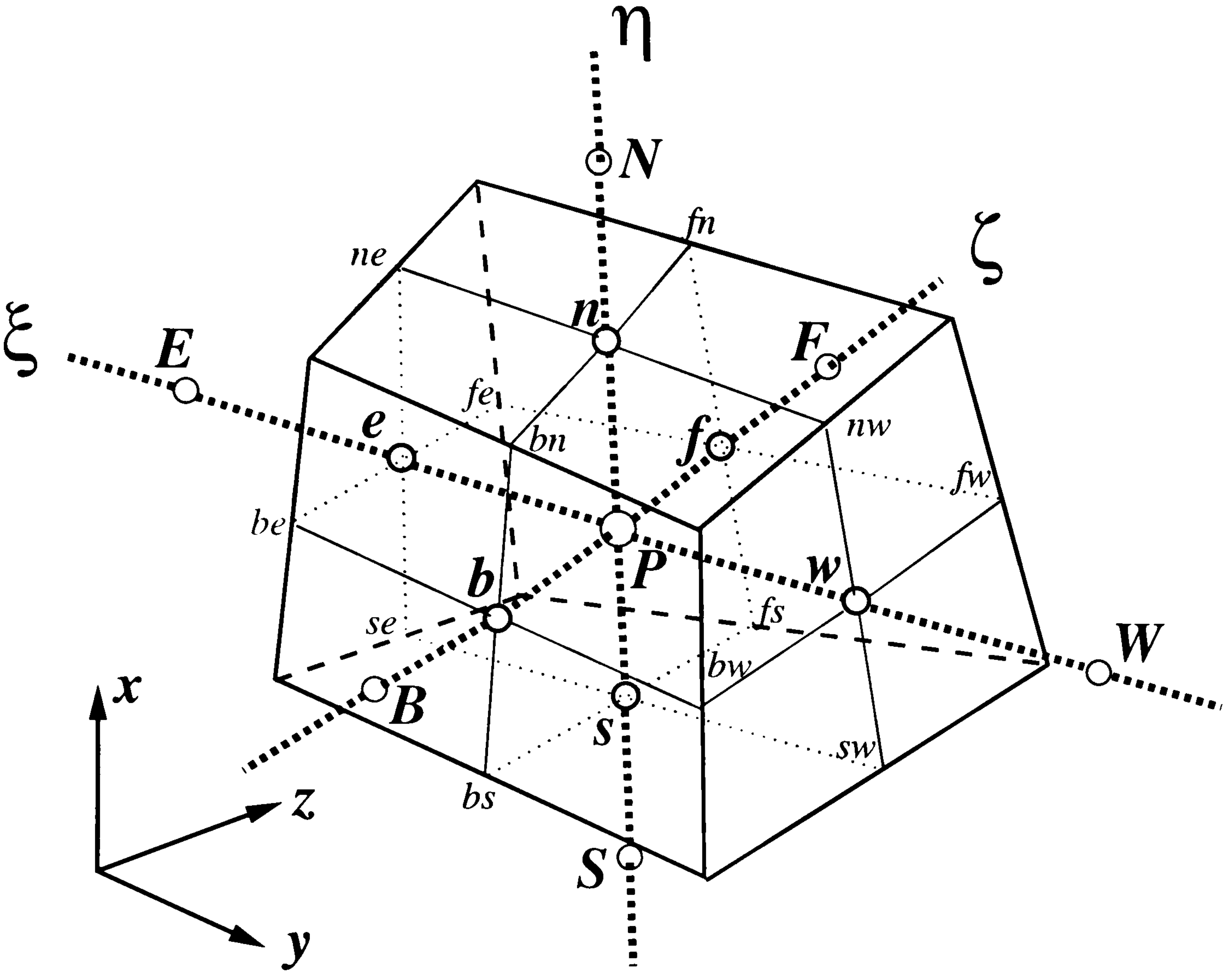

Figure 5.1: **A Control volume and notation**

the volume faces.

The transport equation for a scalar variable Φ, which is a typical steady convection-diffusion equation, can be written in the following form:

$$\nabla \cdot (\rho \Phi \vec{\mathbf{V}}) = \nabla \cdot (\Gamma_\Phi \nabla \Phi) + S_\Phi \tag{5.10}$$

Formal integration over a three-dimensional control volume V_p yields

$$\int_{V_p} \nabla \cdot (\rho \Phi \vec{\mathbf{V}}) dV_p = \int_{V_p} \nabla \cdot (\Gamma_\Phi \nabla \Phi) dV_p + \int_{V_p} S_\Phi dV_p \tag{5.11}$$

On the control volume Gauss's divergence theorem is applied, where the integral of the divergence of a vector variable $\vec{\mathbf{f}}$ over a volume is equal to the component of $\vec{\mathbf{f}}$ in the direction normal to the surface which bounds the volume integrated over the entire bounding surface S, expressed in the following equation.

$$\int_{V_p} \nabla \cdot \vec{\mathbf{f}} dV_p = \oint_S \vec{\mathbf{n}} \cdot \vec{\mathbf{f}} dS = \oint_S \vec{\mathbf{f}} \cdot d\vec{\mathbf{S}} \tag{5.12}$$

The mean value theorem is utilised to provide the value of Φ at the surfaces of the control volume. For example, at "east" surface

$$\Phi_e = \frac{\int_{S_e} \Phi dS_e}{\int_{S_e} dS_e} \tag{5.13}$$

The transport Equation (5.11) can be written as follows

$$\oint_S (\rho\Phi\vec{V}) \cdot d\vec{\mathbf{S}} = \oint_S (\Gamma_\Phi \nabla \Phi) \cdot d\vec{\mathbf{S}} + \int_{V_p} S_\Phi dV_p \tag{5.14}$$

This equation represents the flux balance in a control volume. In other words, the net convective flux equals to the sum of the net diffusive flux plus the generation or destruction of the property Φ within the control volume.

5.3.2 Discretization of the Convection Term

The convection term in the transport equations can be discretized into the following form around the control volume

$$I^C = \oint_S (\rho\vec{\mathbf{V}}\Phi) \cdot d\vec{\mathbf{S}} = I_e^C - I_w^C + I_n^C - I_s^C + I_f^C - I_b^C \tag{5.15}$$

where

$$\begin{aligned}
I_e^C &= \int_{S_e} (\rho V\Phi) dS &= F_e\Phi_e, \quad &where \quad F_e = &(\rho V\delta\eta\delta\zeta)_e \\
I_w^C &= \int_{S_w} (\rho V\Phi) dS &= F_w\Phi_w, \quad &where \quad F_w = &(\rho V\delta\eta\delta\zeta)_w \\
I_n^C &= \int_{S_n} (\rho U\Phi) dS &= F_n\Phi_n, \quad &where \quad F_n = &(\rho U\delta\xi\delta\zeta)_n \\
I_s^C &= \int_{S_s} (\rho U\Phi) dS &= F_s\Phi_s, \quad &where \quad F_s = &(\rho U\delta\xi\delta\zeta)_s \\
I_f^C &= \int_{S_f} (\rho W\Phi) dS &= F_f\Phi_f, \quad &where \quad F_f = &(\rho W\delta\xi\delta\eta)_f \\
I_b^C &= \int_{S_b} (\rho W\Phi) dS &= F_b\Phi_b, \quad &where \quad F_b = &(\rho W\delta\xi\delta\eta)_b
\end{aligned} \tag{5.16}$$

where I^C represents the convection term and F is the mass flux.

The values of velocity components U, V and W and the scalar quantity Φ at control volume faces are estimated with corresponding values stored in neighbouring control volumes by using approximate numerical schemes which will be discussed in Section 5.4.

The continuity equation contains only convective terms when $\Phi = 1$ and can be expressed in the following form:

$$F_e - F_w + F_n - F_s + F_f - F_b = 0 \tag{5.17}$$

5.3.3 Discretization of the Diffusion Term

The integration of the diffusion term in the transport equations can be discretized in the following form:

$$I^D = \oint_S (\Gamma_\Phi \nabla \Phi) \cdot d\vec{S} = I_e^D - I_w^D + I_n^D - I_s^D - I_f^D - I_b^D \tag{5.18}$$

The diffusion term I^D consists of two parts: the "normal" diffusion terms I^{DN} where the first derivative of Φ is normal to the volume faces, and the "cross" diffusion terms where the first derivatives of Φ is crossing the volume faces. For example, at the "e" face of the control volume

$$I_e^D = (\Gamma_\Phi \nabla \Phi)_e \cdot A_e = \left[J\Gamma_\Phi \left(\frac{\partial \Phi}{\partial \xi} g^{11} + \frac{\partial \Phi}{\partial \eta} g^{12} + \frac{\partial \Phi}{\partial \zeta} g^{13} \right) \right]_e (\delta\eta\delta\zeta)_P \tag{5.19}$$

$$I_e^D = I_e^{DN} + I_e^{DC} \tag{5.20}$$

where

$$I_e^{DN} = \left[J\Gamma_\Phi \left(\frac{\partial \Phi}{\partial \xi} g^{11} \right) \right]_e (\delta\eta\delta\zeta)_P$$

$$I_e^{DC} = \left[J\Gamma_\Phi \left(\frac{\partial \Phi}{\partial \eta} g^{12} + \frac{\partial \Phi}{\partial \zeta} g^{13} \right) \right]_e (\delta\eta\delta\zeta)_P$$

By applying the central difference scheme to the following first derivatives of Φ , we obtain:

$$\left(\frac{\partial \Phi}{\partial \xi} \right)_e = \frac{\Phi_E - \Phi_P}{(\delta\xi)_e}$$

$$\left(\frac{\partial \Phi}{\partial \eta} \right)_e = \frac{(\Phi_n - \Phi_s)_e}{(\delta\eta)_e} = \frac{\Phi_{ne} - \Phi_{se}}{(\delta\eta)_P}$$

$$\left(\frac{\partial \Phi}{\partial \zeta} \right)_e = \frac{(\Phi_f - \Phi_b)_e}{(\delta\zeta)_e} = \frac{\Phi_{fe} - \Phi_{be}}{(\delta\zeta)_P}$$

where the values of Φ_{ne}, Φ_{se}, Φ_{fe} and Φ_{be} are obtained from the neighbouring nodal values through approximate interpolation based on central differencing scheme. Then the "normal" and "cross" diffusion terms can be expressed as follows:

$$I_e^{DN} = D_e(\Phi_E - \Phi_P) \qquad where \qquad D_e = \left(\frac{J\Gamma_\Phi g^{11}}{\delta\xi} \right)_e (\delta\eta\delta\zeta)_P \tag{5.21}$$

$$I_e^{DC} = (J\Gamma_\Phi g^{12})_e(\Phi_{ne} - \Phi_{se})(\delta\zeta)_P + (J\Gamma_\Phi g^{13})_e(\Phi_{fe} - \Phi_{be})(\delta\eta)_P \tag{5.22}$$

In a similar way on other cell faces, the normal diffusion terms can be expressed as:

$$\begin{aligned}
I_w^{DN} &= D_w(\Phi_P - \Phi_W), \quad where \quad D_w = \left(\frac{J\Gamma_\Phi g^{11}}{\delta\xi}\right)_w (\delta\eta\delta\zeta)_P \\
I_n^{DN} &= D_n(\Phi_N - \Phi_P), \quad where \quad D_n = \left(\frac{J\Gamma_\Phi g^{22}}{\delta\eta}\right)_n (\delta\xi\delta\zeta)_P \\
I_s^{DN} &= D_s(\Phi_P - \Phi_S), \quad where \quad D_s = \left(\frac{J\Gamma_\Phi g^{22}}{\delta\eta}\right)_s (\delta\xi\delta\zeta)_P \\
I_f^{DN} &= D_f(\Phi_F - \Phi_P), \quad where \quad D_f = \left(\frac{J\Gamma_\Phi g^{33}}{\delta\zeta}\right)_f (\delta\xi\delta\eta)_P \\
I_b^{DN} &= D_b(\Phi_P - \Phi_B), \quad where \quad D_b = \left(\frac{J\Gamma_\Phi g^{33}}{\delta\zeta}\right)_b (\delta\xi\delta\eta)_P
\end{aligned} \tag{5.23}$$

and the cross diffusion terms can be expressed as:

$$\begin{aligned}
I_w^{DC} &= (J\Gamma_\Phi g^{12})_e(\Phi_{nw} - \Phi_{sw})(\delta\zeta)_P + (J\Gamma_\Phi g^{13})_e(\Phi_{fw} - \Phi_{bw})(\delta\eta)_P \\
I_n^{DC} &= (J\Gamma_\Phi g^{21})_e(\Phi_{ne} - \Phi_{nw})(\delta\zeta)_P + (J\Gamma_\Phi g^{23})_e(\Phi_{fn} - \Phi_{bn})(\delta\xi)_P \\
I_s^{DC} &= (J\Gamma_\Phi g^{21})_e(\Phi_{se} - \Phi_{sw})(\delta\zeta)_P + (J\Gamma_\Phi g^{23})_e(\Phi_{fs} - \Phi_{bs})(\delta\xi)_P \\
I_f^{DC} &= (J\Gamma_\Phi g^{31})_e(\Phi_{fe} - \Phi_{fw})(\delta\eta)_P + (J\Gamma_\Phi g^{32})_e(\Phi_{fn} - \Phi_{fs})(\delta\xi)_P \\
I_b^{DC} &= (J\Gamma_\Phi g^{31})_e(\Phi_{be} - \Phi_{bw})(\delta\eta)_P + (J\Gamma_\Phi g^{32})_e(\Phi_{bn} - \Phi_{bs})(\delta\xi)_P
\end{aligned} \tag{5.24}$$

5.3.4 Discretization of the Source Term

The source term in the transport equations includes the pressure gradient term $(\partial p/\partial x_i)$, cross diffusion term (I^{DC}) and the rest of the terms (S_Φ) not included in the convection and normal diffusion terms.

The pressure term is separated from the source term because of its significance for the calculation of the pressure field with pressure correction approach. It is integrated approximately over the control volume by

$$\begin{aligned}
S^{PGT} &= \int_{V_p} \left(-\frac{\partial p}{\partial x_i}\right) dV_p \\
&= -\int_{V_p} \left(\frac{\partial p}{\partial \xi}\xi_{x_i} + \frac{\partial p}{\partial \eta}\eta_{x_i} + \frac{\partial p}{\partial \zeta}\zeta_{x_i}\right) dV_p \\
&= -\left(\frac{\partial p}{\partial \xi}\xi_{x_i} + \frac{\partial p}{\partial \eta}\eta_{x_i} + \frac{\partial p}{\partial \zeta}\zeta_{x_i}\right)_P (J\delta\xi\delta\eta\delta\zeta)_P
\end{aligned} \tag{5.25}$$

The pressure gradients may be approximated by the following formula:

$$\left(\frac{\partial p}{\partial \xi}\right)_P = \frac{p_e - p_w}{(\delta\xi)_P}, \quad \left(\frac{\partial p}{\partial \eta}\right)_P = \frac{p_n - p_s}{(\delta\eta)_P}, \quad \left(\frac{\partial p}{\partial \zeta}\right)_P = \frac{p_f - p_b}{(\delta\zeta)_p} \tag{5.26}$$

The volume integral of the source term (S_Φ) is approximated by:

$$I^{S_\Phi} = \int_{V_p} S_\Phi dV_p = (S_\Phi)_P (J\delta\xi\delta\eta\delta\zeta)_P \tag{5.27}$$

where $(S_\Phi)_P$ is the average value of S_Φ in the control volume and stored at the centre of the volume, V_p is the volume of the control volume surrounding the node P. According to Patankar [135] the source term S_Φ can be linearised into two distinct parts and expressed by

$$S_\Phi = S'_\Phi + S''_\Phi \Phi \tag{5.28}$$

The sign of S''_Φ is chosen to be negative to ensure realistic solutions. In such cases, the discretization of the source term can be expressed as

$$\begin{aligned} I^{S_\Phi} &= (S'_\Phi + S''_\Phi \Phi)_P (J\delta\xi\delta\eta\delta\zeta)_P \\ &= I^{S'_\Phi} + I^{S''_\Phi}\Phi_P \end{aligned} \tag{5.29}$$

where

$$I^{S'_\Phi} = (S'_\Phi)_P (J\delta\xi\delta\eta\delta\zeta)_P \tag{5.30}$$

$$I^{S''_\Phi} = (S''_\Phi)_P (J\delta\xi\delta\eta\delta\zeta)_P \tag{5.31}$$

The source term $I^{S''_\Phi}\Phi_P$ is lumped into the central node term of the discretized equation. Eventually, the integrated source term in the discretized equation becomes:

$$S_P = I^{S'_\Phi} + S^{PGT} + S^{CDT} \tag{5.32}$$

where S^{CDT} includes all the cross diffusion terms and is expressed by

$$S^{CDT} = I_e^{DC} - I_w^{DC} + I_n^{DC} - I_s^{DC} + I_f^{DC} - I_b^{DC} \tag{5.33}$$

5.3.5 General Form of the Discretized Equations

After the discretization of all the terms of the integrated transport equations on a control volume, they can be combined together and expressed in the following typical form:

$$A_P\Phi_P = A_E\Phi_E + A_W\Phi_W + A_N\Phi_N + A_S\Phi_S + A_F\Phi_F + A_B\Phi_B + S_P \tag{5.34}$$

or

$$A_P\Phi_P = \sum_{nb} A_{nb}\Phi_{nb} + S_P \tag{5.35}$$

where the coefficients $A_{nb}(nb = E, W, N, S, F, B, P)$ are obtained from the combination of discretized convection and diffusion terms which will be discussed in the next section; S_P is determined by Equation (5.32) and the coefficient of central node term is

$$A_P = \sum_{nb} A_{nb} - I^{S''_{\Phi}} \tag{5.36}$$

5.4 Numerical Schemes for the Convection Term

Properties of Numerical Schemes

The values of the independent variables in the convection terms of the transport equations have to be estimated in terms of their values at the neighbouring grid points during the discretization process. Different numerical differential schemes have been developed for such estimation. According to Versteeg et al. [180], numerical results may theoretically be indistinguishable from the "exact" solution of the transport equations when the number of computational volumes is infinitely large irrespective of the differencing method used. However in practice, only a finite number of volumes can be used and the numerical results will only be physically realistic when the discretization scheme has certain fundamental properties. The most important ones are stated below, Versteeg et al. [180]:

Conservativeness

The discretization of the transport equations over control volumes yields a set of discretized conservation equations involving the flux of the transported property Φ through the volume faces. To ensure the conservation of Φ for the whole solution domain, the flux of Φ leaving a control volume across a certain face must be equal to the flux entering the adjacent control volume through the same face. This can only be achieved when the flux through a common face is represented by the same expression in adjacent control volumes.

Boundedness

Normally iterative numerical techniques are used to solve a set of discretized algebraic equations for a solution domain. This iteration process starts from a guessed distribution of the variable Φ and perform successive updates until a converged solution is obtained. A sufficient condition known as Scarborough criterion for a convergent iteration method can be expressed in terms of the coefficients of the discretized Equation (5.34):

$$\frac{\sum_{nb} |A_{nb}|}{|A_P|} \begin{cases} \leq 1 & \text{at all nodes} \\ < 1 & \text{at one node at least} \end{cases} \tag{5.37}$$

Here A_P is the net coefficient of the central node P and the summation in the numerator is taken over all the neighbouring nodes (nb). If the differencing scheme produces coefficients that satisfy the above criterion the resulting matrix of coefficients is diagonally dominant.

Diagonal dominance is desirable for satisfying the "boundedness" criterion which means that the internal nodal value of Φ should be between its minimum and maximum boundary values. Another essential requirement for boundedness is that all coefficients of the discretized equations should have the same sign (usually all positive) which physically implies that an increase in variable Φ at one node should result in an increase in Φ at neighbouring nodes. If the discretization scheme does not satisfy the boundedness requirements the solution may not converge at all or contains "wiggles".

Transportiveness

The transportiveness of a numerical scheme is the relationship between the magnitude of the Peclet number (Pe) and the directionality of influencing of flows. The non-dimensional volume Peclet number is defined as a ratio between convection and diffusion and as a measure of the relative strength of convection and diffusion.

$$P_e = \frac{F}{D} = \frac{Convection}{Diffusion} \tag{5.38}$$

The features of the transportiveness can be described by two extreme cases: in the case of pure diffusion the fluid is stagnant ($P_e = 0$) and the diffusion process tends to spread Φ equally in all directions; in the case of pure convection ($P_e = \infty$) all of property Φ propagating from the source immediately transported downstream or the flow properties have no influence on the upstream regions. If the discretization scheme does not satisfy the features of transportiveness. the unrealistic results will be produced.

Central Difference Scheme

The central difference provides an approximation of property Φ at a certain position from a linear interpolation between its bracketing nodal values. For ex-

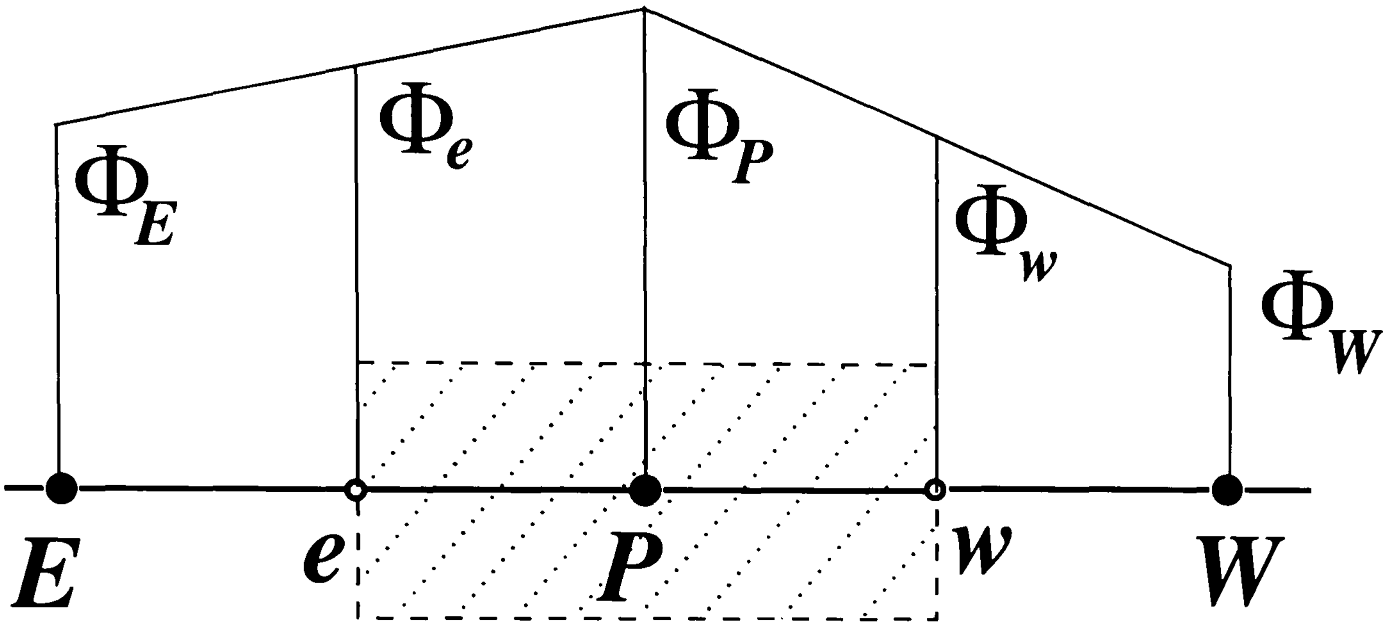

Figure 5.2: **Central difference scheme**

ample, this scheme is shown in Figure 5.2 in a one dimensional situation. Based on the above definition, the scalar quantity Φ on the control volume faces are estimated with the following expressions:

$$\begin{aligned} \Phi_e &= f_P^\xi \Phi_P &+(1-f_P^\xi)\Phi_E \\ \Phi_w &= f_W^\xi \Phi_W &+(1-f_W^\xi)\Phi_P \end{aligned} \tag{5.39}$$

where f_P^ξ and f_W^ξ are interpolation factors and defined as:

$$f_P^\xi = \frac{\overline{eE}}{\overline{Pe}+\overline{eE}}, \qquad f_W^\xi = \frac{\overline{wP}}{\overline{Ww}+\overline{wP}} \tag{5.40}$$

where the overbar denotes distance. Similar expressions can be obtained in other coordinates. The coefficients corresponding to the variables of discretized transport Equation (5.34) can be expressed as:

$$\begin{aligned} A_E &= D_e + F_e(1-f_P^\xi), & A_W &= D_w + F_w f_W^\xi \\ A_N &= D_n + F_n(1-f_P^\eta), & A_S &= D_s + F_s f_S^\eta \\ A_F &= D_f + F_f(1-f_P^\zeta), & A_B &= D_b + F_b f_B^\zeta \end{aligned} \tag{5.41}$$

$$\begin{aligned} A_P &= A_E + A_W + A_N + A_S + A_F + A_B + \\ &+(F_e - F_w + F_n - F_s + F_f - F_b) \end{aligned} \tag{5.42}$$

When the mass continuity equation is satisfied, we obtain:

$$A_P = \sum_{nb} A_{nb}, \qquad nb = E, W, N, S, F, B \tag{5.43}$$

Discussion

1. The central difference scheme uses consistent expressions so the scheme is conservative.

2. In the case of a high Peclet number (Pe) which means the convection dominates the flows, some of the coefficients are negative. This violates one of the requirements of boundedness and may lead to physically impossible solutions.

3. The central difference scheme does not recognise the direction of the flow or the strength of convection relative to diffusion, so it does not possess the transportiveness property at high Pe.

4. The central difference scheme is the second order in terms of Taylor series truncation error. This scheme is more suitable for flows with a small Peclet number ($Pe < 2$).

Upwind Difference Scheme

The upwind difference scheme takes into account the flow direction when determining the convected value of Φ at a certain point: it is taken to be equal to the value at the upstream node. In Figure 5.3 when the flow is in the positive direction (from E to W), i.e. $u_w > 0$, $u_e > 0$ ($Fw > 0, Fe > 0$), the upwind scheme sets face values as:

$$\Phi_w = \Phi_P \qquad and \qquad \Phi_e = \Phi_E \tag{5.44}$$

When the flow is in the negative direction, i.e. $u_w < 0$, $u_e < 0$ ($F_w < 0, F_e < 0$), the scheme takes the form:

$$\Phi_w = \Phi_W \qquad and \qquad \Phi_e = \Phi_P \tag{5.45}$$

Similar expressions can be obtained in other coordinates. So the coefficients of the discretized transport Equation (5.34) are

$$\begin{aligned} A_E &= D_e + max(0, F_e), & A_W &= D_w + max(0, -F_w) \\ A_N &= D_n + max(0, F_n), & A_S &= D_s + max(0, -F_s) \\ A_F &= D_f + max(0, F_f), & A_B &= D_b + max(0, -F_b) \end{aligned} \tag{5.46}$$

where "max" means maximum value. The central coefficient is calculated by

$$\begin{aligned} A_P &= A_E + A_W + A_N + A_S + A_F + A_B + \\ &+ \quad (F_e - F_w + F_n - f_s + F_f - F_b) \end{aligned} \tag{5.47}$$

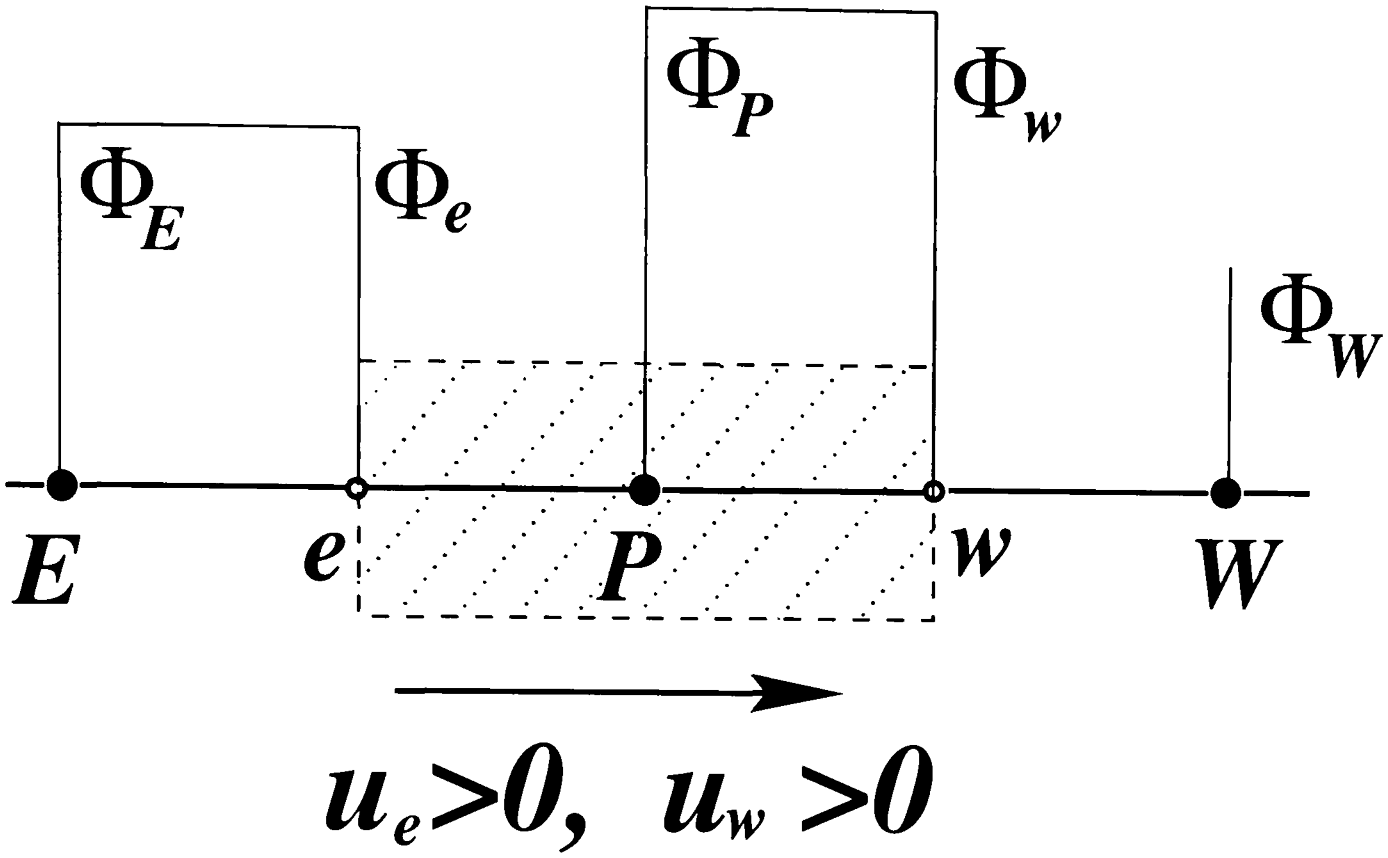

Figure 5.3: **Upwind difference scheme**

When the mass continuity equation is satisfied, the central coefficient becomes

$$A_P = \sum_{nb} A_{nb}, \qquad nb = E, W, N, S, F, B \tag{5.48}$$

Discussion

1. The upwind scheme is conservative because consistent expressions are utilised for flux calculation through the volume faces.
2. The coefficients of the discretized equation are always positive and $A_p = \sum_{nb} A_{nb}$ when the flow satisfies mass continuity. Therefore, the requirements of the boundedness are satisfied and stable iterative solutions can be obtained.
3. The scheme accounts for the flow direction so it is transportive.
4. The accuracy of the upwind scheme is only the first order on the basis of the Taylor series truncation error. Therefore, the upwind difference scheme is not entirely suitable for accurate flow prediction but has the favourite advantage of strong stability.

5. This scheme is more suitable for flows with a high Peclet number ($Pe \geq 2$).

QUICK Scheme

The first order upwind scheme is very stable and obeys the transportiveness requirements but is prone to numerical diffusion errors due to its first order accuracy. The central difference scheme which has second-order accuracy proved to be unstable and does not possess the transportiveness property. So higher order schemes, which preserve upwinding for stability and sensitivity to the flow direction, reduce the discretization errors by employing higher order discretization and bring in a wider influence, are required, Versteeg et al. [180]. One of the most popular higher order schemes is the Quadratic Upstream Interpolation for Convection Kinetics (*QUICK*) scheme developed by Leonard [110], which uses a three-point upstream-weighted quadratic interpolation for cell face values. This scheme was improved by several researchers such as Hayse et al. [75] who generalised the approach for re-arranging *QUICK* schemes and derived a stable and fast converging variant which is described in detail below.

The face value of Φ is obtained from two bracketing nodes (on each side of the face) and a further upstream node with a quadratic function. In one-dimensional case where uniform grids are employed, the face value of Φ at "e" is given by the following formula when $u_e > 0, u_w > 0$ ($F_e > 0, F_w > 0$), Figure 5.4(a):

$$\Phi_e = \Phi_E + \frac{1}{8}(3\Phi_P - 2\Phi_E - \Phi_{EE}) \tag{5.49}$$

$$\Phi_w = \Phi_P + \frac{1}{8}(3\Phi_W - 2\Phi_P - \Phi_E) \tag{5.50}$$

and when $u_e < 0, u_w < 0$ ($F_e < 0, F_w < 0$), Figure 5.4(b):

$$\Phi_e = \Phi_P + \frac{1}{8}(3\Phi_E - 2\Phi_P - \Phi_W) \tag{5.51}$$

$$\Phi_w = \Phi_W + \frac{1}{8}(3\Phi_P - 2\Phi_W - \Phi_{WW}) \tag{5.52}$$

Similar face values can be obtained in other coordinate directions. The above expressions are derived from uniform grids but applied to non-uniform grids for simplicity. Therefore the coefficients of the discretized transport equation are given by the following expressions:

$$\begin{aligned} A_E &= D_e + max(0, F_e), & A_W &= D_w + max(0, -F_w) \\ A_N &= D_n + max(0, F_n), & A_S &= D_s + max(0, -F_s) \\ A_F &= D_f + max(0, F_f), & A_B &= D_b + max(0, -F_b) \end{aligned} \tag{5.53}$$

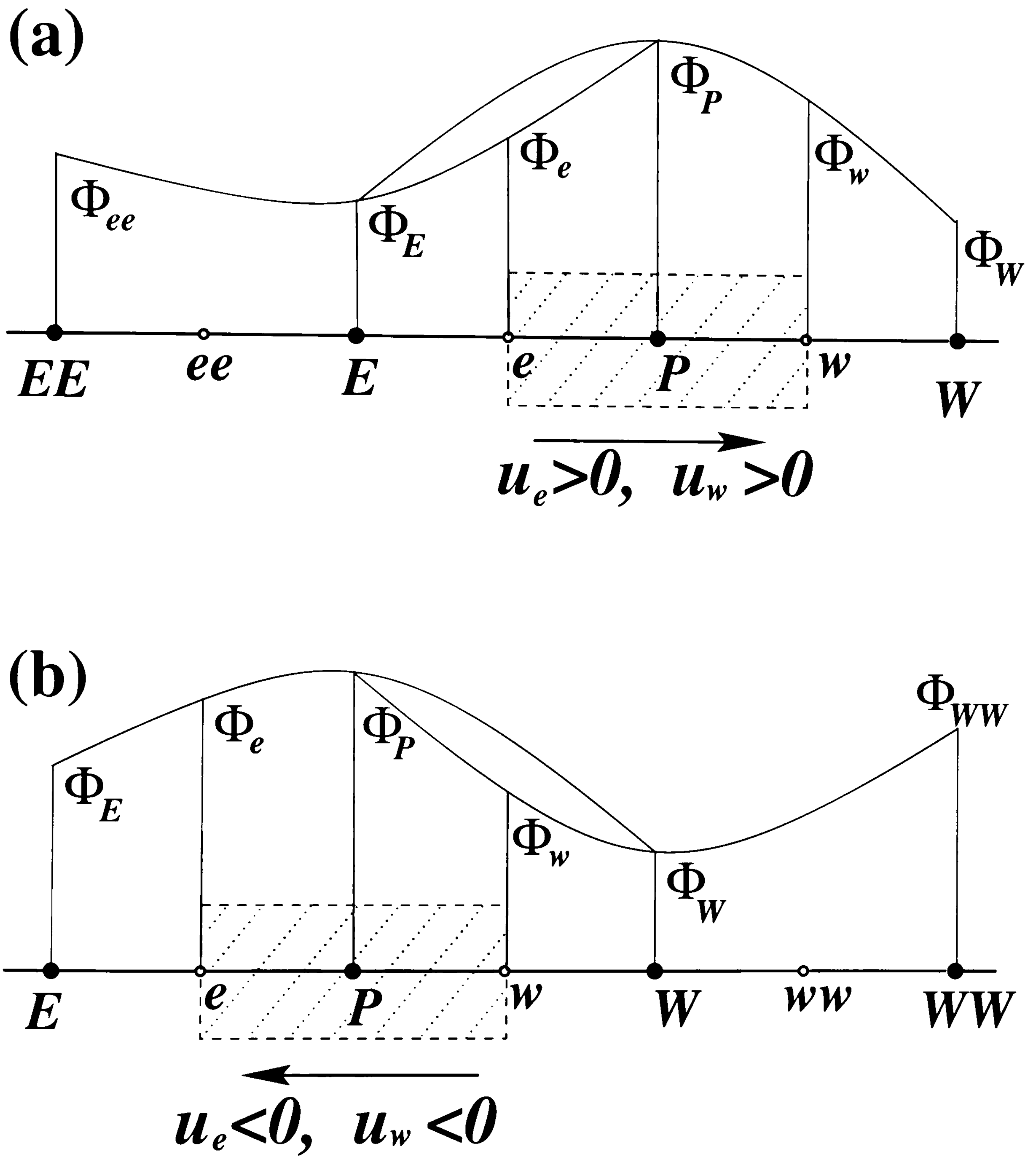

Figure 5.4: *QUICK* scheme

where "max" and "min" mean maximum and minimum values, respectively. The central coefficient is calculated by

$$\begin{aligned} A_P &= A_E - A_W + A_N - A_S + A_F - A_B + \\ &+ (F_e - F_w + F_n - F_s + F_f - F_b) \end{aligned} \tag{5.54}$$

When the mass continuity is satisfied, the expression of A_P becomes:

$$A_P = \sum_{nb} A_{nb}, \qquad nb = E, W, N, S, F, B \tag{5.55}$$

Other terms not included in the above coefficients are put into a high order term (S^{HOT}) and lumped into the source term:

$$S_P = S_P + S^{HOT} \tag{5.56}$$

where in one-dimensional case

$$\begin{aligned} S^{HOT} &= \frac{1}{8}(3\Phi_P - 2\Phi_E - \Phi_{EE})max(0, F_e) + \\ &+ \frac{1}{8}(3\Phi_W - 2\Phi_P - \Phi_E)max(0, F_w) + \\ &+ \frac{1}{8}(3\Phi_E - 2\Phi_P - \Phi_W)min(0, -F_e) + \\ &+ \frac{1}{8}(3\Phi_P - 2\Phi_W - \Phi_{WW})max(0, -F_w) \end{aligned} \tag{5.57}$$

The expression of the high order term (S^{HOT}) can be extended to three-dimensional cases in a similar manner.

Discussion:

1. The scheme uses consistent quadratic profiles and is therefore conservative.

2. In the original $QUICK$ scheme developed by Leonard (1979), the discretized equation includes not only immediate neighbouring nodes but also those further away and the coefficients corresponding to $\Phi_{EE}, \Phi_{WW}, \Phi_{NN}, \Phi_{SS}, \Phi_{FF}$ and Φ_{BB} are not guaranteed to be positive. This gives rise to stability problems and unbounded solutions under certain flow conditions. Therefore, the original $QUICK$ scheme is conditionally stable. In the improved $QUICK$ scheme (Hayse et al.[75]), the discretized equations involve only the immediate neighbouring nodes by lumping other terms into the source terms of the transport equations and the coefficients are always kept positive. In addition, when the flow field satisfies mass continuity the coefficient A_P equals the sum of all neighbouring coefficients. Therefore, this scheme is diagonally dominant, stable and fast converging in most cases.

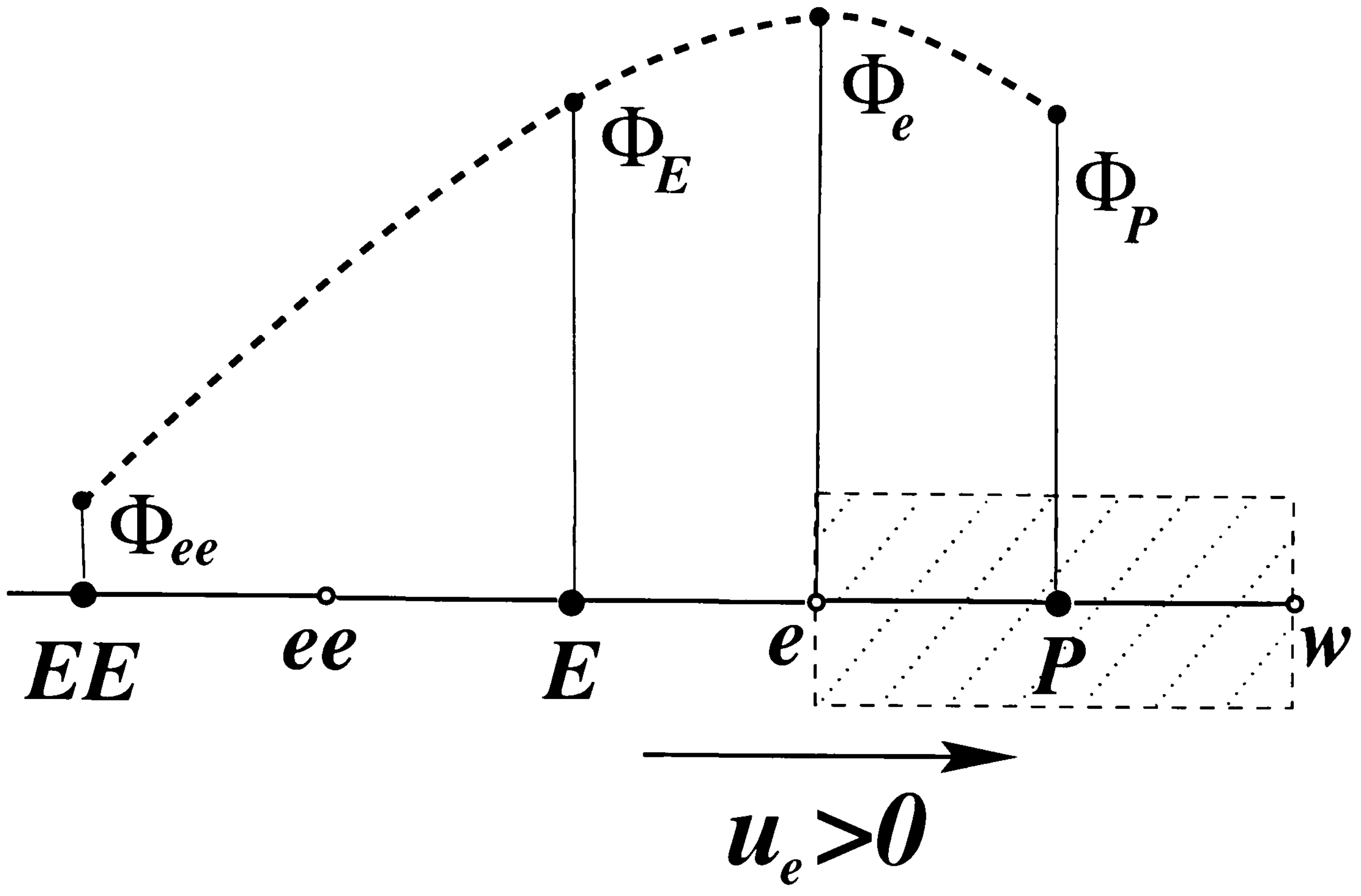

Figure 5.5: **"Overshoot" phenomenon produced by *QUICK* scheme**

3. The *QUICK* schemes have the transportiveness property because the quadratic function is based on two upstream and one downstream nodal values.

4. The accuracy of the *QUICK* scheme is third order in terms of Taylor series truncation error.

5. The *QUICK* scheme has the tendency to cause "overshoots" or "undershoot" during numerical transition and therefore in this situation does not satisfy the requirement of boundedness. This problem is schematically shown in Figure 5.5 for a one-dimensional case. When $\Phi_E \approx \Phi_P$, the value Φ_e obtained from the interpolation can be higher than the values in the surrounding nodes. This phenomenon can lead to non-linear instability.

Other High Order Schemes

As mentioned in *QUICK* scheme, the problem of "overshoots" or "undershoots" in numerical processes exist for high order schemes without any constraints. In order to overcome this problem, a correction boundedness criterion

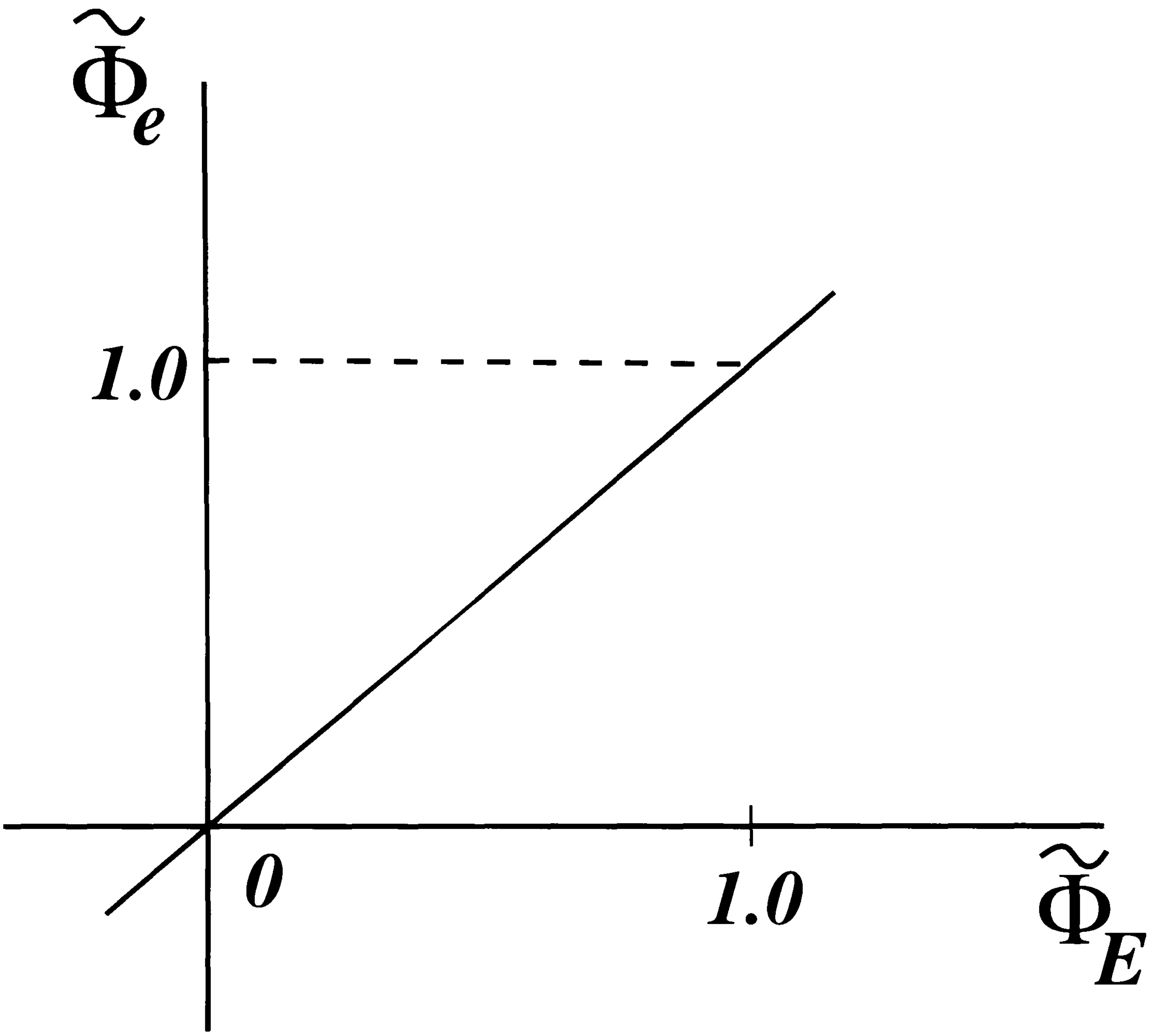

Figure 5.6: **Convection boundedness criterion in** NVD

was defined by Gaskell and Lau [59]. Therefore, different limiters or constraints imposed by the boundedness were introduced to limit the variable values on a cell face obtained from high order schemes before being used in the transport equations. The logic of the limiters or constraints in a one-dimensional case (Figure 5.5). Botte [19] is:

1. in locally monotonic regions, the value on a cell face should lie between adjacent nodal values, i.e. $\Phi_e \in [\Phi_E, \Phi_P]$. if the upstream value Φ_E is bounded by the values in upstream and downstream nodes, i.e. $\Phi_E \in [\Phi_{EE}, \Phi_P]$.
2. if $\Phi_E \notin [\Phi_{EE}, \Phi_P]$, no information is available to limit the interpolated value; in this case, a lower-order scheme is used, such as first order Upwind scheme which is always bounded.

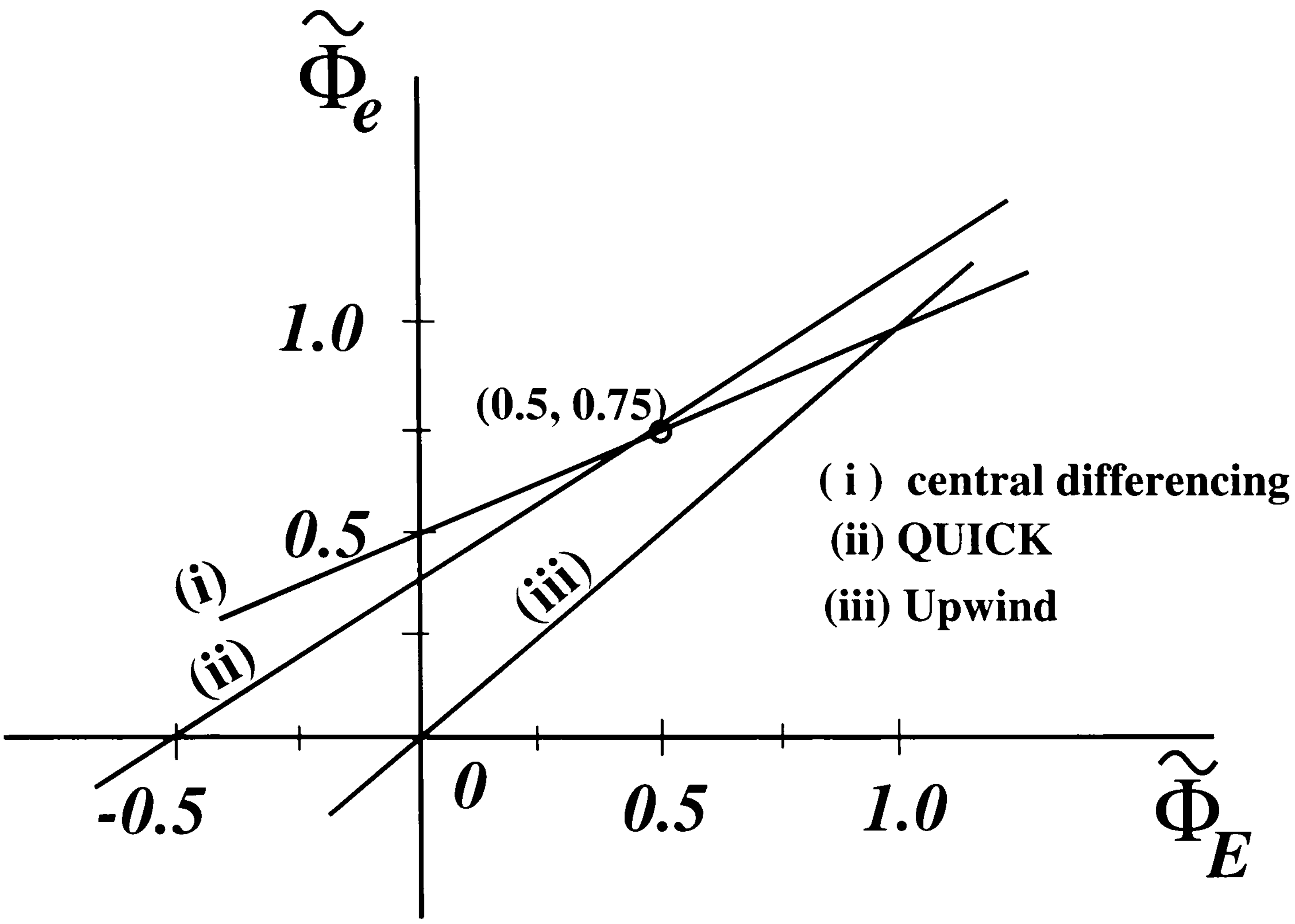

Figure 5.7: **Different Schemes in normalized variable diagram**

Leonard and Mokhtari [112] defined a normalised variable $\tilde{\Phi}$ with which all the schemes can be expressed with the variable in a similar way. The definition of the normalised variable is:

$$\tilde{\Phi} = \frac{\Phi - \Phi_{EE}}{\Phi_P - \Phi_{EE}} \tag{5.58}$$

which results in $\tilde{\Phi}_{EE} = 0$ and $\tilde{\Phi}_P = 1$. The convection boundedness criterion then can be represented in the Normalized Variable Diagram (NVD) shown in Figure 5.6 and expressed as:

- for $\tilde{\Phi}_E \in [0, 1]$, $\tilde{\Phi}_E \leq \tilde{\Phi}_e \leq 1$;
- for $\tilde{\Phi}_E \notin [0, 1]$, $\tilde{\Phi}_e = \tilde{\Phi}_E$

The functional relationships of all previously mentioned schemes can also be plotted in the normalised variable diagram (NVD) (Figure 5.7) and expressed as follows:

- first order Upwind scheme

$$\Phi_e = \Phi_E \qquad or \qquad \tilde{\Phi}_e = \tilde{\Phi}_E \tag{5.59}$$

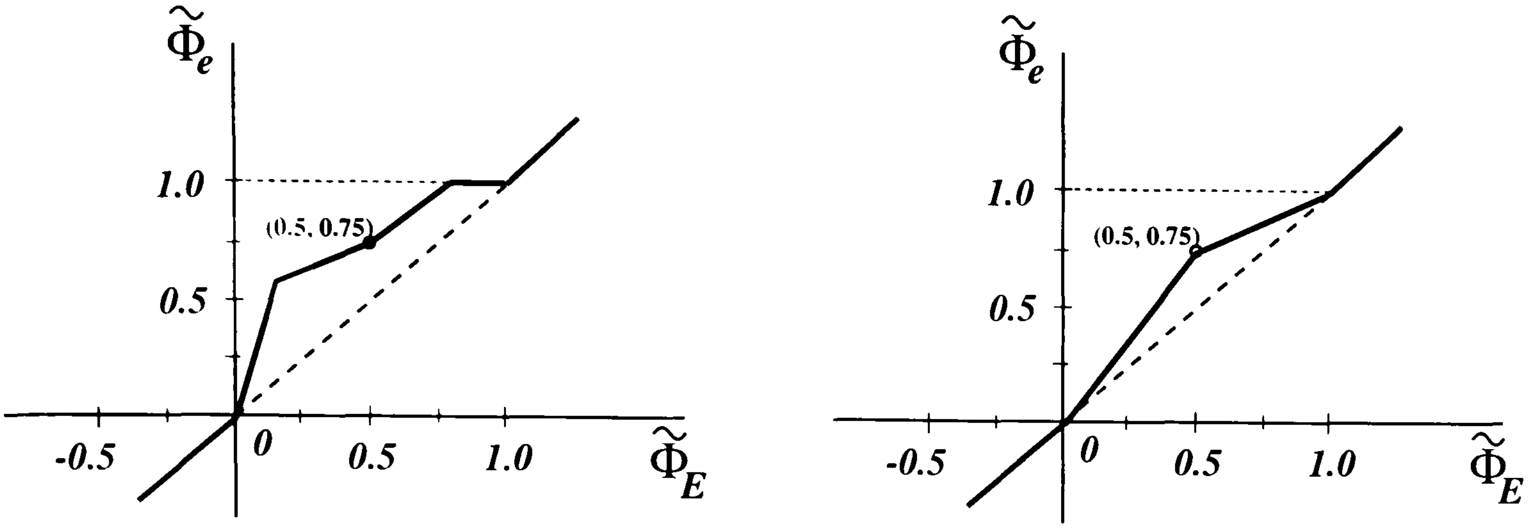

(a) STOIC **(b) SOUCOUP**

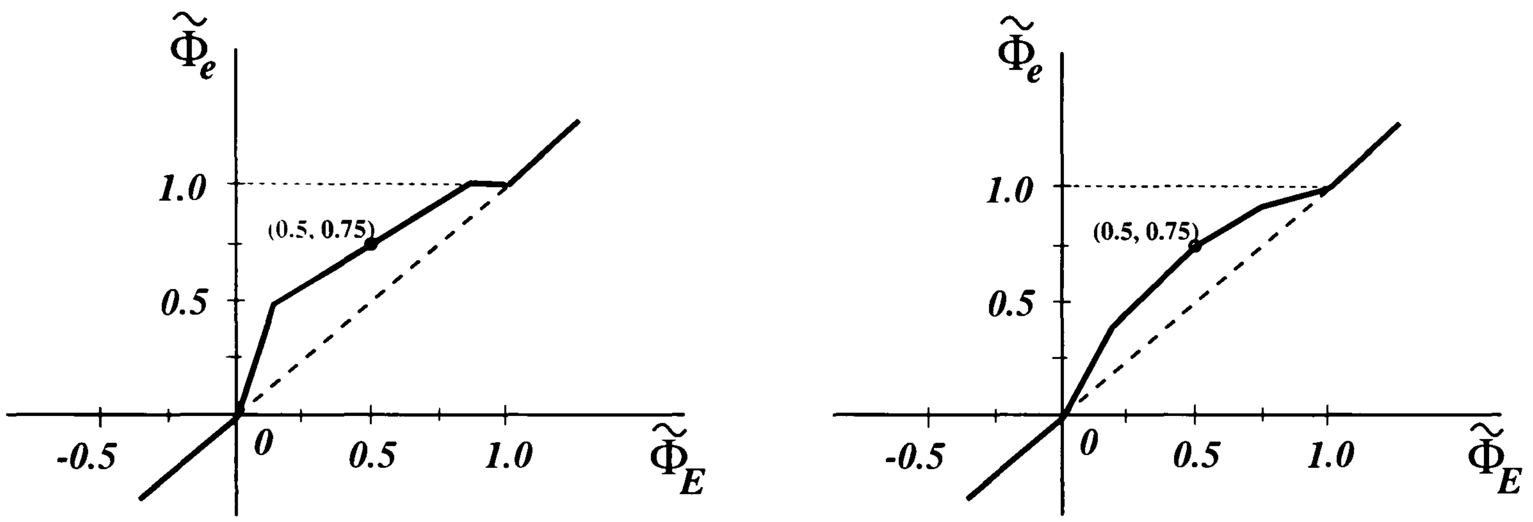

(c) SMART **(d) EULER**

Figure 5.8: **Advanced composite schemes in *NVD***

- second order central difference scheme

$$\begin{aligned} \Phi_e &= \frac{1}{2} * (\Phi_E + \Phi_P) \\ or \quad \tilde{\Phi}_e &= \frac{1}{2} * (1 + \tilde{\Phi}_E) \end{aligned} \tag{5.60}$$

- third-order *QUICK* scheme

$$\begin{aligned} \Phi_e &= \frac{1}{2}(\Phi_E + \Phi_P) - \frac{1}{8}(\Phi_P - 2\Phi_E + \Phi_{EE}) \\ or \quad \tilde{\Phi}_e &= \frac{3}{8} + \frac{3}{4}\tilde{\Phi}_E \end{aligned} \tag{5.61}$$

It is obvious that high order schemes, such as the second-order central difference and the third-order *QUICK* schemes, can not achieve boundedness and accuracy simultaneously. Therefore, several combinations have been proposed to obtain a high-resolution bounded scheme. Some of them are: second and third order interpolation for convection (*STOIC*) from Darwish [35], second-order upwind central differencing first-order upwind (*SOUCOUP*) of Zhu and Rodi [198], sharp and monotonic algorithm for realistic transport by convection (*SMART*) of Gaskell and Lau [59] and exponential upwinding or linear extrapolation refinement (*EULER*) of Leonard [112]. The *NVD* plots for all these schemes are illustrated in Figure 5.8.

5.5 Boundary Conditions

The boundary conditions employed for the computational domains of compressor blade rows in the predictions are as follows:

1. On all solid surfaces, i.e. the blade surfaces, inner and outer annulus walls, non-slip condition is used for velocity and zero gradient condition for static pressure. The values of k and ϵ are specified near the wall with standard wall function, which is described in detail in Chapter 4.
2. Periodic conditions are implemented for all the parameters on both sides of upstream and downstream extensions and also applied to both sides of tip clearance domain.
3. The cylindrical interface between the two rotor blocks is treated by means of halo cells extended from one block into the interior of the adjacent one. Interpolation is used to exchange information between the two blocks.
4. For the computational domain of each blade, spanwise distributions of velocity, k and ϵ either transfered from upstream blade domain or fixed to experimental data are applied at the inlet of the domain of each blade passage. Zero gradient condition for static pressure is applied at the inlet interface of each domain.
5. At the exit interface of the computational domain of each blade row, spanwise static pressure distribution is imposed when there is a downstream blade row or a zero gradient condition with a specified average value for static pressure is imposed when there is no downstream blade row. Zero gradient condition is used for velocity, k and ϵ at the exit interface of the computational domain of each blade row.

6. The inlet and exit boundary conditions of compressor stages can also be set with the repeating stage model described in Chapter 6.

5.6 Solution of Discretised Algebraic Equation System

After the control volume discretization of convection, diffusion and source terms and the combination of these terms, the full discretized form of the transport equation has the following typical form:

$$A_P^{ijk} = \sum_{nb} A_{nb}^{ijk} \Phi_{nb}^{ijk} + S_P^{ijk} \qquad (5.62)$$

Where i, j, k are coordinates of the central nodal point of a control volume in the computational space: $nb = E, W, N, S, F, B$; $i = 0$ to I, $j = 0$ to J and $k = 0$ to K; A_{nb}^{ijk} are the coefficients corresponding to the variable Φ at the neighbouring volumes around volume P. There are N such equations for all control volumes as a whole and

$$N = (I+1)(J+1)(K+1) \qquad (5.63)$$

where I, J and K are maximum numbers of nodes in ξ, η and ζ directions respectively.

The system of the discretized equations with N unknowns can be expressed with the general form:

$$[\mathbf{A}]\vec{\mathbf{\Phi}} = \vec{\mathbf{S}} \qquad (5.64)$$

Where $[\mathbf{A}]$ is the coefficient matrix, $\vec{\mathbf{\Phi}}$ is the variable vector and $\vec{\mathbf{S}}$ is the source term vector. In three-dimensional cases, each row of the matrix $[\mathbf{A}]$ normally consists of seven non-zero elements.

There are various methods available to solve the above discretised equation system, such as Gauss-Seidel iteration method, *ADI* (the Alternating Direction Iteration), *TDMA* (Tri-Diagonal-Matrix-Algorithm), etc. which were analysed by Stone [167]. In the present study a "factorisation" strategy known as the Strongly Implicit Procedure (*SIP*) proposed by Stone [167] is used. The idea of the method is to replace the sparse matrix $[\mathbf{A}]$ by a modified matrix $[\mathbf{A}+\mathbf{P}]$ such that the modified matrix can be decomposed into upper and lower triangular sparse matrices denoted by $[\mathbf{U}]$ and $[\mathbf{L}]$, respectively. The manner in which $[\mathbf{P}]$ is selected is that the elements of $[\mathbf{P}]$ are small in magnitude and permit the set of equations to remain implicitly stronger than that of the *ADI* procedure. An iterative procedure is defined by writing $[\mathbf{A}]\vec{\mathbf{\Phi}} = \vec{\mathbf{S}}$ as

$$[\mathbf{A}+\mathbf{P}]\vec{\mathbf{\Phi}}^{(n+1)} = \vec{\mathbf{S}} + [\mathbf{P}]\Phi^{(n)} \tag{5.65}$$

Decomposing $[\mathbf{B}] = [\mathbf{A}+\mathbf{P}]$ into the upper and lower triangular matrix $[\mathbf{U}]$ and $[\mathbf{L}]$ permits the system to be written as

$$[\mathbf{L}][\mathbf{U}]\Phi^{(n+1)} = \vec{\mathbf{S}} + [\mathbf{P}]\Phi^{(n)} \tag{5.66}$$

Defining an intermediate vector as $\vec{\mathbf{V}}^{(n+1)} = [\mathbf{U}]\Phi^{(n+1)}$. a two-step algorithm is formed as follows:

$$\begin{array}{ll} \textbf{Step1}: & [\mathbf{L}]\vec{\mathbf{V}}^{(n+1)} = \vec{\mathbf{S}} + [\mathbf{P}]\Phi^{(n)} \\ \textbf{Step2}: & [\mathbf{U}]\Phi^{(n+1)} = \vec{\mathbf{V}}^{(n+1)} \end{array}$$

which is repeated iteratively. Step 1 consists simply of a forward substitution and step 2 is a backward substitution.

The matrix [**P**] is selected in the way that [**L**] and [**U**] have only four non-zero diagonals with the principle diagonal of [**U**] being the unity diagonal. Furthermore, the elements of [**U**] and [**L**] are determined such that the coefficients in the [**B**] matrix in the location of the non-zero entries of matrix [**A**] are identical with those in [**A**]. Three additional non-zero diagonals appear in [**B**]. The details of the decomposion and solution procedure can be found in Appendix B.

Stone's study shows that. for solutions to two-dimensional Laplace's equations the method requires only around 50-60% of the computational time required by the *ADI* scheme.

Alternatively, other implicit iteration methods like the Modified Strongly Implicit (*MSI*) procedure, Schneider and Zedan [153] and *GMRES* [150] can be incorporated in the solution process of the discretized equation system.

5.7 Application of Under-Relaxation

In order to make the iteration solution process converge smoothly, the change of the magnitude of the variables between successive iterations is controlled with the application of under-relaxation, Patankar [135]. Starting from the general discretized Equation (5.35) the variable at central point P can be expressed as

$$\Phi_P = \frac{\sum\limits_{nb} A_{nb}\Phi_{nb} + S_P}{A_P} \tag{5.67}$$

or in an equivalent form

$$\Phi_P = \Phi_P^* + \left[\frac{\sum\limits_{nb} A_{nb}\Phi_{nb} + S_P}{A_P} - \Phi_P^* \right] \tag{5.68}$$

where nb $(nb = E, W, N, S, F, B)$ denotes the neighbouring nodes and the value of Φ_P^* is obtained in the previous iteration. The change of the magnitude of the variable Φ_P between two successive iterations, which is expressed by the term inside the parenthesies, can be controlled by multiplying an under-relaxation factor ω $(0 \leq \omega \leq 1)$ to the terms inside the parenthesis. So the relation (5.68) becomes

$$\Phi_P = \Phi_P^* + \omega \left[\frac{\sum\limits_{nb} A_{nb}\Phi_{nb} + S_P}{A_P} - \Phi_P^* \right] \tag{5.69}$$

Finally, the following under-relaxed discrete equation is obtained:

$$\frac{A_P}{\omega}\Phi_P = \sum_{nb} A_{nb}\Phi_{nb} + S_P + \left(\frac{1-\omega}{\omega}\right) A_P\Phi_P^* \tag{5.70}$$

The selection of under-relaxation factor ω is very important for cost-effective simulation. Too large a value of ω may lead to oscillation or even divergence to the solution and too small a value of ω will result in slow convergence. Unfortunately, there is no general rule to choose the optimum value of the under-relaxation factors. They are flow dependent and must be sought on a case–by-case basis with previous experience.

5.8 Pressure-Velocity Coupling Approach

5.8.1 Introduction

The pressure gradient term in momentum equations is an important term among source terms. If the flow is incompressible the density is constant, there is no link between density and pressure but strong link between pressure and velocity. The difficulty of the problem concerned is how to calculate the pressure field and make the velocity field satisfy both the momentum and continuity equations. This kind of problems can be resolved by using the so-called pressure correction methods first introduced by Caretto et al. [28] and Patankar and Spalding [136].

Several pressure correction methods have been developed. One of the most extensively used pressure correction methods is the *SIMPLE* algorithm (Semi

Implicit Method for Pressure Linked Equations), Caretto et al. [28] and Patankar and Spalding [136], where a pressure correction equation is derived from the discretized continuity and momentum equations and gives rise to appropriete corrections of the pressure and velocity fields obtained from the momentum equations. In addition, a number of pressure correction methods which are improved versions of *SIMPLE* algorithm have been derived, such as *SIMPLER* (*SIMPLE*-Revised) algorithm of Patankar [135], *SIMPLEC* (*SIMPLE*-Consistent) algorithm of Van Doormal and Raithby [178], *PISO* (Pressure Implicit with Splitting of Operators) algorithm of Issa [90], etc..

The pressure correction method used in this study is based on the *SIMPLE* algorithm, Patankar [135]. A collocated grid arrangement in general non-orthogonal curvilinear coordinate system is applied for its convenience in computer programming and boundary treatment. An appropriate technique, originated by Rhie and Chow [147] and developed by Majumdar [119], is utilised to avoid the decoupling between velocity and pressure fields. A method proposed by Giannakoglou et al. [60] is employed to accelerate the convergence of the solution of the pressure correction equation.

5.8.2 The Pressure Correction Equation

The continuity equation is integrated and discretized over a control volume, giving rise to

$$F_e - F_w + F_n - F_s + F_f - F_b = 0 \tag{5.71}$$

or

$$\begin{aligned}&[\rho V]_e(\delta\eta\delta\zeta) - [\rho V]_w(\delta\eta\delta\zeta) + [\rho U]_n(\delta\xi\delta\zeta) - \\ &- [\rho U]_s(\delta\xi\delta\zeta) + [\rho W]_f(\delta\xi\delta\eta) - [\rho W]_b(\delta\xi\delta\eta) = 0\end{aligned} \tag{5.72}$$

When applying the values of provisional contravariant velocity components U^*, V^* and W^* on control volume faces, which can be obtained by initial assumption or previous iteration, to the continuity equation, there will appear a "mass source" term m_p at the right-hand side of the continuity equation instead of zero:

$$\begin{aligned}&[\rho V^*]_e(\delta\eta\delta\zeta) - [\rho V^*]_w(\delta\eta\delta\zeta) + [\rho U^*]_n(\delta\xi\delta\zeta) - \\ &- [\rho U^*]_s(\delta\xi\delta\zeta) + [\rho W^*]_f(\delta\xi\delta\eta) - [\rho W^*]_b(\delta\xi\delta\eta) = m_p\end{aligned} \tag{5.73}$$

where $*$ stands for provisional values.

The calculation of m_p requires the contravariant velocities $U_\pi^*(\pi = 1,2,3)$ at control volume faces. They can be obtained from the momentum equations, which will be described in detail in Section 5.7.4.

The accurate values of u_P, v_P, w_P and p_P can be expressed as their provisional values u_P^*, v_P^*, w_P^* and p_P^* plus corresponding correction values u_P', v_P', w_P' and p_P' respectively. Hence

$$\begin{aligned} u_P &= u_P^* + u_P' \\ v_P &= v_P^* + v_P' \\ w_P &= w_P^* + w_P' \\ p_P &= p_P^* + p_P' \end{aligned} \tag{5.74}$$

Both set of values u_P, v_P, w_P, p_P and u_P^*, v_P^*, w_P^*, p_P^* satisfy the momentum equations:

$$A_P^u u_P = \sum_{nb} A_{nb}^u u_{nb} + S_u^{HOT} + S_u^{CDT} + S_u^{OT} + (p_\xi \xi_x + p_\eta \eta_x + p_\zeta \zeta_x)(J\delta\xi\delta\eta\delta\zeta) \tag{5.75}$$

$$A_P^v v_P = \sum_{nb} A_{nb}^v v_{nb} + S_v^{HOT} + S_v^{CDT} + S_v^{OT} + (p_\xi \xi_y + p_\eta \eta_y + p_\zeta \zeta_y)(J\delta\xi\delta\eta\delta\zeta) \tag{5.76}$$

$$A_P^w w_P = \sum_{nb} A_{nb}^w w_{nb} + S_w^{HOT} + S_w^{CDT} + S_w^{OT} + (p_\xi \xi_z + p_\eta \eta_z + p_\zeta \zeta_z)(J\delta\xi\delta\eta\delta\zeta) \tag{5.77}$$

and

$$A_P^u u_P^* = \sum_{nb} A_{nb}^u u_{nb}^* + S_u^{HOT} + S_u^{CDT} + S_u^{OT} + (p_\xi^* \xi_x + p_\eta^* \eta_x + p_\zeta^* \zeta_x)(J\delta\xi\delta\eta\delta\zeta) \tag{5.78}$$

$$A_P^v v_P^* = \sum_{nb} A_{nb}^v v_{nb}^* + S_v^{HOT} + S_v^{CDT} + S_v^{OT} + (p_\xi^* \xi_y + p_\eta^* \eta_y + p_\zeta^* \zeta_y)(J\delta\xi\delta\eta\delta\zeta) \tag{5.79}$$

$$A_P^w w_P^* = \sum_{nb} A_{nb}^w w_{nb}^* + S_w^{HOT} + S_w^{CDT} + S_w^{OT} + (p_\xi^* \xi_z + p_\eta^* \eta_z + p_\zeta^* \zeta_z)(J\delta\xi\delta\eta\delta\zeta) \tag{5.80}$$

Subtracting Equations (5.75) to (5.77) by Equations (5.78) to (5.80) respectively produces the following relations relating to the velocity corrections with the pressure correction:

$$A_P^u u_P' = \sum_{nb} A_{nb}^u u_{nb}' - (p_\xi' \xi_x + p_\eta' \eta_x + p_\zeta' \zeta_x)(J\delta\xi\delta\eta\delta\zeta) \tag{5.81}$$

$$A_P^v v_P' = \sum_{nb} A_{nb}^v v_{nb}' - (p_\xi' \xi_y + p_\eta' \eta_y + p_\zeta' \zeta_y)(J\delta\xi\delta\eta\delta\zeta) \tag{5.82}$$

$$A_P^w w_P' = \sum_{nb} A_{nb}^w w_{nb}' - (p_\xi' \xi_z + p_\eta' \eta_z + p_\zeta' \zeta_z)(J\delta\xi\delta\eta\delta\zeta) \tag{5.83}$$

The first term of the right-hand side of Equations (5.81) to (5.83) can be neglected because u_P', v_P' and w_P' tend to be zero when convergence is achieved. Substituting Equation (5.74) into simplified Equations (5.81) to (5.83) gives rise to

$$u_P = u_P^* + (B^u p_\xi' + C^u p_\eta' + D^u p_\zeta') \tag{5.84}$$

$$v_P = v_P^* + (B^v p'_\xi + C^v p'_\eta + D^v p'_\zeta) \tag{5.85}$$

$$w_P = w_P^* + (B^w p'_\xi + C^w p'_\eta + D^w p'_\zeta) \tag{5.86}$$

where

$$\begin{aligned}
B^u &= -\xi_x \frac{(J\delta\xi\delta\eta\delta\zeta)}{A_P^u}, & C^u &= -\eta_x \frac{(J\delta\xi\delta\eta\delta\zeta)}{A_P^u}, & D^u &= -\zeta_x \frac{(J\delta\xi\delta\eta\delta\zeta)}{A_P^u} \\
B^v &= -\xi_y \frac{(J\delta\xi\delta\eta\delta\zeta)}{A_P^v}, & C^v &= -\eta_y \frac{(J\delta\xi\delta\eta\delta\zeta)}{A_P^v}, & D^v &= -\zeta_y \frac{(J\delta\xi\delta\eta\delta\zeta)}{A_P^v} \\
B^w &= -\xi_z \frac{(J\delta\xi\delta\eta\delta\zeta)}{A_P^w}, & C^w &= -\eta_z \frac{(J\delta\xi\delta\eta\delta\zeta)}{A_P^w}, & D^w &= -\zeta_z \frac{(J\delta\xi\delta\eta\delta\zeta)}{A_P^w}
\end{aligned} \tag{5.87}$$

Substituting Equations (5.84) to (5.86) into Equations (3.29) to (3.31) produces the expressions of the contravariant velocities U_P, V_P and W_P:

$$\begin{aligned}
U_P = U_P^* \; & +J(B^u\xi_x + B^v\xi_y + B^w\xi_z)p'_\xi \\
& \underline{+J(C^u\xi_x + C^v\xi_y + C^w\xi_z)p'_\eta} \\
& \underline{+J(D^u\xi_x + D^v\xi_y + D^w\xi_z)p'_\zeta}
\end{aligned} \tag{5.88}$$

$$\begin{aligned}
V_P = V_P^* \; & \underline{+J(B^u\eta_x + B^v\eta_y + B^w\eta_z)p'_\xi} \\
& +J(C^u\eta_x + C^v\eta_y + C^w\eta_z)p'_\eta \\
& \underline{+J(D^u\eta_x + D^v\eta_y + D^w\eta_z)p'_\zeta}
\end{aligned} \tag{5.89}$$

$$\begin{aligned}
W_P = W_P^* \; & \underline{+J(B^u\zeta_x + B^v\zeta_y + B^w\zeta_z)p'_\xi} \\
& \underline{+J(C^u\zeta_x + C^v\zeta_y + C^w\zeta_z)p'_\eta} \\
& +J(D^u\zeta_x + D^v\zeta_y + D^w\zeta_z)p'_\zeta
\end{aligned} \tag{5.90}$$

The cross terms, marked with under-line, appear due to the non-orthogonality of the coordinate system and can be neglected without affecting the converged solution, so the simplified expression for U_P, V_P and W_P becomes:

$$\begin{aligned}
U_P &= U_P^* + & B p'_\xi \\
V_P &= V_P^* + & C p'_\eta \\
W_P &= W_P^* + & D p'_\zeta
\end{aligned} \tag{5.91}$$

where

$$\begin{aligned}
B &= J(B^u\xi_x + B^v\xi_y + B^w\xi_z) \\
C &= J(C^u\eta_x + C^v\eta_y + C^w\eta_z) \\
D &= J(D^u\zeta_x + D^v\zeta_y + D^w\zeta_z)
\end{aligned} \tag{5.92}$$

Substituting Equation (5.91) into (5.72) and combined with Equation (5.73) and rearranging the equations, we eventually obtain the pressure correction equation as follows:

$$A_P^p p'_P = A_E^p p'_E + A_W^p p'_W + A_N^p p'_N + A_S^p p'_S + A_F^p p'_F + A_B^p p'_B - m_p \tag{5.93}$$

where

$$\begin{aligned} A_E^p &= (\rho B)_e(\delta\eta\delta\zeta)_e & A_W^p &= (\rho B)_w(\delta\eta\delta\zeta)_w \\ A_N^p &= (\rho C)_n(\delta\eta\delta\zeta)_n & A_S^p &= (\rho C)_s(\delta\eta\delta\zeta)_s \\ A_F^p &= (\rho D)_f(\delta\eta\delta\zeta)_f & A_B^p &= (\rho D)_b(\delta\eta\delta\zeta)_b \\ A_P^p &= A_E^p + A_W^p + A_N^p + A_S^p + A_F^p + A_B^p \end{aligned} \tag{5.94}$$

and

$$\begin{aligned} m_p = \; & [\rho V^*]_e(\delta\eta\delta\zeta) - [\rho V^*]_w(\delta\eta\delta\zeta) + [\rho U^*]_n(\delta\xi\delta\zeta) - \\ & - [\rho U^*]_s(\delta\xi\delta\zeta) + [\rho W^*]_f(\delta\xi\delta\eta) - [\rho W^*]_b(\delta\xi\delta\eta) \end{aligned} \tag{5.95}$$

The solution procedure of the pressure correction equation is prone to oscillation or even divergence unless some under-relaxation is used during the iteration process. The new, updated, pressure field is obtained by

$$p_P = p_P^* + \omega_p p_P' \tag{5.96}$$

where ω_p is the under-relaxation factor for the pressure equation, which is between 0 and 1.

The term m_p is the "mass source" (Patankar [135]) of the pressure correction equation and is actually the left hand side of the discretized continuity equation evaluated in terms of the provisional velocities. When m_p becomes zero, the continuity equation is satisfied and no corrections for both pressure and velocity fields are required.

It can be seen that the Equation (5.93) has similar form to the general discrete transport Equation (5.34). This provides the convenience that the solution process of the pressure correction equation can be performed in a similar way as that of the general discrete transport equation system which is described in Section 5.5.

5.8.3 Acceleration to Pressure Correction Equation

The set of pressure correction equations for the whole flow field, derived in a similar way to that of the governing equations and written in the form of Equation (5.97), can be iteratively solved using the same approximate factorisation scheme, i.e. *SIP* (Strongly Implicit Procedure) described in Appendix C.

$$[\mathbf{B}]\vec{\mathbf{p}'} = \vec{\mathbf{S}^*} \tag{5.97}$$

where $\mathbf{B}$ is the coefficient matrix, $\vec{p'}$ the pressure correction vector and $\vec{\mathbf{S}^*}$ the "mass source" vector.

In this study, the convergence of the pressure correction equation is accelerated by imposing residual minimisation constraints, Giannakoglou and Politis [60]. The detailed method was also described and used by Politis and Giannakoglou [139] and they are stated as follows.

Firstly, [**B**] is approximately decomposed into an upper and lower triangular matrices, i.e.

$$[\mathbf{B}] \approx [\mathbf{P}]^{-1} = [\mathbf{L}][\mathbf{U}] \tag{5.98}$$

and a preconditioned pressure correction is obtained based on *SIP*, Stone [167]

$$\vec{\mathbf{p}'} = [\mathbf{P}]\vec{\mathbf{S}^*} \tag{5.99}$$

where [**P**] is the approximate inverse of the coefficient matrix [**B**]. Then a preconditioned residual

$$\vec{\mathbf{R}}^{(n)} = [\mathbf{P}]([\mathbf{B}]\vec{\mathbf{p}'}^{(n)} - \vec{\mathbf{S}^*}^{(n)}) \tag{5.100}$$

is minimized. In order to advance the solution from iteration (n) to iteration $(n+1)$, the preconditionaed residual multiplied by an acceleration parameter β is added to the existing solution vector $\vec{\mathbf{p}'}^{(n)}$ according to the expression

$$\vec{\mathbf{p}'}^{(n+1)} = \vec{\mathbf{p}'}^{(n)} + \beta\vec{\mathbf{R}}^{(n)} \tag{5.101}$$

The calculation of β is based on the minimisation of the preconditioned residual at the next iteration $(n+1)$ and its final expression is given by:

$$\beta = \frac{\alpha_1}{\alpha_1^2 + \alpha_2^2} \tag{5.102}$$

where

$$\alpha_1 = \vec{\gamma} \cdot \frac{\vec{\mathbf{R}}}{\| \vec{\mathbf{R}} \|} \tag{5.103}$$

$$\alpha_2 = \left\| \vec{\gamma} - \alpha_1 \frac{\vec{\mathbf{R}}}{\| \vec{\mathbf{R}} \|} \right\| \tag{5.104}$$

According to Equation (5.104), vector $\vec{\gamma}$ is calculated through the definition of an intermediate vector $\vec{\gamma}''$ and the following two step procedure:

$$\begin{aligned} &\textbf{Step1}: \quad & [\mathbf{L}]\vec{\gamma}'' = [\mathbf{B}]\frac{\vec{\mathbf{R}}}{\| \vec{\mathbf{R}} \|} \\ &\textbf{Step2}: \quad & [\mathbf{U}]\vec{\gamma} = \vec{\gamma}'' \end{aligned}$$

Actually, this approach employs a weighted, over the whole field, correction to the values of pressure correction obtained from *SIP*. This method was proved more efficient by Giannakoglou and Politis [60].

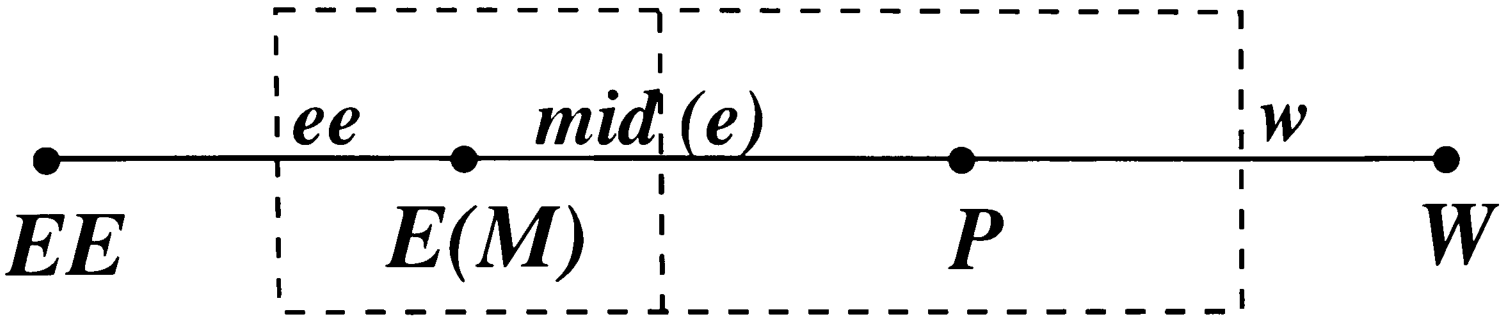

Figure 5.9: **Schematical expression of control volumes and nodes**

5.8.4 Remedy to Pressure Oscillations

The arrangement of a non-staggered grid does provide convenience in computer programming and the treatment of boundary conditions. However, an oscillatory pressure field may appear due to the second-order centred $2\delta\xi_i$-difference approximation of the pressure gradient at the grid nodes, Rhie and Chow [147]. One of the remedies to remove the oscillation is by using a staggered grid, but it cannot be applied to a collocated grid system.

Rhie and Chow [147] proposed a remedy to overcome the pressure oscillations in a non-staggered grid system, which is called Rhie and Chow scheme or Momentum Interpolation scheme. Tourlidakis [173] applied this method in his calculations, which proved to be very effective. The idea of the method is to introduce two different expressions for the two pressure gradient terms in the contravariant velocity component expressions to sense $1\delta\xi_i$-pressure difference. The detailed expression for contravariant velocity component, for example at "e" volume face schematically shown in Figure 5.9, is as follows:

$$U_e = \overline{U_e^*} + \overline{B_e}\left[\left(\frac{\partial p^*}{\partial \xi}\right)_e - \overline{\left(\frac{\partial p^*}{\partial \xi}\right)_e}\right] \tag{5.105}$$

where the first pressure gradient term $\left(\frac{\partial p^*}{\partial \xi}\right)_e$ is calculated by the $1\delta\xi_i$-centre pressure on the volume face:

$$\left(\frac{\partial p^*}{\partial \xi}\right)_e = \frac{p_E^* - p_P^*}{(\delta\xi)_e} \tag{5.106}$$

The second pressure gradient term $\overline{\left(\frac{\partial p^*}{\partial \xi}\right)_e}$ and other terms with overbars are the values obtained from an interpolation between their corresponding values at grid P and E:

$$\overline{\left(\frac{\partial p^*}{\partial \xi}\right)_e} = f_P \left(\frac{\partial p^*}{\partial \xi}\right)_E + (1 - f_P) \left(\frac{\partial p^*}{\partial \xi}\right)_P \tag{5.107}$$

where

$$\left(\frac{\partial p^*}{\partial \xi}\right)_E = \frac{p^*_{EE} - p^*_P}{(\delta\xi)_e + (\delta\xi)_{ee}}$$

$$\left(\frac{\partial p^*}{\partial \xi}\right)_P = \frac{p^*_E - p^*_W}{(\delta\xi)_e + (\delta\xi)_w}$$

and

$$\overline{U_e^*} = f_P U_E^* + (1 - f_P) U_P^* \tag{5.108}$$

$$\overline{B_e^*} = f_P B_E^* + (1 - f_P) B_P^* \tag{5.109}$$

where f_P is the interpolation coefficient determined by volume geometry.

Similar treatment is applied to other contravariant velocity components. After this treatment, m_p can sense the $1\delta\xi_i$-pressure difference and the pressure correction can eventually remove the pressure oscillation during iteration processes.

However, it was found that with Rhie and Chow's scheme the converged result for any flow situation depend on the under-relaxation parameter used for velocity, Majumdar [119]. Thereafter, Majumdar [119] improved the momentum interpolation and make it independent of the under-relaxation parameter used. The method of removing the pressure oscillations used in this study follows the idea suggested by Majumdar [119], which is also described by Giannakoglou and Politis [60]. The details are as follows:

The discretized momentum equations give the expression for the contravariant velocity component at nodes P and E, Figure 5.9:

$$(U_\pi)_P = H_P - \left(\frac{J}{A_P}\right)_P \left[\frac{\partial p}{\partial \xi_j}\frac{\partial \xi_j}{\partial x_i}\frac{\partial \xi_\pi}{\partial x_i}\right]_P \qquad (\pi = 1, 2, 3) \tag{5.110}$$

$$(U_\pi)_M = H_M - \left(\frac{J}{A_P}\right)_M \left[\frac{\partial p}{\partial \xi_j}\frac{\partial \xi_j}{\partial x_i}\frac{\partial \xi_\pi}{\partial x_i}\right]_M \qquad (\pi = 1, 2, 3) \tag{5.111}$$

where M denotes a neighbouring node and H includes all the terms on the right-hand side of the discrtized momentum equation except the pressure gradient term:

$$H = \frac{1}{A_P}\left[\left(\sum_{nb} A_{nb} u^*_{i,nb}\right)\frac{\partial \xi_\pi}{\partial x_i}\right] + \frac{1}{A_P}\left[(S_i^{HOT} + S_i^{CDT} + S_i^{OT})\frac{\partial \xi_\pi}{\partial x_i}\right] \tag{5.112}$$

An under-relaxation parameter ω is incorporated for stability reason to update the cell centre velocity components as:

$$(U_\pi)_P = \omega\left[H_P - \left(\frac{J}{A_P}\right)_P\left(\frac{\partial p}{\partial \xi_j}\frac{\partial \xi_j}{\partial x_i}\frac{\partial \xi_\pi}{\partial x_i}\right)_P\right] + (1-\omega)(U_\pi)_P^{(n)} \tag{5.113}$$

$$(U_\pi)_M = \omega\left[H_M - \left(\frac{J}{A_P}\right)_M\left(\frac{\partial p}{\partial \xi_j}\frac{\partial \xi_j}{\partial x_i}\frac{\partial \xi_\pi}{\partial x_i}\right)_M\right] + (1-\omega)(U_\pi)_M^{(n)} \tag{5.114}$$

where $(U_\pi)_P^{(n)}$ and $(U_\pi)_M^{(n)}$ are values of $(U_\pi)_P$ and $(U_\pi)_M$ at the previous iteration level. This scheme assumed a linear variation between nodes for velocity, source term H and the quantity $\left(\frac{J}{A_P}\right)$. Therefore, the contravariant velocity component at the cell face may be written as:

$$(U_\pi)_{mid} = \omega\left[\overline{H} - \left(\overline{\frac{J}{A_P}}\right)\left(\frac{\partial p}{\partial \xi_j}\frac{\partial \xi_j}{\partial x_i}\frac{\partial \xi_\pi}{\partial x_i}\right)\right] + (1-\omega)(U_\pi)_{mid}^{(n)} \tag{5.115}$$

where

$$\overline{H} = f_M H_P + (1-f_M)H_M$$

$$\left(\overline{\frac{J}{A_P}}\right) = f_M\left(\frac{J}{A_P}\right)_P + (1-f_M)\left(\frac{J}{A_E}\right)_P$$

$$(U_\pi)_{mid}^{(n)} = f_M(U_\pi)_P^{(n)} + (1-f_M)(U_\pi)_E^{(n)} \tag{5.116}$$

where f_M is the interpolation coefficient determined by volume geometry; "*mid*" is any face centre lying between the central node P and the neighbouring node M; and the overbar represents the quantities transferred to the volume faces by interpolation over the adjacent central nodes.

Equation (5.115) clearly shows that the cell face contravariant velocity $(U_\pi)_{mid}$, during the iteration process, is made up of the ω portion of the value resulting from the momentum interpolation and the $(1-\omega)$ portion of the value from the linear interpolation.

The last term in Equation (5.115) is treated explicitly in order to prevent any dependence of the solution on the under-relaxation factor. The pressure gradient term at volume faces in the equation is calculated with pressure difference between grid nodes P and M:

$$\frac{\partial p}{\partial \xi_j} = \frac{p_M - p_P}{(\delta\xi_j)_{mid}} \tag{5.117}$$

In this way, the "mass source" of the pressure correction equation m_p calculated with contravariant velocity components can sense the $1\delta\xi_j$-pressure difference and the pressure oscillation can be removed during the iteration process.

5.9 Solution Procedure of *SIMPLE* Algorithm

So far,the transport equations have been discretized and the pressure correction equation has been derived. With approximate implementation of boundary conditions which will be discussed in calculation cases in the next chapter, a complete set of discrete equations is to be solved with some kind of iterative procedure in order to get solutions of the flow fields for certain cases.

The *SIMPLE* algorithm provides a method of calculating pressure and velocity fields for incompressible flows. The method is iterative and the procedure of the *SIMPLE* algorithm is outlined as follows:

1. Guess the initial values of parameters $u^*, v^*, w^*, p^*, k^*, \epsilon^*, \mu^*$, etc., as provisional values for all the nodes in the flow field. The initial values are expected to be not too far from reality. Otherwise, it may cause divergence.
2. Calculate the coefficients of the momentum equations and solve the discrete momentum equations to obtain a new velocity field.
3. Calculate the coefficients of k and ϵ equations and solve the discrete k and ϵ equations to get new values of k, ϵ and turbulent viscosity μ_T.
4. Calculate the new value of "mass source" m_p and the coefficients of the pressure correction equation. Solve the pressure correction equation to obtain the pressure correction field.
5. Update the pressure field and the velocity field with the pressure correction field.
6. Check if the convergence criteria are satisfied. If not, return to step (2) and repeat the process until convergence is achieved.

5.10 Convergence Criteria

During an iteration process of the *SIMPLE* algorithm, the iteration process is checked and is stopped when certain criteria are satisfied.

In the case of a single blade passage domain, a solution is supposed to be converged when the residuals of all the flow variables satisfy the following two conditions:

$$
\begin{aligned}
\log_{10}\left[\sum_{n} |A_P\Phi_P - \sum_{nb} A_{nb}\Phi_{nb} - S_P|\right] &< \delta_\Phi \\
\log_{10}\left[max\left(|A_P\Phi_P - \sum_{nb} A_{nb}\Phi_{nb} - S_P|_n\right)\right] &< \delta_\Phi
\end{aligned}
\qquad (5.118)
$$

where n is the nodal index ($n = 0$ to N) and δ_Φ is a negative number, normally equals to -2.5. The first equation means that the summation of residuals of all the control volumes in the computational domain satisfies the criteria, and the second equation means that the maximum residual in the whole domain satisfies the criteria.

Chapter 6

Prediction and Analysis of a Low Speed Research Compressor

6.1 Introduction

The physical and mathematical models and numerical algorithm towards the three-dimensional simulation of multistage turbomachinery flows have been described in previous chapters. Two types of approaches for flow simulation in multistage axial flow compressors have been used and developed in the current study, one is based on the mixing plane approach and the other is a deterministic stress model based on the average passage approach described by Adamczyk [2]. The tip leakage flow in rotor blade rows is rigorously simulated with a two block grid system. Two repeating stage models have been developed aiming at simplifying the aerodynamic boundary setting when simulating flows in rear stages of multistage axial flow compressors.

The test case used in this study is the Cranfield 4-stage Low Speed Research Compressor (*LSRC*). Numerical simulations with different approaches have been carried out for both the third stage and the complete 4-stage compressor. Detailed comparison between the numerical results and the experimental data is made in this chapter in order to assess the prediction accuracy of different approaches. Performance prediction of the third stage working at off-design conditions and the analysis of entropy generation rate are also carried out.

6.2 Cranfield Low Speed Research Compressor

The Cranfield University (CU) Low Speed Research Compressor ($LSRC$) consists of four repeating stages. The design of the blading and the aerodynamic measurements were carried out within the BRITE EURAM project $AC3A$ (Advanced Civil Core Compressor Aerodynamics), Swoboda et al. [170]. The experimental investigation was carried out at Cranfield University.

For multistage low speed research compressors with identical stages, it has been found that the flow approaches a repeating flow pattern after several stages (at least two stages). Four stage research machines have been adopted in a number of cases for this reason, where the first two stages function as leading stages where the flow fully develops and reaches a repeating pattern, and the fourth stage functions as a trailing stage providing representative back conditions to the third stage which is the stage under investigation . The third stage, the study stage, demonstrates major flow features of a typical rear stage with repeating flow features working in a multistage environment. More description of the Cranfield Low Speed Research Compressor ($LSRC$) can be found in Appendix B.

6.3 Brief Description of Computational Methods

6.3.1 Governing Equations and Numerical Algorithm

The flow in the compressor is assumed to be incompressible, three-dimensional, adiabatic, steady in a relative frame of reference and turbulent.

The governing equations for the flow problems concerned are the mass continuity and momentum equations which are described in Chapter 3. The form of the ensemble averaged Navier-Stokes equations are used in the predictions with the mixing plane approaches where the unsteady term is ignored. The form of the time averaged Navier-Stokes equations are used in the predictions with the deterministic stress approaches. The standard $k-\epsilon$ turbulence model, Launder and Spalding [106], is used to "close" the Reynolds averaged equation system and the overlapped solution approach is used to "close" the time averaged equation system. The standard wall function method is introduced to simplify the treatment of near wall regions.

The third order $QUICK$ scheme is applied to the momentum equations and the first order upwind scheme is applied to the k and ϵ equations. The $QUICK$ scheme is more accurate than the upwind scheme but is prone to instabilities or even divergence as it remains unbounded. For this reason, *QUICK* scheme is only used in momentum equations. Central differencing is applied to the pressure gradient terms and other source terms of the governing equations.

The *SIMPLE* approach, Patankar and Spalding [136], is used to update the velocity and pressure fields in an iterative way. Stone's Strongly Implicit Procedure (*SIP*) (Stone [167]) is applied to the discretised momentum equations to obtain a solution. The strongly implicit procedure combined with the residual minimisation constraints, Giannakoglou and Politis [60], accelerates the solution convergence of the pressure correction equation. Approximate under-relaxation is used for the equation system to enhance the convergence of each equation.

6.3.2 Computational Grids

In order to predict the flow rigorously in both the main passage and the tip clearance of a rotor blade row, a H-type two-block grid is used for a rotor passage. A single H-type block grid is used for a shrouded stator passage. In the rotor passage including its upstream and downstream extensions, the first block fills the main passage below the cylindrical blade-to-blade surface at the blade tip radius and defined by two successive blades, and the second block , the tip block, fills the remaining part of the flow domain lying between the blade tip radius and the outer annulus. In the stator passage, a single block is used to describe the domain between two shrouded stator blades including its upstream and downstream extensions, where the stator hub cavity is ignored. The grid block arrangement and the grids for the third stage of *LSRC* used in the mixing plane approaches are shown in Figure 6.1. In the predictions with the deterministic stress model, the grid for each blade passage has a further downstream extension which covers the flow passage of the following blade row. The grids for the third stage of *LSRC* used in the deterministic stress approaches are shown in Figure 6.2. The grids for other stages of *LSRC* are the same as those for the third stage because the geometry of every stage is the same. The number of the grid nodes used in the prediction are shown in Table 6.1. More details about the grid generation are described in Chapter 2.

6.3.3 Boundary Conditions

Detailed boundary conditions for each computational domain of blade rows are described in Chapter 5 and will not be repeated here. The inlet and outlet

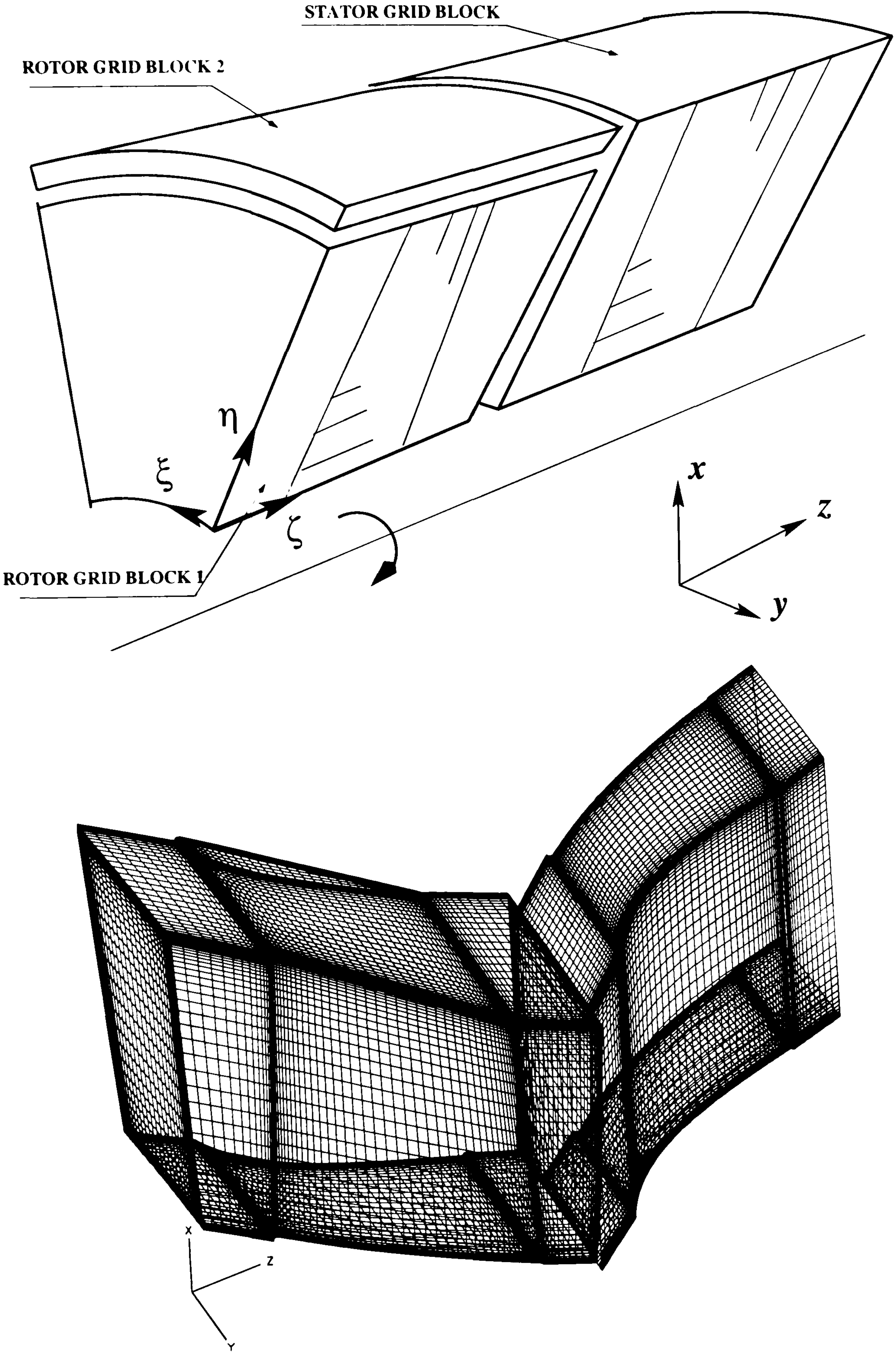

Figure 6.1: **Grids for *LSRC* third stage**

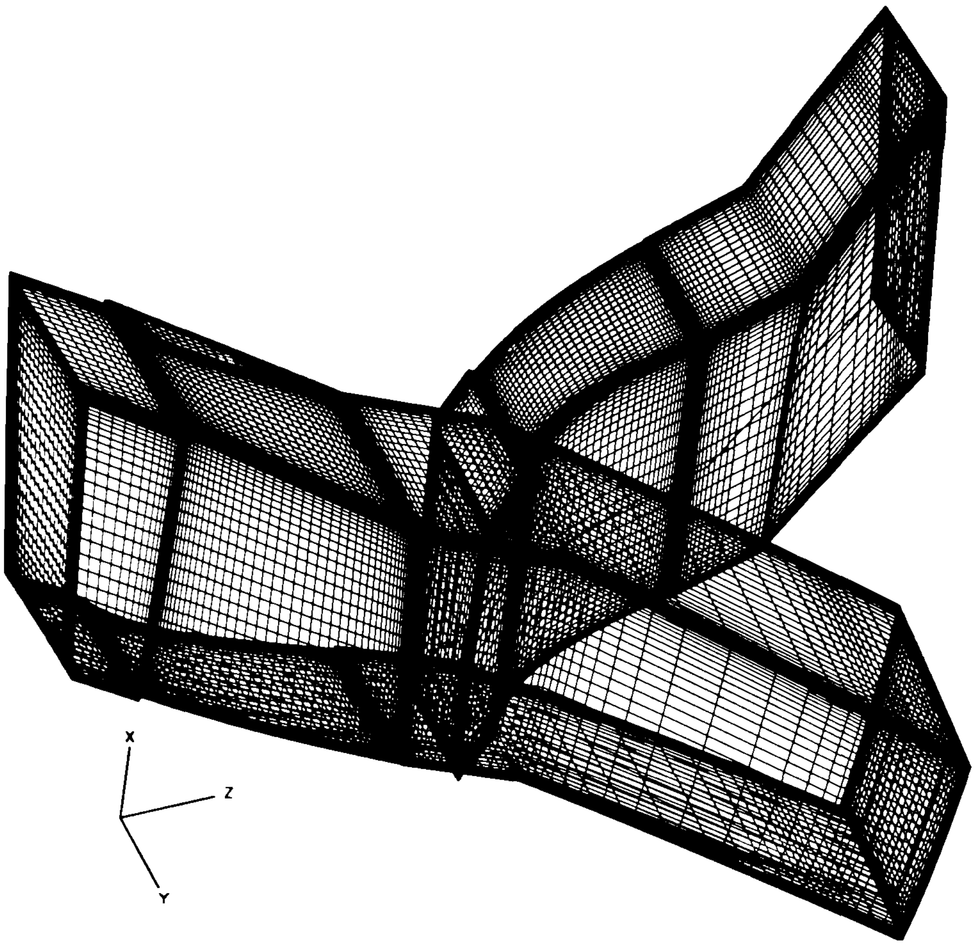

Figure 6.2: **Grids with downstream extension for *LSRC* third stage**

Parameter	Rotor	Stator
Grids (for Deterministic Stress Model)	35x35x115(main) 40x9x115 (tip)	35x35x115
Total number of grid points	182,275	140,875
Grids (for Mixing Plane Model)	35x35x75(main) 40x9x75(tip)	35x35x75
Total number of grid points	118,875	91,875

Table 6.1: **Number of grid nodes**

boundary conditions for the third stage or the complete four stages of *LSRC* in different computation cases are presented in the following sections.

6.3.4 Under-Relaxation Factors

In global iterations, under-relaxation is used to enhance the consistency of all the parameters at the interfaces between blade rows. The relaxation factors for global iterations normally take a value of 0.7 in the first several iterations and about 0.9 in the following iterations.

Under-relaxation is used to enhance the convergence of the governing equations during the local iterations. The relaxation factors for all the equations normally take the value of 0.10 in the first global iteration and 0.15 for the stator and 0.25 to 0.30 for the rotor in the following global iterations.

In general, the determination of the under-relaxation factors are problem dependent and based on previous experience.

6.3.5 Computation Time Required

The computational time requirement on a DEC ALPHA FARM for each inner iteration is approximately 5 seconds for a grid which only covers a blade passage without an extension and 7.5 seconds for a grid which has further downstream extension covering the flow passage of the following blade row. Typically, a maximum number of 5,000 inner iterations is used locally for each blade row to satisfy numerical convergence criteria for the governing equations and about 15 to 20 global iterations are required for global convergence of a single stage computation and about 40 global iterations for a four stage computation.

6.3.6 Convergence Criteria

In order to achieve a converged solution, two types of convergence criteria must be satisfied. The first one refers to the numerical convergence criterion for the governing equations on each blade row, which is satisfied when the residuals of all the governing equations are sufficiently small. This type of criteria is discussed in detail in Chapter 5. The second type is a physical convergence criterion for the global iterations when physical flow quantities of the flow (mass flow rate, velocity, static and total pressure, k and ϵ) in each computational domain stop changing and provide consistency of all the parameters at the interfaces between blade rows with global iteration count. Specified target mass flow rate for each blade row as a constraint is used globally to enhance convergence and avoid accumulated mass flow rate error.

6.3.7 Computer Code

A computer code *MSTurbo3D* originated from code *ELISA*, Politis et al. [141] has been developed in this project based on the physical and mathematical models and the numerical algorithm described in this thesis. The structure of the code is demonstrated in Appendix D and the format of input data files is described in Appendix E.

6.4 Prediction *I*: *LSRC* Third Stage with Conventional Boundary Setting and Mixing Plane Model

The layout of the computational domains and boundary condition setting for the third stage of *LSRC* is shown in Figure 6.3. There are three mixing planes used for the stage analysis, one at the inlet of the rotor, one at the interface between the rotor and the stator and one at the exit of the stator. The spanwise velocity profile at the stage inlet is set equal to the experimental data, Figure 6.5. k and ϵ distribution at the stage inlet are calculated with the local velocity value and imposed at the inlet. The mixing plane models are used to pass information between the rotor and the stator computational domains at the interface located halfway between the two blade rows, where the velocity, k and ϵ propagate downstream and the static pressure upstream.

Performance comparisons of the third stage of *LSRC* are carried out at the operating point of peak efficiency, at the inlet, the exit and the interface between the blade rows in terms of total pressure, static pressure, flow angle and velocity components. In addition, static pressure distributions on the rotor and the stator blade surfaces near blade hub, at midspan and near blade tip are also compared against experimental data. The experimental data are obtained from the *AC3A* project where the total pressure, static pressure and flow angle distributions were directly measured whereas the velocity components were calculated from them.

The predicted area averaged static pressure and total pressure distributions in

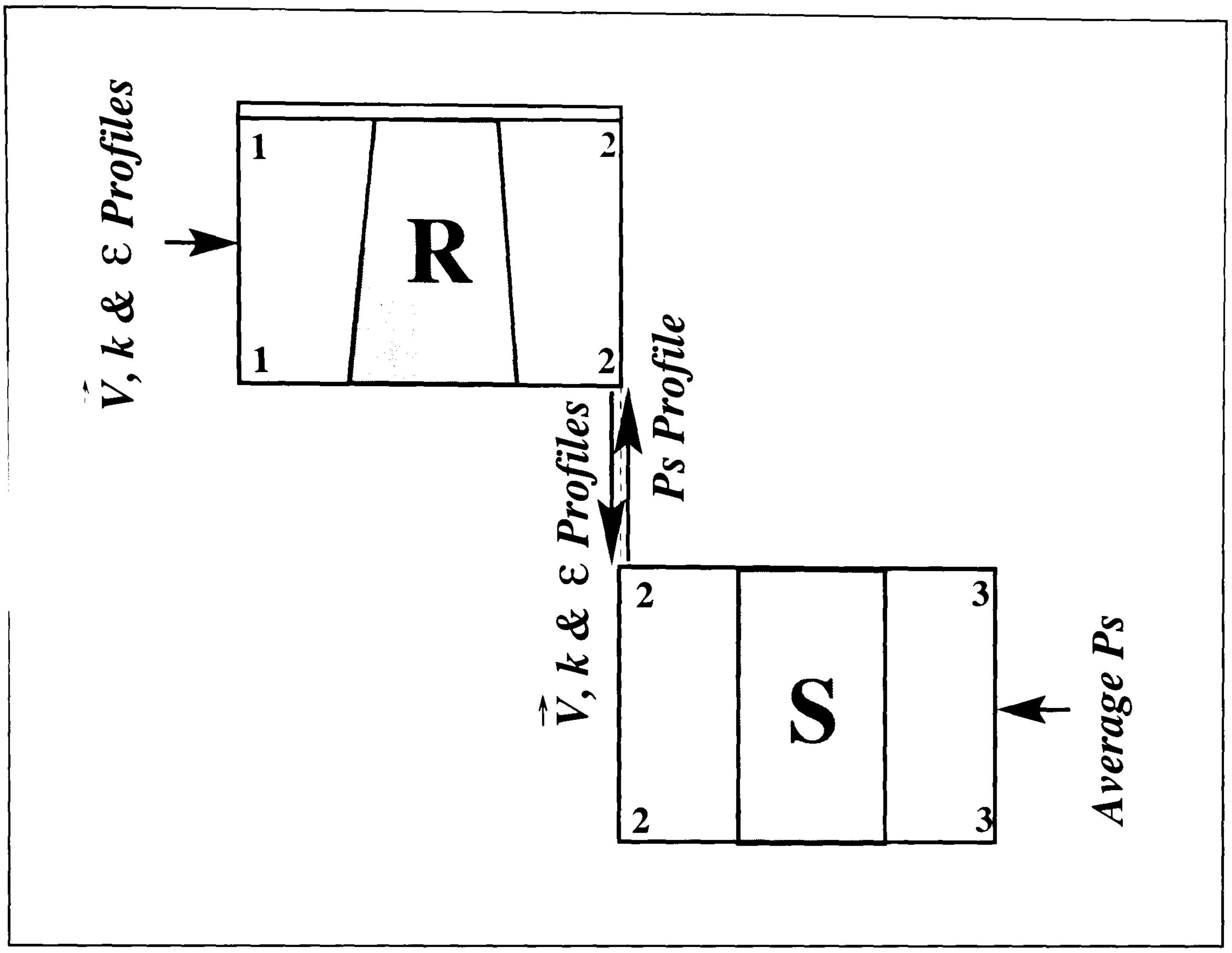

Figure 6.3: **Boundary conditions for Prediction** *I*

the axial direction of the third stage are presented in Figure 6.4. Compared with the experimental data at three stations of the stage. the inlet, the interface between the two blade rows and the exit. good agreement between the computational and the experimental data is shown in the figure although there are small discrepancies. When an average static pressure is fixed at the stator exit. static pressure ratio was over-predicted by about 2% in the stator and under-predicted by about 2% in the rotor. Regarding the total pressure, the prediction provides about 2% over-predicted pressure ratio throughout the stage. Sudden changes of average static pressure and total pressure appear near the leading and trailing edges of each blade row. showing that there are strong interaction between the blades and the flow and significant influence of the sudden change in passage area.

The difference between the total pressure on both sides of the mixing plane is nearly negligible. showing that the discontinuity of the momentum resulted from the mixing-plane model is very small and can be neglected at peak efficiency for this compressor.

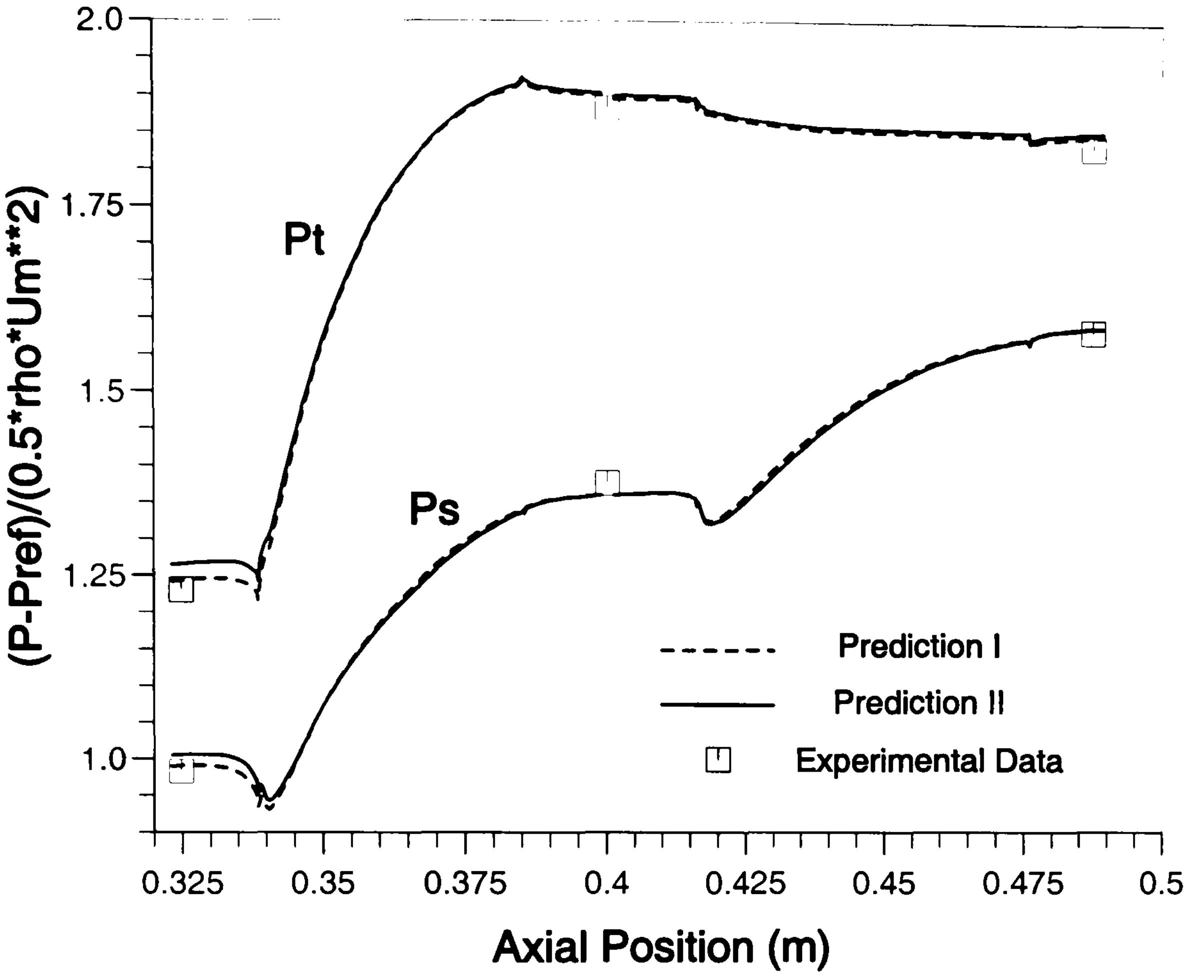

Figure 6.4: **Axial Pt & Ps distribution from Prediction** *I* **&** *II*

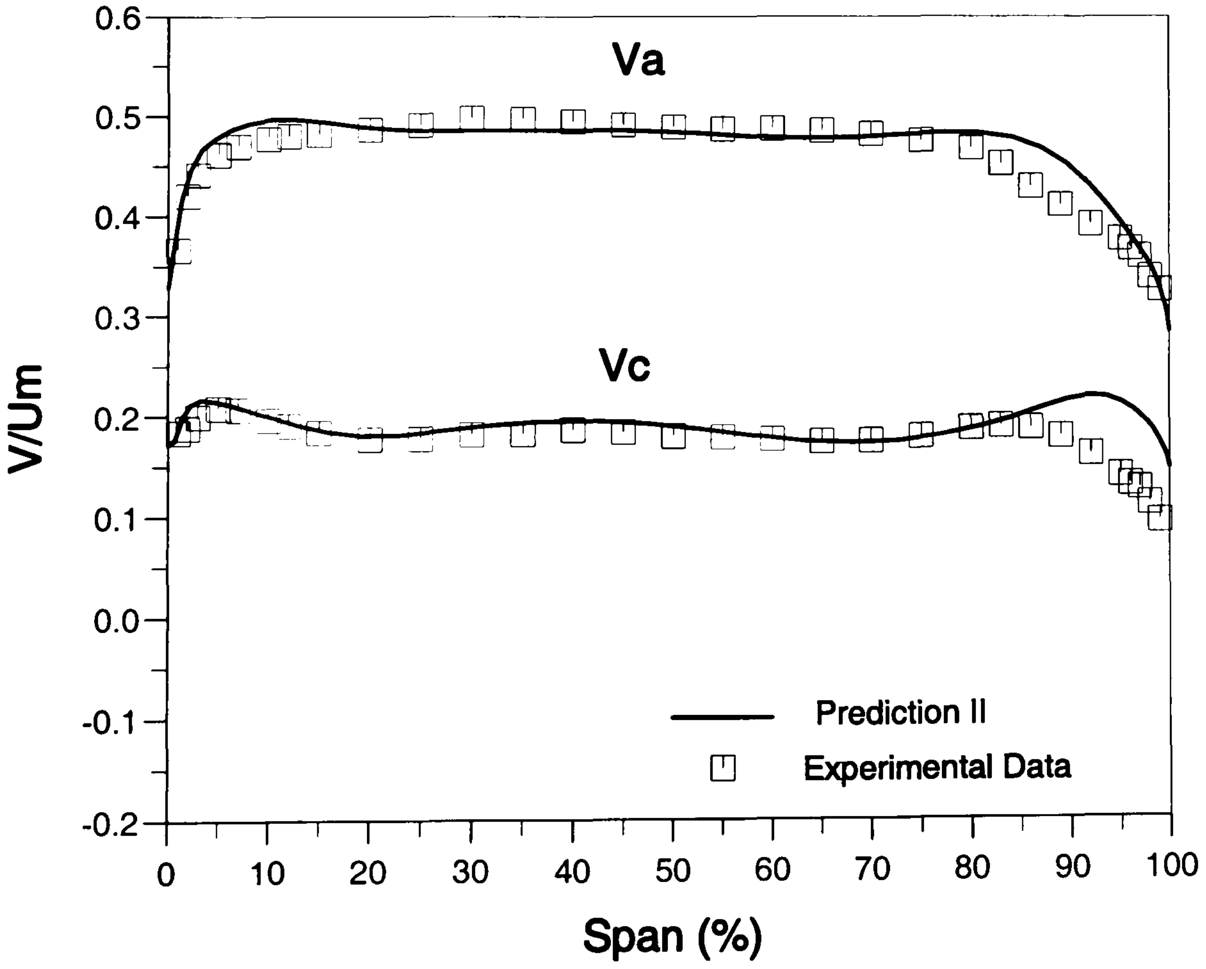

Figure 6.5: **Spanwise velocity at stage inlet from Prediction** *I* **&** *II*

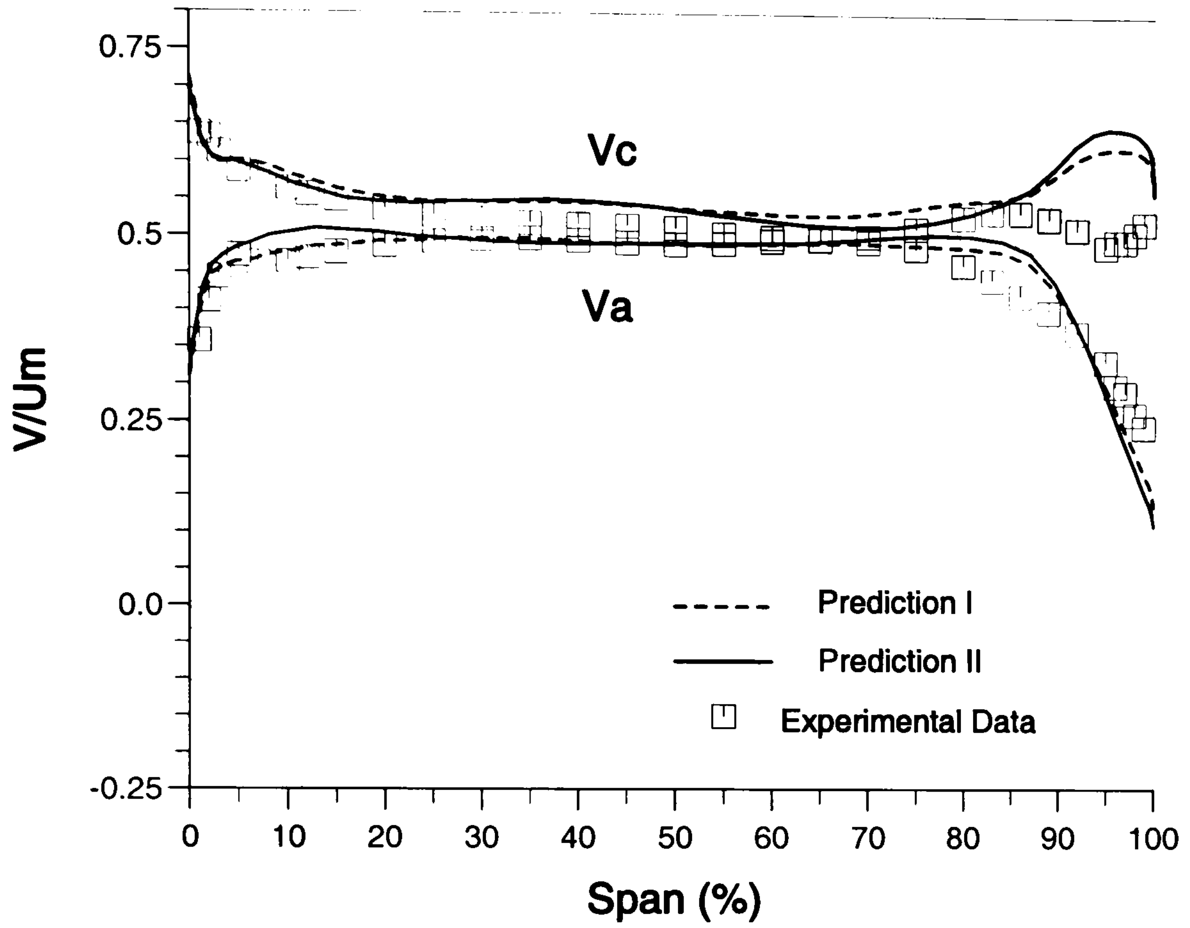

Figure 6.6: Spanwise velocity at interface from Prediction *I* & *II*

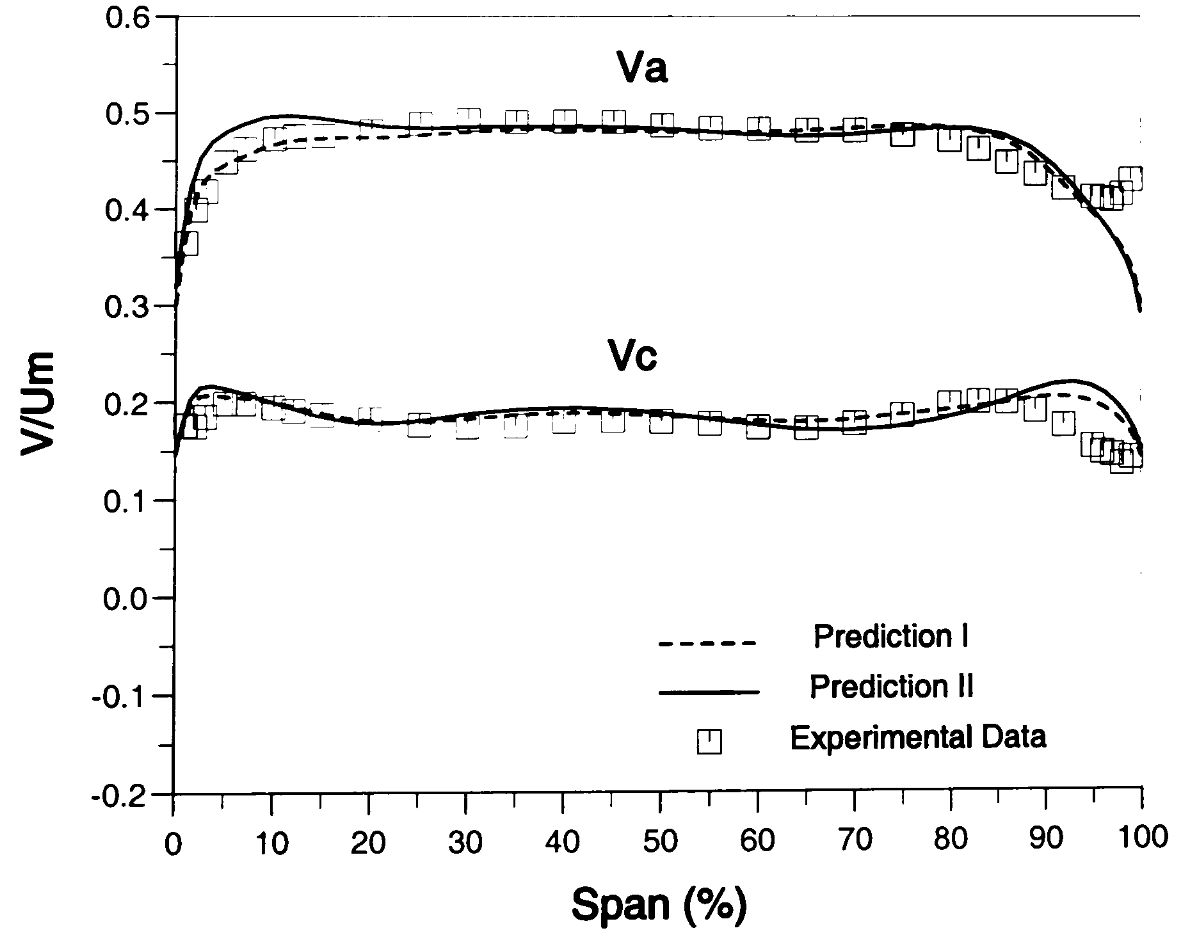

Figure 6.7: Spanwise velocity at stage exit from Prediction *I* & *II*

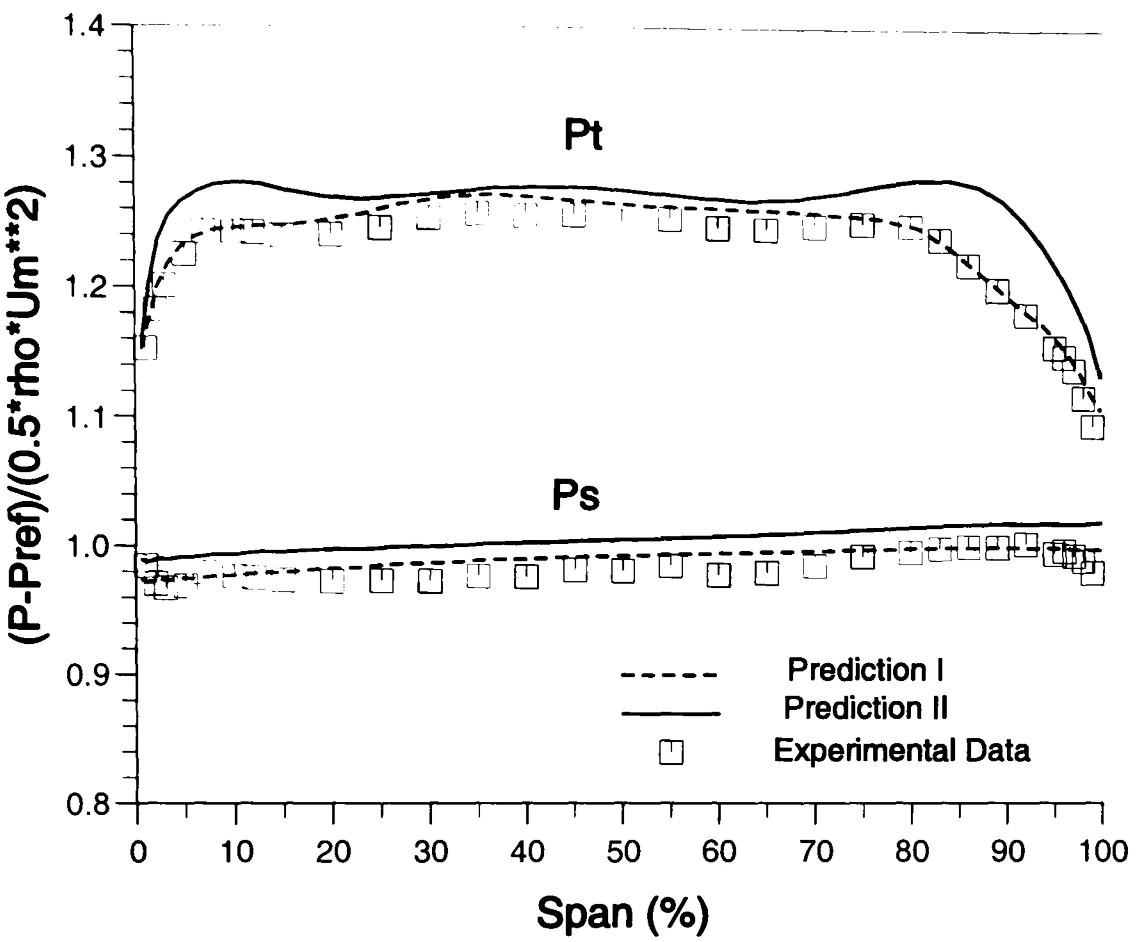

Figure 6.8: Spanwise *Pt* & *Ps* at stage inlet from Prediction *I* & *II*

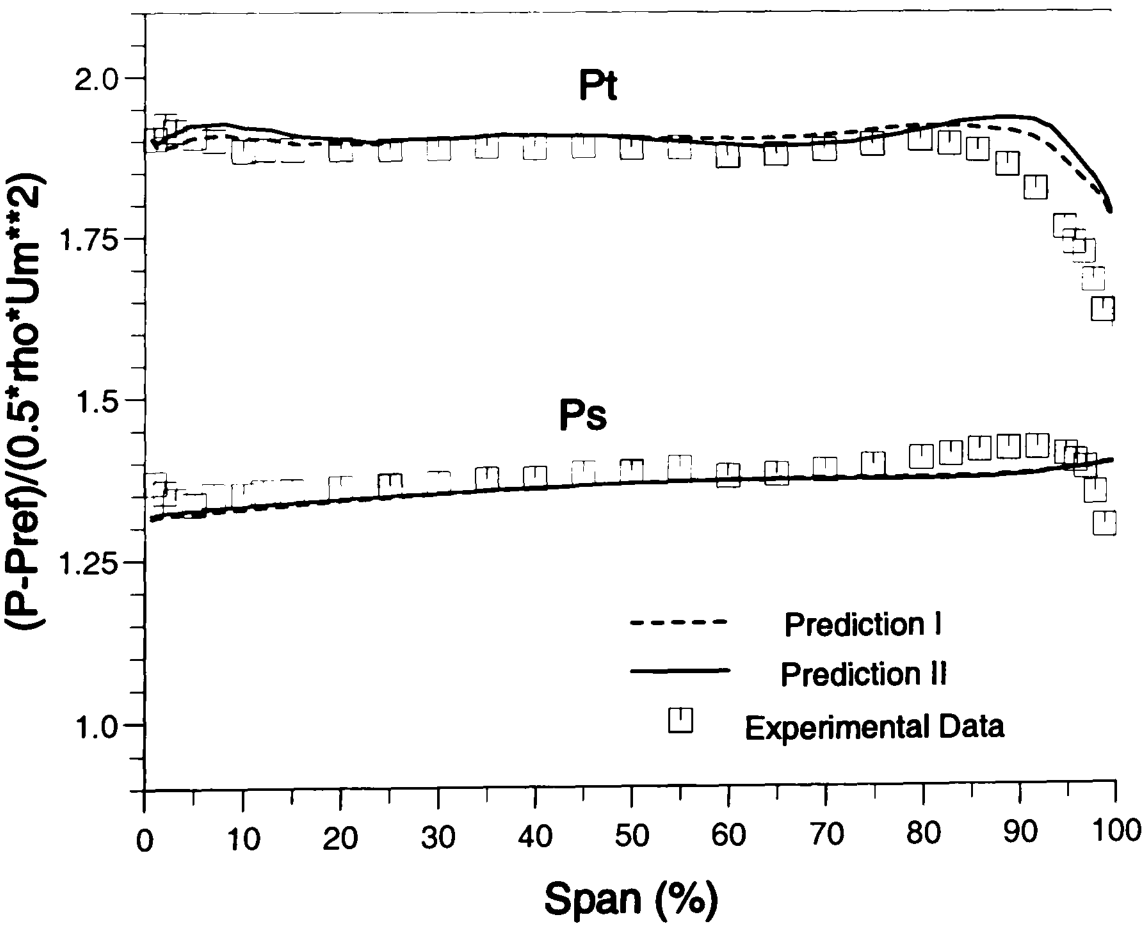

Figure 6.9: Spanwise *Pt* & *Ps* at interface from Prediction *I* & *II*

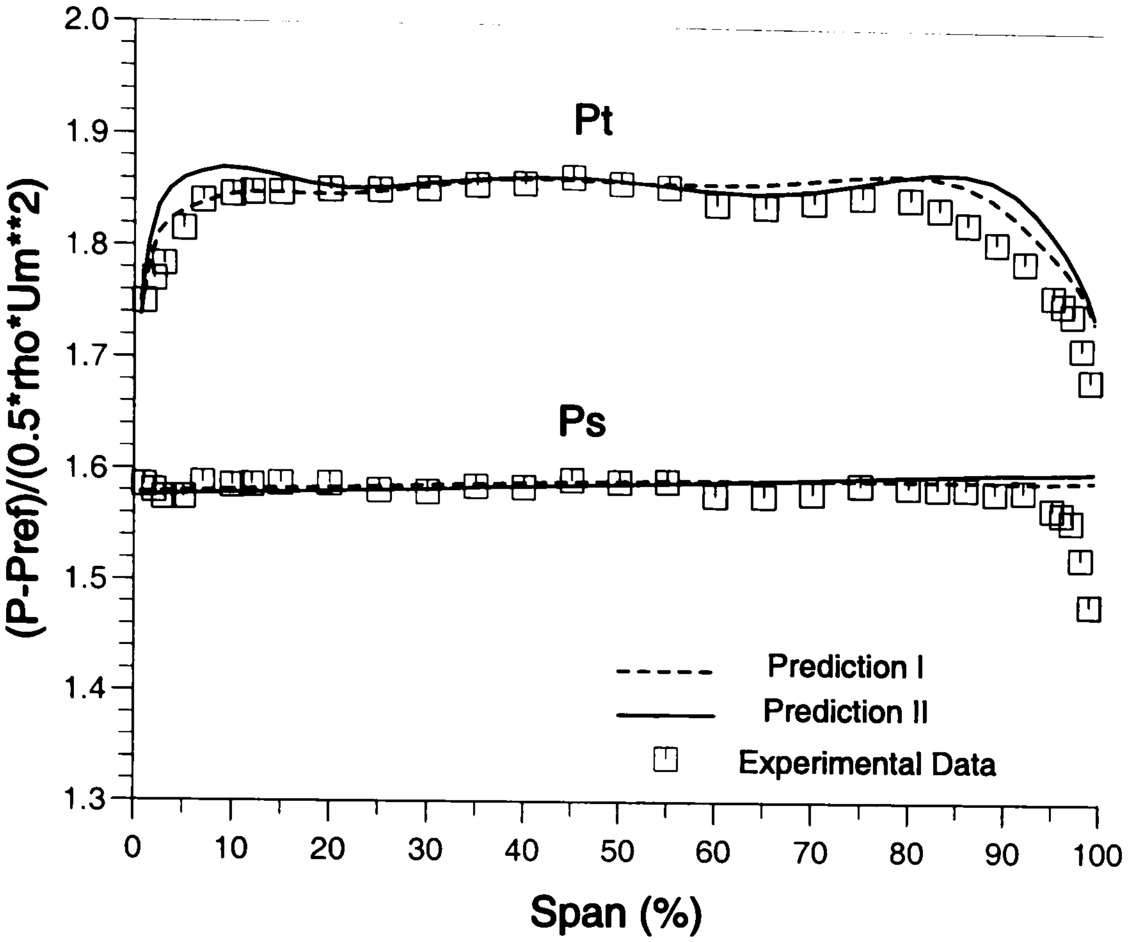

Figure 6.10: Spanwise Pt & Ps at stage exit from Prediction I & II

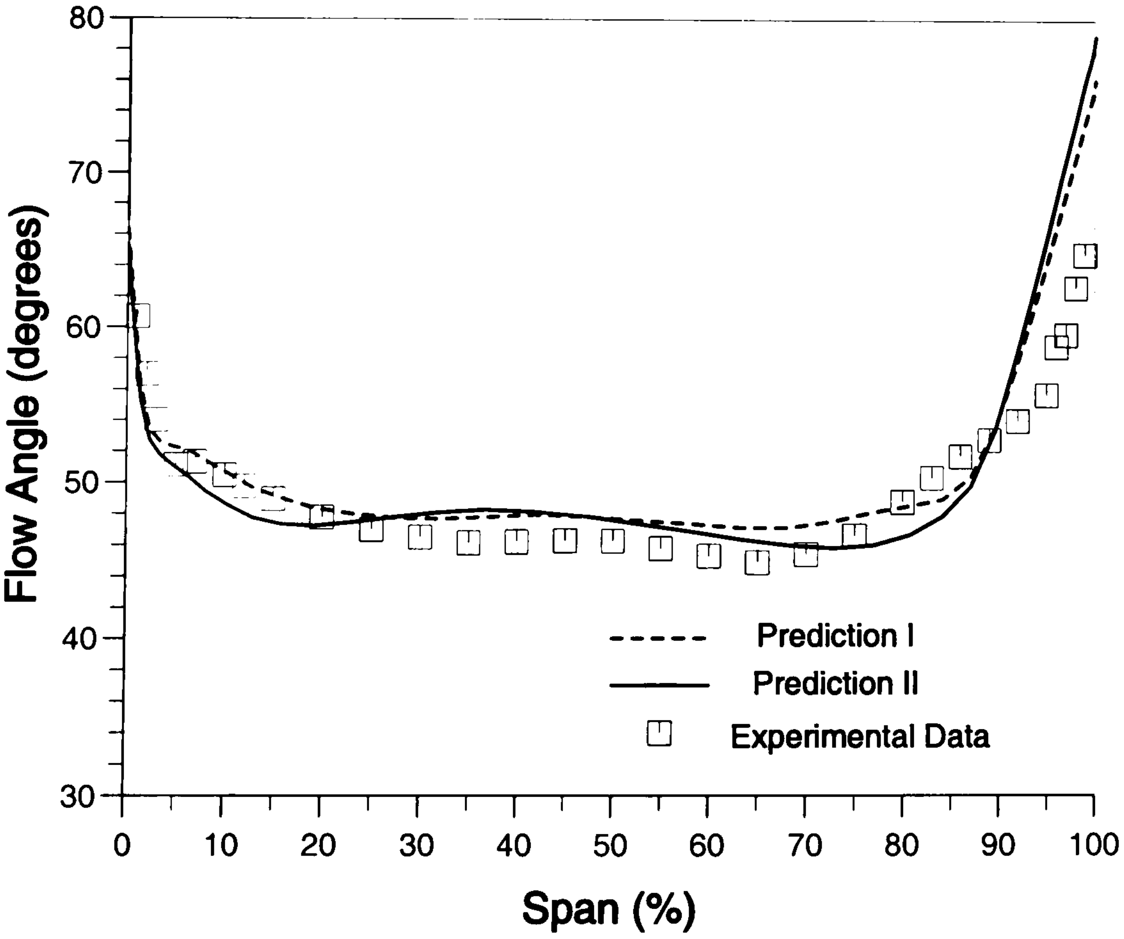

Figure 6.11: Spanwise flow Angle at interface from Prediction I & II

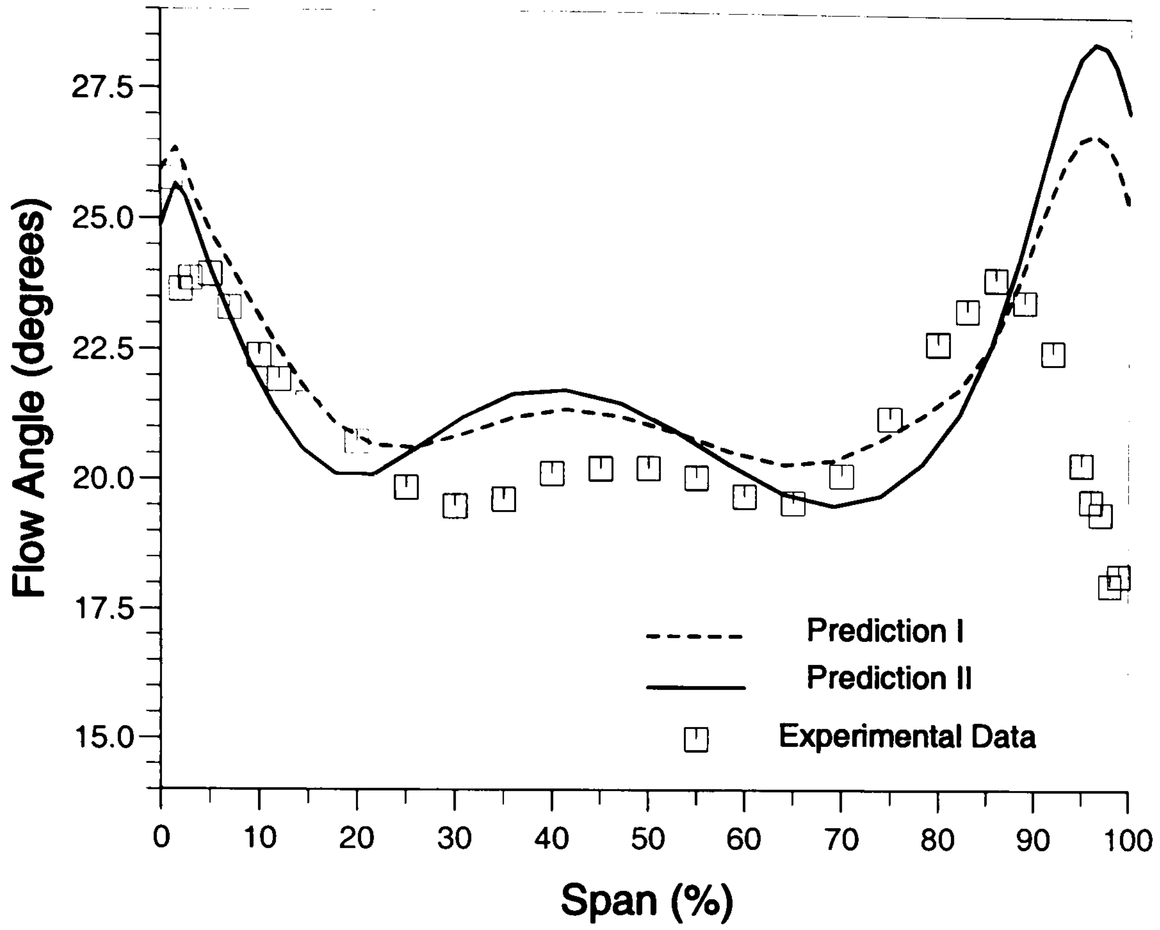

Figure 6.12: **Spanwise flow angle at stage exit from Prediction *I* & *II***

The calculated spanwise distribution of velocity components at the interface between the two blade rows and the stator exit match very well with the experimental data for most part of the blade span although with some discrepancies in the area between 80% and 100% span near the rotor tip, see Figures 6.6 to 6.7. The discrepancies at the rotor exit are very likely due to numerical inaccuracies in resolving the complex, unsteady tip clearance flows because even when the inlet velocity profile is set equal to the experimental data these discrepancies still exist. Downstream the stator passage these discrepancies become smaller because there is no tip clearance in the stator.

In Figures 6.8 to 6.10 the spanwise distributions of static and total pressure are presented for the three locations. Good predictions of static pressure at the three stations are shown with slight under-predicted static pressure at the interface. The sudden changes of experimental static pressure near the annulus wall are not physical and susceptible to measurement error due to the presence of the solid walls (Howard et al., [88]). Hence, the difference in static pressure between experiment and prediction near the blade tip should not be as large as shown in Figures 6.9 and 6.10.

The spanwise total pressure distributions are well predicted as compared with

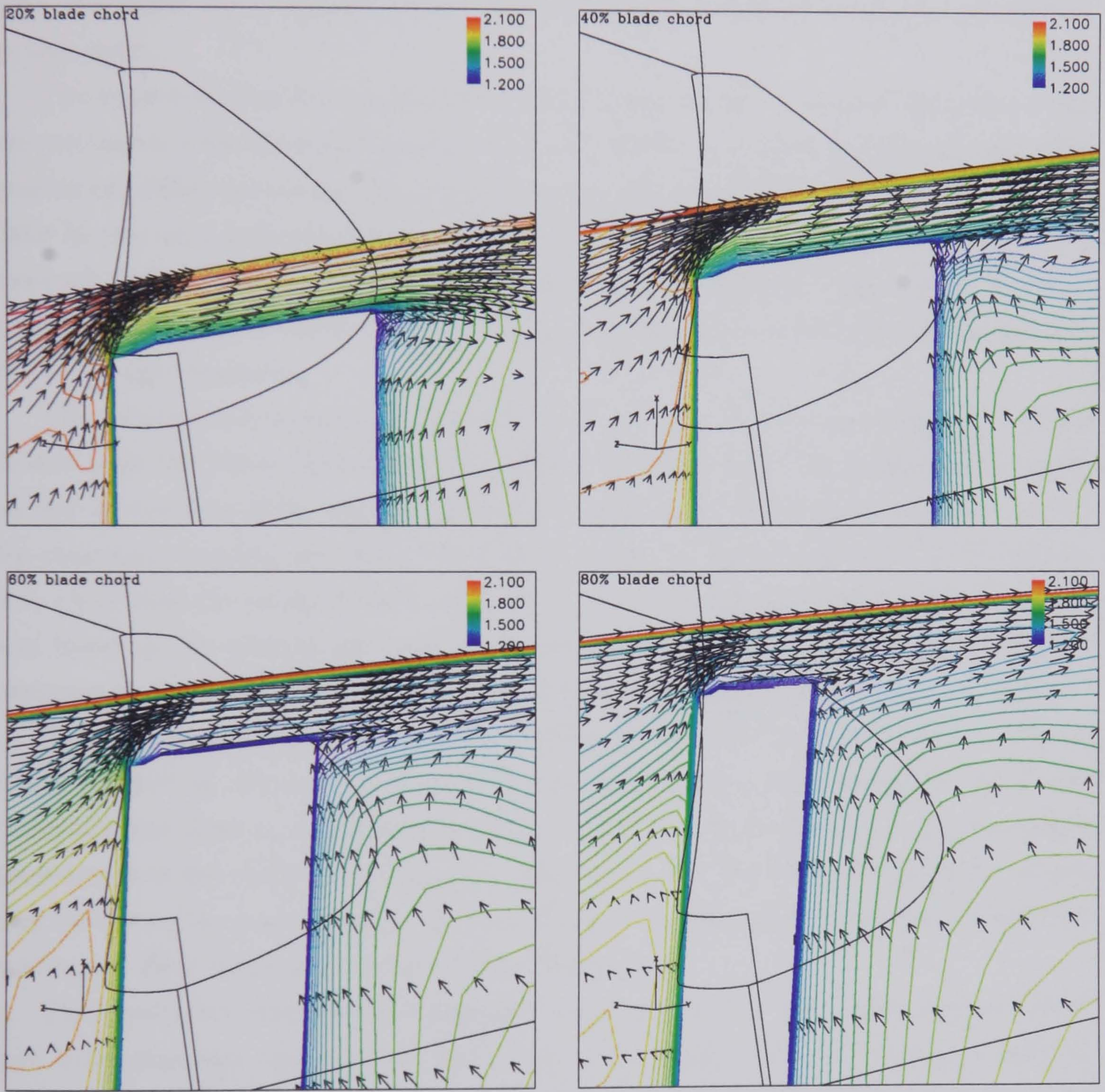

Figure 6.13: **Cross plane views of velocity vectors and relative total pressure $(P_t - P_{ref})/(0.5\rho U_m^2)$ contours in and near Rotor 3 tip clearance at different axial locations (Prediction I)**

the experimental data except for the area between 80% and 100% span at the mid-interface and the stator exit. In the case concerned the flow in the compressor is of low speed and is assumed to be incompressible and the total pressure is calculated using static pressure and velocity values so the discrepancy of the total pressure near the blade tip is caused by the inaccurate prediction of velocity distribution in this area.

The spanwise distribution of relative flow angles at the rotor and the stator exits are compared with the experimental data in Figures 6.11 and 6.12 respectively. The maximum difference of the flow angle between the prediction and the experimental data in the area between 0% to 90% span is less than 2 degrees, but in the area between 90% to 100% blade height it reaches approximately 8 degrees in the rotor and about 10 degrees in the stator due to the inaccurate prediction of the flow in the rotor tip clearance.

The relative total pressure contours and velocity vectors in cross plane views in and near the blade tip clearance at 20%, 40%, 60% and 80% blade chord downstream Rotor 3 leading edge are shown in Figure 6.13. Strong crossing flow in the tip clearance causing secondary flow near the tip is also illustrated in the figure. It is clear that the relative total pressure is higher in the pressure side of the blade and lower in the suction side and tip clearance. Larger values of the relative total pressure and velocity near outer casing is due the relative moving of the casing.

Static pressure distributions on both the rotor and the stator blade surfaces are presented in Figures 6.14 to 6.19 and show very good agreement with the experimental data in most of the blade chord. Some discrepancies in the static pressure near the stator blade leading edge at tip are shown in Figure 6.19, which may be due to the inaccurate prediction of rotor tip leakage flow and the subsequent inaccurate flow incidence to the stator blades.

The predicted relative total pressure contours at the rotor exit and the absolute total pressure contours at the stator exit are plotted and compared against the corresponding experimental contours. In Figure 6.20 which is viewed from the front of the stage in the relative frame of reference, clear wakes at downstream of the rotor are well predicted. The calculated tangential gradients are in agreement with the experimental contours but with smaller average values. The peak point of the total pressure in the prediction appears at about 67% of the blade height and half way between the blade pressure and suction surfaces, while in the experimental contours the peak point appears at about the same blade height but close to the blade pressure surface. Deeper wakes are predicted compared with the exper-

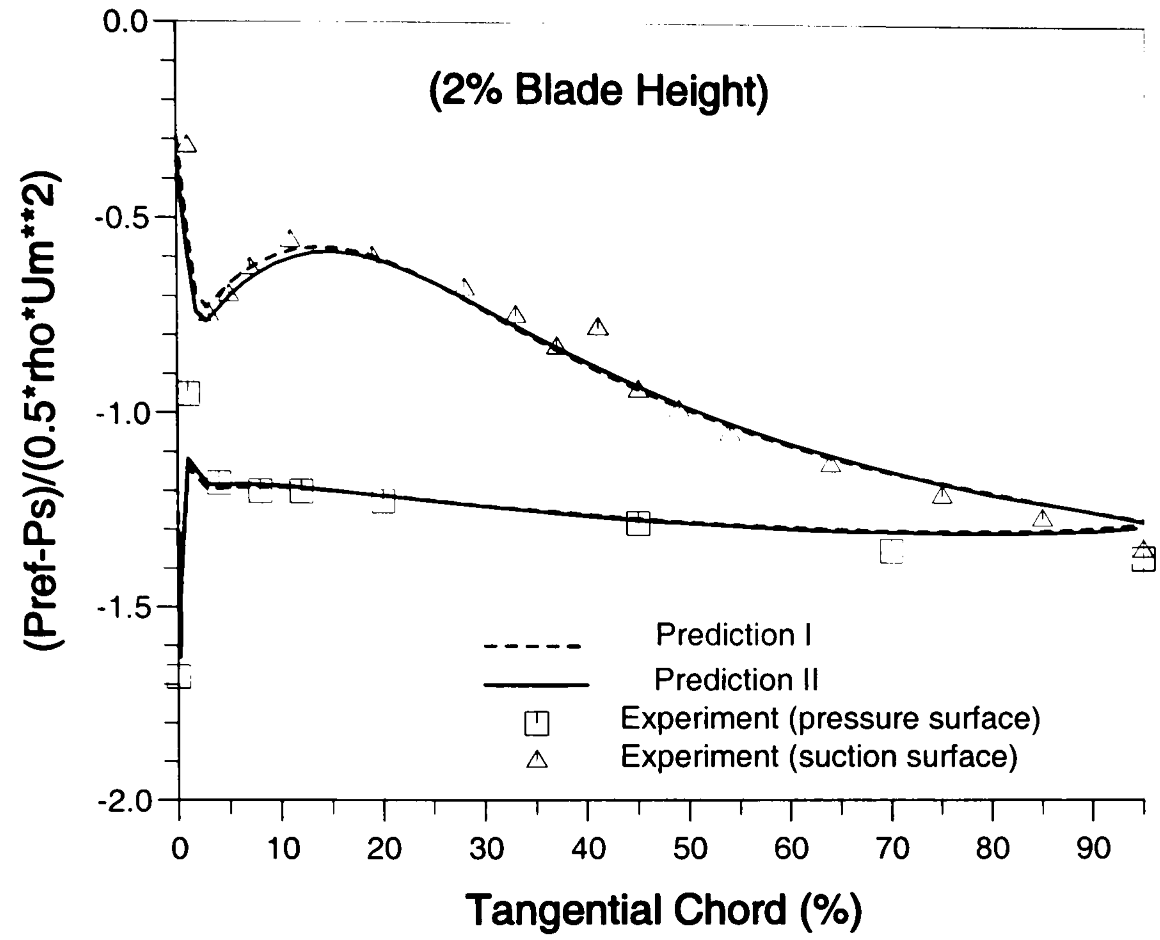

Figure 6.14: *Ps* on rotor hub surface from Prediction *I* & *II*

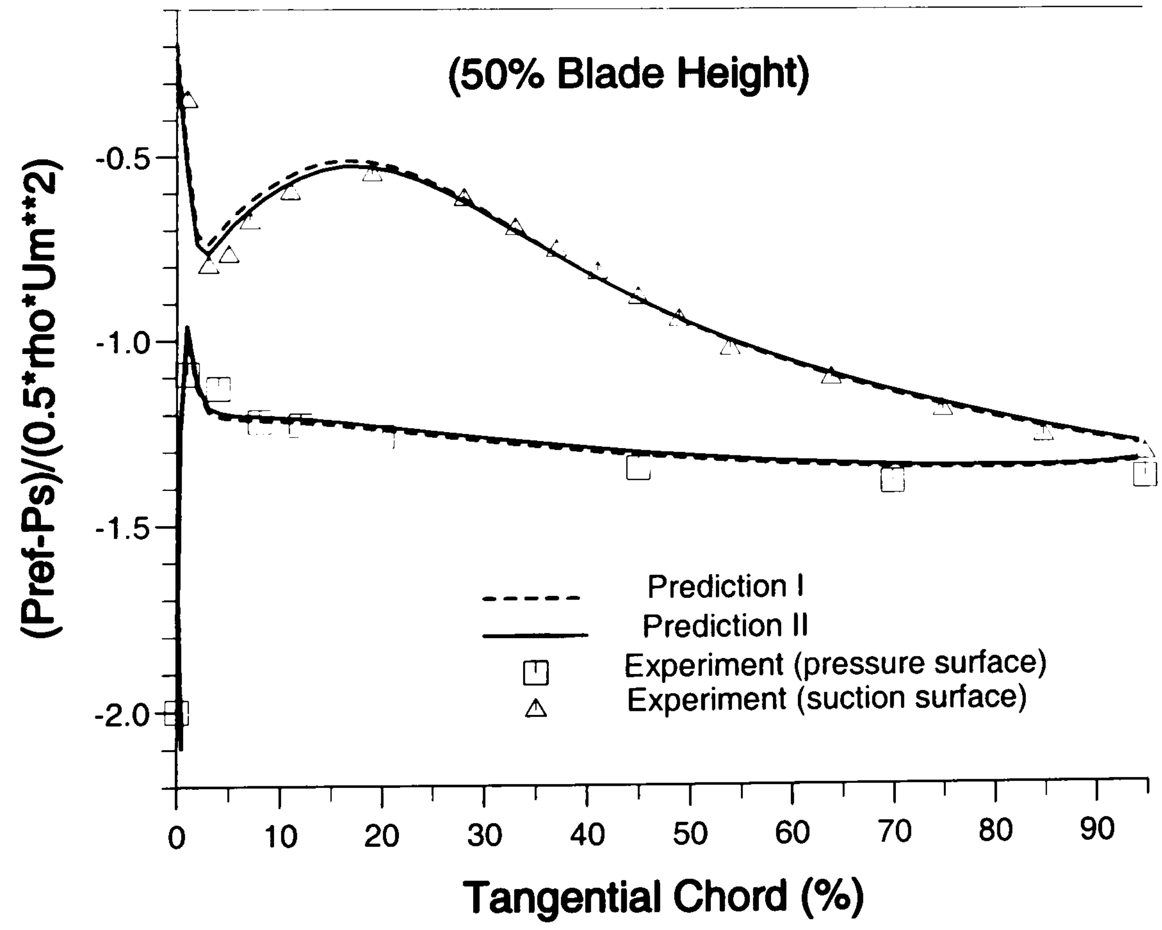

Figure 6.15: *Ps* on rotor midspan surface from Prediction *I* & *II*

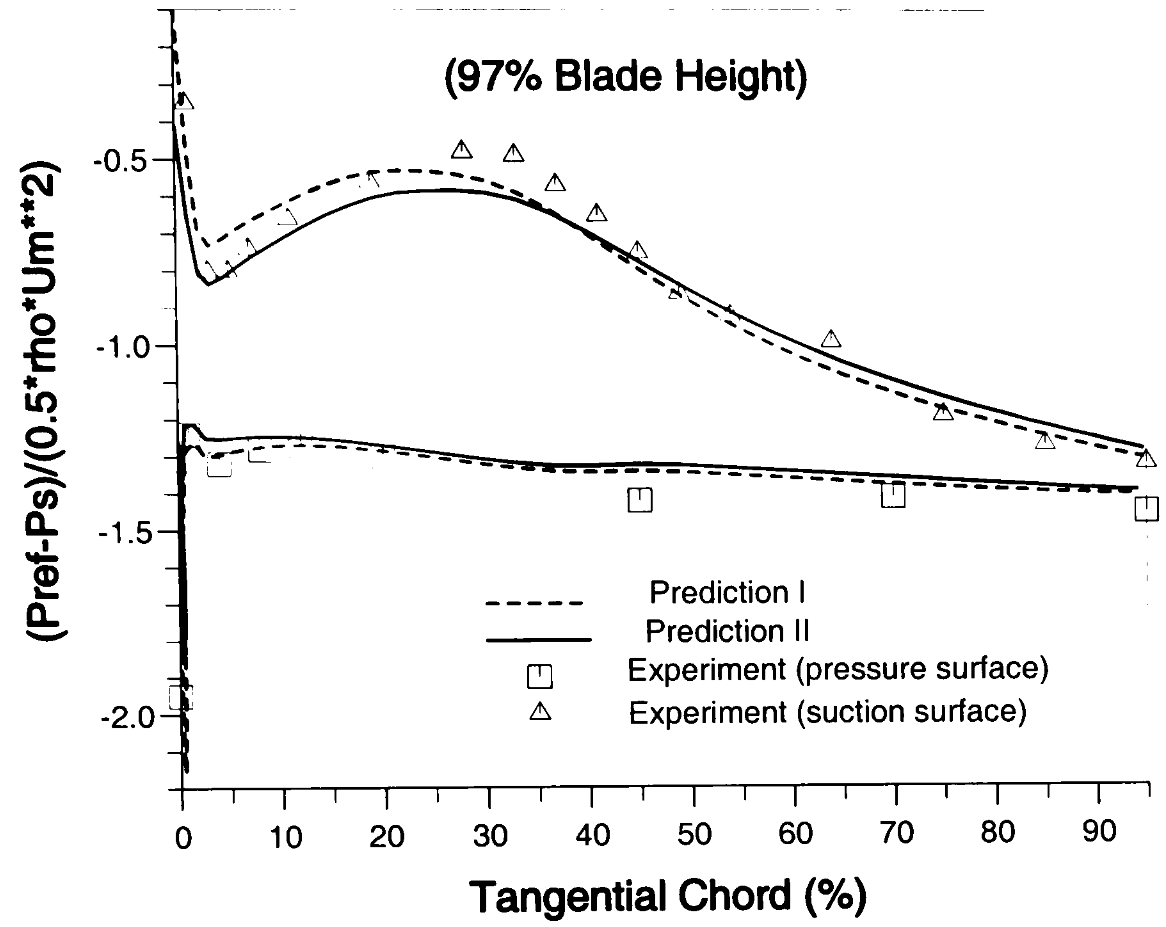

Figure 6.16: *Ps* on rotor near tip surface from Prediction *I* & *II*

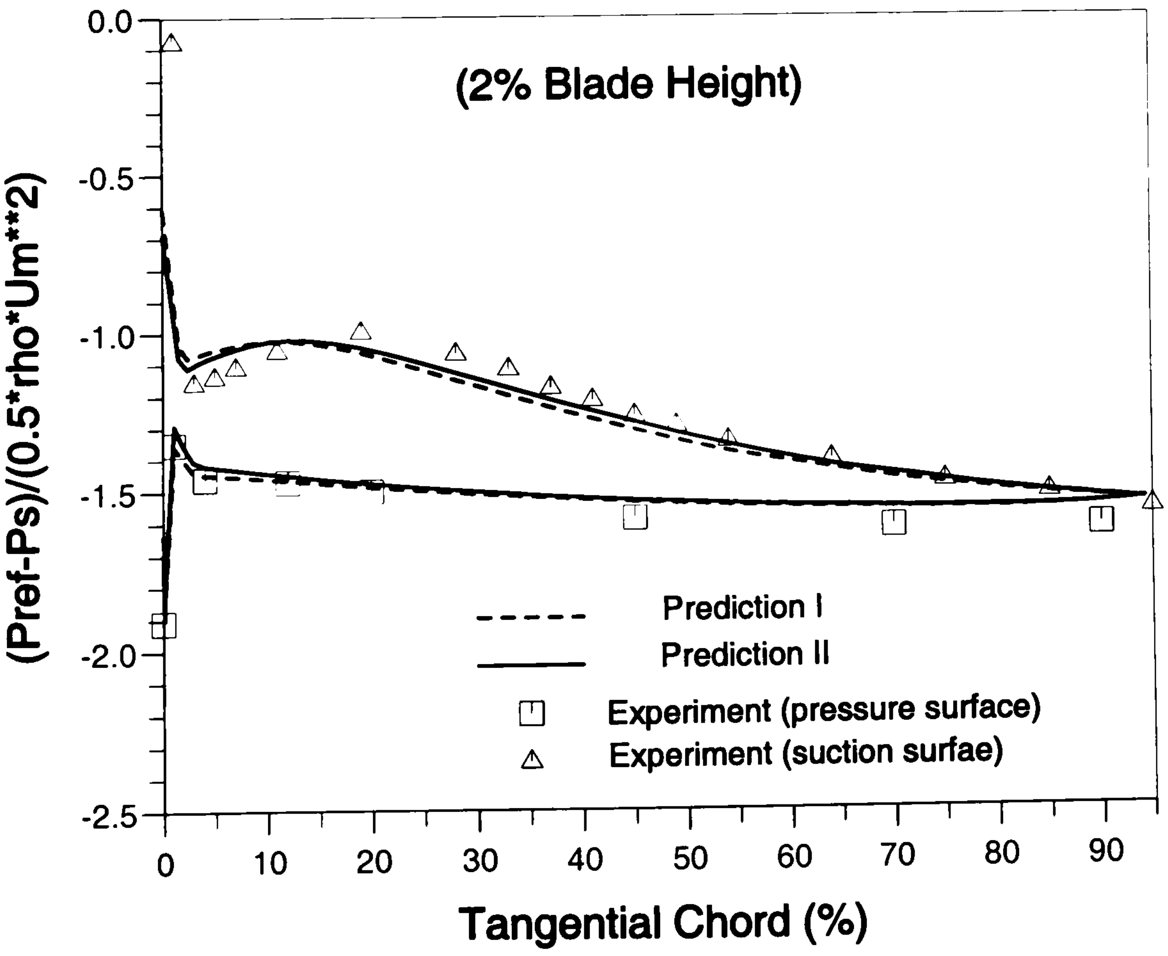

Figure 6.17: *Ps* on stator hub surface from Prediction *I* & *II*

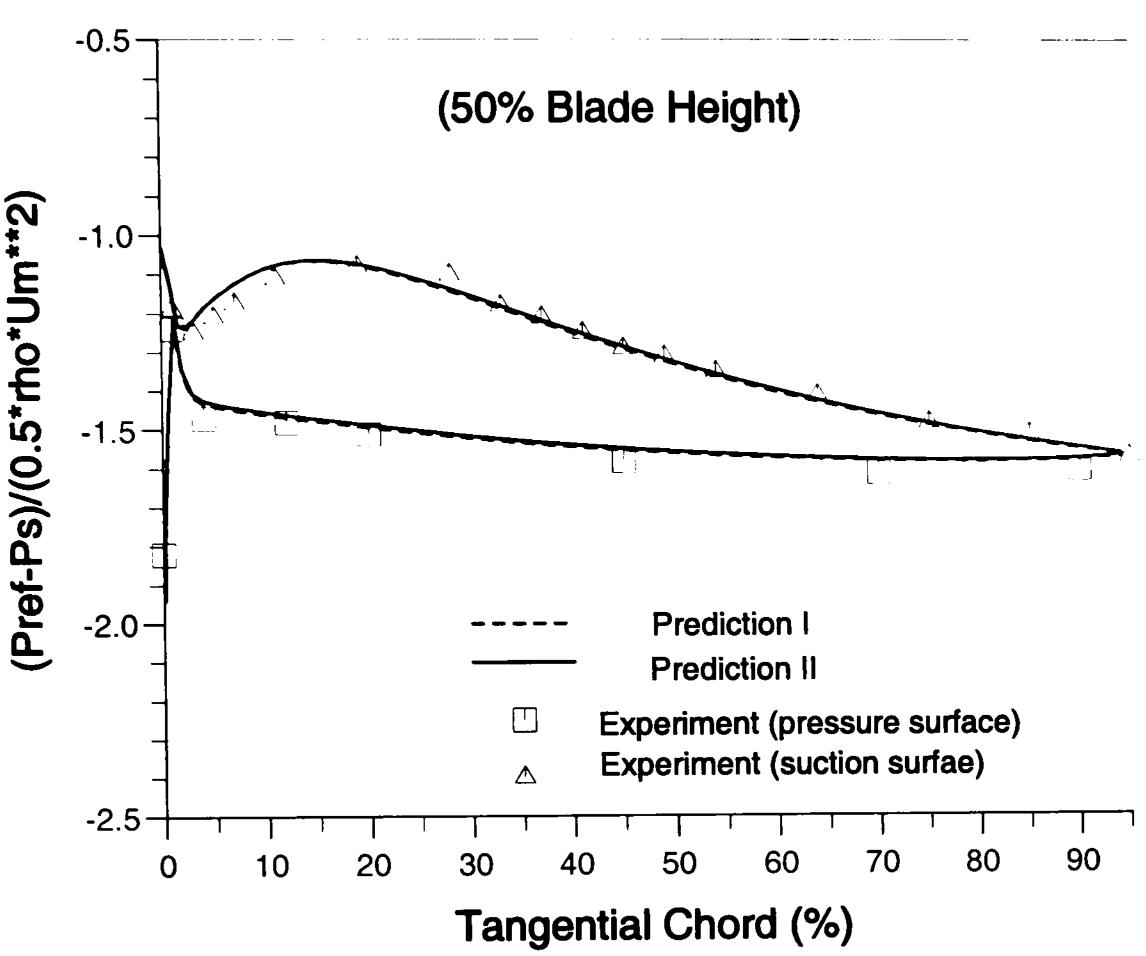

Figure 6.18: Ps on stator midspan surface from Prediction I & II

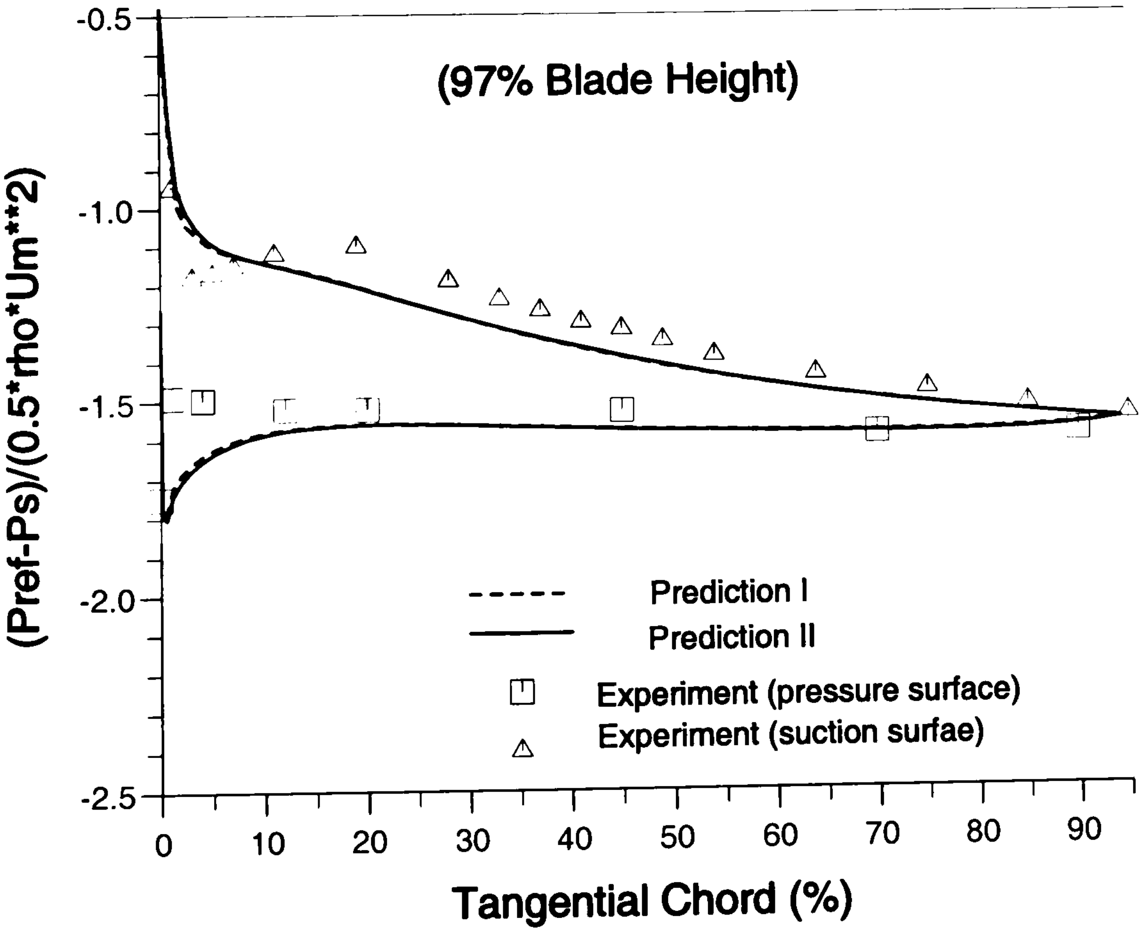

Figure 6.19: Ps on stator near tip surface from Prediction I & II

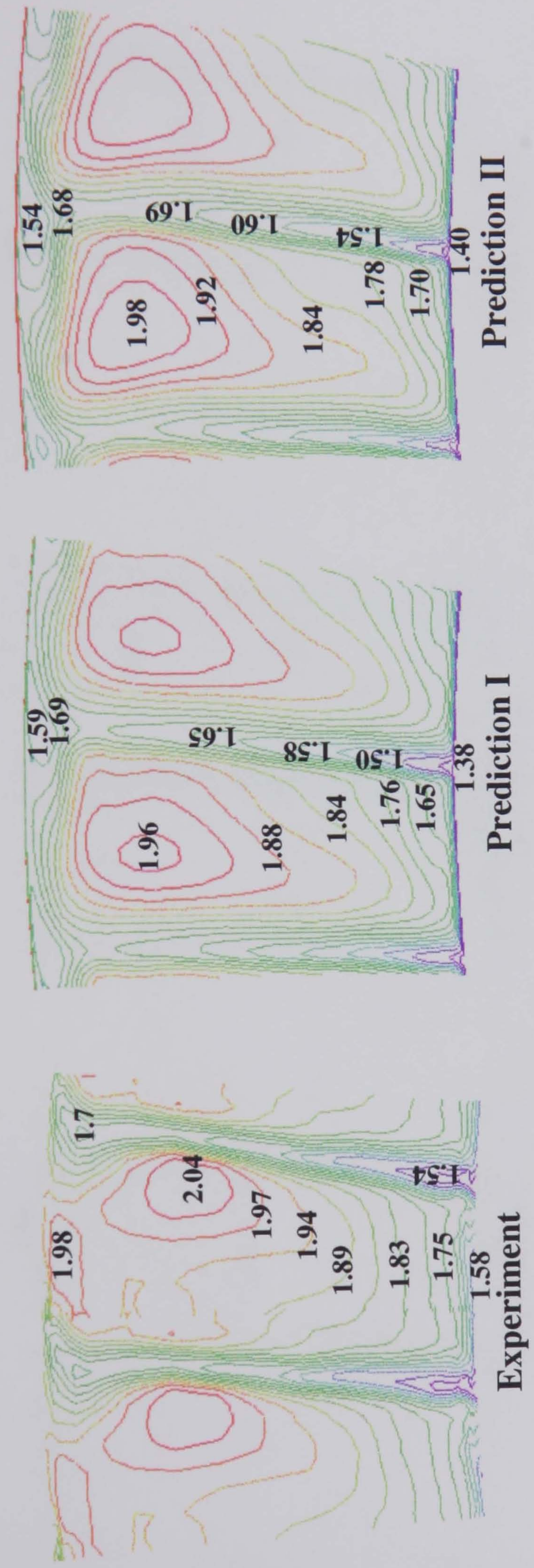

Figure 6.20: **Relative total pressure $(P_t - P_{ref})/(\frac{1}{2}\rho U_m^2)$ contours at Rotor 3 exit**

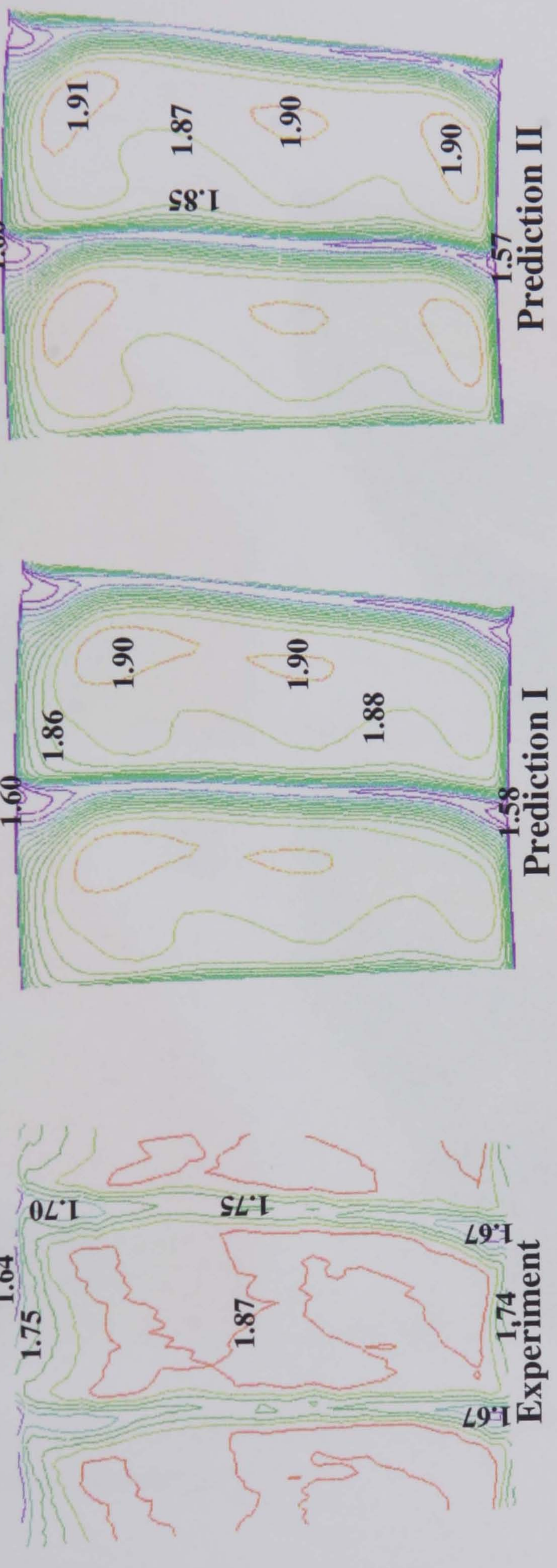

Figure 6.21: **Absolute total pressure** $(P_t - P_{ref})/(\frac{1}{2}\rho U_m^2)$ **contours at Stator 3 exit**

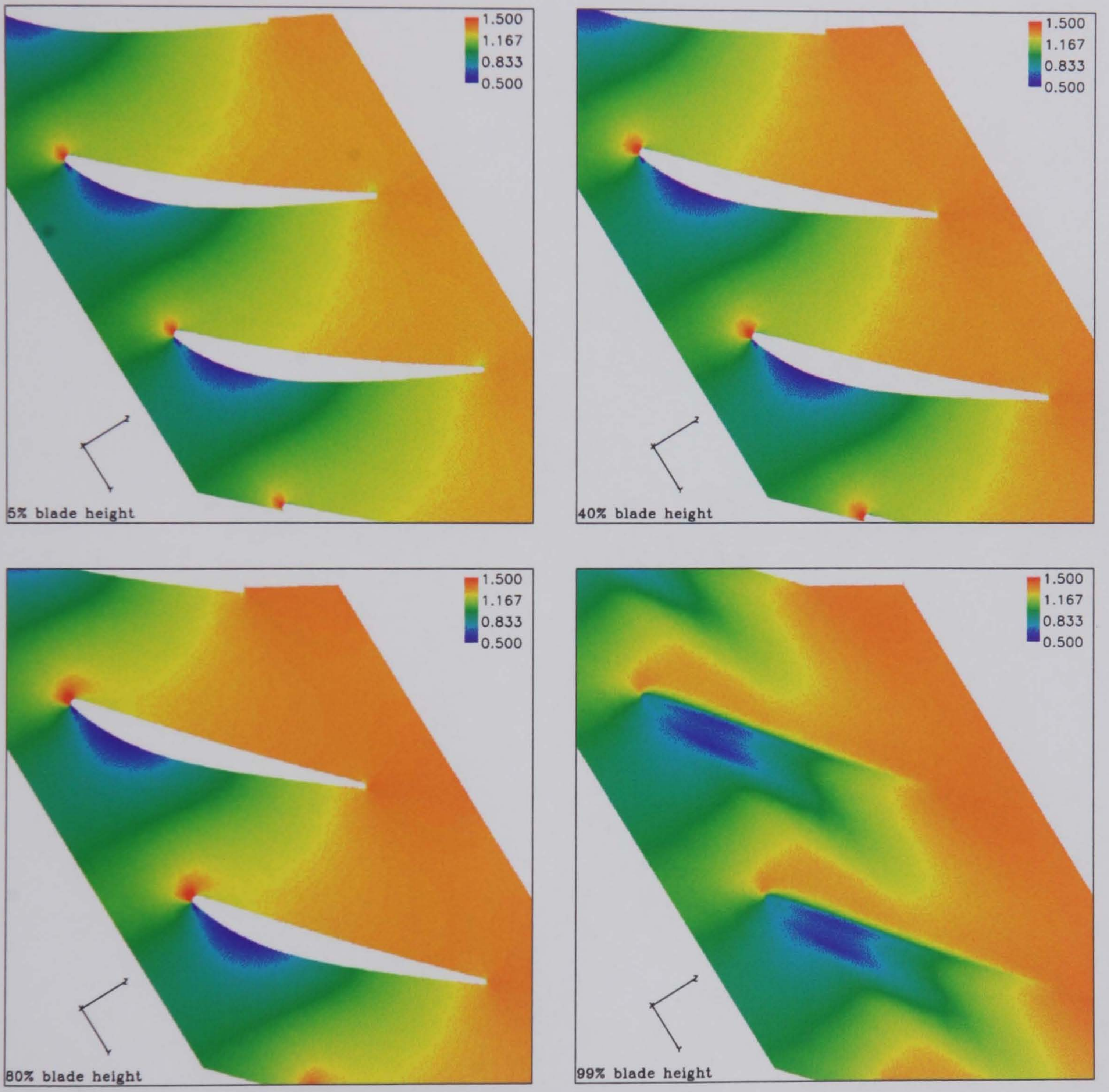

Figure 6.22: $(P_s - P_{ref})/(\frac{1}{2}\rho U_m^2)$ **distribution at blade-to-blade surfaces of Rotor 3 passage from Prediction** *I*

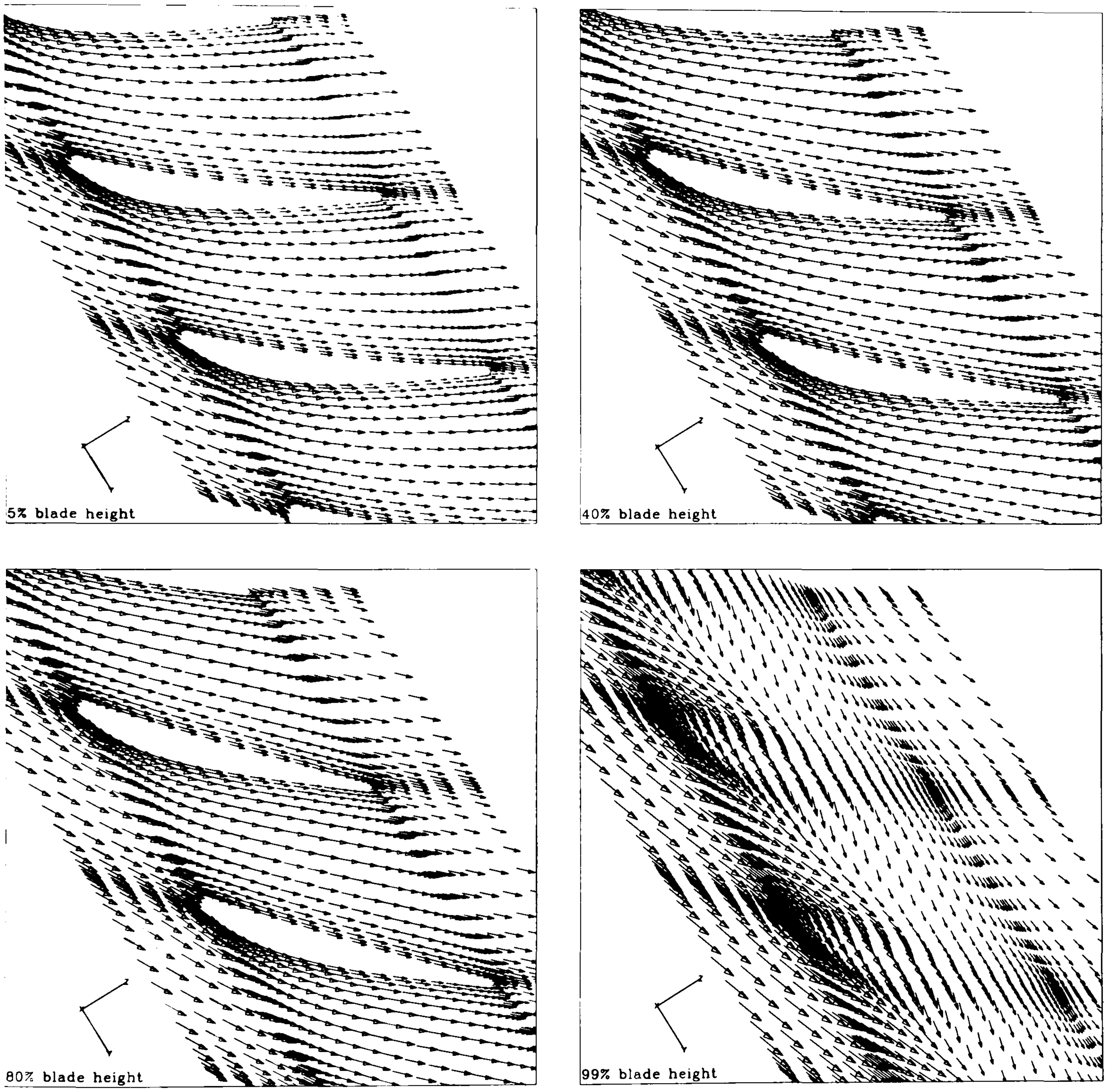

Figure 6.23: **Velocity vectors at blade-to-blade surfaces of Rotor 3 passage from Prediction** *I*

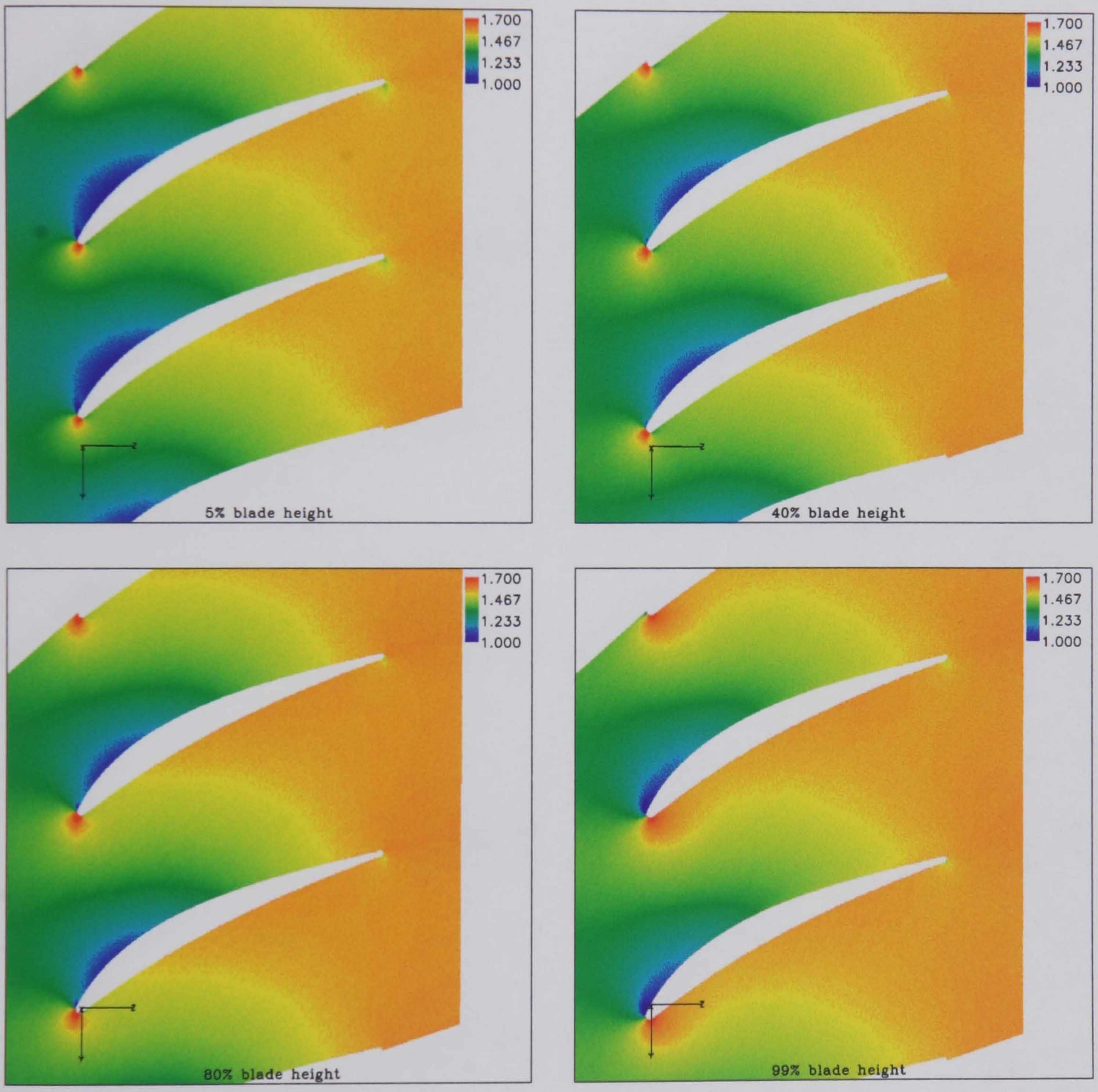

Figure 6.24: $(P_s - P_{ref})/(\frac{1}{2}\rho U_m^2)$ **distribution at blade-to-blade surfaces of Stator 3 passage from Prediction** *I*

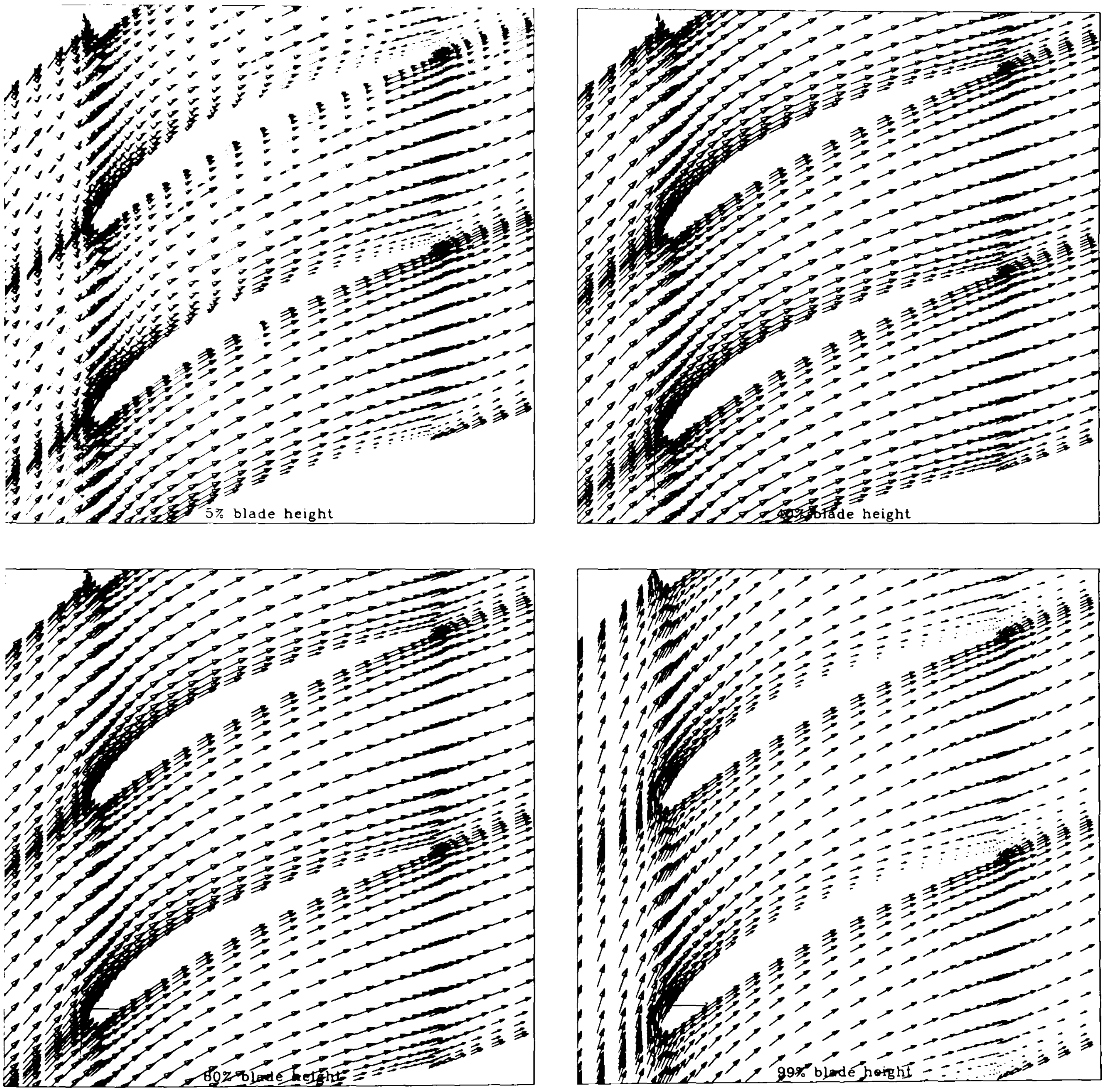

Figure 6.25: **Velocity vectors at blade-to-blade surfaces of Stator 3 passage from Prediction** *I*

imental data especially near the hub and the tip. At the exit plane of the stator, Figure 6.21, quite similar total pressure contours are predicted as compared with the experimental ones, but with around 0.3 higher value in $(P_t - P_{ref})/(\frac{1}{2}\rho U_m^2)$ peak value in the main passage. In the areas between 5% to 80% blade span of the main passage, the predicted total pressure values are nearly uniform as found in the experiment as well. Obvious deficits are predicted at the flow region originated from the shroud suction surface corner that may be due to the separation of the flow which does not appear in the experimental contours.

The static pressure and velocity vectors distributions in blade-to-blade surfaces at 5%, 40%, 80% and 99% blade heights of the Rotor 3 passage are shown in Figures 6.22 and 6.23, giving a detailed description of the flow inside the flow passage. In the rotor tip clearance area (99% blade height), low pressure area can be spotted above the blade between 10% to 30% of blade chord downstream the leading edge and the strong crossing flow is apparent in the velocity vector distribution. In the Stator 3 passage, the static pressure and velocity vector distribution in blade-to-blade surfaces at different blade heights are shown in Figures 6.24 and 6.25. Flow separations on the blade suction surfaces near the trailing edge can be observed in Figure 6.25 near the hub (5% blade height) and the tip (99% blade height). The influence of the separation on the downstream flow can also be seen in Figure 6.102 where the low total pressure areas appear near the hub and the tip in the wake area.

In conclusion, the mixing plane approach combined with conventional boundary setting is a fast and effective method for flow and performance prediction of low speed axial flow compressor stages working near peak efficiency. The discontinuity of aerodynamic parameters at the interface between blade rows does not introduce large prediction errors when the machines operate near their peak efficiency condition.

6.5 Prediction *II*: *LSRC* Third Stage with Repeating Stage and Mixing Plane Models

The repeating stage Model *I* combined with the mixing plane model is described in Chapter 4 and is used to simulate the flow field in the *LSRC* third stage. The detailed computational results are described and analysed in this section. In this prediction case, most of the physical and numerical models are similar to those in Prediction *I*. The only difference lies in the aerodynamic boundary conditions

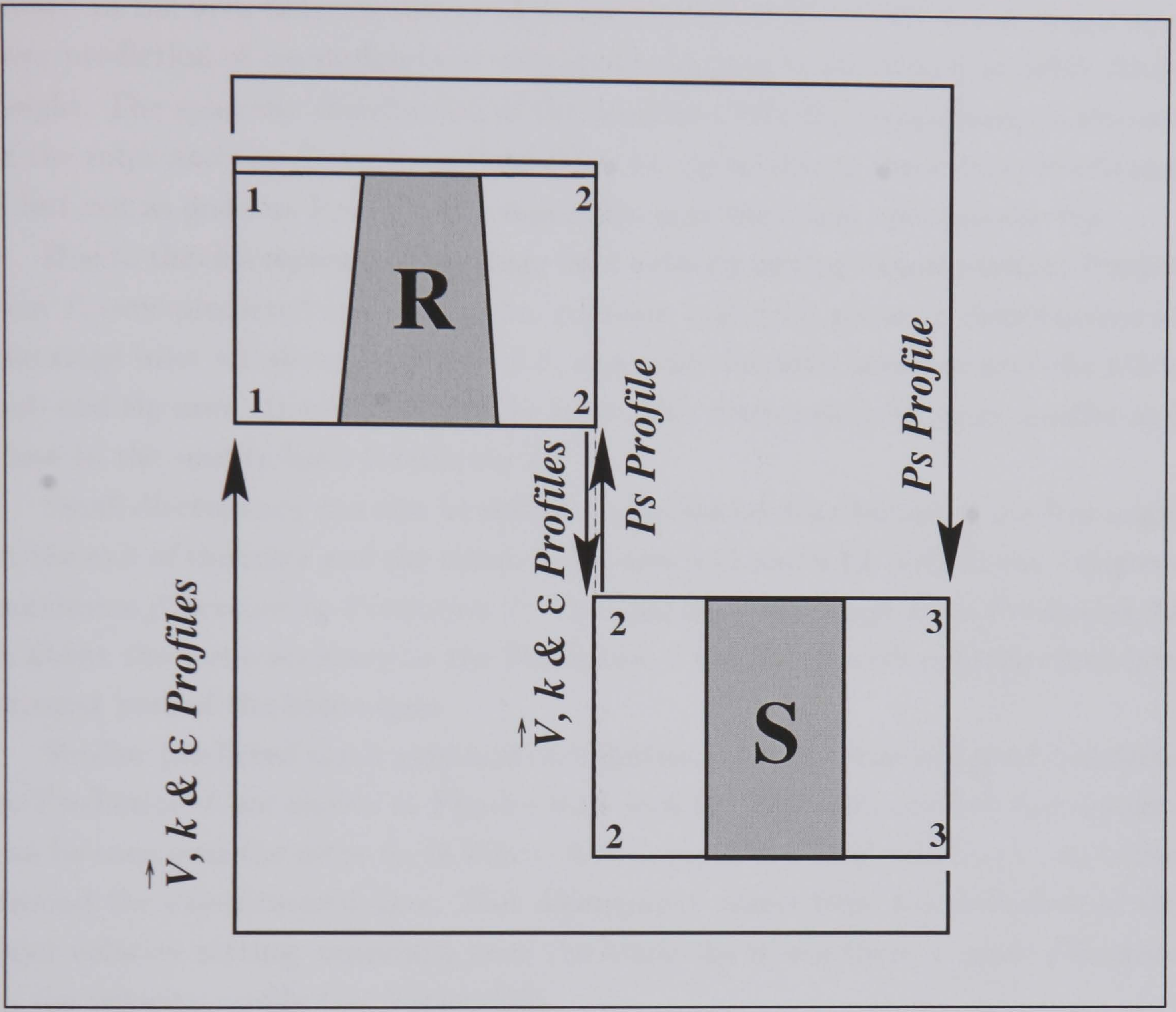

Figure 6.26: **Boundary setting for Prediction** *II*

which is schematically shown in Figure 6.26. With the repeating stage model *I* the requirement of inlet and outlet boundary conditions is significantly simplified. The only requirement is a total mass flow rate and stage exit average static pressure. The predicted results with this approach at the same working condition of the same compressor stage are compared with the experimental data and those from Prediction *I* as follows.

The area averaged static pressure and total pressure along the axial direction of the compressor stage are shown in Figure 6.4. Good agreement is achieved in most axial locations except in the rotor upstream extension. Compared with Prediction *I*, the discrepancy from Prediction *II* comes from the different stage inlet velocity profile which is set to be equal to that at the stage exit.

Figures 6.5 to 6.7 show that the predicted velocity profiles match well with the experimental data in most of the blade span. Over-prediction of axial velocity is shown in the area between 3% to 15% and between 80% to 92% blade height and over-prediction of circumferential velocity in the area between 85% to 100% blade height. The spanwise distribution of the predicted velocity components at the exit of the rotor and the stator from Prediction *II* are similar to those from Prediction *I* but not as good as Prediction *I* especially near the blade hub and the tip.

Due to the discrepancy of the stage inlet velocity setting as compared to Prediction *I*, over-predicted spanwise static pressure and total pressure distributions at the stage inlet are shown in Figure 6.8, especially for total pressure near the blade hub and tip area. Downstream of the stage, this discrepancy becomes smaller and close to the results from Prediction *I*.

Small discrepancy can also be seen in the spanwise distribution of the flow angle at the exit of the rotor and the stator in Figures 6.11 and 6.12, with about 2 degrees maximum difference to Prediction *I*. The spanwise flow angle from Prediction *II* is about the same accuracy to the Prediction *I* compared with experimental data in most part of the blade span.

Similar predicted static pressure distributions on the rotor and stator surfaces to Prediction *I* are shown in Figures 6.14 to 6.19. The only obvious discrepancy can be seen near the rotor tip in Figure 6.16 compared with Prediction *I* but is also around the experimental data. This discrepancy comes from the difference in the inlet velocity setting, especially near the blade tip where there is more difference in the velocity profile (see Figure 6.5).

The total pressure contours agree well for Predictions *I* and *II*, Figures 6.20 and 6.21. At the exit of Rotor 3, Prediction *II* shows larger calculated relative total pressure values near about 67% and 15% blade height due to the larger velocity values at the same locations, Figure 6.6. In general, the difference of the calculated total pressure contours between the two predictions is very small.

To conclude, the repeating stage model is an effective tool to simplify the boundary conditions for the analysis of rear stages of multistage axial flow compressors. The predicted results with this model for the third stage of the *LSRC* provides comparable accuracy to those with conventional setting of boundary conditions.

6.6 Prediction *III*: *LSRC* Third Stage with Conventional Boundary Setting and Deterministic Stress Model

In this section, the predicted results of the flow with the more rigorous deterministic stress model for the third stage of *LSRC* are presented and compared with those from Prediction *I* and with the experimental data, aiming to show any improvements from the deterministic stress model to the prediction.

The layout of the computational domains and the setting of the boundary conditions are shown in Figure 6.27. Because of the implementation of the overlapped domain approach, Stator 2 domain provides an upstream flow environment and a deterministic stress field to the third rotor and Rotor 4 domain provides a downstream flow environment to the third stator. The inlet velocity profile and the exit average static pressure to the third stage are set to the experimental values, which is also the case for Prediction *I*. By taking advantage of the repeating nature of the compressor stages in order to simplify the boundary conditions, the inlet velocity, k and ϵ profiles of Stator 2 are set to be the same as those at Stator 3 inlet (Interface 2).

Compared with the mixing plane model used in Prediction *I*, the deterministic stress model has the advantage that the momentum terms are continuous at interfaces by introducing the deterministic stresses in the momentum equations. For example, circumferentially area-averaged spanwise distribution of the momentum terms at Rotor 3 inlet at Interface 1 before and after the interface are compared in Figure 6.28 where two different models, the mixing plane model and the deterministic stress model, are used to calculate the momentum terms across the interface. The difference between the momentum terms before and after the interface with the mixing plane model is obvious. With the implementation of the deterministic stresses the calculated momentum terms after the interface with the deterministic stress model keep almost unchanged. Minor inconsistency in momentum terms is due to numerical errors.

The circumferentially area-averaged body force component distribution in cylindrical coordinates in the downstream of Rotor 3 and Stator 3 are illustrated in Figures 6.29 and 6.30. The axial body force component contributes to the pressure distribution and part of momentum change in the axial direction, the circumferential body force component contributes to the turning of the flow in the circumferential direction and the radial body force component contributes to the

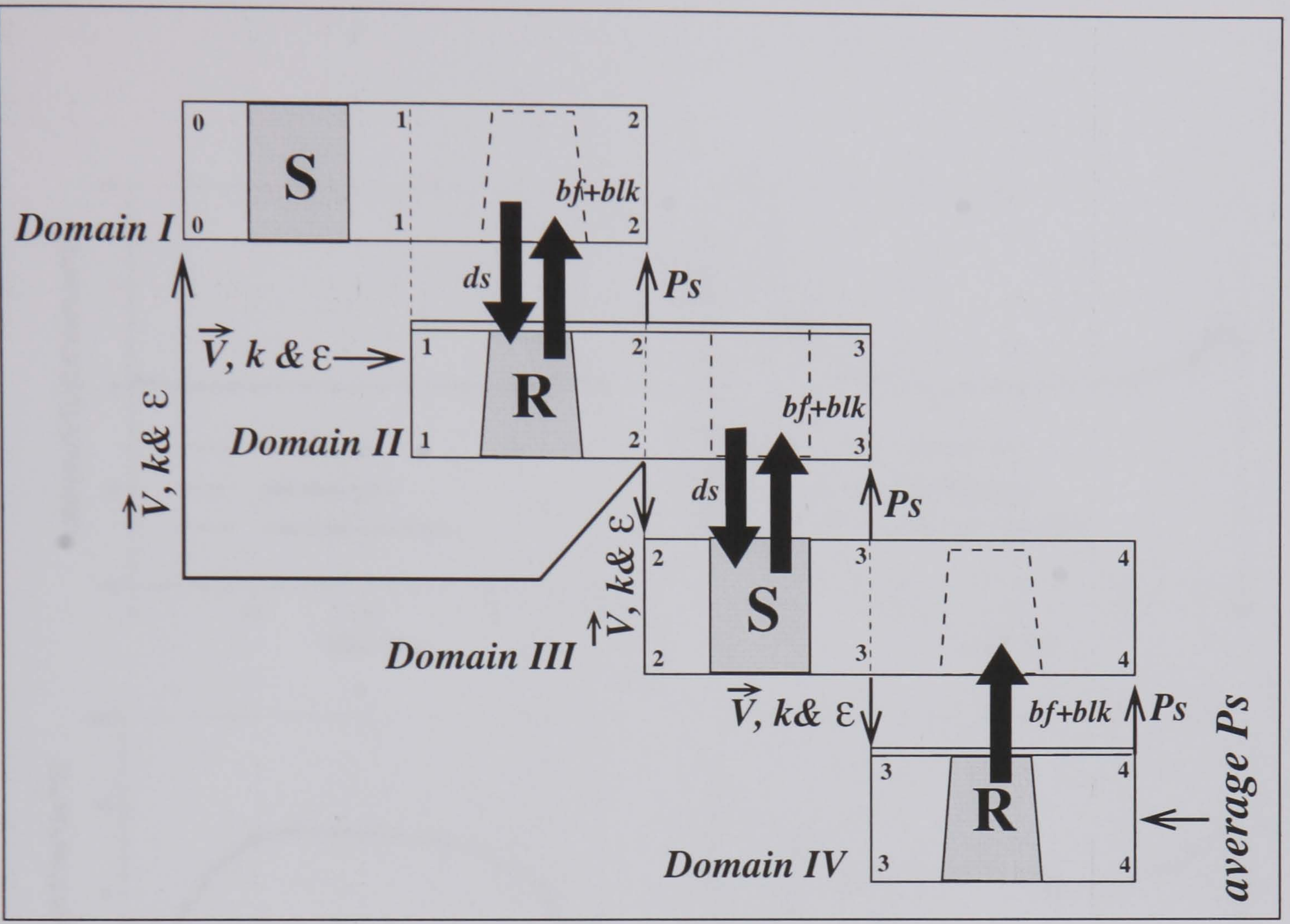

Figure 6.27: **Boundary setting for Prediction** *III*

static pressure and mass flow rate distribution in the radial direction.

The circumferentially area-averaged deterministic stress component distribution in cylindrical coordinates at downstream of Stator 2 and Rotor 3 are shown in Figures 6.31 and 6.32. The deterministic stresses generated by Stator 2, Figure 6.31, are imposed on the Rotor 3 passage and the deterministic stresses generated by Rotor 3, Figure 6.32, are imposed on the Stator 3 passage. It can be seen in Figure 6.31 that the deterministic stresses have larger values in the area close to the hub and the tip in the stator downstream domain than in the central domain of the passage due to the flow separations in the blade passage near the hub and the tip. These separations generate larger periodic flow variation propagating downstream. It can also be observed that the deterministic stress components shown in Figure 6.31 have their largest values near the trailing edge of Stator 2 and deteriorate very rapidly downstream the Stator 2 blade trailing edge and become very small at the interface. In Rotor 3 downstream domain, Figure 6.32, the deterministic stress components containing $\widehat{v}_r$ are about ten times smaller than others and have the largest values near the tip due to the influence of the rotor tip clearance flow. In

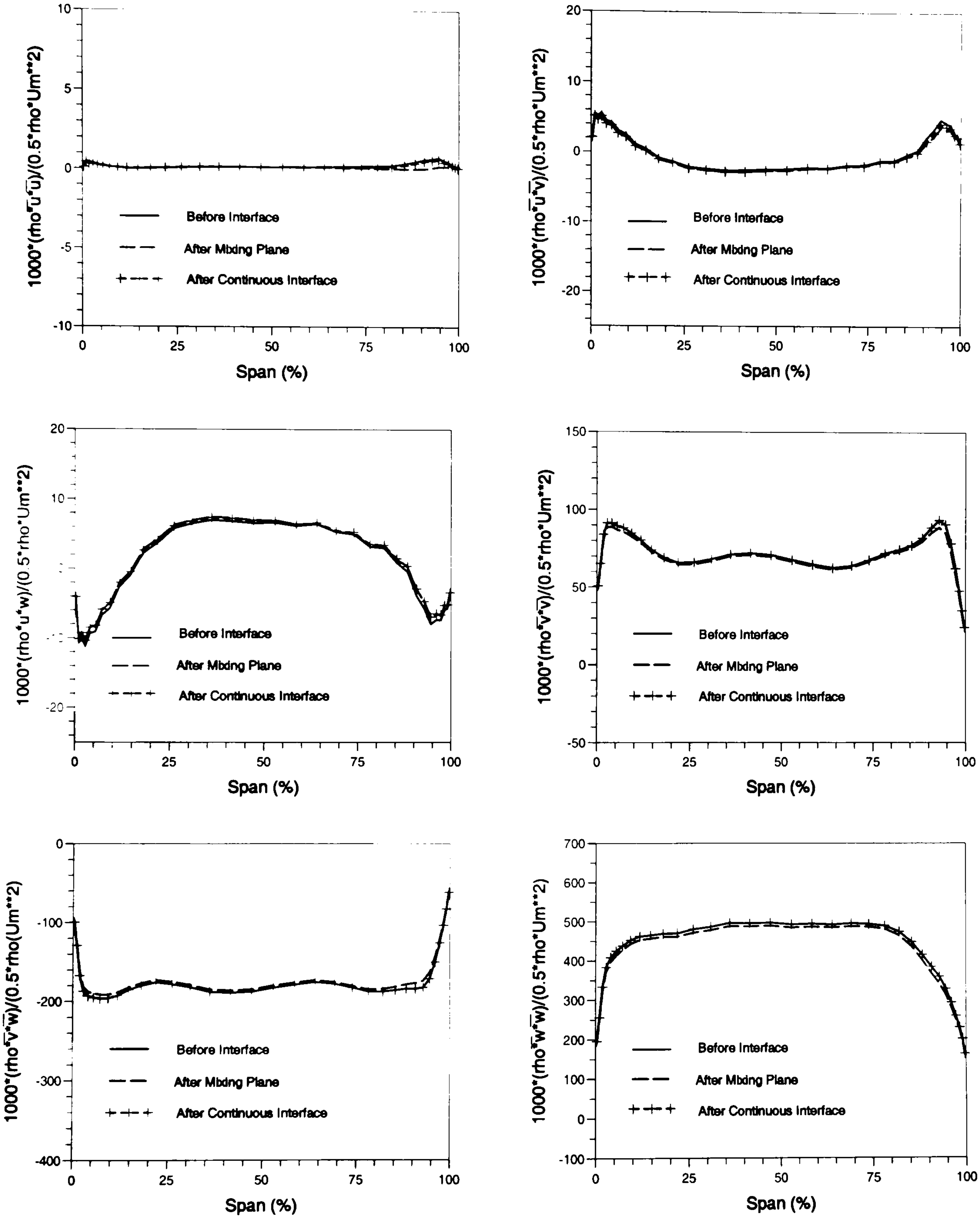

Figure 6.28: **Momentum terms at Rotor 3 inlet at interface 1**

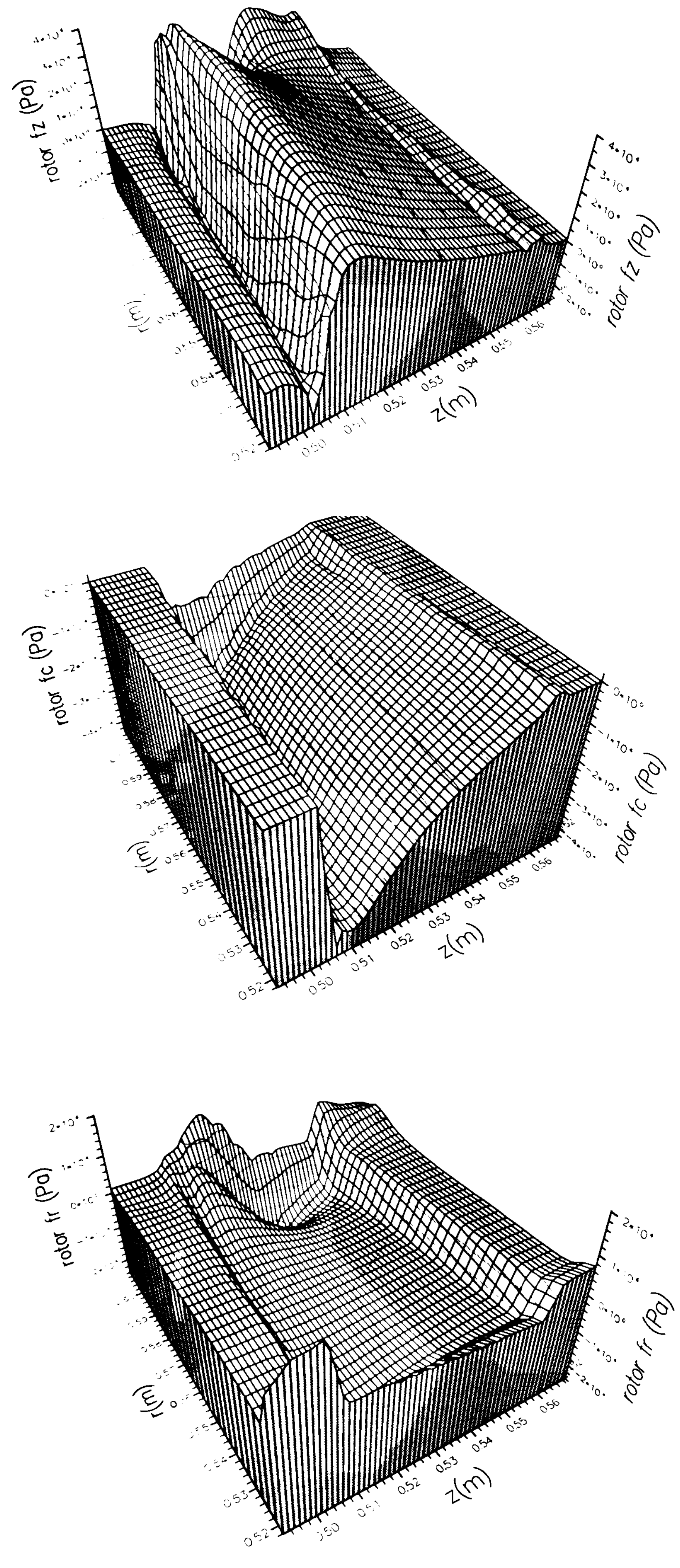

Figure 6.29: **Bodyforce components generated by Rotor 3**

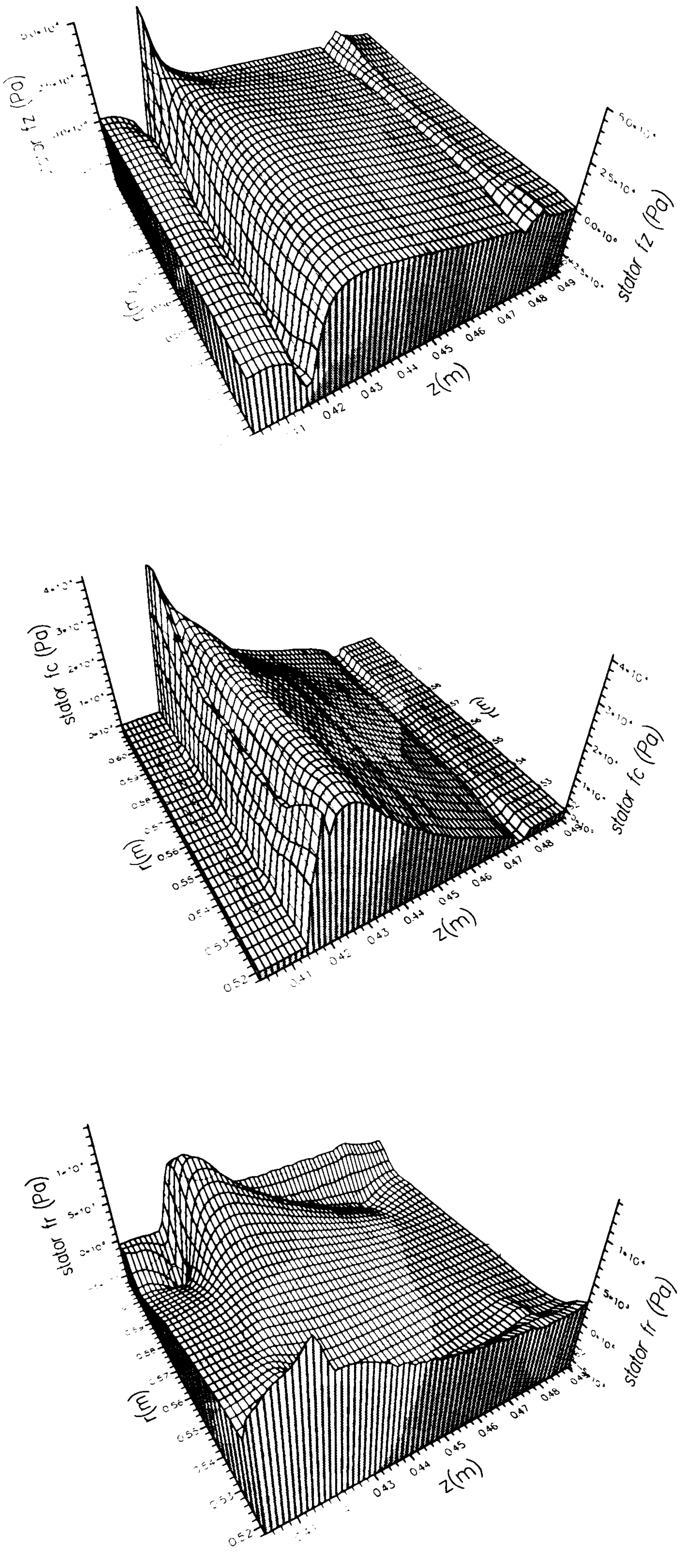

Figure 6.30: **Bodyforce components generated by Stator 3**

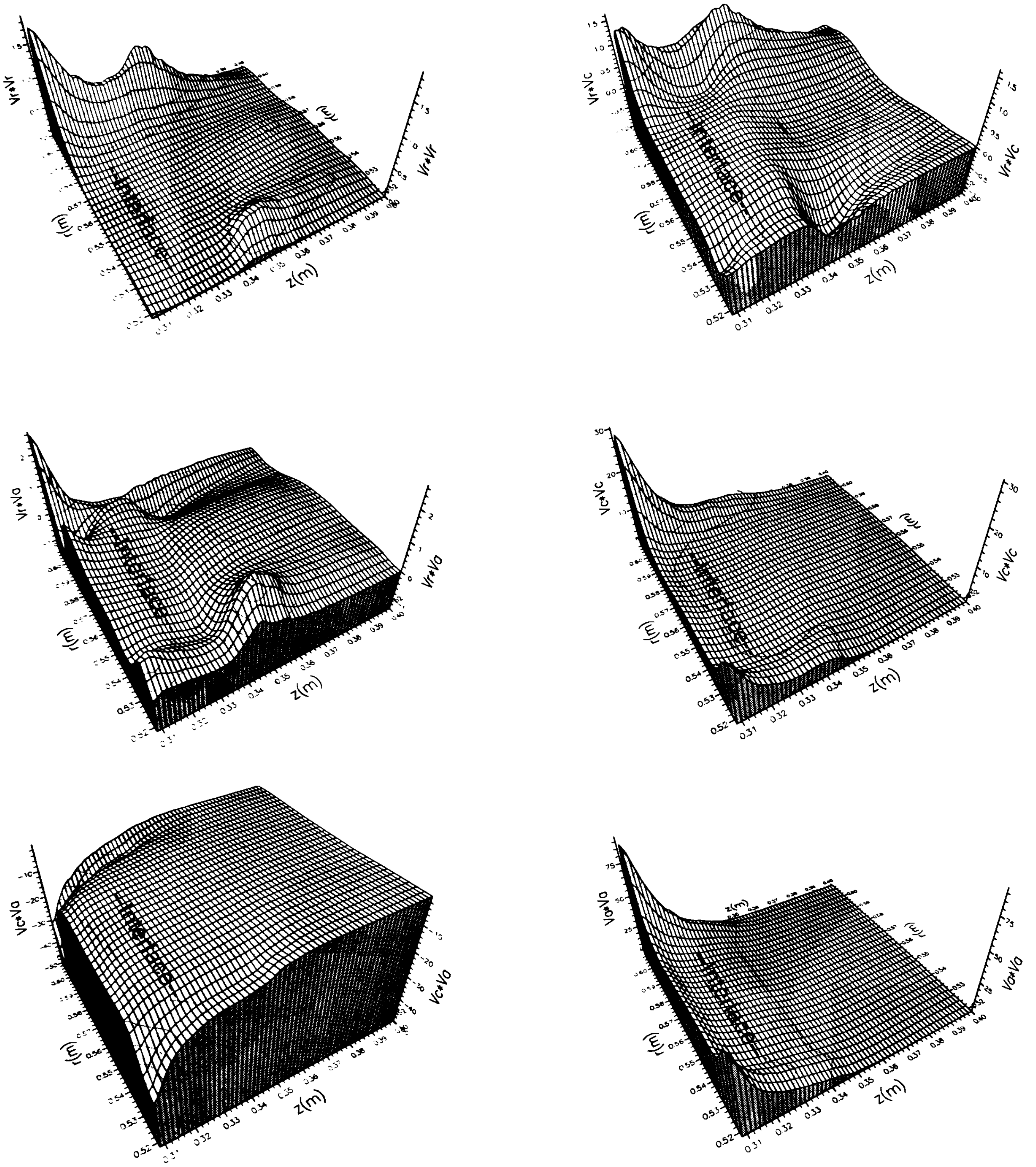

Figure 6.31: **Tangentially area-averaged deterministic stresses at Stator 2 downstream starting from Stator 2 trailing edge**

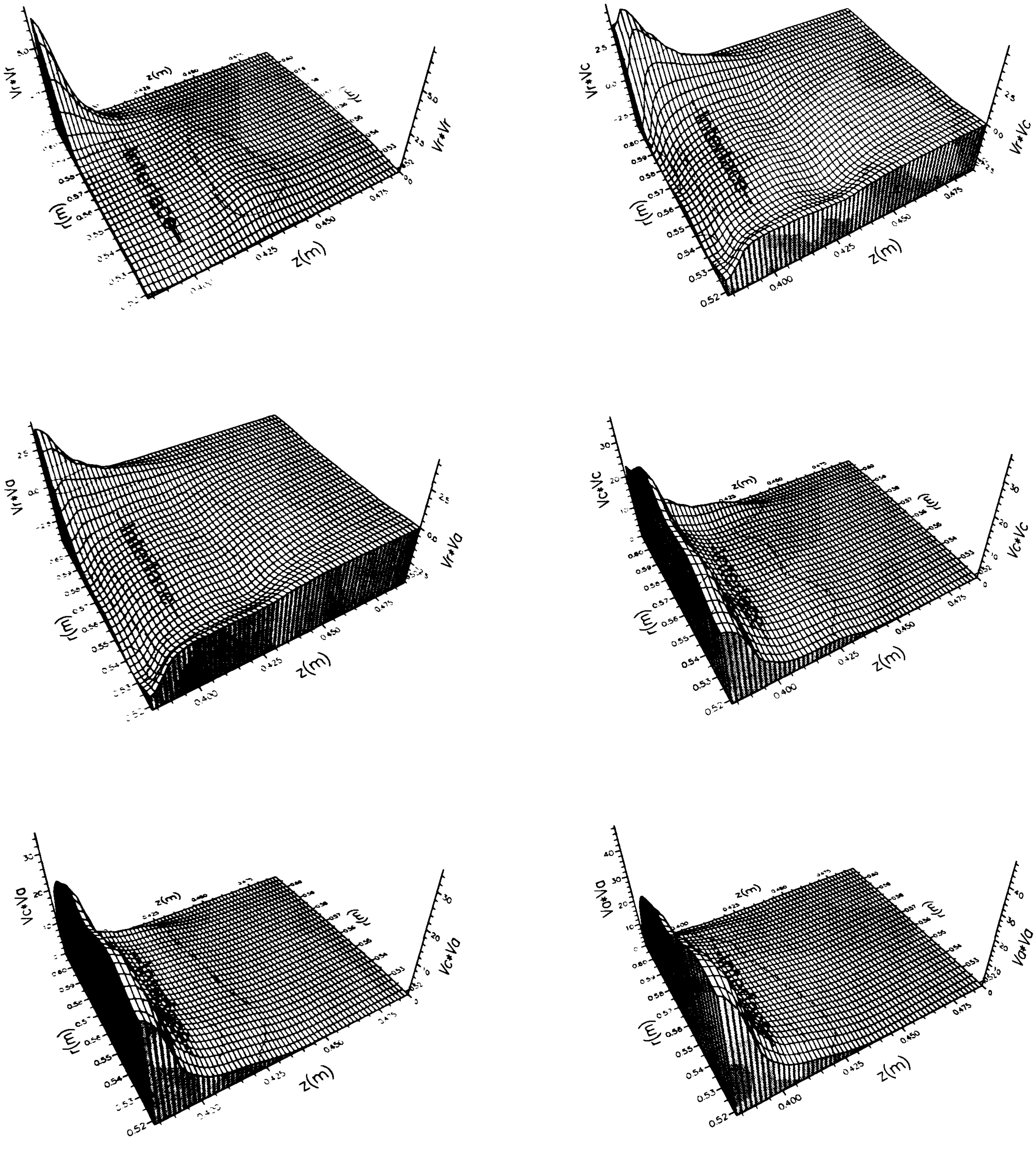

Figure 6.32: Tangentially area-averaged deterministic stresses at Rotor 3 downstream starting from Rotor 3 trailing edge

axial direction, all the components have the largest values near the rotor trailing edge and deteriorate very rapidly downstream. This means that for this low pressure compressor the non-uniformity of the flow from a blade row is mixed out very quickly and the benefit from the implementation of the deterministic stresses will not be significant, which can be seen from the following performance comparison.

The contours of the deterministic stress components at the exit planes of Rotor 3 and Stator 3 from the experiment are compared with those from Prediction *III* in Figures 6.33 to 6.38. The predicted deterministic stress distribution match very well with those from experiments. At the exit of Rotor 3, the maximum values of the predicted deterministic stress components are about half of the corresponding values from the experiment. The reason for this discrepancy is that the predicted wake generated by the rotor blade is not as strong as the actual wake measured in the experiment, which can be seen in Figures 6.61 and 6.62 where the circumferential distributions of the axial velocity and the total pressure at midspan of Rotor 3 outlet are shown. At the exit of Stator 3 the peak values of the calculated deterministic stresses are slightly larger than those from the experiment because the predicted wakes are stronger than obtained in the experiment, as shown in Figures 6.63 and 6.64.

The contours of the turbulence kinetic energy distributions at the exit planes of Rotor 3 and Stator 3 are shown in Figure 6.39. We can see that the peak values of the turbulence kinetic energy is much smaller than those of the major deterministic stress components.

In addition, the contours of total viscous stress components at the exits of Rotor 3 and Stator 3 are plotted in Figures 6.40 and 6.41 and the expressions of these components are presented by Equations (6.1) expressed in cylindrical coordinates. Obviously, they are also much smaller than the deterministic stress components.

$$\begin{aligned}
\tau_{rr} &= 2(\mu+\mu_T)\frac{\partial v_r}{\partial r} \\
\tau_{\theta\theta} &= 2(\mu+\mu_T)\left(\frac{\partial v_\theta}{r\partial\theta}+\frac{v_r}{r}\right) \\
\tau_{zz} &= 2(\mu+\mu_T)\frac{\partial v_z}{\partial z} \\
\tau_{r\theta} &= \tau_{\theta r} = (\mu+\mu_T)\left(\frac{\partial v_r}{r\partial\theta}+\frac{\partial v_\theta}{\partial r}-\frac{v_\theta}{r}\right) \\
\tau_{\theta z} &= \tau_{z\theta} = (\mu+\mu_T)\left(\frac{\partial v_\theta}{\partial z}+\frac{1}{r}\frac{\partial v_z}{\partial\theta}\right) \\
\tau_{zr} &= \tau_{rz} = (\mu+\mu_T)\left(\frac{\partial v_z}{\partial r}+\frac{\partial v_r}{\partial z}\right)
\end{aligned} \tag{6.1}$$

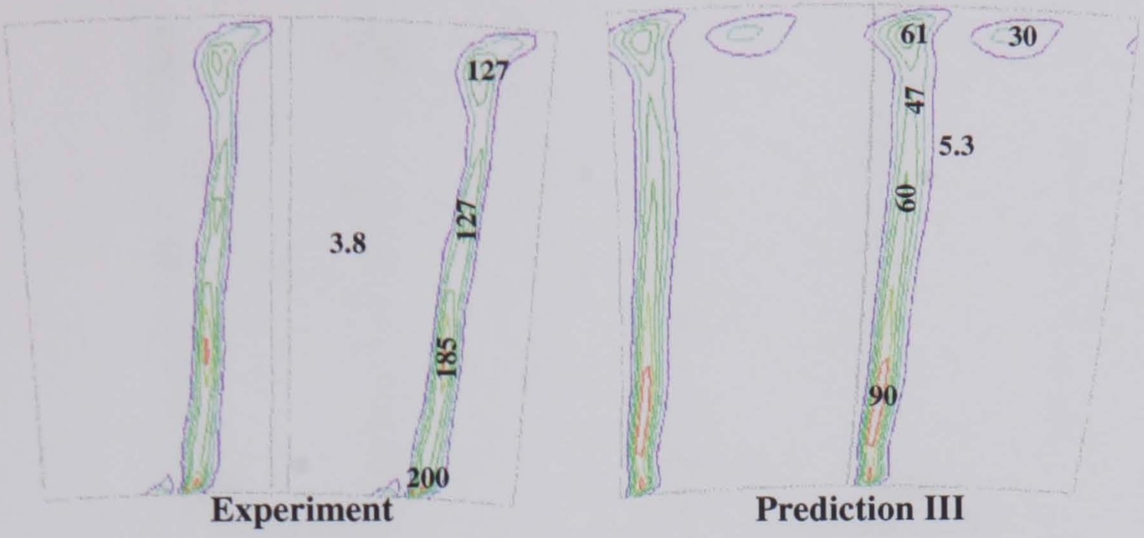

Figure 6.33: **Deterministic stress** $\overline{\rho}\overline{\overline{\widehat{V_c}\widehat{V_c}}}$ **at Rotor 3 Exit**

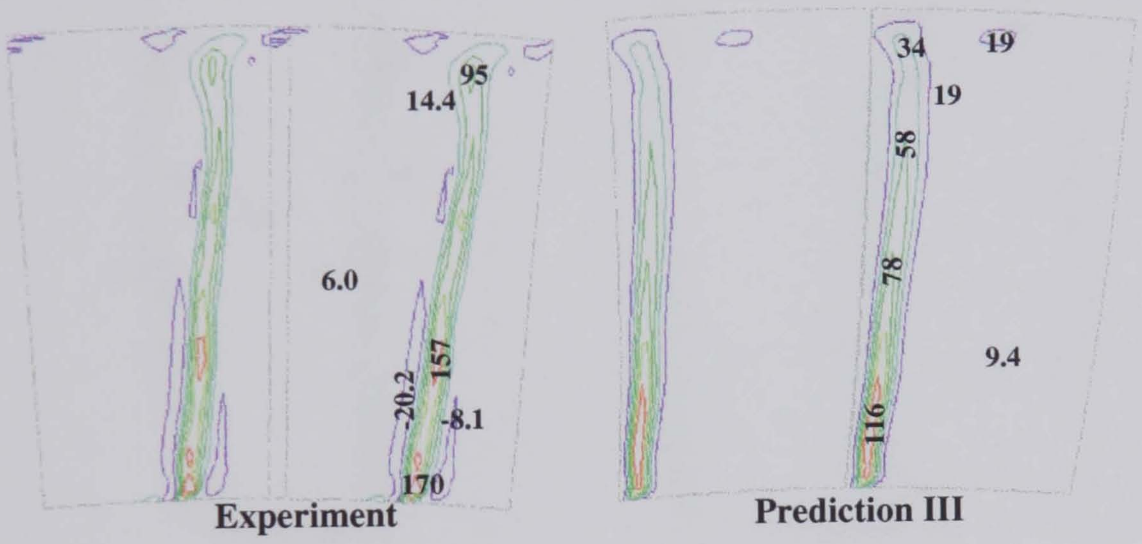

Figure 6.34: **Deterministic stress** $\overline{\rho}\overline{\overline{\widehat{V_c}\widehat{V_a}}}$ **at Rotor 3 Exit**

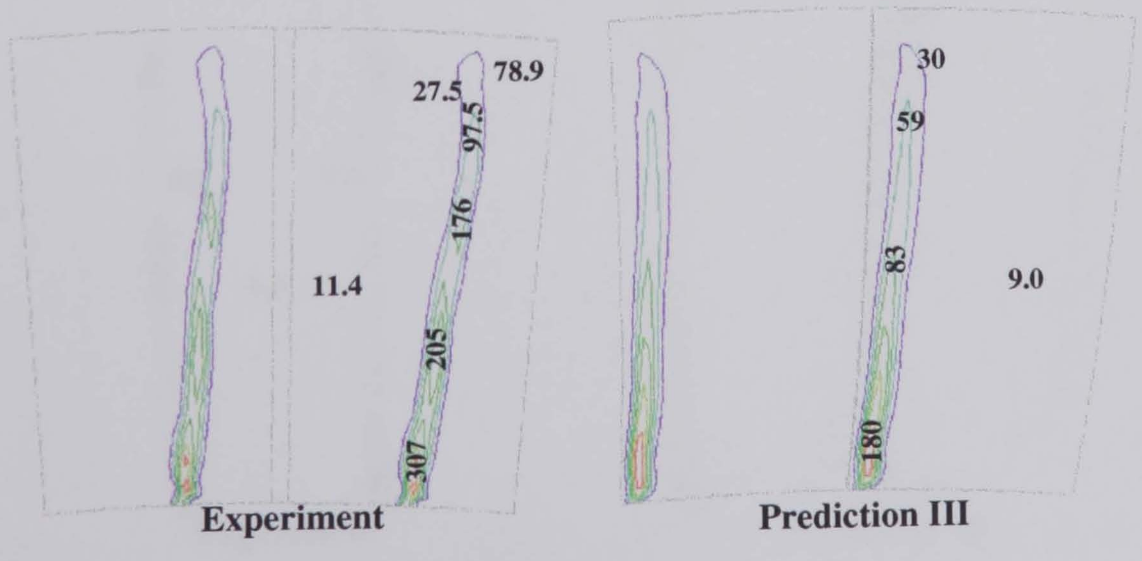

Figure 6.35: **Deterministic stress** $\overline{\rho}\overline{\overline{\widehat{V_a}\widehat{V_a}}}$ **at Rotor 3 Exit**

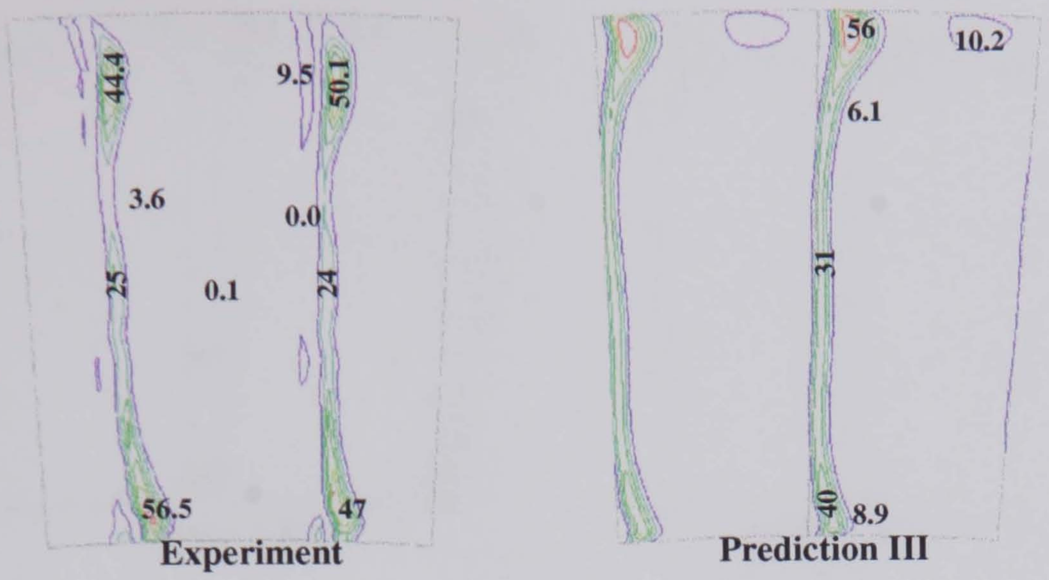

Figure 6.36: **Deterministic stress $\overline{\rho}\,\overline{\overline{\widehat{V_c}\widehat{V_c}}}$ at Stator 3 Exit**

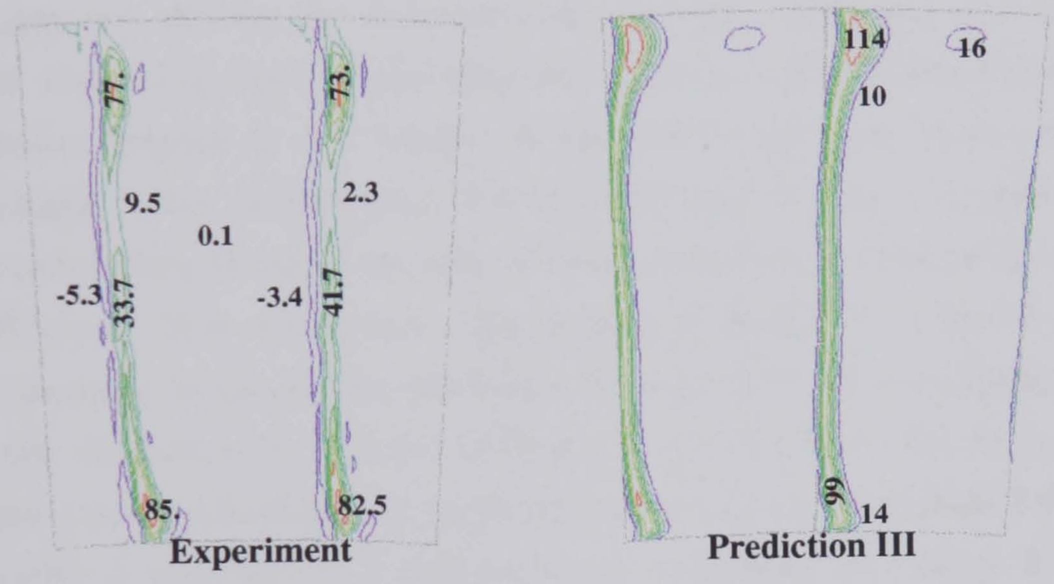

Figure 6.37: **Deterministic stress $\overline{\rho}\,\overline{\overline{\widehat{V_c}\widehat{V_a}}}$ at Stator 3 Exit**

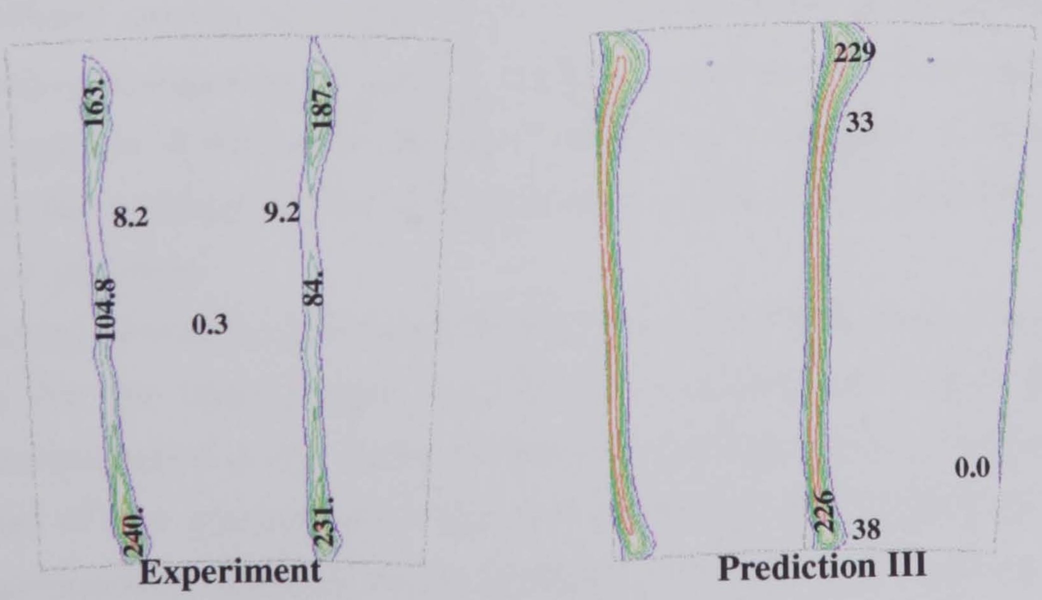

Figure 6.38: **Deterministic stress $\overline{\rho}\,\overline{\overline{\widehat{V_a}\widehat{V_a}}}$ at Stator 3 Exit**

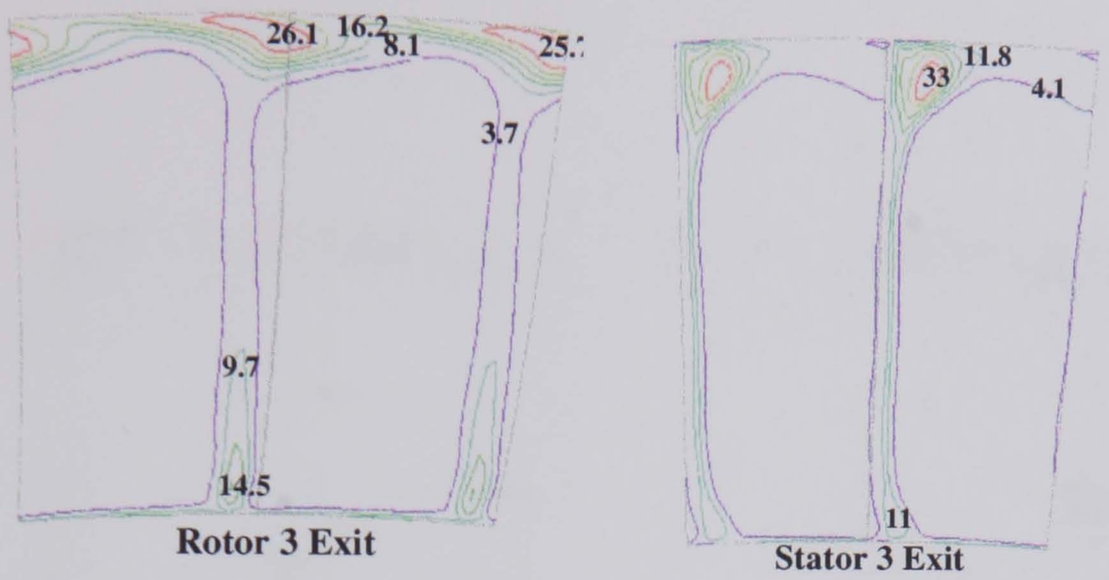

Figure 6.39: **Turbulent kinetic energy k at Rotor 3 and Stator 3 Exit**

The comparison among the deterministic stresses, turbulent kinetic energy (k) and the total viscous stresses shows that the influence of the deterministic stresses on the upstream extension of a blade row should be stronger than others.

The blockage factor distribution for Rotor 3 and Stator 3 is shown in Figure 6.42 which contributes to another part of axial momentum change inside the blade passages. Without this correction, the predicted momentum and total pressure inside blade passage in the blade extension domains will be completely wrong. For example in the downstream domain of Rotor 3 which covers the Stator 3 passage, area averaged static pressure and momentum terms in axial direction calculated from the Stator 3 and Rotor 3 domains are compared in Figure 6.43. For the Rotor 3 domain, two results are presented, one taking into account the blockage and the other without taking into account the blockage. Figure 6.43 shows that the result without taking into account the blockage effect gives wrong prediction of the momentum component $\left(\frac{1}{2}\rho w^2\right)$, which contributes to the wrong prediction of the total pressure distribution in the downstream extension of Rotor 3, Figure 6.44, because the increase of the total pressure in the stator passage downstream the flow is not physical.

Performance comparisons among Prediction III, Prediction I and the experimental data for the third stage of $LSRC$ are carried out in this section. The predicted area-averaged static pressure and the total pressure distributions in the axial direction of the compressor stage are presented in Figure 6.45. Compared with the experimental data at three stations, the Rotor 3 inlet at Interface 1, Interface 2 between the two blade rows and the Stator 3 outlet at Interface 3, good agreement between computational and experimental data is shown. It can

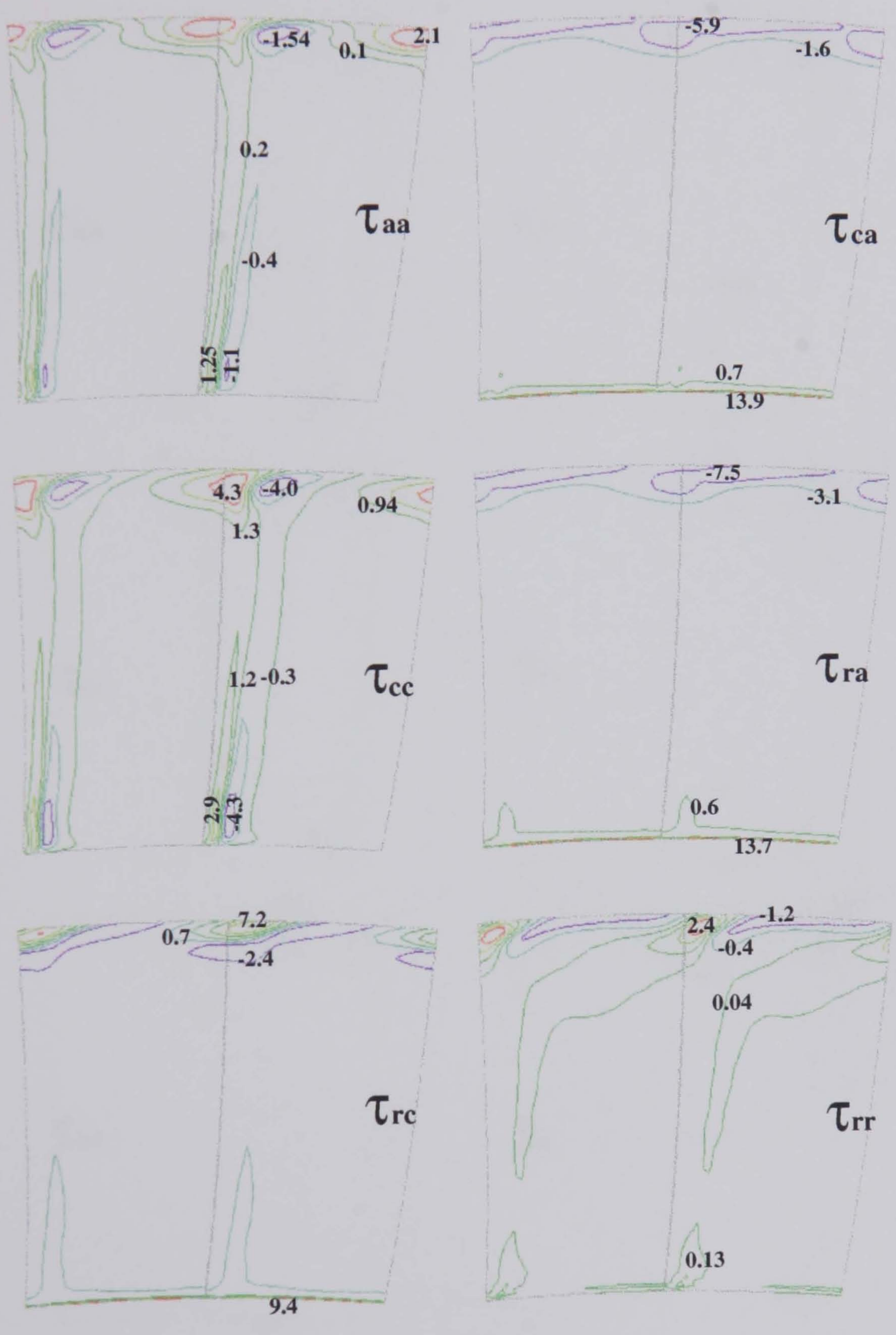

Figure 6.40: **Total viscous stress components at Rotor 3 exit**

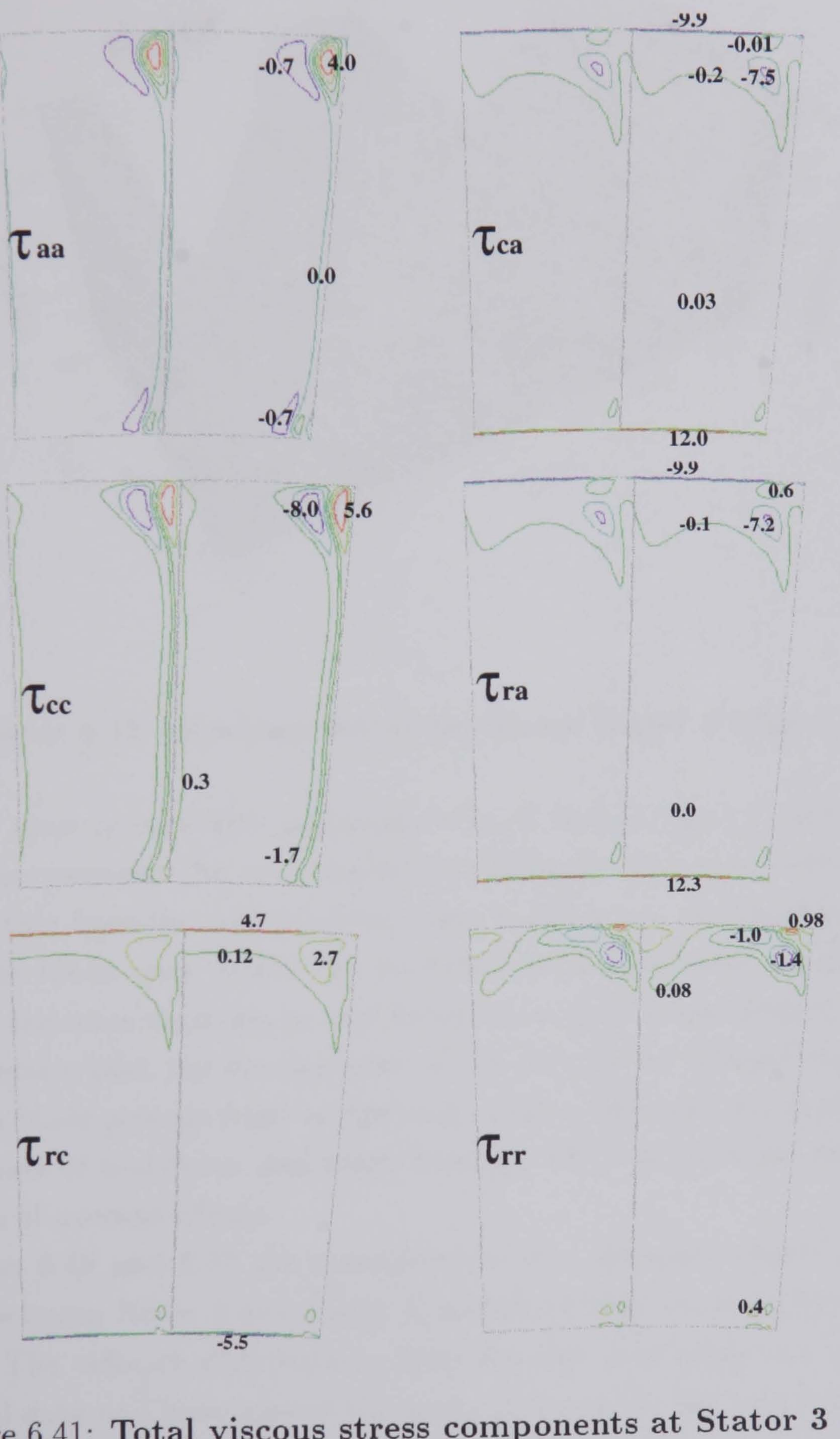

Figure 6.41: **Total viscous stress components at Stator 3 exit**

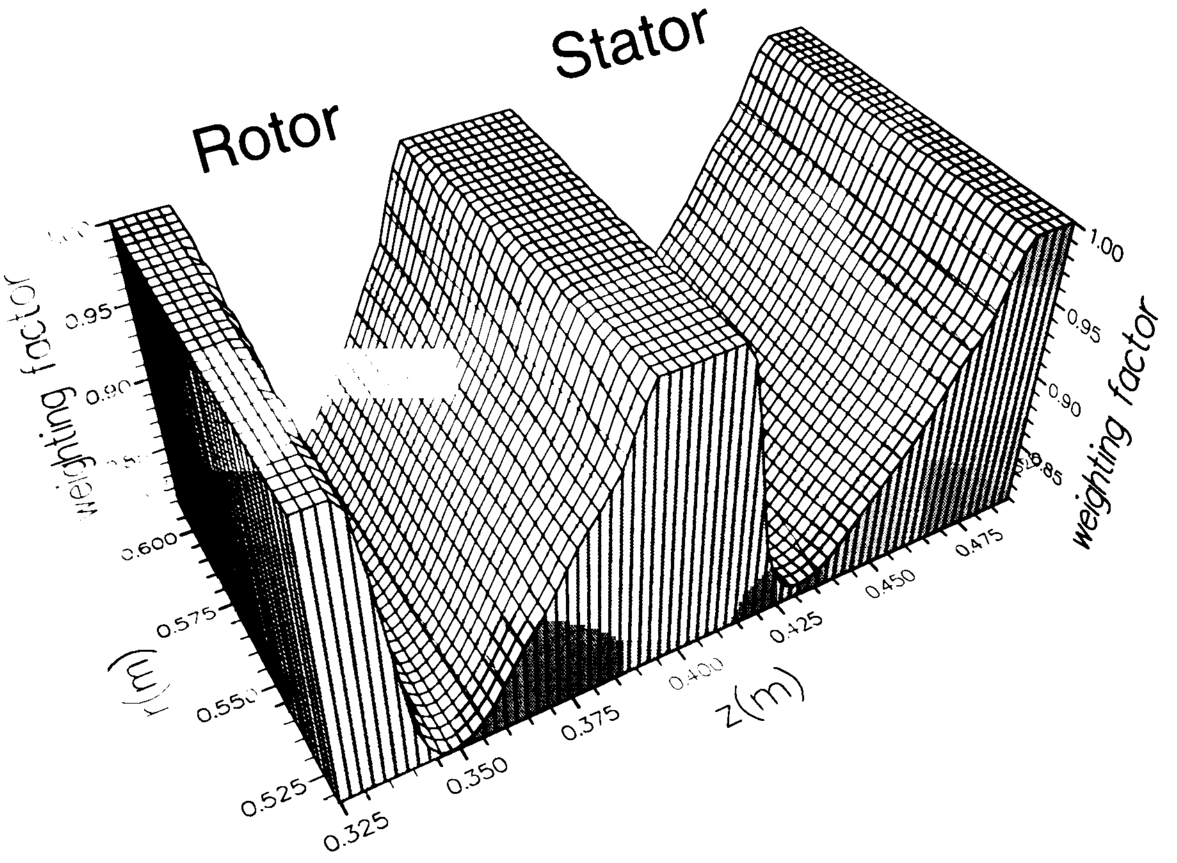

Figure 6.42: **Blockage factor for Rotor 3 and Stator 3**

be seen that there is very little difference in axial distribution of static and total pressure values between the two predictions. However, the most interesting part of the prediction from the deterministic stress model is the downstream extension domain of the blade rows, where the predicted axial distribution of the pressure show almost the same variation to that from the analysis of the downstream blade row. This means that the development of the flow in the domain which covers the following blade passage from an upstream blade row is well predicted with the implementation of bodyforce and blade blockage effect of the downstream blade row in terms of average effects.

In Figures 6.46 and 6.47 the comparison of the spanwise velocity profiles at Interface 2 between Rotor 3 and Stator 3, and the Stator 3 exit at Interface 3 are illustrated. The velocity distributions from the two predictions are close to the experimental data and have almost the same accuracy. In the area between 80 % to 100 % blade span at the exit of Stator 3, the deterministic stress model provides slightly better prediction of velocity profile than the mixing plane model, Figure 6.47. This proves that the deterministic stress model provides slight improvement to the velocity distribution.

In Figure 6.48, Prediction *III* provides improvement for the spanwise static pressure distribution and maintains almost unchanged to the total pressure distribution as compared to Prediction *I*. At the interface between Rotor 3 and Stator 3, the spanwise distributions of the static pressure and the total pressure in Prediction *III* can be obtained from both Rotor 3 and Stator 3 domains. The predicted P_s and P_t distributions from the Rotor 3 domain are very close to those from Prediction *I*. In the Stator 3 domain of Prediction *III*, the predicted spanwise P_s distribution between 0% to 50% span is closer to the experimental data than Prediction *I* and the predicted spanwise P_t in the same span area is slightly over-predicted, while in the area between 65% and 100% span the P_s distribution is under-predicted compared to Prediction *I* and the P_t distribution is obviously better than that from Prediction *I*. At the Stator 3 exit, Figure 6.50, two predictions of spanwise static pressure distribution are close to the experimental data with almost the same accuracy although they differ with each other. For the spanwise total pressure distribution, Prediction *III* gives better distribution near the tip (between 70% to 100% blade height), Prediction *I* gives better distribution near the hub (between 0% to 50%) and the two computations provide similar distribution near midspan.

As mentioned in Chapter 4, the spanwise static pressure distributions obtained from the Rotor 3 domain and the Stator 3 domain at Interface 2 between Rotor 3 and Stator 3 is not consistent, which is shown in Figure 6.49. The maximum difference of the static pressure values between two sides of the interface appearing near the blade tip, is about 0.12% of the pressure ratio of the third stage.

In terms of flow angles, Prediction *III* demonstrates about 1 to 1.5 degrees improvement in its spanwise distribution than Prediction *I* in the area between 5% to 80% blade height at Interface 2 and also in the area between 0% to 75% blade height at Stator 3 exit (Interface 3). Near the tip area, Prediction *I* shows slightly better prediction for spanwise flow angle distribution than Prediction *III* in the area between 94% to 100% blade height at interface 2 and between 87% to 95% blade height at Stator 3 exit (Interface 3).

The total pressure contours in the relative frame of reference at the exit of Rotor 3 and in the absolute frame of reference at the exit of Stator 3 are compared with those from the experiment and Prediction *I*, Figures 6.53 and 6.54, and the contours from the two predictions are very similar to each other especially for those at the exit of Rotor 3. The small discrepancy between the two predictions at Stator 3 exit (Figure 6.54) is that the peak value area of the contours from

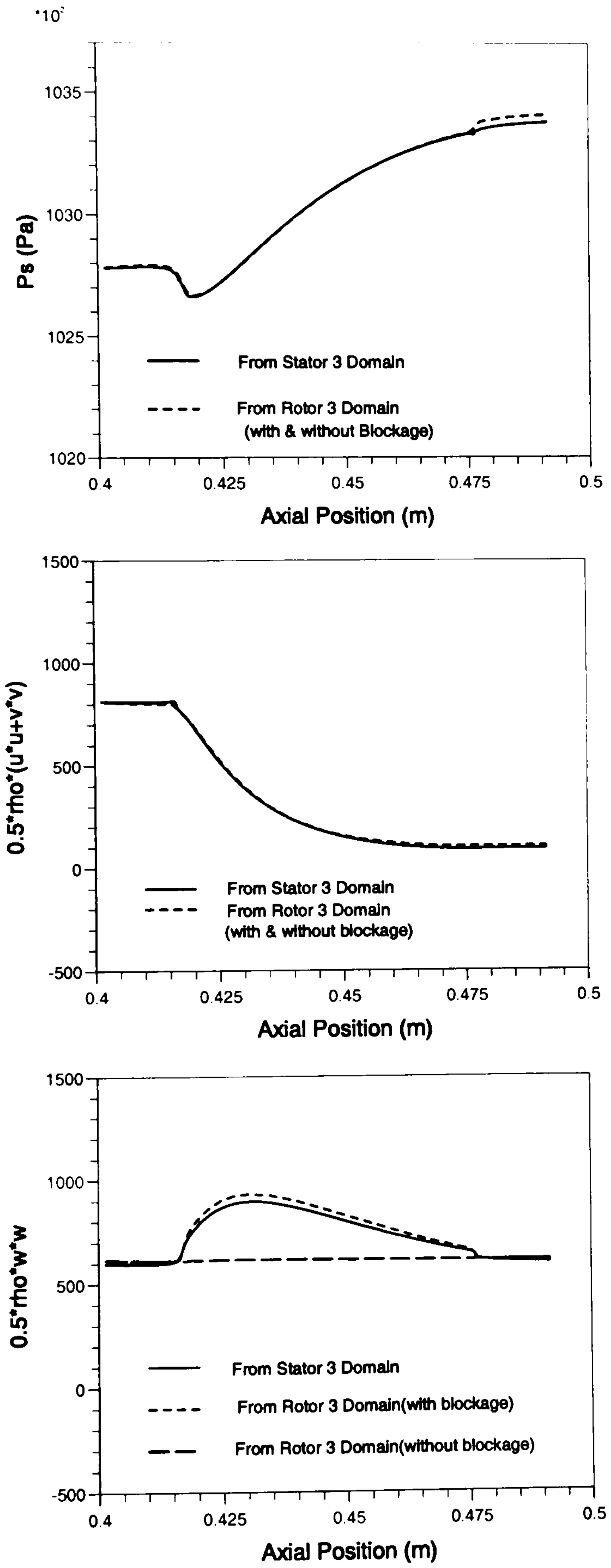

Figure 6.43: Comparison of area-averaged P_s & momentum terms in axial direction

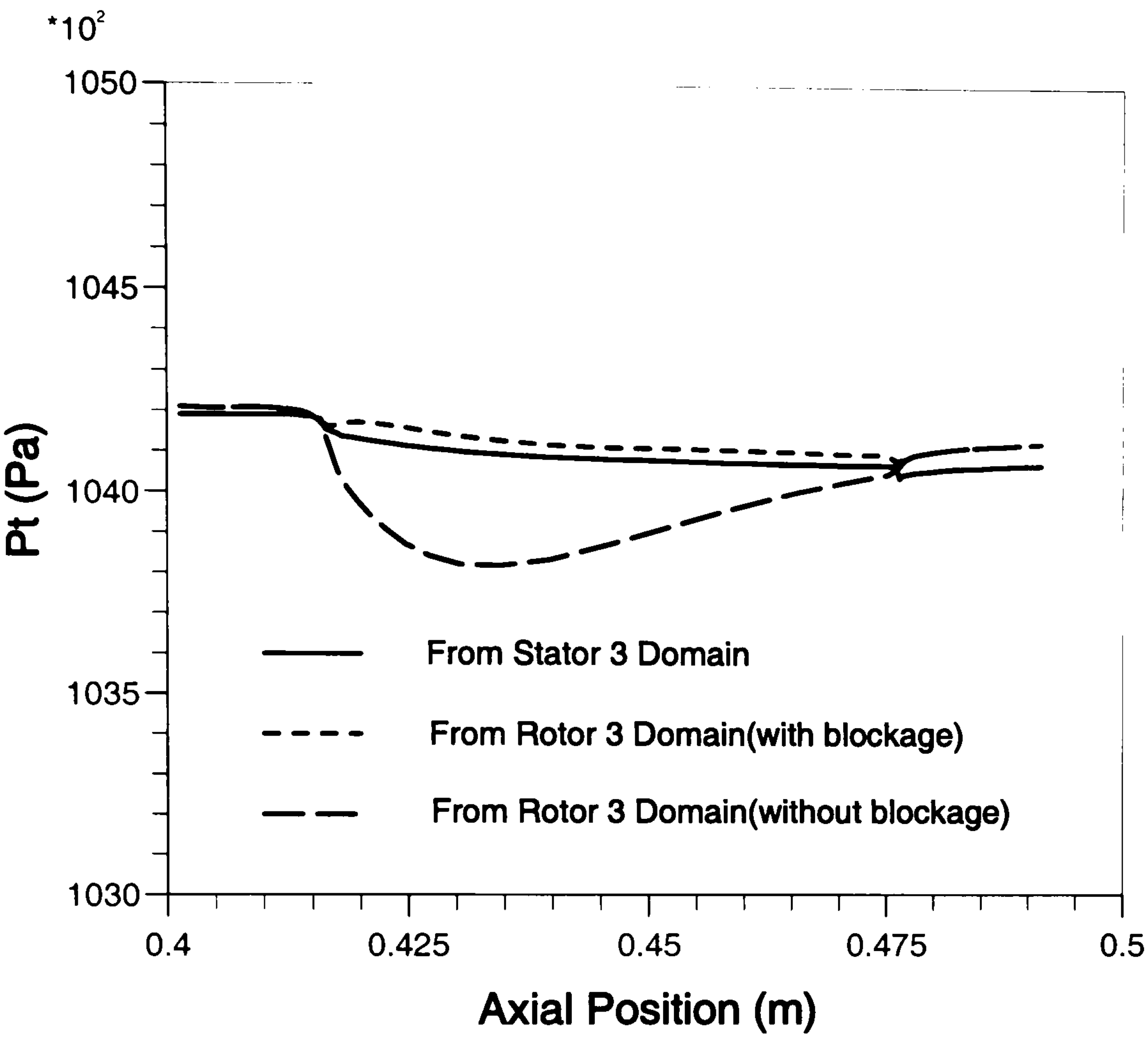

Figure 6.44: Comparison of area-averaged P_t in axial direction

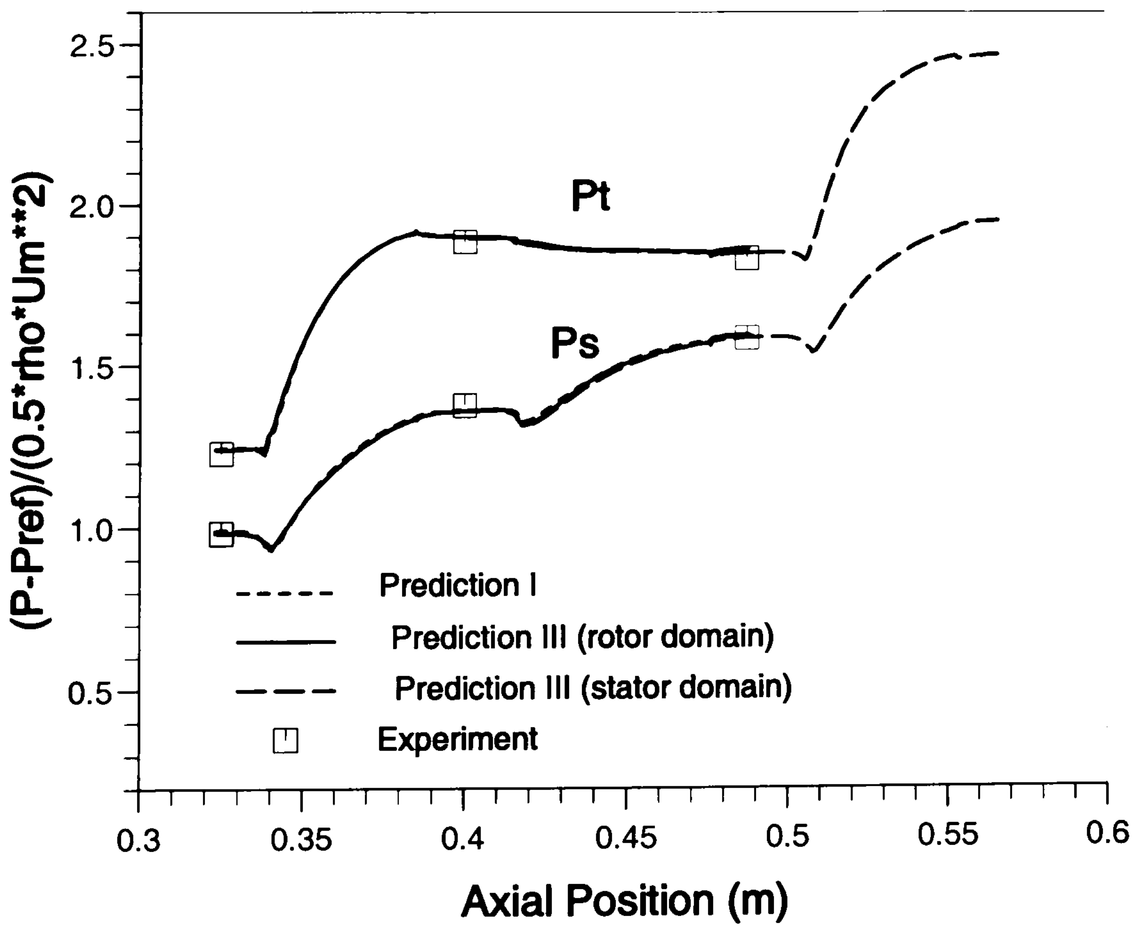

Figure 6.45: Axial Pt & Ps distribution from Prediction $I\&III$

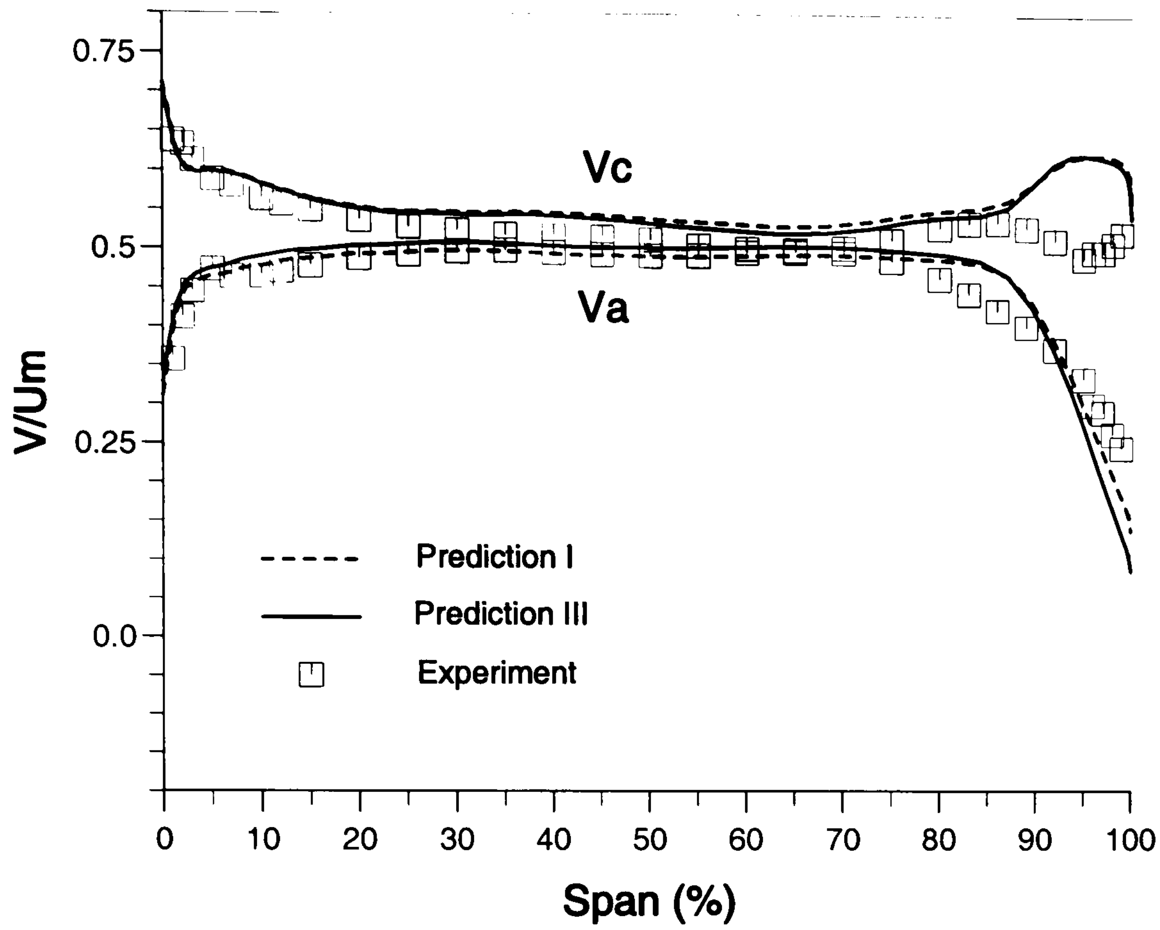

Figure 6.46: Spanwise velocity at Rotor 3 exit from Prediction *I* & *III*

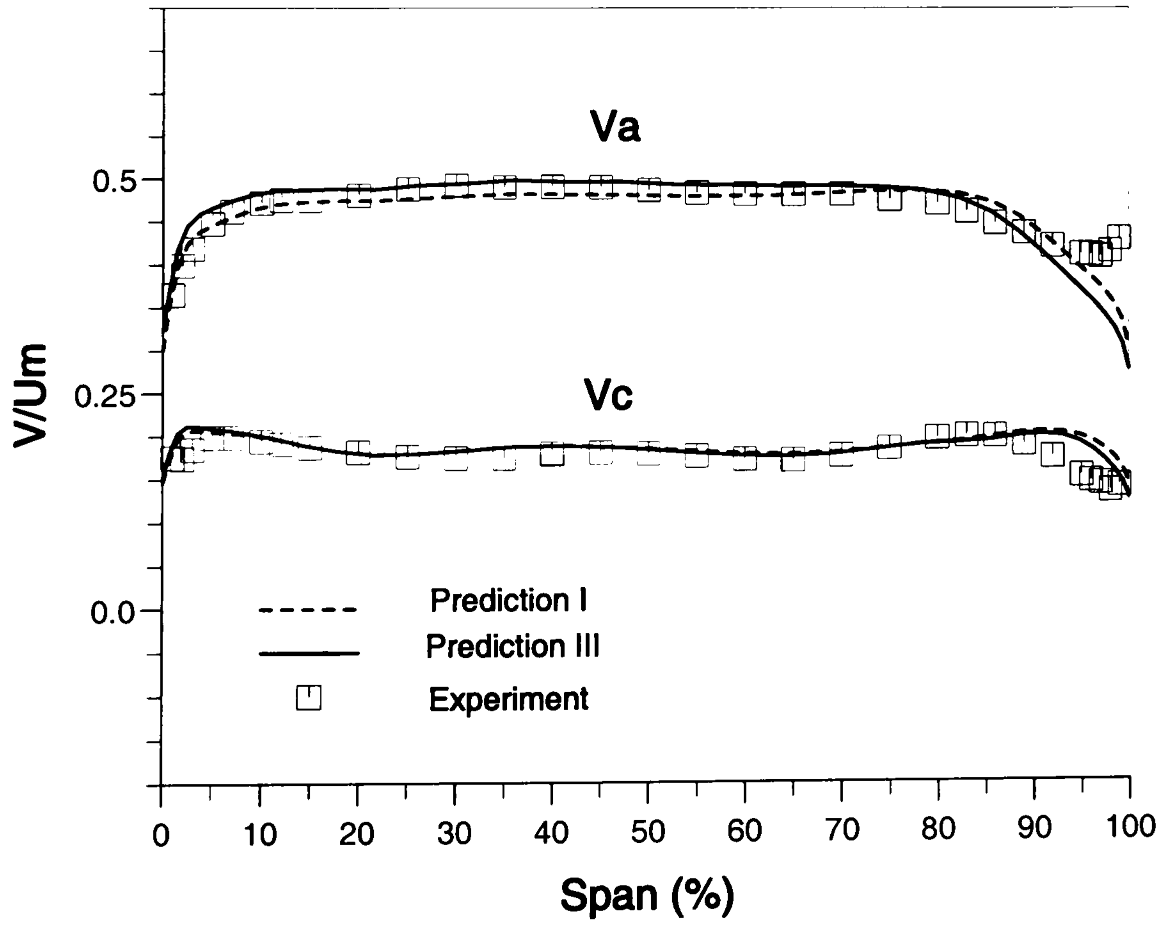

Figure 6.47: Spanwise velocity at Stator 3 exit from Prediction *I* & *III*

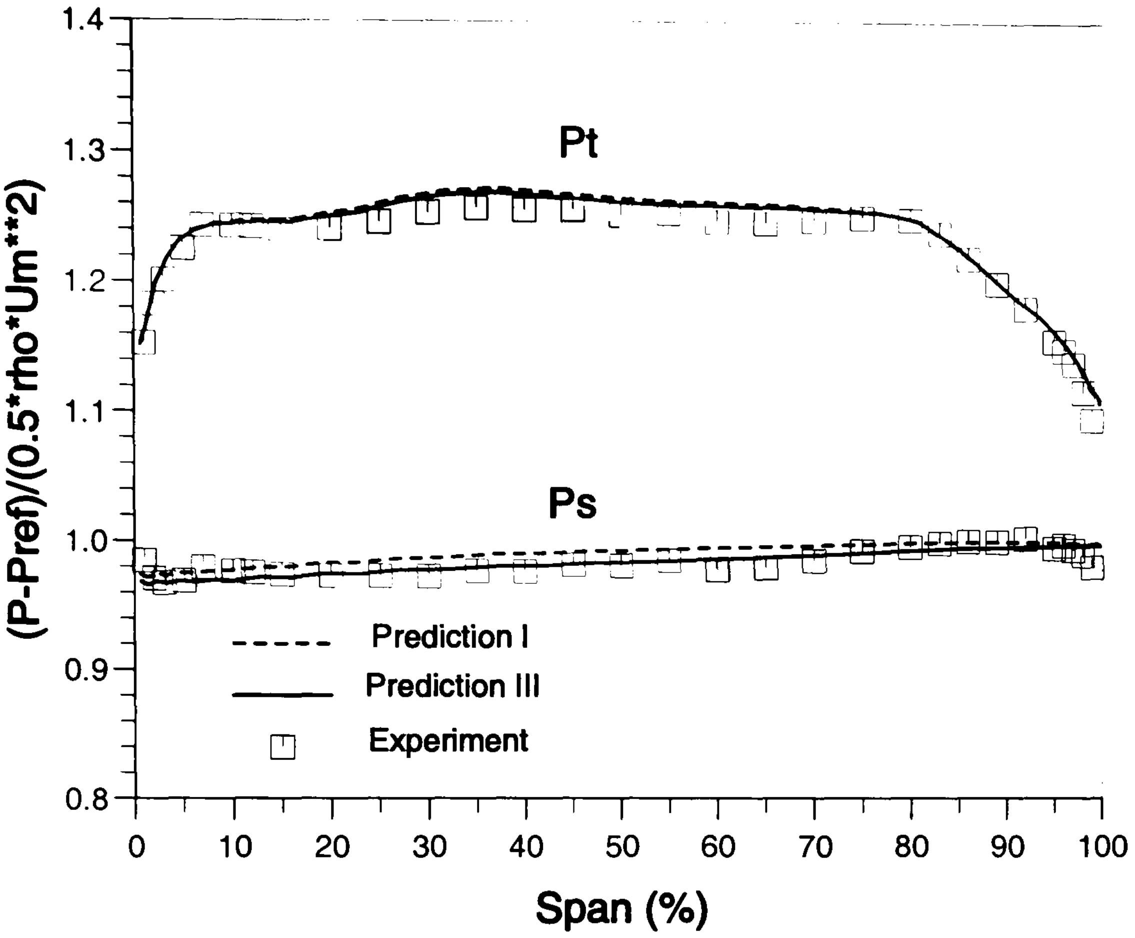

Figure 6.48: **Spanwise** *Pt* **&** *Ps* **at Rotor 3 inlet from Prediction** *I* **&** *III*

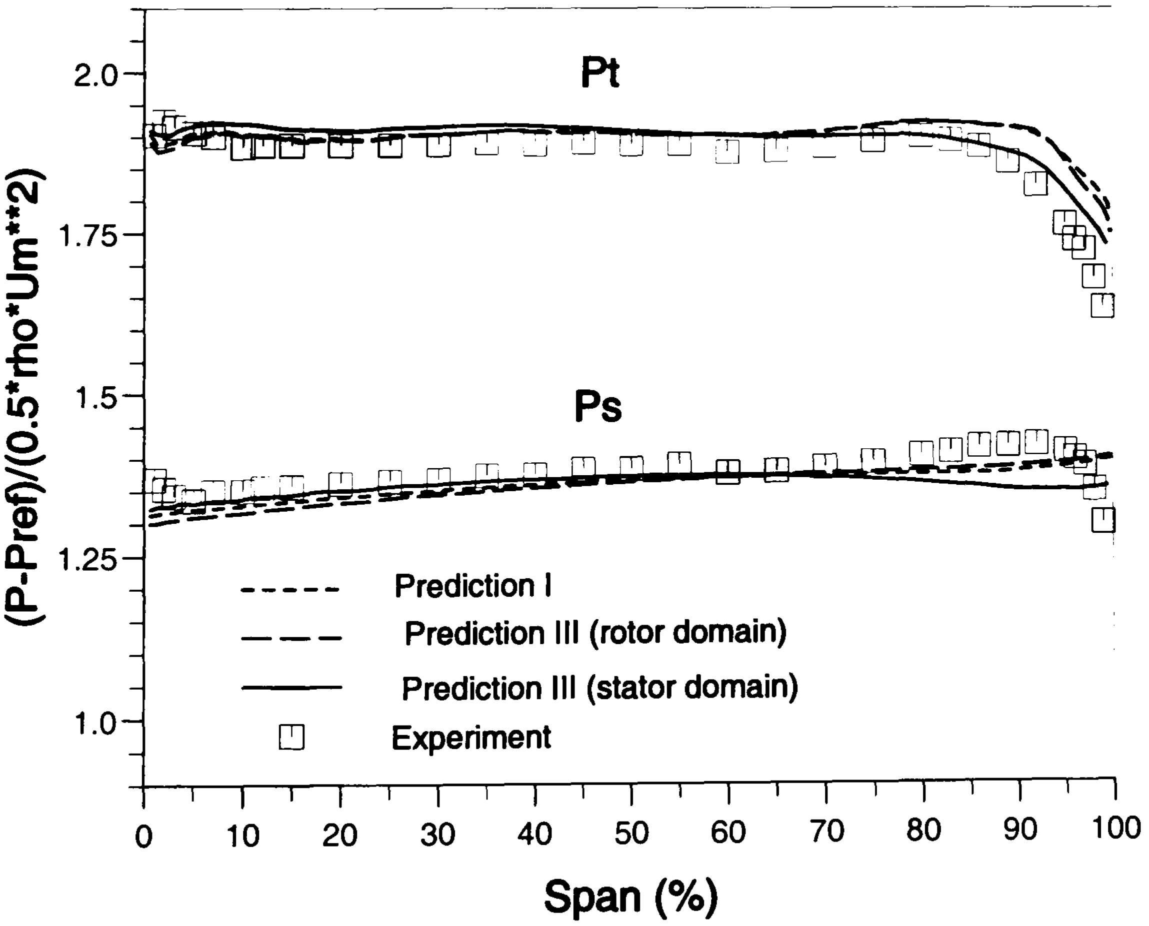

Figure 6.49: **Spanwise** *Pt* **&** *Ps* **at Rotor 3 exit from Prediction** *I* **&** *III*

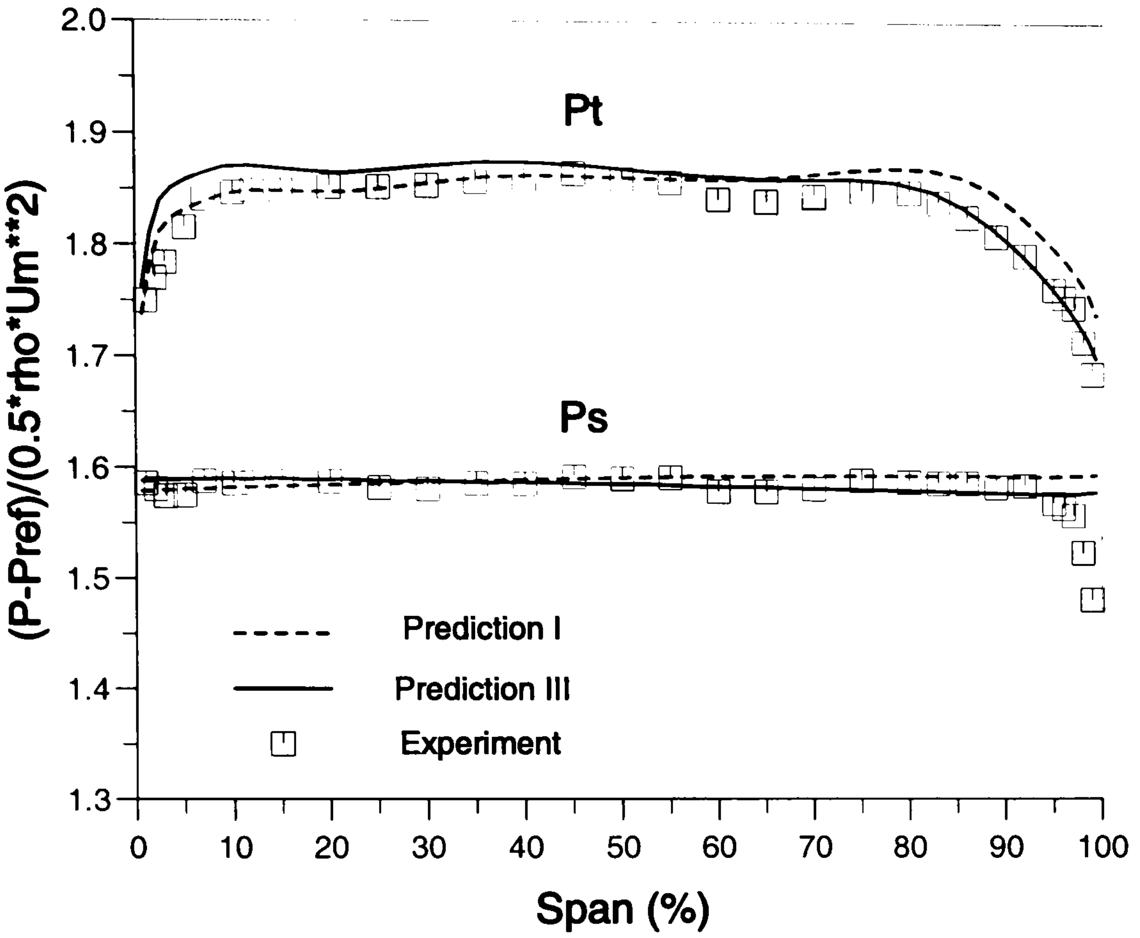

Figure 6.50: Spanwise *Pt* & *Ps* at Stator 3 exit from Prediction *I* & *III*

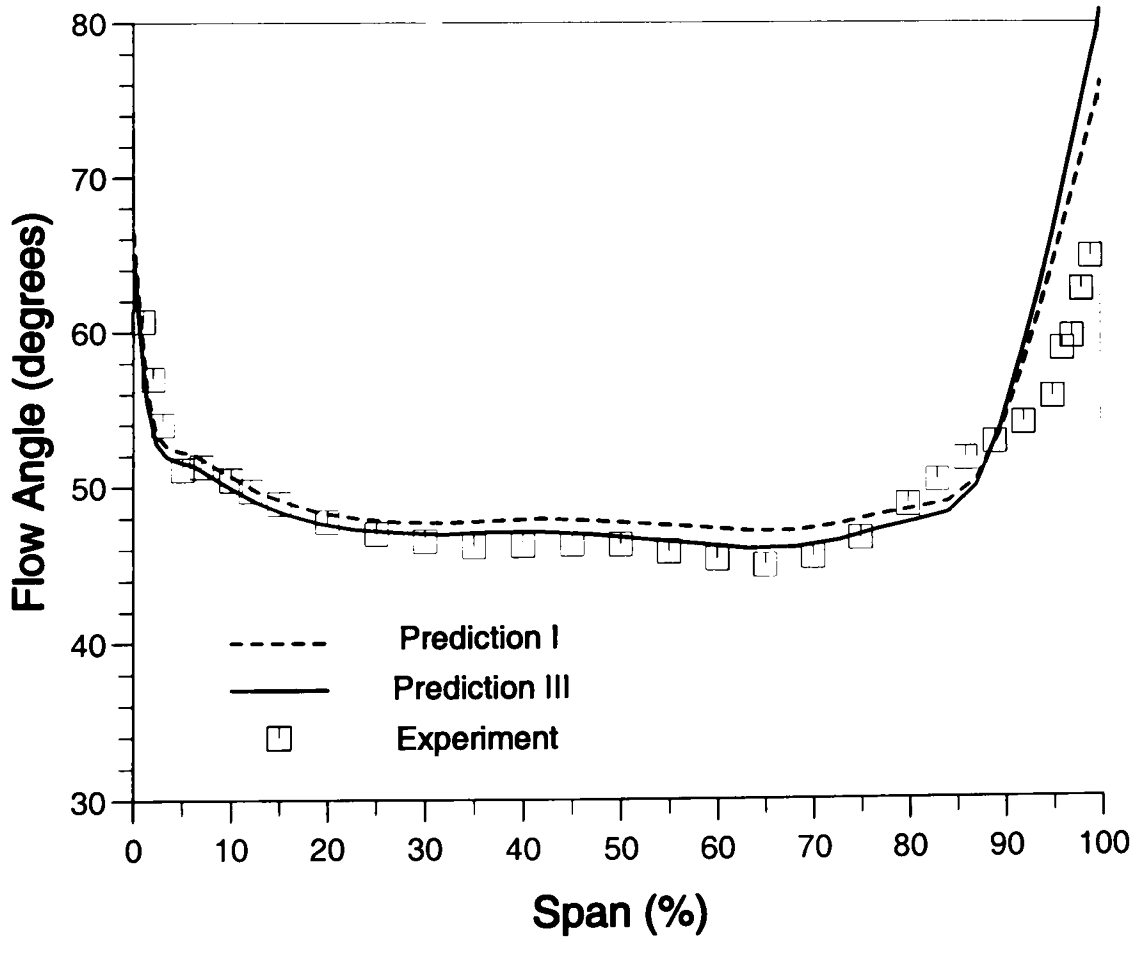

Figure 6.51: Spanwise flow angle at Rotor 3 exit from Prediction *I* & *III*

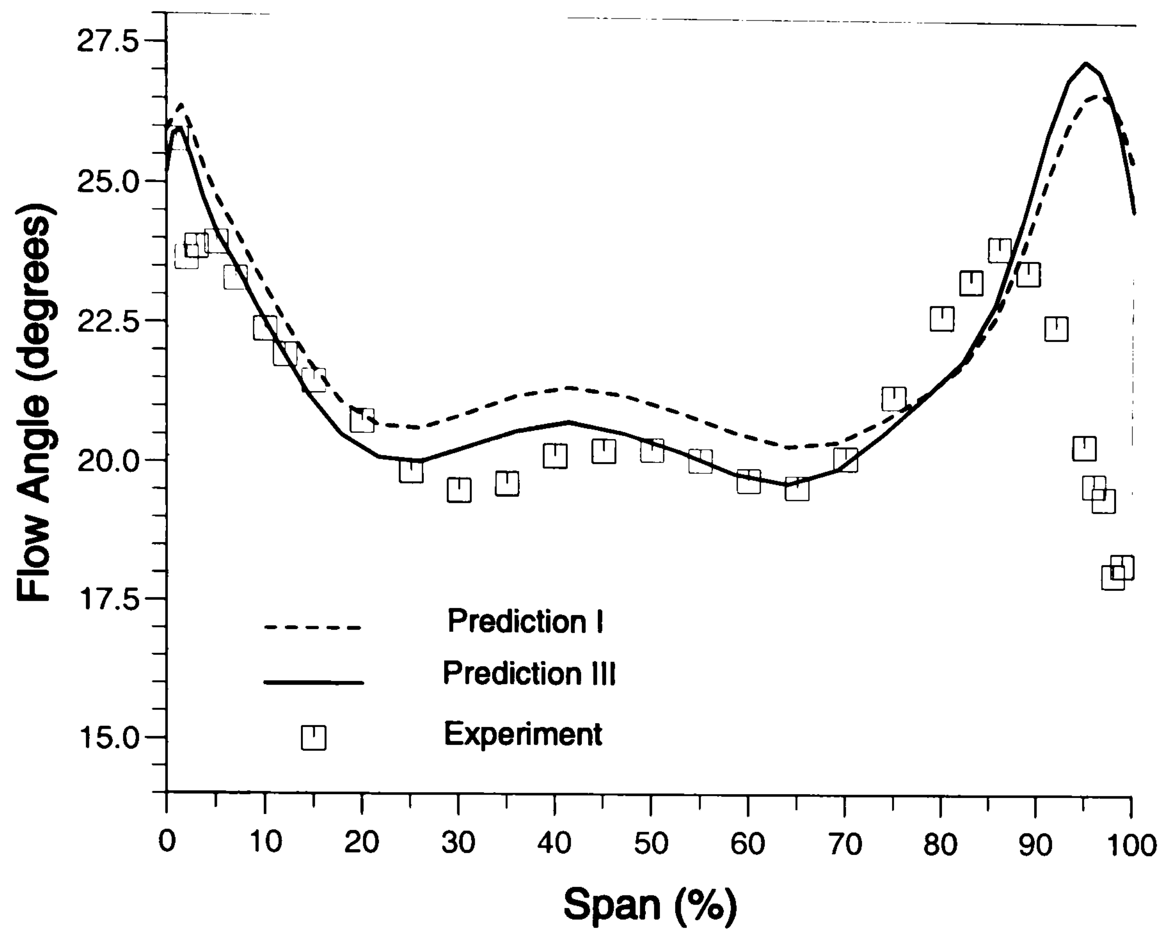

Figure 6.52: **Spanwise flow angle at Stator 3 exit from Prediction** *I* **&** *III*

Prediction *III* is in the lower part of the passage while the peak value area of the contours in Prediction *I* is in the upper part of the passage.

The static pressure and the velocity vector distributions in blade-to-blade surfaces at different blade height are illustrated in Figures 6.55 and 6.56 for the Rotor 3 domain and in Figures 6.57 and 6.58 for the Stator 3 domain. It can be seen that in the downstream extension of each domain the axial variations are well predicted which is corresponding to the average flow in the following blade passage while the circumferential variations are smeared with the action of the downstream relatively rotating blade row. The turning of the flow in the downstream extension of Rotor 3 with the action of its downstream blade row is demonstrated with the streamlines in a blade-to-blade surface at midspan in Figure 6.59.

The wakes generated by Rotor 3 and Stator 3 blades are well predicted with the comparison of the circumferential variation of the axial velocity component and the relative total pressure in the rotating frame of reference for Rotor 3 at midspan of Rotor 3 exit (at Interface 2 of the Rotor 3 domain) and in the absolute frame of reference for Stator 3 at midspan of Stator 3 exit (at Interface 3 of Stator 3 domain) in Figures 6.61 to 6.64. The deterioration of the wakes, schematically illustrated in figure 6.60, are due to the "chopping" of their downstream relatively

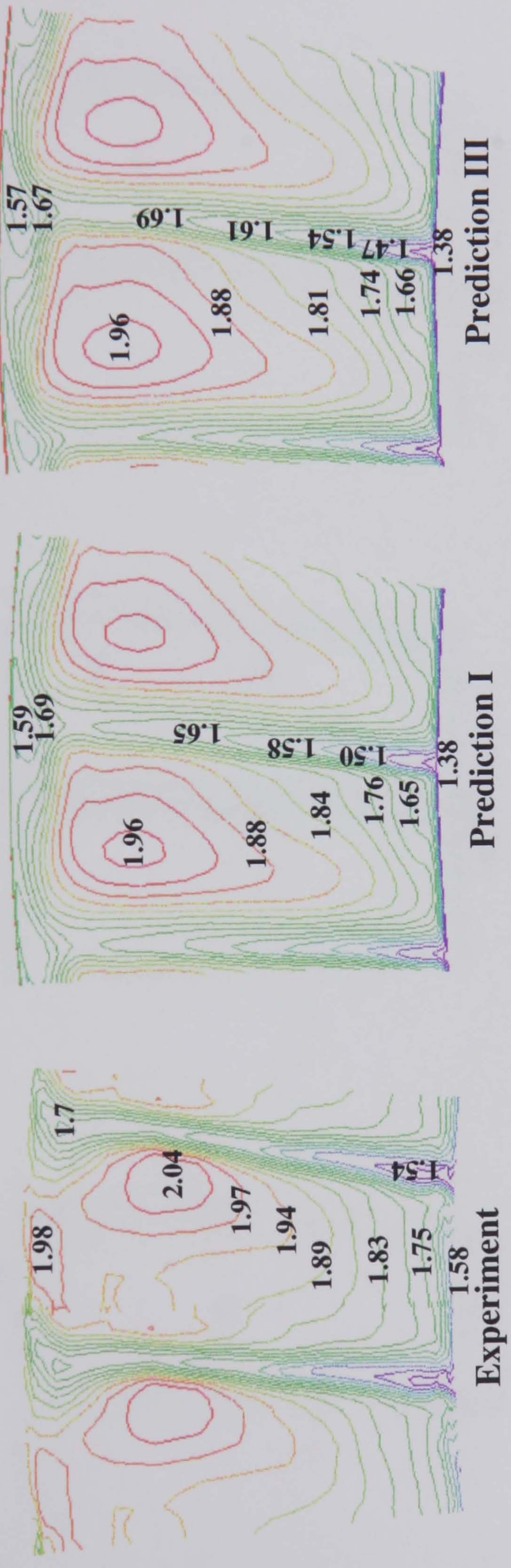

Figure 6.53: **Relative total pressrue $(P_t - P_{ref})/(\frac{1}{2}\rho U_m^2)$ contours at Rotor 3 exit**

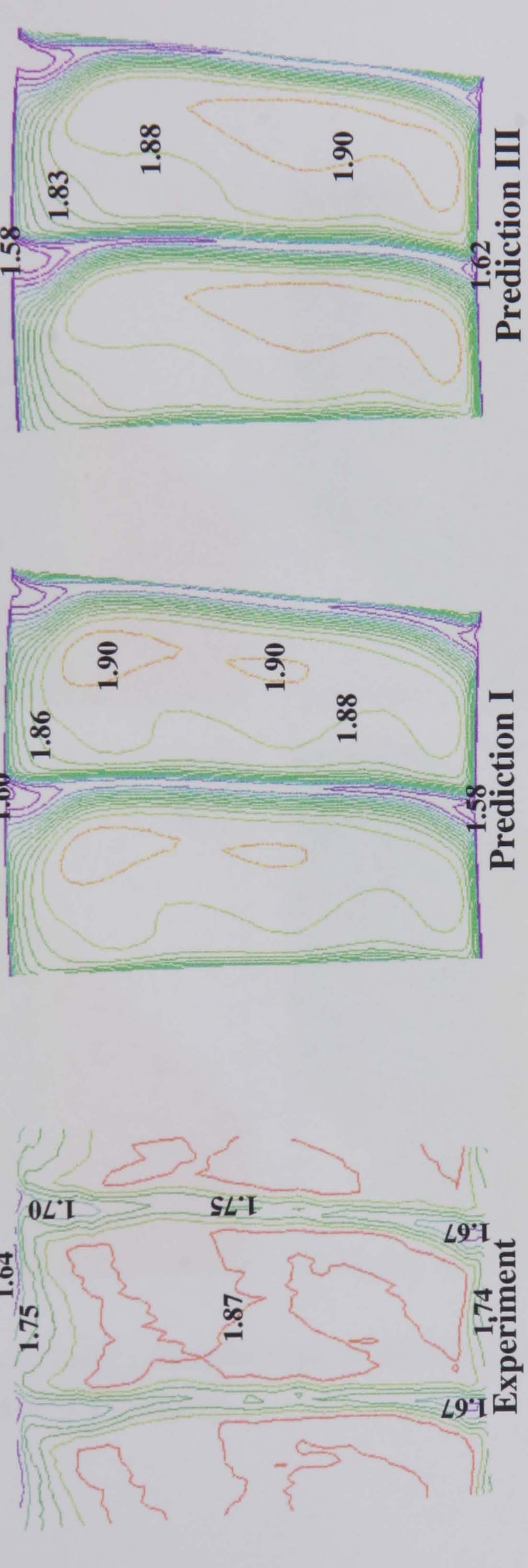

Figure 6.54: **Absolute total pressure $(P_t - P_{ref})/(\frac{1}{2}\rho U_m^2)$ contours at Stator 3 exit**

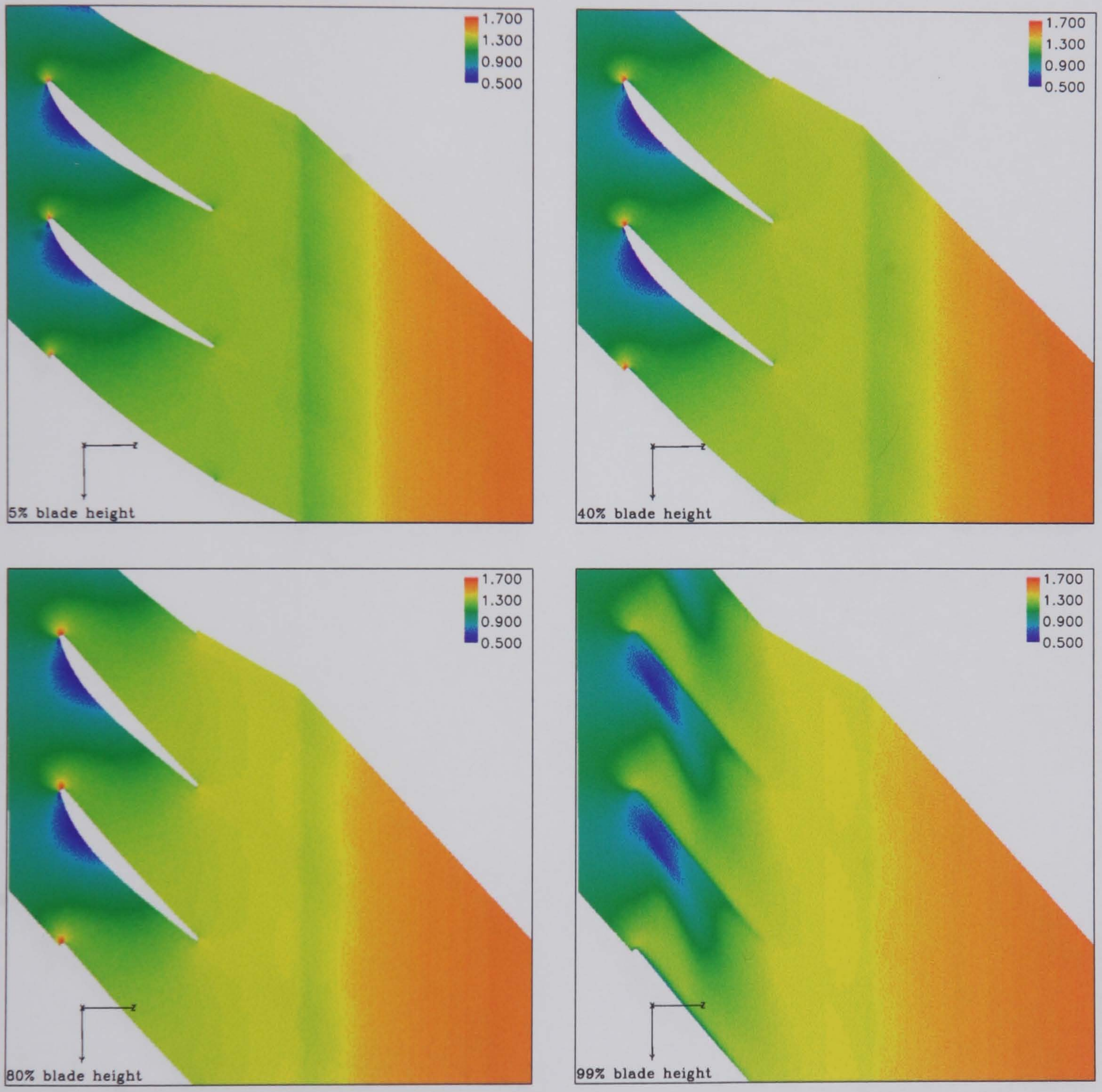

Figure 6.55: $(P_s - P_{ref})/(\frac{1}{2}\rho U_m^2)$ **distribution at blade-to-blade surfaces from Prediction** *III* **(Rotor 3 Domain)**

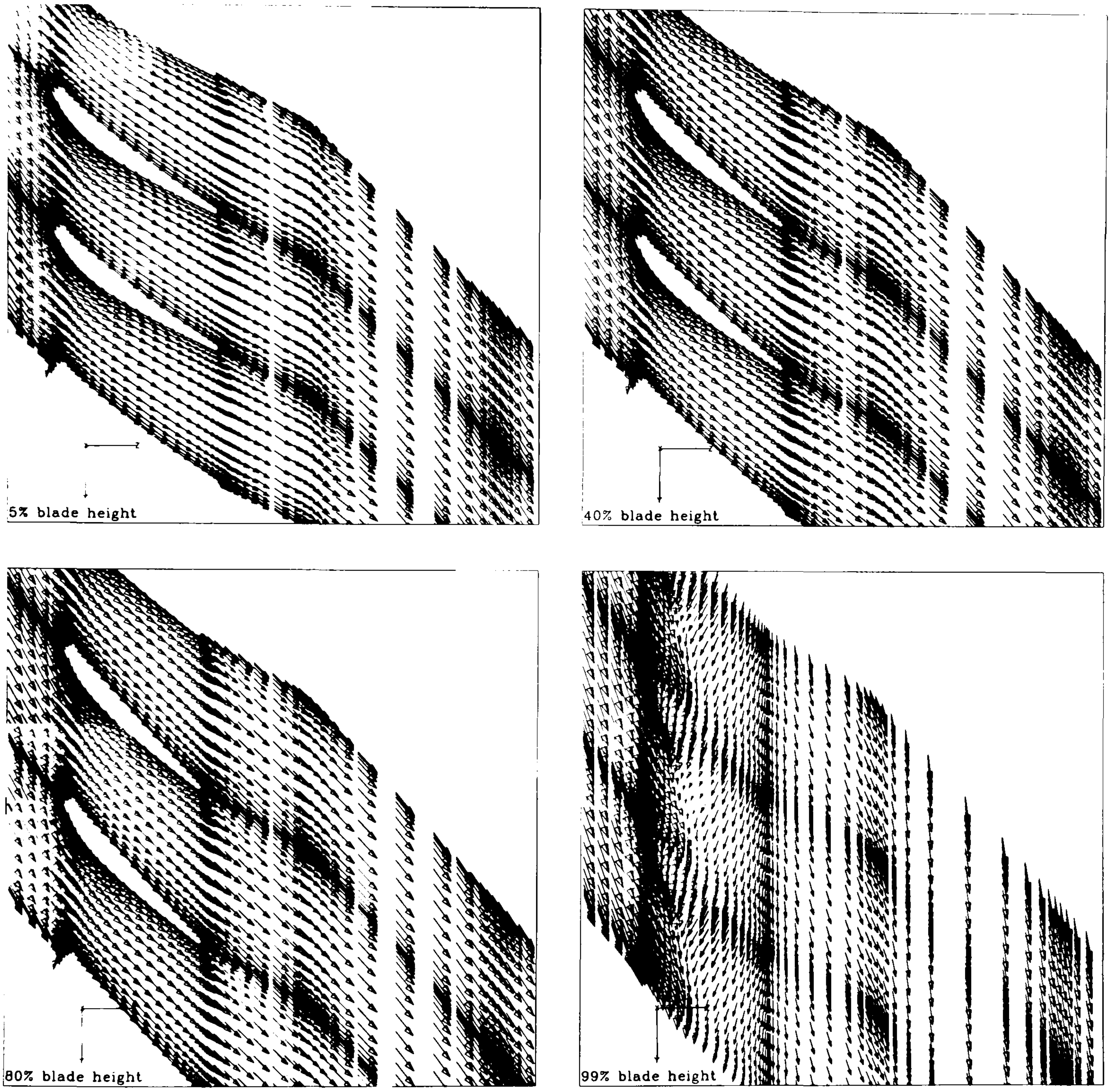

Figure 6.56: **Velocity vectors at blade-to-blade surfaces from Prediction** *III* **(Rotor 3 domain)**

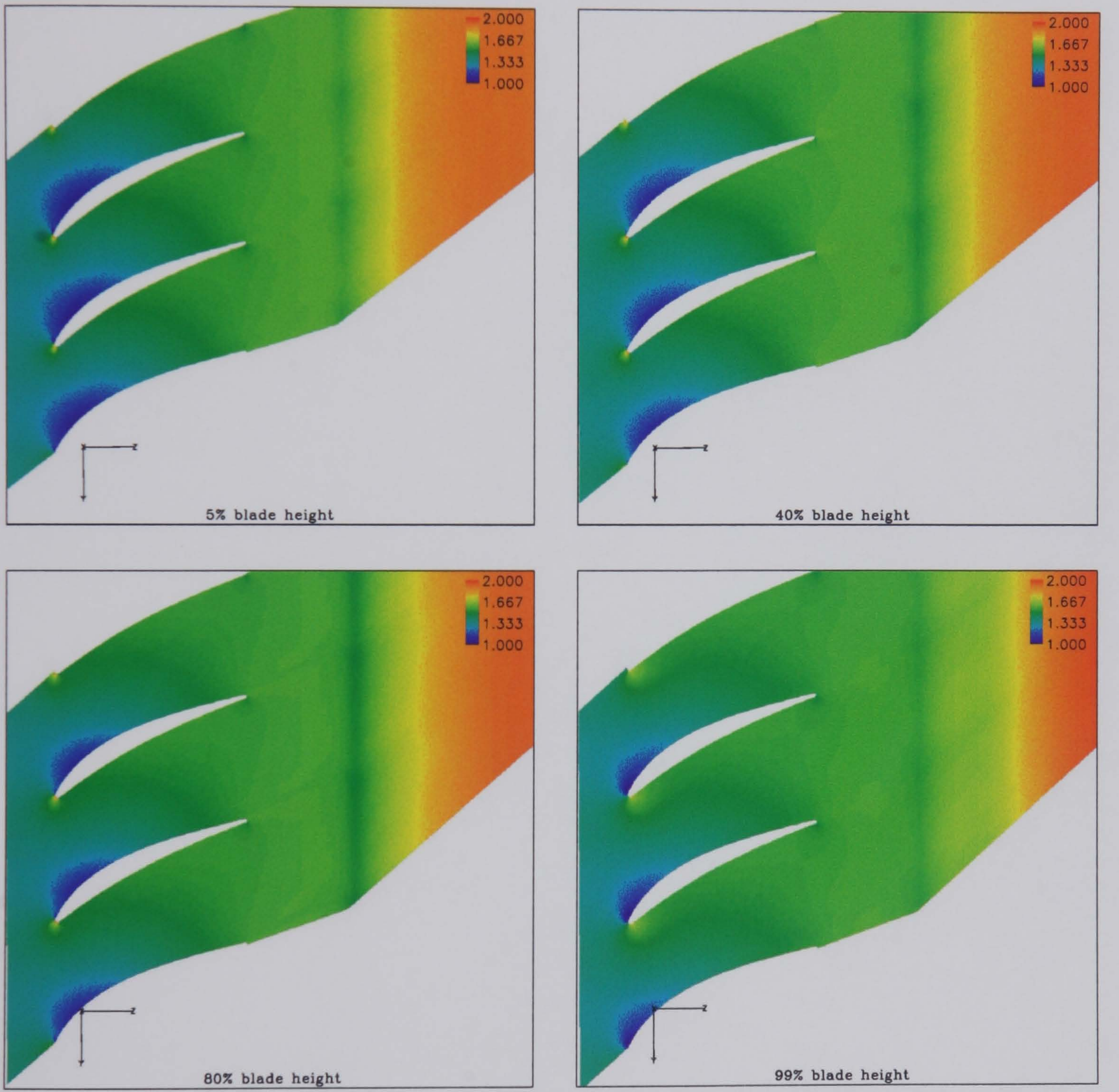

Figure 6.57: $(P_s - P_{ref})/(\frac{1}{2}\rho U_m^2)$ **distribution at blade-to-blade surfaces from Prediction** III **(Rotor 3 domain)**

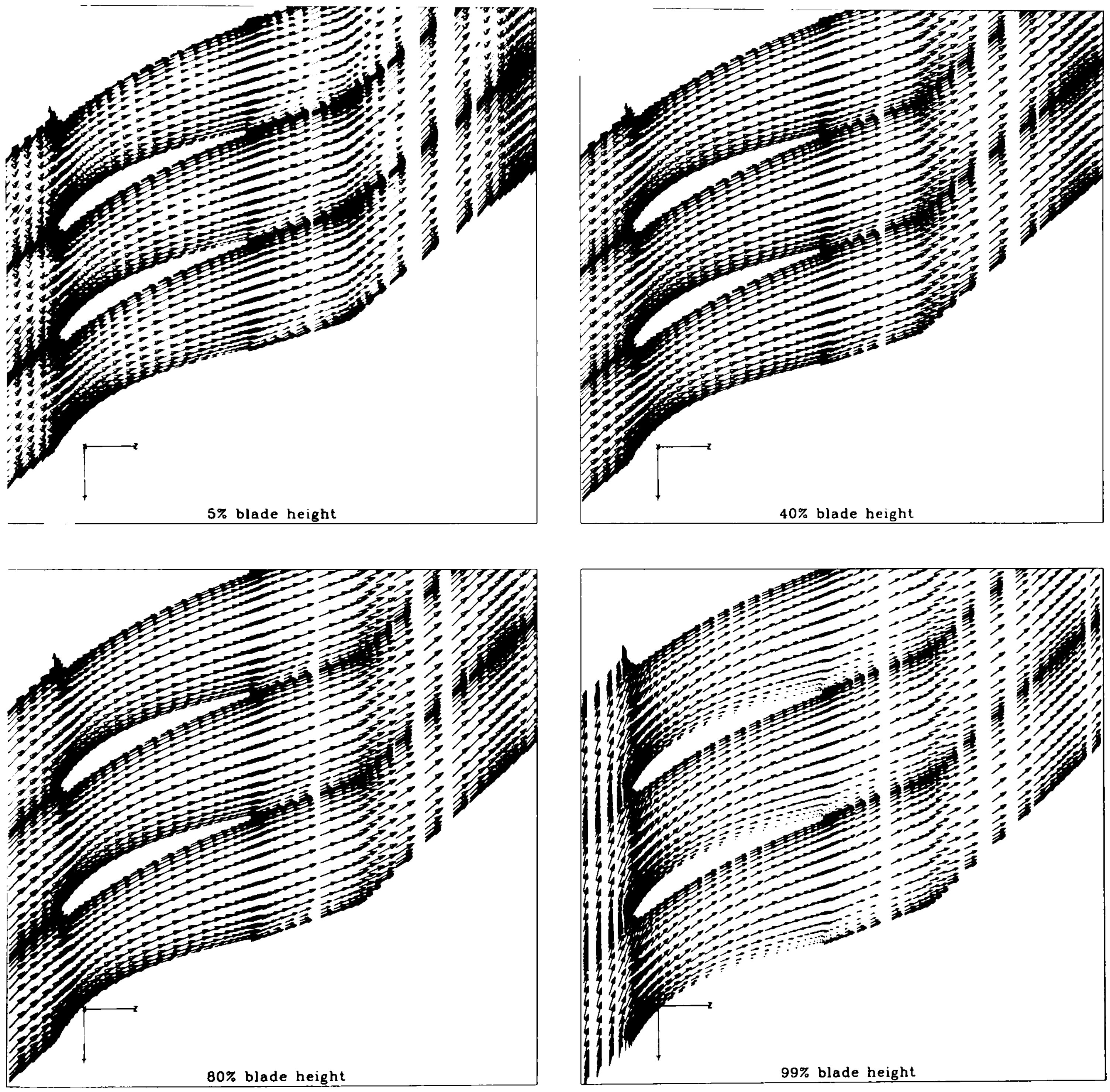

Figure 6.58: **Velocity vectors at blade-to-blade surfaces from Prediction** *III* **(Rotor 3 domain)**

Figure 6.59: **Stream lines on a blade-to-blade surface from Prediction *III* (Rotor 3 domain)**

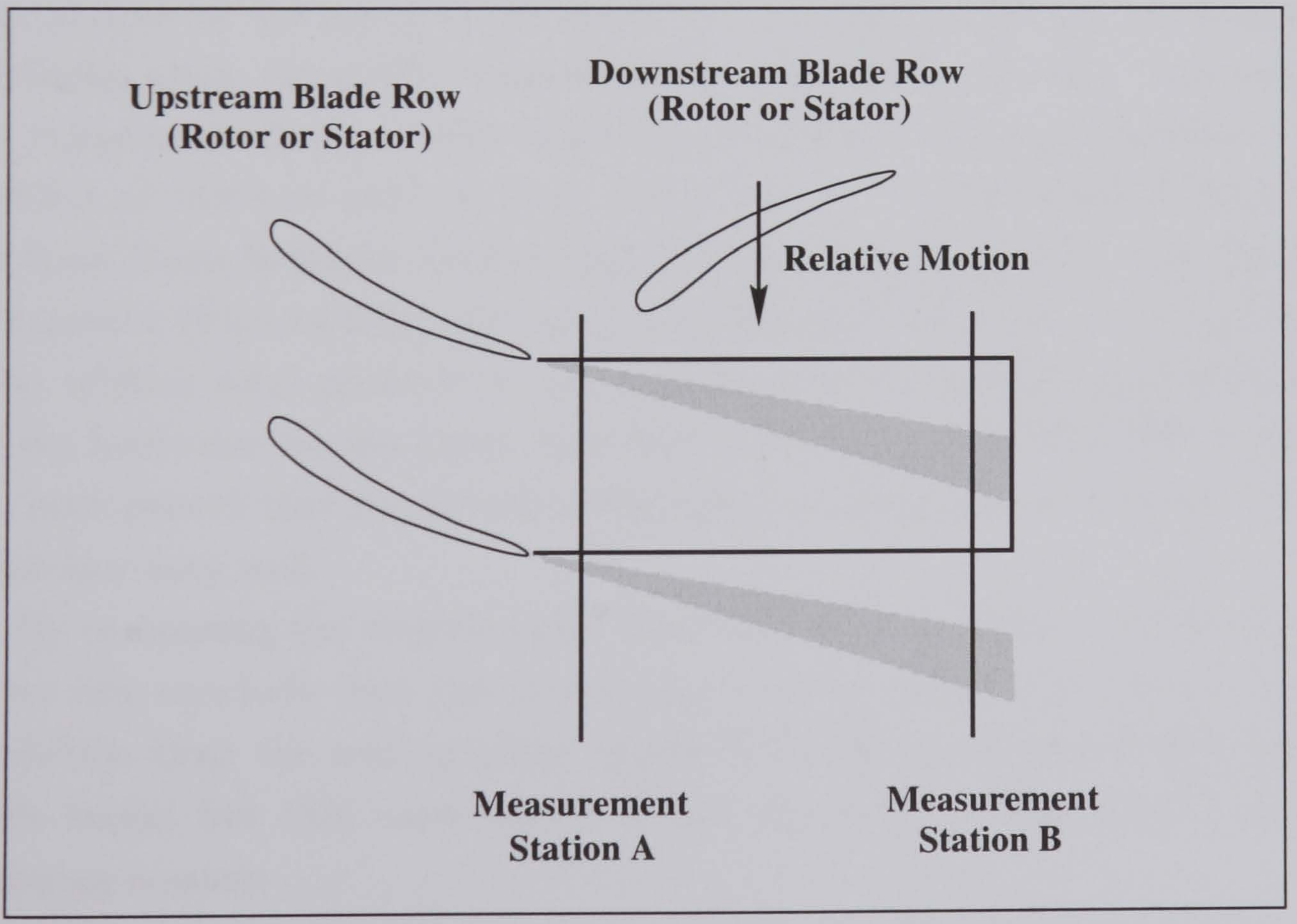

Figure 6.60: **Illustration of development of wakes chopped by downstream relative rotating blades, Hall [73]**

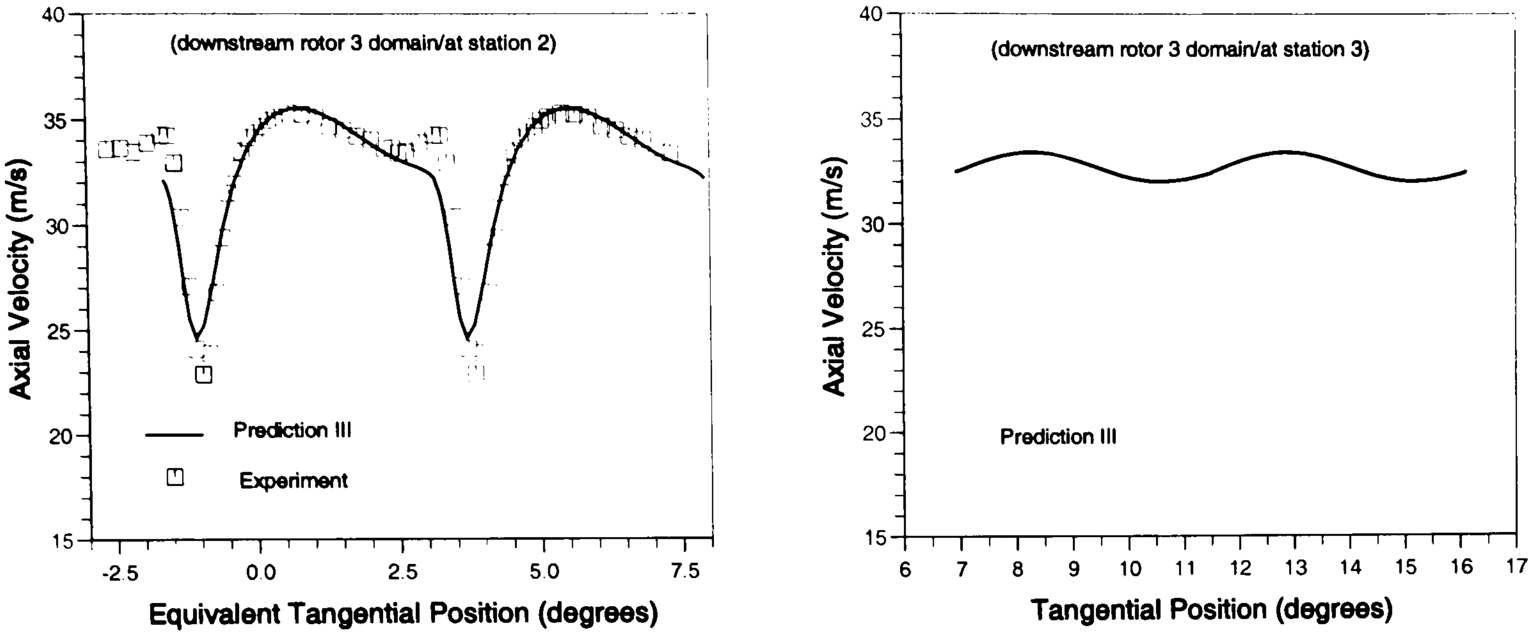

Figure 6.61: **Tangential distribution of axial velocity at Rotor 3 exit midspan and its development (in relative frame of reference)**

rotating blades. The circumferential variations of the axial velocity component and the relative total pressure at the same span position after the "chopping" at Interface 3 of the Rotor 3 domain are plotted in Figures 6.61 and 6.62 and at Interface 4 of the Stator 3 domain in Figures 6.63 and 6.64. Although the experimental data for the decay of the wakes for Cranfield *LSRC* are not available, the prediction show the similar tangential variation of time-average total pressure to the experimentally measured tangential variation of time-averaged relative total pressure at midspan position both before and after a downstream blade row for the Iowa State Research Compressor (Figure 6.65) and NASA Low Speed Axial Compressor (Figures 6.66) and the predicted tangential variation of time-averaged rotor relative total pressure at midspan position both before and after a downstream blade row for the Penn State Research Compressor, Hall[73]. Therefore, it has been proved that the deterministic stress model is able to reproduce the wake behaviour very well.

By comparing the experimental data with the results from Prediction *III* & *I*, we can conclude that the deterministic stress model does provide improved prediction than the mixing plane approach in the area between 50% and 100% blade height but this improvement is not significant. This may be due to the following reasons:

- The implemented deterministic stresses have larger influence on the upstream extension of a blade domain than on the following downstream domain. The deterministic stresses decay rapidly and have little influence downstream

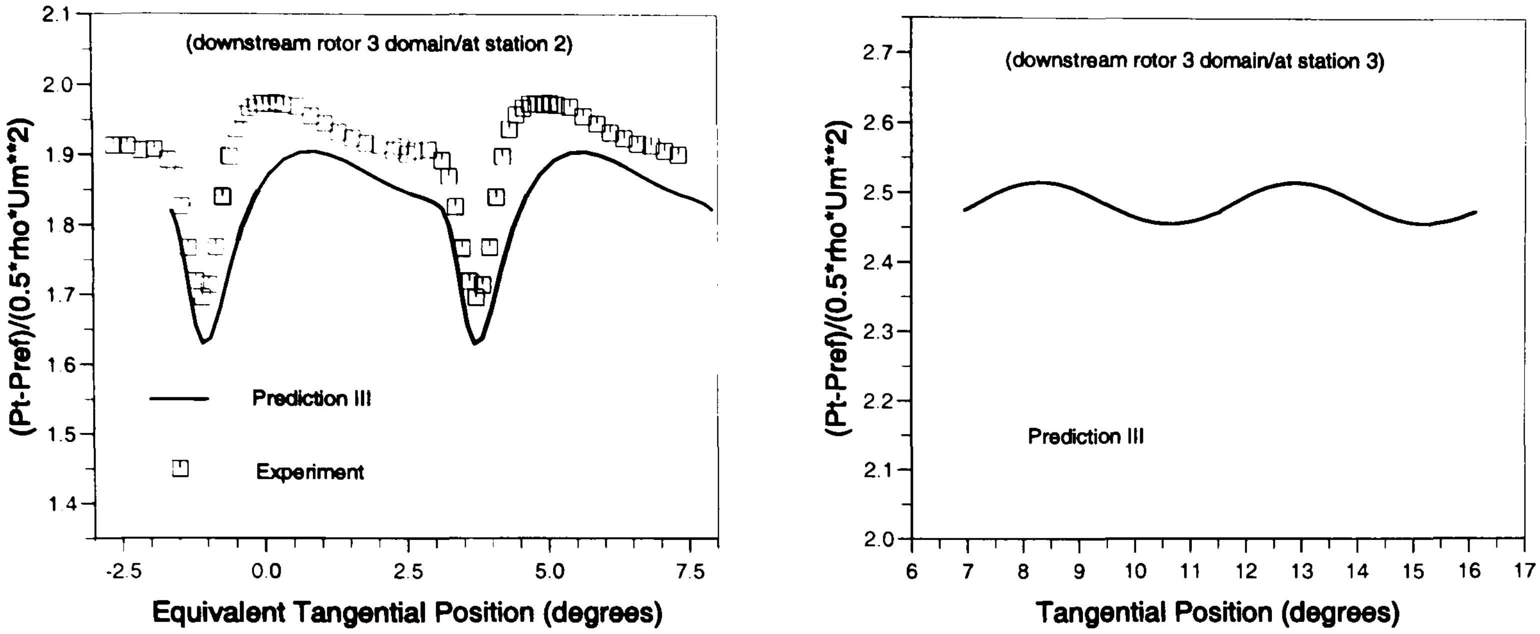

Figure 6.62: Tangential distribution of total pressure at Rotor 3 exit midspan and its development (in relative frame of reference)

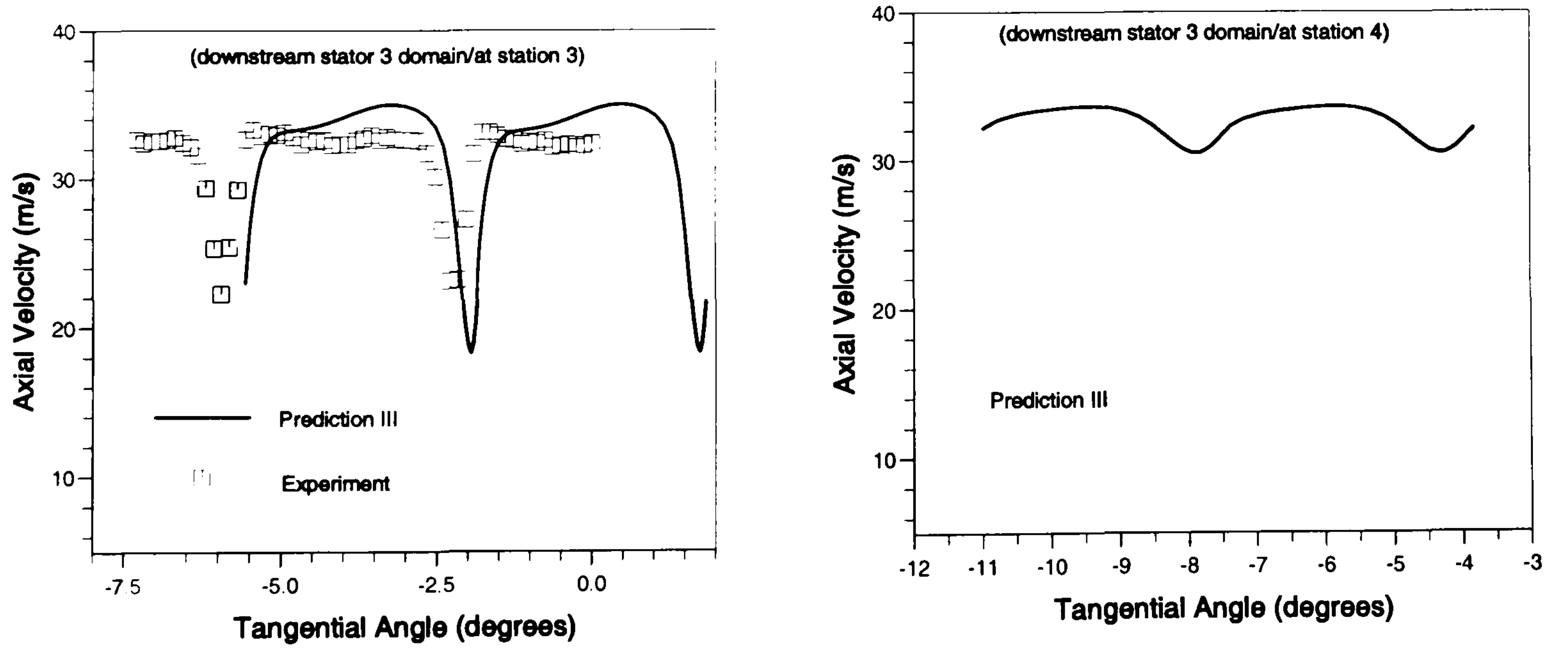

Figure 6.63: Tangential distribution of axial velocity at Stator 3 exit midspan and its development (in absolute frame of reference)

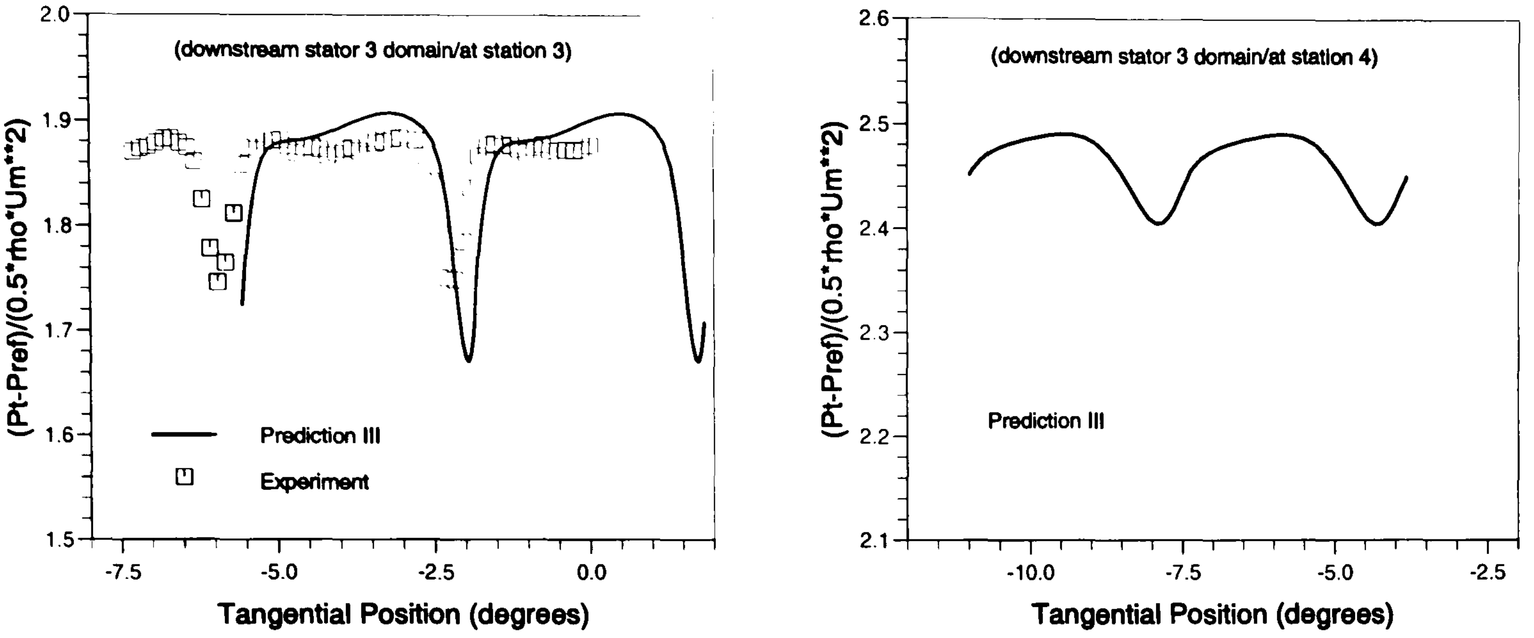

Figure 6.64: Tangential distribution of total pressure at Stator 3 exit midspan and its development (in absolute frame of reference)

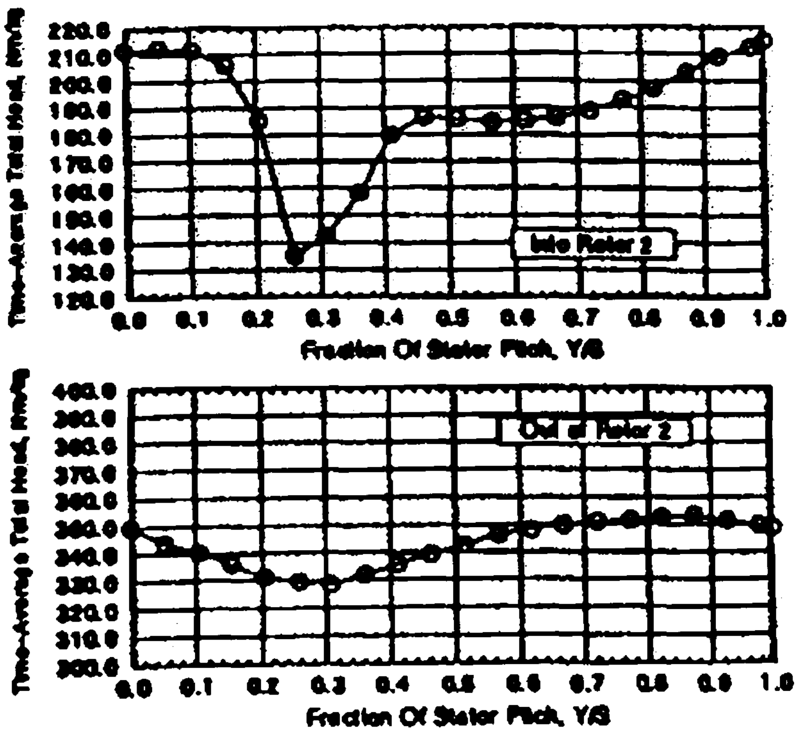

Figure 6.65: Experimental circumferential variation (near midspan) of time-averaged total pressure both before and after a downstream blade row for the Iowa State Research Compressor, Hall[73]

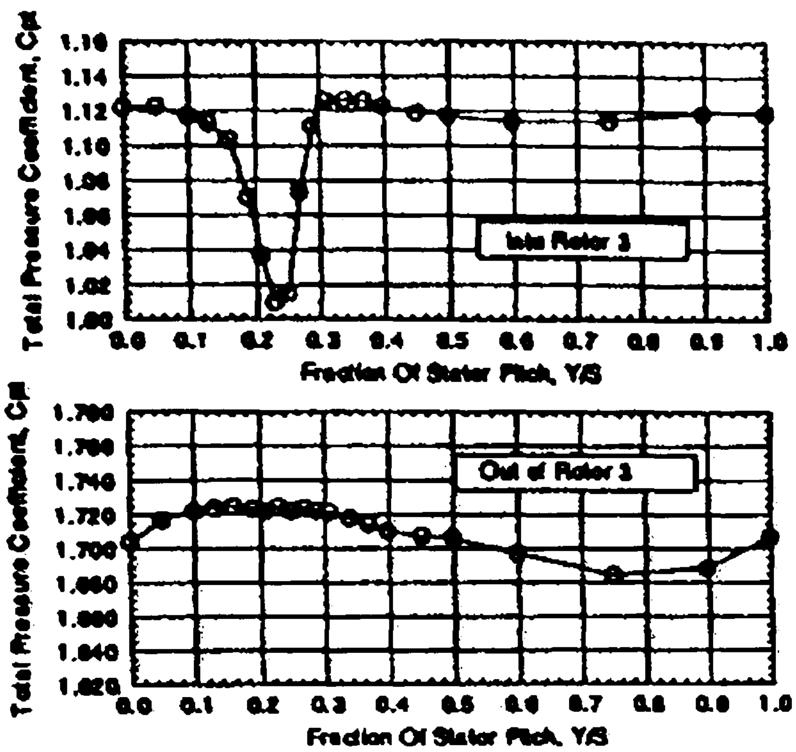

Figure 6.66: Experimental circumferential variation (near midspan) of time-averaged total pressure both before and after a downstream blade row for the NASA Low Speed Axial Compressor, Hall[73]

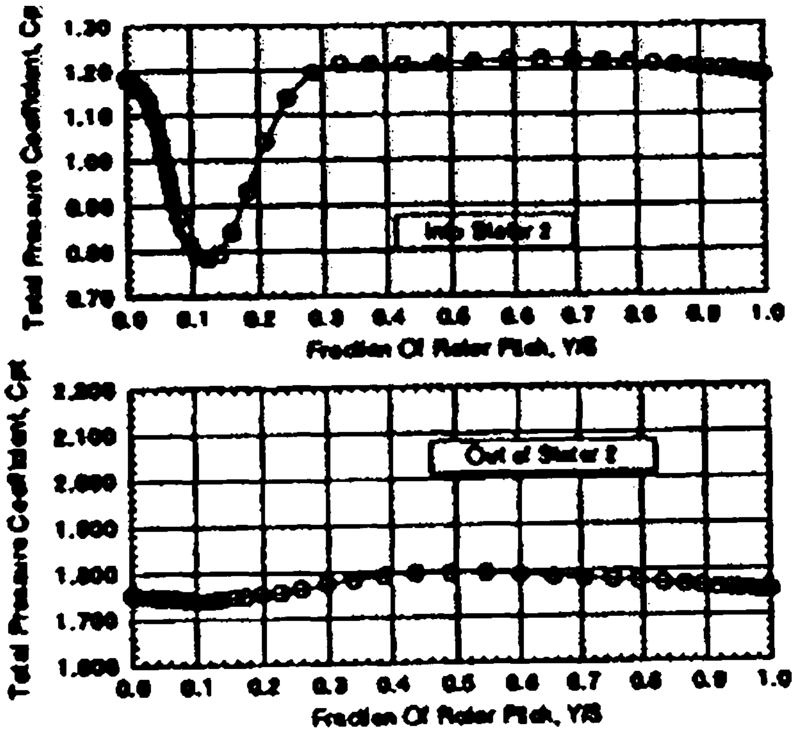

Figure 6.67: Predicted circumferential variation (near midspan) of time-averaged total pressure both before and after a downstream blade row for the Penn State Research Compressor, Hall[73]

blade leading edge.

- The rotor tip leakage flows have significant influence on the flow and this influence is comparable to the improvement from the implementation of the deterministic stresses.
- The inaccurate prediction of the rotor tip leakage flows is obvious. The deterministic stress model does not have the capability to solve the problem.

Generally speaking, the deterministic stress model does provide better prediction of the flow and performance of the third stage of *LSRC* but this improvement is not significant. It is likely that the deterministic stress model can provide more benefits than the mixing plane model for high pressure multistage axial flow compressors with small axial gaps.

6.7 Prediction *IV*: *LSRC* Third Stage with Repeating Stage Model and Deterministic Stress Model

A numerical prediction with the deterministic stress model in combination with the repeating stage model is presented in this section and the results are compared with Prediction *II* which uses the mixing plane model combined with the repeating stage model. The only difference between Prediction *II* and *IV* is the treatment of the interfaces. Through the comparison of the two predictions on the third stage of *LSRC*, the benefits of the deterministic stress model will be further presented.

The details of the second repeating stage model used in Prediction *IV* is described in Chapter 4 and will not be repeated here. The layout of the computational domains for the third stage and the setting of boundary conditions are illustrated in Figure 6.68. This prediction consists of two global iterations. One is the *Computation I* which is a repeating stage approach similar to Prediction *II* by imposing the deterministic stress field on the flow field. The other, the *Computation II*, is a deterministic stress approach similar to Prediction *III* whose boundary conditions come from *Computation I*. The *Computation II* which is carried out once after every 4 to 5 global iterations of *ComputaitonI* provides a deterministic stress field to *Computation I*. Of the two computations in Prediction *IV* the results from the *Computation I* are more concerned and are compared

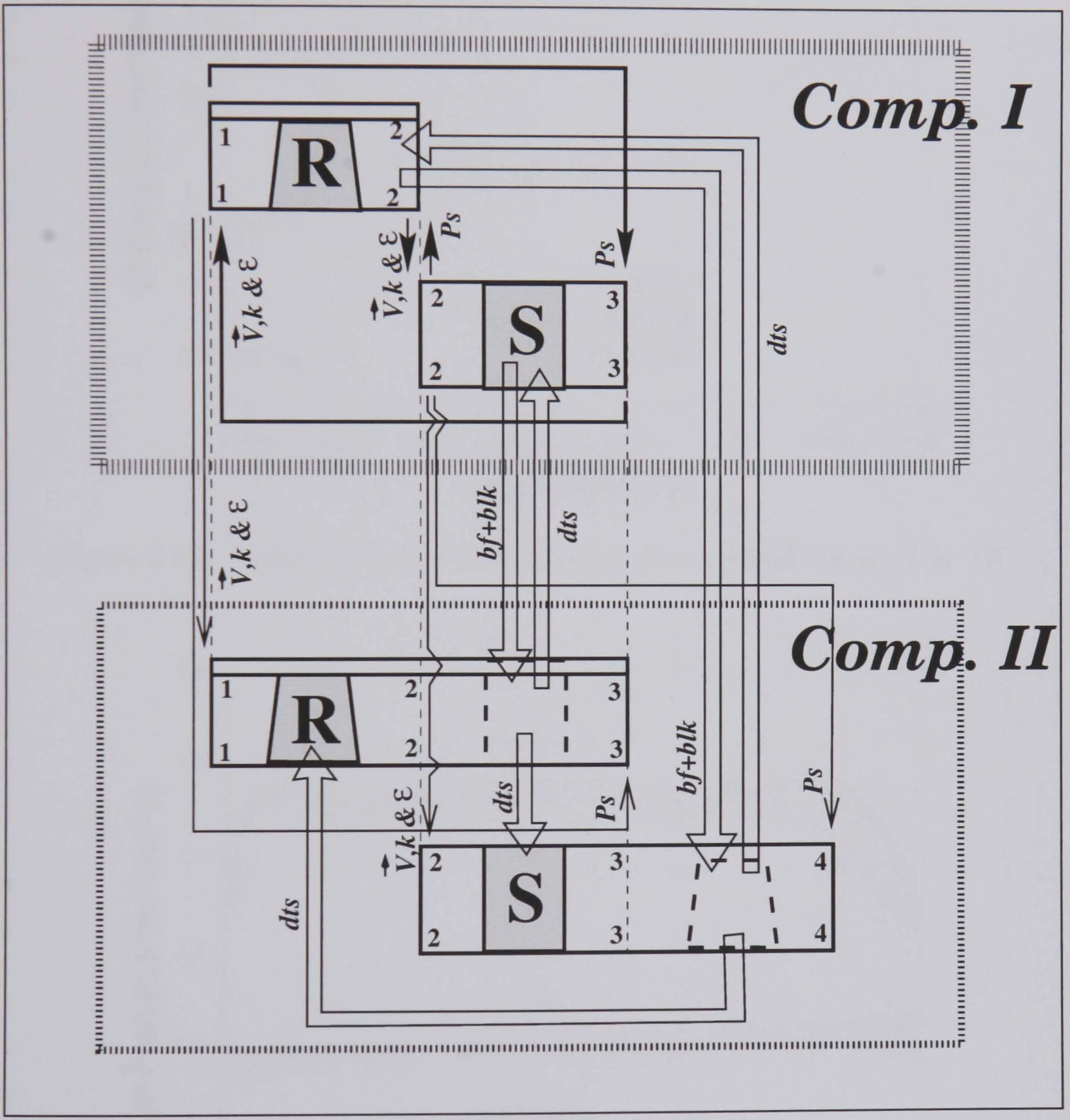

Figure 6.68: **Boundary setting for Prediction** *IV*

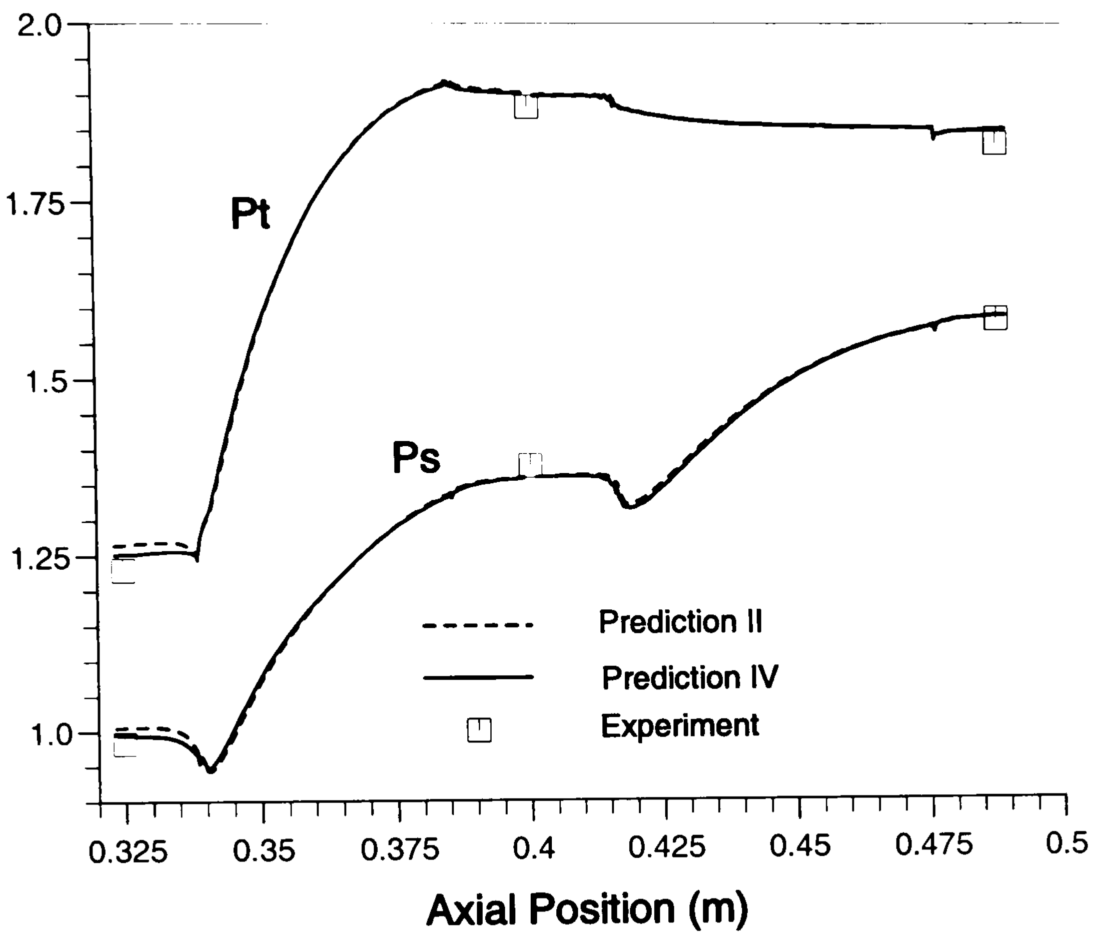

Figure 6.69: Axial Pt & Ps distribution from Prediction II & IV

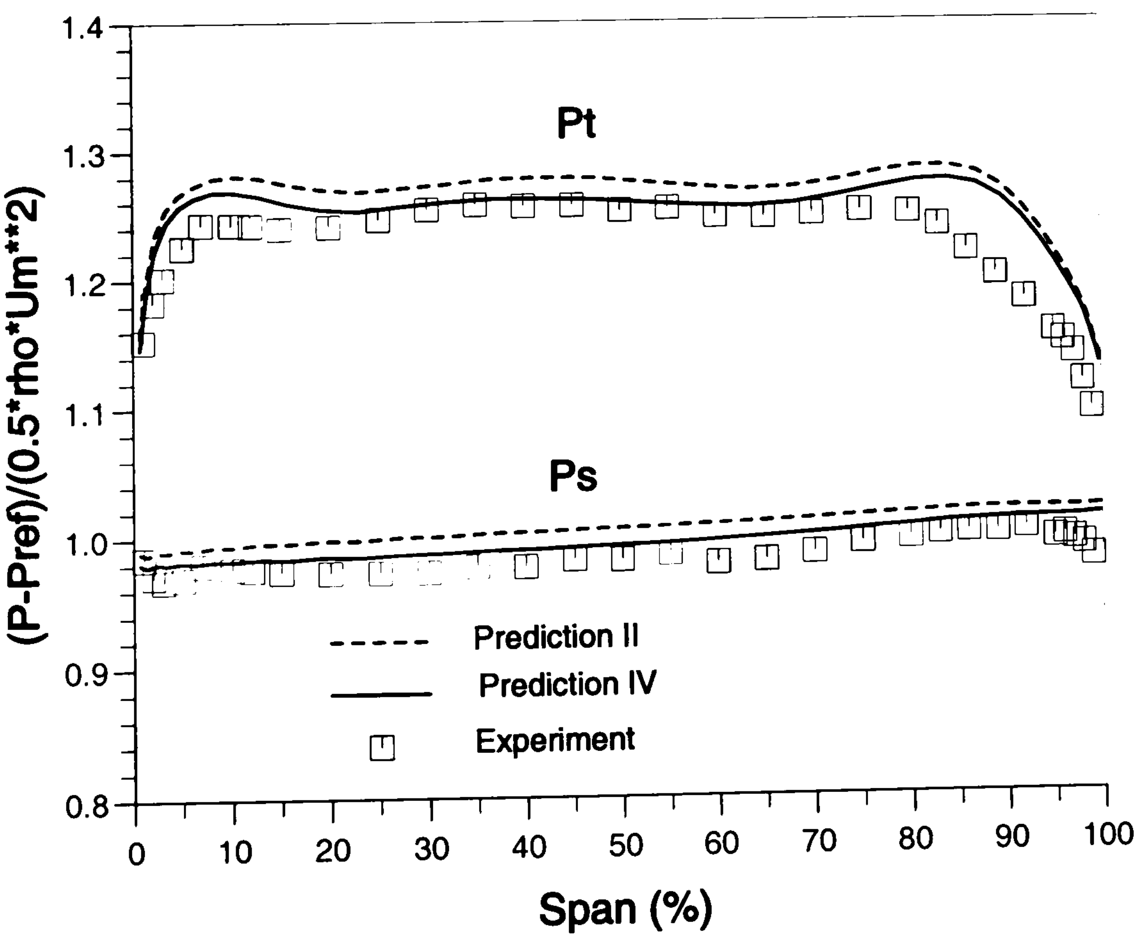

Figure 6.70: Spanwise Pt & Ps at Rotor 3 inlet from Prediction II & IV

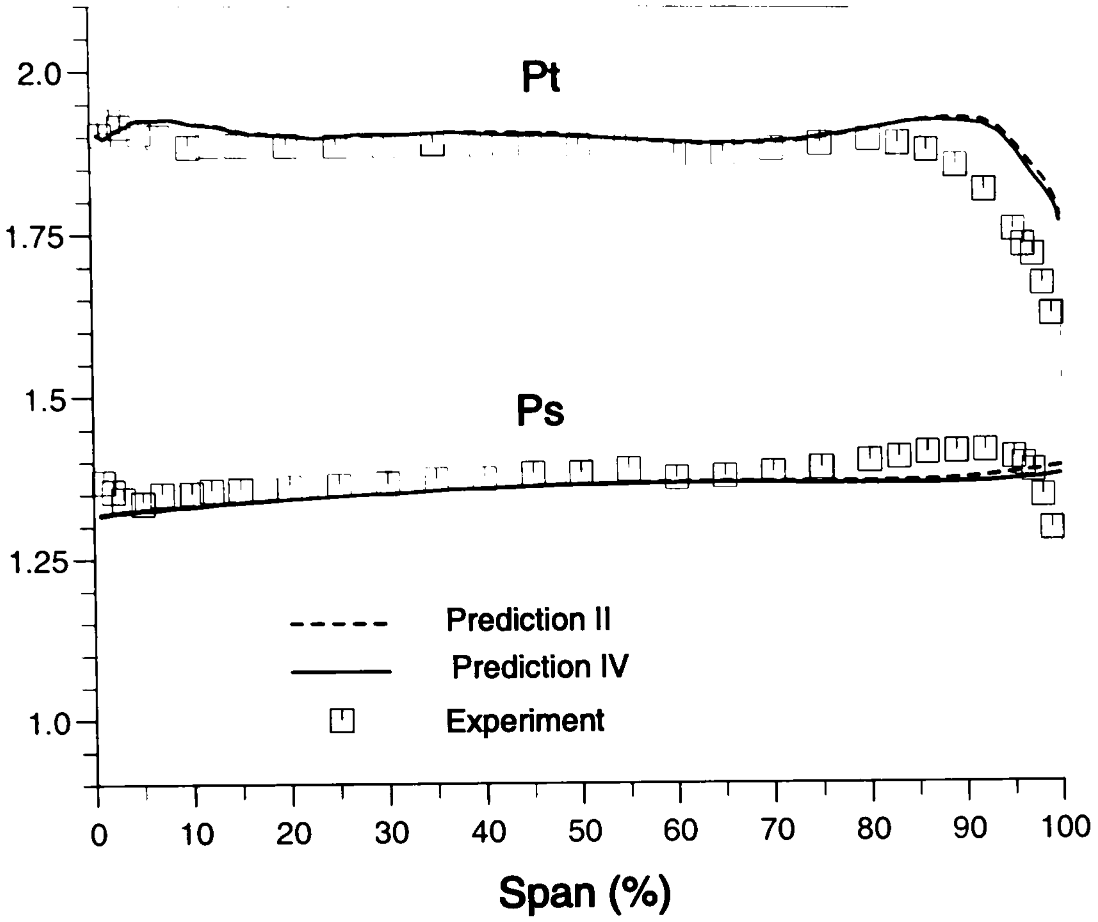

Figure 6.71: Spanwise *Pt* & *Ps* at **Rotor 3 exit from Prediction** *II* & *IV*

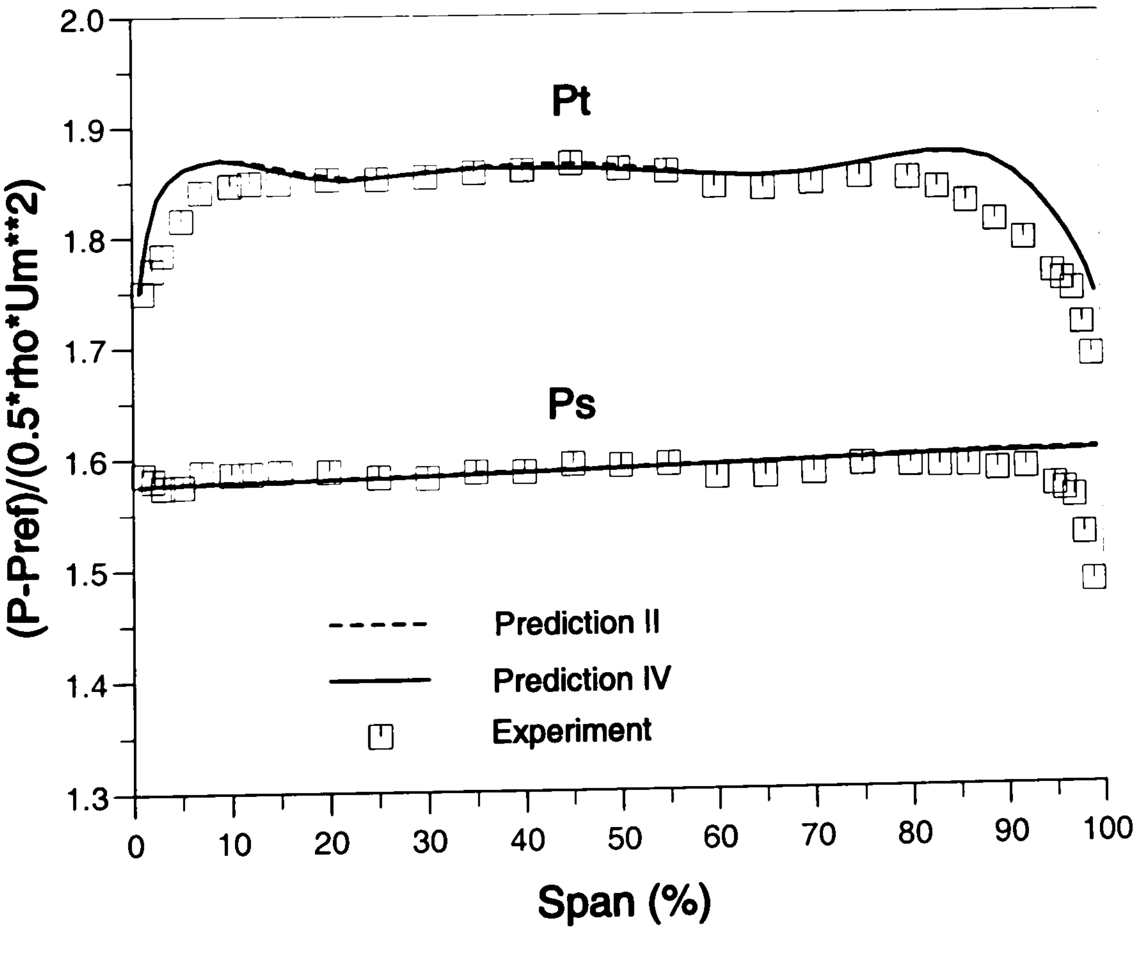

Figure 6.72: Spanwise *Pt* & *Ps* at **Stator 3 exit from Prediction** *II* & *IV*

with Prediction *II*, which shows the difference between the repeating stage models with and without deterministic stresses implemented in the governing equations. The *Computation II* provides similar result to *Computation I* and provides more details about the interaction between the flow and the blade rows.

The total and static pressure distributions along the axial direction of the third stage of *LSRC* from *Computation I* of Prediction *IV* and Prediction *II* are illustrated in Figure 6.69. Both predictions match very well with the experimental data and Prediction *IV* gives better result than Prediction *II* in the rotor upstream extension. This improvement is illustrated more clearly in Figure 6.70. The spanwise distributions of the total and static pressure at the exit of Rotor 3 and Stator 3 from Prediction *IV* is almost the same as those from Prediction *II*, which are shown in Figures 6.71 and 6.72.

The spanwise velocity distributions from Prediction *IV* and *II* are compared with the experimental data in Figures 6.73 to 6.75, which show very little difference between the two predictions.

The two predictions show very little difference in flow angle at the exit of the two blade rows. The spanwise flow angle distributions from the two predictions are almost the same at the exit of Rotor 3 and less than 1 degree difference at the exit of Stator 3, Figures 6.76 and 6.77.

The total pressure contours from Prediction *IV* at the exit of Rotor 3 and Stator 3 also show very similar distribution with those from Prediction *II*, which are shown in Figures 6.78 and 6.79, respectively. The difference between the experimental and predicted contours are discussed in Section 6.6 and will not be discussed here again.

From the comparison, it can be seen that the improvement for the current case only appears in the rotor upstream extension in terms of the static and the total pressure distributions and keep almost the same for all the parameters downstream the stage. The reasons for this may be as follows:

1. According to the distribution of circumferentially area averaged deterministic stress components, Figures 6.31 and 6.32, the significant values of deterministic stresses which are imposed on a computational domain always appear at the inlet of the domain. The magnitude of the deterministic stresses deteriorate very rapidly downstream the flow passages. Therefore the significant influence of the deterministic stress should appear in the upstream extension of a blade passage.

2. Comparing the deterministic stress components imposed on the computa-

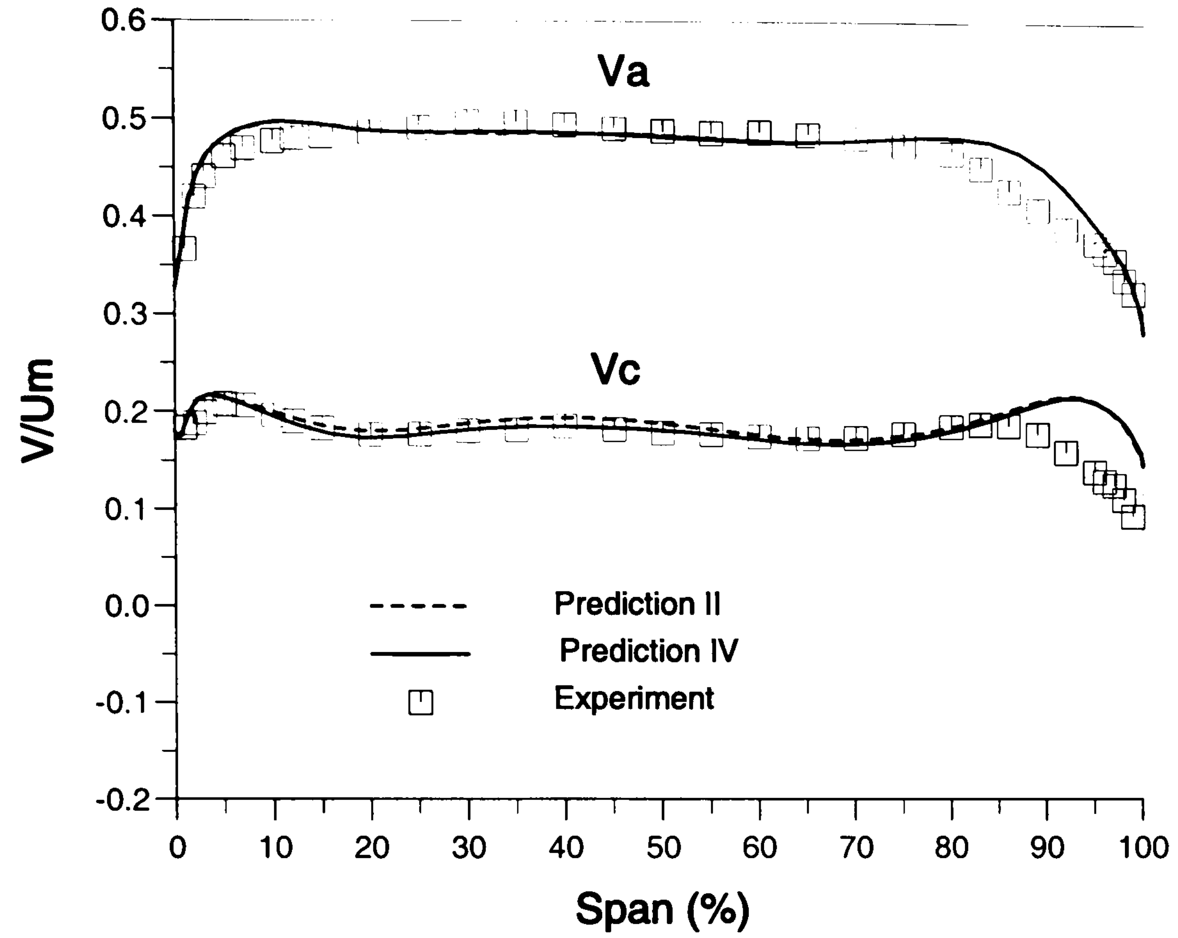

Figure 6.73: Spanwise velocity at Rotor 3 inlet from Prediction *II* & *IV*

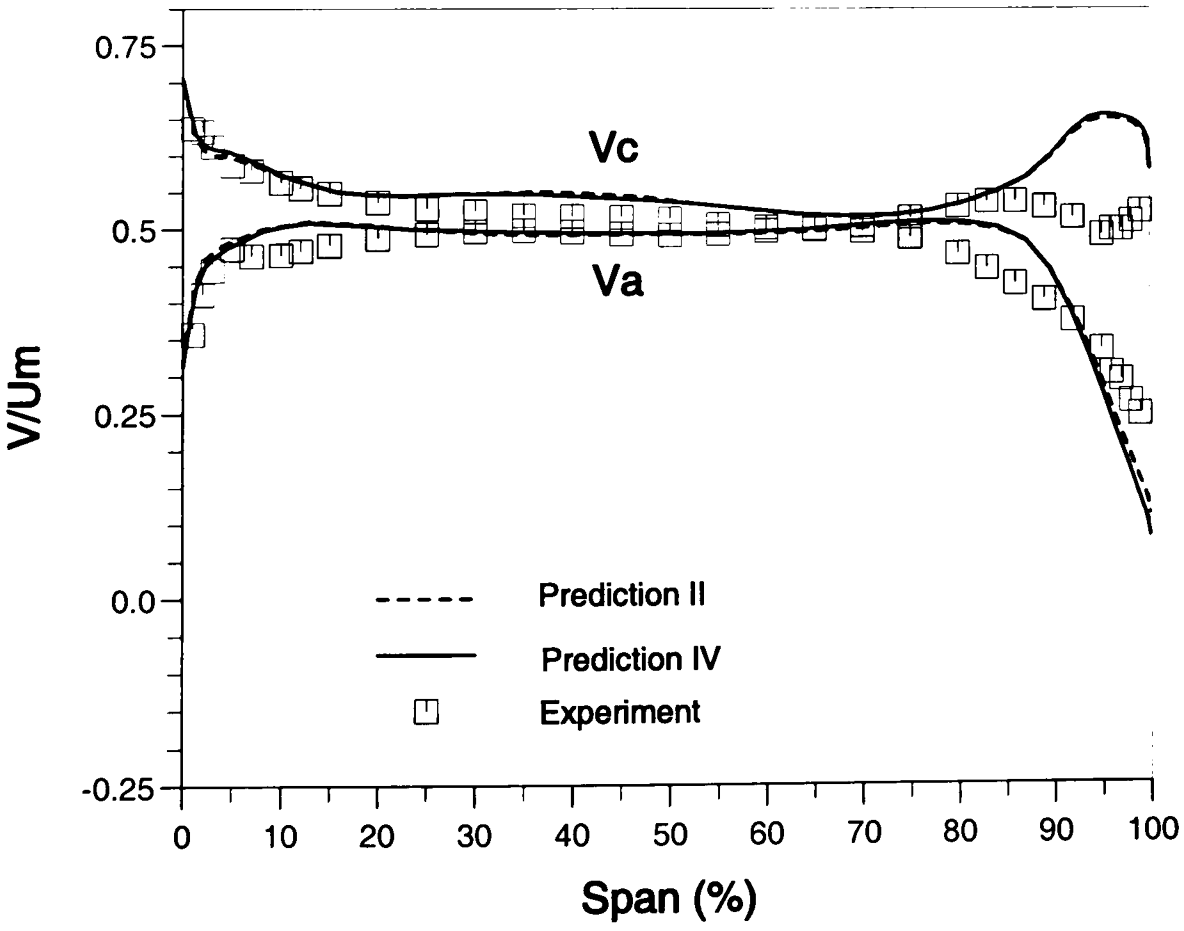

Figure 6.74: Spanwise velocity at Rotor 3 exit from Prediction *II* & *IV*

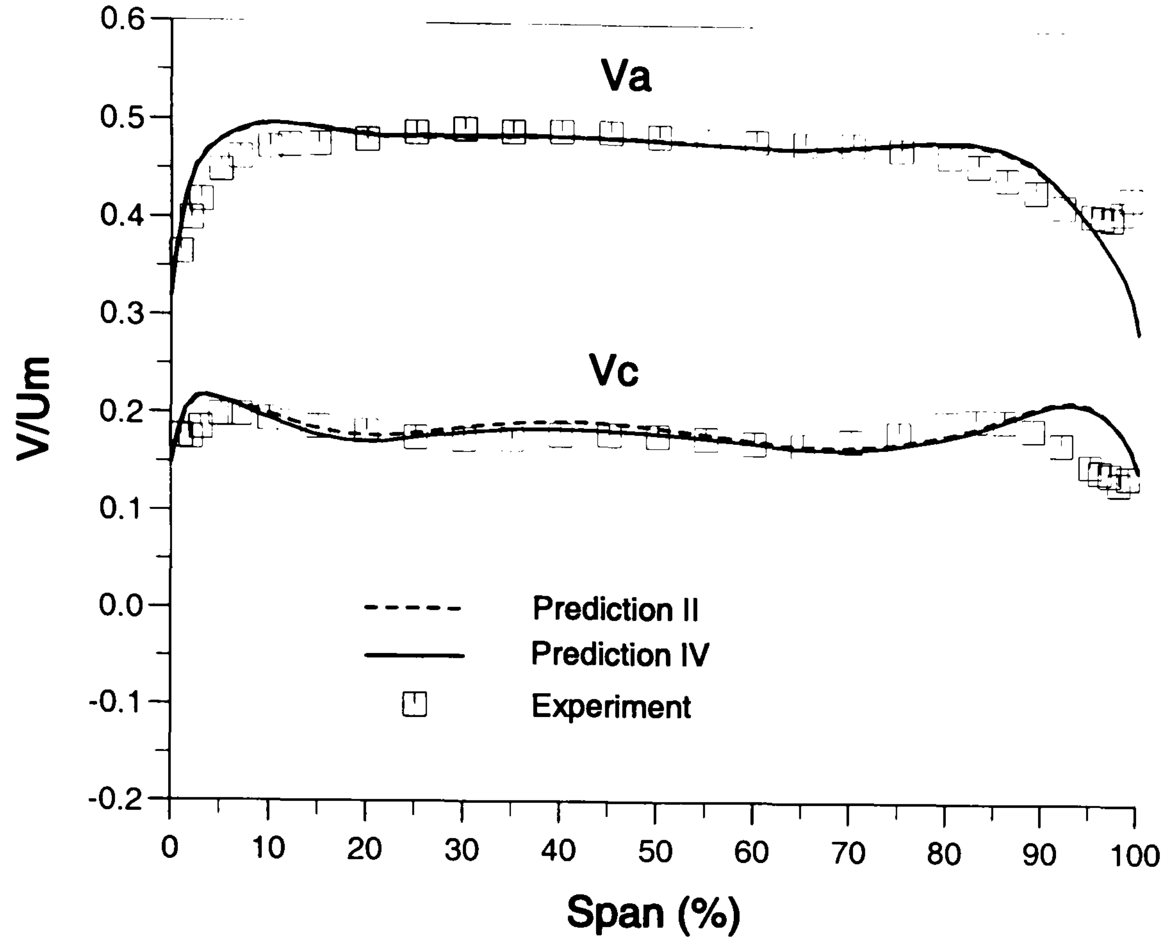

Figure 6.75: Spanwise velocity at Stator 3 exit from Prediction *II* & *IV*

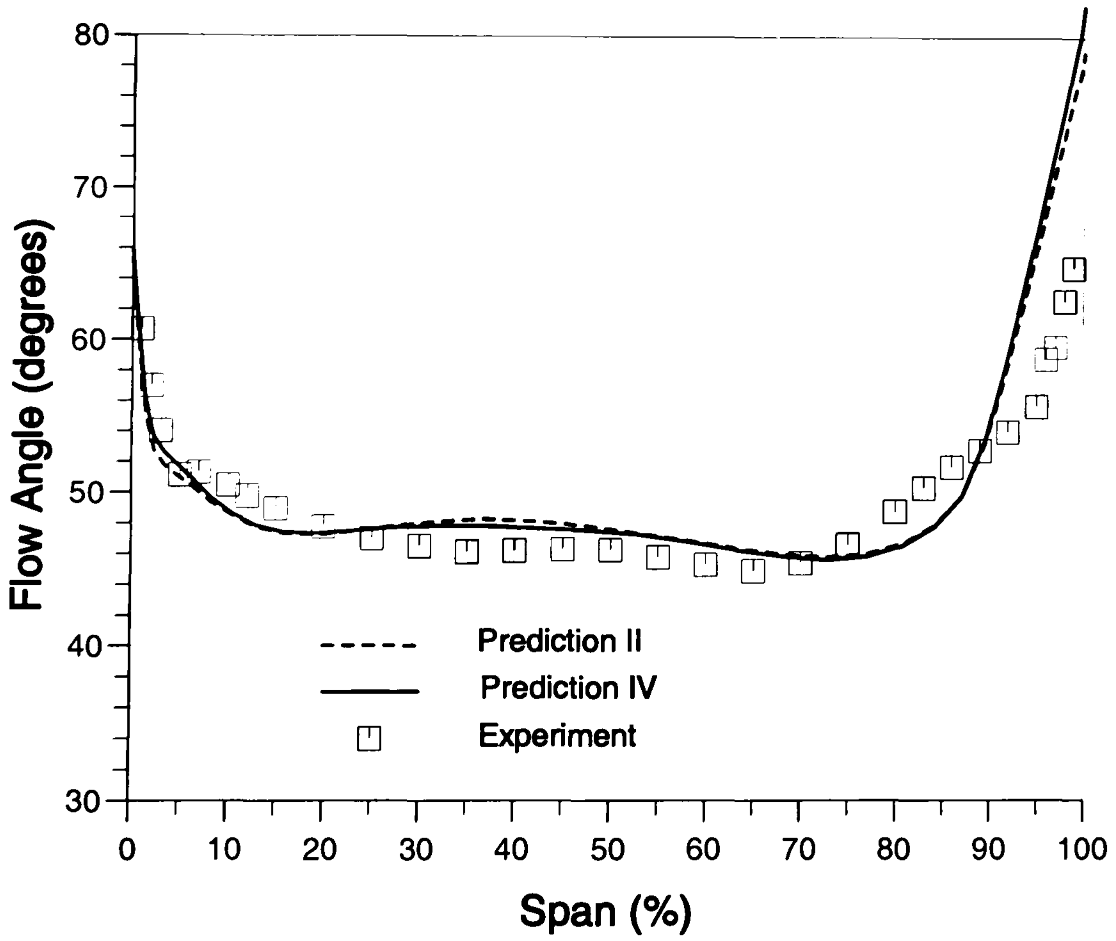

Figure 6.76: Spanwise flow angle at Rotor 3 exit from Prediction *II* & *IV*

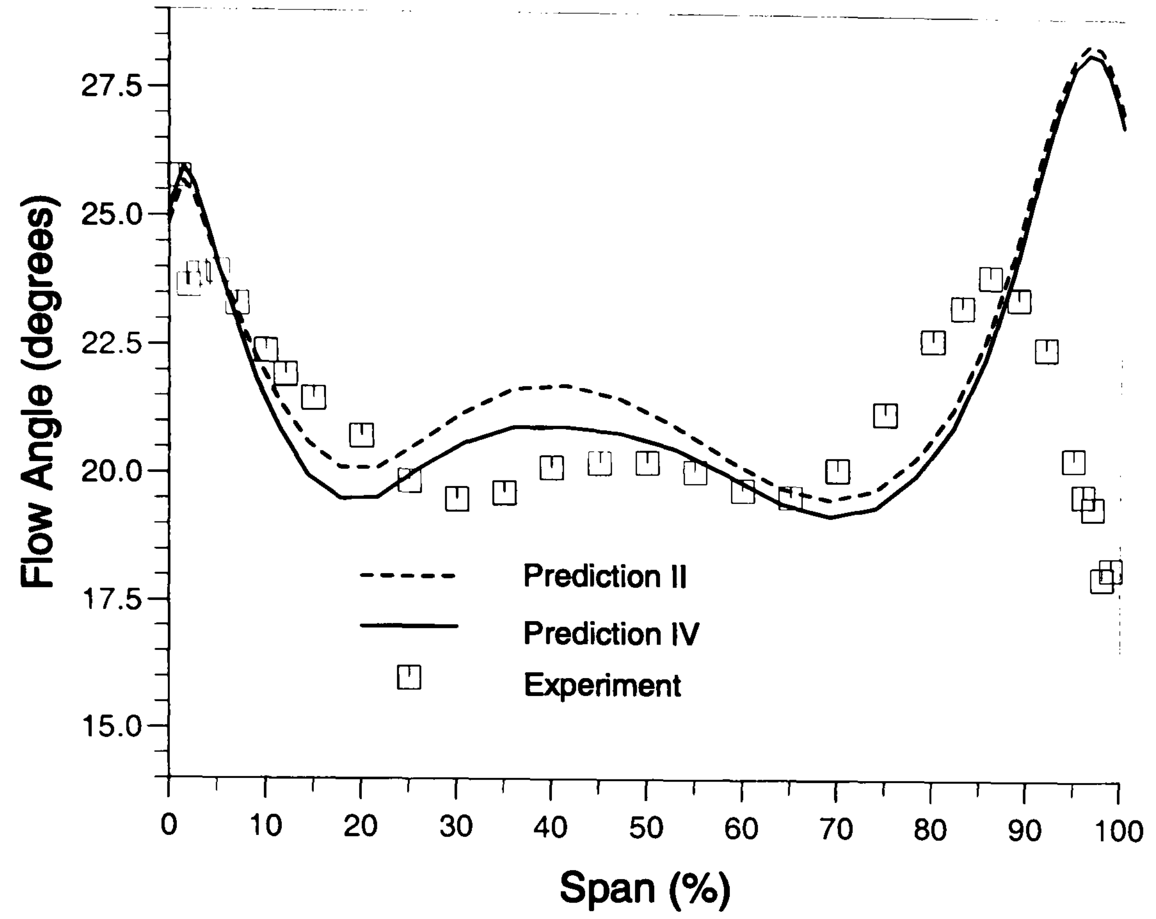

Figure 6.77: **Spanwise flow angle at Stator 3 exit from Prediction *II* & *IV***

tional domain of Rotor 3 (Figure 6.31) and the deterministic stress components imposed on the domain of Stator 3, we can see that the most significant components are $\overline{\rho\widehat{V_c}\widehat{V_c}}$, $\overline{\rho\widehat{V_c}\widehat{V_a}}$ and $\overline{\rho\widehat{V_a}\widehat{V_a}}$, and the deterministic stress field imposed on the Rotor 3 domain is comparable to that imposed on the Stator 3 domain except for the component $\overline{\rho\widehat{V_a}\widehat{V_a}}$ where the difference is about 30% in magnitude at the inlet interface between the two domains. Other deterministic stress components are much smaller and can be ignored.

3. The flow in the Stator 3 passage is less sensitive to the deterministic stresses than the Rotor 3 passage.

Based on the above comparison and analysis, it has been proven again that the deterministic stress model dose not provide significant benefits to the prediction of low speed compressors when the deterministic unsteadiness generated by neighbouring blade rows is small.

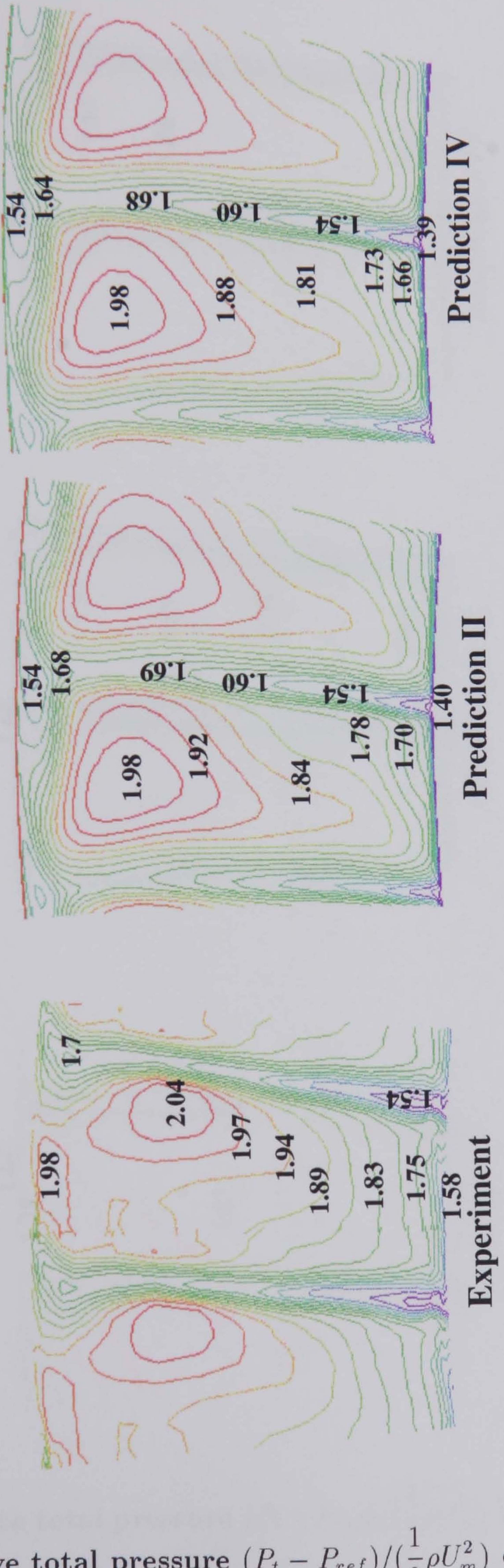

Figure 6.78: **Relative total pressure** $(P_t - P_{ref})/(\frac{1}{2}\rho U_m^2)$ **contours at Rotor 3 exit**

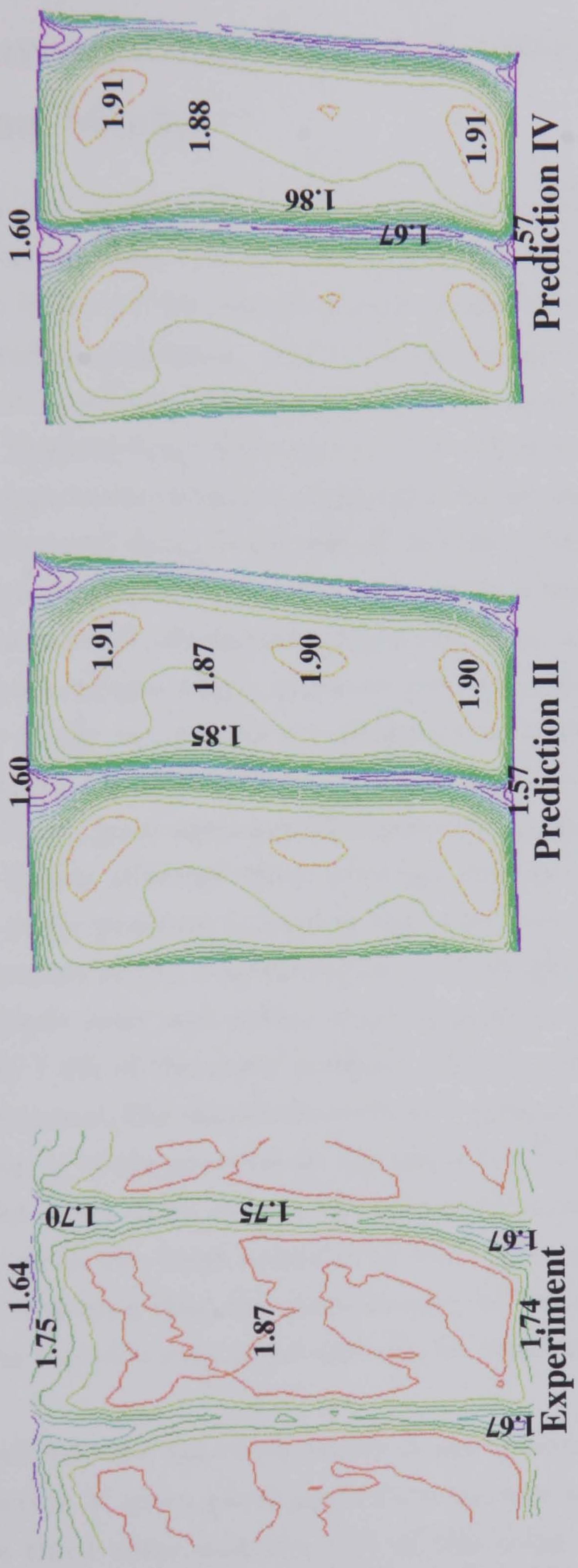

Figure 6.79: **Absolute total pressure** $(P_t - P_{ref})/(\frac{1}{2}\rho U_m^2)$ **contours at Stator 3 exit**

6.8 Prediction *V*: *LSRC* Complete Four Stages with Conventional Boundary Setting and Mixing Plane Model

In this prediction case, the flow field and the performance of the complete four stages of the Cranfield Low Speed Research Compressor (*LSRC*) are simulated. Figure 6.80 shows the layout of the computational domains for all blade rows and the setting of the boundary conditions. Mixing planes are used at the inlet and the exit of every domain of blade rows and the mixing plane model is used to transfer information between neighbouring blade rows. The velocity, k and ϵ profiles at the inlet and the average static pressure at the exit of the compressor are set to be equal to the experimental data. Local and global iterations are carried out to satisfy the convergence criteria of the governing equations and the consistency of aerodynamic parameters at all interfaces between the blade rows.

The predicted area averaged static pressure and total pressure distributions in the axial direction of the compressor are presented in Figure 6.81. Compared with the experimental data at five stations, Rotor 1 inlet and exit, Rotor 3 inlet and exit and Stator 3 exit, good agreement between the predicted results and the experimental data is shown although there are slight discrepancies. In Prediction *V* where the average static pressure is fixed at the compressor exit, the numerical error of the static pressure in the calculation are accumulated through the calculation of the whole blade rows and obtain their maximum value at the Rotor 1 inlet at approximately 1.4% of the static pressure ratio for the whole compressor. Regarding the total pressure, the maximum error also appears at Rotor 1 inlet due to the maximum error in static pressure at the same location where the velocity profile at Rotor 1 inlet is set to be exactly the same to the experimental data.

The difference between the total pressure on both sides of the mixing planes are nearly negligible, showing that the discontinuity of the momentum resulted from the mixing-plane model is very small and can be neglected at peak efficiency for the compressor.

In Figures 6.82 and 6.83 the spanwise distributions of static and total pressure are presented. Prediction *V* gives good predictions for the static pressure at the inlet and exit of the third rotor and the exit of the third stator with a slight over-estimated average value at Rotor 3 inlet and under-estimated average value at Rotor 3 exit. Due to the accumulated error in static pressure further upstream the compressor, under-estimated spanwise distributions of static pressure at Rotor

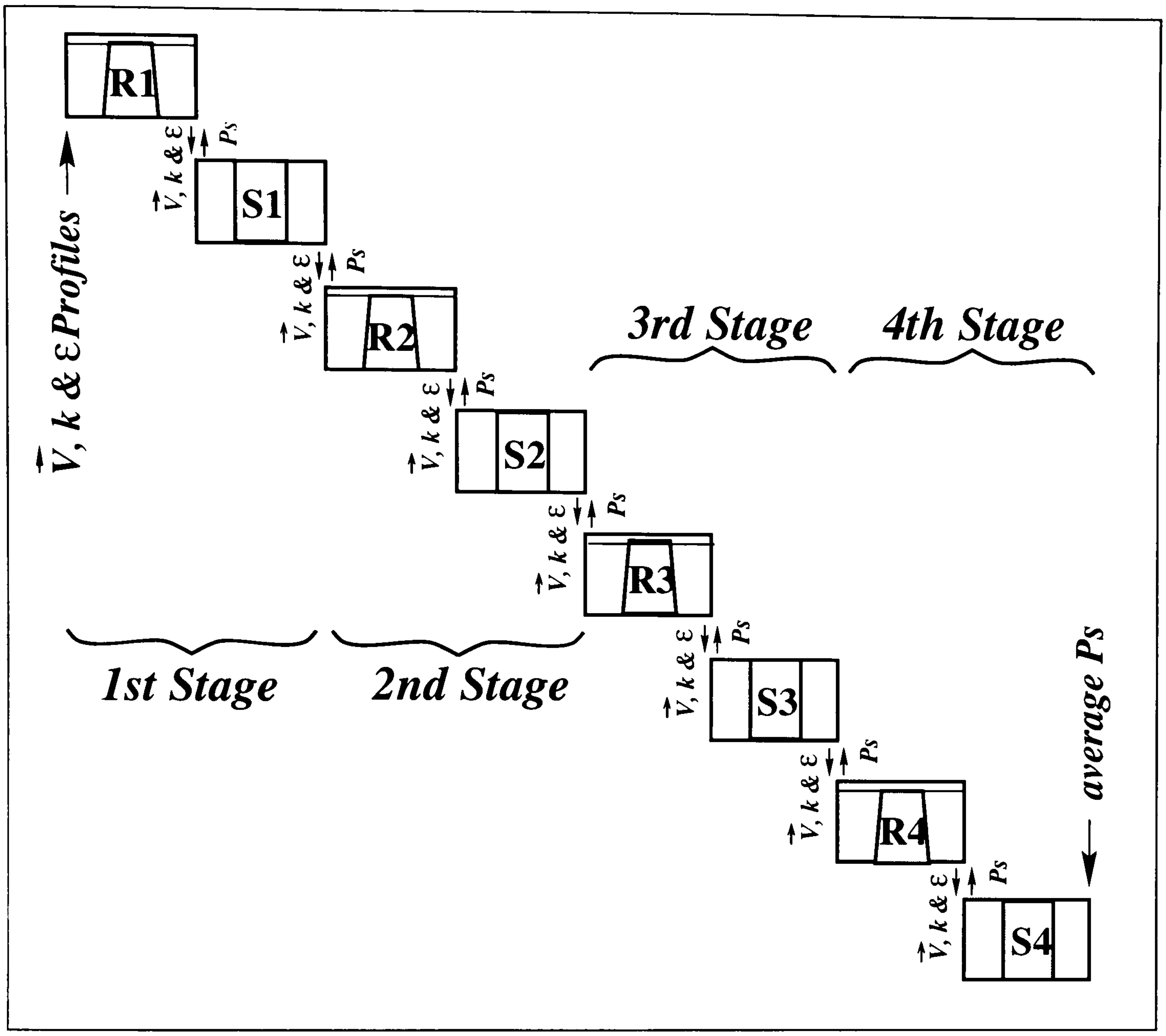

Figure 6.80: **Boundary setting for Prediction** *V*

1 inlet and exit are obvious, which can also be seen in Figure 6.81. This error in static pressure also contributes to the error in total pressure at the same location, Figure 6.83. The sudden changes of experimental static pressure near the walls are not physical and susceptible to measurement error due to the presence of the solid walls (Howard et al. [88]). Hence, the difference in static pressure between experiment and prediction near the blade tip should not be as large as shown in Figures 6.82. The spanwise total pressure distribution at Rotor 3 inlet and exit and Stator 3 exit match very well with the experimental ones in the area between 0% to 85% blade height. The over-prediction in total pressure in the area between 85% to 100% blade span are very likely due to the inaccurate prediction of the rotor tip clearance flows, which can also be seen in Prediction *I*.

The calculated spanwise distribution of velocity components from Prediction *V*

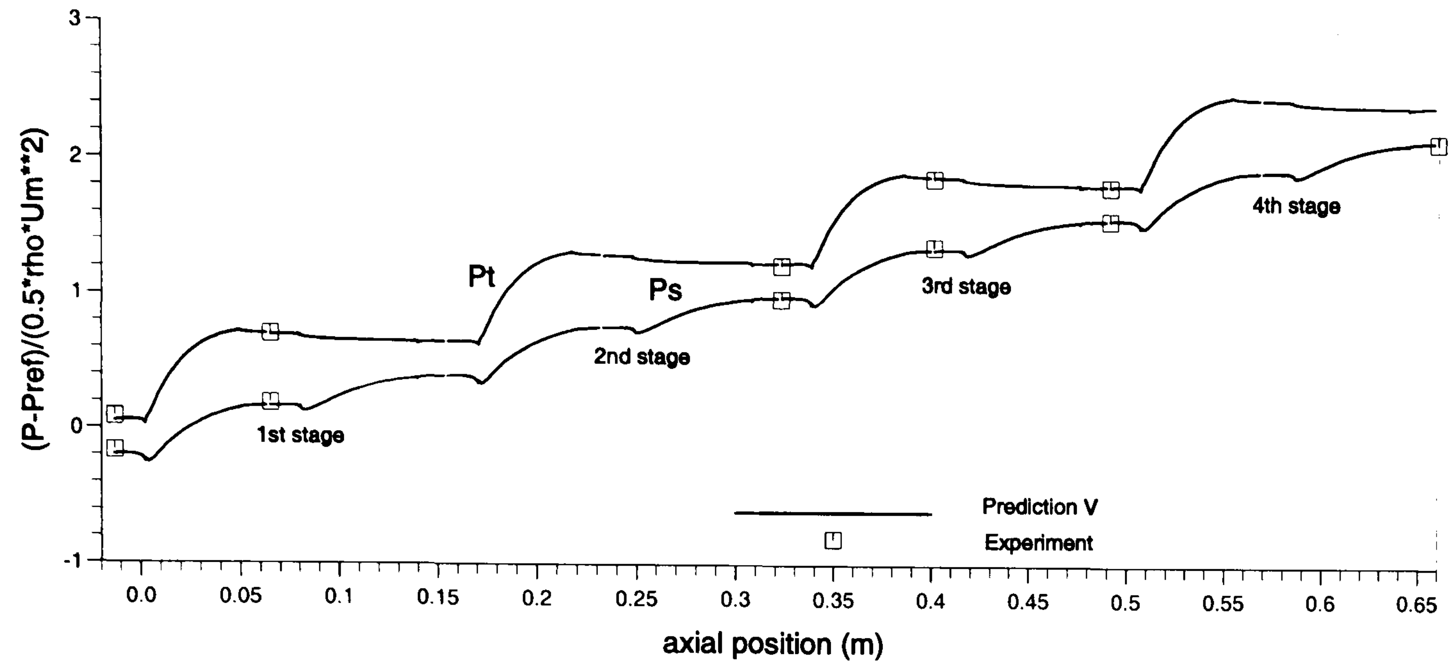

Figure 6.81: **Axial *Pt* & *Ps* distribution from Prediction *V***

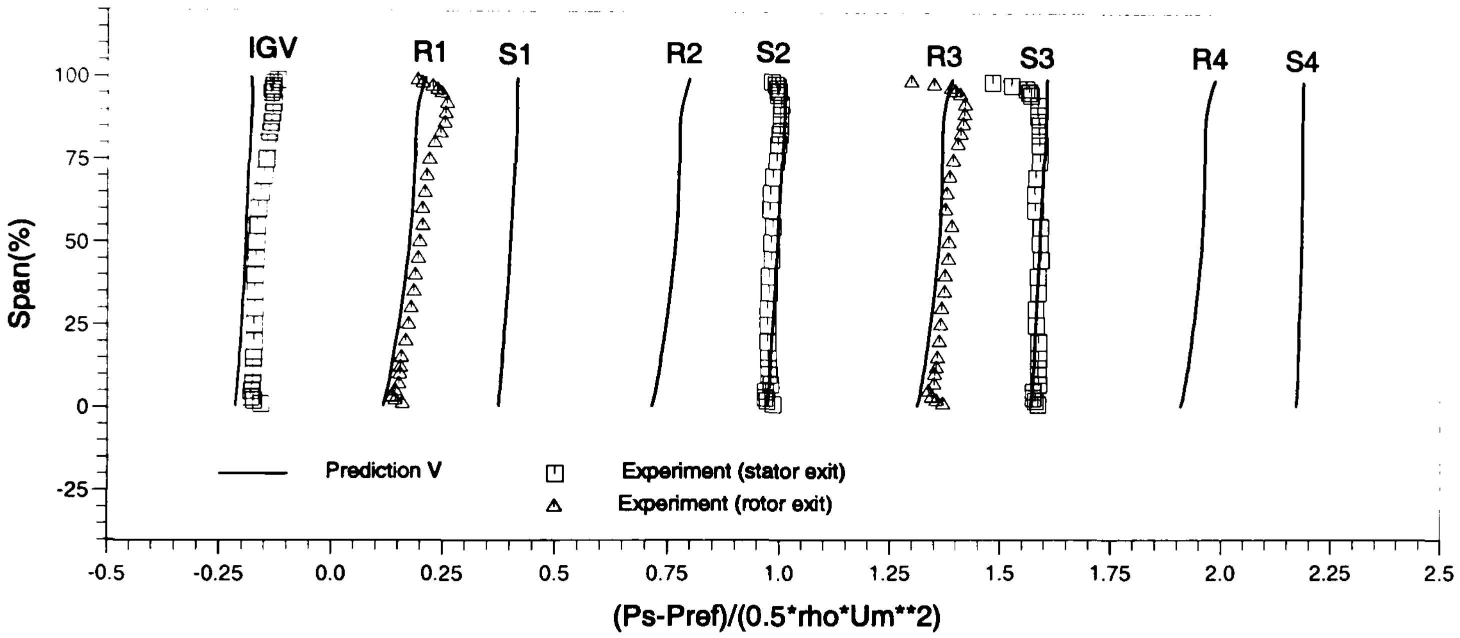

Figure 6.82: **Spanwise *Ps* at exit of LSRC blade rows**

at Rotor 1 exit, Rotor 3 inlet and exit and Stator 3 exit match very well with the experimental data for most part of the blade span although with some discrepancies in the area between 80% and 100% span near the blade tip, Figure 6.85 to 6.88. These discrepancies are very likely due to the numerical inaccuracies in resolving the complex, tip clearance flows.

The above mentioned inaccurate flow prediction in rotor tip clearances also contribute to the discrepancy of the flow angle near the tip, which are illustrated in Figures 6.89 to 6.92 and are of about the same accuracy to that in other prediction cases.

The total pressure contours at Rotor 3 exit and Stator 3 exit are compared with the experimental total pressure contours in Figures 6.93 to 6.94. These predicted

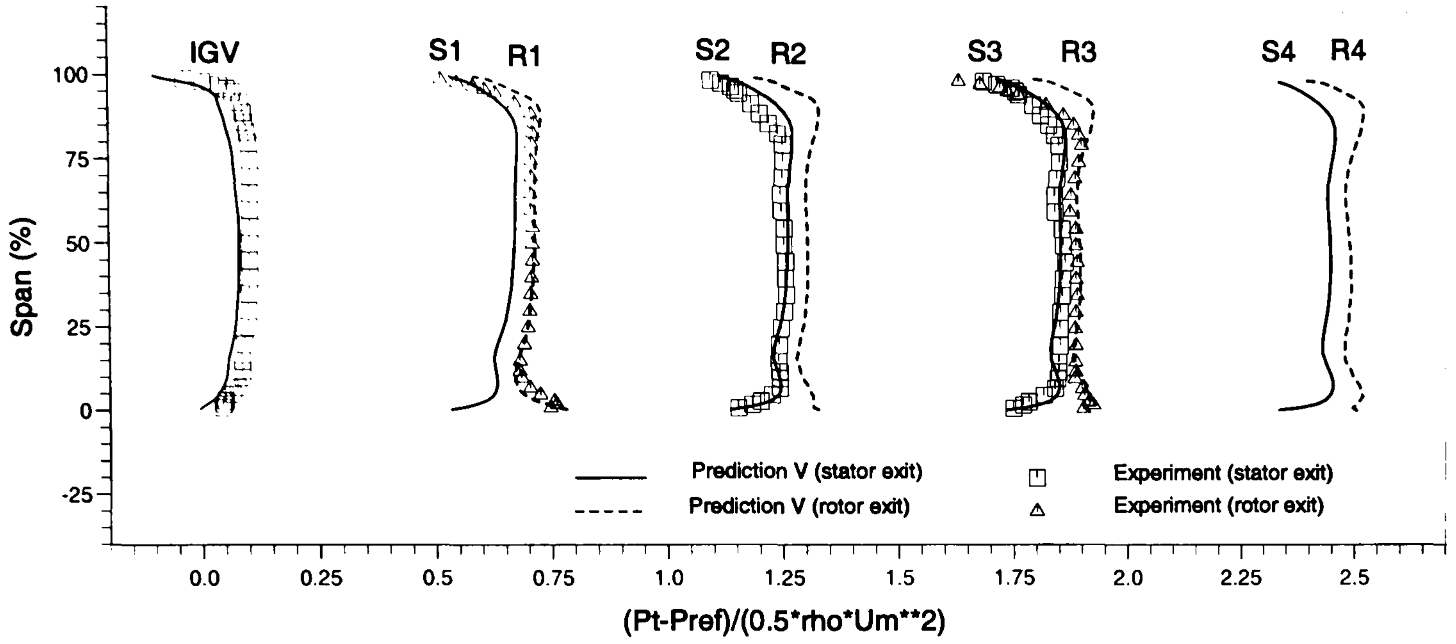

Figure 6.83: Spanwise Pt at exit of LSRC blade rows

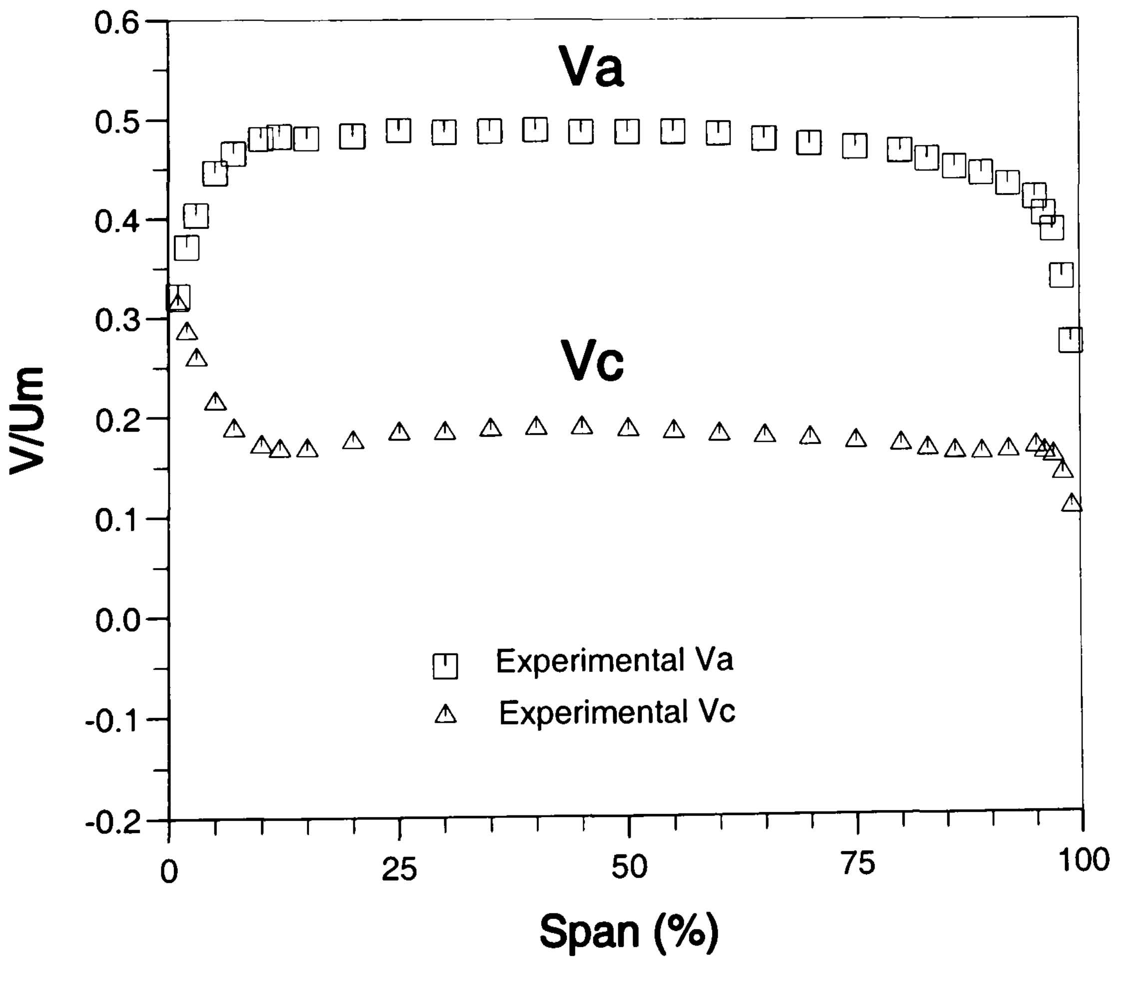

Figure 6.84: Spanwise velocity at IGV exit from Prediction V

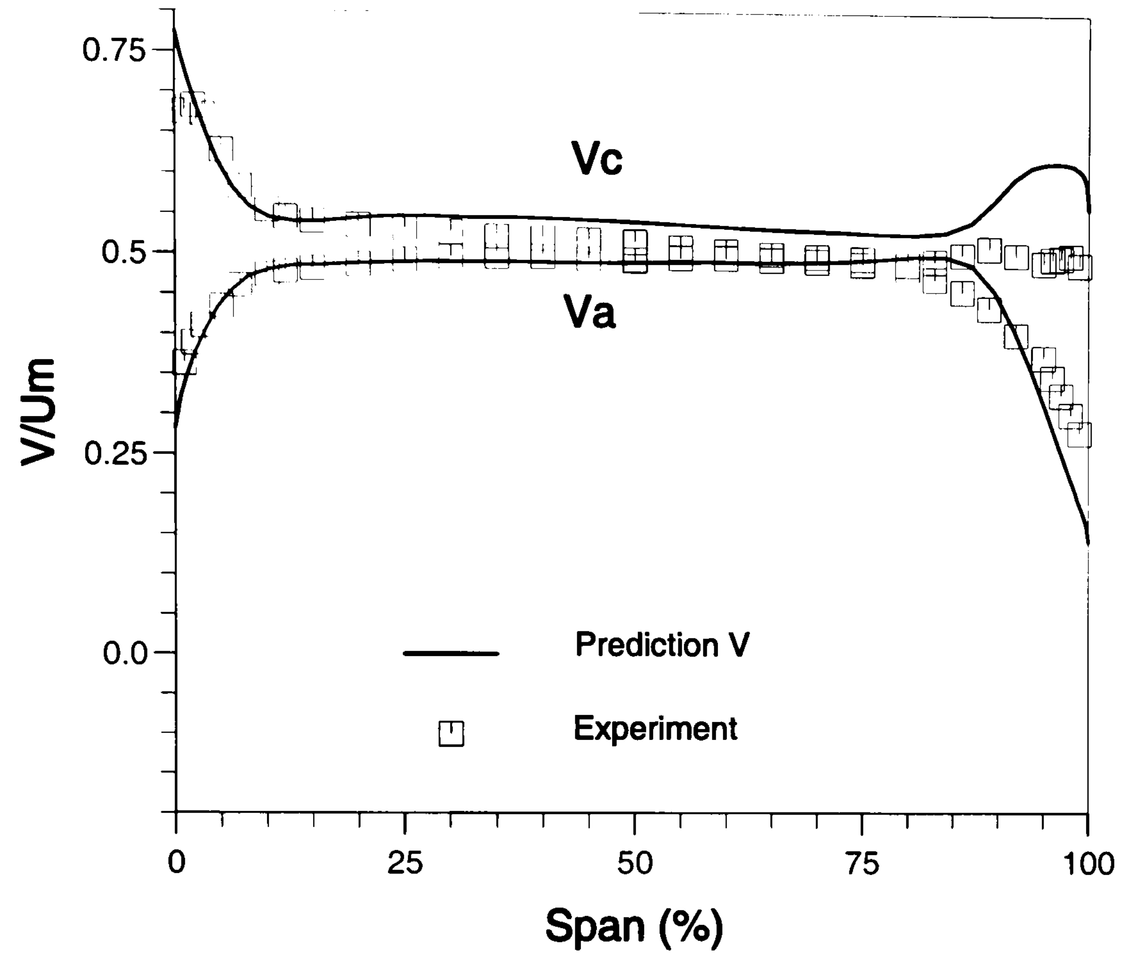

Figure 6.85: Spanwise velocity at Rotor 1 exit from Prediction *V*

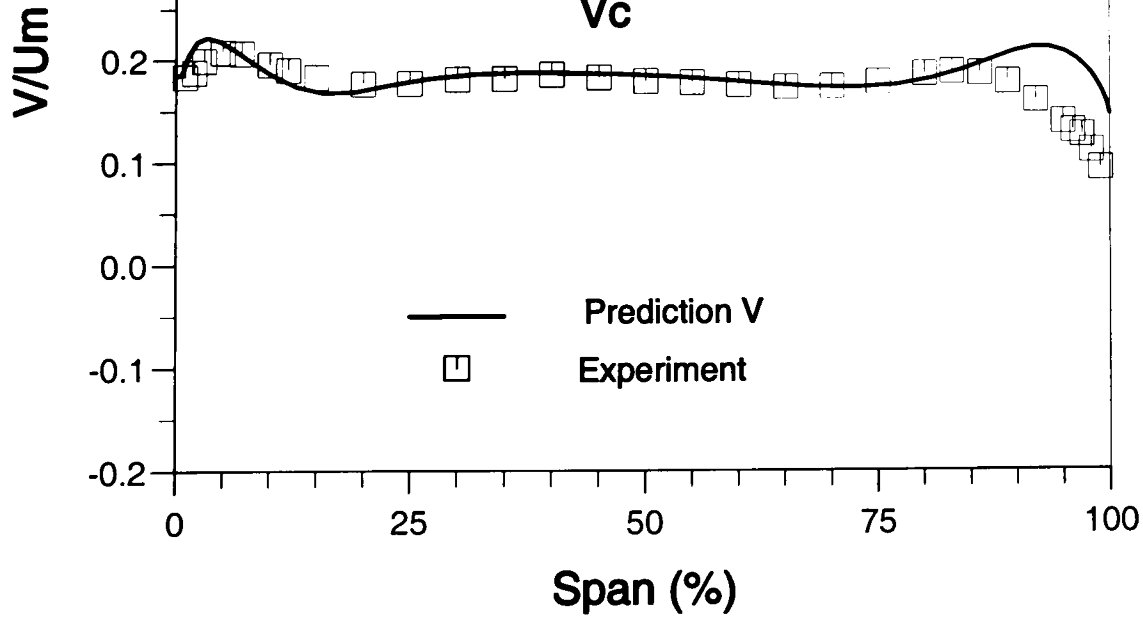

Figure 6.86: Spanwise velocity at Stator 2 exit from Prediction *V*

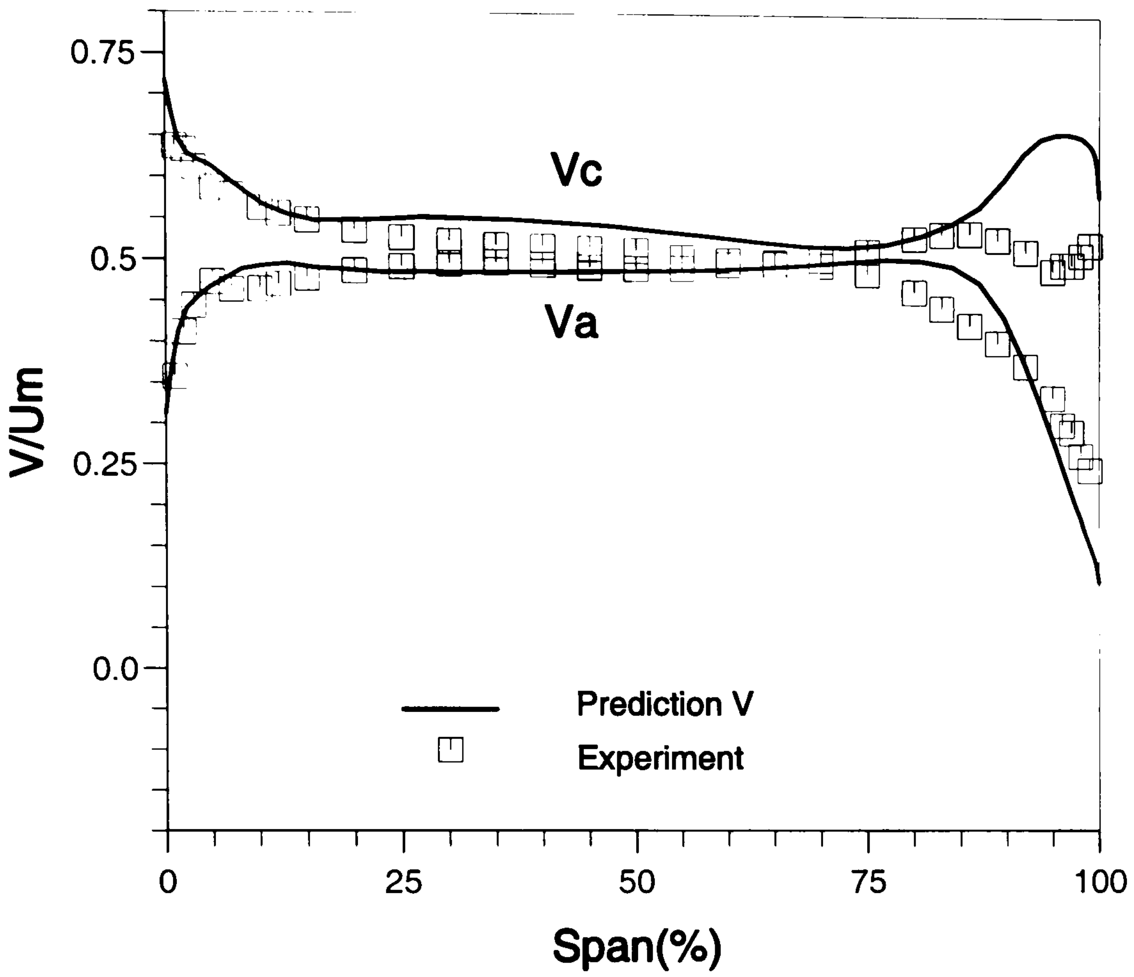

Figure 6.87: Spanwise velocity at Rotor 3 exit from Prediction V

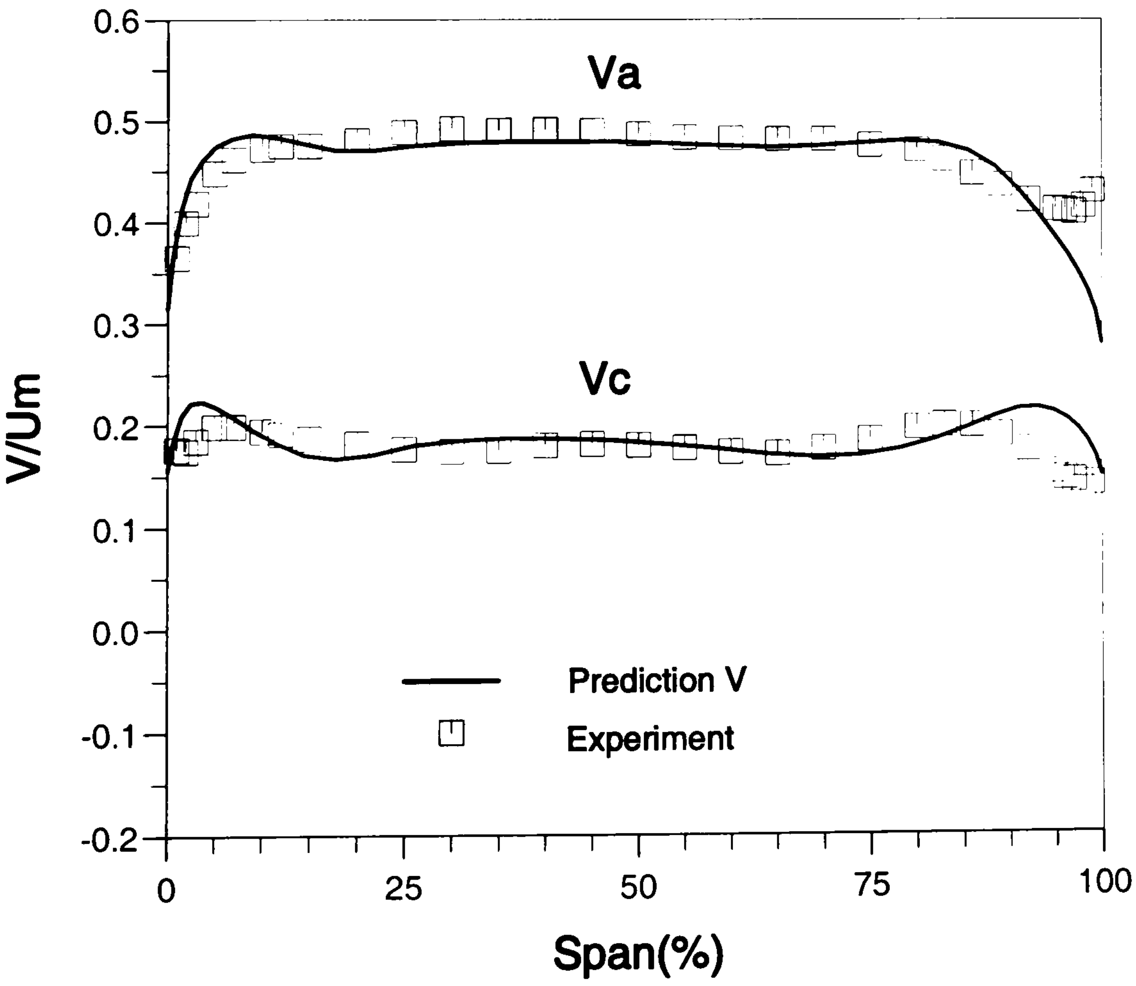

Figure 6.88: Spanwise velocity at Stator 3 exit from Prediction V

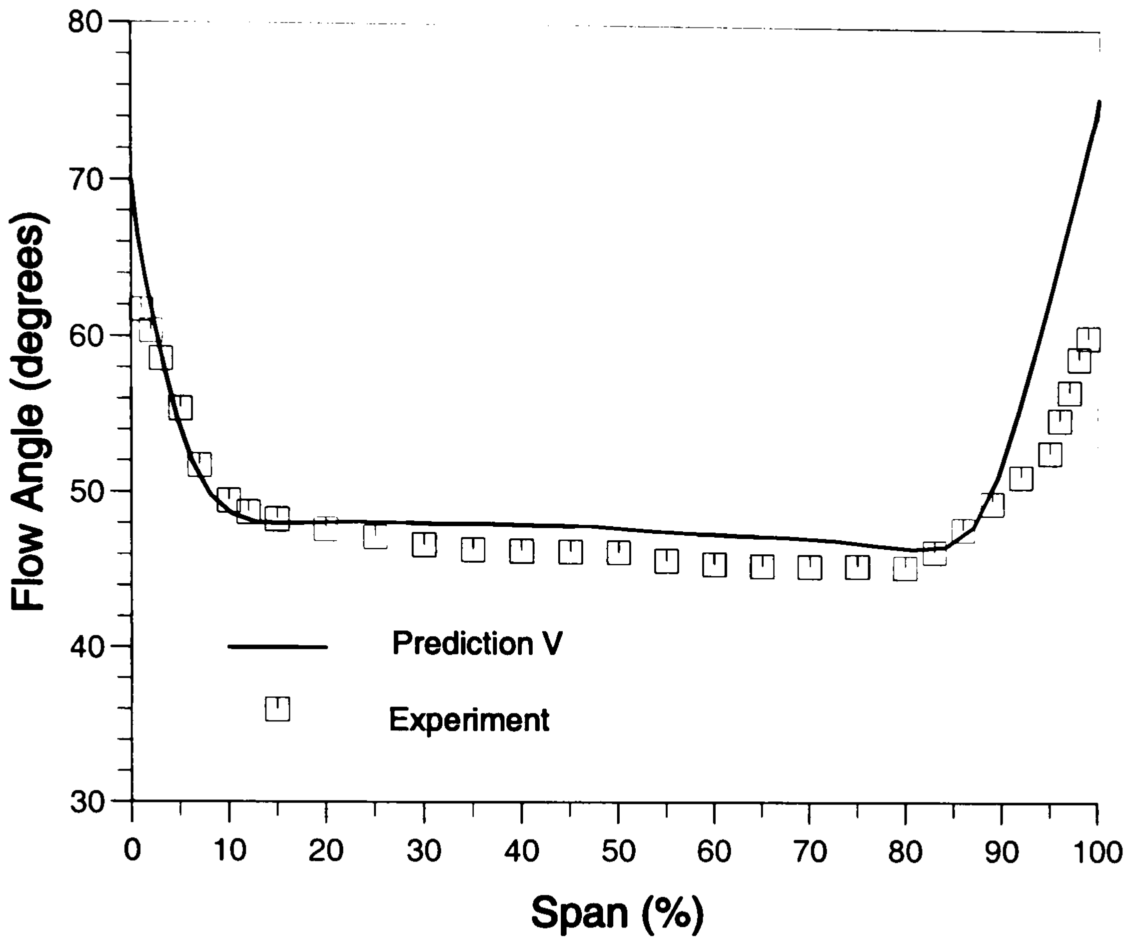

Figure 6.89: Spanwise flow angle at Rotor 1 exit from Prediction *V*

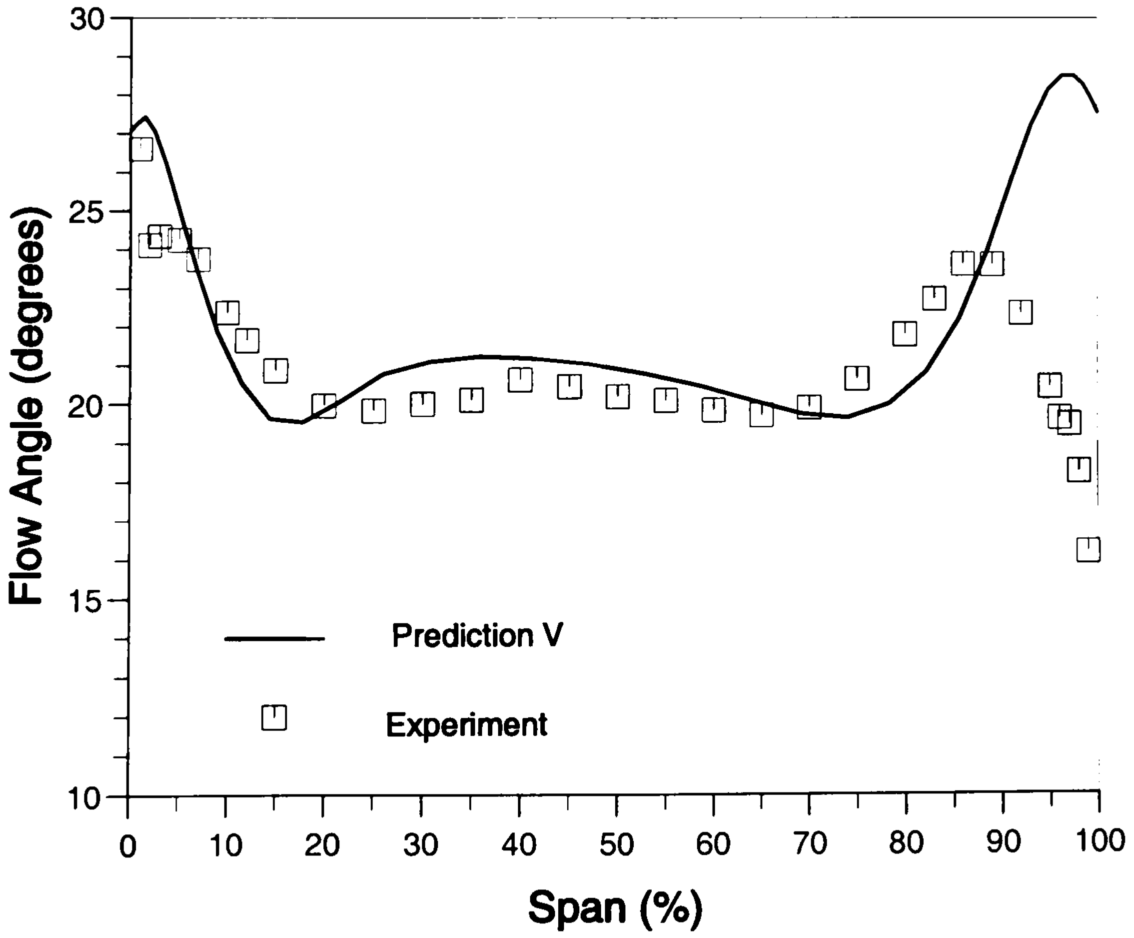

Figure 6.90: Spanwise flow angle at Stator 2 exit from Prediction *V*

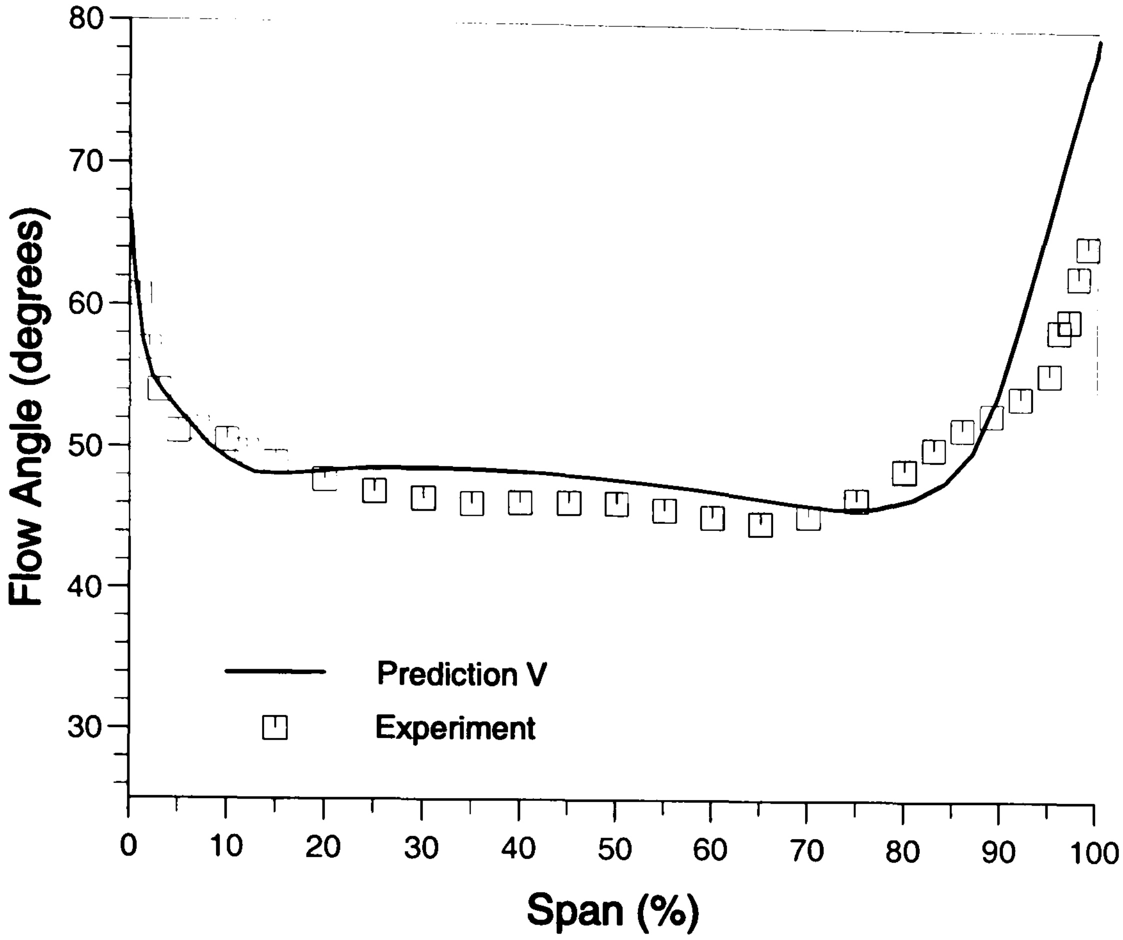

Figure 6.91: Spanwise flow angle at Rotor 3 exit from Prediction *V*

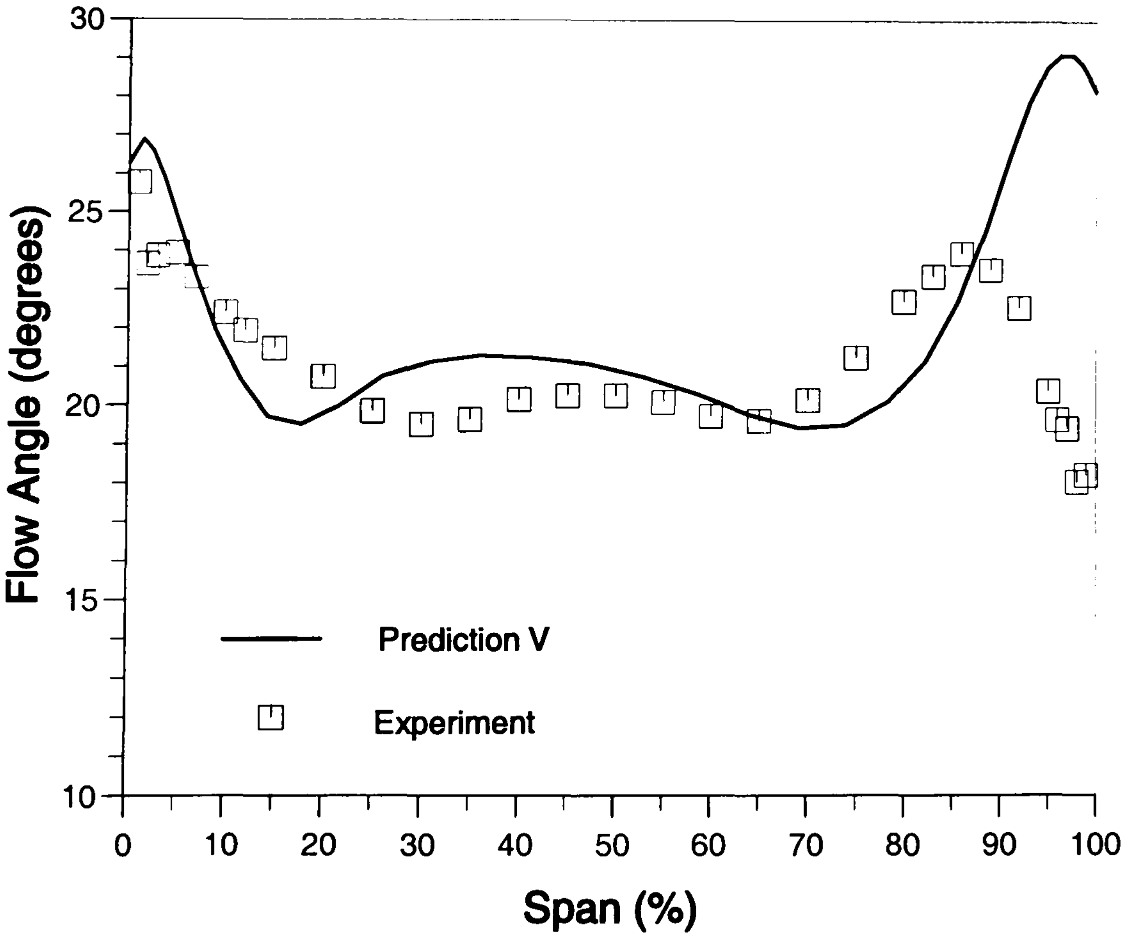

Figure 6.92: Spanwise flow angle at Stator 3 exit from Prediction *V*

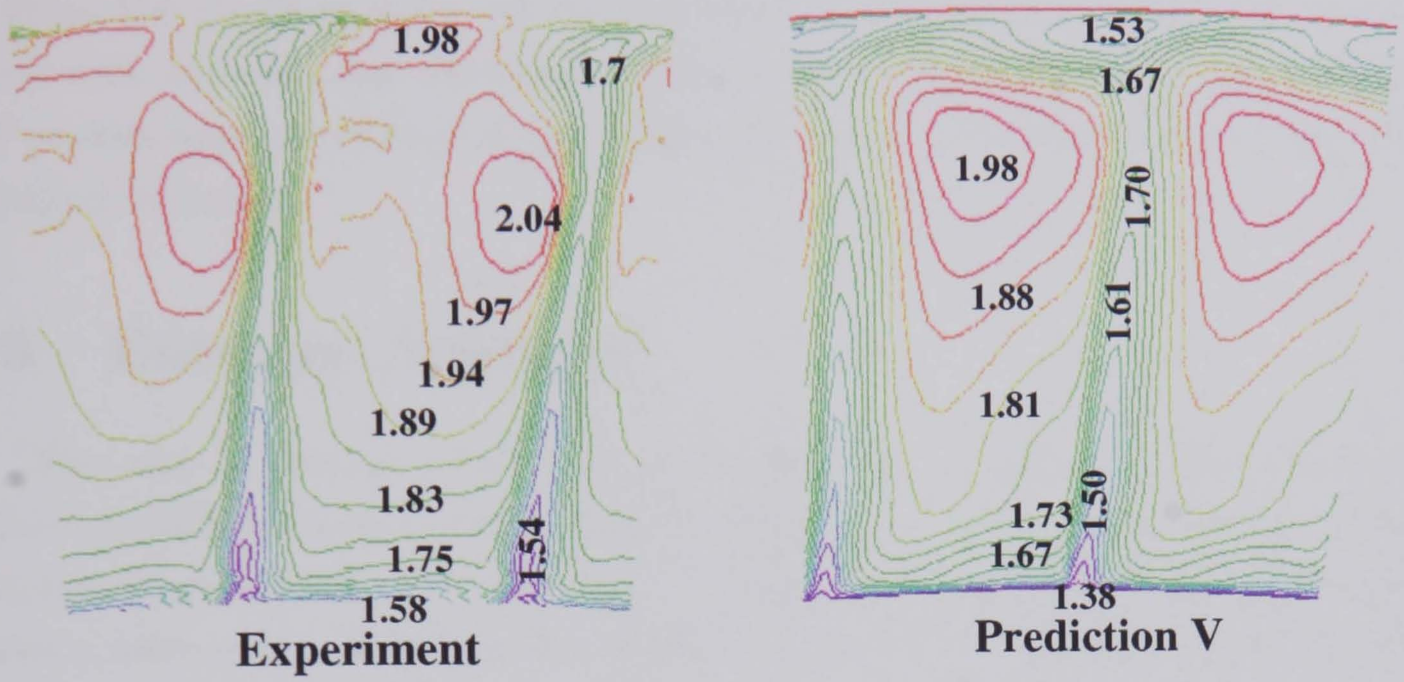

Experiment **Prediction V**

Figure 6.93: **Relative total pressure** $(P_t - P_{ref})/(\frac{1}{2}\rho U_m^2)$ **contours at Rotor 3 exit**

Experiment **Prediction V**

Figure 6.94: **Absolute total pressure** $(P_t - P_{ref})/(\frac{1}{2}\rho U_m^2)$ **contours at Stator 3 exit**

contours are more or less the same with those from Prediction *I* which is a similar prediction case, therefore the detailed analysis is not discussed any further.

From the above analysis, we can conclude that the mixing plane model combined with conventional boundary setting is an effective approach for the flow and performance prediction of multistage low speed axial flow compressors with satisfying accuracy.

6.9 Entropy Analysis

The rate of entropy generation is a parameter to measure the significance of irreversibilities related to heat transfer, friction, and other nonidealities within systems, Sciubba [154]. The analysis of entropy generation inside turbomachinery allows a more exact understanding of losses in the flow path than is possible with traditional methods involving the application of empirical correlations.

With the first law of thermodynamics and the governing equations of flows (i.e. the continuity, momentum and energy equations), an entropy equation can be derived (see Appendix F) and is expressed as follows:

$$\nabla \cdot (\rho \vec{V} s) = \frac{1}{T}\varepsilon_\nu - \frac{1}{T}(\nabla \cdot \vec{q}) \tag{6.2}$$

where ε_ν is a non-negative dissipation term which behaves as a non-reversible heat source and may be expressed by the product of the viscous stress tensor τ and the rate of deformation $(\nabla \cdot \vec{V})$:

$$\varepsilon_\nu = \tau \cdot (\nabla \cdot \vec{V}) = \tau_{ij}\frac{\partial v_i}{\partial x_j} \qquad (i,j = 1,2,3) \tag{6.3}$$

where

$$\tau_{ij} = \mu_T \left[\left(\frac{\partial v_i}{\partial x_j} + \frac{\partial v_j}{\partial x_i} \right) - \frac{2}{3}\delta_{ij}\frac{\partial v_k}{\partial x_k} \right] \qquad (i,j = 1,2,3)$$

The heat flux may be expressed as:

$$\vec{q} = -k(\nabla T)$$

The entropy equation (6.2) states that the difference between the rate flow of entropy out of a fluid element and into the element equals the rate of entropy generation inside the element either from the dissipation of mechanical energy into entropy (loss work) or the dissipation of thermal energy into entropy (loss heat).

For adiabatic flows ($k = 0$), the entropy equation becomes:

$$\nabla \cdot (\rho \vec{V} s) = \frac{1}{T}\left[\tau \cdot (\nabla \cdot \vec{V})\right] \tag{6.4}$$

or

$$\nabla \cdot (\rho \vec{V} s) = \frac{1}{T}\varepsilon_{\nu} \tag{6.5}$$

It can be seen from Equation (6.5) that the entropy increase in a fluid element in adiabatic flows is due to the non-reversible heat source generated by viscous and turbulent stresses. The right hand side of the entropy equation (6.5) is actually the local entropy generation rate s', which can be calculated based on available flow field as follows:

$$s' = \frac{1}{T}\varepsilon_{\nu} = \frac{1}{T}\tau_{ij}\frac{\partial v_i}{\partial x_j} \qquad (i, j = 1, 2, 3) \tag{6.6}$$

The entropy generation rate inside the blade passage of the third stage of the Cranfield *LSRC* can be calculated from the predicted flow field, for example from Prediction *I*. The distribution of entropy generation rate in both Rotor 3 and Stator 3 passages are illustrated in Figures 6.95 to 6.100, where blade-to-blade views at different blade heights and cross plane views at different axial positions are shown. It can be seen that large entropy generation rate appears in the areas with large velocity gradient, such as those near solid boundaries especially near blade leading and trailing edges, in the areas near blade suction surfaces with flow separations and in the downstream area of blade trailing edges where strong wakes exist. Unfortunately, the predicted large value of entropy generation rate near blade leading edge is not physical and is due to the incorrect prediction of large value of turbulence in that area with the two-equation turbulence model.

Relative total pressure is another parameter to assess the efficiency of the flow inside the machine. As a comparison to the entropy generation rate, the total pressure distribution in relative frame of reference at the same locations are also plotted in Figures 6.101 to 6.106. The distribution of relative total pressure shows that in most area where there is large entropy generation rate the relative total pressure is low and vice versa.

With the obtained entropy generation rate, the increase of entropy in axial direction in both Rotor 3 and Stator 3 can be calculated through the following integration:

$$S = S_{ref} + N * \sum_{k=1}^{nz}\left[\sum_{i=1}^{I}\sum_{j=1}^{J}\left(\rho \bigtriangleup V_{ijk} s'_{ijk}\right)\right] \quad (nz \leq K) \tag{6.7}$$

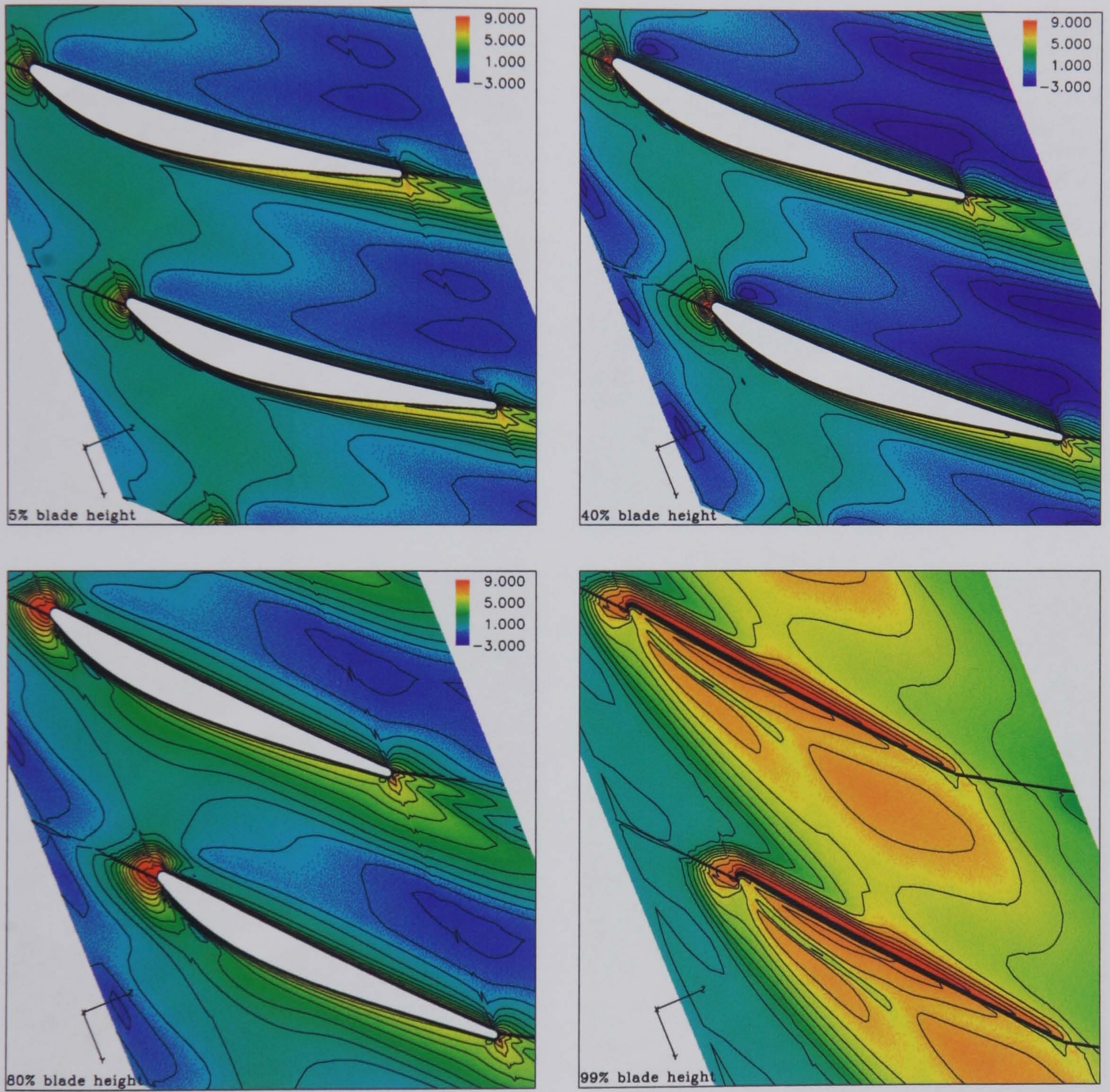

Figure 6.95: **Distribution of entropy generation rate** $\ln(s')$ **at blade-to-blade surfaces at different blade height from Prediction** I **(Rotor 3 domain)**

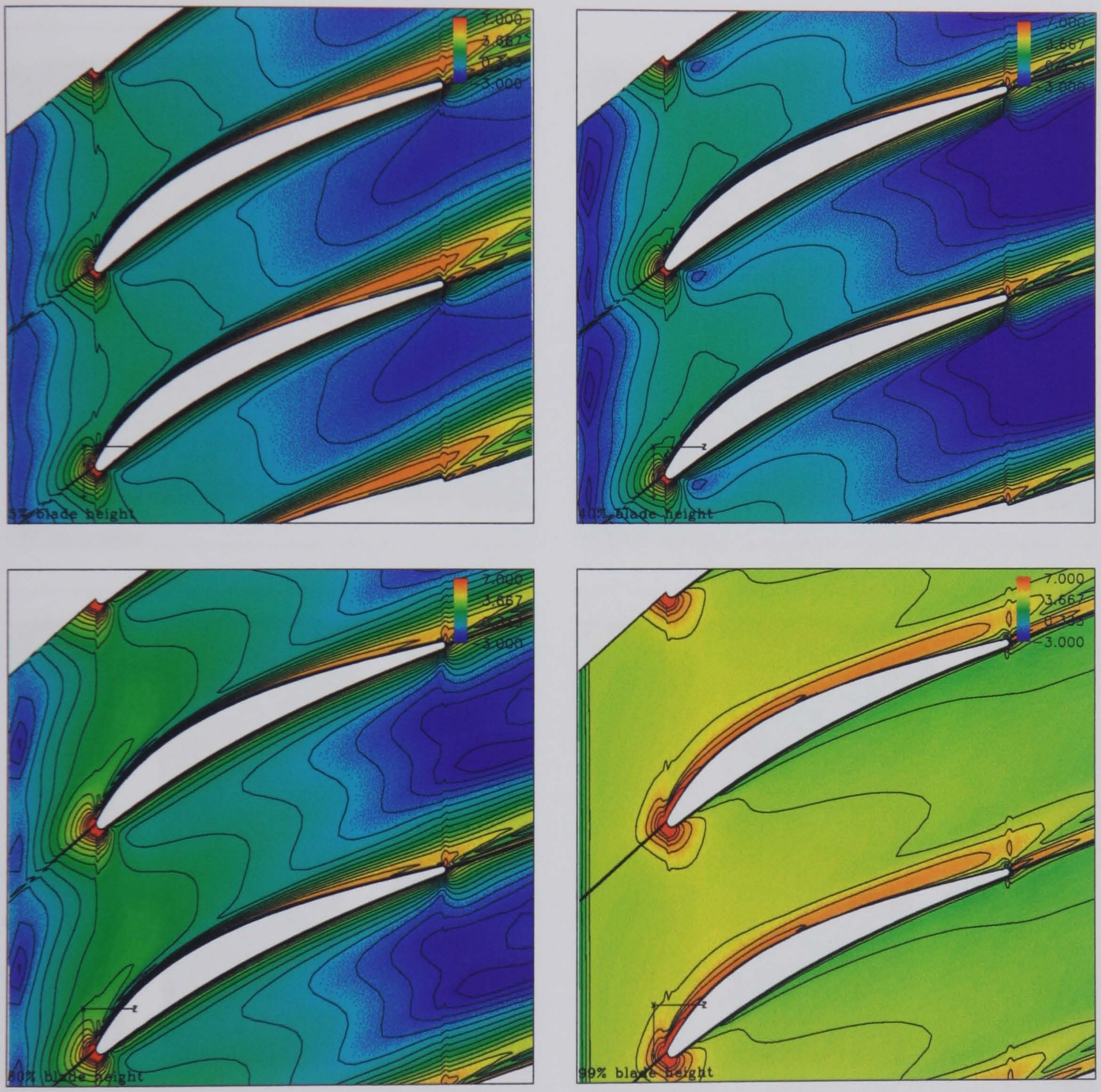

Figure 6.96: **Distribution of entropy generation rate** $\ln(s')$ **at blade-to-blade surfaces at different blade height from Prediction** I **(Stator 3 domain)**

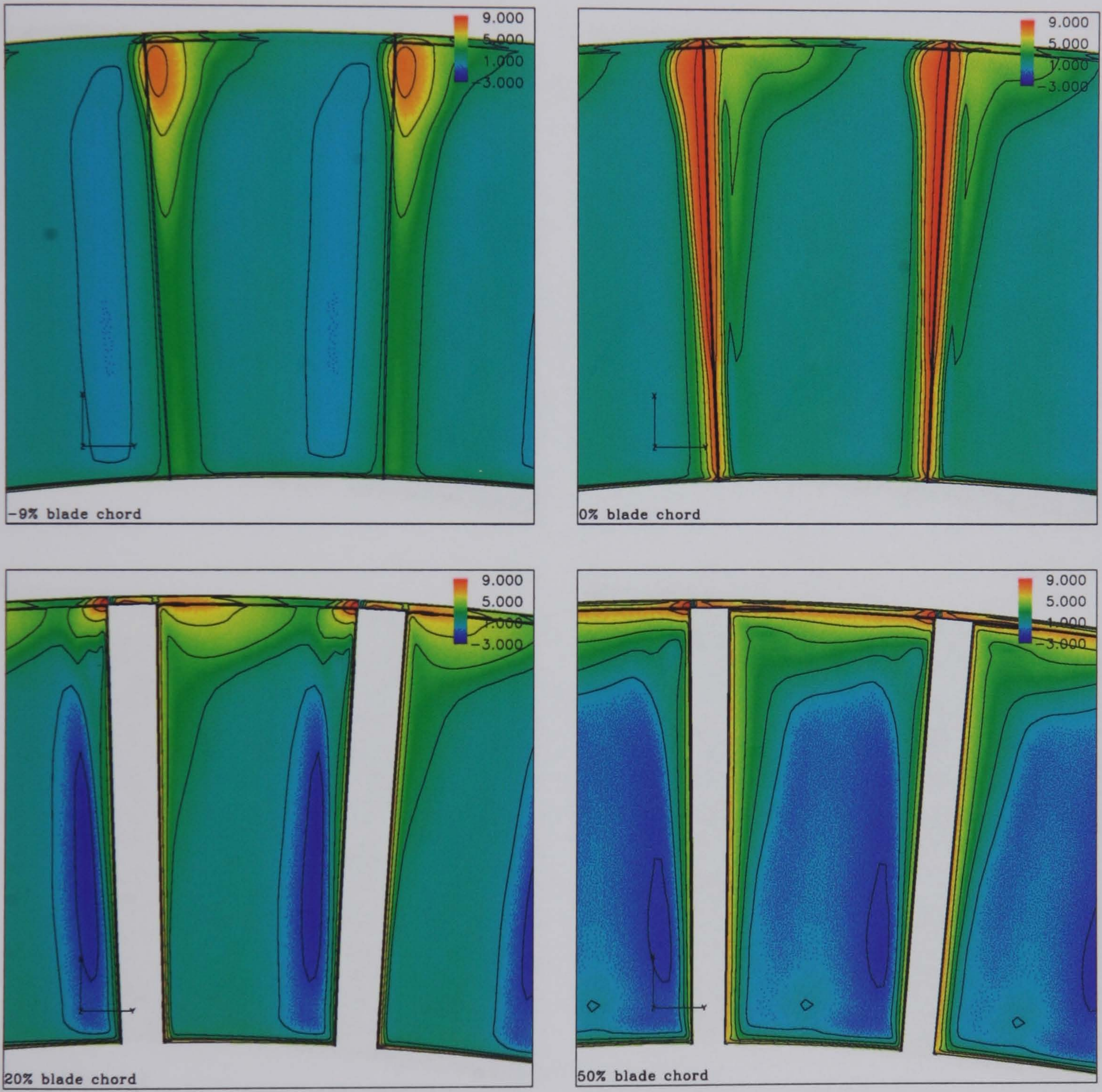

Figure 6.97: **Distribution of entropy generation rate $\ln(s')$ at cross plane surfaces at different axial position from Prediction I (Rotor 3 domain)**

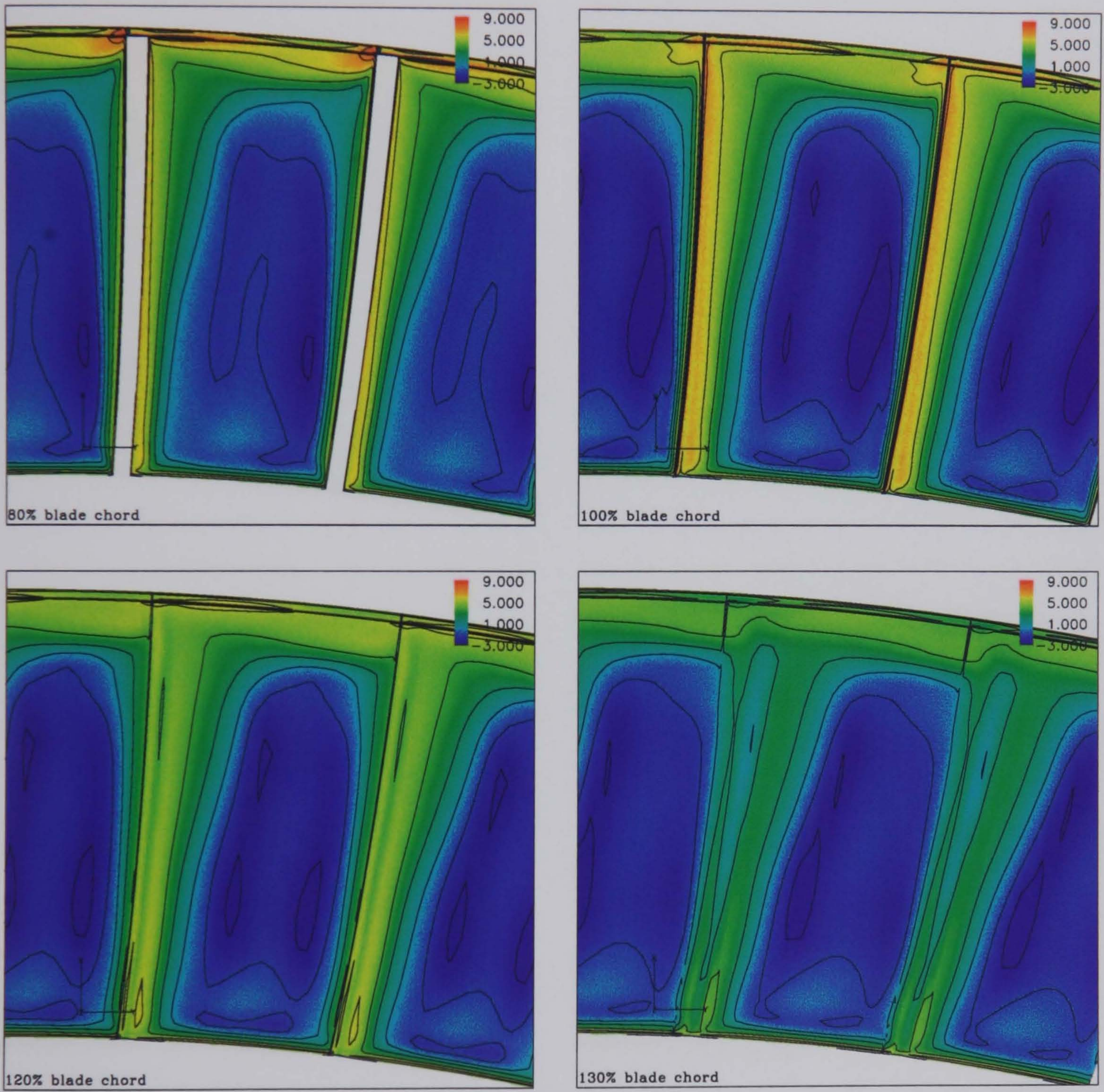

Figure 6.98: **Distribution of entropy generation rate $\ln(s')$ at cross plane surfaces at different axial position from Prediction I (Rotor 3 domain)**

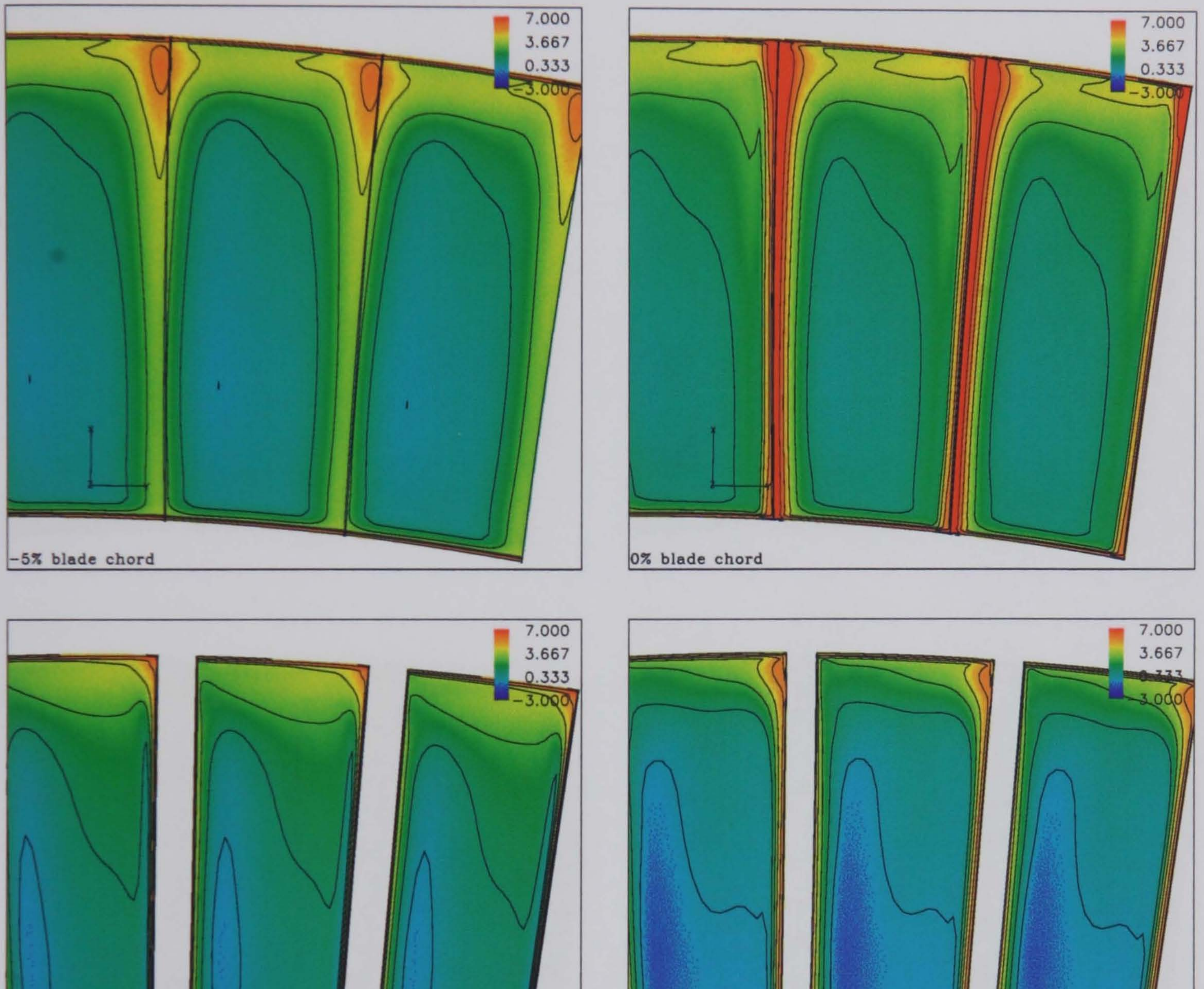

Figure 6.99: **Distribution of entropy generation rate $\ln(s')$ at cross plane surfaces at different axial position from Prediction I (Stator 3 domain)**

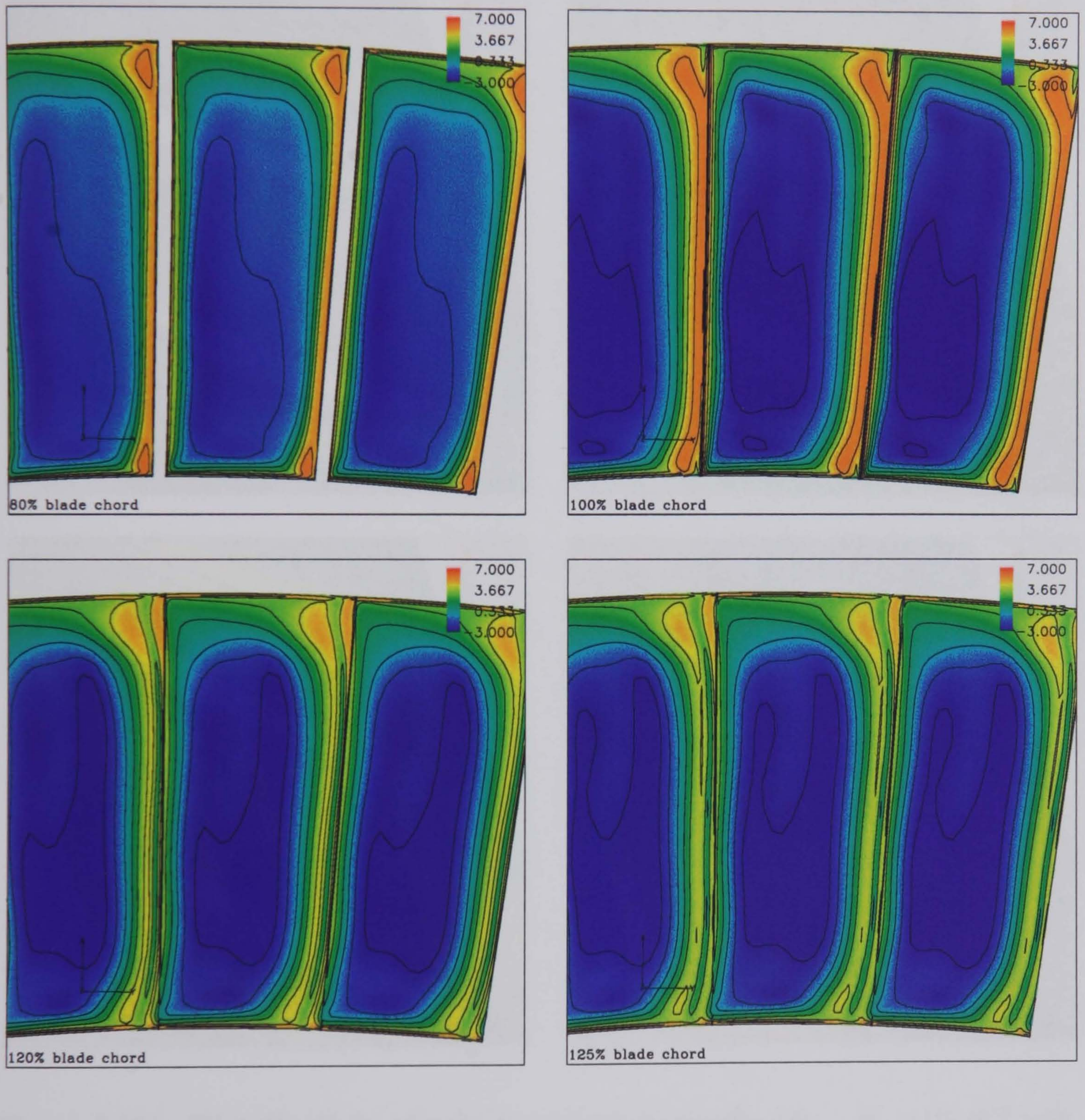

Figure 6.100: **Distribution of entropy generation rate $\ln(s')$ at cross plane surfaces at different axial position from Prediction I (Stator 3 domain)**

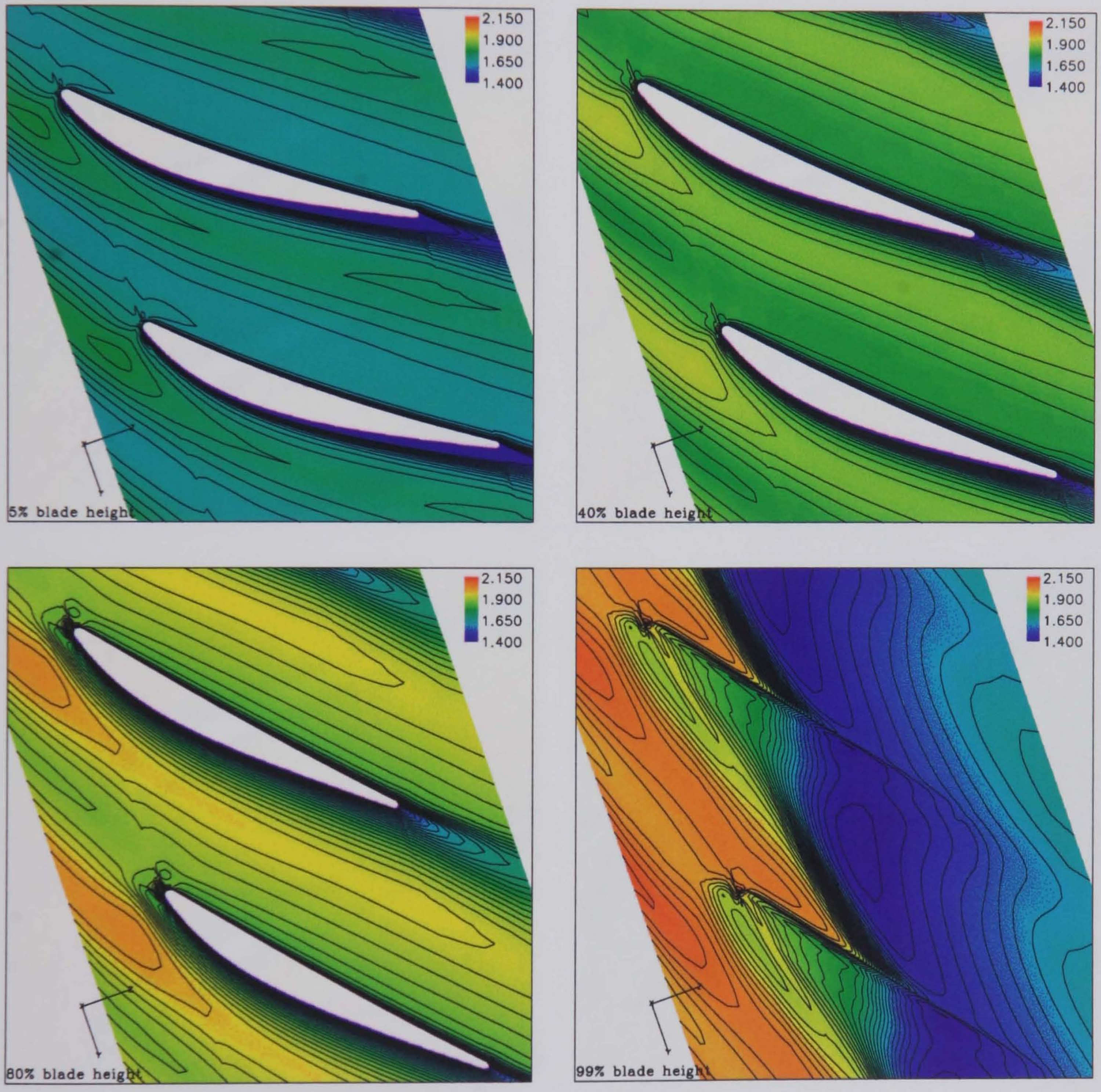

Figure 6.101: **Distribution of relative total pressure $(P_t - P_{ref})/(\frac{1}{2}\rho U_m^2)$ at blade-to-blade surfaces at different blade height from Prediction I (Rotor 3 domain)**

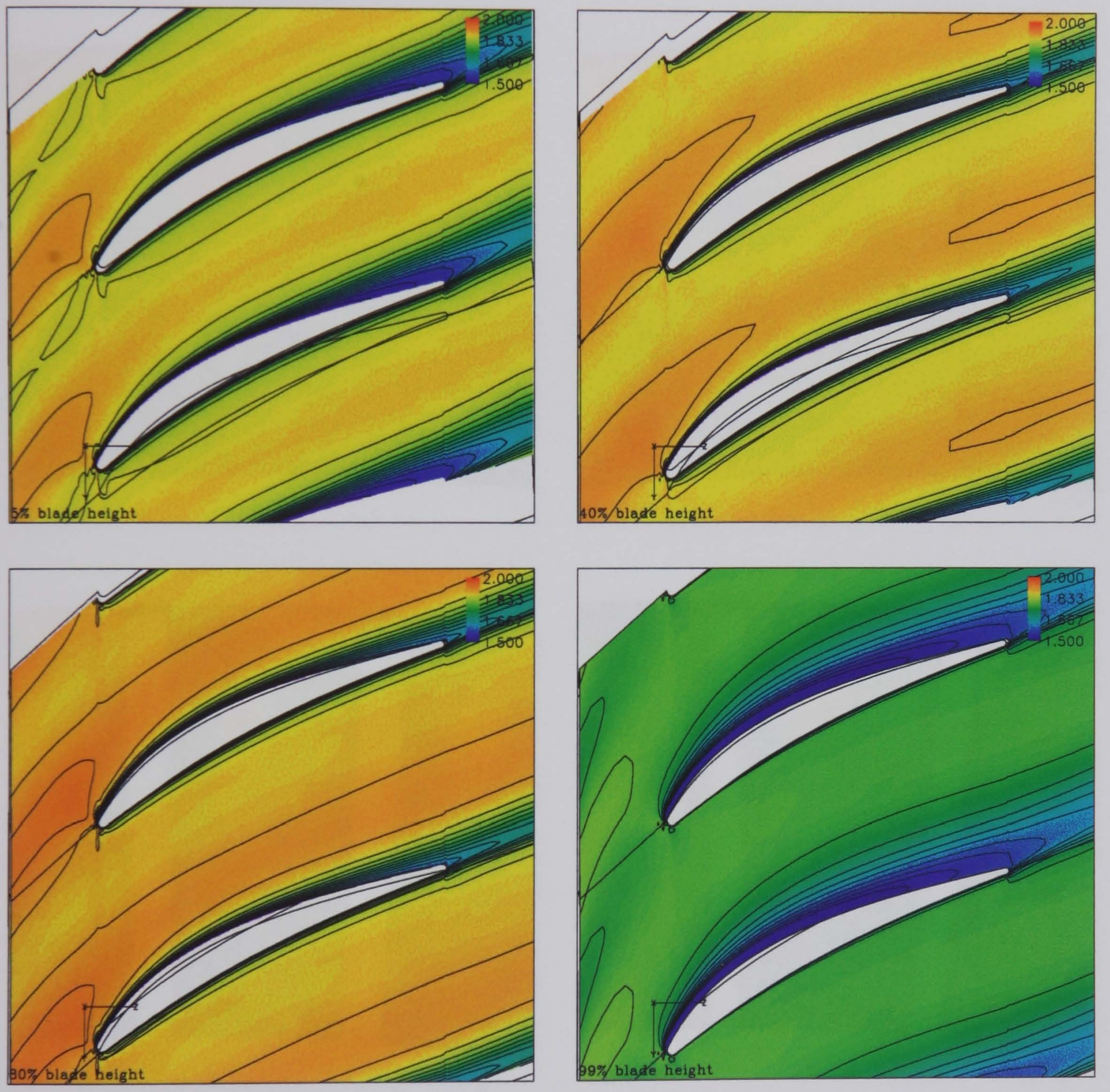

Figure 6.102: **Distribution of total pressure $(P_t - P_{ref})/(\frac{1}{2}\rho U_m^2)$ at blade-to-blade surfaces at different blade height from Prediction I (Stator 3 domain)**

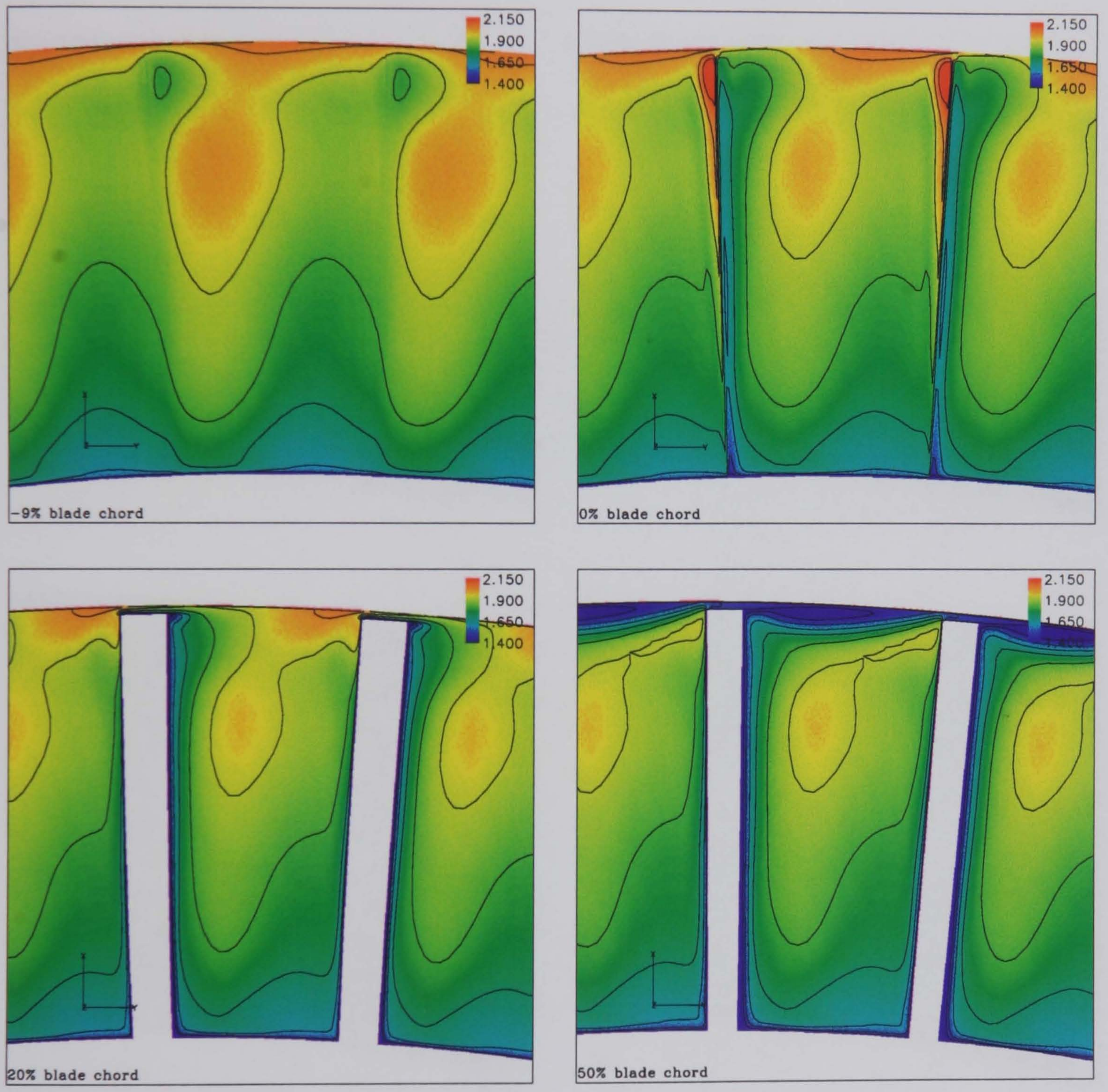

Figure 6.103: **Distribution of relative total pressure $(P_t - P_{ref})/(\frac{1}{2}\rho U_m^2)$ at cross plane surfaces at different axial position from Prediction I (Rotor 3 domain)**

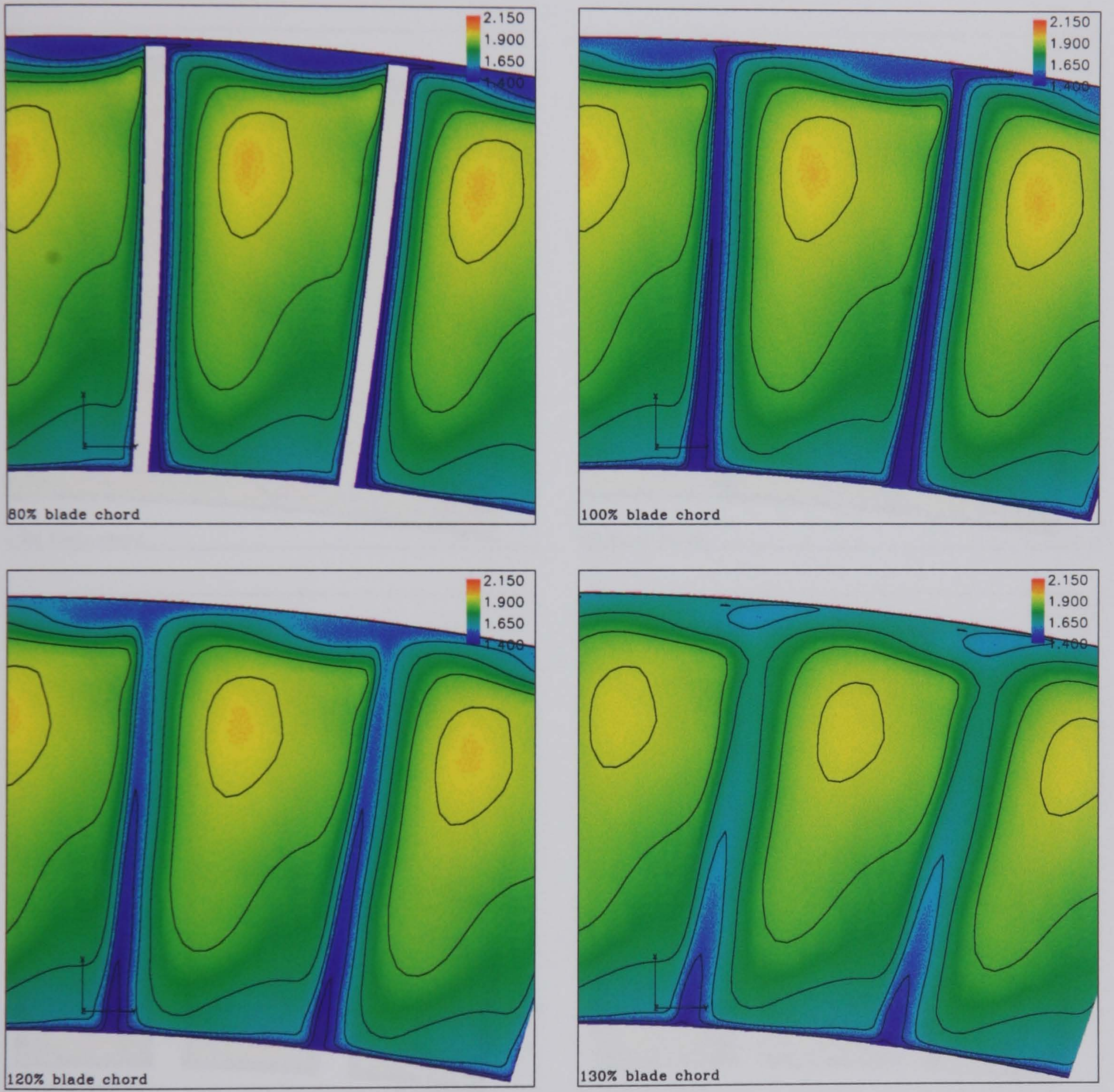

Figure 6.104: **Distribution of relative total pressure $(P_t - P_{ref})/(\frac{1}{2}\rho U_m^2)$ at cross plane surfaces at different axial position from Prediction I (Rotor 3 domain)**

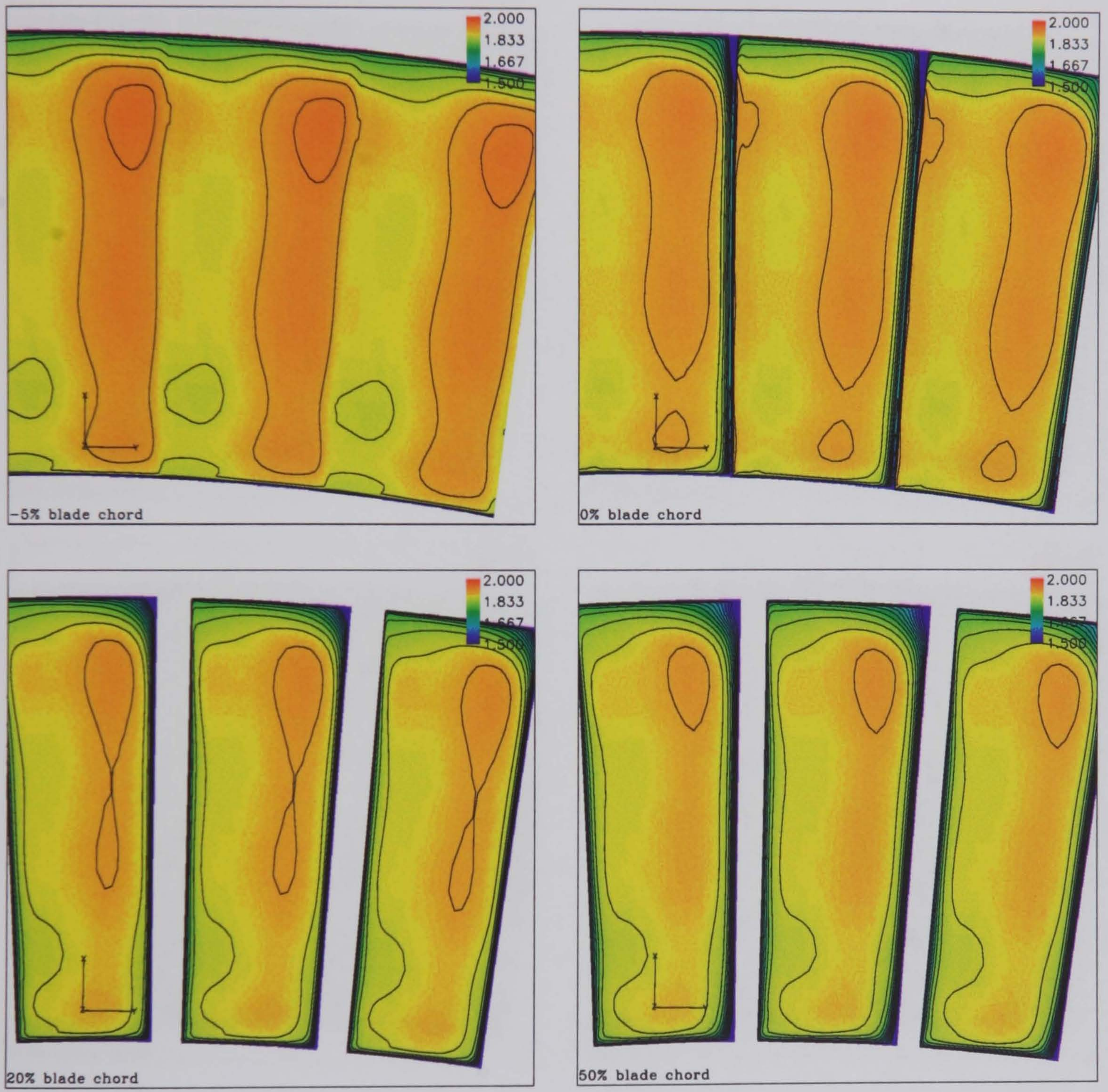

Figure 6.105: **Distribution of total pressure $(P_t - P_{ref})/(\frac{1}{2}\rho U_m^2)$at cross plane surfaces at different axial position from Prediction I (Stator 3 domain)**

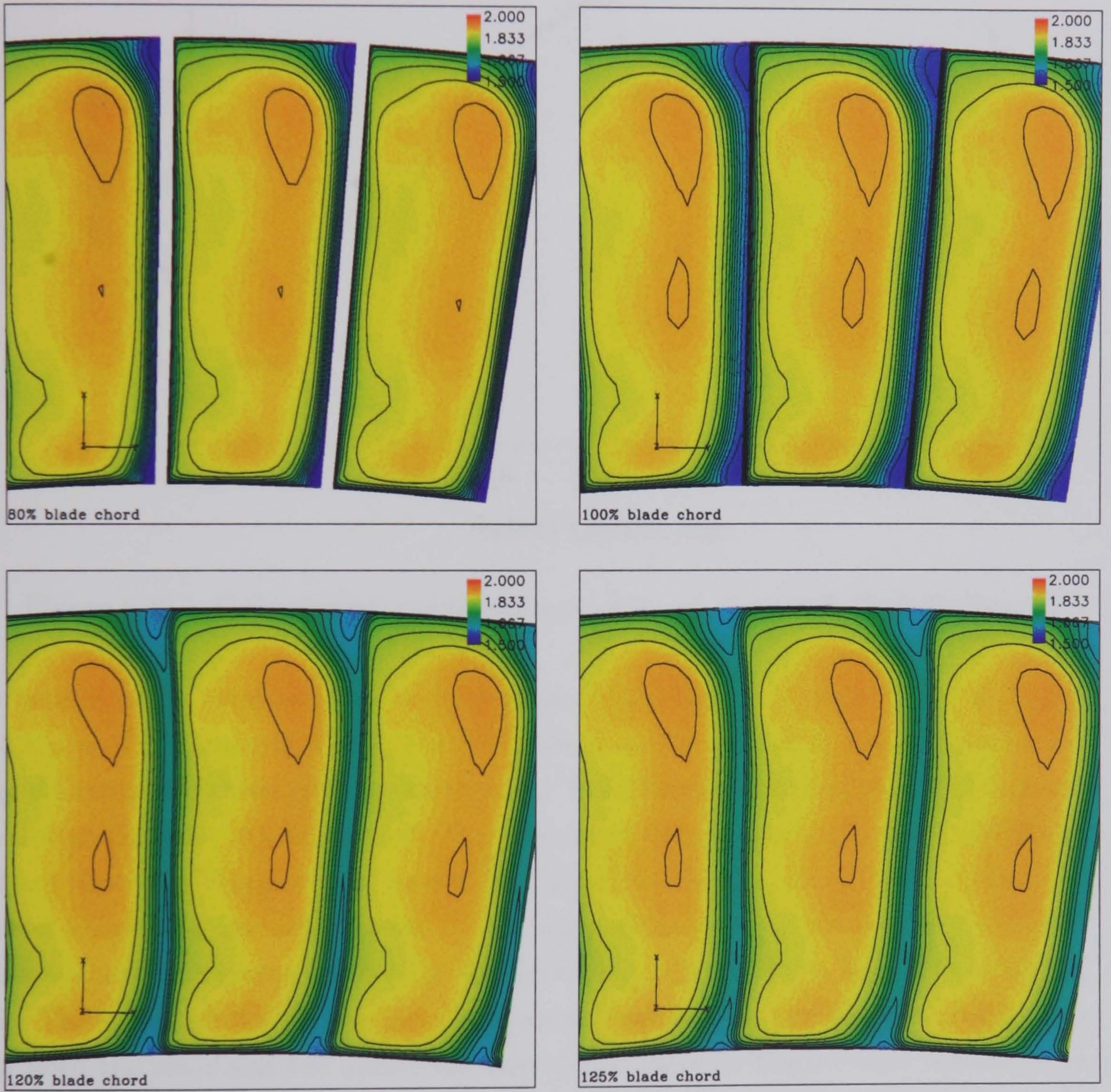

Figure 6.106: **Distribution of total pressure $(P_t - P_{ref})/(\frac{1}{2}\rho U_m^2)$ at cross plane surfaces at different axial position from Prediction I (Stator 3 domain)**

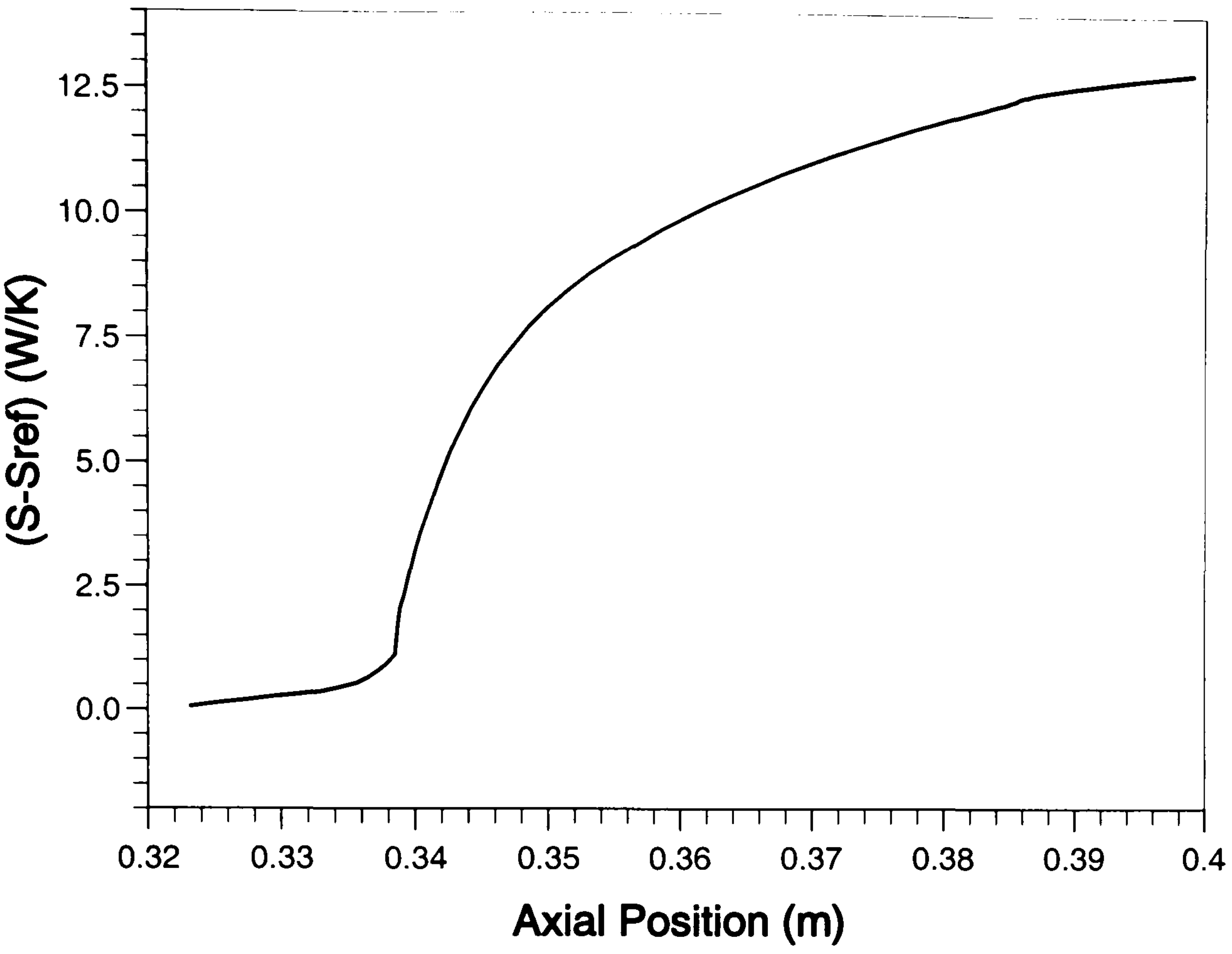

Figure 6.107: **Calculated axial entropy rise in Rotor 3 (Prediction *I*)**

where S is the total entropy at certain axial location. N is the number of blades, ΔV_{ijk} is the volume of a cell, ρ is the density, and I, J and K are the numbers of grid lines in the three grid line directions. The reference entropy normally takes its value at the inlet of a blade row. The calculated entropy rise in Rotor 3 and Stator 3 are shown in Figures 6.107 and 6.108. From the figures, it can be seen that the most significant increase appear in the blade passage area between 0% and 30% blade chord downstream from the blade leading edge for both Rotor 3 and Stator 3. The losses of the flow in the wake areas downstream the blade trailing edges of both the rotor and the stator are also shown through the increase of entropy in these areas.

According to the basic theory of thermodynamics, the efficiency of a compressor stage can be calculated with the following equation, Denton [48]:

$$\eta_c \approx 1 - \frac{T_2(S_2 - S_1)}{\dot{m}(h_2 - h_1)} \tag{6.8}$$

where η_c is the thermal efficiency of the compressor stage, T_2 is the exit average temperature of the stage and the subscripts 1 and 2 mean the inlet and the exit of the stage, Figure 6.109. The total entropy rise across the stage can be obtained by

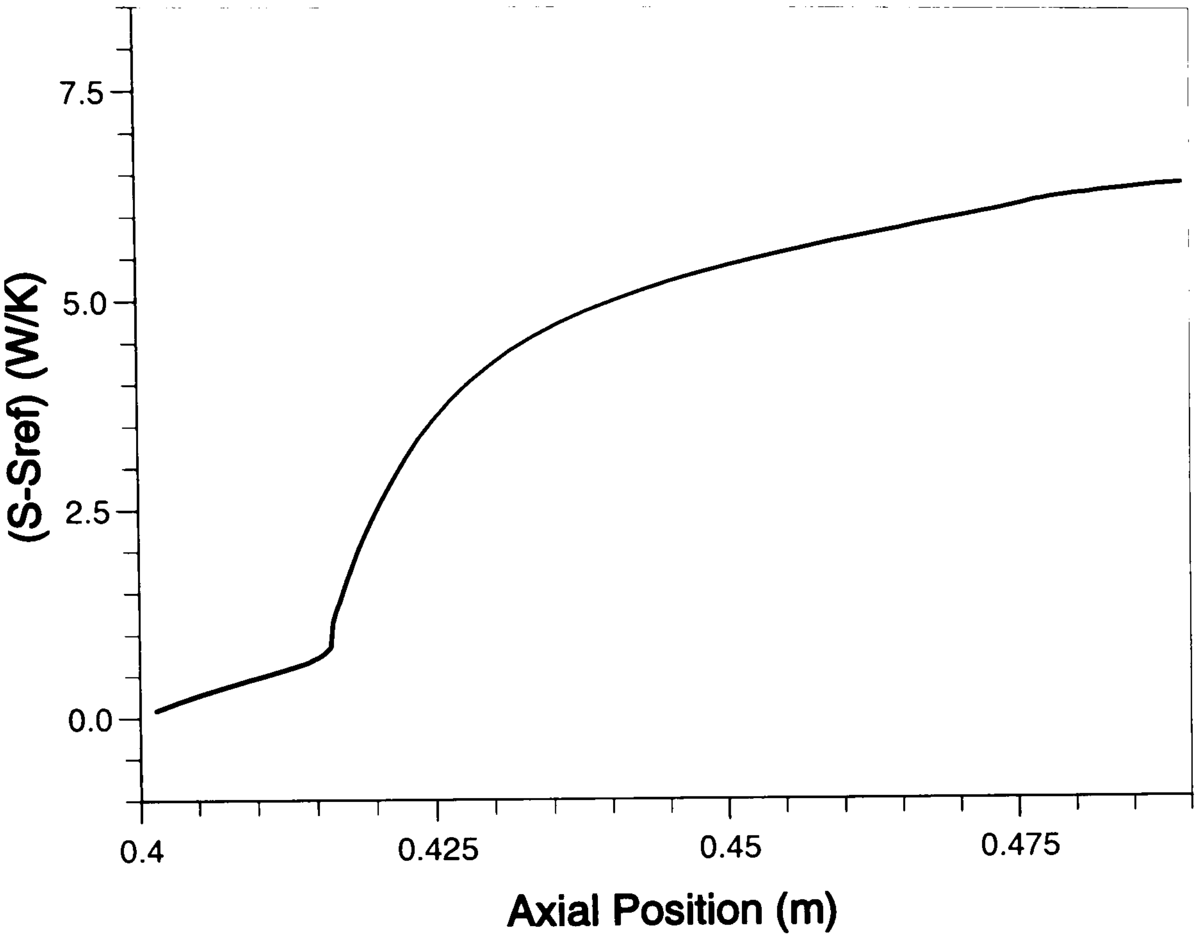

Figure 6.108: **Calculated axial entropy rise in Stator 3 (Prediction *I*)**

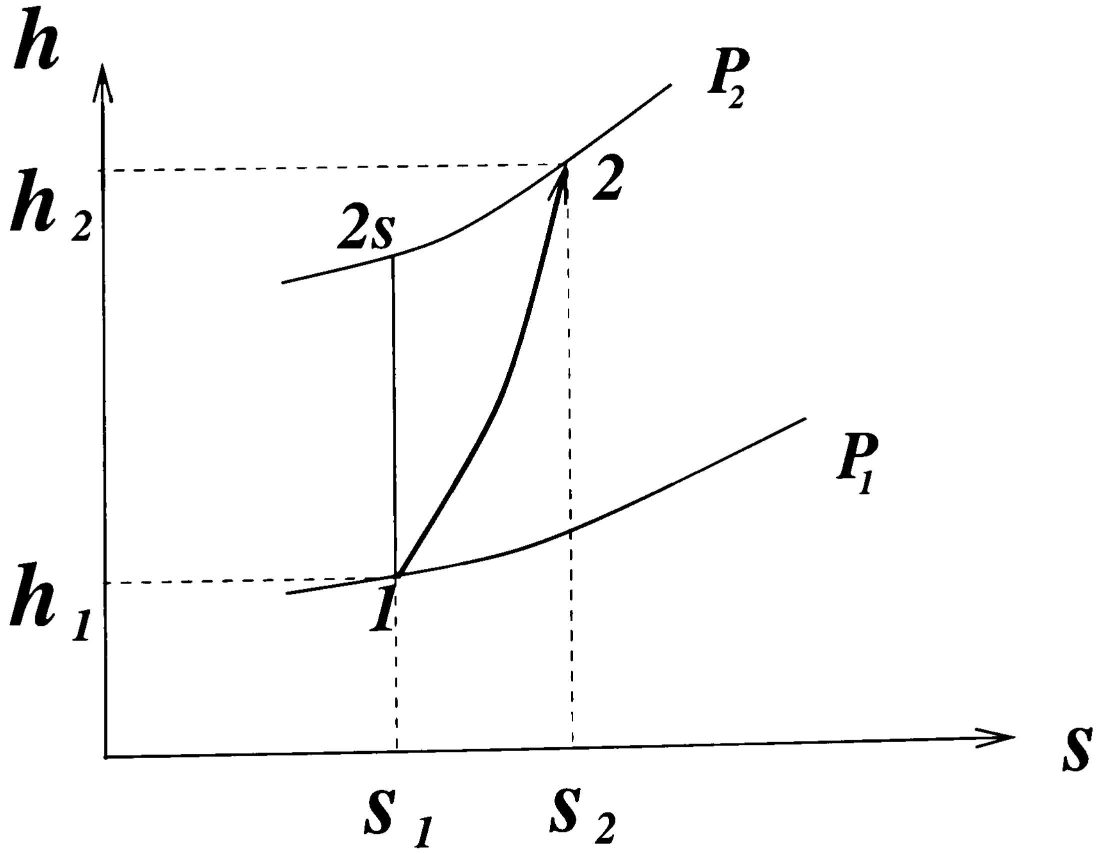

Figure 6.109: **Enthalpy-entropy diagram for compressor flow**

adding the entropy rises in Rotor 3 and Stator 3 together (the entropy rise in the third stage is 19.1335 W/K). The temperature may be calculated with the state equation of ideal gas (for the third stage the calculated inlet temperature is 283.8 K and the outlet temperature is 288.2 K). Eventually, the efficiency of the third stage can be calculated with Equation (6.8) and the calculated efficiency is 89.8%, which is a very satisfactory result as compared to the experimental data (around 88% to 89%).

Loss analysis using entropy-generation rate due to heat and fluid flow is a relative new technique for assessing turbomachinery performance, Sciubba [154]. It will become a better analysis method to the understanding of the loss of the flow in turbomachinery and will be beneficial to the design of more advanced turbomachines.

6.10 Prediction of *LSRC* Third Stage at Off-Design Conditions

Performance predictions with the current computational method at off-design conditions of the Cranfield *LSRC* were carried out and show valuable result. The repeating stage model in combination with the mixing plane model was used in the computation . which is similar to Prediction *II* taking advantage of the repeating flow nature of the compressor and simplify the setting of the boundary conditions. The only difference to Prediction *II* is that the inlet velocity profiles used in this computation are scaled experimental velocity profiles according to the mass flow rate instead of using the calculated stage exit velocity profile. The reason for this is to reduce the accumulated prediction error resulted from the repeating stage model during the global iterations due to the following two reasons: (1) the further the compressor works away from its peak efficiency point, the more the repeating nature of the compressor stages reduces, and (2) if the stage exit velocity profile is used as the stage inlet velocity boundary condition which has significant influence on the flow prediction, the difference of the velocity distributions between the inlet and the exit of the stage will be amplified during the global iterations and the converged result will be far from reality.

Two off-design operating points of the third stage of the Cranfield *LSRC* with the same rotational speed (1100 rpm) have been analysed and plotted in the stage characteristic map, Figure 6.110, one with 2% less mass flow rate and the other with 5% more mass flow rate than the design point. Compared with two test points

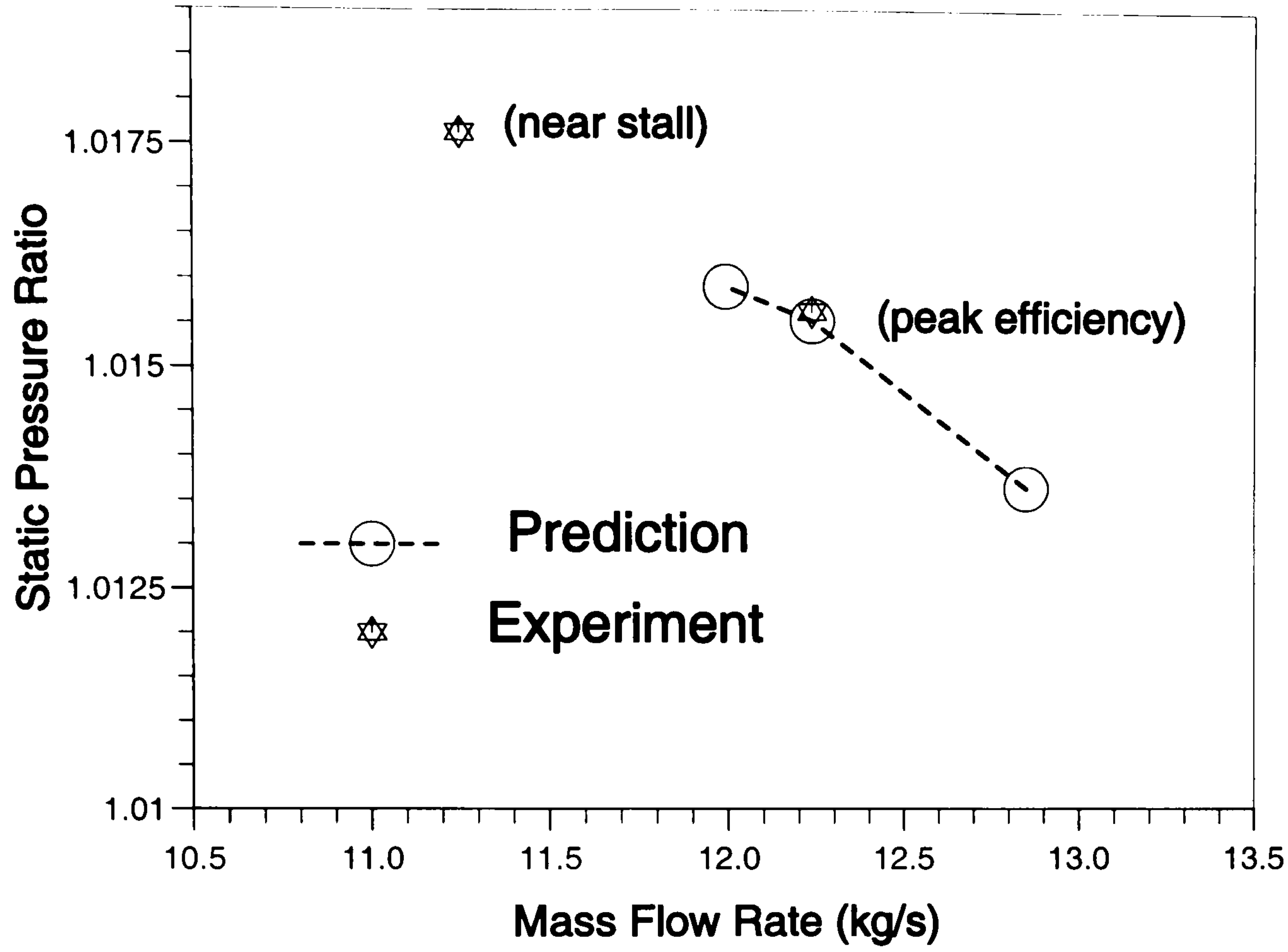

Figure 6.110: **Characteristics of the third stage of** *LSRC*

in the map, it is shown that the predicted pressure ratio of the stage reasonably varies with the mass flow rate. Unfortunately, it is difficult to judge the accuracy of the off-design point predictions because there are no corresponding experimental data available to compared with.

Attempts have also been made to simulate the flow in the third stage of the Cranfield low speed research compressor (*LSRC*) working at an operating condition near stall. Unfortunately, no satisfying results have been obtained.

The effort of the near stall flow simulations in the third stage of *LSRC* was started by setting the inlet velocity profile and the exit static pressure profile to both the rotor and stator domains based on the experimental data. In the rotor domain, the predicted spanwise velocity distribution and the total and the static pressure distributions at the rotor exit are close to the experimental profiles while the spanwise total and static pressure distributions at the rotor inlet are similar to the experimental ones in shape but over-predicted in magnitude. In other words, the total and static pressure ratios in the rotor are obviously under-predicted. In the stator domain, the static pressure distributions at both the inlet and the exit of the stator are close to the experimental ones. The spanwise distribution of the velocity, especially the axial velocity component, is far away from the experimental data, where much higher predicted axial velocity appears in the area between 0% and 70% blade span and much lower predicted axial velocity appears in the area between 70% and 100% span. This means that there is a large flow separation in the predicted stator flow passage near the blade tip which does not appear in the measured field. The inaccurate prediction in the velocity distribution results in the inaccurate prediction of the total pressure distribution. Under these circumstances, simulation with the mixing plane approach did not proceed any further.

Similar simulation for the near stall flow in the *LSRC* third stage blade rows with downstream extended computational domains were also carried out by implementing the deterministic stresses, bodyforce and blockage effect to the computation. Similar predicted results to the mixing plane approach were also obtained. The only difference between the two predictions was that large flow separations in the predicted stator flow passage appear near both the blade hub and tip, resulting in much higher axial velocity component at midspan and much lower axial velocity components near both the hub and the tip in the downstream stator passage. Hence, it has been proven that the deterministic stress model cannot improve the prediction of the flow when the compressor stage works far from the peak efficiency point.

Similar difficulties were also experienced in the simulation of the Lewis low speed axial compressor, Adamczyk [6], which is a four stage machine with an inlet guide vane. This compressor, which is similar to Cranfield low speed research compressor, also has four geometrically identical stages and is representative of the rear stages of a high pressure compressor. The simulation accounted for the rotor tip clearance and did not include the stator hub cavity and hub leakage. The simulation results for the compressor working near the peak efficiency are in good agreement with the measurement, while the simulation of a working point near peak pressure (near stall point) failed to converge.

In conclusion, the developed computer code in this study with current steady state CFD approaches, like other CFD codes, is not able to accurately predict the flow field of multistage axial flow compressors working far off the peak efficiency points.

Chapter 7

Conclusions and Future Work

7.1 Conclusions

- In this study, simulation approaches of three dimensional internal flow and performance of multistage axial flow compressors have been investigated, developed and analysed in great detail based on the original ideas of Denton [47] and Adamczyk [2]. A computational procedure has been developed and proved to be successful. Flow and performance predictions with different models are presented and compared with each other and with available experimental data.

- The surface fitting method to generate boundary grid points of blade passages and the algebraic interior grid generation and clustering have been proven to be fast and effective. The developed computer code for grid generation is successful.

- The system of governing equations, the Navier-Stokes equations, have been averaged with three averaging operators: the ensemble averaging operator, the time averaging operator and the passage-to-passage averaging operator. As the result of these averaging processes, the Reynolds stresses, the deterministic stresses and the stresses related to the aperiodic unsteadiness together with bodyforce and blade blockage appear in the averaged Navier-Stokes equations which take into account different types of unsteady effects and raise the issues of closure modelling. The stresses related to the aperiodic unsteadiness are ignored in this study because it is much smaller than the turbulence unsteadiness and the periodic unsteadiness.

- The two equation turbulence model provides an effective approach in this study to the modelling of Reynolds stresses. It is one of the best among turbulence models in terms of accuracy, computation speed and robustness.

- An overlapped solution domain approach combined with detailed simulation of bodyforce and blade blockage effect provides an effective way of implementing the deterministic stresses in flow simulations. The developed approximation of bodyforce and blade blockage effect is very effective in the flow simulation and simple in programming. This type of deterministic stress model provides spanwise continuous interfaces for mass flow rate, momentum, velocity, k and ϵ when they are transfered across interfaces between blade rows. Unfortunately, spanwise static and total pressure distributions are not continuous at interfaces due to model and numerical errors. This inconsistency is small and can be negligible.

- The mixing plane models are adopted in the study and have been proven to be very effective in the simulation of multistage axial flow compressors. Although they can not provide continuity for some aerodynamic parameters when they are transfered across the interfaces between the blade rows, they provide satisfactory prediction of the flows when the machines have low pressure ratios and work near peak efficiency.

- The deterministic stress model is an improvement to the mixing plane approach. It has taken into account the periodic unsteadiness generated by neighbouring blade rows and provides continuous interfaces between neighbouring blade rows for all the aerodynamic parameters except pressure. By implementing this model into the flow simulation of the third stage of Cranfield low speed compressor ($LSRC$) and comparing the results with those from similar simulations with the mixing plane model, we can see that the deterministic stress model shows only slightly better improvement than the mixing plane model. The reasons for this may be that (1) the compressor under investigation is a low speed compressor with large axial space between blade rows so the influence of the deterministic stress is not significant, and (2) the effectiveness of the model itself is limited and is not able to improve the prediction accuracy significantly, which has been proven in the predictions for the Cranfield low speed compressor ($LSRC$) working both at peak efficiency operation point and near stall point.

- Two repeating stage models have been developed in this study based on the repeating flow behaviour always appearing in the rear stages of multistage axial flow compressors. One of the models works together with the mixing plane model and the other with the deterministic stress model. With the repeating stage models, the aerodynamic boundary conditions for the simulation of rear stages of multistage axial flow compressors can be significantly simplified and the only requirement of the boundary input is a total mass flow rate and average static pressure at the stage exit. The predicted flow field and the performance of the third stage of *LSRC* with the repeating stage models match very well with the experimental data and demonstrate equivalent accuracy to the predictions with conventional boundary setting. It has been proven that the repeating stage models are effective and are economic alternatives to the simulation of complete multistage axial flow compressors when only the flow in the rear stages are concerned and the spanwise distribution of the aerodynamic parameters at the inlet and the exit of these stages are difficult to be obtained.

- The governing equations are expressed in a general non-orthogonal curvilinear coordinate system, which make them easy to be applied to different compressors with complex geometries. This equation system is discretized in finite control volumes with variables stored at the control volume centres. The application of collocated grids minimises the estimation of the coefficients of the discretized equations and simplify the treatment of the boundary volumes. The *SIMPLE* method is utilised in the solution procedure and the numerical scheme originated by Rhie and Chow [147] and developed by Majumdar [119] is used as a remedy to the pressure oscillations and decoupling between pressure and momentum fields. The discretized equation system is solved efficiently with Stone's Strongly Implicit Procedure (*SIP*), Stone [167].

- The calculated distribution of entropy generation rate inside the flow passages of the compressor blade rows gives a clear and accurate description of the fluid losses resulted from viscous stresses. The predicted thermal efficiency for the third stage of the Cranfield *LSRC* working at peak efficiency operation point is very satisfactory.

- The developed simulation methods and computer code are able to predict pretty well the internal flow and performance of low speed axial flow compressor stages working at off-design conditions not far from peak efficiency point but not able to provide good prediction when the machine works near stall point. The computer code has been proven to be a robust analysis tool in simulating flows inside the Cranfield low speed compressor ($LSRC$) and can be easily modified to simulate flows in other low speed multistage turbomachinery.

7.2 Future Work

- **Compressible Flow Simulation of Multistage Axial Flow Compressors**
  Because of the assumption of the incompressibility of the flow in the current study, the developed computer code was only implemented for the flow simulation of a low speed axial flow compressor where the compressibility of the flow can be ignored. By introducing the energy equation into the system and taking into account the compressibility of the flow, the computer code can be extended to simulate flows in high speed multistage axial flow compressors. It is also possible to extend the code to simulate transonic and supersonic flows and capture shock waves in high speed multistage axial flow compressors with additional modifications.

- **Improved Repeating Stage Model**
  The repeating stage models presented in this thesis have the limitation that they were only applied to the stages with constant inner and outer diameters and the flow is supposed to be incompressible. If the compressor annulus is convergent downstream and the flow is compressible, the repeating stage models need to be modified.

- **Unsteady Flow Prediction in Multistage Compressors**
  The mixing plane approach has the limitation when applied to multistage turbomachinery flow simulations that they only behave well when the machines work near peak efficiency. The deterministic stress model is an improvement to the mixing plane model and is a simplified alternative to the complete unsteady simulation of multistage turbomachinery. Unfortunately, the deterministic stress model is not good enough to replace the direct unsteady simulation. With the development of modern computers, it is possible to simulate three dimensional unsteady flows and rotor-stator interactions directly with an unsteady Navier-Stokes approach. A lot of effort has been

devoted in this field during the last decade, which is reviewed in Chapter 1.

- **Acceleration of the Code with Parallel Computation**
  Flow predictions of multistage compressors are very time consuming, even with steady state approaches. In order to accelerate the computation significantly, it is suggested that parallel computations (for example, using *PVM*) be used in the simulation and it is expected that the computational speed could be increased by many times depending on the number of computers used and the parallelisation techniques applied. Parallelisation is a great potential to speed up the simulations.

- **Influence of Stator Hub Cavity Flow**
  The stator hub cavity flows in multistage axial flow compressors, which are ignored in the present study, exist in all multistage axial flow compressors. The influence of the cavity flow sometimes plays an important role to the performance of high speed axial flow compressors. By implementing the cavity domains into the simulation system, the developed computer code can be extended to investigate the rigorous influence of the cavity flows on the main passage flows and the whole compressor performance. Numerical investigation of cavity flows in axial flow compressors have been carried out by some researchers, such as LeJambre et al. [109], Heideggar et al. [77], Campobasso et al. [27] and Scott et al. [155].

Appendix A

Composite Surfaces and Patches

Usually, a three-dimensional surface can be described with an implicit equation of the following form:

$$f(x, y, z) = 0 \tag{A.1}$$

It is also possible to describe the surface in terms of parametric coordinates. In practice, most geometries such as compressor blades cannot be defined by an accurate expression of form (A.1), but are defined by sets of discrete networked points. For example in Figure A.1, a surface is shown on which two families of intersecting curves u and v are drawn. The surface can be viewed as a rectangular plane in the parametric coordinates u and v where these two families of curves can be represented by parametric curves. There is a one-to-one correspondence between the points on the physical and parametric spaces.

An isolated patch is shown in Figure A.2 , defined in parametric coordinate vectors as $\vec{\mathbf{r}}(u, v)$, $0 \leq u \leq 1$, $0 \leq v \leq 1$. The four corners are $\vec{\mathbf{r}}(0,0)$, $\vec{\mathbf{r}}(1,0)$, $\vec{\mathbf{r}}(0,1)$ and $\vec{\mathbf{r}}(1,1)$, and their coordinates are assumed to be known. The four edges which represent the boundary curves are defined as $\vec{\mathbf{r}}(u,0)$, $\vec{\mathbf{r}}(u,1)$, $\vec{\mathbf{r}}(0,v)$ and $\vec{\mathbf{r}}(1,v)$. The required interpolant form for the patch, often called **Coons patch**, Faux [56] is

$$\vec{\mathbf{r}}(u, v) = \vec{\mathbf{r}}_1(u, v) + \vec{\mathbf{r}}_2(u, v) - \vec{\mathbf{r}}_3(u, v) \tag{A.2}$$

where

$$\begin{aligned} \vec{\mathbf{r}}_1(u, v) = \; & (1-u)\vec{\mathbf{r}}(0, v) + u\vec{\mathbf{r}}(1, v) \\ \vec{\mathbf{r}}_2(u, v) = \; & (1-v)\vec{\mathbf{r}}(u, 0) + v\vec{\mathbf{r}}(u, 1) \\ \vec{\mathbf{r}}_3(u, v) = \; & (1-u)(1-v)\vec{\mathbf{r}}(0,0) + u(1-v)\vec{\mathbf{r}}(1,0) + \\ & (1-u)v\vec{\mathbf{r}}(0,1) + uv\vec{\mathbf{r}}(1,1) \end{aligned} \tag{A.3}$$

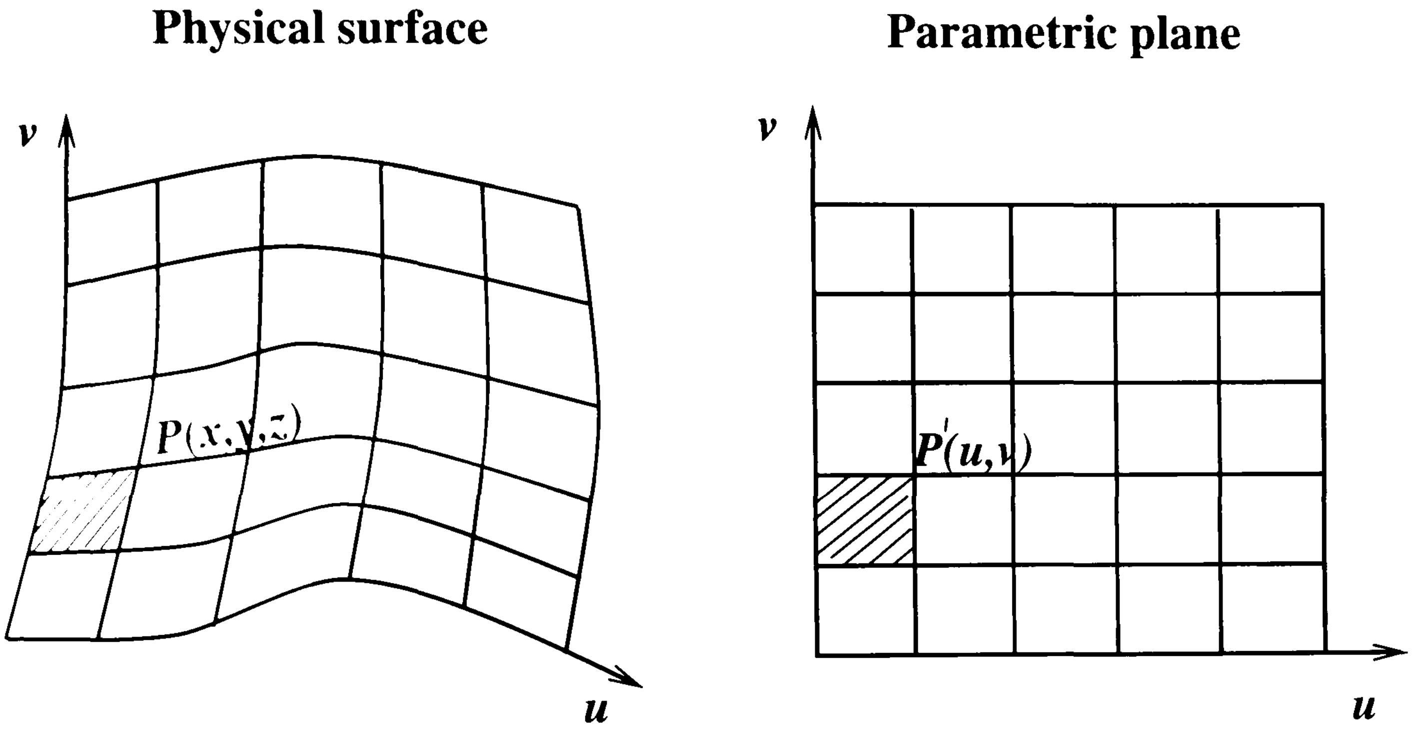

Figure A.1: **Relationship between physical surface and parametric plane**

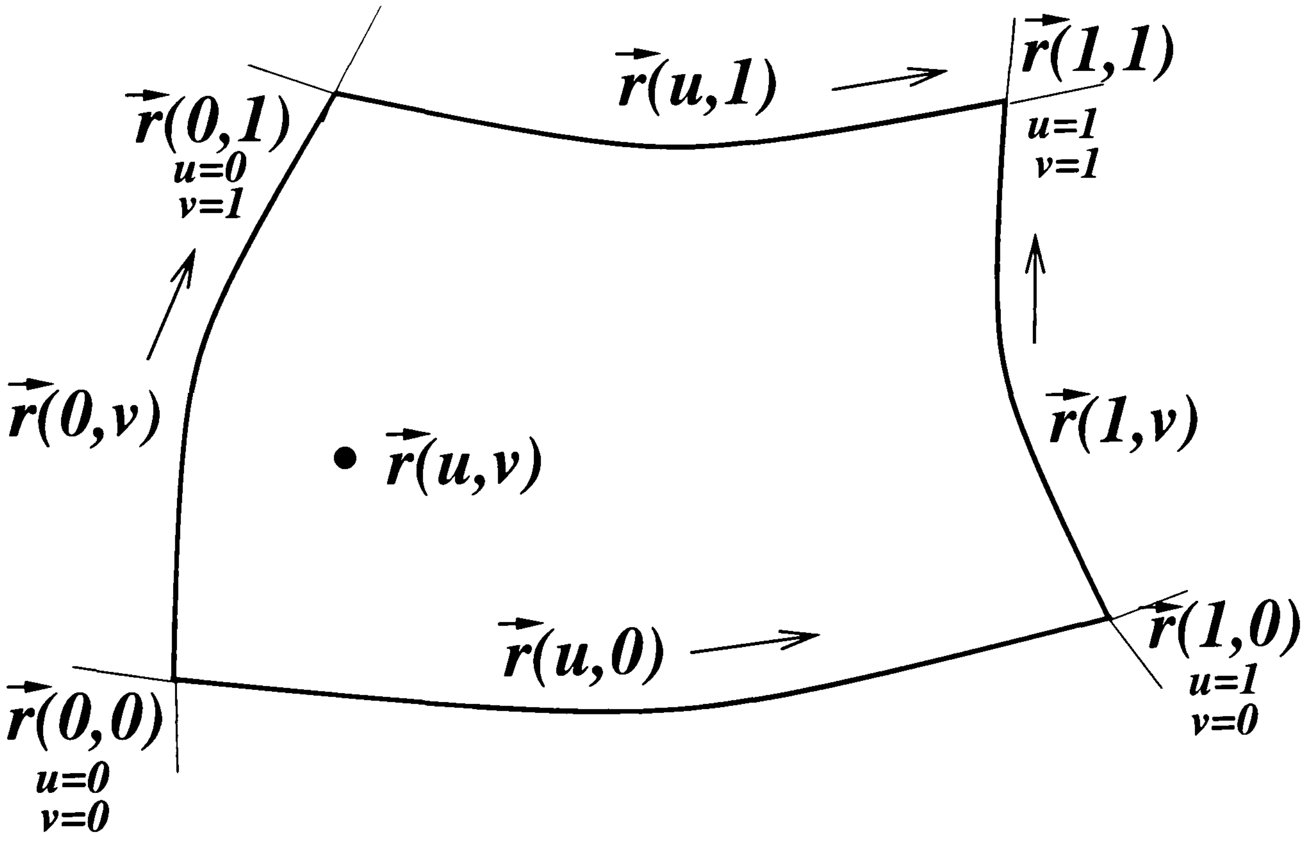

Figure A.2: **Isolated patch on a physical surface**

The above expression can be written in a matrix form:

$$\vec{\mathbf{r}}(u,v) = \begin{bmatrix} (1-u) & u \end{bmatrix} \begin{bmatrix} \vec{\mathbf{r}}(0,v) \\ \vec{\mathbf{r}}(1,v) \end{bmatrix} + \begin{bmatrix} \vec{\mathbf{r}}(u,0) & \vec{\mathbf{r}}(u,1) \end{bmatrix} \begin{bmatrix} 1-v \\ v \end{bmatrix} - \begin{bmatrix} (1-u) & u \end{bmatrix} \begin{bmatrix} \vec{\mathbf{r}}(0,0) & \vec{\mathbf{r}}(0,1) \\ \vec{\mathbf{r}}(1,0) & \vec{\mathbf{r}}(1,1) \end{bmatrix} \begin{bmatrix} 1-v \\ v \end{bmatrix} \tag{A.4}$$

This patch, obtained from the information given on the boundaries is the most elementary of a class of surface originally studied by Coons, Weatherill [184]. The function u, $(1-u)$, v and $(1-v)$ are called **blending functions** since their role is to blend together geometrical information from the four boundaries. A generalisation of the above blending function can be made to provide:

$$\vec{\mathbf{r}}(u,v) = \begin{bmatrix} \alpha_0(u) & \alpha_1(u) \end{bmatrix} \begin{bmatrix} \vec{\mathbf{r}}(0,v) \\ \vec{\mathbf{r}}(1,v) \end{bmatrix} + \begin{bmatrix} \vec{\mathbf{r}}(u,0) & \vec{\mathbf{r}}(u,1) \end{bmatrix} \begin{bmatrix} \alpha_0(v) \\ \alpha_1(v) \end{bmatrix} - \begin{bmatrix} \alpha_0(u) & \alpha_1(u) \end{bmatrix} \begin{bmatrix} \vec{\mathbf{r}}(0,0) & \vec{\mathbf{r}}(0,1) \\ \vec{\mathbf{r}}(1,0) & \vec{\mathbf{r}}(1,1) \end{bmatrix} \begin{bmatrix} \alpha_0(v) \\ \alpha_1(v) \end{bmatrix} \tag{A.5}$$

where

$$\alpha_0(0) = 1 \qquad \alpha_0(1) = 0$$
$$\alpha_1(0) = 0 \qquad \alpha_1(1) = 1$$

The blending functions are usually chosen to be continuous and monotone. The type of patch described above ensures continuity at patch boundaries, but, in general will result in discontinuities in slope, curvature etc. To ensure continuity in slope at patch boundaries it is necessary to introduce a cross boundary slope $\vec{\mathbf{r}}_v(u,0)$, $\vec{\mathbf{r}}_u(1,v)$, $\vec{\mathbf{r}}_v(u,1)$ and $\vec{\mathbf{r}}_u(0,v)$ into the interpolation process. The equation for such a patch utilises generalised Hermite interpolation rather than linear interpolation. The resulting equation is

$$\begin{aligned} \vec{\mathbf{r}}(u,v) &= \begin{bmatrix} \alpha_0(u) & \alpha_1(u) & \beta_0(u) & \beta_1(u) \end{bmatrix} \begin{bmatrix} \vec{\mathbf{r}}(0,v) \\ \vec{\mathbf{r}}(1,v) \\ \vec{\mathbf{r}}_u(0,v) \\ \vec{\mathbf{r}}_u(1,v) \end{bmatrix} + \\ &+ \begin{bmatrix} \vec{\mathbf{r}}(u,0) & \vec{\mathbf{r}}(u,1) & \vec{\mathbf{r}}_v(u,0) & \vec{\mathbf{r}}_v(u,1) \end{bmatrix} \begin{bmatrix} \alpha_0(v) \\ \alpha_1(v) \\ \beta_0(v) \\ \beta_1(v) \end{bmatrix} - \end{aligned} \tag{A.6}$$

$$-\begin{bmatrix} \alpha_0(u) & \alpha_1(u) & \beta_0(u) & \beta_1(u) \end{bmatrix} \begin{bmatrix} \vec{\mathbf{r}}(0,0) & \vec{\mathbf{r}}(0,1) & \vec{\mathbf{r}}_v(0,0) & \vec{\mathbf{r}}_v(0,1) \\ \vec{\mathbf{r}}(1,0) & \vec{\mathbf{r}}(1,1) & \vec{\mathbf{r}}_v(1,0) & \vec{\mathbf{r}}_v(1,1) \\ \vec{\mathbf{r}}_u(0,0) & \vec{\mathbf{r}}_u(0,1) & \vec{\mathbf{r}}_{uv}(0,0) & \vec{\mathbf{r}}_{uv}(0,1) \\ \vec{\mathbf{r}}_u(1,0) & \vec{\mathbf{r}}_u(1,1) & \vec{\mathbf{r}}_{uv}(1,0) & \vec{\mathbf{r}}_{uv}(1,1) \end{bmatrix} \begin{bmatrix} \alpha_0(v) \\ \alpha_1(v) \\ \beta_0(v) \\ \beta_1(v) \end{bmatrix}$$

where

$$\begin{array}{ll} \alpha_0(0) = 1 & \alpha_0(1) = 0 \\ \alpha_1(0) = 0 & \alpha_1(1) = 1 \\ \beta_0'(0) = 1 & \beta_0'(1) = 0 \\ \beta_1'(0) = 0 & \beta_1'(1) = 1 \end{array} \tag{A.7}$$

and

$$\begin{array}{lllll} \alpha_0'(0) & = \alpha_0'(1) & = \alpha_1'(0) & = \alpha_1'(1) & = 0 \\ \beta_0 & = \beta_0(1) & = \beta_1(0) & = \beta_1(1) & = 0 \end{array} \tag{A.8}$$

It is possible to simplify the Coons patch equation (A.6) by defining suitable boundary curves and cross-boundary gradients. If a curve segment is defined in term of its end points and end tangents then

$$\vec{\mathbf{r}}(u,v) = \vec{\mathbf{F}}(u)\, Q\, \vec{\mathbf{F}}^T(v) \tag{A.9}$$

where

$$\vec{\mathbf{F}}(u) = \begin{bmatrix} \alpha_0(u) & \alpha_1(u) & \beta_0(u) & \beta_1(u) \end{bmatrix} \tag{A.10}$$

and

$$Q = \begin{bmatrix} \vec{\mathbf{r}}(0,0) & \vec{\mathbf{r}}(0,1) & \vec{\mathbf{r}}_v(0,0) & \vec{\mathbf{r}}_v(0,1) \\ \vec{\mathbf{r}}(1,0) & \vec{\mathbf{r}}(1,1) & \vec{\mathbf{r}}_v(1,0) & \vec{\mathbf{r}}_v(1,1) \\ \vec{\mathbf{r}}_u(0,0) & \vec{\mathbf{r}}_u(0,1) & \vec{\mathbf{r}}_{uv}(0,0) & \vec{\mathbf{r}}_{uv}(0,1) \\ \vec{\mathbf{r}}_u(1,0) & \vec{\mathbf{r}}_u(1,1) & \vec{\mathbf{r}}_{uv}(1,0) & \vec{\mathbf{r}}_{uv}(1,1) \end{bmatrix} \tag{A.11}$$

Such a patch is often called a tensor-product patch. The simplest set of polynomial blending functions satisfying conditions (A.7) and (A.8) consist of the following cubics

$$\begin{array}{ll} \alpha_0(u) & = 1 - 3u^2 + 2u^3 \\ \alpha_1(u) & = 3u^2 - 2u^3 \\ \beta_0(u) & = u - 2u^2 + u^3 \\ \beta_1(u) & = -u^2 + u^3 \end{array} \tag{A.12}$$

If such blending functions are used in Equation (A.9) then a composite surface is defined, which is made of Ferguson cubic curve segment. In this case the blending function vector

$$\begin{aligned}\vec{\mathbf{F}}(u) &= \begin{bmatrix} \alpha_0(u) & \alpha_1(u) & \beta_0(u) & \beta_1(u) \end{bmatrix} \\ &= \begin{bmatrix} 1 & u & u^2 & u^3 \end{bmatrix} \begin{bmatrix} 1 & 0 & 0 & 0 \\ 0 & 0 & 1 & 0 \\ -3 & 3 & -2 & -1 \\ 2 & -2 & 1 & 1 \end{bmatrix} \\ &= \vec{\mathbf{U}}C\end{aligned} \tag{A.13}$$

$$\begin{aligned}\vec{\mathbf{F}}^T(v) &= \begin{bmatrix} \alpha_0(v) \\ \alpha_1(v) \\ \beta_0(v) \\ \beta_1(v) \end{bmatrix} = \begin{bmatrix} 1 & 0 & -3 & 2 \\ 0 & 0 & 3 & -2 \\ 0 & 1 & -2 & 1 \\ 0 & 0 & -1 & 1 \end{bmatrix} \begin{bmatrix} 1 \\ v \\ v^2 \\ v^3 \end{bmatrix} \\ &= C^T\vec{\mathbf{V}}\end{aligned} \tag{A.14}$$

The Ferguson surface patch can then be expressed as

$$\vec{\mathbf{r}}(u, v) = \vec{\mathbf{U}}CQC^T\vec{\mathbf{V}} = \vec{\mathbf{U}}A\vec{\mathbf{V}} \tag{A.15}$$

where

$$A = CQC^T$$

Such a surface representation is widely used in geometry modelling.

Appendix B

Cranfield Low Speed Research Compressor

The compressor investigated in this project is the Cranfield University (*CU*) Low Speed Research Compressor (*LSRC*). A photograph of the *LSRC* installed on a test rig is shown in Figure B.1. A schematic drawing of the *LSRC* is given in Figure B.2 and a diagrammatic view of the blading of the compressor is shown in Figure B.3. The compressor consists of an inlet guide vane (*IGV*) followed by four identical stages and an outlet guide vane (*OGV*). The *IGV* is used to ensure that inlet conditions of the compressor are representative and thus to set up the correct levels of swirl and the *OGV* is to establish the required downstream flow environment. The annulus of the compressor has constant radius on the inner and outer wall. The blades are of a modern controlled diffusion type and provide a desired non-dimensional velocity distribution typical of a high speed design. The chosen aspect ratio and solidity are typical of modern HP compressor geometries. Therefore the stage loading was set to $\psi = 0.35$ at a flow coefficient $\phi = 0.5$. The test case which is used in this study has a tip clearance of 2% blade height, which is also a typical size in rear stages of high pressure axial flow compressors. Some details of the compressor working at peak efficiency are described in Table B.1 and B.2. Details about the blading is described in [172].

Conventional traverse measurement of total pressure, static pressure and flow angle was performed at downstream of

- IGV
- Rotor 1
- Stator 1

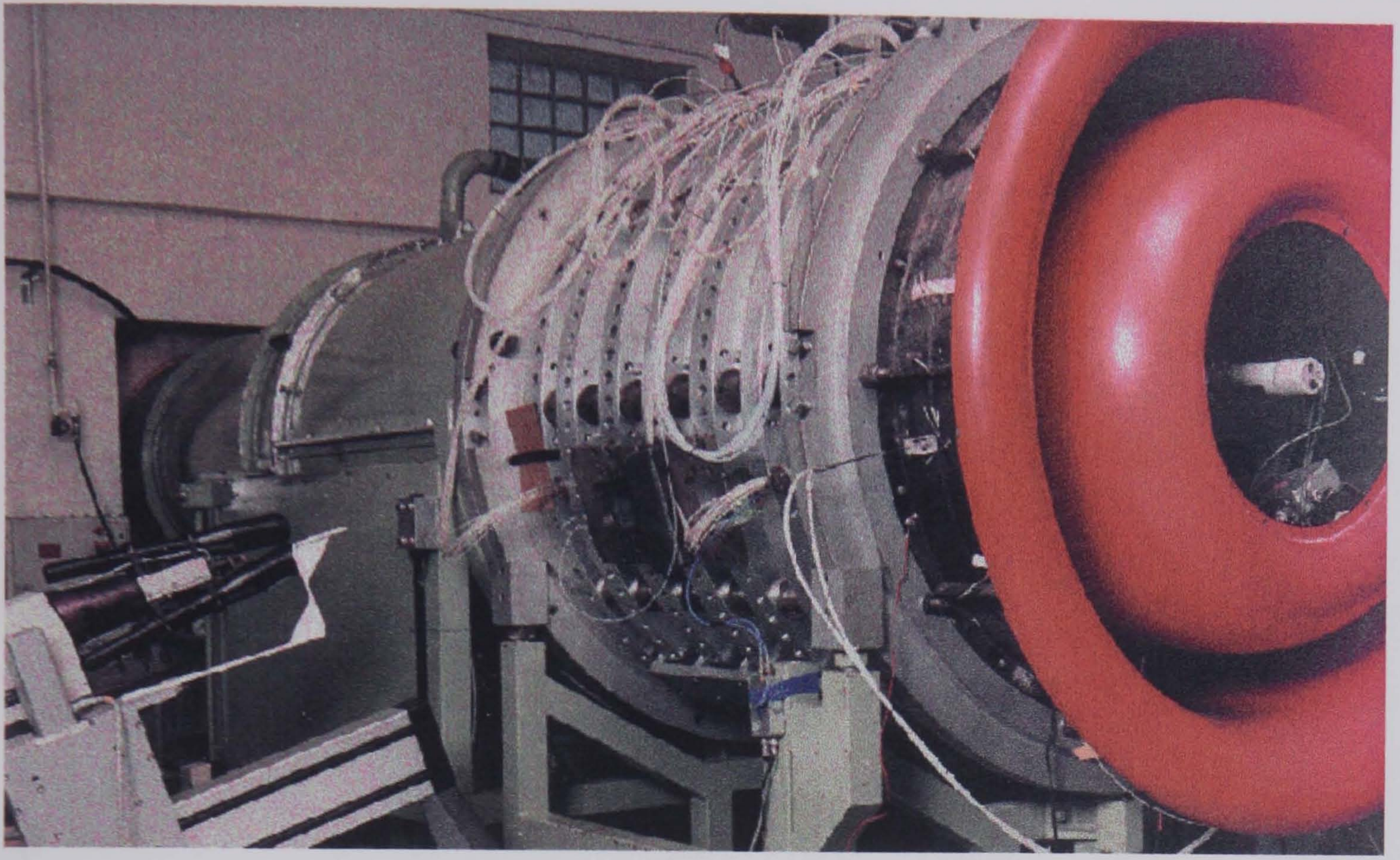

Figure B.1: *LSRC* **on test rig**

- Stator 2
- Rotor 3
- Stator 3

Advanced measurement of total pressure, static pressure and flow angle in rotating frame of reference with a rotating gear at downstream of rotor 3 was also carried out. Wall static pressure at the outer annular wall was measured as well. Additionally, the blade static pressure distributions at the hub, the midspan and the tip of the third stage was also measured.

The third stage is the main study stage, the first two are used to cause the flow to establish a repeating multistage behaviour and the fourth stage provides representive outlet flow conditions.

More details about the experimental work is described in [1] and [164].

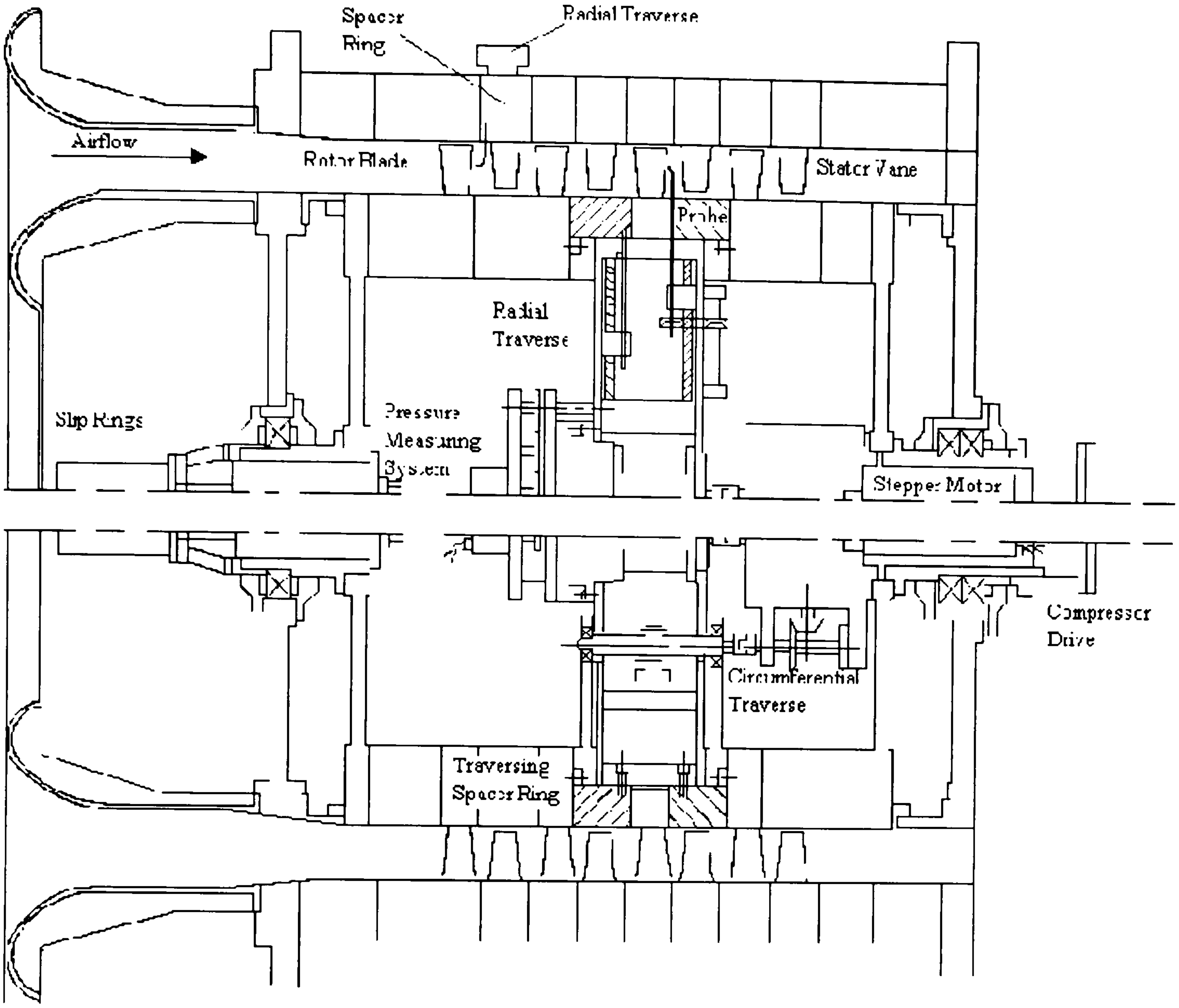

Figure B.2: **Structure of** ***LSRC***

Parameter	Values
Mass Flow Rate (kg/s)	12.24
Flow Density (kg/s^3)	1.25
Inlet Pressure (KPa)	101.28
Inlet Temperature (K)	288.15
Rotational Speed (rpm)	1100
Stage Loading $(\Delta H/U^2)$	0.35
Flow Coefficient (C_{ax}/U)	0.5
Stage Pressure Ratio	1.017
Degree of Reaction	0.64

Table B.1: **General parameters of** ***LSRC***

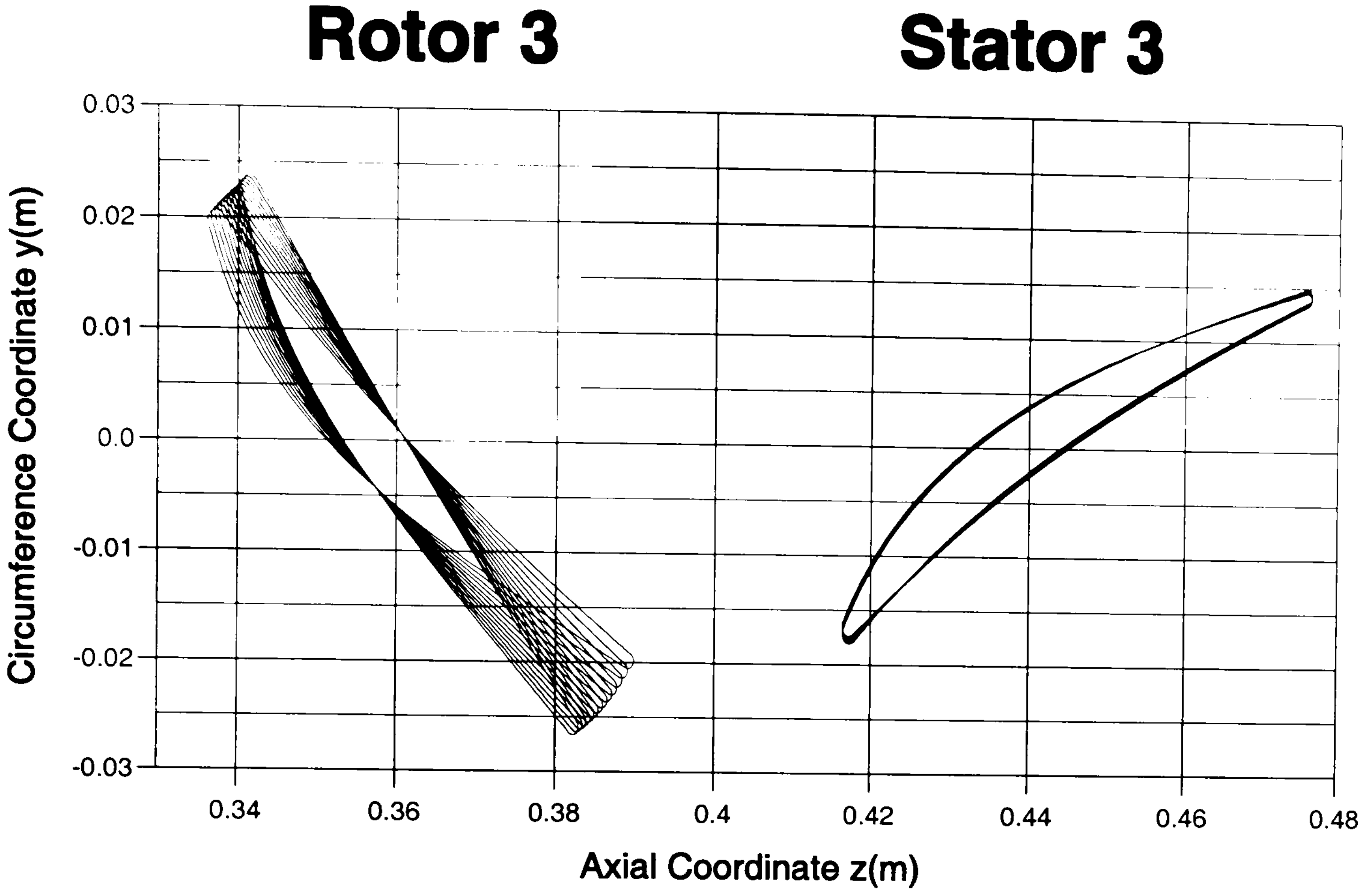

Figure B.3: **Blading geometry of *LSRC* Stage 3**

Parameter	Rotor	Stator
Number of Blades	75	96
Aspect Ratio	1.36	1.36
Space Chord	0.71	0.55
Thickness Chord	0.095	0.088
Turning (degree)	15.7	26.7
Exit Whirl (degree)	42.8	20.5
Diffusion Factor	0.42	0.41
Reynolds Number	2.9×10^5	2.3×10^5

Table B.2: **Parameters of *LSRC* Rotor 3 and Stator 3 blades**

Appendix C

Strongly Implicit Procedure(SIP)

This appendix describes the iterative procedure of an implicit approximation of three dimensional partial differential equations suggested by Stone [167] for solving a class of elliptic partial differential equations (PDE's). This procedure is used to solve the algebraic equations arising from the finite volume representation of the governing equations described in Chapter 3, which belongs to the elliptic class of equations.

The algorithm is developed to handle a seven-point algebraic equation in three dimensional cases, which may be represented in the following form:

$$\begin{aligned} A_b^{ijk}\phi^{i,j,k-1} \quad & + A_n^{ijk}\phi^{i,j-1,k} + A_w^{ijk}\phi^{i-1,j,k} + A_p^{ijk}\phi^{i,j,k} + \\ & + A_e^{ijk}\phi^{i+1,j,k} + A_s^{ijk}\phi^{i,j+1,k} + A_f^{ijk}\phi^{i,j,k+1} = S^{i,j,k} \end{aligned} \tag{C.1}$$

where the subscripts i, j and k refer to location within the grid network rather than the matrix row-column designation, the subscripts are used to identify the coefficients corresponding to the variables at different grid points, and the ϕ represent unknown quantities, see Figure C.1

Since one such equation exists for each grid point (i,j,k), there is a total of $n = (I+1)(J+1)(K+1)$ equations for the unknown variables. The equations can be written in the form

$$[\mathbf{A}]\,\vec{\mathbf{\Phi}} = \vec{\mathbf{S}} \tag{C.2}$$

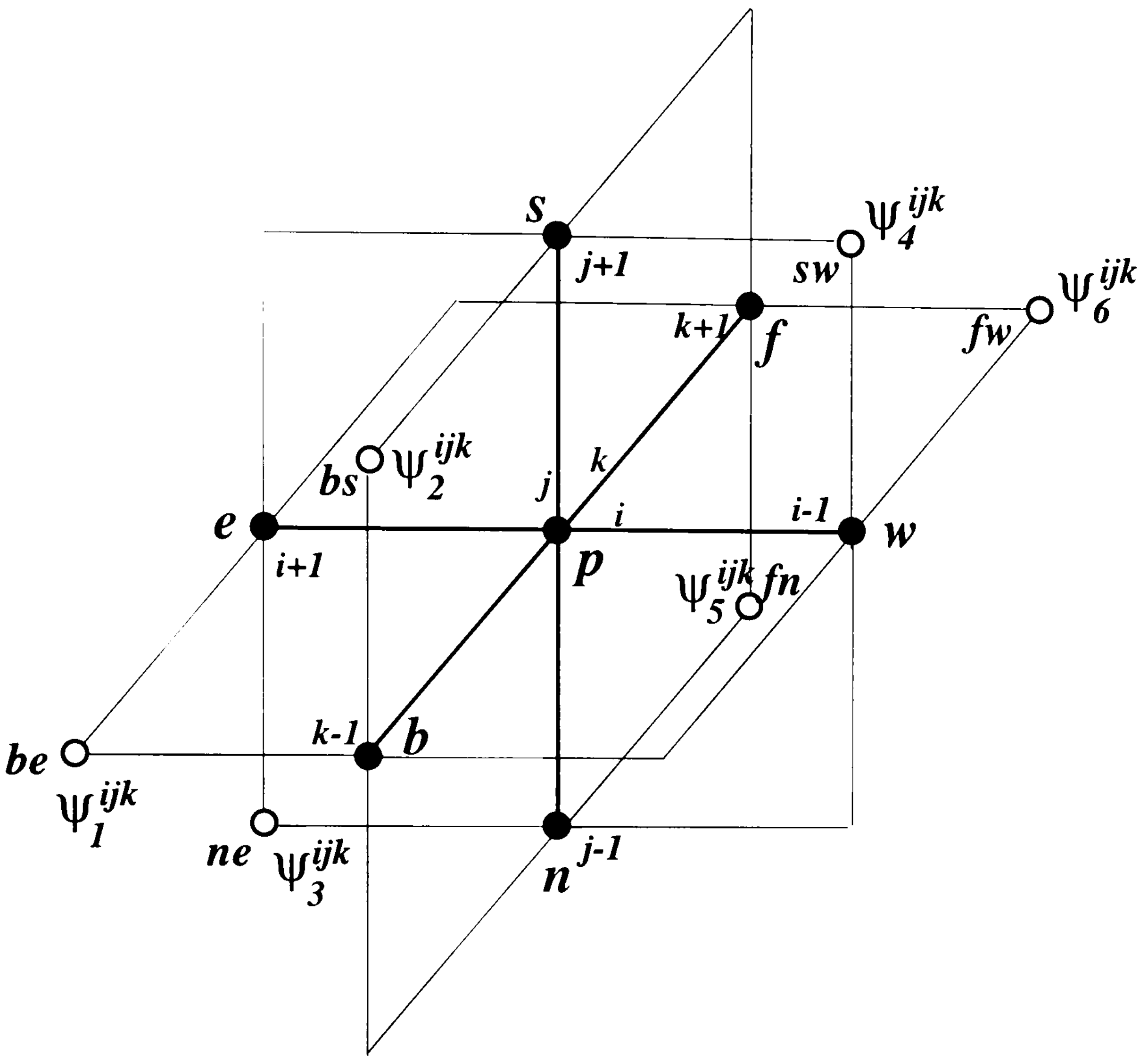

Figure C.1: **Schematical layout of grid network and symbols**

or in a expanded form given in Equation (C.3):

$$\begin{bmatrix}
\ddots & \ddots & & \ddots & & \ddots & & & & & \\
\ddots & \ddots & \ddots & & \ddots & & \ddots & & & & \\
 & \ddots & \ddots & \ddots & & \ddots & & \ddots & & & \\
\ddots & & \ddots & \ddots & \ddots & & \ddots & & A_f^{ijk} & & \\
 & \ddots & & \ddots & \ddots & \ddots & & A_s^{ijk} & & \ddots & \\
\ddots & & \ddots & & A_w^{ijk} & A_p^{ijk} & A_e^{ijk} & & \ddots & & \ddots \\
 & \ddots & & A_n^{ijk} & & \ddots & \ddots & \ddots & & \ddots & \\
 & & A_b^{ijk} & & \ddots & & \ddots & \ddots & \ddots & & \ddots \\
 & & & \ddots & & \ddots & & \ddots & \ddots & \ddots & \\
 & & & & \ddots & & \ddots & & \ddots & \ddots & \ddots \\
 & & & & & \ddots & & \ddots & & \ddots & \ddots
\end{bmatrix}
\begin{bmatrix} \vdots \\ \vdots \\ \vdots \\ \vdots \\ \vdots \\ \phi^{i,j,k} \\ \vdots \\ \vdots \\ \vdots \\ \vdots \\ \vdots \end{bmatrix}
=
\begin{bmatrix} \vdots \\ \vdots \\ \vdots \\ \vdots \\ \vdots \\ s^{i,j,k} \\ \vdots \\ \vdots \\ \vdots \\ \vdots \\ \vdots \end{bmatrix}
\tag{C.3}$$

We now construct another matrix

$$[\mathbf{B}] = [\mathbf{A} + \mathbf{P}] \tag{C.4}$$

such that $[\mathbf{B}]$ can be decomposed into a lower and an upper triangular matrix $[\mathbf{L}]$ and $[\mathbf{U}]$. It is required that $[\mathbf{L}]$ and $[\mathbf{U}]$ have only four nonzero elements in each row, regardless of the size of I, J or K. The $[\mathbf{L}]$ and $[\mathbf{U}]$ matrices have the form

$$[\mathbf{L}] = \left[\begin{array}{cccccccc}
\ddots & & & & & & & \\
\ddots & \ddots & & & & & & \\
\ddots & \ddots & \ddots & & & & & \\
\ddots & \ddots & \ddots & \ddots & & & & \\
 & a^{i,j,k} & b^{i,j,k} & c^{i,j,k} & d^{i,j,k} & & & \\
 & & \ddots & \ddots & \ddots & \ddots & & \\
 & & & \ddots & \ddots & \ddots & \ddots & \\
 & & & & \ddots & \ddots & \ddots & \ddots
\end{array}\right] \tag{C.5}$$

$$[\mathbf{U}] = \left[\begin{array}{cccccccc}
\ddots & \ddots & \ddots & \ddots & & & & \\
 & \ddots & \ddots & \ddots & \ddots & & & \\
 & & \ddots & \ddots & \ddots & \ddots & & \\
 & & & 1 & e^{i,j,k} & f^{i,j,k} & h^{i,j,k} & \\
 & & & & \ddots & \ddots & \ddots & \ddots \\
 & & & & & \ddots & \ddots & \ddots \\
 & & & & & & \ddots & \ddots \\
 & & & & & & & \ddots
\end{array}\right] \tag{C.6}$$

The equations to be used to determine the coefficients of $[\mathbf{L}]$ and $[\mathbf{U}]$ such that the original seven coefficients in $[\mathbf{A}]$ remain unchanged in $[\mathbf{B}]$ are

$$\begin{aligned}
a^{i,j,k} &= A_b^{ijk} \\
b^{i,j,k} &= A_n^{ijk} \\
c^{i,j,k} &= A_w^{ijk} \\
c^{i,j,k}e^{i-1,j,k} + d^{i,j,k} + b^{i,j,k}f^{i,j-1,k} + a^{i,j,k}h^{i,j,k-1} &= A_p^{ijk} \\
d^{i,j,k}e^{i,j,k} &= A_e^{ijk} \\
d^{i,j,k}f^{i,j,k} &= A_s^{ijk} \\
d^{i,j,k}h^{i,j,k} &= A_f^{ijk}
\end{aligned} \tag{C.7}$$

The modified coefficient matrix $[\mathbf{B}] = [\mathbf{A} + \mathbf{P}]$ has the form

$$
[\mathbf{B}] = \begin{bmatrix}
\ddots & \ddots & & \ddots & \ddots & & \ddots & & \ddots & \ddots & & \\
\ddots & \ddots & \ddots & & \ddots & \ddots & & \ddots & & \psi_6^{ijk} & A_f^{ijk} & \\
 & \ddots & \ddots & \ddots & & \ddots & \ddots & & \psi_5^{ijk} & & \ddots & \ddots \\
\ddots & & \ddots & \ddots & \ddots & & \psi_4^{ijk} & A_s^{ijk} & & \ddots & & \ddots \\
\ddots & \ddots & & \ddots & \ddots & A_e^{ijk} & & \ddots & \ddots & & \ddots & \\
 & \ddots & \ddots & & \ddots & A_p^{ijk} & \ddots & & \ddots & \ddots & & \ddots \\
\ddots & & \ddots & \ddots & & A_w^{ijk} & \ddots & \ddots & & \ddots & \ddots & \\
 & \ddots & & \ddots & \ddots & & \ddots & \ddots & \ddots & & \ddots & \ddots \\
\ddots & & \ddots & & A_n^{ijk} & \psi_3^{ijk} & & \ddots & \ddots & \ddots & & \ddots \\
\ddots & \ddots & & \psi_2^{ijk} & & \ddots & \ddots & & \ddots & \ddots & \ddots & \\
 & A_b^{ijk} & \psi_1^{ijk} & & \ddots & & \ddots & \ddots & & \ddots & \ddots & \ddots \\
 & & \ddots & \ddots & & \ddots & & \ddots & \ddots & & \ddots & \ddots
\end{bmatrix}
\tag{C.8}
$$

The elements in $[\mathbf{B}]$ denoted by ψ_1^{ijk}, ψ_2^{ijk}, ψ_3^{ijk}, ψ_4^{ijk}, ψ_5^{ijk} and ψ_5^{ijk} are determined from

$$
\begin{aligned}
\psi_1^{ijk} &= a^{i,j,k} e^{i,j,k-1} \\
\psi_2^{ijk} &= a^{i,j,k} f^{i,j+1,k-1} \\
\psi_3^{ijk} &= b^{i,j,k} e^{i,j-1,k} \\
\psi_4^{ijk} &= c^{i,j,k} f^{i-1,j,k} \\
\psi_5^{ijk} &= b^{i,j,k} h^{i,j-1,k} \\
\psi_6^{ijk} &= c^{i,j,k} h^{i-1,j,k}
\end{aligned}
\tag{C.9}
$$

The numerical molecular associated with matrix $[\mathbf{B}]$ is shown schematically in Figure C.1.

Stone employed Talyor-series expansions to obtain values of $\phi^{i+1,j,k+1}$, $\phi^{i,j+1,k-1}$, $\phi^{i+1,j-1,k}$, $\phi^{i-1,j+1,k}$, $\phi^{i,j-1,k+1}$ and $\phi^{i-1,j,k+1}$ in terms of $\phi' s$ in the original seven-point molecular to partially cancel the influence of the additional ϕ^{ijk} terms in the $[\mathbf{B}]$ matrix. These are

$$
\begin{aligned}
\phi^{i+1,j,k-1} &= -\phi^{ijk} + \phi^{i,j,k-1} + \phi^{i+1,j,k} \\
\phi^{i,j+1,k-1} &= -\phi^{ijk} + \phi^{i,j+1,k} + \phi^{i,j,k-1} \\
\phi^{i+1,j-1,k} &= -\phi^{ijk} + \phi^{i+1,j,k} + \phi^{i,j-1,k} \\
\phi^{i-1,j+1,k} &= -\phi^{ijk} + \phi^{i-1,j,k} + \phi^{i,j+1,k} \\
\phi^{i,j-1,k+1} &= -\phi^{ijk} + \phi^{i,j-1,k} + \phi^{i,j,k+1} \\
\phi^{i-1,j,k+1} &= -\phi^{ijk} + \phi^{i-1,j,k} + \phi^{i,j,k+1}
\end{aligned}
\tag{C.10}
$$

An iterative parameter α is used to implement partial cancellation of the influence of the $\phi^{i,j,k}$ terms appearing in [**B**]. This is done by using a modified seven-point scheme in the form

$$\begin{aligned}
&A_b^{ijk}\phi^{i,j,k-1} + A_n^{ijk}\phi^{i,j-1,k} + A_w^{ijk}\phi^{i-1,j,k} + A_p^{ijk}\phi^{i,j,k} + \\
&+A_e^{ijk}\phi^{i+1,j,k} + A_s^{ijk}\phi^{i,j+1,k} + A_f^{ijk}\phi^{i,j,k+1} + \\
&+\psi_1^{ijk}[\phi^{i+1,j,k-1} - \alpha(-\phi^{i,j,k} + \phi^{i+1,j,k} + \phi^{i,j,k-1})] + \\
&+\psi_2^{ijk}[\phi^{i,j+1,k-1} - \alpha(-\phi^{i,j,k} + \phi^{i,j+1,k} + \phi^{i,j,k-1})] + \\
&+\psi_3^{ijk}[\phi^{i+1,j-1,k} - \alpha(-\phi^{i,j,k} + \phi^{i+1,j,k} + \phi^{i,j-1,k})] + \\
&+\psi_4^{ijk}(\phi^{i-1,j+1,k} - \alpha(-\phi^{i,j,k} + \phi^{i-1,j,k} + \phi^{i.j+1,k})] + \\
&+\psi_5^{ijk}[\phi^{i,j-1,k+1} - \alpha(-\phi^{i,j,k} + \phi^{i,j-1,k} + \phi^{i,j,k+1})] + \\
&+\psi_6^{ijk}[\phi^{i-1,j,k+1} - \alpha(-\phi^{i,j,k} + \phi^{i-1,j,k} + \phi^{i,j,k+1})] = s^{ijk}
\end{aligned} \tag{C.11}$$

Equation (C.11) is re-arranged to produce the modified expression of Equation (C.7) to include the partial cancellation:

$$\begin{aligned}
a^{i,j,k} &= A_b^{ijk} - \alpha(\psi_1^{ijk} + \psi_2^{ijk}) \\
b^{i,j,k} &= A_n^{ijk} - \alpha(\psi_3^{ijk} + \psi_5^{ijk}) \\
c^{i,j,k} &= A_w^{ijk} - \alpha(\psi_4^{ijk} + \psi_6^{ijk}) \\
c^{i,j,k}e^{i-1,j,k} &+ d^{i,j,k} + b^{i,j,k}f^{i,j-1,k} + a^{i,j,k}h^{i,j,k-1} \\
&= A_p^{ijk} + \alpha(\psi_1^{ijk} + \psi_2^{ijk} + \psi_3^{ijk} + \psi_4^{ijk} + \psi_5^{ijk} + \psi_6^{ijk}) \\
d^{i,j,k}e^{i,j,k} &= A_e^{ijk} - \alpha(\psi_1^{ijk} + \psi_3^{ijk}) \\
d^{i,j,k}f^{i,j,k} &= A_s^{ijk} - \alpha(\psi_2^{ijk} + \psi_4^{ijk}) \\
d^{i,j,k}h^{i,j,k} &= A_f^{ijk} - \alpha(\psi_5^{ijk} + \psi_6^{ijk})
\end{aligned} \tag{C.12}$$

The explicit evaluation of the elements of [**L**] and [**U**] are:

$$\begin{aligned}
a^{i,j,k} &= \frac{A_b^{ijk}}{1 + \alpha(e^{i,j,k-1} + f^{i,j+1,k})} \\
b^{i,j,k} &= \frac{A_n^{ijk}}{1 + \alpha(e^{i,j-1,k} + h^{i,j-1,k})} \\
c^{i,j,k} &= \frac{A_w^{ijk}}{1 + \alpha(f^{i-1,j,k} + h^{i-1,j,k})} \\
d^{i,j,k} &= A_p^{ijk} + \alpha(a^{i,j,k}e^{i,j,k-1} + a^{i,j,k}f^{i,j+1,k} + b^{i,j,k}e^{i,j-1,k} + \\
&\quad + c^{i,j,k}f^{i-1,j,k} + b^{i,j,k}h^{i,j-1,k} + c^{i,j,k}h^{i-1,j,k}) - \\
&\quad - c^{i,j,k}e^{i-1,j,k} - b^{i,j,k}f^{i,j-1,k} - a^{i,j,k}h^{i,j,k-1} \\
e^{i,j,k} &= \frac{1}{d^{i,j,k}}[A_e^{ijk} - \alpha(a^{i,j,k}e^{i,j,k-1} + b^{i,j,k}e^{i,j-1,k})] \\
f^{i,j,k} &= \frac{1}{d^{i,j,k}}[A_s^{ijk} - \alpha(a^{i,j,k}f^{i,j+1,k} + c^{i,j,k}f^{i-1,j,k})] \\
h^{i,j,k} &= \frac{1}{d^{i,j,k}}[A_f^{ijk} - \alpha(b^{i,j,k}h^{i,j-1,k} + c^{i,j,k}h^{i-1,j,k})]
\end{aligned} \tag{C.13}$$

The iterative sequence is developed as follows. Adding $[\mathbf{P}]\vec{\mathbf{\Phi}}$ to both sides of Equation (C.2) gives:

$$[\mathbf{A}+\mathbf{P}]\vec{\mathbf{\Phi}} = \vec{\mathbf{S}} + [\mathbf{P}]\vec{\mathbf{\Phi}} \tag{C.14}$$

We evaluate the unknowns on the right-hand side at the n iteration level to write

$$[\mathbf{A}+\mathbf{P}]\vec{\mathbf{\Phi}}^{n+1} = \vec{\mathbf{S}} + [\mathbf{P}]\vec{\mathbf{\Phi}}^{n} \tag{C.15}$$

Decomposing $[\mathbf{A}+\mathbf{P}]$ into $[\mathbf{L}]$ and $[\mathbf{U}]$ matrices gives

$$[\mathbf{L}][\mathbf{U}]\vec{\mathbf{\Phi}}^{n+1} = \vec{\mathbf{S}} + [\mathbf{P}]\vec{\mathbf{\Phi}}^{n} \tag{C.16}$$

Defining an iterative vector $\vec{\mathbf{V}}^{n+1}$ by

$$\vec{\mathbf{V}}^{n+1} = [\mathbf{U}]\vec{\mathbf{\Phi}}^{n+1} \tag{C.17}$$

Then a two-step process is employed:

$$\begin{array}{ll} \textbf{Step1}: & [\mathbf{L}]\vec{\mathbf{V}}^{n+1} = \vec{\mathbf{q}} + [\mathbf{P}]\vec{\mathbf{\Phi}}^{n} \\ \textbf{Step2}: & [\mathbf{U}\vec{\mathbf{\Phi}}^{n+1} = \vec{\mathbf{V}}^{n+1} \end{array} \tag{C.18}$$

The process represented in Step 1 of Equation (C.18) consists of a forward substitution starting with

$$v^{0,0,0} = s^{0,0,0}/d^{0,0,0} \tag{C.19}$$

and continuing with

$$\begin{aligned} v^{i,j,k} &= \frac{1}{d^{i,j,k}}[s^{i,j,k} - a^{i,j,k}v^{i,j,k-1} - b^{i,j,k}v^{i,j-1,k} - c^{i,j,k}v^{i-1,j,k}] \\ &(i = 1,2,....,I; j = 1,2,...,J; k = 1,2,...,K) \end{aligned} \tag{C.20}$$

The process represented in Step 2 of Equation (C.18) consists of a backward substitution starting with

$$\phi^{I,J,K} = v^{I,J,K} \tag{C.21}$$

and continuing with

$$\begin{aligned} \phi^{i,j,k} &= v^{i,j,k} - e^{i,j,k}\phi^{i+1,j,k} - f^{i,j,k}\phi^{i,j+1,k} - h^{i,j,k}\phi^{i,j,k+1} \\ &(i = I-1, I-2, ..., 0; j = J-1, j-2, ..., 0; k = K-1, K-2, ..., 0) \end{aligned} \tag{C.22}$$

The elements of $[\mathbf{P}]$ are simply ψ_1^{ijk}, ψ_2^{ijk}, ψ_3^{ijk}, ψ_4^{ijk}, ψ_5^{ijk} and ψ_6^{ijk} values determined by Equation (C.9).

Alternatively, we can define a differential vector

$$\vec{\delta}^{n+1} = \vec{\mathbf{\Phi}}^{n+1} - \vec{\mathbf{\Phi}}^{n} \tag{C.23}$$

and a residual vector

$$\vec{\mathbf{R}}^n = \vec{\mathbf{S}} - [\mathbf{A}]\vec{\mathbf{\Phi}}^n \tag{C.24}$$

so that Equation (C.15) becomes:

$$[\mathbf{A}+\mathbf{P}]\vec{\delta}^{n+1} = \vec{\mathbf{R}}^n \tag{C.25}$$

Replacing $[\mathbf{A}+\mathbf{P}]$ by the $[\mathbf{L}][\mathbf{U}]$ product gives

$$[\mathbf{L}][\mathbf{U}]\vec{\delta}^{n+1} = \vec{\mathbf{R}}^n \tag{C.26}$$

Defining an intermediate vector $\vec{\mathbf{W}}^{n+1}$ by

$$\vec{\mathbf{W}}^{n+1} = [\mathbf{U}]\vec{\delta}^{n+1} \tag{C.27}$$

The solution procedure can again be written as a two-step process:

$$\begin{array}{ll} \mathbf{Step1}: & [\mathbf{L}]\vec{\mathbf{W}}^{n+1} = \vec{\mathbf{R}}^n \\ \mathbf{Step2}: & [\mathbf{U}]\vec{\delta}^{n+1} = \vec{\mathbf{W}}^{n+1} \end{array} \tag{C.28}$$

Similar process represented in Equation (C.28) are a forward process starting with

$$w^{0,0,0} = r^{0,0,0}/d^{0,0,0} \tag{C.29}$$

and continuing with

$$\begin{aligned} w^{i,j,k} &= \frac{1}{d^{i,j,k}}[r^{i,j,k} - a^{i,j,k}w^{i,j,k-1} - b^{i,j,k}w^{i,j-1,k} - c^{i,j,k}w^{i-1,j,k}] \\ & (i = 1,2,...,I; j = 1,2,...,J; k = 1,2,...,K) \end{aligned} \tag{C.30}$$

and a backward process starting with

$$\delta_{I,J,K} = w^{I,J,K} \tag{C.31}$$

and continuing with

$$\begin{aligned} \delta_{i,j,k} &= w^{i,j,k} - e^{i,j,k}\delta_{i+1,j,k} - f^{i,j,k}\delta_{i,j+1,k} - h^{i,j,k}\delta_{i,j,k+1} \\ & (i = I-1, I-2, ...0; j = J-1, j-2, ..., 0; k = K-1, K-2, ..., 0) \end{aligned} \tag{C.32}$$

The coefficients remain unchanged for the iterative process. The right-hand side of Equation (C.28) is then updated and the process is repeated until a converged solution is obtained.

Appendix D

Structure of the Computer Code *MSTurbo3D*

Figures D.1 to D.3 show the flow charts of the main program and the subprograms of the computer code *MSTurbo3D*.

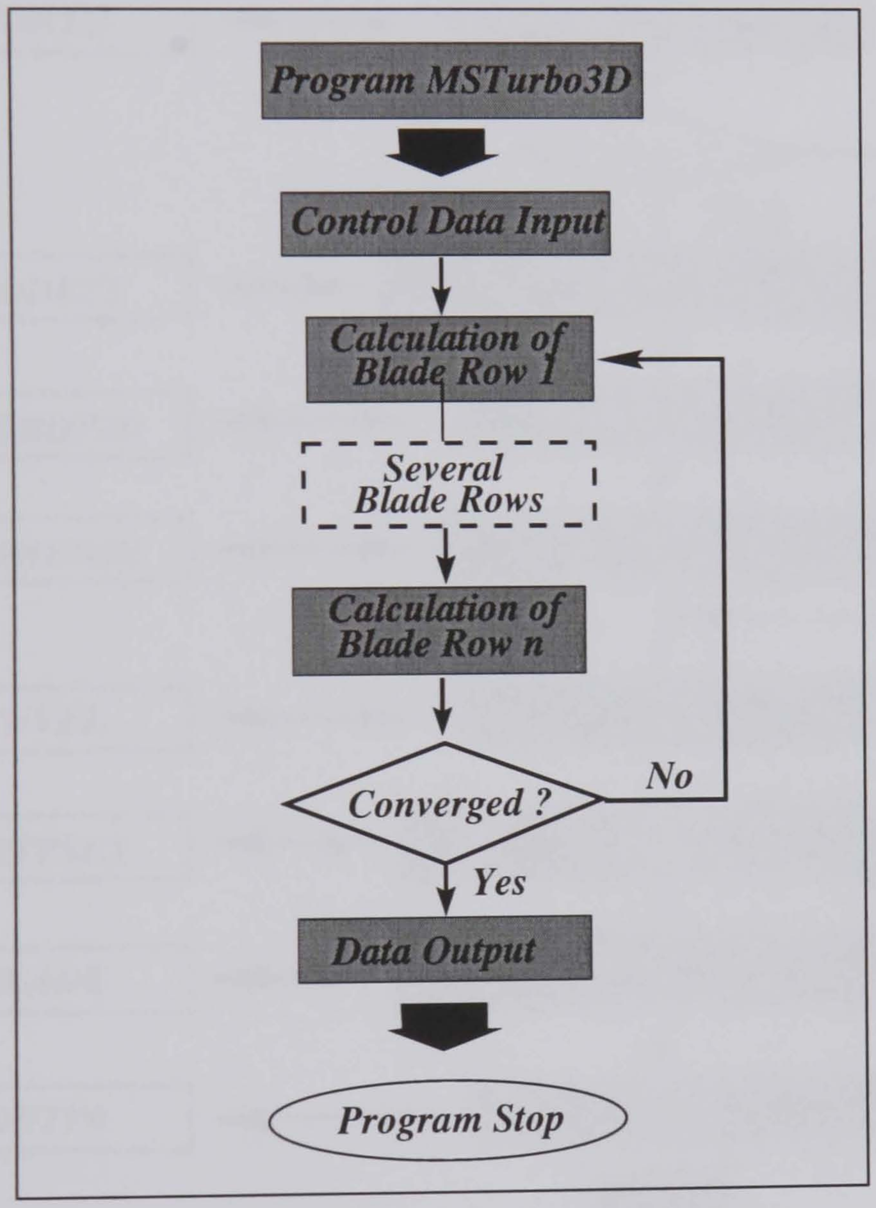

Figure D.1: **Global structure of computer code** $MSTurbo3D$

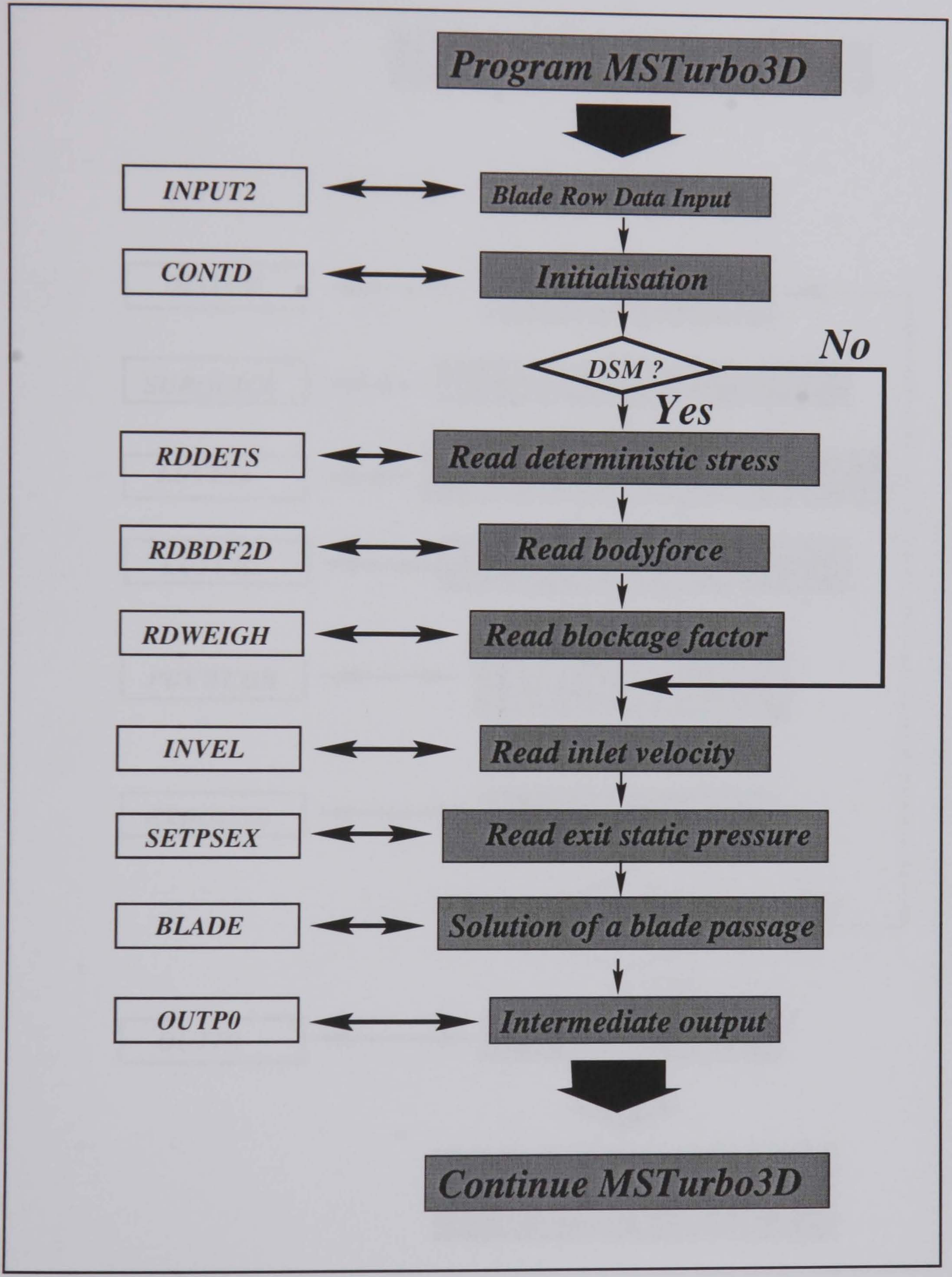

Figure D.2: Subprogram for the calculation of a blade row

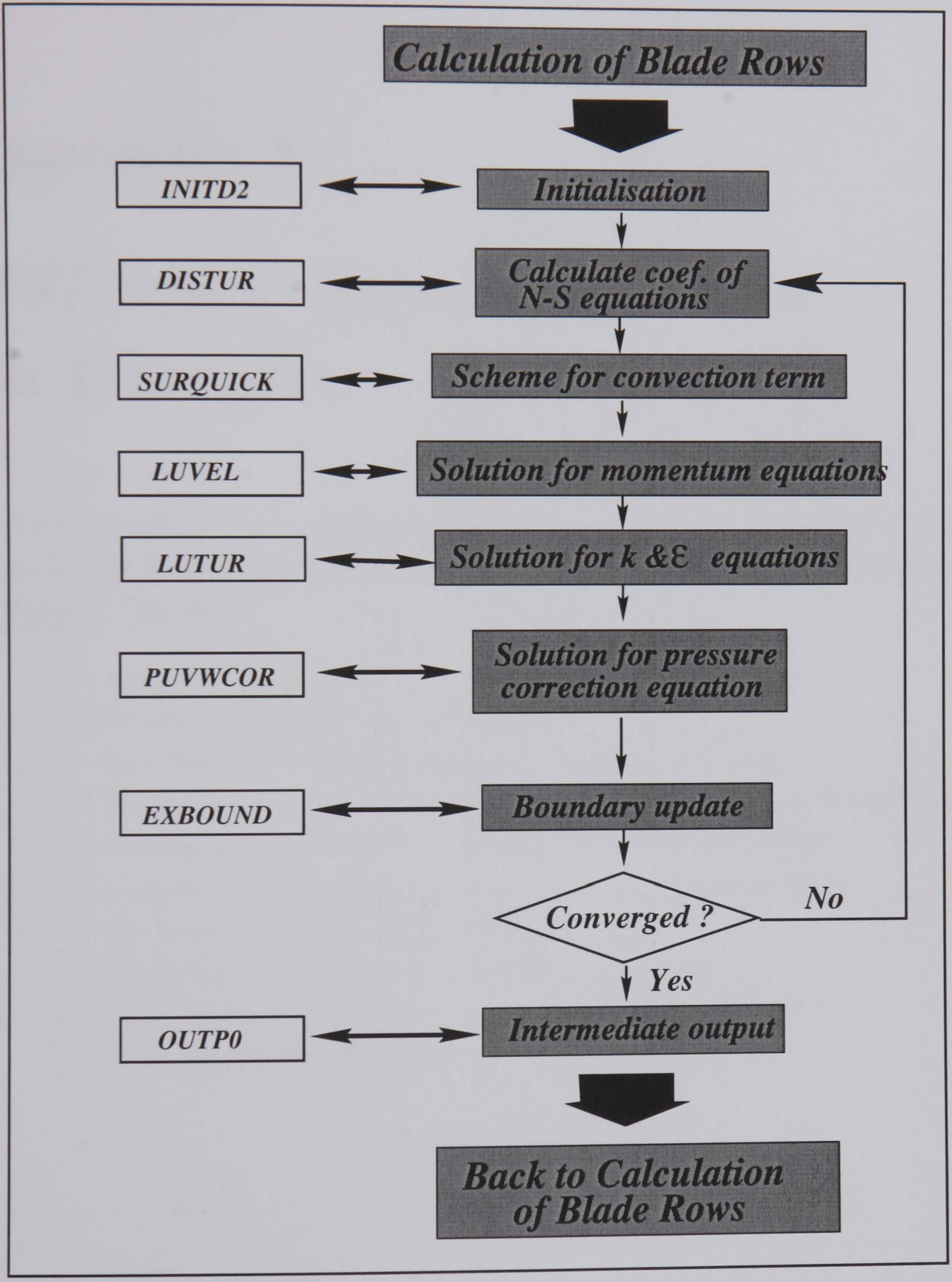

Figure D.3: Subprogram for the solution of N-S equations

Appendix E

MSTurbo3D Input Data Files – An Example

The appendix presents a typical input data file to the computer code *MSTurbo3D* which controls the process of the code. The format of the file "input" is as follows:

Typical "input"

```
2        —- number of blade rows
1        —- format of data file: 1–ascii, 2–binary
1        —- Interface type : 1–mixing plane, 2–continuous interface
3        —- Boundary setting : 1–set inlet Pt&angle, 2–set inlet vel. 3–repeating stages
2        —- Mixing model : 1–circum. uniform , 2–circum. non-uniform
1        —- computation choice : 1–initial computation, 2–continuation
1        —- the blade row from which calculation starts
2        —- discretisation : 1–upwind, 2–QUICK, 3–Zijlema
1        —- initial global iterations
0        —- Additional global Iterations
```

Following is an example of input data file "inicit" which read in detailed data of every blade row.

Typical "inicit"

```
*****  BLADE ROW R3
-1.1-  case counter          : 0-1 domain,      1-2 domains (with tip)
       1
-1.2-  blade type            : 1-rotor,      2-stator
       1
-1.3-  hub type              : 1-moving,     2-stationary
       1
-1.4-  inlet velocity type:      1-read INLETV,      2-Log profile
       1
-1.5-  inlet velocity file name
       EXITV2
-1.6-  Exit velocity file name
       EXITV1
-1.7-  Inlet static pressure file name
       INLTPS1
-1.8-  Exit static pressure file name
       INLTPS2
-1.9-  Inlet tke file name
       EXTKE2
-1.0-  Exit tke file name
       EXTKE1
-1.1-  main grid file name
       grrman.dat
-1.2-  tip grid file name
       grrtip.dat
-1.3-  connection file name (dom2->1)
       connect.up
-1.4-  connection file name (dom1->2)
       connect.low
-1.5-  average residual file name (domain 1)
       conv11.dat
-1.6-  average residual file name (domain 2)
       conv12.dat
```

```
-1.7-   maximum residual file name (domain 1)
        cavr11.dat
-1.8-   maximum residual file name (domain 2)
        cavr12.dat
-1.9-   intermediate CFD results file name (binary, domain 1)
        rescc11
-1.0-   intermediate CFD results file name (binary, domain 2)
        rescc12
-1.1-   intermediate CFD results file name (ASCII, domain 1)
        rescv11
-1.2-   intermediate CFD results file name (ASCII, domain 2)
        rescv12
-1.3-   ptotin    ttotin   flrate     angle1    psout     numbld
          -1.0    290.4    0.163168   1000.     102838.   75
-1.4-   relax: u,    v,     w,     tke,    ted,    h,     p,     rho,    emu
               0.25  0.25   0.25   0.25    0.25    1.0    0.25   1.0    1.0    1.0
-1.5-   Inlet total pressure file name
        INLPT1
-1.6-   Inlet flow angle file name
        INANG1
-1.7-   ksymm
        0
-1.8-   coords-multiplier;   rotational speed;    rescv file output(0-no,1-yes)
              1.000               -1100.                    0
-1.9-   igmon.   ixmon.   iymon.   izmon (monitoring point)
          1        15       15        1
-1.0-   rschek(allowed error)       amschek
              -2.5                  0.0001
-1.1-   inner iteration No.         iplrs(printout step)
              5000                    100
-1.2-   Density
        1.2500
****    BLADE ROW S3
-2.1-   case counter       : 1-tip clearance,       0-1 domain
        0
-2.2-   blade type         : 1-rotor,       2-stator
```

```
         2
-2.3-    hub type        : 1-moving,      2-stationary
         2
-2.4-    inlet velocity type: 1-read INLETV,        2-Log profile
         1
-2.5-    inlet velocity file name
         EXITV1
-2.6-    Exit velocity file name
         EXITV2
-2.7-    Inlet static pressure file name
         INLTPS2
-2.8-    Exit static pressure file name
         INLTPS1
-2.9-    Inlet tke file name
         EXTKE1
-2.0-    Exit tke file name
         EXTKE2
-2.1-    grid file name
         grsman.dat
-2.2-    average residual file name(domain 1)
         conv21.dat
-2.3-    maximum residual file name(domain 1)
         cavr21.dat
-2.4-    intermediate CFD results (binary, domain 1)
         rescc21
-2.5-    intermediate CFD results (ASCII, domain 1)
         rescv21
-2.6-    ptotin     ttotin     flrate     angle1    psout      numbld
         104760.    290.4      0.127475   0.        103391.6   96
-2.7-    relax: u.      v,      w,      tke,     ted,     h,     p,     rho,     emu
            0.10   0.10   0.10    0.10    0.10    1.0   0.10    1.0    1.0    1.0
-2.8-    ksymm
         0
-2.9-    coords-multiplier;       rotational speed;     rescv file output(0-no,1-yes)
             1.000                      -1100.                     0
-2.0-    igmon,   ixmon,   iymon,    izmon (monitoring point)
```

	1 15	15 1
-2.1-	rschek(allowed error)	amschek
	-2.5	0.0001
-2.2-	inner iteration No.	iplrs(printout step)
	5000	100
-2.3-	Density	
	1.2500	

Appendix F

Entropy Equation

The first law of thermodynamics may be expressed as:

$$dQ + dW = dU \tag{F.1}$$

Combined with the definition of enthalpy $h = e + pv$ and the state equation of ideal gas $pv = \rho RT$. another form of the equation is obtained:

$$T \nabla s = \nabla h - \frac{1}{\rho} \nabla p \tag{F.2}$$

The continuity equation of mass is:

$$\frac{D\rho}{Dt} - \rho(\nabla \cdot \vec{V}) = 0 \tag{F.3}$$

where

$$\frac{D}{Dt} = \frac{\partial}{\partial t} + \vec{V} \cdot \nabla$$

or

$$\frac{\partial \rho}{\partial t} + \nabla \cdot (\rho \vec{V}) = 0 \tag{F.4}$$

For steady state flow the equation becomes

$$\nabla \cdot (\rho \vec{V}) = 0 \tag{F.5}$$

The momentum equation takes the following form:

$$\rho \frac{D\vec{V}}{Dt} = - \nabla p + \nabla \tau + \rho \vec{f} \tag{F.6}$$

For steady state flow it becomes

$$\rho \vec{V} \cdot (\nabla \cdot \vec{V}) = - \nabla p + \nabla \cdot \tau + \rho \vec{f} \tag{F.7}$$

The energy equation has the following form:

$$\frac{\partial E}{\partial t} + \nabla \cdot (E\vec{V}) = \frac{\partial Q}{\partial t} - \nabla \cdot \vec{q} + \rho \vec{f} \cdot \vec{V} - \nabla \cdot (p\vec{V}) + \nabla \cdot (\tau \cdot \vec{V}) \tag{F.8}$$

where

$$E = \rho \left(\epsilon + \frac{\vec{V}^2}{2} \right)$$

$$\vec{q} = -k \nabla T$$

For steady state flow, substituting the continuity equation (F.5) into Equation (F.8) gives:

$$\rho\vec{V} \cdot \nabla\epsilon + \rho\vec{V} \cdot (\vec{V} \cdot \nabla\vec{V}) = -\nabla \cdot \vec{q} + \rho\vec{f} \cdot \vec{V} - \nabla \cdot (p\vec{V}) + \nabla \cdot (\tau \cdot \vec{V}) \tag{F.9}$$

Forming the scalar dot product of momentum equation (F.7) with the velocity vector $\vec{V}$ allows one to obtain:

$$\rho\vec{V} \cdot \nabla\epsilon + \left[\nabla \cdot (p\vec{V}) - \nabla p \cdot \vec{V}\right] = -\nabla \cdot \vec{q} + \left[\nabla(\tau \cdot \vec{V}) - (\nabla \cdot \tau) \cdot \vec{V}\right] \tag{F.10}$$

With continuity equation (F.5) we obtain:

$$\nabla \cdot (\rho\vec{V}) = \rho\vec{V} \cdot \nabla(\frac{p}{\rho}) \tag{F.11}$$

Substituting Equation (F.11) into (F.10) obtains:

$$\rho\vec{V} \cdot \nabla h - \nabla p \cdot \vec{V} = -\nabla \cdot \vec{q} + \tau \cdot (\nabla\vec{V}) \tag{F.12}$$

Forming a scalar dot product of Equation (F.2) with $\vec{V}$ gives:

$$\rho T\vec{V} \cdot \nabla s = \rho\vec{V} \cdot \nabla h - \vec{V} \cdot \nabla p \tag{F.13}$$

Combining Equations (F.12) and (F.13) obtains the following steady state entropy equation:

$$\rho T\vec{V} \cdot \nabla s = -\nabla \cdot \vec{q} + \varepsilon_\nu \tag{F.14}$$

where ε_ν is called non-negative dissipation term and may be expressed as:

$$\varepsilon_\nu = \tau \cdot (\nabla \cdot \vec{V}) = \tau_{ij}\frac{\partial v_i}{\partial x_j} \tag{F.15}$$

Substituting the continuity equation (F.5) into Equation (F.14) obtains:

$$\nabla \cdot (\rho\vec{V}s) = \frac{1}{T}(\nabla \cdot \vec{q}) + \frac{1}{T}\left[\tau \cdot (\nabla \cdot \vec{V})\right] \tag{F.16}$$

where the term

$$s' = -\frac{1}{T}(\nabla \cdot \vec{q}) + \frac{1}{T}\left[\tau \cdot (\nabla \cdot \vec{V})\right]$$

is the rate of entropy generation.

The entropy equation is not independent from the energy equation. Note also that the entropy is not a "conserved" quantity in the sense of the derived conserved form of governing equations, Hirsch [79].

Bibliography

[1] "Advanced Civil Core Compressor Aerodynamics: Final Technical Report", IMT AER2-CT92-0039. 1996.

[2] Adamczyk J. J. (1984) "Model Equation for Simulating Flows in Multistage Turbomachinery". NASA TM-86869; ASME paper, 85-GT-226.

[3] Adamczyk J.J., Mulac R.A. and Celestina M.L. (1986) "A Model for Closing the Inviscid Form of the Average-Passage Equation System", *Journal of Turbomachinery*, Vol. 108, pp. 180-186.

[4] Adamczyk J.J., Celestina M.L., Beach T.A. and Barnett M. (1990) "Simulation of Three-Dimensional Viscous Flow Within a Multistage Turbine", *Journal of Turbomachinery*, Vol. 112, pp. 370-376.

[5] Adamczyk J.J., Celestina M.L., and Chen J. P. (1994) "Wake-Induced Unsteady Flows: Their Impact on Rotor Performance and Wake Rectification", ASME Paper 94-GT-219.

[6] Adamczyk J.J. (1999) "Aerodynamic Analysis of Multistage Turbomachinery Flows in Support of Aerodynamic Design", ASME Paper 99-GT-80.

[7] Adler D. and Krimerman Y. (1978) "The Complete 3-Dimensional Calculation of the Compressible Flow Field in Turbo Impellers", *Journal of Mechanical Engineering Science*, Vol. 20, p. 149.

[8] Adler D. and Krimerman Y. (1974) "The Numerical Calculation of the Meridional Flow Field in Turbomachines Using the Finite Element Method", *Israel Journal of Technology*, Vol. 12, No. 34.

[9] Adler D. and Krimerman Y. (1977) " The Numerical Calculation of the Blade-to-Blade Flow Field in Turbomachines Using the Finite Element Method", *Journal of Mechanical Engineering Science*, Vol. 19, p. 108.

[10] Anderson J.D. (1995) "Computational Fluid Dynamics", McGraw-Hill, Inc.

[11] Baldwin B.S. and Lomax H. (1978) "Thin Layer Approximation and Algebraic Model for Separated Turbulent Flows", AIAA Paper AIAA-78-257.

[12] Baldwin B.S. and Barth T.J. (1991) "A One-Equation Turbulence Transport Model for High Reynolds Number Wall-Bounded Flows". AIAA Paper 91-0610.

[13] Beam R.M. and Warming R.F. (1976) "An Implicit Finite-Difference Algorithm for Hyperbolic Systems in Conservation-Law Form", *Journal of Computational Physics*, Vol. 22, p. 87.

[14] Beam R.M. and Warming R.F. (1978) "An Implicit Factored Scheme for the Compressible Navier-Stokes Equations", *AIAA Journal*, Vol. 16, No. 4, pp. 393-402.

[15] Bell D. and He L. (2000) "Three-Dimensional Unsteady Flow for an Oscillating Turbine Blades, and the Influence of Tip Leakage", *Journal of Turbomachinery*, Vol. 122, No. 1.

[16] Bindon J. R. (1973) "Stability and Convergence of Streamline Curvature Flow Analysis Procedures", *Int. Journal for Numerical Methods in Engineering*, Vol. 7, pp. 69-83.

[17] Bosman C. and El-Shaarawi M.A.I. (1976) "Quasi-3-Dimensional Numerical Solution of Flow in Turbomachineries", ASME paper 76-FE-23.

[18] Bosman C. and Highton J. (1979) "A Calculation Procedure for Three-Dimensional, Time-Dependent, Inviscid, Compressible Flow Through Turbomachine Blades of Any Geometry", *Journal of Mechanical Engineering Engineering Science*, Vol. 21, p.39.

[19] Botte V. (1999) "A Robust and Accurate Navier-Stokes Algorithm for Three-Dimensional Applications Adopting Arbitrary Modelling of the Reynolds Stresses", PhD Thesis, Cranfield University.

[20] Boyle R.J. and Giel P.W. (1995) "Three-Dimensional Navier Stokes Heat Transfer Prediction for Turbine Blade Rows", *J. Propulsion and Power*, Vol. 11, No. 6, pp 1179-1186.

[21] Bradshaw P., Ferriss D.H. and Atwell N.P. (1967) "Calculation of Boundary Layer Development Using the Turbulenct Energy Equation", *Journal of Fluid Mechanics*, Vol. 28, Part 3, pp. 593-616.

[22] Briley W.R. and McDonald H. (1975) "Solution of the Three-Dimensional Compressible Navier-Stokes Equations By An Implicit Techniques". *Proceedings 4th International Conference on Numerical Methods In Fluid Dynamics*, Boulder, Springer-Verlag, p. 105.

[23] Briley W.R. and McDonald H. (1976) "Solution of the Multidimensional Compressible Navier-Stokes Equations by a Generalized Implicit Method", *Journal of Computational Physics*, Vol. 24, p. 372.

[24] Busby J., Sondak D., Stauback B. and Dasvis R. (1999) "Deterministic Stress Modelling of Hot Gas Segregation in a Turbine", ASME Paper 99-GT-76.

[25] Calvert W.J. and Smith D.J.L. (1976) "A Digital Computer Program for the Subsonic Flow Past Turbomachine blades Using a Matrix Method", ARC R & M. 3838.

[26] Cambier L., Escande B. and Veuillot J.P. (1986) "Calcul d'ecoulement internes a grand nombre de Reynold par resolution numerique des equations de Navier Stokes". AGARD CP 401.

[27] Campobasso M.S., Mattheiss A., Wenger U., Arnone A. and Boncinelli P. (1999) "Complementary Use of CFD and Experimental Measurements to Assess the Impact of Shrouded and Cantilevered Stator in Axial Compressors", ASME Paper 99-GT-208.

[28] Caretto L.S., Gosman A.D., Patankar S.V. and Spalding D.B.(1972) "Two Calculation Procedures for Steady Three-Dimensional Flows with Recirculation", Proceedings of the Third International Conference on Numerical Methods in Fluid Dynamics, Springer-Veriag, New York.

[29] Celestina M.L., Mulac R.A. and Adamczyk J.J. (1986) "A Numerical Simulation of the Inviscid Flow Through a Counterrotating Propeller", *Journal of Turbomachinery*, Vol. 108, pp. 187-193.

[30] Chen J.P., Celestina M.L. and Adamczyk J.J. (1994) "A New Procedure for Simulating Unsteady Flows Through Turbomachinery Blade Passages", ASME Paper 94-GT-151.

[31] Chen S.H. and Prueger G.H. (1993) "Multistage Turbomachinery Flow Solution Using Three-Dimensional Implicit Euler Method", AIAA paper, AIAA-93-2382.

[32] Chima R.V. (1998) "Calculation of Multistage Turbomachinery Using Steady Characteristic Boundary Conditions", AIAA-98-0968.

[33] Chorin A.J. (1967) "A Numerical Method for Solving Incompressible Viscous Flow Problems", *Journal of Computational Physics*, Vol. 2, pp. 12-26.

[34] Chorin A.J. (1968) "Numerical Solution of the Navier-Stokes Equations", *Mathematics of Computation*, Vol. 22, pp. 745-762.

[35] Darwish M.S. (1993) "A New High-Resolution Scheme Based on the Normalized Variable Formulation", *Numerical Heat Transfer*, Part B, Vol. 24, pp. 353-371.

[36] Davis R.L., Shang T., Butean J. and Ni.R.H. (1996) "Prediction of 3-D Unsteady Flow in Multi-Stage Turbomachinery Using Implicit Dual Time-Step Approach", AIAA paper, AIAA-96-2565.

[37] Davis W.R. and Millar D.A.J. (1972) "A Discussion of the Marsh Matrix Technique Applied to Fluid Flow Problems", *Canadian Aeronautics and Space Journal*.Vol. 5, p. 64.

[38] Davis W.R. and Millar D.A.J. (1973) "Axial Flow Compressor Analysis Using a Matrix Method", Carleton University Report MEA73-1.

[39] Dawes W.N. (1986) "A Numerical Analysis of Three-Dimensional Viscous Flow in a Transonic Compressor Rotor and Comparison with Experimental Data", ASME Paper 86-GT-16.

[40] Dawes W.N. (1991) "The Development of a Solution Adaptive 3D Navier-Stokes Solver for Turbomachinery", AIAA 91-2469.

[41] Dawes W.N. (1992) "Toward Improved Throughflow Capability:The Use of Three-Dimensional Viscous Flow Solvers in a Multistage Environment", *Journal of Turbomachinery*, Vol. 114, pp. 8-17.

[42] Demeulenaere A. and Van den Braembussche R. (1996) "Three Dimensional Inverse Design Method for Turbomachinery Blading Design", ASME Paper 96-GT-39.

[43] Denton J.D. (1975) "A Time Marching Method for Two- and Three-Dimensional Blade-to-Blade Flow", Aeronautical Research Council R&M 3775.

[44] Denton J.D. (1976) "Extension of the Finite Area Time Marching to Three Dimensions", *VKI Lecture Series*, Vol. 84.

[45] Denton J.D. (1982) "An Improved Time-Marching Method for Turbomachinery Flow Calculation", ASME Paper 82-GT-239.

[46] Denton J.D. (1985) "Calculation of Three Dimensional Flow Through any Type of Turbomachine", AGARD Lecture Series 140.

[47] Denton J.D. (1992) "The Calculation of Three-Dimensional Viscous Flow Through Multistage Turbomachineries", *Journal of Turbomachinery*, Vol. 114, pp. 18-26.

[48] Denton J.D. (1993) "Loss Mechanism in Turbomachines", *Journal of Turbomachinery*, Vol. 115, No. 4, pp. 621-656.

[49] Denton J.D. and DawesW.N. (1998) "CFD for Turbomachinery Design" *The Successful Exploitation of CFD in Turbomachinery Design*, IMechE Seminar, London. 19 March 1998.

[50] Denton J.D. and Singh U.K. (1979) "Time Marching Methods for Turbomachinery Flow Calculation. Part I Basic Principles, and Part II Three-Dimensional Flows", *VKI Lecture Series*, Application of numerical methods to flow calculations in turbomachines, 1979-7.

[51] Dorney D.J., Davis R.L., Edwards D.E. and Madavan N.K. (1990) "Unsteady Analysis of Hot Streak Migration in a Turbine Stage", AIAA Paper 90-2354.

[52] Ecer A. and Akay H.U. (1981) "Solution of Steady Euler Equations for Flows Using a Variational Finite Element Formulation", Open Forum,AIAA 5th Computational Fluid Dynamics Conference,Palo Alto.

[53] Emmons H.W. (1954) "Shear Flow Turbulence", Proceedings of the 2nd US Congress of Applied Mechanics, ASME.

[54] Falchetti F. (1992) "Advanced CFD Simulation and Testing of Compressor Blading in the Multistage Environment", AIAA paper, AIAA-92-3040.

[55] Farn C.L. and Whirlow D.K. (1977) "Application of Time-Dependent Finite Volume Method to Transonic Flow in Large Turbines", *Transonic Flow Problems in Turbomachinery*, Washington, D. C., Hemisphere Publ. Corp. pp. 208-227.

[56] Faux I.D. and Pratt M.J.(1979) "Computational Geometry for Design and Manufacture", *Series: Mathematics and its Applications*, Ellis Horwood Publishers.

[57] Fenain M. (1977) "Méthodes de Relaxation Pour la Rásolution d'équations elliptiques dans les Domaines de Frontiéres Quelconques. Applications au Calcul d'écoulements Subscritiques", *J. de Mécanique Appliquée*, Vol. 1, pp. 27-67.

[58] Gallimore S.J. (1998) "Axial Flow Compressor Design", The Successful Exploitation of CFD in Turbomachinery Design, IMechE, HQ, London.

[59] Gaskell P.H. and Lau A.K.C. (1988) "Curvature-Compensated Convective Transport: SMART, a New Boundedness-Preserving Transport Algorithm", *Int. J. Num. Methods in Fluids*, Vol. 8, pp 617.

[60] Giannakoglou K.C. and Politis E.S. (1995) "A Segregated Implicit Solution Algorithm for 2D and 3D Laminar Incompressible Flows", *International Journal for Numerical Methods in Fluids*, Vol. 21, pp. 1067-1086.

[61] Giles M.B. (1990) "Stator/Rotor Interaction in a Transonic Turbine", *AIAA Journal of Propusion and Power*, Vol. 6, p. 621.

[62] Giles M. B. and Drela M. (1987) "Two Dimensional Transonic Aerodynamic Design Method", *AIAA Journal*, Vol. 25, No. 9.

[63] Glushko G. (1965) "Turbulent Boundary Layer on a Flat Plate in a Incompressible Fluid". Izvestia Academy Nauk SSSR Mekh., No. 4, p. 13.

[64] Gundy-Burlet K.L., Rai M.M. and Dring R.P. (1989) "Two-Dimensional Computations of Multistage Compressor Flows Using a Zonal Approach", AIAA Paper 89-2452.

[65] Gundy-Burlet K.L., Rai M.M., Stauter R.C. and Dring R.P. (1991) "Temporally and Spatially Resolved Flow in a Two-Stage Axial Compressor, Part 2 - Computational Assessment", *Journal of Turbomachinery*, Vol. 113, No. 2, pp. 227-232.

[66] Gundy-Burlet K.L. (1992) "Navier-Stokes Simulation of Multistage Turbomachinery Flow", *Computing Systems in Engineering*, Vol. 3, No. 1-4, pp. 231-240.

[67] Gundy-Burlet K.L., Rai M.M. and Madavan N.K. (1993) "Unsteady, Three-Dimensional Navier-Stokes Simulation of Multistage Turbomachinery Flows", AIAA paper, AIAA-93-1979.

[68] Hafez M., South J. and Murman E. (1979) "Artificial Compressibility Methods for Numerical Solution of Transonic Full Potential Equations", *AIAA Journal*, Vol. 17, p. 838.

[69] Hafez M. and Lovell D. (1981) "Numerical Solution of Transonic Stream Function Equation", AIAA Paper, AIAA-81-1017.

[70] Hah C. (1984) "A Navier-Stokes Analysis of 3D Turbulent Flows Inside Turbine Blade Rows", *ASME Journal Eng. Power*, Vol. 106, pp. 421-429.

[71] Hah C. (1987) "Numerical Solution of Three-Dimensional Flows for Modern Gas Turbine Components", ASME Paper 87-GT-84.

[72] Hall E. J. (1997) "Aerodynamic Modelling of Multistage Compressor Flowfield - Part 1: Analysis of Rotor/Stator/Rotor Aerodynamic Interaction", ASME Paper 97-GT-344.

[73] Hall E.J. (1997) "Aerodynamic Modelling of Multistage Compressor Flowfield - Part 2: Modelling Deterministic Stresses", ASME Paper 97-GT-345.

[74] Hamrick J.T., Ambrose G., and Walter M.O. (1950) "Method of Analysis for Compressible Flow Through Mixed-Flow Centrifugal Impellers of Arbitrary Design", NACA Report 1082.

[75] Hayase T., Humphrey J.A.C. and Greif R. (1992) "A Consistently Formulated QUICK Scheme for Fast and Stable Convergence Using Finite-Volume Iterative Calculation Procedure", *Journal of Computational Physics*, Vol. 98, pp. 108-118.

[76] He L. (2000) "3D Navier-Stokes Analysis of Rotor-Stator Interation in Axial Flow Turbines", Proc. IMech.E, Part A, *Journal of Power and Energy*, Vol.214.

[77] Heideggar N.J., Hall E.J. and Delaney R.A. (1996) "Parameterized Study of High-Speed Compressor Seal Cavity Flow", AIAA-96-2807.

[78] Hinze J.O. (1975) "Turbulence", New York: McGraw-HIll.

[79] Hirsch C. (1988) "Numerical Computation of Internal and External Flows. Volume 1 Fundamentals of Numerical Discretization", John Wiley & Sons Ltd.

[80] Hirsch C. (1994) "CFD Modelling and Validation for Turbomachinery Flows", AGARD Lecture Series on "Turbomachinery Design Using CFD".

[81] Hirsch C. and Denton J.D. (1981) "Through-Flow Calculation in Axial Turbomachineries", AGARD-AR-175

[82] Hirsch C. and Warzee G. (1976) "A Finite Element Method for Through-Flow Calculation in Turbomachines", ASME Paper 76-GT-12.

[83] Hirsch C. and Warzee G. (1979) "An Integrated Quasi-3-Dimensional Finite Element Calculation Program for Turbomachinery Flows", ASME *Journal of Engineering for Power*, Vol. 101, p.141.

[84] Hodson H.P. and Dawes W.N. (1998) "On the Interaction of Measured Profile Losses in Unsteady Wake-Turbine Blade Interaction Studies", *Journal of Turbomachinery*, Vol. 120, p. 276.

[85] Hoffmann K.A. and Chiang S.T. (1993), "Computational Fluid Dynamics for Engineers–Volume I", A publication of Engineering Education System, Wichita, Kansas, USA.

[86] Hoffmann K.A. and Chiang S.T. (1993), "Computational Fluid Dynamics for Engineers–Volume II", A publication of Engineering Education System, Wichita, Kansas, USA.

[87] Howard M.A. and Gallimore S.J. (1993) "Viscous Throughflow Modelling for Multi-Stage Compressor Design", ASME *Journal of Turbomachinery*, Vol. 115, p. 296.

[88] Howard M.A., Ivey P.C., Barton J.P. and Young K.F. (1994) "Endwall Effects at Two Tip-Clearances in a Multistage Axial Flow Compressor with Controlled Diffusion Blading", *Journal of Turbomachinery*, Vol. 116, No. 4, pp. 269-289.

[89] Howell A.R., and Calvert W.J. (1978), "A New Stage Stacking Technique for Axial-Flow Compressor Performance Prediction", *Journal of Engineering for Power*, Transactions of ASME Vol. 100, pp. 698-703.

[90] Issa R.I. (1982) "Solution of the Implicitly Discretised Fluid Flow Equations by Operator-Splitting", Fluids Section Report FS/82/15, Mech. Eng. Dept., Imperial College, London.

[91] Ivanov M.Y. and Kimasov Y.I. (1978) "Numerical Solution of the Problem of Determining the Average, Axisymmetric Flow of an Ideal Gas Through Turbomachine Stages", *Fluid Mechanics - Soviet Research*, Vol. 7, No. 4, pp. 143-152.

[92] Jameson A. (1974) "Iterative Solution of Transonic Flows Over Airfoils and Wings Including Flows at Mach 1", *Communications of Pure and Applied Math*, Vol. 27, pp. 283-304.

[93] Jameson A., Schmidt W. and Turkel E. (1981) "Numerical Solution of the Euler Equations by Finite Volume Methods Using Runge-Kutta Time Stepping Schemes", AIAA Paper 81-1259.

[94] Jennions I.K. and Turner M.J. (1992) "Three-Dimensional Navier-Stokes Computations of Transonic Fan Flow Using an Explicit Flow Solver and an Implicit $k - \epsilon$ Solver", ASME 92-GT-309.

[95] Johnson R.W. and Adamczyk J.J. (1989) "Kinetic Energy Equations for the Average-Passage Equation System", *Journal of Propulsion*, Vol. 2, pp. 252-254.

[96] Katsanis T. (1968) "Computer Program for Calculating Velocities and Streamlines on a Blade to Blade Streamsurface of Turbomachines", NASA TN D 4525.

[97] Katsanis T. (1969) "FORTRAN Program for Calculating Transonic Velocities on a Blade-to-Blade Stream Surface of a Turbomachine", NASA TN D-5427.

[98] Katsanis T. and McNally W.D. (1974) "Quasi-3-Dimensional Flow Solution by Meridional Plane Analysis", SAE Paper 740850.

[99] Katsanis T. and McNally W.D. (1977) "Revised FORTRAN Program for Calculating Velocities and Streamlines on the Hub-Shroud Midchannel Stream

Surface of an Axial, Radial,or Mixed-Flow Turbomachine or Annular Duct, I-User's Manual", NASA TN D-8430.

[100] Kirtley K. and Lakshminaarayana B. (1988) "Computation of Three Dimensional Turbulent Flow Using a Coupled Parabolic Marching Method", ASME *Journal of Turbomachinery*, Vol. 110, p. 549.

[101] Kirtley K.R., Turner M.G. and Saeidi S. (1999) "An Average Passage Closure Model for General Meshes", ASME Paper 99-GT-77.

[102] Krimerman Y. and Adler D. (1976) "Calculation of the Blade to Blade Compressible Flow Field in Turbo Impellers Using the Finite Element Method", Fac. Mech. Eng. Technion, Israel Inst. of Technology, Haifa.

[103] Lacor C. and Hirsch C. (1982) "Rotational Flow Calculation In Three-Dimensional Blade Passage", ASME Paper 82-GT-316.

[104] Lakshminarayana B. (1991) "An Assessment of Computational Fluid Dynamic Techniques in the Analysis and Design of Turbomachinery—The 1990 Freemen Scholar Lecture", *Journal of Fluids Engineering*, Vol. 113, pp. 315-352.

[105] Lapworth B.L. (1987) "Three Dimensional Elliptic Compressor for Viscous Turbomachinery Flows", PhD Thesis, Cranfield Institute of Technology.

[106] Launder B.E. and Spalding D.B. (1974) "The Numerical Computation of Turbulent Flows", *Computer Methods in Applied Mechanics and Engineering*, Vol. 3, pp. 269-289.

[107] Lawaczeck O. "Verfahren zur Ermittlung der Asbtrömgrossen Transsonischer Turbinegitter", AVA Göttingen Bericht 68 A 62.

[108] Lax P.D. and Wendroff B. (1964) "Difference Schemes for Hyperbolic Equations with High Order Accuracy", *Comm. Pure App. Math*, Vol. 17, pp.381-398.

[109] LeJambre C.R., Zacharias R.M., Biederman B.P., Gleixner A.J. and Yetka C.J. (1995) "Development and Application of a Multistage Navier-Stokes Flow Solver. Part II: Application to a High Pressure Compressor Design", ASME paper, 95-GT-343.

[110] Leonard B.P. (1979) "A Stable and Accurate Convective Modelling Procedure Based on Quadratic Upstream Interpolation", *Comp. Meth. Appl. Mech. Engg.*, Vol. 19, pp. 59-98.

[111] Leonard B.P. (1988) "Universal Limiter for Transient Interpolation Modelling of the Advective Transport Equation: The Ultimate Conservative Difference Scheme", NASA TM-100916 (ICOMP 88-11).

[112] Leonard B.P. and Mokhtari S. (1990) "Beyond First-Order Upwinding: the ULTRA-SHARP Alternative for Non-Oscillatory Steady-State Simulation of Convection", *Int. J. Num. Methods in Engrg.*, Vol. 30, pp 729.

[113] Li Y.G., Tourlidakis A. and Elder R.L. (1999) "Three-Dimensional Performance Prediction of Multistage Axial Flow Compressors With a Repeating Stage Model", ASME TURBO EXPO'99, ASME Paper 99-GT-290, Indianapolis, USA, June 1999.

[114] Li Y.G., Tourlidakis A. and Elder R.L. (1999) "Three-Dimensional Viscous Flow Analysis of Multistage Axial Flow Compressors", The IVX International Symposium of Air Breathing Engines, ISABE 99-7064, Florence, Italy, September 1999.

[115] Lymberopoulos N. Giannakoglou K., Nikolaou I., Papailiou K.D., Tourlidakis A. and Elder R.L. (1993) "Modelling of Tip Clearance Flows Through an Improved 3-D Pressure Correction Navier-Stokes Solver", ASME paper, 93-GT-374.

[116] MacCormack R.W. (1969) "The Effect of Viscosity in Hypervelocity Impact Catering", AIAA 69-345.

[117] Magnus R. and Yoshihara H. (1972) "Steady Inviscid Transonic Flow Over Planar Airfoils – A Research for Simplified Procedure", NACA CR 2186.

[118] Magnus R. and Yoshihara H. (1970) "Inviscid Transonic Flow Over Airfoils", *AIAA Journal*, Vol. 8, No. 2, pp. 2157-2162.

[119] Majumdar S. (1988) "Role of Underrelaxation in Momentum Interpolation for Calculation of Flow with Nonstaggered Grids", *Numerical Heat Transfer*, Vol. 13, pp. 125-132.

[120] Marsh H (1968) "A Digital Computer Program for the Through-Flow Fluid Mechanics in an Arbitrary Turbomachine Using a Matrix Method", Aeronautical Research Council R&M 3509.

[121] Matuso Y. (1991) "Computations of Three-Dimensional Viscous Flows in Turbomachinery Casades", AIAA 91-2237.

[122] McDonald P.W. (1971) "The Computation of Transonic Flow Through Two-Dimensional Gas Turbine Cascades", ASME Paper 71-GT-89.

[123] McNally W.D. and Sockol P.M. (1985) "REVIEW-Computational Methods for Internal Flows With Emphasis on Turbomachinery", *Transaction of ASME, Journal of Fluids Engineering*, Vol. 107, pp. 6-22.

[124] Moore J. and Moore J.G. (1979) "A calculation Procedure for 3D Viscous Compressible Duct Flow. Part 1 & 2", *ASME Journal Fluid Eng.*, Vol. 101.

[125] Morice P. (1978) "Une Méthode Numérique Basée Sur Les Principes Variationnels Pour Des Écoulements Avec Frontiéres Libres", ONERA TP 1978-40.

[126] Mulac R.A. and Adamczyk J.J. (1992) "The Numerical Simulation of a High-Speed Axial Flow Compressor", *Journal of Turbomachinery*, Vol. 114, pp. 517-527.

[127] Murman E.M. and Cole J.D. (1971) "Calculation of Plane,Steady Transonic Flows", *AIAA Journal*, Vol. 9, p. 114.

[128] Nallasamy M. (1987) "Turbulence Models and Their Applications to the Prediction of Internal Flows: A Revies", *Computers and Fluids*, Vol. 15, No. 2, pp. 151-194.

[129] Nee V.W. and Kovasznay L.S.G. (1968) "The Calculation of the Incompressible Turbulent Boundary Layer by a Simple Theory", *Physics of Fluids*, Vol. 12, p. 473.

[130] Ni R.H. (1981) "A Multiple Grid Scheme for Solving the Euler Equations", AIAA Paper 81-1025.

[131] Ni R.H. (1987) "Flow Simulation in Multistage Turbine", presented at the NASA Marshall Space Flight and Computational Fluid Dynamics Workshop.

[132] Nozaki O., Kikuchi K., Nishizawa T. and Mastsuo Y. (1999) "Unsteady Three-Dimensional Viscous Flow Computations of Multiple-Blade-Row Interactions", 14th International Symposium of Air Breathing Engines, Florence, Italy, September 1999.

[133] Orkwis P.D., Turner M.G. and Barter J.W. (1999) "Deterministic Stress Source Terms for Turbine Hot Streak Applications Derived from Linear Unsteady Solutions", 14th International Symposium of Air Breathing Engines (ISABE), Florence, Italy, September 1999.

[134] Osher S. and Salomon F. (1982) "Upwind Scheme for Hyperbolic Systems of Conservation Laws", *Mathematics of Computation*, Vol. 38, p. 339.

[135] Patankar S.V. (1980), "Numerical Heat Transfer and Fluid Flow", McGraw-Hill, New York.

[136] Patankar S.V. and Spalding D.B. (1972) "A Calculation Procedure for Heat, Mass and Momentum Transfer in Three-Dimensional Parabolic Flows", *International Journal of Heat and Mass Transfer*,Vol. 15, pp. 1787-1806.

[137] Perot J.B. and Moin P. (1995) "Shear-Free Turbulent Boundary Layers. Part 2. New Concept for Reynolds Stress Transport Equation Modelling of Inhomogeous Flows", *J. Fluid Mech.*, Vol.295, pp.229-245.

[138] Perot J.B. (1997) "A New Approach to Turbulence Modeling", SBIR Phase I Final Report", Aquasions, Inc.

[139] Politis E.S. and Giannakoglou K.C. (1997) "An Elliptic Implicit Solution Algorithm", Private Communication.

[140] Politis E.S., Giannakoglou K.C. and Papailiou K.D. (1995) "A Successive Implicit Method for Incompressible Flow Calculation in Three-Dimensional Ducts and Cascades", In: ISABE–International Symposium on Air Breathing Engines, 12th, Melbourne, Australia, Proceedings, Vol. 1, pp. 612-620.

[141] Politis E.S., Giannakoglou K.C. and Papailiou K.D. (1997) "Axial Compressor Stage Analysis Through a Multi-Block 3D Navier-Stokes Solution Method", ASME paper, 97-GT-93 .

[142] Prandtl L. (1925) "Bericht uber Untersuchungen zur ausgebilteten Turbulenz", ZAMM Vol.5, No.2

[143] Prandtl L. (1945) "Über ein neues Formelsystem für die ausgebildete Turbulenz", Nacr. Akad. Wiss. Göttingen, Math-Phys. Kl. 1945, pp. 6-19.

[144] Prato J., Lakshminarayana B. and Suryavamshi N. (1998) "Steady and Unsteady Three-Dimensional Flow Field Downstream of an Embedded Stator in a Multistage Axial Flow Compressor - Part 1: Unsteady Velocity Field", ASME Paper 98-GT-521.

[145] Rai M.M. (1987) "Unsteady Three-Dimensional Simulation of Turbine Rotor-Stator Interaction", AIAA Paper 87-2058.

[146] Rai M.M. and Dring R.P. (1987) "Navier-Stokes Analysis of the Redistribution of INlet Temperature Distribution in a Turbine", AIAA Paper 87-2146.

[147] Rhie C.M. and Chow W.L. (1983) "Numerical Study of the Turbulent Flows Past an Airfoil With Trailing Edge Separation", *AIAA Journal*, Vol. 21, pp. 1525-1532.

[148] Rhie C. M., Gleixner A. J., Spear D.A., Fischbery C.J. and Zacharias R.M. (1995) "Development and Application of a Multistage Navier-Stokes Solver. Part I: Multistage Modelling Using Bodyforce and Deterministic Stress", ASME paper, 95-GT-342.

[149] Rodi W. (1976) "A New Algebraic Relation for Calculating Reynolds Stress", *ZAMM*, Vol. 56, pp. 219.

[150] Saad Y. and Schultz M.H. (1986) "GMRES: A Generalised Minimal Residual Algorithm for Solving Non-Symmetric Linear Systems", *SIAM J. Sci. Comput.*, Vol. 7, pp. 856-869.

[151] Schiff L.B. and Steger J.L. (1980) "Numerical Simulation of Steady Supersonic Viscous Flow", *AIAA Journal*, Vol. 18, No. 12, pp. 1421-1430.

[152] Schlichting H. (1955) "Berechnung Der Reibungslosen Incompressiblen Ströming *für* Ein Vorgegebenes Ebenes Schaufelgitter", VKI Forschungsheft 447-B 21.

[153] Schneider G.E. and Zedan M. (1981) "A Modified Strongly Implicit Procedure for the Numerical Solution of Field Problems", *Numerical Heat Transfer*, Vol. 4, pp. 1-19.

[154] Sciubba E. (1997) "Calculating Entropy with CFD", *Mechanical Engineering*, Vol. 119, No. 10.

[155] Scott R.M., Childs P.R.N., Hills N.J. and Millward J.A. (2000) "Radial Inflow into the Downstream Cavity of a Compressor Stator Well", ASME Paper 2000-GT-0507.

[156] Shapiro A. (1953) "The Dynamics and Thermodynamics of Compressible Fluid Flow", The Ronald Press Company, New York.

[157] Sharma O.P., Pickett G.F. and Ni R.H. (1992) "Assessment of Unsteady Flows in Turbines", *ASME Journal of Turbomachinery*, Vol. 114.

[158] Smith D.J.L. and Frost D.H. (1970) "Calculation of the Flow Past Turbomachine Blades", *Proceedings of the Institution of Mechanical Engineers*, Vol. 184, p. 72.

[159] Smith D.J.L. (1974) "Computer Solutions of Wu's Equations for the Compressible Flow Through Turbomachines", Fluid Mechanics, Acoustics, and Design of Turbomachinery, Part I, NASA SP-304.

[160] Spalding D.B. (1980) "A Mathematical Modelling of Fluid Dynamics, Heat Transfer and Mean Transfer Processes", Imperial College (London) Report hts/8011.

[161] Sondak D.L., Dorney D.J. and Davis R.L. (1996) "Modelling Turbomachinery Unsteadiness with Lumped Deterministic Stresses", ASME Paper 96-GT-2570.

[162] Sondak D.L. and Pletcher R.H. (1995) "Application of Wall Function to Generalized Nonorthogonal Curvilinear Coordinate Systems", *AIAA Journal*, Vol. 33, No. 1, pp. 33-41.

[163] Spalart P.R. and Allmaras S.R. (1992) "A One-Equation Turbulence Model for Aerodynamic Flows", AIAA Paper 92-0439.

[164] "Status of *LSRC* Measurements First Results With RBB Blading. Part A: Meeting on IMTAC3A Programme at BMW Rolls Royce", Dahlewitz, July 1995.

[165] Steger J.L. (1978) "Implicit Finite-Difference Simulation of Flow About Arbitrary Two-Dimensional Geometries", *AIAA Journal*, Vol. 16, p. 679.

[166] Steger J.L., Pulliam T.H. and Chima R.V. (1980) "An Implicit Finite Difference Code for Inviscid and Viscous Cascade Flow", AIAA Paper 80-1428.

[167] Stone H.L. (1968) "Iterative Solution of Implicit Approximations of Multidimensional Partial Differential Equations", SIAM *Journal of Numerical Analysis*, Vol. 5, pp. 530-558.

[168] Suryavamshi N., Lakshminarayana B. and Prato J. (1998) "Steady and Unsteady Three-Dimensional Flow Field Downstream of an Embedded Stator in a Multistage Axial Flow Compressor - Part 3: Deterministic Stress and Heat-Flux Distribution and Average-Passage Equation System", ASME Paper 98-GT-523.

[169] Swoboda M., Ivey P.C, Wenger U. and Gummer V. (1998) "An Experimental Examination of Cantilevered and Shrouded Stator in a Multistage Axial Compressor". ASME Paper, 98-GT-282, 1998.

[170] Swoboda M., Wenger U., and Gummer V. (1996) "BRITE EURAM (Project AC3A) Blading Desigh Report for the 4-Stage CU (Cranfield University) Low Speed Research Compressor (LSRC)". Brite Euram Report 11-BRR-02. 1996.

[171] "TASKflow3D Version 2.4: Theory Documentation", Advanced Scientific Computing Ltd., 1995.

[172] "Technical Report". E-TR37496-(IR)ISS00, 1996.

[173] Tourlidakis A. (1992). "Numerical Modelling of Viscous Turbomachinery Flows with a Pressure Correction Method", PhD Thesis, Cranfield Institute of Technology.

[174] Tourlidakis A. and Elder R.L. (1991) "Computation of Three-Dimensional Viscous Turbulent Flows in Centrifugal Compressors With Tip Leakage", IMechE 1991, C423050.

[175] Traupel W. (1942) "Neue allgemeine theorie der mehrstufigen axialen turbomaschinen", Zurich, Leeman.

[176] Tsuei H.H. and Perot J.B. (2000) "Advanced Turbulence Model for Transitional and Rotational Flows in Turbomachinery", AIAA-2000-0134.

[177] Turner M.G., Vitt P.H., Topp D.A., Saeidi S., Hunter S.D., Dailey L.D. and Beach T.A. (1999) "Multistage Simulation of the GE90 Turbine", ASME Paper 99-GT-98.

[178] Van Doormaal J.P. and Raithby G.D. (1984) "Enhancements of the SIMPLE Method for Predicting Incompressible Fluid Flows", *Numerical Heat Transfer*, Vol. 7, No. 2, pp. 147-163.

[179] Vanka (1986) "Block Implicit Multigrid Calculation of the Two Dimensional Recirculating Flow", *Computer Methods in Applied Mechanics and Engineering*, Vol. 59, pp. 29-48.

[180] Versteeg H.K. and Malalasekera W. (1995) "An Introduction to Computational Fluid Dynamics–The Finite Volume Method", Longman Science & Technical.

[181] Veuillot J.P. and Viviand H. (1979) "A Pseudo-Unsteady Method for the Computation of Transonic Potential Flows", *AIAA Journal*, Vol. 17.

[182] Viviand H. and Veuillot J.P. (1978) "Methods Pseudo-Instation-Naires Pour Le Calcul D'Ecoulements Transsoniques", ONERA Publication 1978-4, English Translation ESA.TT.561.

[183] Von Doorrmal J.P. and Raithby G.D. (1990) "Enhancement of the SIMPLE Method for Predicting Incompressible Fluid Flow", *Numerical Heat Transfer*, Vol. 67, p. 147.

[184] Weatherill N.P. (1990) "Numerical Grid Generation", Von Karman Institute for Fluid Dynamics 1990 Lecture Series.

[185] Whitfield D.L., Swafford T.W., Janus J.M., Mulac R.A. and Belk D.M. (1987) "Three-Dimensional Unsteady Euler Solution for Propfan and Counter-rotating Propfans in Transonic Flow", AIAA Paper 87-1197.

[186] Weatherill N.P. (1990) "Structured Grid Generation", Von Karmam Institute for Fluid Dynamics, 1990 Lecture Series.

[187] Whitehead D.S. and Newton S.G. (1985) "Finite Element Method for the Solution of 2D Transonic Flow in Cascade", *Int. J. for Numerical Method in Fluid*, Vol. 5, pp. 115-132.

[188] Wilcox D.C. (1994) "Turbulence Modeling for CFD", DCW Industries, Inc.

[189] Wilkinson D.M. (1970) "Stability, convergence and Accuracy of Two Dimensional Streamline curvature Methods Using Quasi Orthogonals", Thermodynamics and Fluid Mechanics Convertion 1970, Inst. Mech. Engrs.. London, Vol. II.

[190] Wu C.H. (1950), "A General Through-Flow Theory of Fluid with Subsonic or Supersonic Velocity in Turbomachines of Arbitrary Hub and Casing Shapes", NACA TN 2302.

[191] Wu C.H. (1952) "A General Theory of Three-Dimensional Flow in Subsonic and Supersonic Turbomachines of Axial-, Radial-, and Mixed-Flow Types", NACA TN 2604.

[192' Wu C.H. (1952) "A General Theory of Three-Dimensional Flow in Subsonic and Supersonic Turbomachinery of Axial, Radial and Mixed-Flow Types", NACA-TN-2407.

[193] Wu C.H. (1952) "Matrix and Relaxation Solutions that Determine Sobsonic Flow in an Axial-Flow Gas Turbine", NACA TN 2750.

[194] Wu C.H. (1952) "A General Theory of Three-Dimensional Flow in Subsonic and Supersonic Turbomachines of Axial-, Radial-, and Mixed-Flow Types", *Transactions of ASME*. Vol. 74. pp. 1363-1380.

[195] Wu C.H. (1953) "Subsonic Flow of Air Through a Single-Stage and a Seven-Stage Compressor". NACA TN 2961.

[196] Wu Chung-Hua. and Lincoln Wolfenstein. (1950) "Application of Radial-Equilibrium condition to Axial-Flow Compressor and Turbine Design", NACA Report 955.

[197] Yeuan J.J.. Liang T. and Hamed A. (1996) "A 3-D Navier-Stokes Solver for Turbomachinery Blade Rows", AIAA paper, AIAA-96-3308.

[198] Zhu J. and Rodi W. (1991) "A New Dipersion and Bounded Convection Scheme". *Computational Methods in Applied Mechanical Engineering*, Vol. 92, pp. 87-96.